

**EXPLORING MARTIAN AND LUGAR  
GEOCHEMISTRY THROUGH THE STUDY  
OF METEORITES, ANALOGS,  
LABORATORY SIMULATION, AND  
MISSION DATA ANALYSIS**

**PhD Thesis  
JENNIFER HUIDOBRO MARTIN  
2023**

eman ta zabal zazu



Universidad  
del País Vasco

Euskal Herriko  
Unibertsitatea



Universidad del País Vasco    Euskal Herriko Unibertsitatea

Department of Analytical Chemistry

**Exploring Martian and Lunar geochemistry through  
the study of meteorites, analogs, laboratory  
simulations, and analysis of mission data**

Dissertation presented for the international PhD degree

**Jennifer Huidobro Martin**

May 2023

Supervised by:

Juan Manuel Madariaga Mota

Julene Aramendia Gutiérrez



La presente tesis doctoral tiene como objeto el estudio de la geoquímica de Marte y de la Luna a través del análisis de diferentes muestras, como lo son los meteoritos, los análogos y las simulaciones de laboratorio. También se consideran datos de las actuales y pasadas misiones a la superficie de Marte. Con el fin de comprender el contenido de esta tesis, el capítulo introductorio se centra en hacer una revisión de todas las misiones que han aterrizado en Marte. Así como de indicar todos los instrumentos analíticos con los que estaban equipadas dichas naves para estudiar la geoquímica de la superficie del planeta. En total son 10 las naves que desde diferentes países han conseguido aterrizar en Marte. Aunque algunas no lograron cumplir con los objetivos propuestos, perdiéndose la conexión con Tierra antes de realizar su cometido, otras han conseguido enviar a Tierra resultados muy valiosos. Dichos resultados fueron obtenidos a través de instrumentos analíticos que viajaban a bordo de los “rovers” o “landers” de las misiones. Generalmente, estos instrumentos se pueden clasificar en técnicas elementales y moleculares. Por un lado, las técnicas elementales, como su nombre indica, son aquellas que tienen la capacidad de caracterizar, e incluso cuantificar, elementalmente la muestra objeto de estudio. La técnica elemental más pionera en estudiar la geoquímica del planeta rojo fue la espectroscopía de fluorescencia de rayos-X (XRF), la cual viajó a bordo de los landers Viking de la Nasa. Además de XRF, a lo largo de la historia de exploración de la superficie de Marte también se han empleado las siguientes técnicas elementales: espectroscopía de partículas alfa y rayos-X (APXS), electrodos selectivos de iones (ISE) y espectroscopía de ablación laser (LIBS). Por otro lado, han sido varias las técnicas moleculares en estudiar de forma *in situ* la geoquímica de Marte. Entre ellas destacan la cromatografía de gases acoplado a la espectroscopía de masas (GC-MS), el analizador de gases evolucionados térmicamente (TEGA), la espectroscopía Mössbauer (MBS), la difracción de rayos-X (XRD), la espectroscopía infrarroja (IR) y la espectroscopía Raman. Siendo esta última la técnica molecular más novedosa usada para la exploración espacial y en la que más se ha centrado esta tesis. Asimismo, estas técnicas, tanto las elementales como las moleculares, pueden diferenciarse entre destructivas y no destructivas. Cabe destacar que las técnicas no destructivas, como son XRF, la espectroscopía Raman y la IR, son los métodos más utilizadas en laboratorios científicos de estudios planetarios. Esto se debe a que las principales muestras del espacio estudiadas en la Tierra son los meteoritos, siendo muestras muy preciadas y de carácter único. Con el fin de preservarlas y conservarlas para futuros estudios, es crucial analizarlas mediante técnicas no destructivas.

Considerando esto, esta tesis ha realizado una caracterización completa de las diversas muestras citadas anteriormente mediante técnicas espectroscópicas no destructivas.

---

En lo que al estudio de la geoquímica marciana se refiere, en primer lugar, se desarrolló una metodología para la cuantificación del ratio Fe/Mg en olivinos, en función del desplazamiento de sus bandas Raman principales. Con el fin de evitar la desviación inducida por el uso de un determinado instrumento, en este trabajo se emplearon más de 60 referencias bibliográficas diferentes de espectros Raman de olivino adquiridos con diferentes instrumentos y de concentración Fe/Mg perfectamente conocida. A través de estos datos se pudieron desarrollar diferentes modelos de calibración para el cálculo del ratio Fe/Mg con un nivel de precisión elevado en comparación con los modelos existentes hasta el momento. Además, con el fin de corroborar la precisión de los modelos desarrollados, estos se validaron con muestras de concentración conocidas. Pudiéndose concluir que sólo dos de los tres modelos desarrollados fueron lo suficientemente precisos. Mediante el uso de estos dos modelos y de los espectros Raman de granos de olivinos, se calcularon los ratios de Fe/Mg tanto para diversos análogos marcianos como para rocas de Marte analizadas por el espectrómetro Raman del instrumento SuperCam (Mars2020).

Con estos modelos también se estudiaron los olivinos encontrados en dos muestras de meteoritos de Marte (LAR 12095 y RBT 04262). Estos meteoritos también fueron caracterizados a través de técnicas analíticas no destructivas, como lo son el XRF y la espectroscopía Raman. Gracias a estos estudios se pudieron identificar los minerales primarios (origen marciano), los secundarios marcianos (minerales formados a través de la alteración de los primarios en Marte), secundarios terrestres (minerales formados a través de la alteración de los primarios pero en la Tierra) y los de meteorización terrestre (aquellos que no son originales de Marte, sino de la Tierra). Teniendo clara esta clasificación, se pudieron estimar los diferentes procesos de alteración que tuvieron lugar para que los primarios se alteraran a secundarios, tanto en Marte como en la Tierra. En este sentido, se identificaron los siguientes procesos de alteración: alteraciones por altas presiones, por oxidación anaeróbica, por oxidación aeróbica y la alteración hidrotermal. Entre todos los minerales identificados en ambos meteoritos se encontraron varias fases de azufre, como  $S^{2-}$ ,  $S_8$  y  $S^{6+}$ . Los sulfuros y el azufre elemental fueron clasificados como minerales secundarios de Marte, mientras que el origen de los sulfatos fue más abstracto, pudiéndose tratar de minerales secundarios de Marte, de la Tierra o de meteorización terrestre. De tal forma, que uno de los aspectos más novedosos de este trabajo fue la propuesta de los diferentes procesos que pueden dar lugar a la formación de compuestos de azufre tanto en Marte como en la Tierra, obteniéndose así otras fases secundarias.

Considerando el interés científico suscitado en torno a la presencia de sulfatos en Marte, en este trabajo también se llevaron a cabo experimentos

---

de simulación en diferentes condiciones hidrotermales con el fin de recrear los procesos de formación y alteración de algunos sulfatos ya encontrados en Marte, como son el yeso y la anhidrita. Así como la formación de otros sulfatos que aún no se han encontrado pero que se esperan descubrir, como son la syngenite y la görgeyita.

En este sentido, se pudo comprobar que la syngenita y el yeso precipitaban fácilmente a temperatura ambiente (25°C). Sin embargo, la görgeyita requería condiciones hidrotermales para su formación (altas temperaturas). En cualquiera de los casos, la síntesis de estos tres sulfatos requería medio acuoso para su formación. En este sentido, las actuales y futuras misiones a Marte estudian y estudiarán lugares en donde hubo agua en el pasado. Esperando la aparición, de nuevo, de sulfatos.

De la misma forma, se simularon las respuestas de dichos sulfatos a condiciones extremas que podrían sufrir en la superficie marciana. Los procesos de alteración considerados fueron dos. Por un lado, se sometieron los sulfatos a altas y bajas temperaturas para conocer su respuesta espectroscópica a dichas condiciones. Por otro lado, se investigó la deshidratación del yeso a bajas presiones y bajas temperaturas. Gracias a los experimentos de temperatura, se pudo concluir que ni el yeso, ni la syngenita, ni la görgeyita se alteraban químicamente a bajas temperaturas. El cambio observado se basaba en una modificación de la cristalinidad en sus moléculas de hidratación. Sin embargo, cuando dichos minerales fueron sometidos a altas temperaturas, sus bandas Raman se desplazaban hasta que se daba un cambio de fase mineral. Una vez evaluado el efecto que tenían los cambios de temperatura en los espectros Raman de cada compuesto, se calcularon las ecuaciones de regresión de la banda Raman en función de la temperatura. Estos experimentos son cruciales como soporte a las actuales y futuras misiones espaciales que incorporen la espectroscopía Raman entre su equipamiento científico, ya que con ellos se podrá calcular la posición de las bandas Raman de estos sulfatos a una temperatura en concreto. A través del estudio de la deshidratación del yeso a bajas temperaturas y presiones, se pretendió dar respuesta a la coexistencia de las tres formas de hidratación del calcio, la dihidratada, la hemihidratada y la anhidra, correspondiendo al yeso, la bassanita y la anhidrita. Estos tres compuestos fueron detectados simultáneamente por el rover Curiosity. Gracias a este trabajo se pudo comprender que dicha coexistencia se debía a las condiciones variables de humedad y temperatura entre los veranos e inviernos de Marte. Los experimentos determinaron que a bajas temperaturas y presiones el yeso se podía deshidratar a bassanita y, posteriormente, a anhidrita.

Esta tesis doctoral aborda también diferentes escenarios que permiten detectar vida pasada o presente en la superficie marciana. Este hecho es

---

complicado debido a las actuales condiciones de Marte que incluyen una alta radiación ultravioleta, alta radiación de partículas ionizantes, etc. Tales condiciones dificultan la presencia de vida libre en Marte. De tal forma que la forma esperable de encontrar este tipo de señales biológicas es asociada a estructuras geológicas bioprotectoras, entendiéndose como bioprotector a aquellas estructuras o agentes que son capaces de hospedar bioseñales y protegerlas frente a las inhóspitas condiciones marcianas. Para poder estudiar los diferentes bioprotectores, primeramente, fue indispensable estudiar la geoquímica de Marte a través de los datos de misiones pasadas y actuales. Posteriormente se estudiaron dos de los posibles bioprotectores que se esperan encontrar en Marte. En primer lugar, se analizaron los suelos de Marte a través de datos elementales de misiones pasadas y actuales. Se prestó especial atención a aquellos suelos poseyentes de costra, ya que son regolitos compactados que podrían proteger bioseñales bajo la costra. Sin embargo, más estudios deben realizarse acerca la posible habitabilidad bajo las costras de Marte.

Seguidamente, se estudiaron diferentes especies de la familia de las esmectitas. Las esmectitas son filosilicatos dispuestos en láminas que tienen la capacidad de albergar iones y moléculas en las entrecapas. En este sentido, este trabajo se basó en comprender cómo puede introducirse una molécula orgánica de cadena larga en las entrecapas de dos esmectitas. Una muy común en Marte, la montmorillonita, y otra menos común, la hectorita. En este sentido, se hicieron varios experimentos para dopar con ácido laurico las entrecapas de dichas esmectitas. Los compuestos resultantes fueron analizados mediante XRD, microscopía de barrido acoplado a espectroscopía de dispersión de rayos-X (SEM/EDS) e IR. Tras dichos estudios se pudo comprobar que es más favorable la adsorción del ácido laurico a valores de pH bajos, condiciones que se dieron en Marte en el pasado.

Por otro lado, se estudió una muestra de oncolito del Salar Carachi Pampa de Argentina como posible bioprotector. Los oncolitos son un tipo de microbialito que se caracterizan por ser muestras sedimentarias que se forman como consecuencia de la acumulación de materiales carbonatados como productos de excreción de microorganismos. En Marte, estructuras parecidas a estas fueron observadas por el rover Curiosity pero no fueron analizadas en profundidad. Por este motivo, en este trabajo el oncolito fue analizado por varias técnicas analíticas que se encuentran a bordo de la actual misión Mars2020 y de la futura misión Rosalind Franklin: XRF, LIBS, Raman, IR y GC-MS. Combinando dichas técnicas se pudo hacer una caracterización completa y se puso de manifiesto la importancia de la ciencia colaborativa para obtener la máxima información posible.

Finalmente, se estudió la geoquímica de la Luna a través del meteorito Lunar NWA 11273. Dicho meteorito también fue estudiado a través de las

---

técnicas no destructivas espectroscopía Raman y XRF. A través de los minerales identificados y de igual forma que en el anterior caso de estudio de meteoritos marcianos, se pudieron clasificar los minerales en función de su origen y formación (minerales primarios, secundarios de la Luna, secundarios de la Tierra y de meteorización terrestre). Teniendo en cuenta la clasificación, se estimaron los diferentes procesos que los minerales primarios sufrieron para formar los secundarios. La mayoría de las fases secundarias identificadas fueron formadas a través de procesos de oxidación, los cuales también se esperan encontrar en el regolito lunar. Un ejemplo de estos minerales oxidados en el regolito lunar es la ilmenita. Este mineral ya fue previamente identificado en la Luna y su presencia es muy relevante ya que es un compuesto importante para la habitabilidad humana debido a que es capaz de absorber elementos volátiles como H, N, C y He, entre otros. El hecho de haberlo encontrado en el meteorito y que previamente se haya encontrado en la Luna marca una clara similitud entre ambos, lo cual hace pensar que se podrían utilizar los meteoritos lunares meteorizados tanto en la Luna como en la Tierra como caso de estudio para el futuro cultivo de plantas en la Luna. Del mismo modo, los minerales primarios identificados en el meteorito lunar NWA 11273 coincidieron con los ya identificados en el simulante de suelo basáltico lunar LZS-1. Este claro paralelismo entre el meteorito y el simulante ayudarán en un futuro a realizar, por un lado, experimentos de habitabilidad a gran escala utilizando el simulante y, por otro lado, experimentos a baja escala con el meteorito NWA 11273. De tal forma que, en este trabajo se propone como trabajo futuro detectar si en el simulante también se encuentran los minerales oxidados identificados previamente en el meteorito. También se llevarán a cabo pruebas oxidativas ácidas para detectar nuevas fases minerales y compuestos liberados en ambos materiales que puedan servir para una futura misión que considere la habitabilidad Lunar mediante el cultivo de plantas.

Con los trabajos llevados a cabo en esta tesis ha sido posible generar información sobre la geoquímica tanto marciana como lunar, lo cual sirve como soporte científico a las misiones actuales y futuras. Asimismo, se han podido comprobar las ventajas de la ciencia colaborativa, así como las técnicas analíticas más sensibles para la identificación de orgánicos. Esta tesis también ha contribuido a la propuesta de futuros experimentos para la búsqueda de recursos naturales lunares con el fin de permitir la habitabilidad a través del cultivo de plantas.

---

---

---

## Acknowledgements

---

This PhD Thesis has been developed thanks to the people, institutions and funding support, related below. First, Jennifer Huidobro Martin is grateful to the Basque Country Government for her pre-doctoral contract (January 2020 – May 2023) and to the University of the Basque Country for being her alma mater and allowing her to carry out this doctoral thesis. She would like to thank the Department of Analytical Chemistry and the IBeA Research Group for their constant support.

Several funding agencies and projects have provided samples and resources to afford the studies related to this PhD Thesis:

1. The *Raman On Mars* project: “Contribution of the Raman spectroscopy to the exploration of Mars and Martian Moons: ExoMars, Mars 2020 and MMX missions (RamOnMars)” (Grant No. PID2019-107442RB-C31), funded by the Spanish Agency for Research (through the Spanish Ministry of Science and Innovation, MICINN, and the European Regional Development Fund, FEDER).
2. The Excellence Research Groups program, funded by the Basque Country Government (Grants Nos. IT 1213/19 and IT 1446/22).
3. The Strategic Project “Terrestrial and Planetary Alteration Processes” (Grant No. UPV/EHU PES18/57), funded by the University of the Basque Country (UPV/EHU).
4. The Thematic Network SIGUE-Mars (Grant No. RED2018-102600-T), funded by the Spanish AEI/MICINN/FEDER, their member staff for the fruitful discussions and in particular to Dr. Daniel Carrizo from the Centro de Astrobiología (CAB, INTA-CSIC) for providing the oncoïd sample from the Atacama Desert.
5. The Johnson Space Center, NASA, for providing the LAR 12095 and RBT 04262 Martian meteorite samples, through its agreement with the University of the Basque Country (UPV/EHU)

Part of the analyses performed in this work were carried out in the General X-Ray Service of Rocks and Minerals, and in the General X-Ray Service of Molecules and Materials Unit from the Research General Services of the UPV/EHU (SGIKER). Specially, we would like to thanks Francisco Javier Sangüesa Aguerri and Aitor Larrañaga Varga.

Likewise, some of the activities developed in this PhD Thesis were performed in the laboratories of members of the Thematic Network SIGUE-Mars. In this sense, we would like to give special thanks to the CAB-INTA-CSIC, to the LaserLab Research Group of the University of Málaga (UMA), to the ERICA Research Group of the University of Valladolid (UVa) and to the Geoscience Institute (IGEEO, CSIC-UCM).

---

I would like to thank NASA, the Mars 2020 Project, the SuperCam, and specially to the PIs Dr. Roger Wiens and Dr. Sylvestre Maurice for inviting me to be a member of both the Mars 2020 and the SuperCam Science Teams. I would like to thank also ESA and the Rosalind Franklin mission to Mars for including me in the ExoMars Science Team (current Rosalind Franklin mission) through the PI of the RLS Science Team, Prof. Fernando Rull. This PhD Thesis is primarily focused on supporting these two and upcoming missions to Mars and the Moon.

Finally, I would like to acknowledge Prof. Elisabeth M. Hausrath and her entire research team for welcoming me to her laboratory in the Geoscience Department at the University of Las Vegas, Nevada (UNLV), USA, where I develop part of this thesis work.

Tras los agradecimientos más formales me gustaría resaltar la gran dedicación y apoyo que he tenido por parte de mis dos directores, Juanma y Julene.

Por un lado, tenemos a la directora joven, la chica de las ganas por cosas nuevas, la tenaz, la directora/compañera, con la que he reído y he llorado a la vez. Jul gracias por no soltarme de la mano en ningún momento y, sobretodo, gracias por entenderme en la montaña rusa de la ciencia. Tu apoyo y tu “hay relativizar” me ha ayudado a crecer personalmente, a ser valiente y a quererme un poco más. A ti, gracias por acogerme tan bien, por enseñarme mano a mano y, en definitiva, por ser mi hermana de la ciencia.

Y Juanma, ¿qué decir de ti? Mi padre de la ciencia. Eres el director que siempre quiere ir más allá con todo, al que nada le parece una locura y el que está convencido de nada se le pondrá en el camino. Creo que es más que evidente lo buen director que eres, solo hace falta ver que confiaste en una niña de 20 años y, tras 6 años, aquí estamos, defendiendo la tesis. Espero que estés orgulloso de los discípulos que estás dejando en este largo camino. Gracias por abrirme camino y guiarme en la investigación.

A los dos, gracias por confiar tanto en mí incluso cuando ni si quiera yo misma confiaba.

También tengo que agradecer esta tesis a la gente con la que he compartido laboratorio, tanto los que ya no están, como los que están. Os lo agradezco a todos, pero me gustaría hacer especial mención a dos grupos de personas que me han marcado un antes y un después en este camino. Por un lado, Patri, Imanol, Cris, Silvis, aunque ya no estéis cerca, os quiero dar las gracias ya que no he podido tener mejores compis de inicio de tesis. Me acogisteis como una igual, me ayudasteis a ubicarme y me habéis seguido ayudando hoy en día.

---

## Acknowledgements

---

Aunque me doctore, creo que seguiré mandándoos WhatsApps con dudas existenciales... No os vais a librar de mi tan fácilmente 😊.

Por otro lado, las chicas del actual labo: Ila, Ido y Reahitxu. Chicas, sois lo MÁS! Gracias por estar y gracias por aguantarme tanto, sobre todo en estos últimos duros meses. A partir de esta defensa prometo no lloriquear tanto, irme con vosotras a escalar, a Yoga de guiris o al monte, donde haga falta, siempre y cuando nos espere una caña al final! Las tres me parecéis mujeres super fuertes, super valientes, super resolutivas, buenas compañeras y muy buenas personas. En la ciencia o en otro campo, os llevo siempre conmigo ♥.

Seguimos con el team espacio. Gorka y Kepa, aunque no seáis mis directores más directos, estoy muy agradecida de vuestros comentarios y sugerencias. Siempre me han enriquecido mucho y estoy muy orgullosa de poder aprender de cada uno de vosotros. Gorka, gracias por tener siempre con una gracia, haces ver la luz al final del túnel. Y Kepa, gracias por velar tanto por tu gente. Para terminar, también tengo que agradecer el apoyo a la última incorporación al team, Iratxe.

I would like to thank all the people I met during my stay at UNLV for their support and help. It was the first time I went abroad on my own and you all made me feel at home. I thank you all, but specially to Theresa, Erika and the Spanish girls, I have brought back to Spain very good friendships. Thank you.

I would also like to thank the brilliant pictures that some Friends and colleagues lent me and that give a visual support to this thesis. Thanks to Erika Valdueza, Luis Santiago Gutiérrez and Didac Mesa Romeu.

En los agradecimientos no puede faltar la gente que me ha ayudado a desconectar, los que antes de empezar la tesis ya confiaban en que iba a salir adelante. Mis chicas sobredosis de moscato, galácticos, las WaveGirls, los amigos de Portu con las arrimadas como yo, mis parejas favoritas y mi gente de Villarcayo. No pongo nombres porque si no tengo que escribir otra tesis doctoral sobre todos vosotros. No sabéis lo increíble que es tener relaciones tan sanas y bonitas. Soy una privilegiada teniéndoo a todos. Gracias por nuestras cenas de los martes, los cafés e infusiones interminables, los jueves de cañas, los findes que no hay nada pero una simple cena lo arregla todo, las charangas, los viajes, las peñas y un largo etcétera. Con todos vosotros cualquier excusa es buena para brindar. Simplemente os doy las GRACIAS.

Gracias a ti también Asier, has confiado siempre en mí y has aguantado mis máximas alegrías y mis mayores caídas.

---

Para terminar, tengo que agradecer todo lo que soy a mi familia. Gracias papá, mamá y Miri por creer tanto en mí. Papá, mamá, me habéis enseñado que con sacrificio y ganas se puede llegar a cualquier sitio. Estoy orgullosa de la familia tan bonita que habéis construido y de lo que estáis consiguiendo conmigo y con mi hermana. No es fácil salir de un pueblo pequeño cuando nadie en la familia ha estudiado una carrera y hay un negocio familiar de por medio. En ese momento lo lógico y sencillo era ponernos a ayudaros y seguir con la empresa. Pero queríais un futuro mejor para nosotras. Nos animasteis a ir contra viento y marea para que pudiéramos formarnos. Os agradezco todo, pero sobretodo, gracias por darnos los valores tan buenos que tenemos. Miri, gracias por ser mi vía de escape y estoy super orgullosa de la buena persona que eres. He de reconocer que esta tesis no tendría estética sin la opinión crítica de mi hermana jeje. A Losi y Blanqui, gracias por ser al mismo tiempo mi refugio y mi diversión.

Esta tesis no hubiera sido posible sin vosotros, osea que esta tesis es tan mía como vuestra. ¡Mil gracias!

*A la persona que más y mejor me quiere - a mi madre*

*To the person who loves me the most and the best - to my mom*

---





---

<b>1. INTRODUCTION.....</b>	<b>1</b>
1.1. SPACE EXPLORATION SINCE THE MIDDLE OF 20 <sup>TH</sup> CENTURY.....	1
1.2. WAYS TO STUDY THE GEOCHEMISTRY OF CELESTIAL BODIES .....	4
1.2.1. <i>Martian meteorites</i> .....	5
1.2.2. <i>Martian analogs</i> .....	8
1.2.3. <i>Landed Martian missions</i> .....	8
1.3. <i>IN SITU</i> ANALYTICAL TECHNIQUES USED ON MARTIAN SURFACE .....	21
1.3.1. <i>In situ analytical techniques used on Martian surface for elemental characterization.....</i>	<i>21</i>
1.3.2. <i>In situ analytical techniques used on Martian surface for molecular analysis.....</i>	<i>31</i>
1.3.3. <i>In situ vs laboratory analytical techniques for geochemical Martian analysis .....</i>	<i>52</i>
1.4. REFERENCES .....	55
<b>2. OBJECTIVES .....</b>	<b>81</b>
<b>3. SAMPLES AND EXPERIMENTAL PROCEDURE.....</b>	<b>84</b>
3.1. SAMPLE DESCRIPTION .....	84
3.1.1. <i>Meteorites</i> .....	84
3.2.1. <i>Terrestrial analogs</i> .....	87
3.2.2. <i>Simulants</i> .....	89
3.3. EXPERIMENTAL PROCEDURE.....	90
3.3.1. <i>Reagents</i> .....	90
3.3.2. <i>Analytical techniques</i> .....	91
3.4. LABORATORY APPARATUS.....	104
3.4.1. <i>PARR 4848B reactor controller</i> .....	104
3.4.2. <i>Freeze-dryer</i> .....	104
3.4.3. <i>pH and redox determination</i> .....	105
3.4.4. <i>Centrifuge</i> .....	106
3.4.5. <i>Shaker water bath</i> .....	106
3.5. MISSION DATA ACQUISITION.....	107
3.6. CHEMICAL AND THERMODYNAMIC MODELING.....	107
3.7. CHEMOMETRICS AND STATISTICS .....	107
3.8. REFERENCES .....	108
<b>4. BEYOND MARTIAN MINERALOGY: ANALYSES OF MARTIAN CHEMICAL PROCESSES THROUGH METEORITES, SIMULATION WORK AND MISISON DATA TO UNDERSTAND MARTIAN GEOCHEMISTRY .....</b>	<b>114</b>
4.1. RAMAN SPECTROSCOPY TO ASCERTAIN THE FA/FO RATIO IN OLIVINES: APPLICATION TO TERRESTRIAL ANALOGS AND JEZERO CRATER, MARS 115	
4.1.1. <i>Methodology</i> .....	116
4.1.2. <i>Calibration models, validation and implementation.....</i>	<i>116</i>

---

---

4.1.3. Discussion .....	132
4.2. MARTIAN METEORITES STUDY - PRESSURE, OXIDATION AND HYDROTHERMAL ALTERATION PROCESSES OBSERVED IN MARTIAN SHERGOTTITES .....	135
4.2.1. LAR 12095 meteorite .....	135
4.2.2. RBT 04262 meteorite .....	148
4.2.3. Discussion .....	154
4.3. MARTIAN SIMULANTS STUDY – HYDROTHERMAL, TEMPERATURE AND PRESSURE PROCESSES .....	157
4.3.1. Mixed-sulfate synthesis under the ancient Martian hydrothermal state .....	159
4.3.2. Temperature-sensitive Martian sulfates studied by Raman Spectroscopy .....	171
4.3.3. Simulation of anhydrite formation at the Delta Front, Jezero crater, Mars .....	187
4.4. CONCLUSIONS .....	197
4.5. REFERENCES .....	199
<b>5. LABORATORY STUDIES TO UNDERSTAND MARTIAN HABITABILITY .....</b>	<b>214</b>
5.1. SOILS AT JEZERO CRATER FLOOR AND AT DIFFERENT LANDING SITES OF PAST MISSIONS .....	215
5.1.1. Soils at the Viking landing site .....	215
5.1.2. Soils at the Pathfinder landing site .....	216
5.1.3. Soils at the MER traverse sites .....	218
5.1.4. Soils at the Phoenix landing site .....	221
5.1.5. Soils at Gale crater up to sol 100. The Rocknest dune shadow and indurated soils .....	222
5.1.6. Crust soils at the Jezero crater, Mars .....	225
5.1.7. Discussion .....	235
5.2. MARTIAN SIMULANT STUDY – CLAY MINERALS AS HOSTS FOR ORGANIC MOLECULES ON MARS .....	237
5.2.1. Samples .....	238
5.2.2. Doping methodology .....	238
5.2.3. Results .....	240
5.2.4. Discussion .....	248
5.3. MARTIAN ANALOG STUDY – THE CASE OF FINDING ORGANIC MOLECULES ON THE CARACHI PAMPA ONCOID .....	250
5.3.1. Mission-like analytical instruments used for the study of habitability in the Carachi Pampa oncoïd .....	251
5.3.2. Results and discussion .....	253
5.3.3. Discussion .....	267
5.4. CONCLUSIONS .....	269
5.5. REFERENCIES .....	271

---

<b>6. POSSIBLE HABITABILITY ON THE MOON? EVALUATING THE MINERALOGY OF THE LUNAR REGOLITH FOR PLANT CULTIVATION .....</b>	<b>288</b>
6.1. MINERALOGY OF LUNAR METEORITES – THE CASE OF THE NWA 11273 LUNAR METEORITE .....	291
6.1.1. <i>Results</i> .....	291
6.1.2. <i>Discussion</i> .....	301
6.2. WEATHERING OF LUNAR SOILS, AS SEEN FROM THE NWA 11273 LUNAR METEORITE, AS THE FIRST STEP FOR PLANT CULTIVATION .....	303
6.3. CONCLUSIONS .....	307
6.4. REFERENCES .....	309
<b>7. GENERAL CONCLUSIONS AND FUTURE WORKS .....</b>	<b>316</b>
<b>8. APPENDICES.....</b>	<b>321</b>
8.1. GLOSSARY OF ACRONYMS .....	321
8.2. GLOSSARY OF MINERAL PHASES .....	325
8.3. ANNEXES WITH DATA .....	327
8.4. SCIENTIFIC PUBLICATIONS.....	333
8.4.1. <i>Published articles</i> .....	333
8.4.2. <i>Articles under review</i> .....	334
8.4.3. <i>Contributions to national and international conferences</i> ..	334
8.5. SCIENTIFIC DISCLOSURE .....	337

---

---

---

# CHAPTER 1

## INTRODUCTION

**“SOMEWHERE, SOMETHING INCREDIBLE IS  
WAITING TO BE KNOWN” – Carl Sagan**

---



## 1. INTRODUCTION

### 1.1. Space exploration since the middle of 20<sup>th</sup> century

Human beings have always been eager to learn about the objects seen during the night skies. After a big effort and thanks to the advances in technologies developed in the 20<sup>th</sup> century, it was possible to send the first machines, animals and, then, people to the outer space. This happened during the Cold War (1954-1989), a period of political enmity between the United States and the Soviet Union. In the course of many years, the space exploration was a competition to achieve quality spaceflights between both rivals. The dispute came to a head in October 1957, when the Soviet Union launched the first artificial satellite to orbit the Earth. It was named Sputnik in honor of the Russian word for satellite <sup>[1]</sup>. The artificial satellite Sputnik orbited the Earth and was visible to the naked eye, so that all the people in the world were able to appreciate it <sup>[2]</sup>. One month later, in November 1957, Soviets achieved another space success of the Sputnik program, the launch of Sputnik II. This was the first spacecraft to carry a living animal into the space, being the first space dog, Laika. The dog survived for four days, until the batteries on the satellite failed and Laika died from overheating <sup>[3]</sup>.

At the same time, the United States were working on its own goals. The U.S Space Agency began in January 1958, when Explorer 1 became the first successfully launched satellite of a large number of Explorer Program Satellites of the United States to orbit the Earth. In contrast to the two Soviet satellites sent before, the Explorer 1 carried the first science instrument into the space. It was a cosmic ray detector designed to measure the radiation environment in Earth orbit <sup>[4]</sup>. In the same year, in July 1958, the United States' space exploration started to be managed by the National Aeronautics and Space Administration (NASA), a civilian agency <sup>[5]</sup>.

In September 1959, the Soviet Union fulfilled the first spacecraft to impact the Moon <sup>[6]</sup>. That mission was called Luna 2, the second of the large program of robotic spacecraft missions that accomplished many discoveries along the space exploration history. Although Luna 1 was the first spacecraft designed to impact on the Moon, it escaped from the Earth-Moon system.

From this moment, both opponents sent several spacecraft into space. However, the following milestone of the space exploration was the journey of the first human into outer space. It was the Soviet cosmonaut Yuri Gagarin, who made one orbit flight around Earth in the capsule Vostok 1 in April 1961 <sup>[7]</sup>. Less than a month later, the American Alan Shepard became the first human to make a suborbital mission on board the Mercury capsule Freedom 7 <sup>[8]</sup>. On the basis of this feat, the American President John F.

Kennedy declared putting human beings in the Moon and their successful return to Earth as NASA's primary goal <sup>[9]</sup>.

Two years after getting a man safely into space, the Soviet Union launched the Vostok 6 mission, which made Valentina Tereshkova the first woman to travel to space <sup>[10]</sup>. Two years later, in March 1965, the cosmonaut Aleksei Leonov made the first spacewalk of the history, leaving the capsule during the Voskhod 2 mission <sup>[11]</sup>. While Americans were concentrated on taking humans to the Moon, Soviets did the first soft landing of a lander on the Moon's surface in January 1966 <sup>[11]</sup>. This mission was called Luna 9 and landed on the Moon's surface the following month after its launch <sup>[12]</sup>. After Luna 9, more missions had the objective to make soft landing on the Moon. However, the Surveyor V of the American Surveyor Program became the first successful soft landing to carry an analytical measurement instrument for conducting experiments on the Moon's surface and did the first *in situ* chemical analyses of the lunar surface <sup>[13]</sup>. Those analyses were performed by an alpha backscattering technique designed by professor Turkevich and his research team <sup>[14]</sup> and was also on board of the next Surveyor VI and VII missions. Considering the success in analyzing the lunar surface, the backscattering spectrometry technique became a common laboratory technique for chemical analysis. With time, this technique was substantially miniaturized and improved. In this way, it acquired the name of Alpha Proton X-ray Spectrometer (APXS) and it was used to obtain, for the first time, the chemical composition of Martian rocks on Pathfinder mission to Mars in 1997 <sup>[14]</sup>.

Using the knowledge acquired to perform soft landings, the most impressive milestone of the 60<sup>th</sup> and 70<sup>th</sup> decades was achieved. This was the arrival of American human being to the Moon's surface and the return of lunar samples. These events happened along the Gemini and Apollo Programs, between 1961 and 1972. Apollo 11 is so far the most famous space mission, as it was the first human landing on the Moon. In July 1969, astronauts Neil Armstrong, Edwin "Buzz" Aldrin and Michael Collins flew to the Moon on board the Command Module Columbia, after which Aldrin and Armstrong transferred to L.M. Eagle for the final descent to the lunar surface. It took place on July 1969, when Aldrin and Armstrong stepped on the Moon's surface and collected samples to bring back to Earth <sup>[15]</sup>. While they were on the surface, the pilot Michael Collins flew the Command Module Columbia in lunar orbit.

With the development of new technologies and the improvement of space missions, Americans considered studying other celestial bodies that had not been previously considered. These were Mercury, Venus and Mars, which missions were gathered into the Mariner program of NASA from 1962 and 1973. At the same time, Soviets designed one of the great successes

of the old Soviet's lunar exploration program, the Lunokhod 1 rover. It was the first robotic space exploration vehicle on the Moon's surface which carried more than one scientific instrument to accomplish experiments on the celestial body's surface. Lunokhod 1 was carried by the Luna 17 probe which landed in November 1970 <sup>[16]</sup>. This vehicle, together with Lunokhod 2 robot of the Luna 21 mission, were the only two automatic mobile laboratories, guided by remote control, in 40 years with the aim of exploring and sending images of the lunar surface to Earth <sup>[16]</sup>. The Lunokhod 1 rover explored the lunar surface using: (1) two low resolution TVs and four high resolution photometers, (2) the Penetrometer PROP to study physical and mechanical properties of the surface material, (3) the X-ray fluorescence spectrometer RIFMA (Roentgen Isotopic Fluorescent Method of Analysis) to measure the elemental composition of the surface material, (4) X-ray telescope to study the cosmic X-ray radiation, (5) a radiometric equipment for the study of cosmic rays of low energy and (6) a laser retroreflector to measure the Earth and Moon distance <sup>[17]</sup>.

In addition to the scientific equipment available on the Lunokhod 1, Lunokhod 2 (launched in 1973) had notable improvements, as (1) a third low resolution TV, (2) a RIFMA spectrometer improved, (3) a ternary ferromagnetometer to measure the magnetization of individual targets on the lunar surface and (4) an astrophotometer for measuring the luminosity of the sky at visible and ultraviolet wavelengths <sup>[18]</sup>.

The next phase of space exploration was marked by space stations. The first space station in Earth orbit was the Soviet Salyut 1, which was launched in April 1971 <sup>[19]</sup>. It was followed by the NASAS's Skylab, which was launched in May 1973 <sup>[20]</sup>.

At this point of the space exploration history, the race between the Soviet Union and NASA took a breath. This happened as they realized the importance of collaborative science to reach more extraordinary goals. Therefore, in July 1975, both worked in the Apollo-Soyuz mission <sup>[11]</sup>. Becoming the first international space mission, in which the United States Apollo module docked with a Soviet Union Soyuz capsule. This fact marked the end of the Space Race and other space agencies joined the space study. These were the Indian Space Research Organisation (ISRO), the European Space Agency (ESA), the China National Space Administration (CNSA) and the Japan Exploration Agency (JAXA), among others. Moreover, one year after the dissolution of the Soviet Union the Russian State Space Corporation (Roscosmos) was born in 1991 to unify the Russian space fields.

In addition to the launch of satellites, animals, humans and space stations, the next landmark was the creation of a modular space station in low Earth orbit, the International Space Station (ISS). The ISS is the result of the

collaboration between 15 countries (Governments of Canada, the United States of America, Japan, Russia and ESA member States). Its construction began in 1998 <sup>[21]</sup>, in order to be a scientific facility, in which international scientists and astronauts cooperate from that moment so far.

This historic review of the emerging of the space exploration highlights the evolution of technology required to face new challenges. This development has allowed increasing the knowledge about the Solar System and even other galaxies.

A key aspect to understand better the origin of the galaxies and their evolution is to ascertain the geochemistry of celestial bodies. The Geochemistry is defined as the science that deals with the chemical study of Earth's natural materials and other rocky bodies. Besides, geochemistry studies the alteration chemical processes that they undergo, both now and in the past <sup>[22]</sup>. This study can be an easy task when it comes to Earth study. However, it becomes more complicated when a far object wants to be analyzed.

## **1.2. Ways to study the geochemistry of celestial bodies**

There are several ways to study the geochemistry of non-terrestrial bodies from Earth <sup>[23]</sup>. These are:

- the characterization of collected meteorites and planetary dust;
- the study of terrestrial analogs that are used to gain a better comprehension about the nature and biogeochemistry processes happened on Earth; and
- the analysis of returned samples.

Aramendia et al. <sup>[24]</sup> summarized the most common analytical techniques used in order to study these samples. Nevertheless, even if valuable information is extracted from these studies, there is a broad gap between the knowledge acquired from these samples and what is discovered from planetary missions, with the exception of return samples. In this way, non-terrestrial samples found on Earth have undergone alteration processes, so the mineral phases found in these samples may not be the original or primary, but secondary ones or weathering/alteration products. Therefore, it is very important to study extraterrestrial material *in situ* so that the primary mineral phases can be unequivocally described <sup>[25]</sup>.

In order to characterize unaltered materials, two approaches have been used in space exploration so far:

- remote observations;

- *in situ* analyses with landed instruments; and
- return samples investigation.

Orbiters are designed to travel to a celestial body and enter into its orbit. After a first reconnaissance of the celestial bodies with flyby spacecraft, orbiters are the next type of spacecraft that are usually sent for macroscopic studies. They cover large portions of planetary bodies, being able to map globally the composition of their surface. Besides, they can acquire high spatial and spectral resolution images and determine the abundance of different elements in the surface and subsurface, among other macroscopic capabilities <sup>[26]</sup>.

*In situ* analyses include the use of landers and/or rovers. Lander spacecraft are designed to reach the surface of a celestial body and survive long enough to telemeter data back to Earth. Sometimes lander spacecraft carry a rover inside them. Rovers are mobile robots, whose main purpose range from taking images, scientific data and collect samples for its analyses on Earth. Therefore, landers and rovers provide many *in situ* analyses on a smaller scale, even microscopic, if they are compared with orbiters.

As explained above, remote sensing instruments installed in orbiters cover large portions of planetary bodies and place geochemistry in a whole-body context. Besides, orbiters are a first reconnaissance of the celestial body, which can be used to identify hotspots for future landing missions. Likewise, landers and rovers are equipped with analytical instruments to provide accurate information on a smaller scale. In this way, it can be seen how the information provided by remote observations and surface measurements are complementary.

Apart from Earth, it is likely that the only planet in the Solar System that met all the favorable conditions for the existence of life was Mars. Analyzing its evolution, Mars can give us clues about how the Earth may evolve over the years. In this sense, nowadays the only way to study its geochemistry is through the analysis of meteorites, analogs and landed missions, since there are no Martian samples on Earth so far.

### **1.2.1. Martian meteorites**

Meteorites were traditionally defined as solid objects that have fallen through the Earth's atmosphere and landed on the Earth's surface <sup>[27]</sup>. However, this definition had to be specified since not all objects falling from space are meteorites and meteorites are not only found on Earth. In this sense, this definition was reformulated by the International Astronomical Union, considering meteorites the natural solid objects that are moving in interplanetary space, on a size considerably smaller than an asteroid and considerably larger than 10  $\mu\text{m}$  in size <sup>[28]</sup>. To be considered as a meteorite, it must be derived from a celestial body that was transported by natural

processes from the body on which it was formed to a region outside the gravitational influence of that body. Then, collided with a natural or artificial body larger than itself <sup>[27,29]</sup>.

Likewise, there are two terms that should not be confused with each other, these are meteoroid and meteor. A meteoroid is a 10  $\mu\text{m}$  to 1 m, in size, natural solid object moving in interplanetary space. When meteoroids enter into an atmosphere, the light phenomenon meteor occurs due to the passage of an object through an atmosphere colliding with the particles in the air, causing the generation of high temperatures and, then, the mineralogical transformation of the crust <sup>[27]</sup>.

Taking into account these definitions, the Martian samples that can be found on Earth are those very small bodies that were formed on Mars, ejected out of Martian gravitational influence, traveled as meteoroids through space, and finally entered into the Earth's atmosphere as meteors, whose fragments survived to those hard conditions. The collected bodies on the Earth surface are called meteorites.

Meteorites can be stony or metallic. The stony ones are only slightly heavier than a standard terrestrial rock of the same size, whereas the metallic ones are much heavier and ring like bell when struck with a metallic object. Meteorites that have fallen recently have a distinctive dark coating called fusion crust, which is glassy and smooth in appearance. Meteorites that have been found later after its arrival are usually weathered and appear to be covered by rather smooth dark brown coating <sup>[30]</sup>.

Although there are several requirements to be satisfied, the positive identification of a meteorite is complicated and requires an expert to do so. The best way to confirm a meteoritic nature of a possible meteorite is to send a small piece to one of many meteorite experts, many of whom are members of the Meteoritical Society, including members at universities and museums. In the case of finding a new meteorite, the Meteoritical Society will name it and give a brief physico-chemical description of the sample. However, a small-scale characterization is not performed, hence, the importance of studying meteorites in depth at laboratories using the top-notch techniques available <sup>[30]</sup>.

In this sense, it has been determined that Martian meteorites represent igneous rocks of basaltic and ultramafic provenance, and they are divided into different categories based on their mineralogical composition and textural characteristics. These are shergottites, nakhlites (clinopyroxenites), chassignites (dunites), and orthopyroxenites <sup>[31]</sup>.

- Shergottites

They are composed of relatively coarse-grained olivine and chromite grains enclosed by large orthopyroxene crystals. Accessory phases, such as maskelynite, pyrrhotite, ilmenite, titanomagnetite, pigeonite, augite and whitlockite, are also present in these samples.

- Nakhilites

They consist of Mg-rich augite and Fe-rich olivine set into a microcrystalline groundmass of mostly crystalline plagioclase, which has not been transformed into maskelynite by shock, pigeonite, ferroaugite, titanomagnetite, pyrite, troilite, chloroapatite and sometimes SiO<sub>2</sub>-rich glass.

- Chassignites

They consist of 90% Fe-rich olivine, 5% pyroxene, 2% feldspar, and 3% accessory phases.

- Orthopyroxenites

The unique orthopyroxenites found so far is the ALH84001, which is a coarse-grained breccia with a modal composition of 96% orthopyroxene, 2% chromite, 1% plagioclase (maskelynite), and 0.15% phosphate. The rest is in the form of accessory phases, such as augite, olivine, pyrite and Fe-Mg-Ca carbonates.

Meteorites found on the Earth's surface can be called falls or findings, depending on the time they have spent on Earth. On the one hand, if they have been found immediately after landing following the meteor's path, they are called falls. On the other hand, if they have been found on Earth and the date of landing is unknown, they are called findings <sup>[32]</sup>. Although both types of meteorites have been exposed to terrestrial oxidation processes, findings are expected to be more weathered than falls due to terrestrial conditions. It is therefore very important to distinguish between primary minerals, Martian secondary, terrestrial secondary and terrestrial weathering mineral phases.

That is, primary minerals, as the name implies, are those igneous materials that are original from Mars and have not undergone any alteration process. Secondary minerals are those that come from primary minerals because they have undergone alteration processes that caused a chemical change, and can be formed both on Mars and/or Earth. Finally, as meteorites are found on the terrestrial surface, they may suffer further terrestrial weathering processes. Thus, detecting terrestrial weathering minerals is crucial to identify which are the main processes that alter or degrade meteorites on the Earth. Once defined these differences, it is possible to

trace the history of meteorites, as well as to understand alteration processes both on Mars and on Earth.

### **1.2.2. Martian analogs**

One of the major goals of space exploration consists of characterizing the geochemistry of the celestial bodies' surface. Although many minerals can be identified during *in situ* and orbital missions, it is necessary to determine the alteration pathways that those minerals follow [33,34]. For this purpose, analyzing terrestrial samples becomes a very important and easy tool to trace the mineralogical history, since planetary exploration is largely based on comparison with Earth. To do so, it is necessary to select terrestrial analogs, which are terrestrial samples or emplacements that have been exposed, at some point of their history, to conditions, processes or environments that may have occurred or occurs on Mars.

With this description, many sites and samples can be considered as Martian analogs. The Atacama Desert (Chile) is one of the most referenced examples of Martian analog, since is one of the driest deserts on Earth and, therefore, matches with the aridity of Mars [35,36]. Due to the cold and weathering environments, the Dry Valleys (Antarctica) has been used as a Martian analog before even before the Viking missions [37,38]. Mojave Desert (USA) was chosen as Martian analog due to its inert hygroscopic features, its availability in a variety of forms and due to its physical and chemical characteristics that are relevant to Martian studies [39,40]. In addition, Rio Tinto (Spain) was selected as a Martian analog for being a sulfate-rich site considering that on Mars, some locations such as Meridiani Planum, Noachian sulfates were discovered, which suggests a past aqueous, acidic and sulfate-rich environment [41]. The submarine volcanos of Meñakotz and Armintza (northern Spain) were described as Martian analogs since it is well known that Mars had volcanic activity and had water in some periods of its history, so it could be possible that some episode of submarine volcanism took place [42,43]. Many more places are classified as terrestrial analogs of Mars. In any case, the characterization of planetary terrestrial analogs becomes an essential tool to understand the geochemistry of Mars and to estimate the potential scientific return of forthcoming missions.

### **1.2.3. Landed Martian missions**

To date, 10 missions have traveled to Mars to study *in situ* the geochemistry of the planet. In addition, two more rovers will be launched in the near future, one to Mars and the other to its moon Phobos.

#### **1.2.3.1. The Viking Project**

NASA's Viking Project became the first mission to land a spacecraft safely on the surface of Mars and to return images. This project consisted of two identical spacecraft missions, the Viking 1 and the Viking 2, whose main

scientific goal was the search for life. Both spacecraft contained a lander (Figure 1.1 A) and an orbiter. Each orbiter-lander pair flew together and entered into Mar's orbit, the lander then separated and descended to the planet's surface.

On the one hand, Viking 1 was launched on August 20<sup>th</sup>, 1975 and the lander touched down at Chryse Planitia (22°N, 312°E) on July 20<sup>th</sup>, 1976. On the other hand, Viking 2 was launched on September 9<sup>th</sup>, 1975 and its spacecraft landed at Utopia Planitia (48°N, 134°E) on September 3<sup>rd</sup>, 1976.

Chryse Planitia region was selected to land because it is close to the terminus of three large channel systems (Ares Vallis, Tiu Vallis and Simud Vallis), which were considered to be primarily fluvial in origin and to have been modified by aeolian processes [44–46].

In contrast, Utopia Planitia is an impact basin located at the northwest of the volcanic province of Elysium Planitia and northeast of Arabia Terra. It was chosen for examination due to the presence of a large number and variety of periglacial features [44–46].

The Viking project was planned to continue for 90 days after landing. Nevertheless, each mission operated far beyond its design lifetime. Viking orbiter 2 was commanded off on July 25<sup>th</sup>, 1978; Viking lander 2 on April 11<sup>th</sup>, 1980 (1360 days at work); Viking orbiter 1 on August 7<sup>th</sup>, 1980 and Viking lander 1 on November 11<sup>th</sup>, 1982 (2260 days at work) [46].

The orbiters' scientific equipment was made up of cameras, an infrared spectrometer for water vapor mapping (MAWD) and an infrared radiometer for thermal mapping (IRTM). Conversely, the landers were composed of different cameras, a thermal volatilization gas chromatograph-mass spectrometer (TV-GC-MS), a seismometer, an X-ray Fluorescence spectrometer (XRF), a weather instrument package (temperature, pressure, wind velocity), a remote sampler arm to take soil samples, and a biology laboratory with three different experiments. The three experiments were called pyrolytic release (PR), labeled release (LR), and gas exchange (GEX) [47].

### **1.2.3.2. The Mars Pathfinder Project – Sojourner rover and Carl Sagan Memorial Station lander**

Mars Pathfinder, a spacecraft composed of a lander and a rover, was the first mission to explore in detail a landing area on Mars with a mobile platform. The lander was later named Carl Sagan Memorial Station in honor of the astronomer Dr. Carl Sagan; while the rover was called Sojourner. The Mars Pathfinder spacecraft was launched on December 4<sup>th</sup>, 1996 and landed on the Mars' Ares Vallis (19.33°N, 33.55°W, local reference frame) on July 4<sup>th</sup>, 1997 [48]. Although the mission was designed to operate

between one week and one month, it worked around three months. Sojourner (Figure 1.1 B), a rover weighing 10.5 kg and having 66 cm long, 48 cm wide and 30 cm tall, crossed over 100 m during its lifetime and extended the radius of investigations to a distance of approximately 12 m from the landing site <sup>[48,49]</sup>. As one of the objectives of this mission was to demonstrate a simple and low-cost system, the communications had to be improved, since the rover and the lander had to work at the same time and send data to Earth. Thus, in order to save rover power and mass, the rover communicated with Earth through the lander, requiring a short rover-lander communication range <sup>[50]</sup>.

After many experiments, the lander battery degraded as expected during the first 30 days, so the spacecraft resulted in progressive cooling (night) and warming (day) cycles, until something in the telecommunications hardware failed. For this reason, the last communication with the main spacecraft was on October 7<sup>th</sup>, 1997 <sup>[51]</sup>.

The Ares Vallis is a large channel that drained into the Chryse Planitia basin. That landscape is the result of ancient outflow channel formation and subsequent aeolian resurfacing of the depositional plain <sup>[52]</sup>. This landing site was selected because it appeared acceptably safe to land and permitted the possibility to investigate a great variety of rock types deposited by catastrophic floods. Moreover, the Ares Vallis enabled to study different scientific questions, such as the differentiation of the crust, the development of weathering products, and the nature of the early Martian environment and its evolution <sup>[53]</sup>.

The primary objective of the Pathfinder mission was to demonstrate a low-cost cruise, entry, descent, and landing system that could safely place a payload on the Martian surface. Moreover, other objectives were related to extend the scientific knowledge about the red planet. These included the study of the surface's morphology and geology, the elemental composition of surface materials, a variety of atmospheric science investigations and rotational and orbital dynamics investigations.

To achieve the scientific goals, both rover and lander were equipped with different instruments. On the one hand, the Sojourner rover carried an alpha proton X-ray spectrometer (APXS) and cameras. On the other hand, the lander carried (1) a spectroscopic imager (the Imager for Mars Pathfinder, IMP) composed of three cameras and (2) an Atmospheric Structure Instrument/Meteorology Package to measure the Martian atmosphere during the spacecraft descent, and to provide meteorology data both before and after landing <sup>[48]</sup>.

### **1.2.3.3. Mars Surveyor 98 – Mars Polar lander**

The Mars Surveyor '98 mission was part of the NASA's Mars Surveyor Program (MSP), which began in 1994 with plans to send a spacecraft to Mars every 26 months. The first spacecraft sent was the Mars Global Surveyor (MGS), a global mapping mission, which was launched in 1996 to orbit Mars. The next mission was the Mars Surveyor '98, which was comprised of two spacecraft, the Mars Climate orbiter, launched on December 11<sup>th</sup>, 1998, and the Mars Polar lander (Figure 1.1 C), launched on January 3<sup>rd</sup>, 1999 <sup>[54,55]</sup>. Both the lander and the orbiter were designed to study the Martian weather, climate, water and carbon dioxide budget of the Martian South Pole.

The orbiter carried a Pressure Modulated Infrared Radiometer (PMIRR) to collect data on the Martian climate and atmospheric/surface processes. Moreover, it also carried a multispectral camera (Mars Color Imager, MARCI) to perform remote sensing measurements using a wide angle and a medium angle cameras <sup>[56]</sup>.

The lander carried a payload, including a robotic arm that deposited soil into a thermal evolved gas analyzer. In addition, the lander was equipped with a Light Detection and Ranging (LIDAR) instrument to measure atmospheric properties and detect sound, a weather station similar to Pathfinder's, and a meteorology equipment <sup>[56]</sup>.

Two small micro-landers, called Deep Space-2, were also carried as technology demonstrators. They were planned to plummet to the surface without parachutes, hoping to plunge into 2 meters, leaving a radio on the surface to link with the MGS orbiter. They were designed to send information about the regolith density, subsurface/surface temperature and pressure, and to capture a subsurface soil sample and analyze its water content <sup>[56]</sup>.

The mission was expected to land in a region known as Planum Australe, due to the interest in studying the only known examples of extraterrestrial ice-sheets comparable to those of the Earth. Previous images received from the Viking and Mariner 9 orbiters allowed to select the landing site <sup>[57]</sup>. Unfortunately, the last contact with the vehicle was on December 3<sup>rd</sup>, 1999, when the spacecraft was entering into the atmosphere and the MGS tried to look for signs of the lander on the surface, but the search resulted fruitless <sup>[54,55]</sup>.

### **1.2.3.4. The Mars Express (MES) – The Beagle 2 lander**

The Mars Express mission was the first planetary mission conducted by the ESA. MES was launched on June 2<sup>nd</sup>, 2003 and it included an orbiter, called the MES orbiter, and a small lander. The lander was named Beagle

2 (Figure 1.1 D) in honor of the ship involved in the epic voyage made by Charles Darwin and Robert FitzRoy during the years 1831 and 1836 that led to publish Darwin's "on the Origin of Species" book <sup>[58]</sup>. The landing site was selected after examining data from the instruments of the Mars Observer, MGS and the Viking orbiters <sup>[59]</sup>. The selected location was the Isidis Planitia (11.6°N, 90.75 °E), which is a large flat sedimentary basin of impact origin straddling the relatively young northern plains and ancient southern highlands, where traces of life could have been preserved <sup>[60]</sup>.

This mission supposed the first opportunity to study *in situ* the Martian mineralogy. The MES orbiter was captured into Mars orbit on December 25<sup>th</sup>, 2003. It was equipped with several instruments to make remote studies of the planet's subsurface, surface and atmosphere. These were: (1) a High-Resolution Stereo Camera (HRSC), (2) an IR-spectro-imager (Observatoire pour la Minéralogie, l'Eau, les Glaces et l'Activité, OMEGA), (3) a Mars Advanced Radar for Subsurface and Ionospheric Sounding (MARSIS), (4) an imager of energetic neutral atoms with an analyzer of space plasmas (Analyzer of Space Plasmas Energetic Neutral Atoms, ASPERA-3), and (5) a Mars Express Radio Science Experiment (MaRS) <sup>[61]</sup>. The orbiter was also equipped with spectrometers, such as (6) an infrared spectrometer (Planetary Fourier Spectrometer, PES) and (7) an ultraviolet spectrometer (Spectroscopy for the Investigation of the Characteristics of the Atmospheric of Mars, SPICAM). Orbital remote sensing observations, such as those made by OMEGA, enable a global characterization of Mars surface. Based on OMEGA operations, a first analysis of the global distribution of key mineral species at low and mid latitudes was performed <sup>[62]</sup>.

The OMEGA analysis revealed general trends of the distribution of surface material on Mars, broadly consistent with previous ground-based and space observations. Apart from many minerals detected such as pyroxene and olivine, among others, hydrated minerals were detected in some spots, mostly within the ancient crust. Hydrated minerals were also detected by further studies performed by the Compact Reconnaissance Imaging Spectrometer for Mars (CRISM) instrument on board the NASA's Mars Reconnaissance orbiter (MRO), which is still active after 17 years of operation <sup>[62,63]</sup>. Those analytical results have been used with scientific purposes and for the selection of the landing site of future missions. Recently, ESA has approved the continuation of the Mars Express mission.

Although the Beagle 2 spacecraft successfully deployed from the Mars Express mother craft on December 19<sup>th</sup>, 2003, six days later, it was not forthcoming. Data from the lander were planned to be relayed back to Earth via the MES orbiter and NASA's Mars Odyssey mission, but the mission only received data from the orbiter, which is still operating <sup>[59]</sup>.

Twelve years later, on January 16<sup>th</sup>, 2015, ESA announced that the probe was found in pictures taken by the NASA's Mars Reconnaissance orbiter. The lander was seen partially deployed on the surface, showing that the entry, descent and landing sequence worked [64].

Beagle 2 was designed to perform a detailed geological, mineralogical and chemical analysis of the site's soils and rocks. For that reason, the Beagle 2 carried a Gas Analysis Package (GAP), the first Mössbauer spectrometer (MIMOS) to analyze the molecular composition of iron minerals and the XRF to characterize the elemental composition of the surface. Besides, it included environmental sensors, cameras (Marine), stereo cameras and a microscope, among others [58].

This lander was the most equipped one sent to Mars, aiming to fully characterize volatiles, soils and rocks around the landing site area. Unfortunately, something happened at the landing phase leaving a great human effort and instrumental developments without any returned data from the *in situ* analysis.

Although the lifetime of the Beagle 2 lander was short, the MRO orbiter has been one of the ESA's greatest achievements, as it is still active and will soon reach 20 years of operation.

### **1.2.3.5. The Mars Exploration rovers (MER) mission – Spirit and Opportunity rovers**

The MER mission (Figure 1.1 E) were part of the NASA's Mars Exploration Program, which by that time, had landed successfully three robots in Mars: the Viking 1 lander, the Viking 2 lander and the Sojourner rover.

The main goal of the MER mission consisted of placing two mobile science laboratories on the surface of Mars in order to conduct *in situ* investigations for at least 90 sols (Martian days). In addition, the science goal of the MER mission was to determine the climatic, aqueous, and geologic history of a pair of sites on Mars where conditions may have been favorable to the preservation of pre-biotic or biotic processes evidences [65]. In this way, the MER-A rover (called Spirit) and the MER-B (called Opportunity) were launched on June 10<sup>th</sup>, 2003, and July 7<sup>th</sup>, 2003, respectively.

Before landing, potential landing sites were mapped by using orbital images from Viking, the Mars Orbital Camera (MOC), and thermal emission imaging system (THEMIS) [66]. Finally, Spirit touched down on January 4<sup>th</sup>, 2004 on the volcanic plains of Gusev Crater, a place where mineral deposits suggested that Mars had a wet history [67].

In order to select Gusev crater as landing site, prelanding orbital images including those acquired by the Viking camera, the Odyssey THEMIS, and the MGS MOC were considered to select the Opportunity landing site [68].

Finally, Opportunity landed on January 24<sup>th</sup>, 2004 on Eagle Crater (Meridiani Planum), a possible ancient lake in a giant impact crater [69].

Even though both rovers were designed for completing 90 sols, Spirit and Opportunity exceeded their lifetime for many years. The Jet Propulsion Laboratory (JPL/NASA) lost contact with Spirit on March 22<sup>nd</sup>, 2010 and with Opportunity on March 10<sup>th</sup>, 2018 [65]. Despite the attempts of JPL to regain contact with both rovers, the missions were declared ended after confirming the lost of contact communications. The Spirit mission finished on March 22<sup>nd</sup>, 2010 and the Opportunity one on February 13<sup>th</sup>, 2019.

Spirit and Opportunity were identical rovers equipped with the Athena Science Payload which was composed of a (1) Panoramic Camera (Pancam), (2) a Miniature Thermal Emission Spectrometer (Mini-TES), (3) Mösbauer Spectrometer (MBS), (4) an APXS (5) a Magnet Array for collecting magnetic dust particles that were, afterwards, analyzed by MBS and APXS, (6) a Microscopic Imager (MI) and (7) a Rock Abrasion Tool (RAT) [70].

#### **1.2.3.6. The Mars Phoenix mission – Phoenix Lander**

The Phoenix mission was the first of the NASA's Scout Program. Its name is related with the mythological bird Phoenix due to the intention to land on the Mars' pole after the failed attempt of the Mars Polar Lander.

The Mars Phoenix lander (Figure 1.1 F) was launched on August 4<sup>th</sup>, 2007, and landed on the northern plains of Mars on May 25<sup>th</sup>, 2008. The landing site was the Green Valley of Vastias Borealis (68.22 °N, 125.7 °W), in the Martian northern hemisphere. Thanks to the data arrived from the High-Resolution Imaging Science Experiment (HiRISE) of the Mars Reconnaissance orbiter, and from the Mars Orbiter Laser Altimeter (MOLA), Green Valley was selected as the Phoenix Lander landing site [71]. The arctic of Mars was selected to land because the primary goals were to study the history and current state of water in the Martian north polar region, and to understand if the landing site represented a habitable zone [72]. Phoenix completed its mission in August 2008, and made a last brief communication with Earth on November 2<sup>nd</sup>, 2008, as available solar power dropped with the Martian winter.

The lander was equipped with several instruments capable of characterizing the ice and surrounding soils: (1) a Robotic Arm, (2) a Microscopy, Electrochemistry and Conductivity Analyzer (MECA) that consisted of a wet chemistry lab (WCL) to extract soluble ions from the Martian soils, an optical and atomic force microscopes, and a thermal and electrical conductivity probe, (3) a Robotic Arm Camera, (4) a Surface Stereo Imager, (5) a Thermal and Evolved Gas Analyzer (TEGA), (6) a

Mars Descent and (7) a Meteorological Station (MET) to record the dialy weather of Mars <sup>[73]</sup>.

One of the greatest success of this mission was the detection of soluble perchlorates in the soils of the Phoenix landing site, confirming the presence of a chloride/perchlorate cycle on Mars.

### **1.2.3.7. The Mars Science Laboratory (MSL) mission – Curiosity rover**

The MSL mission was launched on November 26<sup>th</sup>, 2011, and successfully delivered the rover Curiosity (Figure 1.1 G) to the surface of Mars on August 5<sup>th</sup>, 2012. After having traveled nearly than 30 km, the Curiosity rover remains active on Mars. Gale Crater, the selected landing site, was formed when a meteor hit Mars in its early history, about 3.5 to 3.8 billion years ago. As the meteor impact punched an enormous hole in the terrain (the crater has 154 km in diameter), water was retained in the crater over its history. The remote sensing instruments on board several orbital platforms, including MRO, which carries the Context Imager (CTX), the MiRISE and the CRISM instruments, enabled the selection of Curiosity's landing site. CRISM was used to determine the minerals present at the surface, which helped to detect distinctive geologic units and asses the nature of past aqueous environment. MiRISE and CTX provided morphologic information regarding the minerals' stratigraphic context while also addressing landing site safety concerns <sup>[74]</sup>.

In that way, NASA chose the Gale Crater, in the Aeolis Mensae region on the Southern edge of Elysium Planitia, as the landing site of the Curiosity rover with the aim of assessing whether Mars ever had an environment capable of supporting microbial life <sup>[75]</sup>. The scientific goals were to determine whether life ever arose on Mars, to characterize the climate of Mars, to characterize its geology and to prepare for human exploration. In order to achieve those aims, the MSL Curiosity rover was sent to Mars with a series of science sets, which are classified into contact, remote sensing, environmental, and analytical laboratory instruments.

Firstly, the two contact instruments on board the Curiosity are the APXS and the Mars Hand Lens Imager (MAHLI). Secondly, the Chemical Camera (ChemCam) and the Mast Cameras (Mastcam) are the two remote sensing instruments of the rover to characterize the Martian surface. Thirdly, the Curiosity is provided by an environmental laboratory composed by the following instruments: (a) the Dynamic Albedo of Neutron (DAN), (b) the Mars Descent Imager (MARDI), (c) the Radiation Assessment Detector (RAD), (d) the Rover Environmental Monitoring Station (REMS), and (e) the Mars Science Laboratory Entry Descent and Landing Instrument (MEDLI). Finally, the analytical laboratory system is composed by the

Chemistry and Mineralogy (CheMin) and the Sample Analysis at Mars (SAM) instruments <sup>[76]</sup>.

At the time of writing this work (February 2023), Curiosity had successfully traversed along the Gale Crater for more than 3700 sols <sup>[77]</sup>.

### **1.2.3.8. The Insight mission – Insight lander**

The twelfth mission of NASA's Discovery Program was InSight (Interior Exploration using Seismic Investigations, Geodesy and Heat Transport). This lander was launched on May 5<sup>th</sup>, 2018 and landed on November 26<sup>th</sup>, 2018 <sup>[78]</sup> in Elysium Planitia (4.502 °N, 135.623 °E) <sup>[79]</sup>, in the vicinity of the Curiosity Rover landing site <sup>[80]</sup>. The purpose of the InSight lander was to perform the first comprehensive surface-based geophysical investigation of Mars. This mission was also planned to help scientist answer key questions about the early formation of rocky planets in our inner Solar System (Mercury, Venus, Earth, and Mars), as well as rocky exoplanets.

The scientific goals of this mission consisted of understanding the formation and evolution of terrestrial planets through investigation of the interior structure and Martian processes, apart from determining the presence of tectonic activity and impact flux <sup>[81]</sup>.

The InSight lander carried three instruments: (1) the Seismic Experiment for Interior Structure (SEIS), (2) the Heat Flow and Physical Properties Package (HP<sup>3</sup>) and (3) the Rotation and Interior Structure Experiment (RISE) <sup>[82]</sup>. The lander was also equipped with an Auxiliary Payload Subsystem (APSS) to provide information about the weather. After more than four years of collecting data on seismic activity, the lander ran out of power and could no longer establish contact with its operators on Earth on December, 15<sup>th</sup>, 2022 <sup>[83]</sup>.

### **1.2.3.9. The Mars 2020 mission – Perseverance rover**

On July 30<sup>th</sup>, 2020, NASA launched the Perseverance rover (Figure 1.1 H) of the Mars 2020 mission, which landed in the Jezero Crater, located on the western edge of Isidis Planitia, on February 18<sup>th</sup>, 2021 <sup>[84]</sup>. Recent high-resolution orbital imaging systems have revolutionized the understanding of the Martian surface, and have updated the global geologic map of Mars. Likewise, they have generated numerous local geologic mapping works in which surface and subsurface details are identified <sup>[85]</sup>. Hence, thanks to orbit data, Jezero crater was selected to land as scientists believe that the area was once flooded with water and was home to ancient river delta <sup>[84]</sup>.

The Mars 2020 mission is part of the NASA's Mars Exploration Program. One of its high-priority goals is to answer key questions about the potential life on Mars. The objectives are:

- (1) Investigation of the mineralogy and geology of the Jezero Crater as representative of the ancient Martian environment.
- (2) Evaluation of the habitability of this ancient environment.
- (3) Identification of rocks with a high potential biosignatures preserved.
- (4) The study of the current environmental Martian conditions for the upcoming human exploration.

The rover includes a drill coupled to a catching system that collects samples that will return to Earth in the future Mars Sample Return mission [86]. Besides, it is equipped with seven science instruments: (1) Mastcam-Z, (2) Mars Environmental Dynamics Analyzer (MEDA), (3) Mars Oxygen *In Situ* Resource Utilization Experiment (MOXIE), (4) Planetary Instrument for X-ray Lithochemistry (PIXL), (5) Radar Imager for Mars' Subsurface Experiment (RIMFAX), (6) Scanning Habitable Environments with Radar and Luminescence for Organics and Chemicals (SHERLOC) and (7) SuperCam [87,88].

I belong to the Science Team of SuperCam instrument and, hence, to that of the Mars2020 mission.

#### **1.2.3.10. The Tianwen-1 mission – Tianwen-1 rover**

China's first Mars exploration mission, Tianwen-1, was launched on July 23<sup>rd</sup>, 2020, and entered into the Mars orbit on February 10<sup>th</sup>, 2021. The process of landing site selection for Tianwan-1's rover (Figure 1.1 I) involved both engineering safety and scientific importance. Finally, based on orbiter data the selected site to land was Utopia Planitia, which is the largest recognized impact basin in the northern hemisphere of Mars, where the rover landed on May 15<sup>th</sup>, 2021. The site is located south of the NASA's Viking 2 Lander landing site and northwest of the spot where the NASA's InSight Lander touched down.

The main scientific objectives of Tianwen-1 are to study the characteristics of the Martian topography and geological structure; to study the characteristics of the Martian soils and the distribution of water ice; to investigate the subsurface composition; to study the ionosphere, surface climate and environmental characteristics of Mars; and to study the Martian physical fields and internal structure [89].

To achieve those objectives, Tianwen-1 is equipped with thirteen scientific instruments, seven on the orbiter, six on the rover and two controllers separately installed on the orbiter and the rover, respectively. The scientific payload mounted on the rover includes: (1) Navigation and Terrain Camera (NaTeCam), (2) Multispectral Camera (MSCam), (3) Mars Rover Penetrating Radar (RoPeR), (4) Mars Surface Composition Detector (MarsCoDe), (5) Mars Rover Magnetometer (RoMAG), and (6) Mars Climate Station (MCS).

### 1.2.3.11. The Rosalind Franklin mission – Rosalind Franklin rover

The ESA's Rosalind Franklin mission will consist on the Rosalind Franklin rover. After a journey of nine months, the rover will travel across the Martian surface to search for signs of life, collect samples with a drill and analyze them by *in situ* instruments and by other more sophisticated systems. These last ones will be installed in the Analytical Laboratory Drawer (ALD), a clean laboratory where the samples collected by the drill would be analyzed. The landing site selected is Oxia Planum, which is situated at the eastern margin of the Chryse basin at the outlet of the Coogoon Valles system <sup>[90]</sup>. Oxia Planum is a 200 km-wide low-relief terrain characterized by hydrous clay-bearing bedrock units. This region is of scientific interest as it exhibits at least two distinct aqueous environments, both of which occurred during the Noachian: (1) a first phase that led to the deposition and alteration of 100 m of layered clay-rich deposits and (2) a second one of a fluviodeltaic system that postdates the widespread clay-rich layered unit <sup>[91]</sup>. Those sediments are ideally suited for the exobiology rover.

Rosalind Franklin will be the first mission to combine the capability to move across the surface and to study Mars at variable depths, from surface down to 2 meters <sup>[92]</sup>. The rover will be equipped with nine instruments: (1) PanCam, (2) Close-Up Imager (CLUPI), (3) Water Ice Subsurface Deposit Observation on Mars (WISDOM), (4) Autonomous Detector of Radiation of Neutrons On board Rover at Mars (ADRON-RM), (5) Mars Multispectral Imager for Subsurface Studies (Ma-MISS), and three more instruments installed in the ALD, (6) MicrOmega, (7) Raman Laser Spectrometer (RLS), and (8) Mars Organic Molecule Analyzer (MOMA).

I belong to the Science Team of RLS instrument and, hence, to that of the Rosalind Franklin mission.

### 1.2.3.12. The Martian Moons eXploration (MMX) mission

JAXA is planning to launch the MMX mission in 2024. The MMX mission is a project to explore the Martian moons Phobos and Deimos, which includes a rover (Figure 1.1 J) <sup>[93]</sup>. Its major scientific goal consists of clarifying the origin of the two Martian moons and the evolution process of the Martian sphere (Mars, Phobos and Deimos) <sup>[94]</sup>.

The spacecraft will be inserted into Mars orbit in 2025, and will stay in the Martian area for about three years. It will perform scientific observation of Phobos from low altitudes and select sample collection sites. Then, the spacecraft will land on the surface of Phobos, perform *in situ* science with a small (about 25 Kg) rover, collect samples, and return to Earth in 2029.

Before entering into the orbit to return to Earth, the spacecraft will carry out a flyby observation of Deimos <sup>[93]</sup>.

The main probe will have 7 science instruments: (1) the Telescopic Nadir imager for GeOmOrphology (TENGOO), (2) the Optical Radiometer composed of Chromatic Imagers (OROCHI), (3) a LIDAR to gather information on the shape of Phobos, (4) the MMX Infrared Spectrometer (MIRS), (5) the Mars-moon Exploration with Gamma Rays and Neutrons (MEGANE), (6) the Circum-Martian Dust Monitor (CMDM), and (7) the Mass Spectrum Analyzer (MSA) <sup>[94]</sup>.

The MMX rover will be a contribution by the Centre National d'Etudes Spatiales (CNES) and the German Aerospace Center (DLR). It will be delivered to the surface of Phobos to perform *in situ* science but also to serve as a scout, preparing the landing of the main spacecraft. Its currently considered scientific payload consists of cameras, a Raman Spectrometer (RAX), and a thermal mapper (miniRAD) <sup>[95]</sup>.

As has been seen throughout the review of Martian landed missions, analytical techniques are very important in order to characterize the geochemistry of the planet.

For this reason, the following review summarizes all the *in situ* analytical techniques used on Mars, which can also be used in laboratories on meteorites, analogs and future Martian return samples.

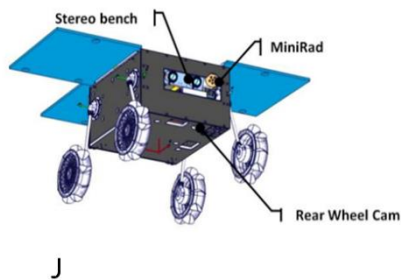
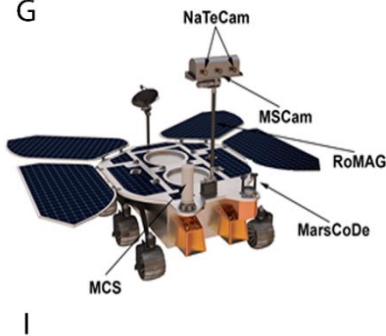
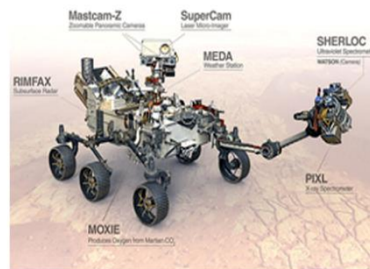
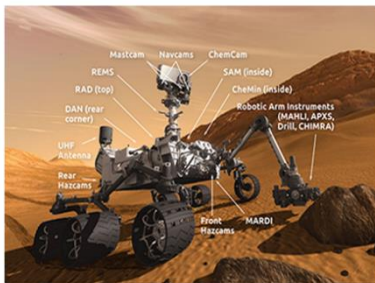
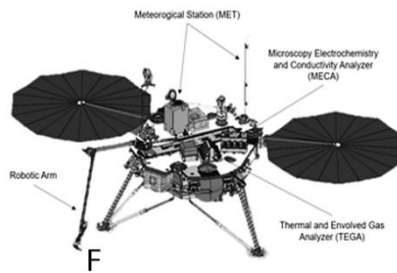
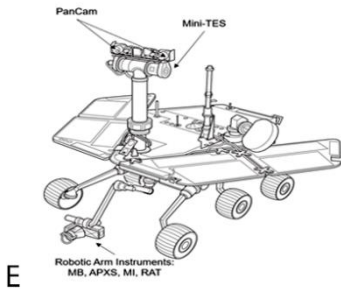
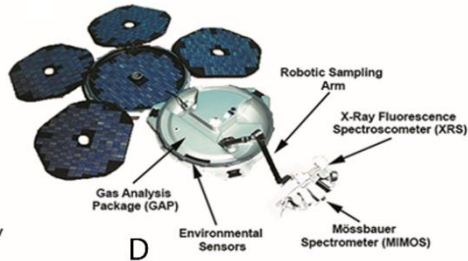
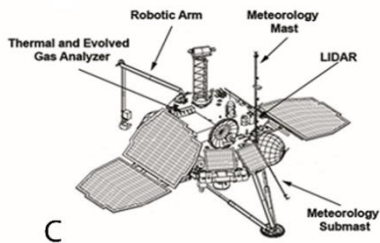
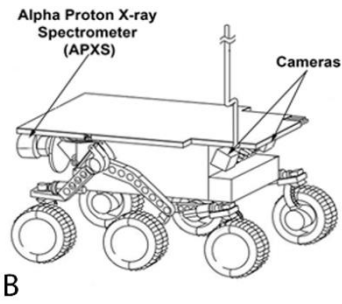
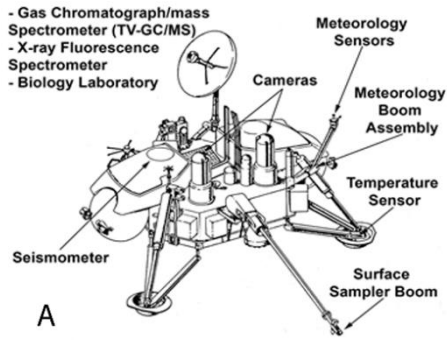


Figure 1.1. Illustration of (A) the Viking lander with its scientific payload shown (this figure has been edited from the original version <sup>[96]</sup>). (B) the Mars Pathfinder's Sojourner rover with its APXS and some cameras shown (this figure has been edited from the original one <sup>[97]</sup>), (C) the Mars Polar lander with its scientific payload shown (this figure has been edited from the original one <sup>[98]</sup>), (D) the ESA's Beagle 2 lander instruments (this figure has been edited from the original version <sup>[99]</sup>), (E) the NASA's MER rovers with its analytical techniques shown (this figure has been edited from the original version <sup>[100]</sup>), (F) the Phoenix lander with its analytical techniques shown (this figure has been edited from the original version <sup>[101]</sup>), (G) the Curiosity rover with its scientific payload shown <sup>[102]</sup>, (H) the Perseverance rover with its analytical techniques shown <sup>[103]</sup>, (I) the Tianwen-1 rover with its scientific payload shown (this figure has been edited from the original version <sup>[104]</sup>), and (J) the MMX rover to Phobos <sup>[95]</sup>.

### 1.3. *In situ* analytical techniques used on Martian surface

All the techniques summarize in this subchapter have been differentiated according to the analysis target, being classified as elemental and molecular techniques.

#### 1.3.1. *In situ* analytical techniques used on Martian surface for elemental characterization

##### 1.3.1.1. X-ray Fluorescence (XRF)

As mentioned above, XRF spectroscopy is one of the most common non-invasive techniques used for elemental characterization of non-terrestrial techniques.

To date three robotic missions have been equipped with an XRF spectrometer: the Viking landers, the Beagle 2 lander and the Perseverance rover. In this way, the XRF on board the Viking landers carried out the first *in situ* geochemical analyses of the Martian regolith.

Initially, the Viking mission's first objective was to study the exobiology of the planet, as it was the first exploratory journey to Mars. Subsequently, as it was decided to extend the scientific payload of the landers, a XRF spectrometer was added (Figure 1.2 A). Unfortunately, as the spacecraft design was already firm, the XRF construction was limited, especially in size and configuration <sup>[105]</sup>, which affected the quality of the results. Each fluorescence analyzer consisted of two pairs of gas proportional counters, with each pair adjacent to a single, sealed radioisotope source. The sources were <sup>55</sup>Fe and <sup>109</sup>Cd, emitting 5.9 keV and 22.2 keV X-rays, respectively <sup>[106]</sup>. As the analytical performance of the instrument was limited by the energy resolution of the gas proportional counters used for X-ray detection, its resolution was 1.2 keV at 5.9 keV (Mn K $\alpha$  line), expressed as full width half maximum (FWHM) <sup>[107]</sup>. Besides, its live time was about 14400 seconds and the limit of detection (LOD) for Rb, Sr and Zr was 42, 42 and 57  $\mu\text{g/g}$ , respectively <sup>[107]</sup>. In analytical tests on unknown samples, the elements detected were measured with accuracies, which

compared favorably with those obtained by wet-chemical methods. As it is known, the accuracy improved with increasing atomic number.

Despite its limitations, the XRF of the Viking landers got interesting results. According to the element concentration results interpreted by Soffen et al. [44], the elemental composition of Chryse and Utopia sites were similar, but they were not so similar to terrestrial soils. The main elements detected by the Viking landers were silicon and iron (supposing the 89 % of elements detected). Then, in less abundance, magnesium, sulfur, aluminum, calcium, titanium, chloride and potassium were identified in decreasing order, and finally, another 2 % of other minor elements were also detected [108,109]. The elemental concentrations were combined to simulate the presence of many types of geochemical compounds in the soils. In this way, there are many mineral models about the geochemistry of the Martian surface thanks to the data provided by Viking XRF [110,111].

Another XRF instrument was on board the Beagle 2 lander (Figure 1.2 B). Although the Beagle 2 lander failed, this instrument incorporated a number of innovative design features. In order to integrate the XRF device at the end of the robotic arm of the Beagle 2 lander, it had to be miniaturized. Its mass was about 0.156 Kg, the detector head assembly dimensions were 47 mm in diameter and 47 mm of length, and the dimensions of the signal processing electronics were 120 x 80 x 15 mm [107].

Most common XRF spectrometers use a dual source to illuminate the sample sequentially. However, the Beagle 2 XRF spectrometers was designed to used both types of sources simultaneously. The primary excitation was provided by two  $^{55}\text{Fe}$  (105.6 MBq) sources (emitting Mn K X-rays of energy 5.9 keV and 6.5 keV) and two  $^{109}\text{Cd}$  (8.77 MBq) sources (emitting Ag K X-rays of 22.2 keV and 24.9 keV) [107]. This improvement was developed in order to avoid the need of a source change mechanism that might have compromised the reliable operation of the instrument and unnecessarily increased its mass.

The FWHM resolution of the flight spare Beagle 2 XRF device was about 0.39 KeV at Mn K $\alpha$  [107]. Regarding to LODs of the Beagle 2 XRF, they were calculated to be 22, 27 and 26  $\mu\text{g/g}$  for the trace elements Rb, Sr and Zr respectively, improving considerably those of Viking [107].

As has been described, the XRF of the Beagle 2 included improvements with respect to the Viking XRF for the study of the Martian surface geochemistry. Unfortunately, as the mission was unsuccessful, there are no real analytical results to compare with those obtained by the XRF of the Viking landers.

Subsequently to the Beagle 2 XRF, a very novel instrument was developed for the Curiosity rover payload. This was the initial CheMin, which combined

X-ray diffraction with XRF. Both techniques aimed to study simultaneously mineralogy and geochemistry of the Martian surface. However, due to the warmth of the landing site, the CCD of the XRF was going to be warmer than expected. This fact was one of the reasons why the CheMin XRF requirement was dropped [114].

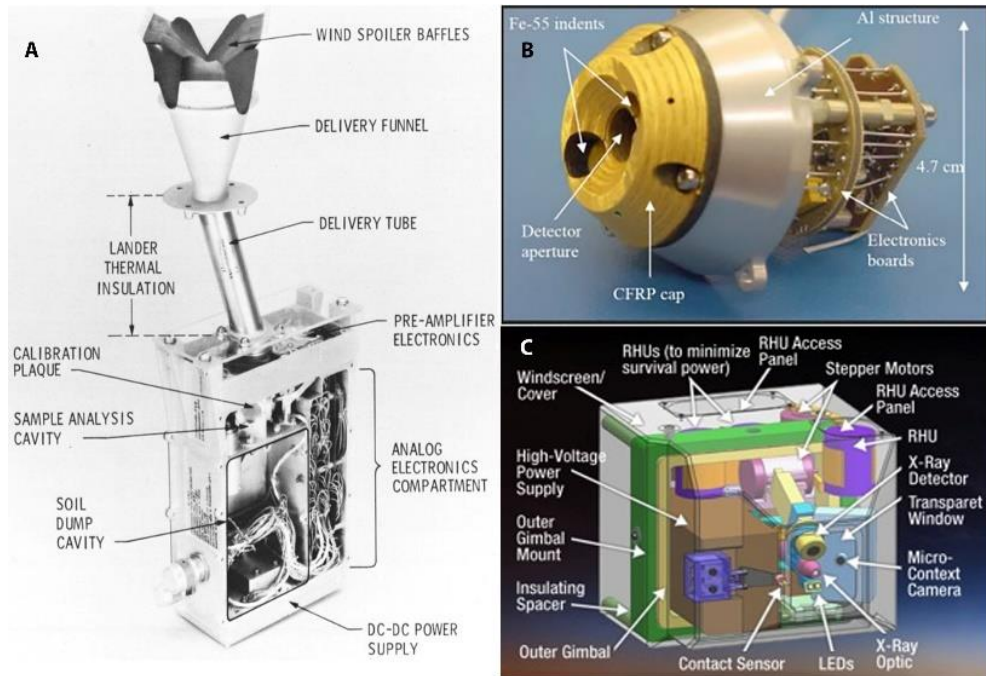


Figure 1.2. (A) Viking XRF instrument [105], (B) Beagle 2 spectrometer [112] and (C) PIXL arm mounted sensor head (Perseverance rover, Mars2020 mission) [113].

More than fifteen years after the second XRF on Mars on board the Beagle 2 lander, the Perseverance rover of the Mars2020 mission has carried a much-improved version of this instrument to Mars. The so-called PIXL (Figure 1.2 C) is mounted on the robotic arm of the rover. One of the most significant improvements of PIXL is that it can acquire high spectral resolution observations of rock and soil chemistry. Over a period of several hours, the instrument can autonomously raster-scan an area of the rock surface and acquire a hyperspectral map composed of several thousand of individual measured points. When correlated to visual image acquired by PIXL's camera, these maps reveal the distribution and abundance of chemical elements making up the rock. It weighs more than the other instruments previously shipped, ~7.9 Kg and its FWHM spectral resolution at Mn K $\alpha$  line is <0.16 KeV [115].

On July 20, 2021 NASA published the first PIXL's chemical maps on its website [116]. These maps correspond to the elements: Na, Si, Cl, Ti, Fe, Mg, P, K, Cr, Ni, Al, S, Ca, Mn and Zn.

### 1.3.1.2. Alpha Proton X-ray Spectrometer (APXS)

The Rutherford alpha backscattering technique was invented to obtain *in situ*, for the first time, the chemical composition of the lunar surface material during the NASA's Surveyor mission in 1967-1968 <sup>[14]</sup>. After the successful performance in the lunar surface, the backscattering spectroscopy technique became a common laboratory technique of chemical analyses. A similar instrument, but substantially miniaturized and improved in its performance, was used to obtain the chemical composition of Martian surface. The APXS was used for the first time during the Pathfinder mission, on board the Sojourner rover. Subsequently, it was used by the MER Spirit and Opportunity, and by the Curiosity rover.

The APXS is based on three different interactions of alpha particles from a radioactive source with matter: Rutherford backscattering (alpha mode), nuclear reactions of alpha particles with some light elements (proton mode), and generation of characteristic X-rays in the sample through ionization by alpha particles (X-ray mode). The alpha mode measures all elements heavier than helium. The X-ray mode measures all elements heavier than Na and the proton mode obtains complementary data for elements in the transition regions, that is for Na, Mg, Si and Al. Combining these three modes, it was possible to measure the abundances of all elements in the sample except for H and He <sup>[117]</sup>. Therefore, the geochemical information obtained by the APXS is more complete than that of XRF (elements lighter than Na are not detected).

The APXS of the Sojourner rover (Figure 1.3 A) consisted of two parts: the sensor head and the electronics box. The electronics box was located inside the rover in a thermally controlled box and its dimensions were about 70 x 80 x 65 mm. The sensor head was mounted on the outside of the rover, with a diameter of 52 mm and a length of 65 mm <sup>[14]</sup>. In this way, the mobility of the rover enabled the instrument to access a wider variety of samples and make the first direct geochemical analyses of rocks. The overall weight was 0.55 Kg, and the power consumption came to only 0.4W <sup>[49]</sup>. The detection limit of the measurements depended on the excitation mechanisms (alpha or X-ray), but in general, the LOD varied between 0.1 to 1 wt. % depending on the element <sup>[49]</sup>. Most of the APXS data were obtained during the nights, when the surface temperature was usually between -50 °C and -90 °C and, therefore, the X-ray mode reached the best resolution <sup>[14]</sup>. The X-ray detector operated without any cooling and achieved an FWHM (5.9 keV) of about 250 eV. The Pathfinder APXS used about 40 mCi of <sup>244</sup>Cm alpha radioactive sources for its operation, and the source emitted a monochromatic beam of 5.8 MeV <sup>[14]</sup>.

As both the Sojourner rover and the Carl Sagan Memorial Station lander were communicated to each other, the IMP provided the necessary

multispectral images of the scene to select the APXS targets. In this way, the rover traversed in a clockwise direction around the lander to make its elemental measurements on the Martian rocks <sup>[51]</sup>.

Many sampling sites, soils, and rocks around the lander were analyzed, such as the Barnacle Bill rock, which became the first rock ever analyzed on Mars (samples analyzed by the Viking landers were just soils) <sup>[49]</sup>. Preliminary APXS results indicated that Si had the higher abundance in all the samples, followed by Fe, Al, Mg, Al, Ca, S, Na, Ti, Cl and K, in decreasing order <sup>[117]</sup>. These elemental results for the rock were similar to those of the soils in the sites measured by the Viking landers. However, the soils measured by Sojourner had generally lower S and higher Cl abundance than the Viking ones. One of the greatest discoveries of the Pathfinder mission was the assumption of the fact that the surfaces of the rocks were covered by varying degrees of adhering dust or a weathering rind similar in composition to the dust. As the Martian soils had more S abundance than the rocks, the rocks probably were covered by a sulfur rind. This theory was proposed because the rock analyses contained appreciably more S than is normally accommodated in magmas or igneous rocks. Therefore, the different amounts of sulfur can come from weathering processes and from volcanic gases <sup>[117]</sup>. Nevertheless, the APXS method cannot discriminate between rock surface and adhering dust that was transported by the wind to rock surfaces. Recalibrated and post-normalized studies exposed that there were also potassium, magnesium and chromium in the Martian samples <sup>[49]</sup>. Based on those elemental results, scientists suggested that the rocks analyzed by Pathfinder had an andesitic to basaltic composition, indicating a certain degree of differentiation from mantle-derived magmas <sup>[51]</sup>.

However, as it happened with the elemental results of the Viking landers, there are not any molecular results to confirm exactly the mineral phases present in the rocks and the soils. In this way, there are several scientific articles that speculate about possible minerals present in the Martian surface by combining APXS and IMP data <sup>[118]</sup>.

A new development of the Pathfinder APXS instrument was used on the two MERs. This technique was part of the Athena Payload (Figure 1.3 B), which was mounted on the instrument deployment devices (IDD) of the two rovers. The high-resolution silicon drift detector was improved with an energy resolution of  $\sim 160$  eV at 5.9 keV <sup>[107]</sup>. The sensitivity of the instrument compared to the Pathfinder APXS was improved for the K lines of elements such as Ni, Zn and Br. This was because the APXS MER used  $\sim 30$  mm of distance between the sample and the detector to acquire the spectrum <sup>[119]</sup>. The temperature at which the best spectra resolution was achieved improved to approximately  $-40$  °C <sup>[119]</sup>. The MER APXS used six <sup>244</sup>Cm sources, its global mass was about 0.37 Kg (almost half comparing

the previous one), and the dimensions of the sensor head had 53 mm of diameter and 90 mm of length, whereas the dimensions of the electronics board were 170 x 100 x 10 mm<sup>3</sup> [107].

Figure 1.3 C shows the X-ray spectra comparison between Athena APXS (MER, in black) and the Pathfinder APXS spare instrument (MPF, in red). Analyses were performed on the same sample (andesite SSK1). The count rates increased by a factor of about 20 and the improvement of the energy resolution was best visible for the low elements Na to Si.

The first measurement with the Opportunity APXS was performed on a soil named Tarmac on the base of Eagle crater. This analytical technique detected in all the targets of Eagle crater Si, Fe, Al, Ca, Mg, Na, Ti, P, Cr, K, S, Cl, Mn, Ni, Z and Br, among others minor elements [120]. The elemental composition of the soils analysed in Meridini Planum was similar to those measured by Spirit and Pathfinder.

The APXS results obtained by Spirit were almost similar to the Opportunity ones. However, the rocks of the Columbia Hills, a range of low hills inside Gusev crater, were chemically distinct from the primitive basalts in the plains. The APXS revealed the important alterations of the rocks in an aqueous and acid environment, because even after the abrasion of outcrops and rocks to a depth of 9 mm there was a high abundance of salts as indicated by the elevated levels of Br, Cl, and S [121]. In addition, when one of Spirit's front-wheel motors failed, the rover had to drive backward and drag along the stuck wheel, creating a shallow trenches. Due to this mishap, the APXS detected pure silica in the trenches [122].

The following APXS to reach Mars was that of the Curiosity rover (Figure 1.3 D), which was further improved. The temperature range spectra was extended upwards to approximately -5 °C, whereas the MER APXS was only capable to function below -40 °C [119]. The FWHM (5.9 keV) at low temperatures improved from ~155 eV to ~140 eV. In addition, the sensitivity (signal per second) was improved of an overall factor of 3, because the spectra was achieved by a closer proximity between the sample and the detector (~19 mm) [119]. The MSL APXS used 30 mCi conventional sealed <sup>244</sup>Cm sources in addition to the alpha emitting 30 mCi <sup>244</sup>Cm to further boost the light Z elements above Fe by a factor of 2. Another advancement was that the internal Peltier cooler of the SDD can be activated, delivering a cooling of the X-ray detector by -35 °C, extending the operation time with respect to the Martian day [119].

Jake\_M, in the Bradbury Group, was the first rock analyzed by the Curiosity APXS instrument. This rock differed substantially in chemical composition from other known Martian igneous rocks, because it was alkaline (>15% normative nepheline) and relatively fractionated. Jake\_M was

compositionally similar to terrestrial mugearites, a rock type typically found in ocean islands and continental rifts. It could have been produced by extensive fractional crystallization of primary alkaline or transitional magma at elevated pressures, with or without elevated water contents. The discovery of Jake\_M suggested that alkaline magmas may be more abundant on Mars than on Earth and that Curiosity could encounter even more fractionated alkaline rocks [126].

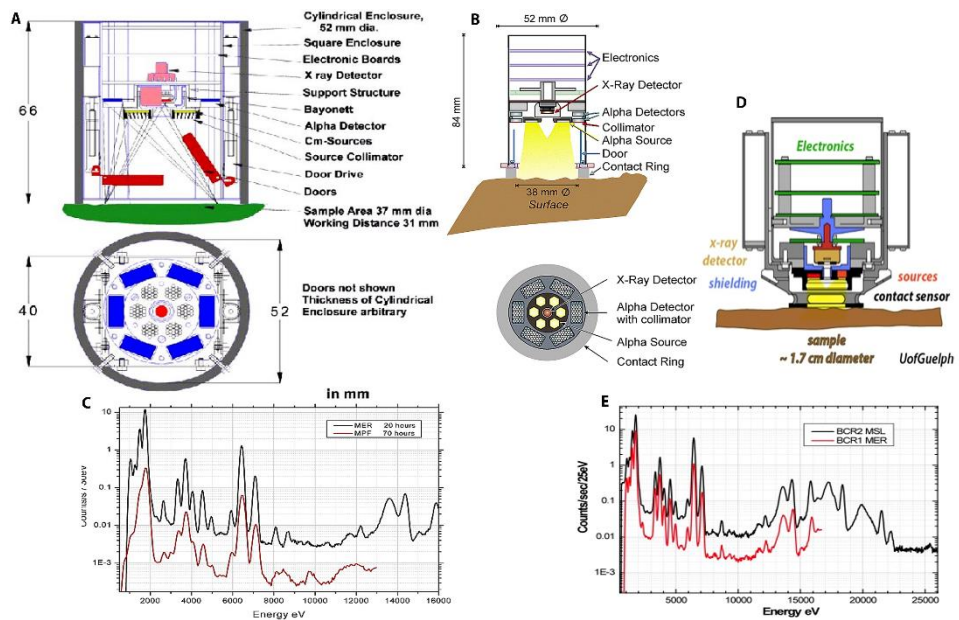


Figure 1.3. (A) APXS of the Mars Pathfinder Sojourner rover [123], (B) Athena APXS for the MERs, (C) X-ray spectra comparison between Athena APXS (MER, in black) and the Pathfinder APXS spare instrument (MPR, in red). Analyses were performed on the same sample (Andesite SSK1) [124], (D) APXS of the Curiosity rover [125], and (E) X-ray spectra comparison between MER (in red) and MSL (in black) APXS instruments on the same sample BCR reference material [125].

Figure 1.3 E shows the X-ray spectra comparison between the MER and the MSL APXS instruments on the same sample BCR reference material. The MSL energy range has been extended to about 25 keV, where additional Compton and Rayleigh backscattered X-ray peaks can be identified. The overall sensitivity (signal per time) is increased by about a factor of 3 for low Z elements and about 6 for high Z elements above Ti due to added 30 mCi sealed Cm244 sources.

### 1.3.1.3. Ion Selective Electrode (ISE)

The Phoenix Mars lander included four chemistry cells, which were known as the WCLs. WCLs took part of the MECA package of the lander. WCLs were designed to address the aqueous chemistry and reactivity of the Martian surface material. By measuring a variety of dust and regolith properties including pH, redox potential, solution electrical conductivity and

soluble ion species, it would be able to better understand Martian chemistry and mineralogy. Up until that moment, there was no research on ionic strength or compounds formed when Martian soil mixed with water. However, this knowledge is critical, both to help to understand the biological potential of Mars and to assess hazards that may be encountered by future human explores. In this way, the MECA package included the first ISEs carried to the surface of Mars. WCL was designed to measure the concentration of the cations  $\text{Ca}^{2+}$ ,  $\text{Mg}^{2+}$ ,  $\text{K}^+$ ,  $\text{Na}^+$  and  $\text{NH}_4^+$ , and the anions  $\text{Cl}^-$ ,  $\text{Br}^-$ ,  $\text{I}^-$ ,  $\text{SO}_4^{2-}$  and  $\text{NO}_3^-/\text{ClO}_4^-$  [127].

Perchlorate salts of calcium, magnesium- and sodium were detected in situ at the Phoenix landing site by the MECA instrument [128]. Unfortunately, ISEs have never again been taken to the surface of Mars to carry out wet analytical chemistry analyses.

#### **1.3.1.4. Laser-Induced Breakdown Spectroscopy (LIBS)**

APXS and XRF used abrasion tools (for example RAT in MER) to remove surface dust and analyze non-weathered material remotely. Later, another analytical instrument for analyzing clean samples remotely emerged, the LIBS instrument.

In this way, the ChemCam team of the Curiosity rover designed the first instrument with the capability to remotely clean and obtain depth profiles of samples by laser ablation. The ChemCam instrument combine the LIBS technique to provide elemental data, and a remote micro imager for context imaging the small LIBS points. In contrast to APXS and XRF, LIBS is a micro-destructive technique, so its use on laboratories has to be limited to samples that can be damaged. However, it offers several advantages in comparison with XRF and APXS. For example, LIBS allows characterizing quantitative elemental compositions including light elements like hydrogen and some other elements for which LIBS is uniquely sensitive (Li, Be, Rb, Sr, Ba, etc.). These abundances are measured from rasters of small observation points 350-550  $\mu\text{m}$  in diameter [129].

All the different sections of ChemCam are mounted at the top of the rover's mast or in the rover body, and the overall weight of the instrument is almost 11 kg. The ChemCam LIBS was designed to obtain major element compositions for rocks and soils within seven meters from the instrument to relative accuracy of  $\pm 10\%$ . Its laser beam is invisible (1067 nm) and the LIBS spectrum covers a range from the deep ultraviolet to the infrared [129].

ChemCam helps to sample geological targets before using other instruments that require longer measurement times (contact XRF/APXS or mass spectrometry). The main differences with the elemental techniques exposed above is that ChemCam observations take approximately 6 minutes once the instrument is ready. In contrast, other techniques need to

acquire, prepare, and then measure the samples. This process may take several sols. In addition, the Curiosity LIBS has very low LODs for certain elements, specifically the alkalis and alkaline earths. These LODs can be in the range of parts per million<sup>[129]</sup>.

ChemCam instrument has analyzed more than 2000 targets throughout the duration of the mission. Generally, ChemCam remote sensing data suggested that the Curiosity landing site was mostly composed by phyllosilicates, sulfates, hydrated sulfates, silica, carbonates and iron oxide minerals that were formed through some combination of fluvial, lacustrine, and aeolian processes <sup>[74]</sup>. For instance, the Yellowknife Bay was chemically basaltic but contained Mg-rich phyllosilicate (~20%), calcium sulfates (2-4%; anhydrite, bassanite) and a significant fraction of amorphous material (~30%).

The instruments of Curiosity are limited mostly to elemental composition rather than mineralogy. In order to fill this gap, the Perseverance rover is equipped with a remote mineral-identification instrument, the SuperCam instrument. SuperCam is a response to this requirement for remote mineralogy while preserving the ability to remove dust prior to making observations of nearby targets, and providing the same or better chemistry and high-resolution imaging as ChemCam.

SuperCam is provided with a number of versatile remote-sensing techniques that can be used at long distance. These include LIBS, remote time-resolved Raman and luminescence spectroscopies, and visible and infrared (VNIR) reflectance spectroscopy. As ChemCam, SuperCam is also equipped with a remote micro imager to high resolution color contact imaging. Moreover, SuperCam includes also a microphone that can be used as a stand-alone tool for environmental studies or to determine physical properties of rocks and soils from the shocks of LIBS.

The Perseverance LIBS is able to detect and quantify the same elements than that of Curiosity, which are ~ 25, and performs analyses with the same distance capability than the Curiosity LIBS (~ 7 m) <sup>[130]</sup>.

The laser used to achieve the plasmas provides up to 14 mJ and > 10 MW/mm<sup>2</sup> of 1064 nm photons per pulse. And the pulsed laser, which is the same one as for Raman, frequency doubled to 532 nm <sup>[130]</sup>. The LOD is different for each element, but it is around 1000 ppm for alkalis and alkaline elements <sup>[130]</sup>.

Perseverance LIBS has no significant analytical improvements over Curiosity LIBS. The current improvement is that the LIBS results are combined with those of the other SuperCam techniques for the same point analyzed, so that geochemistry and mineralogy are studied together. The SuperCam LIBS detected characteristic emission peaks for O, H and the

major constituent elements of smectites (Si, Fe, Mg, etc.) [131,132]. In addition, thanks to LIBS measurements it was possible to detect hydrogen in Jezero rocks, confirming the presence of various hydrated phases, such as Fe-rich clays, oxyhydroxide, hydrated Fe-carbonates and/or sulfates [133]. These minerals suggest aqueous alteration of the basaltic floor on the Jezero crater.

The first Chinese Mars exploration mission also aims to study the Martian surface composition remotely, determining the geochemistry and the mineralogy. The MarSCoDe is a remote sensing instrument suite on board the Tianwen-1 rover. This instrument includes a LIBS to provide elemental composition with a maximum distance of 7 m. For each LIBS measurement, the operation time of the MarSCoDe instrument ranges from 0.3 seconds to 4 minutes. The laser used is of 1064 nm, like the SuperCam one, and its spot is greater when the measurement is done at maximum distance of 7 m, being 0.25 mm. The LIBS spectral range goes from 240 to 850 nm approximately and the laser irradiance on the target with 23 mJ of energy and can soundly exceed 10 MW/mm<sup>2</sup> [134]. Up to now, no analytical results have been published so far.

The MarSCoDe instrument includes as well a Short Wave Infrared (SWIR) spectroscopy to conduct IR reflection analyses, and a telescopic micro imager for high resolution images of targets at different distances.

Unlike the analytical techniques seen previously, LIBS has not been evolving over time. The most remarkable advance of this technique in space exploration is that it will be combined with others to simultaneously study the geochemistry and mineralogy remotely, providing the opportunity to perform collaborative science and, in this way, extract more information.

### **1.3.2. *In situ* analytical techniques used on Martian surface for molecular analysis**

#### **1.3.2.1. Gas Chromatography – Mass Spectroscopy (GC-MS)**

GC has been one of the most frequently used *in situ* techniques for the chemical study of the atmospheres and surfaces of extraterrestrial bodies. This is because it offers great sensitivity and efficiency, is fast, requires low energy consumption, its format is robust, and it can be combined with spectrometric and spectroscopic devices, as well as with column instruments. GC coupled with mass spectroscopy (MS) is the most widely used methodology for the detection of organic matter. GC uses a thin capillary fiber known as column to separate different types of molecules, based on their chemical properties. Each type of molecule passes through the column at a different rate and the temperature of the column determines the rate of separation. Once processed by the GC, the molecules then enter into the mass spectrometer, which evaluates and identifies them by breaking each one into ionized fragments and detecting these fragments using their charge-to-mass ratio. This produced a unique profile of each compound that could be converted into a digital signal and could be transmitted to Earth <sup>[135]</sup>.

So far, 4 spacecrafts equipped with a GC have traveled to Mars: the Viking landers, the Beagle 2 lander and the Curiosity rover. In the future, the Rosalind Franklin rover will also carry a GC in its scientific payload.

The Viking landers were equipped, for the first time ever, with a biology laboratory. This instrument was designed to carry out three different experiments in order to search for evidence of living microorganisms in material sampled from the Martian surface. These three experiments were called: the PR, the LR and the GEX. The PR had the capability to measure the fixation of carbon dioxide or carbon monoxide into organic matter. The LR experiment was designed to detect metabolic processes by monitoring the production of volatile carbon compounds from a radioactively labeled nutrient mixture. The GEX monitored the gas exchanges in the head space above a soil sample which was either incubated in a humid environment or supplied with a rich organic nutrient solution <sup>[47]</sup>. The total mass of the biology laboratory was about 15.5 Kg, with a volume of 2.7 dm<sup>3</sup>. It was designed to consume an average power of 12 W, but it could consume up to 180 W <sup>[47]</sup>.

The changes in gas composition of the GEX were measured by GC-MS (Figure 1.4 A). This was the first time a GC-MS has been taken into space. The Viking GC-MS was designed to take a small soil sample, separate volatile elements using the GC, and analyze their composition with the MS. The GC-MS permitted the release of volatile organic material by

vaporization and thermal decomposition of more refractory substances through heating to various temperatures (50, 200, 350 and 500 °C) [136].

The GC-MS was carefully designed to maximize performance while minimizing weight and power requirements. In this way, the instrument was composed by three tubular sample ovens that after filling it with up to 100 mg of finely grounded (<300 µm) soil, they were tightly sealed into the gas line to assure quantitative transfer of the products. Moreover, the gas chromatographic column was specifically designed to tolerate water and carbon dioxide while transmitting a wide range of organic compounds. The electrically scanning magnetic sector mass spectrometer had a scan range from m/z 12 to 220 [136].

Each of the Viking landers analyzed two basaltic regolith samples using the TV-GC-MS with the goal of finding organic compounds. Both Viking landers detected chlorohydrocarbons, but these were thought to be terrestrial contamination from the solvents used to clean the instruments [137]. However, the Navarro-González et al. work demonstrated that perchlorates could react with organics in sediment samples during heating, causing the release of CO<sub>2</sub> and formation of chlorohydrocarbons. The results from this work suggested that the chlorohydrocarbons detected by the Viking landers may have been the result of organic matter indigenous to the Martian soil reacting with perchlorates during sample heating [137].

Previously to the classification of Martian meteorites, significant abundances of trapped gasses such as argon, krypton, xenon, nitrogen and carbon dioxide were measured in shock-altered phases of the achondritic meteorite Elephant Moraine (EETA) 79001 from Antarctica. Surprisingly, the composition of this trapped gas resembled the Viking data for the Martian atmosphere [138,139]. The work of Treiman et al. shows the close similarity between trapped Shergotty, Nakhla, and Chassigny (SNC) meteorites gas and the Martian atmosphere [140]. In addition, the geochemistry of the SNCs matches that of Martian materials analyzed on Mars [140]. Therefore, Viking results allowed to appropriately classify SNCs meteorites found on Earth.

After Viking landers, the Beagle 2 lander was also equipped with a GC-MS, which was part of the GAP instrument (Figure 1.4 B). GAP was designed to analyze samples of the Martian soil and atmosphere collected by the lander equipment, for evidence of chemical signatures of past biological processes. This instrument was located at the centre of the lander with a total mass of 5.7 Kg, including electronics [112].

The GAP instrument had three operation modes: quantitative analysis, qualitative analysis and precise isotopic measurement. GAP was designed to be fed either by direct atmospheric sampling or via one of the 12 ovens

mounted on the carousel. The material acquired by the sampling tools, in the form of soil or rock, was deposited into one of the ovens, which was then rotated to a tapped station to be connected with the GAP. The ovens withstand temperatures upto 1000 °C <sup>[112]</sup>.

In addition, the GAP instrument presented a great advantage over the GC-MS of the Viking landers: it could operate in one or two ways, either analysing gases directly or from a solid sample producing appropriate analyte gases by chemical processing. In this way, GAP was very flexible, being able to investigate processes of atmospheric evolution, the nature of gases trapped in rocks and soils, low-temperature geochemistry, etc <sup>[112]</sup>.

Regarding the MS, it was a 6 cm-radius magnetic sector spectrometer, which was designed to operate in both dynamic and static modes. It included six ion beam detectors. The main unit was a triple-collector array for the determination of N<sub>2</sub> (m/z 28, 29, 30), O<sub>2</sub> (m/z 32, 33, 34), and CO<sub>2</sub> (m/z 44, 45, 46). When operated dynamically, the MS should be able to measure stable isotope ratios to high degree of precision and accuracy. In contrast, static operation should allow high levels of sensitivity with some reduction in precision of the isotopic measurements <sup>[112]</sup>.

As has been described, the GAP instrument included improvements with respect to the Viking GC-MS. Unfortunately, as mentioned above, there are no real analytical results.

The following GC to reach the Martian surface was on board the Curiosity rover of the NASA's mission. In this case, a new and sophisticated instrument called SAM was designed (Figure 1.4 C). SAM addresses the chemical and isotopic composition of the atmosphere and volatiles extracted from solid samples. To do so, SAM combines three different techniques: the GC, the MS and the tunable laser spectroscopy (TLS). All of them provide complementary information on the same samples. The Curiosity rover's GC-MS has a more novel design than previous landers equipped with a GC-MS, since it also uses the capabilities of the TLS for the measure of methane, carbon dioxide and water vapor in the Martian atmosphere <sup>[141]</sup>.

SAM is a 40 Kg instrument suite located in the interior of the rover. It is able to measure a suite of light isotopes and to analyze volatiles directly from the atmosphere or from solid samples. In addition to measurements of simple inorganic compounds and noble gases, SAM conduct a sensitive search for organic compounds with thermal or chemical extraction from sieved samples delivered by the sample processing system on the Curiosity rover's robotic arm <sup>[141]</sup>.

The GC assembly contains six complementary chromatographic columns. The stationary phases of the columns are selected to provide a broad range

of detection capability for both light and heavy organic molecules for a range of molecular polarity and for inorganic volatiles. The proportional integral differential heater circuit provided by the SAM electronics independently heats each column. Only one column is operated at a time and each column provides a signal independent of the mass spectrometer. The MS can detect the major species contained in the sample down to the part per million level, with a  $10^5$  dynamic linear range <sup>[141]</sup>.

As samples of drilled rock or scooped soil are heated within SAM, components in them are vaporized and piped to the different instruments. The MS separates elements and compound by mass for measurement and identification. The GC separates the volatiles into various components for analysis. The TLS measures the abundance of various isotopes of carbon, hydrogen, and oxygen in atmospheric gases such as methane, water vapor, and carbon dioxide <sup>[142]</sup>. Many sources of organic compounds that SAM might detect could be exogenous, indigenous, or terrestrial contaminations because the exogenously sourced compounds are directly derived from in-fall meteorites, interplanetary dust particles and larger volatile-rich impactors such as comets or carbonaceous asteroids <sup>[141]</sup>. Fortunately, this instrument can differ isotopically between the possible biogenic or abiogenic origin of these compounds. Exogenous organic carbon is expected to share chemical characteristics of carbon-rich meteorites and interplanetary dust <sup>[143]</sup>. It is possible that abiotic photosynthesis and the presence of exogenous material occur in the current Mars. These events coat the planet's surface with small amounts of organic compound. Besides, abiotic photosynthesis could also generate methane, which would be detected by the TLS <sup>[143]</sup>.

Although the SAM instrument was not designed for *in situ* molecular analyses of the organogeochemistry in the Martian surface, it is important to highlight that in all of the analyzed solid compounds SAM detected chlorinated organic compounds above the instrument background levels <sup>[144]</sup>. While some authors argued that the source of these compounds may originate from reactions between oxychlorines and terrestrial organic carbon present in the instrument background, others have demonstrated that it is originated from indigenous organic carbon present in samples <sup>[144,145]</sup>. This finding provides again an evidence of the possible past habitability of Mars, as well as other evidence shown by the other rovers and landers described in this manuscript.

In addition, SAM detected volatiles (water, oxygen, sulfur dioxide, carbon dioxide, and chlorine) in interesting rocks such as Rocknest, which is in the Bradbury Group <sup>[146]</sup>. Samples of the Rocknest aeolian deposit were heated to  $\sim 835$  °C under helium flow and evolved gases analyzed by Curiosity's SAM instrument suite. H<sub>2</sub>O, SO<sub>2</sub>, CO<sub>2</sub>, and O<sub>2</sub> were the major

gases released. Deposition of fine-grained Fe or Mg carbonate was the likely source of much of the evolved CO<sub>2</sub>. Evolved O<sub>2</sub> was coincident with the release of Cl found. This fact suggested that oxygen was produced from thermal decomposition of an oxychloride compound. Carbon isotopes indicated multiple carbon sources and several simple organic compounds were detected [147].

SAM has generated many results and not all of them could be included in this review. In this way, as a summary it can be said that: Organic molecules are the building blocks of life, and they were discovered on Mars after a long search by the SAM instrument in several samples drilled from Mount Sharp and the surrounding plains. The organic molecules found were chlorobenzene, chloromethane, dichloromethane, dimethylsulfide, thiophene, methyl-thiophene, dithiolane, dithiapentane, dithiolane, trihiane, propanethiol, diathiapentane, methyl-naphthalene, benzoic acid and benzothiophene, among others [148,149].

The SAM instrument has found Mars's present atmosphere to be enriched in the heavier forms (isotopes) of argon, carbon, and hydrogen. This indicates that Mars has lost much of its original atmosphere and reservoir of water [150-152].

As can be seen, the SAM instrument has proved to be the best performing GC-MS in the history of gas chromatography on the Martian's surface. This is due to the fact that the Viking results are still being questioned and that the Beagle 2 lander did not manage to operate on Mars.

Following the important results obtained by SAM and based on the objectives of the Rosalind Franklin mission, the future Rosalind Franklin rover will also be equipped with a GC-MS. This combination will be part of the MOMA instrument (Figure 1.4 D), which will be the largest instrument in the rover. This instrument will also include a Laser Desorption coupled to the MS (MOMA LDMS). On the one hand, GC-MS will be used for volatile molecules characterization. Volatile compounds thermally evolved from solid samples in a pyrolysis oven will be separated by the GC and then analyzed individually with the MS. On the other hand, for non-volatile molecules, MOMA will use the LDMS. LDMS will produce gas-phase ions by high-intensity laser pulses applied directly to a crushed sample surface. These ions will be transferred into the MS and analyzed. Both modes of operation will use a common linear ion trap MS for detection and identification of molecular ions [153].

MOMA will achieve the Rosalind Franklin scientific objective to search for signs of past or present life on Mars. It will analyze a wide range of organic compounds that may be found in drill samples acquired up to 2 m below the Martian surface.

As can be seen, MOMA includes further advances over previous GC-MS. The most remarkable one is that it will be able to detect non-volatile organic molecules thanks to the LDMS.

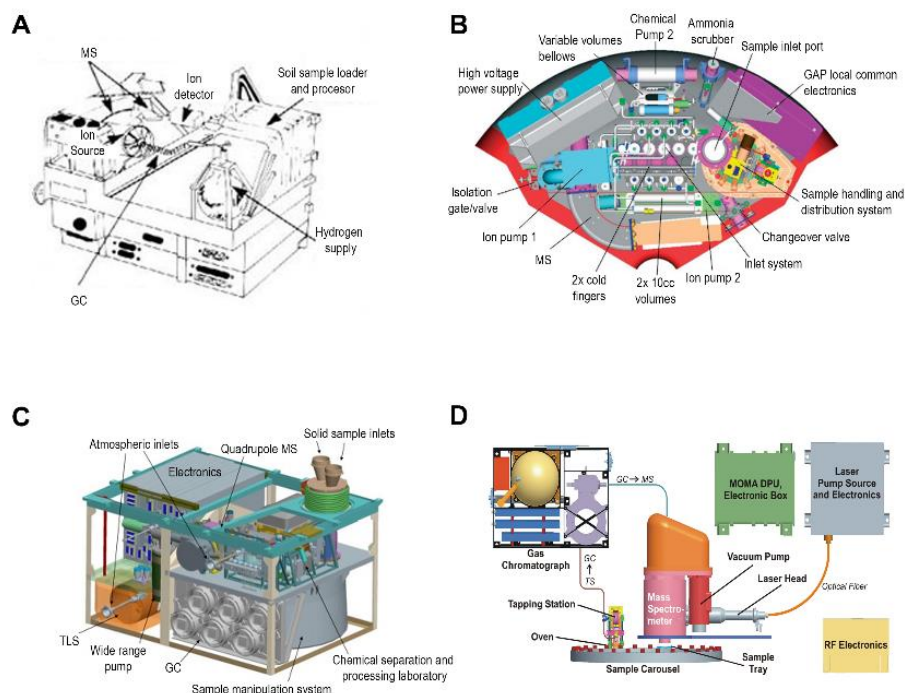


Figure 1.4. (A) Viking GC-MS <sup>[154]</sup>, (B) GAP instrument on board the Beagle 2 lander <sup>[112]</sup>, (C) SAM instrument of the Curiosity rover <sup>[155]</sup> and (D) MOMA instrument of the Rosalind Franklin rover <sup>[156]</sup>.

### 1.3.2.2. Thermal and Evolved Gas Analyzer (TEGA)

One of the main objectives of the Mars pole missions was to study the reservoirs and the behaviour of volatiles. In this way, the TEGA instrument was developed to meet this need, which was on board the Mars Polar lander and on board the Phoenix Mars lander. TEGA is used to study the gas evolved from heated samples that undergone decomposition or desorption. It is always used together with other analytical methods such as MS, Fourier transform spectroscopy, GC, or optical *in situ* evolved gas analysis, among others. Although it was designed primarily to study the volatiles in the Martian atmosphere, it has been also used to analyze the reservoirs of water, CO<sub>2</sub> and some minerals, such as carbonates, in the Martian soils. As samples have to be heated, TEGA is considered as a destructive analytical technique and performs its analysis inside the body of the lander, so it does not have the advantage of working remotely.

The Mars Polar lander of the Mars Surveyor mission was the first spacecraft to deliver a TEGA (Figure 1.5 A) to the Martian surface in order to measure the volatile content of the Martian soil at depth. Specifically, it was used to determine the water and carbon dioxide content, to identify other minerals and to detect oxidizing compounds in the soils.

The instrument was composed of three main components: the main electronics, which are located in the payload electronic box, the auxiliary electronics box, which is located close to the instrument to reduce noise, and the sensor head. The sensor head included (1) eight single use thermal analyzer modules to receive soil samples and perform differential scanning calorimetry (DSC) over the temperature range of Mars ambient to 950 °C; (2) a gas handling system to distribute and control carrier or calibration gas; (3) an oxygen sensor to detect evolved oxygen; and (4) a tunable diode laser spectrometer to determine the amount of water vapor and carbon dioxide evolved from the DSC ovens.

Each thermal analyzer had two identical ovens, one for the sample and one (empty) for a reference. A sample of soil from depth would have been acquired with a robotic arm and deposited into a hooper over the selected thermal analyzer. Then, the DSC would have controlled the first temperature that would have been ramped up and down around the freezing point to detect the abundance of water ice by the influence of ice's latent heat on the power required to heat the sample. The sample would then have been heated up to 950 °C with nitrogen. Subsequently, the TEGA would have analyzed the evolved gases as the ovens were heated to provide knowledge of correlated gas release associated with the phase transitions. TEGA would have determined water and carbon dioxide contents via a high-resolution tunable diode laser absorption spectrometer. Mineral phase transformations would have been calorimetrically detected while evolution of absorbed water and decomposition products would have been carried to the oxygen sensor and finally into the high-resolution tunable diode spectrometer. This spectrometer would have enabled the quantitative determination of the volatile content of the sample, and may constrain the isotopic ratios of the evolved gases. The total mass of TEGA was of 5.71 Kg and its power requirements varied as a function of ambient temperature, the mode in which it is operating, and the temperature of the ovens. It ranged from 9.6 W with all the heaters off to a maximum of 78.0 W with all the heaters operating. Each TEGA experiment would have probably taken 2 days and samples would have been acquired from depths of up to 0.5 m with the robotic arm <sup>[157–159]</sup>.

The combination of DSC and EGA was particularly powerful, since volatile release can be characterized in a correlated way by both components. Unfortunately, the last contact with the vehicle was when it was to enter into the Martian atmosphere, so it could not do any experiment.

The next spacecraft that included a TEGA instrument in its scientific payload was the Phoenix lander (Figure 1.5 B). This one, unlike the Mars Polar lander, did operate on the Martian surface and obtained important results. This instrument was based on the Mars Polar lander's TEGA, but included some improvements. The most notable improvement was that the Phoenix TEGA was a combination of high temperature furnace to heat the samples and a mass spectrometer to determine the amount of volatiles.

The instrument was composed of two main components: the electronics, which were located in the lower section of the EGA package, and the sensor head, which was located in the upper section of the EGA package and it contained the thermal analyzer and the MS. As in the previous TEGA, the thermal analyzer was a calorimeter with a set of eight small ovens. Each one was used once and accepted the sample delivered by the robotic arm. The operation process is exactly the same as for the previous TEGA. However, when the evolved gases were formed, they were transported to the MS by a carrier gas of high-purity nitrogen, which was used to measure the mass and concentrations of specific molecules and atoms in a sample. The MS was sensitive to detection levels on the order of 10 parts per billion, a level that may detect tiny quantities of organic molecules potentially existing in the ice and soil. The MS was a miniature magnetic sector instrument controlled by microprocessor-driven power supplies. One feature was the gas enrichment cell that increased the partial pressures of the noble gases in an atmosphere sample by removing all the active gases, carbon dioxide, and nitrogen, to improve the accuracy of their isotopic ratio measurements <sup>[160]</sup>.

The total mass of the Phoenix TEGA instrument was the same of the other TEGA, but the average of power consumption was of 13 W, less than the other. Its dimensions were 24 x 23 x 18 cm <sup>[160]</sup>.

In its work on Mars, TEGA indicated carbonate thermal decomposition at both low and high temperatures. The low temperature thermal decomposition was consistent with the presence of magnesite or siderite, their solid solution, or any combination of both. The high temperature thermal decomposition was consistent with calcite, dolomite, or ankerite, or any combination of those phases. Those carbonates could be there due to the inheritance of ejecta from the Vastitas Borealis and Scandia region, inherited from material deposited by eolian processes, or formed *in situ* at the site where they were discovered. If this last option was the correct one, the soil would have had the suitable pH for microbial activity <sup>[161]</sup>.

In order to predict salt precipitation sequences during freezing or evaporation of brines, equilibrium models were developed with data about soluble perchlorates, sulfates and carbonates in Martian soils. On the one hand, one of those models was proposed by Toner et al. <sup>[162]</sup>. They built a

Pitzer model in the Na-K-Ca-Mg-Cl-SO<sub>4</sub>-ClO<sub>4</sub>-H<sub>2</sub>O system at 298.15 K using compilations of solubility data in ternary and quaternary perchlorate systems. This model meant an improvement over the FREEZING CHEMISTRY (FREEZCHEM), which was originally designed to simulate salt chemistries and freezing processes at low temperatures (-45 to 25 °C) and 1 atm pressure <sup>[163]</sup>. Over the years, the FREEZCHEM model has been broadened in order to explore cold biochemical processes on Earth, Mars, and Europa <sup>[163]</sup>. Both models, Pitzer and FREEZCHEM, predicted the early precipitation of KClO<sub>4</sub>, hydromagnesite, gypsum, and epsomite, followed by dehydration of epsomite and gypsum to kieserite and anhydrite, respectively <sup>[164]</sup>. The Pitzer model predicted also that at low residual water contents the halite, NaClO<sub>4</sub>·H<sub>2</sub>O, and Mg(ClO<sub>4</sub>)<sub>2</sub>·6H<sub>2</sub>O would precipitate, whereas the FREEZCHEM one predicts that halite and NaClO<sub>4</sub>·H<sub>2</sub>O would never precipitate. According to the latter model, the salts found by the WCL instrument of the Phoenix lander were not formed during evaporation near 298.15 K, but during possible freezing remains. Other models also predicted the freezing of calcite, meridianiite, MgCl<sub>2</sub>·12H<sub>2</sub>O, NaClO<sub>4</sub>·2H<sub>2</sub>O, and Mg(ClO<sub>4</sub>)<sub>2</sub>·6H<sub>2</sub>O at the eutectic (209K) point <sup>[165]</sup>.

### 1.3.2.3. Mössbauer Spectroscopy (MBS)

Mössbauer spectroscopy is an extremely useful tool for quantitative analysis of Fe-bearing compounds and is therefore particularly used for *in situ* studies on the surface of Mars.

The Mössbauer effect provides information about the iron content of mineral samples by measurement of the Doppler shift in the velocity (or energy spectrum) of gamma-rays. These rays are emitted by a stationary target bombarded by an isotopically equivalent gamma-ray source. The absorption characteristics of the atoms give different spectra depending on their valence state and bonding. The signal strength is quantifiable, so the instrument can characterize the mineralogical composition of the rocks and soils. Its ability to measure valence states provides important information about oxidation and a detailed understanding of the weathering environment <sup>[166]</sup>.

MBS leaves a footprint on the sample (in the order of cm). This technique is temperature sensitive as Mössbauer spectra may change drastically with temperature. This fact helps in determining the nature of the Fe-bearing phases. Therefore, Mössbauer measurements are performed at different temperatures, including both the highest (during the day) and the lowest (during the night) temperatures <sup>[166]</sup>. Besides, the MBS spectrometers that are built with backscatter measurement geometry require no sample preparation, a factor important for *in situ* planetary measurements.

So far, the Beagle 2 lander and the two MER rovers were equipped with a MBS. MB's results were helpful to interpret the results of other techniques, such as APXS or XRF and vice versa.

MIMOS II (Figure 1.5 C) was the miniaturized MBS developed for the two MER rovers. The MER MBS was split into two parts: the detector head, which was mounted on a robotic arm, and the printed circuit board, which had the circuitry for the instrument control, data acquisition and storage, and was located in the rover's warm electronics box. The detector head was composed by the  $^{57}\text{Co}$  radiation source and shielding, velocity transducer, and silicon PIN diode radiation detector. The total weight of the MIMOS II was about 500 g (400 g for the detector head and 100 g for the printed circuit board) and the dimensions of the instrument were about 90 x 50 x 40 mm for the sensor head, and 160 x 100 x 25 mm for the electronic board. The power consumption was in the order of 2 W. The instrument was fully tested over the expected temperature range, which was from -120 to 40 °C for the sensor head, and from -50 to 40 °C for the electronics board [167].

The MIMOS II measurements were done by placing the detector head against the rock or soil in order to minimize possible microphonic noise on the velocity-modulated energy of the emitted gamma-rays. The field of view of the instrument was of 1.5 cm of diameter and the average information depth was 200-300  $\mu\text{m}$ , assuming basaltic rock composition. The source intensity of about 300 mCi at launch gave a 6-12 hours of time for acquisition a standard MBS spectrum on Mars, depending on the total Fe content and which Fe-bearing phases were present [167].

The Opportunity MBS revealed four iron-bearing targets at Eagle crater: jarosite and hematite rich outcrop, hematite rich soil, olivine-bearing basaltic soil, and pyroxene-bearing basaltic rock [168].

The Spirit MBS identified eight Fe-bearing phases: olivine, pyroxene, ilmenite, magnetite, nanophase ferric oxide, hematite, goethite and a  $\text{Fe}^{3+}$  sulfate. It was seen that the  $\text{Fe}^{2+}$  from olivine and pyroxene was higher in moderately altered materials than in pervasively ones. Besides, MIMOS II allowed to detect the highest abundance of ilmenite and hematite in the less altered rocks. In contrast, goethite was found specially in Clovis, one of the most altered rocks. Goethite is a mineralogical evidence for aqueous processes because it has structural hydroxide and it is formed under aqueous conditions. Figure 1.5 D represents the Mössbauer spectrum of the Clovis rock, in which the following minerals appear: hematite, silicate, goethite and a nanophase-oxide. Finally, regarding the results provided by MIMOS II, it was seen that every soil measured in Columbia Hills had a high concentration of iron sulfate and magnetite [67,169].

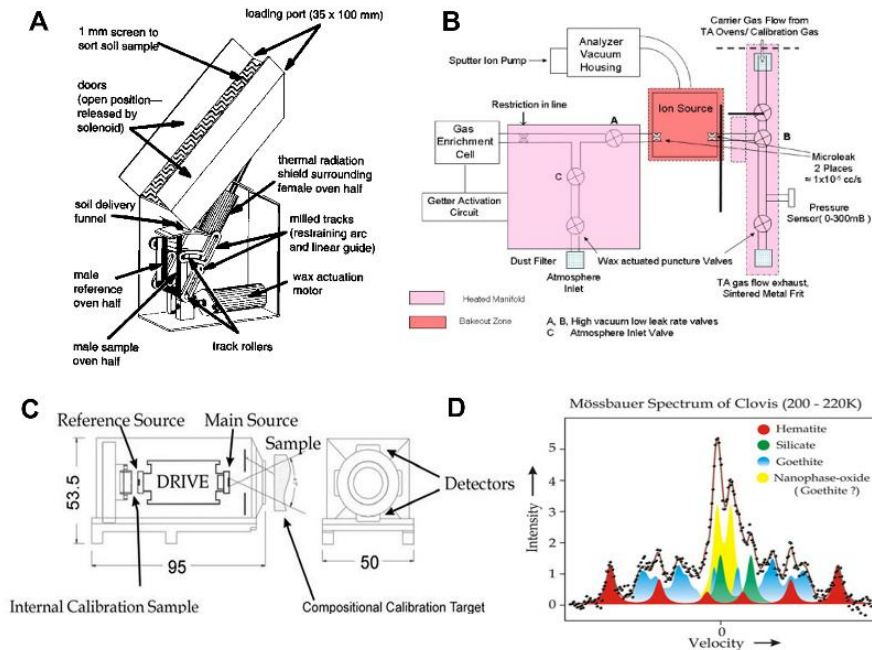


Figure 1.5. (A) Mars Polar TEGA [159], (B) Phoenix lander TEGA [160], (C) MIMOS II instrument [170] and (D) Mössbauer spectrum obtained by the MIMOS II instrument of the Spirit rover in the Clovis rock of Mars [169].

The Beagle 2 MBS was also divided into two parts, the detector head assembly and the electronics. The detector head assembly was located on the body of the rover and contained the radioactive sources, whereas the electronics were located at the base of the arms in the relatively warmer environment of the lander base. Its total weight was 541 g (438 g for the detector head and 102 g for the electronics) and the dimensions of the instrument were about 90 x 50 x 45 mm for the detection head, and 160 x 100 x 30 mm for the electronics. The weight and the dimensions of this MBS are quite similar to those of the MIMOS II. The total consumption was 3 W, higher than MIMOS II. Besides, the instrument was designed to use gamma-rays from the decay of  $^{57}\text{Co}$  to  $^{57}\text{Fe}$ . The footprint of the instrument was to be circular, with a diameter of about 1.5 cm, like MIMOS II, and the average information depth was of the order 100-200 mm, greater than MIMOS II [166].

Unfortunately, as the lander of Mars Express mission was unsuccessful, the Beagle 2 MBS did not make any measurement and there are no real analytical results to compare with those obtained by the MBS of the MER rovers.

### 1.3.2.4. X-ray Diffraction (XRD)

XRF, APXS and LIBS chemical data have been collected *in situ* by robotic spacecraft. These highly successful experiments provided critical constraints on the elements present in the targets, helping us to understand surface processes and planetary evolution. However, the mineralogy remained unknown. In this way, the MSL mission considered to incorporate simultaneous XRD instrument with XRF capabilities in order to analyze the mineralogy and the elemental composition of the Martian soils. This instrument was called CheMin (Figure 1.6 A).

CheMin is located inside the main body of the rover, with a total mass of ~10 Kg, dimensions of 30 x 30 x 30 cm and a power consumption of ~40 W. This instrument returns quantitative powder XRD from scooped soil and rock samples, delivered to it by the Sample Analysis/Sample Processing and Handling (SA/SPaH) and Collection and Handling for *In Situ* Martian Rock Analysis (CHIMRA) systems. Samples of 45-65 mm<sup>3</sup> from material sieved to <150 µm are delivered through a funnel to one of the 27 reusable cells arrayed on a sample wheel (Figure 1.6 B). The sample cells are comprised of 8 mm diameter discs with 7 µm thick Mylar or Kapton windows spaced 170 µm apart. Within this volume, the sample is shaken by piezoelectric vibration a sonic frequency, causing the powder to flow past a narrow, collimated X-ray beam in random orientations over the course of an analysis. In this way, diffraction patterns exhibiting little to no preferred orientations can be obtained even from minerals normally exhibiting strong preferred orientation such as phyllosilicates <sup>[114,171]</sup>.

During an analysis, a collimated X-ray beam from a micro focus X-ray tube source (Co anode and produces X-radiation from a 50 µm diameter spot) is directed through powdered or crushed sample material. Then, an X-ray sensitive CCD imager is positioned on the opposite side of the sample from the source and directly detects X-ray diffracted by the sample. The tube is normally operated at 28 KeV with a filament current of 1.5 A and cathode output of 100 µA. The detector is an E2V CCD-244 X-ray sensitive 600x600 pixel imager. Each CheMin analysis can take up to 10 hours of time over two or more Martian nights. For typical well-ordered minerals, CheMin has a LOD of < 3% by mass, an accuracy better than 15% and a precision better than 10% of the amount present for phases that are in a concentration higher than 12% <sup>[114,171]</sup>.

CheMin has analyzed more than 19 drilled and 3 scooped samples to date, providing a wealth of mineralogical information. Figure 1.6 C shows the Curiosity traverse including the drilling points. To date, the major basaltic minerals identified by CheMin include Mg-Fe-olivines, Mg-Fe-Ca-pyroxenes, and Na-Ca-K-feldspars, while minor primary minerals include magnetite and ilmenite. CheMin also identified secondary minerals formed

during alteration of the basalts, such as calcium sulfates (anhydrite and bassanite), iron oxides (hematite and akaganeite), pyrrhotite, clays and quartz. These secondary minerals form and persist only in limited ranges of temperature, pressure, and environment chemical conditions, and provide clues about the habitability of Mars [172].

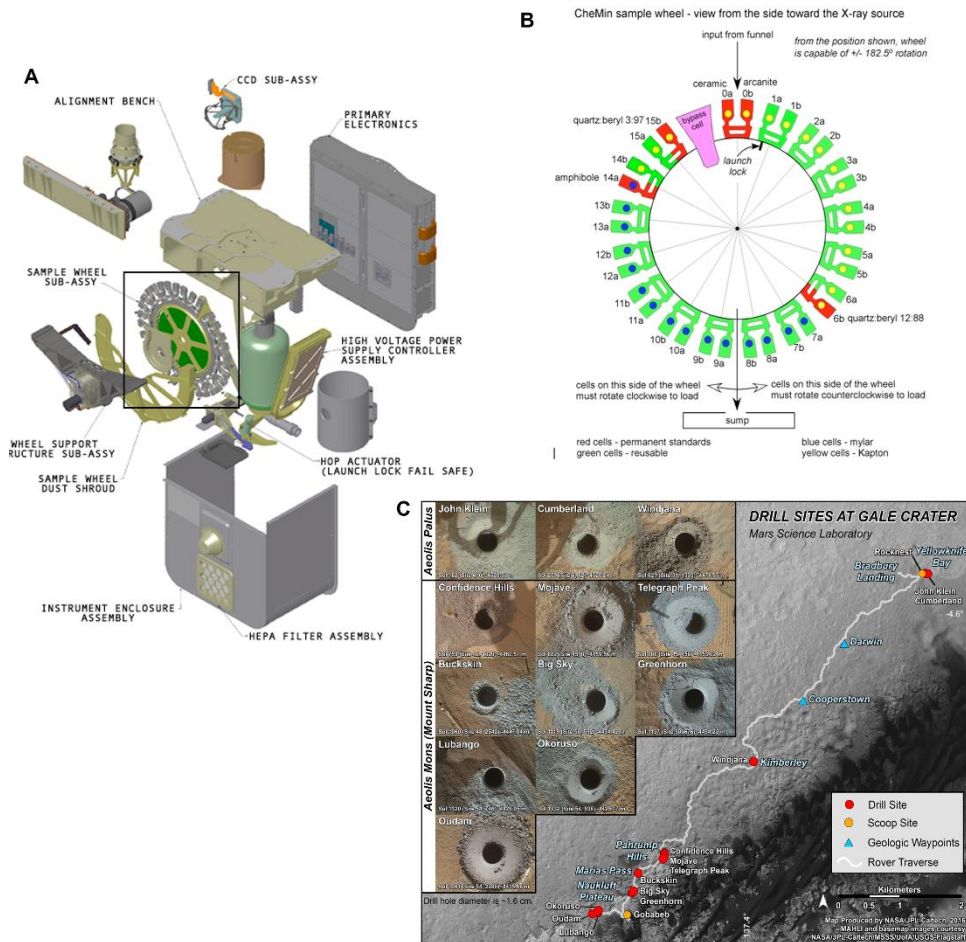


Figure 1.6. (A) CheMin XRD instrument, (B) CheMin sample wheel [114] and (C) Curiosity traverse including the drilling points [173].

### 1.3.2.5. Raman Spectroscopy

Although it is an old-known technique, the benefits of using Raman spectroscopy for the laboratory study of mineralogy and organic compounds present in precious geologic samples has been widely recognized in recent years. This technique allows to analyze samples without destroying them, as it is a non-destructive technique. Moreover, as its portability is also well established in the scientific community, it has become the new key technique to be included in the scientific payload of

the current and future rovers for space surface analysis. These are the Perseverance, the Rosalind Franklin and the MMX rovers.

The Perseverance rover is equipped with two Raman spectrometers located in different instruments: SuperCam, which focuses on general mineral detection with some organic capabilities, and SHERLOC, which focuses on organics with some mineral capabilities.

The SHERLOC instrument (Figure 1.7 A) combines high resolution imaging with ultraviolet (UV) resonance Raman and native deep UV fluorescence spectroscopy in order to identify potential biosignatures and understand the aqueous history of the Jezero region, the landing site of the Perseverance rover. This instrument is located in the arm of the rover and its total mass is of 6.85 Kg <sup>[174]</sup>.

The spectrometer uses a 248.6 nm deep UV excitation laser. This laser generates characteristic Raman and fluorescence photons from the Martian surface within the 100  $\mu\text{m}$  laser spot and with a resolution of 0.31 nm. The laser is co-boresighted to the Autofocusing Contextual Imager (ACI) to facilitate a raster scan across the surface and to produce a chemical and organic maps of the sample. These spectral maps reveal more information than a single spectra by itself by relating minerals and chemicals to textures in a way simple bulk analysis does not. The Raman range goes from 810 to 4000  $\text{cm}^{-1}$ , whereas the fluorescence range goes from 274 to 354 nm. The SHERLOC instrument is designed to detect the bulk organics with a sensitivity of  $10^{-5}$  to  $10^{-6}$  w/w over and 7 x 7 mm spot. Whereas, the fine scale organics should be detected with a sensitivity of  $10^{-2}$  to  $10^{-4}$  w/w spatially resolved at <100  $\mu\text{m}$ . Finally, the organics and astrobiologically relevant minerals should be detected and classified to <100  $\mu\text{m}$  resolution <sup>[174]</sup>. SHERLOC is capable of correlating detected classes of organics with morphology (widths and shapes) to determine whether morphological candidates for microfossils, filaments, or stromatolitic layering are potentially biogenic (Figure 1.7 A) <sup>[175]</sup>. SHERLOC has already made some observations of different types of organics embedded within different lithologies, such as sulfates, carbonates, phosphates and amorphous silica mixtures. Although assignment of fluorescence signatures to specific organic molecules is not conclusive, it is believed to have been found 1- and 2-ring aromatic organics <sup>[176]</sup>.

As mentioned above, the SuperCam instrument of the Perseverance rover is equipped with the first remote time-resolved Raman and luminescence spectrometer in space. Remote Time-Resolved Raman spectroscopy requires the use of a telescope, a pulsed laser, and a time-gated, intensified detector to provide sufficient signal to noise (Figure 1.7 B). The intensified signal is projected in the form of multiple spectral traces onto a single CCD to maximize the product of spectral range and resolution. Moreover, a high-

voltage power supply capable of operating in the Mars environment has been miniaturized, so that it mounts directly beneath the spectrometer [177,178].

The SuperCam Raman can analyze the sample from a measurement distance of 2 to 7 m with its visible laser (532 nm), which laser spot size can reach several mm in diameter. Its FWHM is of  $12\text{ cm}^{-1}$  and the Raman range goes from  $150$  to  $4400\text{ cm}^{-1}$ , due to the fact that  $0$ - $150\text{ cm}^{-1}$  range is cut by filters blocking the Rayleigh-scattered laser light. The total mass of the SuperCam instrument is about 10.4 Kg, including the mast unit (MU), the body unit (BU) and the calibration targets. This is a higher weight than SHERLOC, but it should be noted that SuperCam includes Raman, LIBS and IR spectroscopies [177,178]. There are already results from the SuperCam Raman spectrometer, which was able to identify carbonate-absorption bands and olivine, among other common compounds [179].

The two Mars 2020 Raman spectrometers are fundamentally different. While SuperCam avoids most fluorescence interferences to the Raman signal by time gating, SHERLOC avoids these interferences by operating in the deep UV where fluorescence does not occur. The SHERLOC spectral window starts at  $810\text{ cm}^{-1}$ , missing most oxides and silicate structural signatures, which are the compound SuperCam focuses on.

The Rosalind Franklind rover will be also equipped with the RLS. The RLS (Figure 1.7 C) will provide geological and mineralogical information on igneous, metamorphic, and sedimentary processes, especially regarding water-related interactions. In addition, RLS can contribute to the tactical aspects of exploration by providing a quick assessment of organic content before the analysis with MOMA.

The RLS instrument is composed by the spectrometer unit, the optical head unit, and the electronic control unit, which also will include the laser excitation source. This Raman spectrometer will use a continuous excitation laser of 532 nm with a spot size of  $50\text{ }\mu\text{m}$ . Its spectral range will go from  $150$  to  $3800\text{ cm}^{-1}$  with a Raman resolution between  $6$  and  $8\text{ cm}^{-1}$  in the fingerprint spectral region. To reduce noise and improve the scientific performance, the CCD will operate in the range  $-10$  to  $-40\text{ }^{\circ}\text{C}$ . This temperature will be guaranteed by a current-controlled thermoelectric cooler system that will be placed in contact with the detector [180–182].

In contrast to SuperCam, which performs the measurements remotely and without any sample preparation, RLS will work on the inside the rover's analytical laboratory drawer. The samples will be collected on the surface and subsurface (down to 2 m) with the Rosalind Franklin rover drill. Then, a rock crusher will reduce the sample to particulate matter that will be deposited in a small, refillable container. Finally, a carousel will place the



stabilized during RAX operations to an accuracy of  $\pm 0.1$  K by a thermoelectric module. Its spectral range will reach up  $4000\text{ cm}^{-1}$  with a resolution of  $10\text{ cm}^{-1}$ . In order to perform in situ measurements at different locations on Phobos, RAX will have an integrated autofocus mechanism, which will be used for precisely focusing of the laser beam onto the ground below the rover. Moreover, in order to avoid the influence of ambient lights, the measurements of the RAX instrument will be performed during Phobos nights <sup>[185]</sup>.

### 1.3.2.6. Infrared (IR) Spectroscopy

Visible to near IR spectroscopy has been used from Mars orbit for nearly two decades. However, these spectrometers provide large-scale infrared information and generate large-scale images. Regarding surface located analysis, the MER rovers, the Curiosity rover, the Perseverance rover, the Tianwen-1 rover, the Rosalind Franklin rover and the MMX rover were, are and will be equipped with an infrared spectrometer. Unlike the IR spectrometers of the orbiters, the rover ones are point spectrometers and are designed to analyze the mineralogy of the Martian soils and rocks on a much smaller scale, so more detailed information can be obtained.

The first IR spectrometer reaching the surface of Mars was the Miniature Thermal Emission Spectrometer (Mini-TES) of the MER rovers. Mini-TES was a miniaturized version of the Mars Global Surveyor TES, which was used to map the mineral composition of the Martian surface by scanning the thermal emissions. In this case, Mini-TES measured the different spectrums of IR light, or heat, emitted from different minerals in rocks and soils. It was a Fourier Transform Spectrometer (FTS) that covered the spectral range from 5000 to 29000 nm ( $339.50$  to  $1997.06\text{ cm}^{-1}$ ) and had a spectral resolution of  $10\text{ cm}^{-1}$  <sup>[186]</sup>.

Almost all of the Mini-TES instrumentation was located in the body of the rover at the bottom of the rover neck, its dimensions were  $24 \times 16 \times 16\text{ cm}$  with a total mass of 2.4 Kg and its power consumption ranged from 0.3 W (daily average) to 5.6 W (operating). Unlike other instruments, Mini-TES possessed an uncooled detector (Deuterated Triglycine Sulphate, DTGS), which substantially reduced the complexity of its fabrication, and reached the scientific requirements for investigations. Its telescope was a compact 6.35 cm diameter Cassegrain telescope with an intermediate stop before the afocal section that provided excellent stray light rejection and efficient baffling. The instrument operational temperature range went from  $-10$  to  $30\text{ }^{\circ}\text{C}$  and the diurnal variation of temperature on the surface of Mars excluded night operation when the temperature is too low <sup>[186]</sup>.

The scene around the rover was imaged by Mini-TES at two different spatial scales, creating 3-dimension hyperspectral image cubes. These

remote mineralogical measurements, together with the morphologic and color data from the Pancam, were used to direct the rover to specific targets of interest for detailed study by the full suite of the rover instruments. The mineralogical mappings of Mini-TES met these three requirements: (1) radiometric accuracy and precision necessary to uniquely determine the mineral abundances in mixtures to within 5% absolute relative presence, (2) spectral resolution sufficient to uniquely determine the mineral abundances in mixtures to within 5% relative presence, and (3) spatial resolution  $\leq 25$  cm at 10 m of distance necessary to resolve and identify individual rocks 0.5 m in size or larger in the rover near field <sup>[186,187]</sup>.

The Mini-TES results of the Opportunity rover confirmed the presence of sulfates, hematite, glasses, oxides, feldspar, olivine and pyroxene in all the analyzed targets. The bands of the sulfates infrared spectra were decomposed in order to identify the mixture of sulfates the Martian samples were composed by. In this way, it was suggested that gypsum, bassanite, epsomite, kieserite, glauberite and jarosite could be part of Martian soils <sup>[188]</sup>.

On the other hand, the Mini-TES observations of the Spirit rover discovered a pure silica spectrum. This fact was one of the strongest evidence for concluding that Mars was much wetter than it was on the moment of the measurements, since the processes that could lead to such a concentrated silica require the presence of water <sup>[122]</sup>. Moreover, the Mini-TES indicated that rocks of Gusev crater were olivine-rich basalts with varying degrees of dust and other coatings. The soils were principally composed of pyroxene, sodic to intermediate plagioclase and andesine. However, undisturbed soil spectra showed evidence for minor carbonates and bound water, being the Mg-carbonate the mineral which most fitted with the spectra. Combining the results of all the instruments, it could be concluded that rocks and soils of Gusev crater had a similar composition and that the soils were primarily formed from mechanically abraded ground and then mixed with materials coming from other sources such as any aqueous-altered materials <sup>[189]</sup>. As the Opportunity found, the coatings analyzed by Spirit were related to sulfates, specially with Mg and Ca-sulfates and even Fe-sulfates <sup>[190]</sup>.

It is also considered a suitable technique for gas analyses as the majority of gaseous chemical substances possess their fundamental vibrational absorption bands in the mid-IR spectral region (2000-10000 nm). Moreover, small planetary instruments are not well suited to low abundance of H<sub>2</sub>O and confuse H<sub>2</sub>O, NH<sub>3</sub> and CH<sub>4</sub> isotopic species that overlap in mass number. For this reason, the SAM instrument of the Curiosity rover includes a TLS <sup>[191]</sup>.

The TLS of the Curiosity is based on IR laser absorption within a multipass sample cell to record ultra-high resolution spectra of selected tunes of targeted species. The method is very sensitive (parts per million or parts per trillion), direct, non-destructive, easy to calibrate and unambiguous in species identification and isotopic ratio determinations without interference [141].

In this way, TLS complements the measurements of the MS and focuses on specific measurements for which it offers increased precision. The combination of GC-MS with TLS makes the SAM instrument of the Curiosity rover the instrument with the most significant findings. In order to achieve the objectives of the TLS, two semiconductor continuous-wave laser sources scan over three wavelength regions chosen to target gas abundances and isotopic ratios. These are a near-infrared (NIR) tunable diode laser at 2.78  $\mu\text{m}$  for carbon dioxide and water, and an interband-cascade (IC) laser at 3.27  $\mu\text{m}$  for methane [141].

As it has already indicated in the GC-MS section, the SAM instrument has a total mass of 40 Kg. This is much heavier than the Mini-TES instrument, as it includes the GC-MS. In addition, although Mini-TES had good resolution, it made measurements remotely on a larger scale than TLS, which makes measurements on small grains.

The TLS within the SAM instrument detected a seasonally varying background level of atmospheric methane and observed a ten-fold increase in methane over two-month period. This discovery could suggest that the methane can be produced by living organisms or by chemical reactions between rock and water [192].

The next IR spectrometer reaching the Martian surface has been that of the Perseverance rover. This technique is part of the SuperCam instrument, which together with LIBS and Raman spectroscopy aims to study the chemistry and mineralogy of the Martian regolith. However, unlike the previously mentioned IR spectrometer, the SuperCam one is a passive VNIR, which is known as VIS-NIR-SWIR reflectance spectrometer. Passive VNIR spectroscopy is widely used for the detection and identification of both organic and inorganic compounds. This passive technique does not have any problem with the measurement distance, since they can observe up to the horizon because sunlight is absorbed by molecules so there is no need of any excitation source. The reflectance spectra are characteristic of the molecules composing the target as they absorb at frequencies driven by their vibrational frequencies.

Considering all this, the SuperCam VNIR will be used to identify remotely minerals at the mm-scale from the vicinity of the rover to distant outcrops. It is located on the bottom of the mast unit together with other SuperCam

instruments, such as the RMI, the telescope and the 1064 and 532 nm lasers, among others. The passive VNIR use an acousto-optic tunable filter (AOTF) excited by a RF signal to diffract 256 different wavelengths ranging between 1300 and 2600 nm on two photodiodes to produce a single spectrum in about 80 seconds. The spectral resolution spans from 5 to 20 nm and it has a FWHM of 30 cm<sup>-1</sup>. Its performance temperature range goes from -35 to -5 °C [177,193,194].

Among the three IR spectrometers described so far, the SuperCam spectrometer is the one with the poorest spectral resolution. However, it should be noted that SuperCam is the first instrument of all those described that combines three different spectroscopies simultaneously to measure the same point. Moreover, working remotely will obviously have less accurate results than *in situ* measurements done inside the instruments themselves with sample collection. Although it has less spectral resolution than the other IR spectrometers, the combination of the IR results with the Raman and the LIBS ones will make great advances in the knowledge of the Martian surface mineralogy.

As has been explained above, MarSCoDe has a LIBS spectrometer analyzing the laser-excited plasma from the UV to the NIR. Besides, MarSCoDe is also equipped with a passive spectrometer operating from the NIR to the SWIR. The MarSCoDe is a spectral detection instrument with a combination of active-passive detection techniques. Therefore, by combining the 240-850 nm spectral range of the LIBS module and the 850-2400 nm spectral range of the IR module, it is acquiring the passive mode covering 240-2400 nm [89,134].

The main function of the SWIR is to collect the reflected solar radiation by the Martian surface and transmit it to the SWIR spectrometer. Its spectral resolution ranges between 3 and 12 nm. Like SuperCam's VNIR spectrometer, the SWIR uses an AOTF crystal as the dispersive component and for band selection. The total mass of the MarSCoDe instrument is 16.4 Kg and has a power consumption of 64 W. MarSCoDe is working while the rover is in a stationary mode [89,134].

The next rover to incorporate IR spectrometers in its scientific payload will be the Rosalind Franklin rover. This rover will be equipped with two different IR instruments: Ma-MISS and MicrOmega.

Ma-MISS will be located inside the drill and it will be the instrument in closest contact with the Martian surface. The Martian surface is highly influenced by external processes such as weathering, erosion, sedimentation and impact, which alter its original properties. In this way, Ma-MISS's main science objective is to study the Martian subsurface to analyze partially unaltered material. This instrument will image the walls of

the borehole created by the drill to study the Martian mineralogy and rock formation. As the rover drills into the upper surface of Mars, Ma-MISS will illuminate the hole's cylindrical wall through a transparent window situated in the drill tool. It will capture the reflected light and analyze its spectrum. This instrument will exploit the movement of the drill to acquire data from all around the borehole. The rotation of the instrument as it descends will allow images to be built up in both horizontal (ring image) and vertical sequences (column image). This will provide valuable information for the study of subsurface soil and rock layers, the distribution and state of water-related minerals and it will help to characterize the geophysical Martian environment <sup>[195,196]</sup>.

The spectrometer will perform IR spectral reflectance investigations in the 400 – 2200 nm range to characterize the mineralogy at depths between 0 and 2 m. Besides, it will provide high precision data with 20 nm of spectral resolution <sup>[195,196]</sup>.

*Table 1.1. IR spectrometer features for the in situ study of the Martian mineralogy.*

Instrument	Rover	Analysis site	Type of sample	Type of analysis	Target	Spectral range / nm	Spectral resolution
Mini-TES	Spirit and Opportunity	Inside the rover	Surface	Imaging	Minerals	5000-29000	10 cm <sup>-1</sup>
TLS	Curiosity	Inside the rover	Surface	Punctual	Specific organic molecules	2780 and 3270	Ultra-high
SuperCam	Perseverance	Remotely	Surface	Punctual	Minerals	1300-2600	30 cm <sup>-1</sup>
MarSCoDe	Tianwen-1	Remotely	Surface	Punctual	Minerals	850-2400	3-12 nm
Ma-MISS	Rosalind Franklin	Inside the rover	Subsurface	Imaging	Minerals	400-2200	20 nm
MicrOmega	Rosalind Franklin	Inside the rover	Surface	Punctual and imaging	Minerals	500-3650	20-30 cm <sup>-1</sup>

Finally, MicrOmega will be a micro-imaging system designed to identify, at grain scale, the mineralogical and the molecular composition of the Martian samples collected by the Rosalind Franklin drill. This instrument will be included in the suite of the analytical laboratory together with MOMA and the RLS. All of them will characterize the collected samples and specifically the organic substances they may contain. MicrOmega will consist of a visible light microscope and a near infrared imaging spectrometer. The total mass of the instrument will be less than 2.4 Kg and its dimensions will be 17 x 16 x 11 cm. The instrument will use an AOTF and its associated detector with a high spectral sampling of 2-14 nm. It will acquire high resolution monochromatic images in a spectral range that will go from 500 to 3650 nm <sup>[197]</sup>.

Each of the Rosalind Franklin rover instruments will have a different function, so it is difficult to compare them with each other. Even more

difficult is to compare the seven instruments that use IR spectroscopy as they were built following different needs and for very different aims. Some perform infrared imaging, others small-scale spot analysis, others carry out it remotely at bigger scale, etc. Table 1.1 summarizes some features that allow differentiating between the seven instruments described.

### **1.3.3. *In situ* vs laboratory analytical techniques for geochemical Martian analysis**

Table 1.2 and Table 1.3 show the pros and cons of working in terrestrial laboratories with common analytical techniques or working with *in situ* analytical techniques on Martian samples.

As explained above, meteorites are the only samples available on Earth coming from Mars, which can be analyzed by laboratory analytical techniques. However, minerals found in meteorites cannot be fully used to trace the history of the planet, as they are exposed to terrestrial weathering.

This problem will be solved when the first samples return from Mars. Those samples will be analyzed with the widest analytical techniques available in specialized laboratories. However, this will occur in the early 2030s. Until those dates, Martian meteorites and *in situ* analyses on the Martian surface are the only ways to study real material from Mars.

The number of instruments on board the different missions has increased continuously over time. In fact, the current methodologies used in laboratories for the geochemical characterization of meteorites have been included as part of the instrument payload of Martian rovers and/or landers. In order to introduce the analytical techniques on board the spacecraft, several requirements were satisfied: size was minimized, power consumption reduced, sensitivity and accuracy improved, portability enhanced, mechanical and shock resistance improved, reliability under space conditions, and more.

Therefore, reaching these requirements has been, is and will be a great challenge for the development of analytical chemistry.

For example, as indicated above, the first analytical instrument that went to space with the purpose of studying the geochemistry of a non-terrestrial body was XRF, which was on board the Viking landers. Then, based on the same purpose, the XRF was miniaturized and improved, incorporating it into the Sojourner rover as the APXS instrument.

Thanks to the miniaturization, the APXS could be mounted later on robotic arms (MER rovers), providing the possibility to move the instrument to the target of measurement. Then, the first LIBS instrument was developed for remote analysis in the Curiosity rover, having low weight and good capabilities. Today, the Perseverance rover implements, together with

LIBS, the first XRF imaging spectrometer (PIXL) to improve the characterization of the chemical elements in the samples under analyses.

The MER rovers were equipped with the Athena Science Payload, which is composed by six instruments and a Rock Abrasion Tool working on the same sample <sup>[70]</sup>. Since the MER mission, collaborative science has been possible on Mars. In contrast to the analyses performed in laboratories, several instruments were used to analyze the same sample. The great problem is that at a small scale, it is quite difficult to perform laboratory analyses with several techniques exactly on the same point. However, this capability was achieved for the first time in the MER rovers. The high quality of the results promoted the creation of instruments with several analytical techniques working together, like in the MSL mission <sup>[76]</sup> and nowadays in the Mars 2020 <sup>[130]</sup>.

Table 1.2. Pros and cons of using *in situ* analytical techniques to measure geochemistry of non-terrestrial samples.

<b><i>In situ</i> analytical techniques</b>	
<b>PROS</b>	<b>CONS</b>
<ul style="list-style-type: none"> <li>✓ Latest technology.</li> <li>✓ Downsizing.</li> <li>✓ Automation and monitorization.</li> <li>✓ Samples do not undergo any change in molecular/mineral structure or chemistry as pretreatment is avoided.</li> <li>✓ Same environmental measurement conditions as samples, avoiding terrestrial weathering.</li> </ul>	<ul style="list-style-type: none"> <li>✗ Worse detection limits.</li> <li>✗ Slower but reliable instrument-Earth connections.</li> <li>✗ More expensive.</li> <li>✗ High risk of being damaged.</li> <li>✗ Limitation of the analysis due to environmental conditions and energy constrains.</li> </ul>

Therefore, the advances in analytical instrumentation made in response to the needs of space exploration are not only applicable to *in situ* analysis techniques. As costs have been reduced, these innovative improvements could have been spread to laboratory instrumentation. However, until today very few laboratory analytical instruments can perform collaborative science using a single benchtop. This means that only one laboratory instrument can make measurements with at least 3-4 different analytical techniques on the same microscopic spot, like the SEM/EDS-Raman instrument, which is commonly used to characterize meteorites by our IBeA Research Group <sup>[24]</sup>.

This is the case of the SuperCam instrument onboard the Perseverance rover, which is the most modern analytical instrument used by space exploration. However, it is expected that in few years the concept of collaborative science will be extended to laboratory setups, coupling several analytical techniques in the same benchtop instrument. Even, such

improvements will be implemented in the near future in portable instrument for field analyses.

In the near future, one of the best instrumental suites for *in situ* combined science will be inside the ALD on board the Rosalind Franklin rover. Its carousel will be able to place a small amount of sample under the common observation of the MicrOmega, RLS and MOMA instruments.

Table 1.3. Pros and cons of using laboratory analytical techniques to measure the geochemistry of non-terrestrial samples.

<b>Laboratory analytical techniques</b>	
<b>PROS</b>	<b>CONS</b>
<ul style="list-style-type: none"> <li>✓ Better detection limits.</li> <li>✓ Faster instrument-Earth connections.</li> <li>✓ Cheaper.</li> <li>✓ Downsizing.</li> <li>✓ Some, but not all, are automatic.</li> <li>✓ Low risk of being damaged.</li> <li>✓ Imaging possibility</li> </ul>	<ul style="list-style-type: none"> <li>✗ Samples could undergone some changes in molecular structure or chemistry.</li> <li>✗ Different environmental measurement conditions than those of the samples.</li> </ul>

What is clear is that the future of space exploration is very promising, promoting the creation of combined analytical instruments with robust capabilities.

## 1.4. References

- [1] Siddiqi, A. Sputnik 50 Years Later: New Evidence on Its Origins. *Acta Astronaut.* **2008**, *63*, 529. <https://doi.org/https://doi.org/10.1016/j.actaastro.2007.12.042>.
- [2] Kuznetsov, V. D.; Sinelnikov, V. M.; Alpert, S. N. Yakov Alpert: Sputnik-1 and the First Satellite Ionospheric Experiment. *Adv. Sp. Res.* **2015**, *55*, 2833. <https://doi.org/https://doi.org/10.1016/j.asr.2015.02.033>.
- [3] Wassersug, R. J. Truly Dead or Just Comotose?: The Status of Space Biology at the Half-Century Mark. *Space Policy* **2008**, *24*, 67. <https://doi.org/https://doi.org/10.1016/j.spacepol.2008.03.004>.
- [4] Helvajian, H.; Janson, S. *Small Satellites: Past, Present and Future*; The Aerospace Press: California, 2008.
- [5] Dick, S. J. Origins and Development of NASA's Exobiology Program, 1958–1976. *Acta Astronaut.* **2009**, *65*, 1. <https://doi.org/https://doi.org/10.1016/j.actaastro.2009.01.058>.
- [6] Huntress, W.; Moroz, V. I.; Shevaley, I. L. Lunar and Planetary Robotic Exploration Missions in the 20th Century. *Space Sci. Rev.* **2003**, *107*, 541. <https://doi.org/10.1023/A:1026172301375>.
- [7] Skoog, A. I.; Abramov, I. P.; Stoklitsky, A. Y.; Doodnik, M. N. The Soviet-Russian Space Suits a Historical Overview of the 1960's. *Acta Astronaut.* **2002**, *51*, 113. [https://doi.org/https://doi.org/10.1016/S0094-5765\(02\)00092-9](https://doi.org/https://doi.org/10.1016/S0094-5765(02)00092-9).
- [8] Battin, R. H. Second Breakwell Memorial Lecture: 1961 and All That. *Acta Astronaut.* **1996**, *39*, 407. [https://doi.org/https://doi.org/10.1016/S0094-5765\(96\)00153-1](https://doi.org/https://doi.org/10.1016/S0094-5765(96)00153-1).
- [9] Kauffman, J. NASA's PR Campaign on Behalf of Manned Space Flight, 1961—1963. *Public Relat. Rev.* **1991**, *17*, 57. [https://doi.org/https://doi.org/10.1016/0363-8111\(91\)90006-7](https://doi.org/https://doi.org/10.1016/0363-8111(91)90006-7).
- [10] Thiele, G. Psychology of Space Exploration: Contemporary Research in Historical Perspective. *Space Policy* **2012**, *28*, 206. <https://doi.org/https://doi.org/10.1016/j.spacepol.2012.06.013>.
- [11] Villain, J. A Brief History of Baikonur. *Space Policy* **1996**, *12*, 129. [https://doi.org/https://doi.org/10.1016/0265-9646\(96\)00004-5](https://doi.org/https://doi.org/10.1016/0265-9646(96)00004-5).
- [12] Efanov, V. V.; Dolgoplov, V. P. The Moon: From Research to Exploration (To the 50th Anniversary of Luna-9 and Luna-10 Spacecraft). *Sol. Syst. Res.* **2017**, *51*, 573. <https://doi.org/10.1134/S0038094617070036>.
- [13] Chu, W. K.; Liu, J. R. Rutherford Backscattering Spectrometry: Reminiscences and Progresses. *Mater. Chem. Phys.* **1996**, *46*, 183. [https://doi.org/https://doi.org/10.1016/S0254-0584\(97\)80012-0](https://doi.org/https://doi.org/10.1016/S0254-0584(97)80012-0).
- [14] Economou, T. Chemical Analyses of Martian Soil and Rocks Obtained by the Pathfinder Alpha Proton X-Ray Spectrometer. *Radiat. Phys. Chem.* **2001**, *61*, 191. [https://doi.org/10.1016/S0969-806X\(01\)00240-7](https://doi.org/10.1016/S0969-806X(01)00240-7).

- [15] Sturdevant, R. W. Footprints in the Dust: The Epic Voyages of Apollo, 1969-1975. *Air Power Hist.* **2011**, *58*, 42.
- [16] Mateo Sanguino, T. de J. 50 Years of Rovers for Planetary Exploration: A Retrospective Review for Future Directions. *Rob. Auton. Syst.* **2017**, *94*, 172. <https://doi.org/https://doi.org/10.1016/j.robot.2017.04.020>.
- [17] Basilevsky, A. T.; Abdrakhimov, A. M.; Head, J. W.; Pieters, C. M.; Wu, Y.; Xiao, L. Geologic Characteristics of the Luna 17/Lunokhod 1 and Chang'E-3/Yutu Landing Sites, Northwest Mare Imbrium of the Moon. *Planet. Space Sci.* **2015**, *117*, 385. <https://doi.org/10.1016/j.pss.2015.08.006>.
- [18] Karachevtseva, I. P.; Kozlova, N. A.; Kokhanov, A. A.; Zubarev, A. E.; Nadezhdina, I. E.; Patratiy, V. D.; Konopikhin, A. A.; Basilevsky, A. T.; Abdrakhimov, A. M.; Oberst, J.; Haase, I.; Jolliff, B. L.; Plescia, J. B.; Robinson, M. S. Cartography of the Luna-21 Landing Site and Lunokhod-2 Traverse Area Based on Lunar Reconnaissance Orbiter Camera Images and Surface Archive TV-Panoramas. *Icarus* **2017**, *283*, 104. <https://doi.org/https://doi.org/10.1016/j.icarus.2016.05.021>.
- [19] Sevastiyarov, N. N.; Bryukhanov, N. A. Space Stations: Evolution and New Programs. *Acta Astronaut.* **2007**, *61*, 1, 193. <https://doi.org/https://doi.org/10.1016/j.actaastro.2007.01.041>.
- [20] Whedon, G. D.; Rambaut, P. C. Effects of Long-Duration Space Flight on Calcium Metabolism: Review of Human Studies from Skylab to the Present. *Acta Astronaut.* **2006**, *58*, 2, 59. <https://doi.org/https://doi.org/10.1016/j.actaastro.2005.03.074>.
- [21] Henry Lambright, W. Administrative Leadership and Long-Term Technology: NASA and the International Space Station. *Space Policy* **2019**, *47*, 85. <https://doi.org/https://doi.org/10.1016/j.spacepol.2018.07.003>.
- [22] Trueman, C. N.; Rodgers, K. J.; McLellan, I. S.; Hursthouse, A. S. Geochemistry. Inorganic. In *Encyclopedia of Analytical Science*; Worsford, P., Poole, C., Townshend, A., Miró, M., Eds.; Elsevier, 2019; pp 271–282. <https://doi.org/10.1016/B978-0-12-409547-2.14362-8>.
- [23] Foing, B.; Stoker, C.; Zavaleta, J.; Ehrenfreund, P.; Thiel, C.; Sarrazin, P.; Blake, D.; Page, J.; Pletser, V.; Hendrikse, J.; Direito, S.; Kotler, J.; Martins, Z.; Orzechowska, G.; Gross, C.; Wendt, L.; Clarke, J.; Borst, A.; Peters, S.; Davies. Field Astrobiology Research in Moon-Mars Analogue Environments: Instruments and Methods. *Int. J. Astrobiol.* **2011**, *10*, 141. <https://doi.org/10.1017/S1473550411000036>.
- [24] Aramendia, J.; Gomez-Nubla, L.; Castro, K.; Fdez-Ortiz de Vallejuelo, S.; Arana, G.; Maguregui, M.; Baonza, V. G.; Medina, J.; Rull, F.; Madariaga, J. M. Overview of the Techniques Used for the Study of Non-Terrestrial Bodies: Proposition of Novel Non-

- Destructive Methodology. *Trends Anal. Chem.* **2018**, 98, 36. <https://doi.org/10.1016/j.trac.2017.10.018>.
- [25] Bland, P.; Zolensky, M.; Benedix, G.; Sephton, M. Weathering of Chondritic Meteorites. In *Meteorites and the early solar system*; 2006; Vol. II, pp 853–867.
- [26] Saunders, R. S.; Arvidson, R. E.; Badhwar, G. D.; Boynton, W. V.; Christensen, P. R.; Cucinotta, F. A.; Feldman, W. C.; Gibbs, R. G.; Kloss Jr., C.; Landano, M. R.; Mase, R. A.; McSmith, G. W.; Meyer, M. A.; Mitrofanov, I. G.; Pace, G. D.; Plaut, J. J.; Sidney, W. P.; Spencer, D. A.; Thompson, T. W.; Zeitlin, C. J. 2001 Mars Odyssey Mission Summary. *Space Sci. Rev.* **2004**, 110, 1. <https://doi.org/10.1023/B:SPAC.0000021006.84299.18>.
- [27] Rubin, A. E.; Grossman, J. N. Meteorite and Meteoroid: New Comprehensive Definitions. *Meteorit. Planet. Sci.* **2010**, 45, 114. <https://doi.org/10.1111/j.1945-5100.2009.01009.x>.
- [28] Millman, P. M. Meteor News. *J. R. Astron. Soc. Canada* **1961**, 55, 265.
- [29] Mason, B. *Meteorites*; Wiley: New York, 1962.
- [30] The Meteoritical Society. *Meteorites*. The Meteoritical Society. <https://meteoritical.org/meteorites> (accessed 2023-03-01).
- [31] Nyquist, L. E.; Bogard, D. D.; Shih, C. Y.; Greshake, A.; Stöffler, D.; Eugster, O. Ages and Geologic Histories of Martian Meteorites. In *Chronology and Evolution of Mars 96*; Kallenbach, R., Geiss, J., Hartmann, W. K., Eds.; Kluwer Academic Publishers: Bern, Switzerland, 2001; pp 1005–1164.
- [32] Ostrowski, D.; Bryson, K. The Physical Properties of Meteorites. *Planet. Space Sci.* **2019**, 165, 148. <https://doi.org/10.1016/j.pss.2018.11.003>.
- [33] Dypvik, H.; Hellevang, H.; Krzesińska, A.; Sætre, C.; Viennet, J.-C.; Bultel, B.; Ray, D.; Poulet, F.; Loizeau, D.; Veneranda, M.; Rull, F.; Cousin, A.; Werner, S. C. The Planetary Terrestrial Analogues Library (PTAL) – An Exclusive Lithological Selection of Possible Martian Earth Analogues. *Planet. Space Sci.* **2021**, 208, 105339. <https://doi.org/10.1016/j.pss.2021.105339>.
- [34] Veneranda, M.; Sáiz, J.; Sanz- Arranz, A.; Manrique, J. A.; Lopez-Reyes, G.; Medina, J.; Dypvik, H.; Werner, S. C.; Rull, F. Planetary Terrestrial Analogues Library (PTAL) Project: Raman Data Overview. *J. Raman Spectrosc.* **2020**, 51, 1731. <https://doi.org/10.1002/jrs.5652>.
- [35] Sutter, B.; Dalton, J. B.; Ewing, S. A.; Amundson, R.; McKay, C. P. Terrestrial Analogs for Interpretation of Infrared Spectra from the Martian Surface and Subsurface: Sulfate, Nitrate, Carbonate, and Phyllosilicate-Bearing Atacama Desert Soils. *J. Geophys. Res. Biogeosciences* **2007**, 112, 1. <https://doi.org/10.1029/2006JG000313>.
- [36] Wei, J.; Wang, A.; Lambert, J. L.; Wettergreen, D.; Cabrol, N.;

- Warren-Rhodes, K.; Zacny, K. Autonomous Soil Analysis by the Mars Micro-Beam Raman Spectrometer (MMRS) on-Board a Rover in the Atacama Desert: A Terrestrial Test for Planetary Exploration. *J. Raman Spectrosc.* **2015**, *46*, 810. <https://doi.org/10.1002/jrs.4656>.
- [37] Gibson, E. K.; Wentworth, S. J.; McKay, D. S. Chemical Weathering and Diagenesis of a Cold Desert Soil from Wright Valley, Antarctica: An Analog of Martian Weathering Processes. *J. Geophys. Res.* **1983**, *88*, A912. <https://doi.org/10.1029/JB088iS02p0A912>.
- [38] Cannon, K. M.; Mustard, J. F.; Salvatore, M. R. Alteration of Immature Sedimentary Rocks on Earth and Mars: Recording Aqueous and Surface–Atmosphere Processes. *Earth Planet. Sci. Lett.* **2015**, *417*, 78. <https://doi.org/10.1016/j.epsl.2015.02.017>.
- [39] Salas, E.; Abbey, W.; Bhartia, R.; Beegle, L. W. The Mojave Desert: A Martian Analog Site for Future Astrobiology Themed Missions. In *analogue Sites for Mars Missions: MSL and Beyond*; 2011; Abs 161.
- [40] Peters, G. H.; Abbey, W.; Bearman, G. H.; Mungas, G. S.; Smith, J. A.; Anderson, R. C.; Douglas, S.; Beegle, L. W. Mojave Mars Simulant—Characterization of a New Geologic Mars Analog. *Icarus* **2008**, *197*, 470 <https://doi.org/10.1016/j.icarus.2008.05.004>.
- [41] Amils, R.; Fernández-Remolar, D.; the IPBSL Team. Río Tinto: A Geochemical and Mineralogical Terrestrial Analogue of Mars. *Life* **2014**, *4*, 511. <https://doi.org/10.3390/life4030511>.
- [42] Ruiz-Galende, P.; Fernández, G.; Torre-Fdez, I.; Aramendia, J.; Gomez-Nubla, L.; García-Florentino, C.; Castro, K.; Arana, G.; Madariaga, J. M. Characterization of Sedimentary and Volcanic Rocks in Armintza Outcrop (Biscay, Spain) and Its Implication for Oxia Planum (Mars) Exploration. *Spectrochim. Acta Part A Mol. Biomol. Spectrosc.* **2021**, *251*, 119443. <https://doi.org/10.1016/j.saa.2021.119443>.
- [43] Ruiz- Galende, P.; Torre- Fdez, I.; Aramendia, J.; Gómez- Nubla, L.; Castro, K.; Arana, G.; Madariaga, J. M. Study of a Terrestrial Martian Analogue: Geochemical Characterization of the Meñakoz Outcrops (Biscay, Spain). *J. Raman Spectrosc.* **2020**, *51*, 1603. <https://doi.org/10.1002/jrs.5565>.
- [44] Soffen, G. A. The Viking Project. *J. Geophys. Res.* **1977**, *82*, 3959–3970. <https://doi.org/10.1029/JS082i028p03959>.
- [45] Soffen, G. A.; Snyder, C. W. The First Viking Mission to Mars. *Science.* **1976**, *193*, 759. <https://doi.org/10.1126/science.193.4255.759>.
- [46] Flinn, E. A. Scientific Results of the Viking Project. *J. Geophys. Res.* **1977**, *82*, 722.
- [47] Brown, F. S.; Adelson, H. E.; Chapman, M. C.; Clausen, O. W.; Cole, A. J.; Cragin, J. T.; Day, R. J.; Debenham, C. H.; Fortney, R. E.; Gilje, R. I.; Harvey, D. W.; Kropp, J. L.; Loer, S. J.; Logan, J. L.; Potter, W. D.; Rosiak, G. T. The Biology Instrument for the Viking

- Mars Mission. *Rev. Sci. Instrum.* **1978**, *49*, 139. <https://doi.org/10.1063/1.1135378>.
- [48] Golombek, M. P. The Mars Pathfinder Mission. *J. Geophys. Res. Planets* **1997**, *102*, 3953. <https://doi.org/10.1029/96JE02805>.
- [49] Brückner, J.; Dreibus, G.; Rieder, R.; Wänke, H. Refined Data of Alpha Proton X-Ray Spectrometer Analyses of Soils and Rocks at the Mars Pathfinder Site: Implications for Surface Chemistry. *J. Geophys. Res. Planets* **2003**, *108*, 8094. <https://doi.org/10.1029/2003JE002060>.
- [50] Shirley, D. L. Mars Pathfinder Microrover Flight Experiment — A Paradigm for Very Low-Cost Spacecraft. *Acta Astronaut.* **1995**, *35*, 355. [https://doi.org/10.1016/0094-5765\(94\)00201-V](https://doi.org/10.1016/0094-5765(94)00201-V).
- [51] Golombek, M. P.; Anderson, R. C.; Barnes, J. R.; Bell III, J. F.; Bridger, N. T.; Britt, D. T.; Brückner, J.; Cook, R. A.; Crisp, D.; Economou, T.; Folkner, W. M.; Greeley, R.; Haberle, R. M.; Hargraves, R. B.; Harris, J. A.; Haldemann, A. F. C.; Herkenhoff, K. E.; Hviid, S. F.; Jaumann, R.; Johnson, J. R.; Kallemeyn, P. H.; Keller, H. U.; Kirk, R. L.; Knudsen, J. M.; Larsen, S.; Lemmon, M. T.; Madsen, M. B.; Magalhaes, J. A.; Maki, J. N.; Malin, M. C.; Manning, R. M.; Matijevic, J.; McSween Jr., H. Y.; Moore, H. J.; Murchie, S. L.; Murphy, J. R.; Parker, T. J.; Rieder, R.; Soderblom, L. A.; Spencer, D. A.; Stoker, C. R.; Sullivan, R.; Thomas, N.; Thurman, S. W.; Tomasko, M. G.; Vaughan, R. M.; Wänke, H.; Ward, A. W.; Wilson, G. R. Overview of the Mars Pathfinder Mission: Launch, through Landing, Surface Operations, Data Sets, and Science Results. *J. Geophys. Res.* **1999**, *104*, 8523. <https://doi.org/10.1029/98JE02554>.
- [52] Basilevsky, A. T.; Markiewicz, W. J.; Thomas, N.; Keller, H. U. Morphologies of Rocks within and near the Rock Garden at the Mars Pathfinder Landing Site. *J. Geophys. Res. Planets* **1999**, *104*, 8617. <https://doi.org/10.1029/1998JE900039>.
- [53] Golombek, M. P.; Moore, H. J.; Haldemann, A. F. C.; Parker, T. J.; Schofield, J. T. Assessment of Mars Pathfinder Landing Site Predictions. *J. Geophys. Res. Planets* **1999**, *104*, 8585. <https://doi.org/10.1029/1998JE900015>.
- [54] NASA. Mars Polar Lander. <https://nssdc.gsfc.nasa.gov/nmc/spacecraft/display.action?id=1999-001A> (accessed 2020-12-17).
- [55] NASA. Mars Climate Orbiter. <https://nssdc.gsfc.nasa.gov/nmc/spacecraft/display.action?id=1998-073A> (accessed 2020-12-16).
- [56] Shirley, D. L. Touching Mars: 1998 Status of the Mars Robotic Exploration Program. *Acta Astronaut.* **1999**, *45*, 249. [https://doi.org/10.1016/S0094-5765\(99\)00142-3](https://doi.org/10.1016/S0094-5765(99)00142-3).
- [57] Vasavada, A. R.; Williams, J.-P.; Paige, D. A.; Herkenhoff, K. E.; Bridges, N. T.; Greeley, R.; Murray, B. C.; Bass, D. S.; McBride, K.

- S. Surface Properties of Mars' Polar Layered Deposits and Polar Landing Sites. *J. Geophys. Res. Planets* **2000**, *105*, 6961. <https://doi.org/10.1029/1999JE001108>.
- [58] Wright, I. P.; Sims, M. R.; Pillinger, C. T. Scientific Objectives of the Beagle 2 Lander. *Acta Astronaut.* **2003**, *52*, 219. [https://doi.org/10.1016/S0094-5765\(02\)00160-1](https://doi.org/10.1016/S0094-5765(02)00160-1).
- [59] Bridges, J. C. Selection of the Landing Site in Isidis Planitia of Mars Probe Beagle 2. *J. Geophys. Res.* **2003**, *108*, 5001. <https://doi.org/10.1029/2001JE001820>.
- [60] Chicarro, A.; Martin, P.; Trautner, R. The Mars Express Mission: An Overview. In *Mars Express: a European Mission to the Red Planet*; Wilson, A., Ed.; European Space Agency Publication Division: Noordwijk, 2004; Vol. SP-1240, pp 3–16.
- [61] Fletcher, K. *Mars Express: The Scientific Investigations, ESA SP-1291*; ESA Communication Production Office, ESTEC: Noordwijk, Netherlands, 2009.
- [62] Ody, A.; Poulet, F.; Langevin, Y.; Bibring, J. P.; Bellucci, G.; Altieri, F.; Gondet, B.; Vincendon, M.; Carter, J.; Manaud, N. Global Maps of Anhydrous Minerals at the Surface of Mars from OMEGA/MEX. *J. Geophys. Res.* **2012**, *117*, 1. <https://doi.org/10.1029/2012JE004117>.
- [63] Carter, J.; Poulet, F.; Bibring, J. P.; Mangold, N.; Murchie, S. Hydrous Minerals on Mars as Seen by the CRISM and OMEGA Imaging Spectrometers: Updated Global View. *J. Geophys. Res. Planets* **2013**, *118*, 4, 831. <https://doi.org/10.1029/2012JE004145>.
- [64] ESA. Beagle-2 lander found on Mars. [http://www.esa.int/Science\\_Exploration/Space\\_Science/Mars\\_Express/Beagle-2\\_lander\\_found\\_on\\_Mars](http://www.esa.int/Science_Exploration/Space_Science/Mars_Express/Beagle-2_lander_found_on_Mars) (accessed 2021-01-14).
- [65] Roncoli, R. B.; Ludwinski, J. M. Mission Design over View for the Mars Exploration Rover Mission. In *AIAA/AAS Astrodynamics Specialist Conference and Exhibit*; Monterey, California; Abs AIAA 2002-4823.
- [66] Li, R.; Archinal, B. A.; Arvidson, R. E.; Bell, J.; Christensen, P.; Crumpler, L.; Des Marais, D. J.; Di, K.; Duxbury, T.; Golombek, M.; Grant, J.; Greeley, R.; Guinn, J.; Johnson, A.; Kirk, R. L.; Maimone, M.; Matthies, L. H.; Malin, M.; Parker, T.; Sims, M.; Thompson, S.; Squyres, S. W.; Soderblom, L. A. Spirit Rover Localization and Topographic Mapping at the Landing Site of Gusev Crater, Mars. *J. Geophys. Res. Planets* **2006**, *111*, E2. <https://doi.org/10.1029/2005JE002483>.
- [67] Arvidson, R. E.; Squyres, S. W.; Anderson, R. C.; Bell III, J. F.; Blaney, D.; Brückner, J.; Cabrol, N. A.; Calvin, W.; Carr, M. H.; Christensen, P. R.; Clark, B. C.; Crumpler, L.; Des Marais, D. J.; de Souza Jr., P. A.; D'Uston, C.; Economou, T.; Farmer, J.; Farrand, W.; Folkner, W.; Golombek, M.; Gorevan, S.; Grant, J. A.; Greeley, R.; Grotzinger, J.; Guinness, E.; Hahn, B. C.; Haskin, L.; Herkenhoff,

- K. E.; Hurowitz, J. A.; Hviid, S.; Johnson, J. R.; Klingelhöfer, G.; Knoll, A. H.; Landis, G.; Leff, C.; Lemmon, M.; Li, R.; Madsen, M. B.; Malin, M. C.; McLennan, S. M.; McSween, H. Y.; Ming, D. W.; Moersch, J.; Morris, R. V.; Parker, T.; Rice Jr, J. W.; Ritcher, L.; Rieder, R.; Rodionov, D. S.; Schöder, C.; Sims, M.; Smith, M.; Smith, P.; Soderblom, L. A.; Sullivan, R.; Thompson, S. D.; Tosca, N. J.; Wang, A.; Wänke, H.; Ward, J.; Wdowiak, T.; Wolff, M.; Yen, A. Overview of the Spirit Mars Exploration Rover Mission to Gusev Crater: Landing Site to Backstay Rock in the Columbia Hills. *J. Geophys. Res.* **2006**, *111*, E02S01. <https://doi.org/10.1029/2005JE002499>.
- [68] Li, R.; Arvidson, R. E.; Di, K.; Golombek, M.; Guinn, J.; Johnson, A.; Maimone, M.; Matthies, L. H.; Malin, M.; Parker, T.; Squyres, S. W.; Watters, W. A. Opportunity Rover Localization and Topographic Mapping at the Landing Site of Meridiani Planum, Mars. *J. Geophys. Res.* **2007**, *112*, E02S90. <https://doi.org/10.1029/2006JE002776>.
- [69] Squyres, S. W.; Arvidson, R. E.; Bell III, J. F.; Brückner, J.; Cabrol, N. A.; Calvin, W.; Carr, M. H.; Christensen, P. R.; Clark, B. C.; Crumpler, L.; Des Marais, D. J.; D'Uston, C.; Economou, T.; Farmer, J.; Farrand, W.; Folkner, W.; Golombek, M.; Gorevan, S.; Grant, J. A.; Greeley, R.; Grotzinger, J.; Haskin, L.; Herkenhoff, K. E.; Hviid, S.; Johnson, J.; Klingelhöfer, G.; Knoll, A. H.; Landis, G.; Lemmon, M.; Li, R.; Madsen, M. B.; Malin, M. C.; McLennan, S. M.; McSween, H. Y.; Ming, D. W.; Moersch, J.; Morris, R. V.; Parker, T.; Rice Jr, J. W.; Ritcher, L.; Rieder, R.; Sims, M.; Smith, M.; Smith, P.; Soderblom, L. A.; Sullivan, R.; Wänke, H.; Wdowiak, T.; Wolff, M.; Yen, A. The Opportunity Rover's Athena Science Investigation at Meridiani Planum, Mars. *Science*. **2004**, *306*, 1698. <https://doi.org/10.1126/science.110617>.
- [70] NASA. Mars Exploration Rovers Overview. <https://mars.nasa.gov/mer/mission/overview/> (accessed 2020-12-18).
- [71] Bonfiglio, E. P.; Adams, D.; Craig, L.; Spencer, D. A.; Arvidson, R.; Heet, T. Landing-Site Dispersion Analysis and Statistical Assessment for the Mars Phoenix Lander. *J. Spacecr. Rockets* **2011**, *48*, 5, 784. <https://doi.org/10.2514/1.48813>.
- [72] Tamppari, L. K.; Bass, D.; Cantor, B.; Daubar, I.; Dickinson, C.; Fisher, D.; Fujii, K.; Gunnlauggson, H. P.; Hudson, T. L.; Kass, D.; Kleinböhl, A.; Komguem, L.; Lemmon, M. T.; Mellon, M.; Moores, J.; Pankine, A.; Pathak, J.; Searls, M.; Seelos, F.; Smith, M. D.; Smrekar, S.; Taylor, P.; Holstein-Rathlou, C.; Weng, W.; Whiteway, J.; Wolff, M. Phoenix and MRO Coordinated Atmospheric Measurements. *J. Geophys. Res.* **2010**, *115*, E00E17. <https://doi.org/10.1029/2009JE003415>.
- [73] Cull, S.; Arvidson, R. E.; Mellon, M. T.; Skemer, P.; Shaw, A.; Morris, R. V. Compositions of Subsurface Ices at the Mars Phoenix Landing Site. *Geophys. Res. Lett.* **2010**, *37*, L24203.

- <https://doi.org/10.1029/2010GL045372>.
- [74] Seelos, K. D.; Seelos, F. P.; Viviano-Beck, C. E.; Murchie, S. L.; Arvidson, R. E.; Ehlmann, B. L.; Fraeman, A. A. Mineralogy of the MSL Curiosity Landing Site in Gale Crater as Observed by MRO/CRISM. *Geophys. Res. Lett.* **2014**, *41*, 14, 4880. <https://doi.org/10.1002/2014GL060310>.
- [75] Golombek, M.; Grant, J.; Kipp, D.; Vasavada, A.; Kirk, R.; Fergason, R.; Bellutta, P.; Calef, F.; Larsen, K.; Katayama, Y.; Huertas, A.; Beyer, R.; Chen, A.; Parker, T.; Pollard, B.; Lee, S.; Sun, Y.; Hoover, R.; Sladek, H.; Grotzinger, J.; Welch, R.; Noe Dobrea, E.; Michalski, J.; Watkins, M. Selection of the Mars Science Laboratory Landing Site. *Space Sci. Rev.* **2012**, *170*, 641. <https://doi.org/10.1007/s11214-012-9916-y>.
- [76] Grotzinger, J. P.; Crisp, J.; Vasavada, A. R.; Anderson, R. C.; Baker, C. J.; Barry, R.; Blake, D.; Conrad, P.; Edgett, K. S.; Ferdowski, B.; Gellert, R.; Gilbert, J. B.; Golombek, M.; Gómez-Elvira, J.; Hassler, D. M.; Jandura, L.; Litvak, M.; Mahaffy, P.; Maki, J.; Meyer, M.; Malin, M. C.; Mitrofanov, I.; Simmonds, J. J.; Vaniman, D.; Welch, R. V.; Wiens, R. C. Mars Science Laboratory Mission and Science Investigation. *Space Sci. Rev.* **2012**, *170*, 5. <https://doi.org/10.1007/s11214-012-9892-2>.
- [77] Bedford, C. Distinguish The Geochemical Effects Of Sedimentary Processes And Source Region Characteristics In Gale Crater, Mars, Royal Holloway, University of London, UK, 2019.
- [78] Wippermann, T.; Hudson, T. L.; Spohn, T.; Witte, L.; Scharringhausen, M.; Tsakyridis, G.; Fittock, M.; Krömer, O.; Hense, S.; Grott, M.; Knollenberg, J.; Lichtenheldt, R. Penetration and Performance Testing of the HP3 Mole for the InSight Mars Mission. *Planet. Space Sci.* **2020**, *181*, 10478, 1. <https://doi.org/10.1016/j.pss.2019.104780>.
- [79] Golombek, M.; Williams, N.; Warner, N. H.; Parker, T.; Williams, M. G.; Daubar, I.; Calef, F.; Grant, J.; Bailey, P.; Abarca, H.; Deen, R.; Ruoff, N.; Maki, J.; McEwen, A.; Baugh, N.; Block, K.; Tamppari, L. K.; Call, J.; Ladewing, J.; Stoltz, A.; Weems, W. A.; Mora-Sotomayor, L.; Torres, J.; Johnson, M.; Kennedy, T.; Sklyanskiy, E. Location and Setting of the Mars InSight Lander, Instruments, and Landing Site. *Earth Sp. Sci.* **2020**, *7*, 1. <https://doi.org/10.1029/2020EA001248>.
- [80] Golombek, M.; Kipp, D.; Warner, N.; Daubar, I. J.; Fergason, R.; Kirk, R. L.; Beyer, R.; Huertas, A.; Piqueux, S.; Putzig, N. E.; Campbell, B. A.; Morgan, G. A.; Charalambous, C.; Pike, W. T.; Gwinner, K.; Calef, F.; Kass, D.; Mischna, M.; Ashley, J.; Bloom, C.; Wigton, N.; Hare, T.; Schwartz, C.; Gengl, H.; Redmond, L.; Trautman, M.; Sweeney, J.; Grima, C.; Smith, I. B.; Sklyanskiy, E.; Lisano, M.; Benardini, J.; Smrekar, S.; Lognonné, P.; Banerdt, W. B. Selection of the InSight Landing Site. *Space Sci. Rev.* **2017**, *211*, 5. <https://doi.org/10.1007/s11214-016-0321-9>.

- [81] Banerdt, W. B.; Smrekar, S.; Hurst, K.; Lognonné, P.; Spohn, T.; Asmar, S.; Banfield, D.; Boschi, L.; Christensen, U.; Dehant, V.; Folkner, W.; Giardini, D.; Goetz, W.; Golombek, M.; Grott, M.; Hudson, T.; Johnson, C.; Kargl, G.; Kobayashi, N.; Maki, J.; Mimoun, D.; Mocquet, A.; Morgan, P.; Panning, M.; Pike, W. T.; Tromp, J.; van Zoest, T.; Weber, R.; Wieczorek, M. Insight: A Discovery Mission to Explore the Interior of Mars. In *44th Lunar and Planetary Science Conference*; 2013; Abs 1915.
- [82] Banerdt, W. B.; Smrekar, S.; Bandfield, D.; Giardini, D.; Golombek, M.; Johnson, C. L.; Lognonné, P.; Spiga, A.; Spohn, T.; Perrin, C.; Stähler, S. C.; Antonangeli, D.; Asmar, S.; Beghein, C.; Bowles, N.; Bozdog, E.; Chi, P.; Christensen, U.; Clinton, J.; Collins, G. S.; Daubar, I.; Dehant, V.; Drilleau, M.; Fillingim, M.; Folkner, W.; Garcia, R. F.; Garvin, J.; Grant, J.; Grott, M.; Grygorczuk, J.; Hudson, T.; Irving, J. C. E.; Kargl, G.; Kawamura, T.; Kedar, S.; King, S.; Knapmeyer-Endrun, B.; Knapmeyer, M.; Lemmon, M.; Lorenz, R.; Maki, J. N.; Margerin, L.; McLennan, S. M.; Michaut, C.; Mimoun, D.; Mittelholz, A.; Mocquet, A.; Morgan, P.; Mueller, N. T.; Murdoch, N.; Nagihara, S.; Newman, C.; Nimmo, F.; Panning, M.; Pike, W. T.; Plesa, A.; Rodriguez, S.; Rodriguez-Manfredi, J. A.; Russell, C. T.; Schmerr, N.; Siegler, M.; Stanley, S.; Stutzmann, E.; Teanby, N.; Tromp, J.; van Driel, M.; Warner, N.; Weber, R.; Wieczorek, M. Initial Results from the InSight Mission on Mars. *Nat. Geosci.* **2020**, *13*, 183. <https://doi.org/10.1038/s41561-020-0544-y>.
- [83] NASA. *NASA retires InSight Mars Lander mission after years of science*. InSight Mars Lander. <https://www.nasa.gov/press-release/nasa-retires-insight-mars-lander-mission-after-years-of-science> (accessed 2023-03-01).
- [84] NASA. Mars 2020 mission Perseverance Rover. <https://mars.nasa.gov/mars2020/> (accessed 2021-01-14).
- [85] Stack, K. M.; Williams, N. R.; Calef, F.; Sun, V. Z.; Williford, K. H.; Farley, K. A.; Eide, S.; Flannery, D.; Hughes, C.; Jacob, S. R.; Kah, L. C.; Meyen, F.; Molina, A.; Nataf, C. Q.; Rice, M.; Russell, P.; Scheller, E.; Seeger, C. H.; Abbey, W. J.; Adler, J. B.; Amundsen, H.; Anderson, R. B.; Angel, S. M.; Arana, G.; Atkins, J.; Barrington, M.; Berger, T.; Borden, R.; Boring, B.; Brown, A.; Carrier, B. L.; Conrad, P.; Dypvik, H.; Fagents, S. A.; Gallegos, Z. E.; Garczynski, B.; Golder, K.; Gomez, F.; Goreva, Y.; Gupta, S.; Hamran, S.-E.; Hicks, T.; Hinterman, E. D.; Horgan, B. N.; Hurowitz, J.; Johnson, J. R.; Lasue, J.; Kronyak, R. E.; Liu, Y.; Madariaga, J. M.; Mangold, N.; McClean, J.; Miklusick, N.; Nunes, D.; Rojas, C.; Runyon, K.; Schmitz, N.; Scudder, N.; Shaver, E.; SooHoo, J.; Spaulding, R.; Stanish, E.; Tamppari, L. K.; Tice, M. M.; Turenne, N.; Willis, P. A.; Aileen Yingst, R. Photogeologic Map of the Perseverance Rover Field Site in Jezero Crater Constructed by the Mars 2020 Science Team. *Space Sci. Rev.* **2020**, *216*, 127. <https://doi.org/10.1007/s11214-020-00739-x>.

- [86] NASA. Mars Sample Return. <https://www.jpl.nasa.gov/missions/mars-sample-return-msr/> (accessed 2021-01-07).
- [87] NASA. Instruments Summary of the Mars 2020 mission: Perseverance Rover. <https://mars.nasa.gov/mars2020/spacecraft/instruments/> (accessed 2021-01-07).
- [88] Farley, K. A.; Williford, K. H.; Stack, K. M.; Bhartia, R.; Chen, A.; de la Torre, M.; Hand, K.; Goreva, Y.; Herd, C. D. K.; Hueso, R.; Liu, Y.; Maki, J. N.; Martinez, G.; Moeller, R. C.; Nelessen, A.; Newman, C. E.; Nunes, D.; Ponce, A.; Spanovich, N.; Willis, P. A.; Beegle, L. W.; Bell, J. F.; Brown, A. J.; Hamran, S.-E.; Hurowitz, J. A.; Maurice, S.; Paige, D. A.; Rodriguez-Manfredi, J. A.; Schulte, M.; Wiens, R. C. Mars 2020 Mission Overview. *Space Sci. Rev.* **2020**, *216*, 142. <https://doi.org/10.1007/s11214-020-00762-y>.
- [89] Zou, Y.; Zhu, Y.; Bai, Y.; Wang, L.; Jia, Y.; Shen, W.; Fan, Y.; Liu, Y.; Wang, C.; Zhang, A.; Yu, G.; Dong, J.; Shu, R.; He, Z.; Zhang, T.; Du, A.; Fan, M.; Yang, J.; Zhou, B.; Wang, Y.; Peng, Y. Scientific Objectives and Payloads of Tianwen-1, China's First Mars Exploration Mission. *Adv. Sp. Res.* **2021**, *67*, 812. <https://doi.org/10.1016/j.asr.2020.11.005>.
- [90] Egea-Gonzalez, I.; Jiménez-Díaz, A.; Parro, L. M.; Mansilla, F.; Holmes, J. A.; Lewis, S. R.; Patel, M. R.; Ruiz, J. Regional Heat Flow and Subsurface Temperature Patterns at Elysium Planitia and Oxia Planum Areas, Mars. *Icarus* **2021**, *353*, 113379. <https://doi.org/10.1016/j.icarus.2019.07.013>.
- [91] Quantin-Nataf, C.; Carter, J.; Mandon, L.; Thollot, P.; Balme, M.; Volat, M.; Pan, L.; Loizeau, D.; Millot, C.; Breton, S.; Dehouck, E.; Fawdon, P.; Gupta, S.; Davis, J.; Grindrod, P. M.; Pacifici, A.; Bultel, B.; Allemand, P.; Ody, A.; Lozach, L.; Broyer, J. Oxia Planum: The Landing Site for the ExoMars "Rosalind Franklin" Rover Mission: Geological Context and Prelanding Interpretation. *Astrobiology* **2021**, *21*, 345. <https://doi.org/10.1089/ast.2019.2191>.
- [92] ESA. Robotic Exploration of Mars. <https://exploration.esa.int/web/mars/-/48088-mission-overview> (accessed 2021-01-08).
- [93] Campagnola, S.; Yam, C. H.; Tsuda, Y.; Ogawa, N.; Kawakatsu, Y. Mission Analysis for the Martian Moons Explorer (MMS) Mission. *Acta Astronaut.* **2018**, *146*, 409. <https://doi.org/10.1016/j.actaastro.2018.03.024>.
- [94] JAXA. Martian Moons Exploration. <https://www.mmx.jaxa.jp/en/> (accessed 2021-06-28).
- [95] Ulamec, S.; Michel, P.; Grott, M.; Böttger, U.; Hübers, H.; Murdoch, N.; Vernazza, P.; Karatekin, Ö.; Knollenberg, J.; Willner, K.; Grebenstein, M.; Mary, S.; Chazalnoël, P.; Biele, J.; Krause, C.; Ho, T.; Lange, C.; Grundmann, J. T.; Sasaki, K.; Maibaum, M.;

- Küchemann, O.; Reill, J.; Chalon, M.; Barthelmes, S.; Lichtenheldt, R.; Krenn, R.; Amisek, M.; Bertrand, J.; Moussi, A.; Delmas, C.; Tardivel, S.; Arrat, D.; Ijpelaan, F.; Mélac, L.; Lorda, L.; Remeteau, E.; Lange, M.; Mierheim, O.; Reershemius, S.; Usui, T.; Matsuoka, M.; Nakamura, T.; Wada, K.; Miyamoto, H.; Kuramoto, K.; LeMaitre, J.; Mas, G.; Delpech, M.; Celine, L.; Rafflegeau, A.; Boirard, H.; Schmitter, R.; Virmontois, C.; Cenac-Morthe, C.; Besson, D.; Rull, F. A Rover for the JAXA MMX Mission to Phobos\_IAC-19-A3.4.8. In *70th International Astronautical Congress*; Washington DC, 2019; Abs 1–18.
- [96] NASA. *Viking 1*. <https://solarsystem.nasa.gov/missions/viking-1/in-depth/> (accessed 2021-10-21).
- [97] NASA. Press Kit. *Mars Pathfinder Landing*; 1997.
- [98] NASA. Press Kit. *Mars Polar Lander / Deep Space 2*; 1999.
- [99] ESA. *Beagle 2 lander*. [https://www.esa.int/Science\\_Exploration/Space\\_Science/Mars\\_Express/Beagle\\_2\\_lander](https://www.esa.int/Science_Exploration/Space_Science/Mars_Express/Beagle_2_lander) (accessed 2021-10-21).
- [100] NASA. Press Kit. *Mars Exploration Rover Landings*; 2004.
- [101] NASA. Press Kit. *Phoenix Launch / Mission to the Martian Polar North*; 2007.
- [102] NASA. *Mars Curiosity Rover. Instruments*. <https://mars.nasa.gov/msl/spacecraft/instruments/summary/> (accessed 2021-10-21).
- [103] NASA. *Perseverance Rover. Instruments*. <https://mars.nasa.gov/msl/spacecraft/instruments/summary/> (accessed 2021-10-21).
- [104] Division, N. S. S. *Tianwen-1, el primer rover chino en pisar Marte. Todos sus instrumentos en 3D (Mission Huoxing)*. Tianwen-1, el primer rover chino en pisar Marte. Todos sus instrumentos en 3D (Mission Huoxing) (accessed 2021-10-21).
- [105] Clark, B. C.; Baird, A. K.; Rose, H. J.; Toulmin, P.; Christian, R. P.; Kelliher, W. C.; Castro, A. J.; Rowe, C. D.; Keil, K.; Huss, G. R. The Viking X Ray Fluorescence Experiment: Analytical Methods and Early Results. *J. Geophys. Res.* **1977**, *82*, 4577. <https://doi.org/10.1029/JS082i028p04577>.
- [106] Clark, B. C.; Baird, A. K. Martian Regolith X-Ray Analyzer: Test Results of Geochemical Performance. *Geology* **1973**, *1*, 15. [https://doi.org/10.1130/0091-7613\(1973\)1<15:MRXATR>2.0.CO;2](https://doi.org/10.1130/0091-7613(1973)1<15:MRXATR>2.0.CO;2).
- [107] Talboys, D. L.; Potts, P. J.; Fraser, G. W.; Butcher, G.; Wegrzynek, D. The Comparative Analytical Performance of the Beagle 2 X-Ray Spectrometer for in Situ Geochemical Analysis on Mars. *X-Ray Spectrom.* **2009**, *38*, 417. <https://doi.org/10.1002/xrs.1198>.
- [108] Clark, B. C.; Baird, A. K.; Weldon, R. J.; Tsusaki, D. M.; Schnabel, L.; Candelaria, M. P. Chemical Composition of Martian Fines. *J. Geophys. Res.* **1982**, *87*, 10059. <https://doi.org/10.1029/JB087iB12p10059>.

- [109] Bairs, A. K.; Toulmin III, P.; Clark, B. C.; Rose, H. J.; Keil, K.; Christian, R. P.; Gooding, J. L. Mineralogic and Petrologic Implications of Viking Geochemical Results From Mars: Interim Report. *Science*. **1976**, *194*, 1288. <https://doi.org/10.1126/science.194.4271.1288>.
- [110] Clark, B. C. Geochemical Components in Martian Soil. *Geochim. Cosmochim. Acta* **1993**, *57*, 4575. [https://doi.org/10.1016/0016-7037\(93\)90183-W](https://doi.org/10.1016/0016-7037(93)90183-W).
- [111] Clark, B. C.; Baird, A. K. Is the Martian Lithosphere Sulfur Rich? *J. Geophys. Res.* **1979**, *84*, 8395. <https://doi.org/10.1029/JB084iB14p08395>.
- [112] Pullan, D.; Sims, M. R.; Wright, I. P.; Pillinger, C. T.; Trautner, R. Beagle 2: The Exobiological Lander of Mars Express. In *Mars Express: the scientific payload*; ESA Special Publication, 2004; Abs SP1240.
- [113] NASA. *X-ray Instrument for Mars 2020 Rover PIXL*. <https://mars.nasa.gov/resources/6476/x-ray-instrument-for-mars-2020-rover-is-pixl/> (accessed 2021-10-21).
- [114] Blake, D.; Vaniman, D.; Achilles, C.; Anderson, R.; Bish, D.; Bristow, T.; Chen, C.; Chipera, S.; Crisp, J.; Des Marais, D.; Downs, R. T.; Farmer, J.; Feldman, S.; Fonda, M.; Gaihanou, M.; Ma, H.; Ming, D. W.; Morris, R. V.; Sarrazin, P.; Stolper, E.; Treiman, A.; Yen, A. Characterization and Calibration of the CheMin Mineralogical Instrument on Mars Science Laboratory. *Space Sci. Rev.* **2012**, *170*, 341. <https://doi.org/10.1007/s11214-012-9905-1>.
- [115] Allwood, A. C.; Wade, L. A.; Foote, M. C.; Elam, W. T.; Hurowitz, J. A.; Battel, S.; Dawson, D. E.; Denise, R. W.; Ek, E. M.; Gilbert, M. S.; King, M. E.; Liebe, C. C.; Parker, T.; Pedersen, D. A. K.; Randall, D. P.; Sharrow, R. F.; Sondheim, M. E.; Allen, G.; Arnett, K.; Au, M. H.; Basset, C.; Benn, M.; Bousman, J. C.; Braun, D.; Calvet, R. J.; Clark, B.; Cinquini, L.; Conaby, S.; Conley, H. A.; Davidoff, S.; Delaney, J.; Denver, T.; Diaz, E.; Doran, G. B.; Ervin, J.; Evans, M.; Flannery, D. O.; Gao, N.; Gross, J.; Grotzinger, J.; Hannah, B.; Harris, J. T.; Harris, C. M.; He, Y.; Heirwegh, C. M.; Hernandez, C.; Hertzberg, E.; Hodyss, R. P.; Holden, J. R.; Hummel, C.; Jadusingh, M. A.; Jørgensen, J. L.; Kawamura, J. H.; Kitiyakara, A.; Kozaczek, K.; Lambert, J. L.; Lawson, P. R.; Liu, Y.; Luchik, T. S.; Macneal, K. M.; Madsen, S. N.; McLennan, S. M.; McNally, P.; Meras, P. L.; Muller, R. E.; Napoli, J.; Naylor, B. J.; Nemere, P.; Ponomarev, I.; Perez, R. M.; Pootrakul, N.; Romero, R. A.; Rosas, R.; Sachs, J.; Schaefer, R. T.; Schein, M. E.; Setterfield, T. P.; Singh, V.; Song, E.; Soria, M. M.; Stek, P. C.; Tallarida, N. R.; Thompson, D. R.; Tice, M. M.; Timmermann, L.; Torossian, V.; Treiman, A.; Tsai, S.; Uckert, K.; Villalvazo, J.; Wang, M.; Wilson, D. W.; Worel, S. C.; Zamani, P.; Zappe, M.; Zhong, F.; Zimmerman, R. PIXL: Planetary Instrument for X-Ray Lithochemistry. *Space Sci. Rev.* **2020**, *216*, 134. <https://doi.org/10.1007/s11214-020-00767-7>.

- [116] NASA. PIXL's First Chemical Maps. <https://mars.nasa.gov/resources/26060/pixls-first-chemical-maps/> (accessed 2023-03-14).
- [117] Rieder, R.; Economou, T.; Wänke, H.; Turkevich, A.; Crisp, J.; Brückner, J.; Dreibus, G.; McSween, H. Y. The Chemical Composition of Martian Soil and Rocks Returned by the Mobile Alpha Proton X-Ray Spectrometer: Preliminary Results from the X-Ray Mode. *Science*. **1997**, *278*, 1771. <https://doi.org/10.1126/science.278.5344.1771>.
- [118] Bell, J. F.; McSween, H. Y.; Crisp, J. A.; Morris, R. V.; Murchie, S. L.; Bridges, N. T.; Johnson, J. R.; Britt, D. T.; Golombek, M. P.; Moore, H. J.; Ghosh, A.; Bishop, J. L.; Anderson, R. C.; Brückner, J.; Economou, T.; Greenwood, J. P.; Gunnlaugsson, H. P.; Hargraves, R. M.; Hviid, S.; Knudsen, J. M.; Madsen, M. B.; Reid, R.; Rieder, R.; Soderblom, L. Mineralogic and Compositional Properties of Martian Soil and Dust: Results from Mars Pathfinder. *J. Geophys. Res. Planets* **2000**, *105*, 1721. <https://doi.org/10.1029/1999JE001060>.
- [119] Gellert, R.; Campbell, J. L.; King, P. L.; Leshin, L. A.; Lugmair, G. W.; Spray, J. S.; Squyres, S. W.; Yen, A. S. The Alpha-Particle-X-Ray-Spectrometer (APXS) for the Mars Science Laboratory (MSL) Rover Mission. In *40th Lunar and Planetary Science Conference*; 2009; Abs 2364.
- [120] Rieder, R.; Gellert, R.; Anderson, R. C.; Brückner, J.; Clark, B. C.; Dreibus, G.; Economou, T.; Klingelhöfer, G.; Lugmair, G. W.; Ming, D. W.; Squyres, S. W.; D'Uston, C.; Wänke, H.; Yen, A.; Zipfel, J. Chemistry of Rocks and Soils at Meridiani Planum from the Alpha Particle X-Ray Spectrometer. *Science*. **2004**, *306*, 1746. <https://doi.org/10.1126/science.1104358>.
- [121] Gellert, R.; Rieder, R.; Brückner, J.; Clark, B. C.; Dreibus, G.; Klingelhöfer, G.; Lugmair, G. W.; Ming, D. W.; Yen, A.; Zipfel, J.; Squyres, S. W. Alpha Particle X-Ray Spectrometer (APXS): Results from Gusev Crater and Calibration Report. *J. Geophys. Res.* **2006**, *111*, E02S0.
- [122] Ruff, S. W.; Farmer, J. D.; Calvin, W. M.; Herkenhoff, K. E.; Johnson, J. R.; Morris, R. V.; Rice, M. S.; Arvidson, R. E.; Bell, J. F.; Christensen, P. R.; Squyres, S. W. Characteristics, Distribution, Origin, and Significance of Opaline Silica Observed by the Spirit Rover in Gusev Crater, Mars. *J. Geophys. Res.* **2011**, *116*, E00F23. <https://doi.org/10.1029/2010JE003767>.
- [123] Kim, K. J.; Lee, J. H.; Lee, S. R.; Sim, E. S. X-Ray Spectroscopy for Planetary Surface Analysis and Future Trend. *J. Petrol. Soc. Korea* **2010**, *19*, 4, 245.
- [124] Rieder, R.; Gellert, R.; Brückner, J.; Klingelhöfer, G.; Dreibus, G.; Yen, A.; Squyres, S. W. The New Athena Alpha Particle X-Ray Spectrometer for the Mars Exploration Rovers. *J. Geophys. Res. Planets* **2003**, *108*, 8066. <https://doi.org/10.1029/2003JE002150>.

- [125] NASA. *APXS for Scientists. Mars Curiosity Rover*. <https://mars.nasa.gov/msl/spacecraft/instruments/apxs/for-scientists/> (accessed 2021-10-21).
- [126] Stolper, E. M.; Baker, M. B.; Newcombe, M. E.; Schmidt, M. E.; Treiman, A. H.; Cousin, A.; Dyar, M. D.; Fisk, M. R.; Gellert, R.; King, P. L.; Leshin, L.; Maurice, S.; McLennan, S. M.; Minitti, M. E.; Perrett, G.; Rowland, S.; Sautter, V.; Wiens, R. C.; MarsScienceLaboratoryTeam. The Petrochemistry of Jake\_M: A Martian Mugearite. *Science*. **2013**, *341*, 6153. <https://doi.org/10.1126/science.1239463>.
- [127] Kounaves, S. P.; Hecht, M. H.; West, S. J.; Morookian, J.-M.; Young, S. M. M.; Quinn, R.; Grunthaner, P.; Wen, X.; Weilert, M.; Cable, C. A.; Fisher, A.; Gospodinova, K.; Kapit, J.; Stroble, S.; Hsu, P.-C.; Clark, B. C.; Ming, D. W.; Smith, P. H. The MECA Wet Chemistry Laboratory on the 2007 Phoenix Mars Scout Lander. *J. Geophys. Res.* **2009**, *114*, E00A19. <https://doi.org/10.1029/2008JE003084>.
- [128] Fischer, E. Searching for Brine on Mars Using Raman Spectroscopy. *Física la Tierra* **2016**, *28*, 181. [https://doi.org/10.5209/rev\\_FITE.2016.v28.53903](https://doi.org/10.5209/rev_FITE.2016.v28.53903).
- [129] Wiens, R. C.; Maurice, S.; Barraclough, B.; Saccoccio, M.; Barkley, W. C.; Bell, J. F.; Bender, S.; Bernardin, J.; Blaney, D.; Blank, J.; Bouyé, M.; Bridges, N.; Bultman, N.; Cais, P.; Clanton, R. C.; Clark, B.; Clegg, S.; Cousin, A.; Cremers, D.; Cros, A.; DeFlores, L.; Delapp, D.; Dingler, R.; D'Uston, C.; Darby Dyar, M.; Elliott, T.; Enemark, D.; Fabre, C.; Flores, M.; Forni, O.; Gasnault, O.; Hale, T.; Hays, C.; Herkenhoff, K.; Kan, E.; Kirkland, L.; Kouach, D.; Landis, D.; Langevin, Y.; Lanza, N.; LaRocca, F.; Lasue, J.; Latino, J.; Limonadi, D.; Lindensmith, C.; Little, C.; Mangold, N.; Manhes, G.; Mauchien, P.; McKay, C.; Miller, E.; Mooney, J.; Morris, R. V.; Morrison, L.; Nelson, T.; Newsom, H.; Ollila, A.; Ott, M.; Pares, L.; Perez, R.; Poitrasson, F.; Provost, C.; Reiter, J. W.; Roberts, T.; Romero, F.; Sautter, V.; Salazar, S.; Simmonds, J. J.; Stiglich, R.; Storms, S.; Striebig, N.; Thocaven, J.-J.; Trujillo, T.; Ulibarri, M.; Vaniman, D.; Warner, N.; Waterbury, R.; Whitaker, R.; Witt, J.; Wong-Swanson, B. The ChemCam Instrument Suite on the Mars Science Laboratory (MSL) Rover: Body Unit and Combined System Tests. *Space Sci. Rev.* **2012**, *170*, 167. <https://doi.org/10.1007/s11214-012-9902-4>.
- [130] Wiens, R. C.; Maurice, S.; Robinson, S. H.; Nelson, A. E.; Cais, P.; Bernardi, P.; Newell, R. T.; Clegg, S.; Sharma, S. K.; Storms, S.; Deming, J.; Beckman, D.; Ollila, A. M.; Gasnault, O.; Anderson, R. B.; André, Y.; Angel, S. M.; Arana, G.; Auden, E.; Beck, P.; Becker, J.; Benzerara, K.; Bernard, S.; Beyssac, O.; Borges, L.; Bousquet, B.; Boyd, K.; Caffrey, M.; Carlson, J.; Castro, K.; Celis, J.; Chide, B.; Clark, K.; Cloutis, E.; Cordoba, E. C.; Cousin, A.; Dale, M.; Deflores, L.; Delapp, D.; Deleuze, M.; Dirmyer, M.; Donny, C.; Dromart, G.; Duran, M. G.; Egan, M.; Ervin, J.; Fabre, C.; Fau, A.; Fischer, W.;

- Forni, O.; Fouchet, T.; Fresquez, R.; Frydenvang, J.; Gasway, D.; Gontijo, I.; Grotzinger, J.; Jacob, X.; Jacquiod, S.; Johnson, J. R.; Klisiewicz, R. A.; Lake, J.; Lanza, N.; Laserna, J.; Lasue, J.; Le Mouélic, S.; Lucero, B.; Madariaga, J. M.; Madsen, M.; Madsen, S.; Mangold, N.; Manrique, J. A.; Martinez, J. P.; Martinez-Frias, J.; McCabe, K. P.; McConnochie, T. H.; McGlown, J. M.; McLennan, S. M.; Melikechi, N.; Meslin, P.; Michel, J. M.; Mimoun, D.; Misra, A.; Montagnac, G.; Montmessin, F.; Mousset, V.; Murdoch, N.; Newsom, H.; Ott, L. A.; Ousnamer, Z. R.; Pares, L.; Parot, Y.; Pawlucyk, R.; Peterson, C. G.; Pilleri, P.; Pinet, P.; Pont, G.; Poulet, F.; Provost, C.; Quertier, B.; Quinn, H.; Rapin, W.; Reess, J.; Regan, A. H.; Reyes-Newell, A. L.; Romano, P. J.; Royer, C.; Rull, F.; Sandoval, B.; Sarrao, J. H.; Sautter, V.; Schoppers, M. J.; Schöder, S.; Seitz, D.; Shepherd, T.; Sobron, P.; Dubois, B.; Sridhar, V.; Toplis, M. J.; Torre-Fdez, I.; Trettel, I. A.; Underwood, M.; Valdez, A.; Valdez, J.; Venhaus, D.; Willis, P. The SuperCam Instrument Suite on the NASA Mars 2020 Rover: Body Unit and Combined System Tests. *Space Sci. Rev.* **2021**, *217*, 4. <https://doi.org/10.1007/s11214-020-00777-5>.
- [131] Anderson, R. B.; Forni, O.; Cousin, A.; Wiens, R. C.; Clegg, S. M.; Frydenvang, J.; Gabriel, T. S. J.; Ollila, A.; Schröder, S.; Beyssac, O.; Gibbons, E.; Vogt, D. S.; Clavé, E.; Manrique, J.-A.; Legett, C.; Pilleri, P.; Newell, R. T.; Sarrao, J.; Maurice, S.; Arana, G.; Benzerara, K.; Bernardi, P.; Bernard, S.; Bousquet, B.; Brown, A. J.; Alvarez-Llamas, C.; Chide, B.; Cloutis, E.; Comellas, J.; Connell, S.; Dehouck, E.; Delapp, D. M.; Essunfeld, A.; Fabre, C.; Fouchet, T.; Garcia-Florentino, C.; García-Gómez, L.; Gasda, P.; Gasnault, O.; Hausrath, E. M.; Lanza, N. L.; Laserna, J.; Lasue, J.; Lopez, G.; Madariaga, J. M.; Mandon, L.; Mangold, N.; Meslin, P.-Y.; Nelson, A. E.; Newsom, H.; Reyes-Newell, A. L.; Robinson, S.; Rull, F.; Sharma, S.; Simon, J. I.; Sobron, P.; Fernandez, I. T.; Udry, A.; Venhaus, D.; McLennan, S. M.; Morris, R. V.; Ehlmann, B. Post-Landing Major Element Quantification Using SuperCam Laser Induced Breakdown Spectroscopy. *Spectrochim. Acta Part B At. Spectrosc.* **2022**, *188*, 106347. <https://doi.org/10.1016/j.sab.2021.106347>.
- [132] Sarkar, S.; Bose, N.; Bhattacharya, S.; Bhandari, S. Identification of Smectites by IR and LIBS Instruments of SuperCam Suite Onboard Mars 2020 Perseverance Rover: Comments on the Non-Retrieval of First Frill Core. *Curr. Sci.* **2022**, *123*, 93.
- [133] Beck, P.; Forni, O.; Meslin, P. Y.; Benzerana, K.; Beyssac, O.; Lasue, J.; Quantin-Nataf, C.; Poulet, F.; Royer, C.; Mandon, L.; Rapin, W.; Clavé, E.; Cousin, A.; Schöder, S.; Le Mouélic, S.; Gasnault, O.; Ollila, A. M.; Hausrath, E.; Maurice, S.; Wiens, R. C.; SuperCamTeam. Hydrogen in Rocks from Jezero Crater Investigated with SuperCam LIBS. In *53rd Lunar and Planetary Science Conference*; The Woodlands, TX, USA, 2022; Abs 1178.

- [134] Xu, W.; Liu, X.; Yan, Z.; Li, L.; Zhang, Z.; Kuang, Y.; Jiang, H.; Yu, H.; Yang, F.; Liu, C.; Wang, T.; Li, C.; Jin, Y.; Shen, J.; Wang, B.; Wan, W.; Chen, J.; Ni, S.; Ruan, Y.; Xu, R.; Zhang, C.; Yuan, Z.; Wan, X.; Yang, Y.; Li, Z.; Shen, Y.; Liu, D.; Wang, B.; Yuan, R.; Bao, T.; Shu, R. The MarSCoDe Instrument Suite on the Mars Rover of China's Tianwen-1 Mission. *Space Sci. Rev.* **2021**, *217*, 64. <https://doi.org/10.1007/s11214-021-00836-5>.
- [135] NASA. *Searching for Life on Mars: The Development of the Viking Gas Chromatograph Mass Spectrometer (GCMS)*. [https://appel.nasa.gov/critical-knowledge/case-studies/appel-case-studies/viking\\_gcms-html/](https://appel.nasa.gov/critical-knowledge/case-studies/appel-case-studies/viking_gcms-html/) (accessed 2023-03-14).
- [136] Biemann, K. On the Ability of the Viking Gas Chromatograph-Mass Spectrometer to Detect Organic Matter. *Proc. Natl. Acad. Sci.* **2007**, *104*, 10310. <https://doi.org/10.1073/pnas.0703732104>.
- [137] Clark, J.; Sutter, B.; Archer, P. D.; Ming, D.; Rampe, E.; McAdam, A.; Navarro-González, R.; Eigenbrode, J.; Glavin, D.; Zorzano, M.-P.; Martin-Torres, J.; Morris, R.; Tu, V.; Ralston, S. J.; Mahaffy, P. A Review of Sample Analysis at Mars-Evolved Gas Analysis Laboratory Analog Work Supporting the Presence of Perchlorates and Chlorates in Gale Crater, Mars. *Minerals* **2021**, *11*, 475. <https://doi.org/10.3390/min11050475>.
- [138] Bogard, D. D.; Johnson, P. Martian Gases in an Antarctic Meteorite? *Science*. **1983**, *221*, 651. <https://doi.org/10.1126/science.221.4611.651>.
- [139] Udry, A.; Howarth, G. H.; Herd, C. D. K.; Day, J. M. D.; Lapen, T. J.; Filiberto, J. What Martian Meteorites Reveal About the Interior and Surface of Mars. *J. Geophys. Res. Planets* **2020**, *125*, e2020JE006523. <https://doi.org/10.1029/2020JE006523>.
- [140] Treiman, A. H.; Gleason, J. D.; Bogard, D. D. The SNC Meteorites Are from Mars. *Planet. Space Sci.* **2000**, *48*, 1213. [https://doi.org/10.1016/S0032-0633\(00\)00105-7](https://doi.org/10.1016/S0032-0633(00)00105-7).
- [141] Mahaffy, P. R.; Webster, C. R.; Cabane, M.; Conrad, P. G.; Coll, P.; Atreya, S. K.; Arvey, R.; Barciniak, M.; Benna, M.; Bleacher, L.; Brinckerhoff, W. B.; Eigenbrode, J. L.; Carignan, D.; Cascia, M.; Chalmers, R. A.; Dworkin, J. P.; Errigo, T.; Everson, P.; Franz, H.; Farley, R.; Feng, S.; Frazier, G.; Freissinet, C.; Glavin, D. P.; Harpold, D. N.; Hawk, D.; Holmes, V.; Johnson, C. S.; Jones, A.; Jordan, P.; Kellogg, J.; Lewis, J.; Lyness, E.; Malespin, C. A.; Martin, D. K.; Maurer, J.; McAdam, A. C.; McLennan, D.; Nolan, T. J.; Noriega, M.; Pavlov, A. A.; Prats, B.; Raaen, E.; Sheinman, O.; Sheppard, D.; Smith, J.; Stern, J. C.; Tan, F.; Trainer, M.; Ming, D. W.; Morris, R. V.; Jones, J.; Gundersen, C.; Steele, A.; Wray, J.; Botta, O.; Leshin, L. A.; Owen, T.; Battel, S.; Jakosky, B. M.; Manning, H.; Squyres, S.; Navarro-González, R.; McKay, C. P.; Raulin, F.; Sternberg, R.; Buch, A.; Sorensen, P.; Kline-Schoder, R.; Coscia, D.; Szopa, C.; Teinturier, S.; Baffes, C.; Feldman, J.; Flesch, G.; Forouhar, S.; Garcia, R.; Keymeulen, D.; Woodward, S.; Block,

- B. P.; Arnett, K.; Miller, R.; Edmonson, C.; Gorevan, S.; Mumm, E. The Sample Analysis at Mars Investigation and Instrument Suite. *Space Sci. Rev.* **2012**, *170*, 401. <https://doi.org/10.1007/s11214-012-9879-z>.
- [142] NASA. Mars Curiosity Rover, the SAM instrument. <https://mars.nasa.gov/msl/spacecraft/instruments/sam/> (accessed 2021-07-10).
- [143] Franz, H. B.; Mahaffy, P. R.; Webster, C. R.; Flesch, G. J.; Raaen, E.; Freissinet, C.; Atreya, S. K.; House, C. H.; McAdam, A. C.; Knudson, C. A.; Archer, P. D.; Stern, J. C.; Steele, A.; Sutter, B.; Eigenbrode, J. L.; Glavin, D. P.; Lewis, J. M. T.; Malespin, C. A.; Millan, M.; Ming, D. W.; Navarro-González, R.; Summons, R. E. Indigenous and Exogenous Organics and Surface–Atmosphere Cycling Inferred from Carbon and Oxygen Isotopes at Gale Crater. *Nat. Astron.* **2020**, *4*, 526. <https://doi.org/10.1038/s41550-019-0990-x>.
- [144] Millan, M.; Szopa, C.; Buch, A.; Coll, P.; Glavin, D. P.; Freissinet, C.; Navarro-Gonzalez, R.; François, P.; Coscia, D.; Bonnet, J. Y.; Teinturier, S.; Cabane, M.; Mahaffy, P. R. In Situ Analysis of Martian Regolith with the SAM Experiment during the First Mars Year of the MSL Mission: Identification of Organic Molecules by Gas Chromatography from Laboratory Measurements. *Planet. Space Sci.* **2016**, *129*, 88. <https://doi.org/10.1016/j.pss.2016.06.007>.
- [145] Millan, M.; Szopa, C.; Buch, A.; Cabane, M.; Teinturier, S.; Mahaffy, P.; Johnson, S. S. Performance of the SAM Gas Chromatographic Columns under Simulated Flight Operating Conditions for the Analysis of Chlorohydrocarbons on Mars. *J. Chromatogr. A* **2019**, *1598*, 183. <https://doi.org/10.1016/j.chroma.2019.03.064>.
- [146] Blake, D. F.; Morris, R. V.; Kocurek, G.; Morrison, S. M.; Downs, R. T.; Bish, D.; Ming, D. W.; Edgett, K. S.; Rubin, D.; Goetz, W.; Madsen, M. B.; Sullivan, R.; Gellert, R.; Campbell, I.; Treiman, A. H.; McLennan, S. M.; Yen, A. S.; Grotzinger, J.; Vaniman, D. T.; Chipera, S. J.; Achilles, C. N.; Rampe, E. B.; Sumner, D.; Meslin, P.-Y.; Maurice, S.; Forni, O.; Gasnault, O.; Fisk, M.; Schmidt, M.; Mahaffy, P.; Leshin, L. A.; Glavin, D.; Steele, A.; Freissinet, C.; Navarro-González, R.; Yingst, R. A.; Kah, L. C.; Bridges, N.; Lewis, K. W.; Bristow, T. F.; Farmer, J. D.; Crisp, J. A.; Stolper, E. M.; Des Marais, D. J.; Sarrazin, P.; MarsScienceLaboratoryTeam. Curiosity at Gale Crater, Mars: Characterization and Analysis of the Rocknest Sand Shadow. *Science*. **2013**, *341*, 12395. <https://doi.org/10.1126/science.1239505>.
- [147] Leshin, L. A.; Mahaffy, P. R.; Webster, C. R.; Cabane, M.; Coll, P.; Conrad, P. G.; Archer, P. D.; Atreya, S. K.; Brunner, A. E.; Buch, A.; Eigenbrode, J. L.; Flesch, G. J.; Franz, H. B.; Freissinet, C.; Glavin, D. P.; McAdam, A. C.; Miller, K. E.; Ming, D. W.; Morris, R. V.; Navarro-González, R.; Niles, P. B.; Owen, T.; Pepin, R. O.; Squyres, S.; Steele, A.; Stern, J. C.; Summons, R. E.; Sumner, D. Y.; Sutter,

- B.; Szopa, C.; Teinturier, S.; Trainer, M. G.; Wray, J. J.; Grotzinger, J. P.; MarsScienceLaboratoryTeam. Volatile, Isotope, and Organic Analysis of Martian Fines with the Mars Curiosity Rover. *Science*. **2013**, *341*, 12389. <https://doi.org/10.1126/science.1238937>.
- [148] Freissinet, C.; Glavin, D. P.; Mahaffy, P. R.; Miller, K. E.; Eigenbrode, J. L.; Summons, R. E.; Brunner, A. E.; Buch, A.; Szopa, C.; Archer, P. D.; Franz, H. B.; Atreya, S. K.; Brinckerhoff, W. B.; Cabane, M.; Coll, P.; Conrad, P. G.; Des Marais, D. J.; Dworkin, J. P.; Fairén, A. G.; François, P.; Grotzinger, J. P.; Kashyap, S.; ten Kate, I. L.; Leshin, L. A.; Malespin, C. A.; Martin, M. G.; Martin-Torres, F. J.; McAdam, A. C.; Ming, D. W.; Navarro-González, R.; Pavlov, A. A.; Prats, B. D.; Squyres, S. W.; Steele, A.; Stern, J. C.; Sumner, D. Y.; Sutter, B.; Zorzano, M. -P. Organic Molecules in the Sheepbed Mudstone, Gale Crater, Mars. *J. Geophys. Res. Planets* **2015**, *120*, 495. <https://doi.org/10.1002/2014JE004737>.
- [149] Millan, M.; Williams, A. J.; McAdam, A.; Eigenbrode, J. L.; Freissinet, C.; Glavin, D. P.; Szopa, C.; Buch, A.; Williams, R. H.; Navarro-González, R.; Lewis, J. M. T.; Fox, V.; Bryk, A. B.; Bennet, K.; Steele, A.; Teinturier, S.; Malespin, C. A.; Johnson, S. S.; Mahaffy, P. R. Organic Molecules Revealed in Glen Torridon by the SAM Instrument, No. 2548. In *52nd Lunar and Planetary Science Conference*; 2021; Abs 2039.
- [150] Webster, C. R.; Mahaffy, P. R.; Flesch, G. J.; Niles, P. B.; Jones, J. H.; Leshin, L. A.; Atreya, S. K.; Stern, J. C.; Christensen, L. E.; Owen, T.; Franz, H.; Pepin, R. O.; Steele, A. Isotope Ratios of H, C, and O in CO<sub>2</sub> and H<sub>2</sub>O of the Martian Atmosphere. *Science*. **2013**, *341*, 260. <https://doi.org/10.1126/science.1237961>.
- [151] Mahaffy, P. R.; Webster, C. R.; Stern, J. C.; Brunner, A. E.; Atreya, S. K.; Conrad, P. G.; Domagal-Goldman, S.; Eigenbrode, J. L.; Flesch, G. J.; Christensen, L. E.; Franz, H. B.; Freissinet, C.; Glavin, D. P.; Grotzinger, J. P.; Jones, J. H.; Leshin, L. A.; Malespin, C.; McAdam, A. C.; Ming, D. W.; Navarro-Gonzalez, R.; Niles, P. B.; Owen, T.; Pavlov, A. A.; Steele, A.; Trainer, M. G.; Williford, K. H.; Wray, J. J. The Imprint of Atmospheric Evolution in the D/H of Hesperian Clay Minerals on Mars. *Science*. **2015**, *347*, 412. <https://doi.org/10.1126/science.1260291>.
- [152] Mahaffy, P. R.; Webster, C. R.; Atreya, S. K.; Franz, H.; Wong, M.; Conrad, P. G.; Harpold, D.; Jones, J. J.; Leshin, L. A.; Manning, H.; Owen, T.; Pepin, R. O.; Squyres, S.; Trainer, M.; MarsScienceLaboratoryTeam. Abundance and Isotopic Composition of Gases in the Martian Atmosphere from the Curiosity Rover. *Science*. **2013**, *341*, 263. <https://doi.org/10.1126/science.1237966>.
- [153] Goesmann, F.; Brinckerhoff, W. B.; Raulin, F.; Goetz, W.; Danell, R. M.; Getty, S. A.; Silijeström, S.; Mibach, H.; Steininger, H.; Arevalo, R. D.; Buch, J. A.; Freissinet, C.; Grubisic, A.; Meierhenrich, U. J.; Pinnick, V. T.; Stalport, F.; Szopa, C.; Vago, J. L.; Lindner, R.; Schulte, M. D.; Brucato, J. R.; Glavin, D. P.; Grand, N.; Li, X.; van

- Amerom, F. H. W. The Mars Organic Molecule Analyzer (MOMA) Instrument: Characterization of Organic Material in Martian Sediments. *Astrobiology* **2017**, *17*, 655. <https://doi.org/10.1089/ast.2016.1551>.
- [154] Thomas, A. Mutch Has Described the History of the Lander Camera. In *The Martian Landscape, NASA SP-425*; 1978; pp 3–31.
- [155] NASA. *SAM for Scientists. Mars Curiosity Rover*. <https://mars.nasa.gov/msl/spacecraft/instruments/sam/for-scientists/> (accessed 2021-10-21).
- [156] Goetz, W.; Brinckerhoff, W. B.; Arevalo, R.; Freissinet, C.; Getty, S.; Glavin, D. P.; Siljeström, S.; Buch, A.; Stalport, F.; Grubisic, A.; Li, X.; Pinnick, V.; Danell, R.; van Amerom, F. H. W.; Goesmann, F.; Steininger, H.; Grand, N.; Raulin, F.; Szopa, C.; Meierhenrich, U.; Brucato, J. R. MOMA: The Challenge to Search for Organics and Biosignatures on Mars. *Int. J. Astrobiol.* **2016**, *15*, 239. <https://doi.org/10.1017/S1473550416000227>.
- [157] Boynton, W. V.; Lorenz, R. D.; Bailey, S. H.; Williams, M. S.; Hamara, D. K. The Thermal and Evolved Gas Analyzer (TEGA) on the 1998 Mars Polar Lander. In *1st International Conference on Mars Polar Science*; Houston, Texas, 1998; Abs 3047.
- [158] Boynton, W. V.; Bailey, S. H.; Hamara, D. K.; Kring, D. K.; Lorenz, R. D.; Ward, M.; Williams, M. S. The Thermal and Evolved Gas Analyzer (TEGA) on the Mars Polar Lander. In *Lunar and Planetary Science XXX*; Houston, Texas, 1999; Abs 1914.
- [159] Boynton, W. V.; Bailey, S. H.; Hamara, D. K.; Williams, M. S.; Bode, R. C.; Fitzgibbon, M. R.; Ko, W.; Ward, M. G.; Sridhar, K. R.; Blanchard, J. A.; Lorenz, R. D.; May, R. D.; Paige, D. A.; Pathare, A. V.; Kring, D. A.; Leshin, L. A.; Ming, D. W.; Zent, A. P.; Golden, D. C.; Kerry, K. E.; Lauer, H. V.; Quinn, R. C. Thermal and Evolved Gas Analyzer: Part of the Mars Volatile and Climate Surveyor Integrated Payload. *J. Geophys. Res. Planets* **2001**, *106*, 17683. <https://doi.org/10.1029/1999JE001153>.
- [160] Hoffman, J. H.; Chaney, R. C.; Hammack, H. Phoenix Mars Mission—The Thermal Evolved Gas Analyzer. *J. Am. Soc. Mass Spectrom.* **2008**, *19*, 1377. <https://doi.org/10.1016/j.jasms.2008.07.015>.
- [161] Sutter, B.; Boynton, W. V.; Ming, D. W.; Niles, P. B.; Morris, R. V.; Golden, D. C.; Lauer, H. V.; Fellows, C.; Hamara, D. K.; Mertzman, S. A. The Detection of Carbonate in the Martian Soil at the Phoenix Landing Site: A Laboratory Investigation and Comparison with the Thermal and Evolved Gas Analyzer (TEGA) Data. *Icarus* **2012**, *2018*, 290. <https://doi.org/10.1016/j.icarus.2011.12.002>.
- [162] Toner, J. D.; Catling, D. C.; Light, B. Modeling Salt Precipitation from Brines on Mars: Evaporation versus Freezing Origin for Soil Salts. *Icarus* **2015**, *250*, 451. <https://doi.org/10.1016/j.icarus.2014.12.013>.

- [163] Marion, G. M.; Kargel, J. S. *Cold Aqueous Planetary Geochemistry with FREZCHEM. From Modeling to the Search for Life at the Limits*; Springer: Berlin/Heidelberg, 2008.
- [164] Kounaves, S. P.; Hecht, M. H.; Kapit, J.; Quinn, R. C.; Catling, D. C.; Clark, B. C.; Ming, D. W.; Gospodinova, K.; Hredzak, P.; McElhoney, K.; Shusterman, J. Soluble Sulfate in the Martian Soil at the Phoenix Landing Site. *Geophys. Res. Lett.* **2010**, *37*, L09201. <https://doi.org/10.1029/2010GL042613>.
- [165] Toner, J. D.; Catling, D. C.; Light, B. A Revised Pitzer Model for Low-Temperature Soluble Salts Assemblages at the Phoenix Site, Mars. *Geochim. Cosmochim. Acta* **2015**, *166*, 327. <https://doi.org/10.1016/j.gca.2015.06.011>.
- [166] Pullan, D.; Sims, M. R.; Wright, I. P.; Pillinger, C. T.; Trautner, R. Beagle 2: The Exobiological Lander of Mars Express. In *Mars Express: the scientific payload*; Wilson, A., Ed.; ESA Publications Division: Noordwijk, Netherlands, 2001; pp 165–204.
- [167] Klingelhöfer, G.; Morris, R. V.; de Souza, P. A.; Bernhardt, B.; Team, A. S. The Miniaturized Mössbauer Spectrometer MIMOS II of the Athena Payload for the 1003 MER Mission. In *6th International Conference on Mars*; 2003; Abs 3132.
- [168] Klingelhöfer, G.; Morris, R. V.; Bernhardt, B.; Schöder, C.; Rodionov, D. S.; de Souza Jr., P. A.; Yen, A.; Gellert, R.; Evlanov, E. N.; Zubkov, B.; Foh, J.; Bonnes, U.; Kankleit, E.; Gütlich, P.; Ming, D. W.; Renz, F.; Wdowiak, T.; Squyres, S. W.; Arvidson, R. E. Jarosite and Hematite at Meridiani Planum from Opportunity's Mössbauer Spectrometer. *Science*. **2004**, *306*, 1740. <https://doi.org/10.1126/science.1104653>.
- [169] Morris, R. V.; Klingelhöfer, G.; Schöder, C.; Rodionov, D. S.; Yen, A.; Ming, D. W.; de Souza, P. A.; Fleischer, I.; Wdowiak, T.; Gellert, R.; Bernhardt, B.; Evlanov, E. N.; Zubkov, B.; Foh, J.; Bonnes, U.; Kankleit, E.; Gütlich, P.; Renz, F.; Squyres, S. W.; Arvidson, R. E. Mössbauer Mineralogy of Rock, Soil, and Dust at Gusev Crater, Mars: Spirit's Journey through Weakly Altered Olivine Basalt on the Plains and Pervasively Altered Basalt in the Columbia Hills. *J. Geophys. Res.* **2006**, *111*, E02S1. <https://doi.org/10.1029/2005JE002584>.
- [170] Klingelhöfer, G.; Bernhardt, B.; Foh, J.; Bonnes, U.; Rodionov, D.; de Souza, P. A.; Schröder, C.; Gellert, R.; Kane, S.; Gütlich, P.; Kankleit, E. The Miniaturized Mössbauer Spectrometer MIMOS II for Extraterrestrial and Outdoor Terrestrial Applications: A Status Report. *Hyperfine Interact.* **2002**, *144–145*, 371. [https://doi.org/10.1007/978-94-010-0045-1\\_36](https://doi.org/10.1007/978-94-010-0045-1_36).
- [171] Blake, D. F.; Vaniman, D.; Anderson, R.; Bish, D.; Chipera, S.; Chemtob, S. M.; Crisp, J.; Des Marais, D. J.; Downs, R. T.; Farmer, J.; Gailhanou, M.; Ming, D.; Morris, D.; Stolper, E.; Sarrazin, P.; Treiman, A.; Yen, A. The CheMin Mineralogical Instrument on the

- Mars Science Laboratory Mission. In *40th Lunar and Planetary Science Conference*; 2009; Abs 1484.
- [172] Downs, R. T.; Team, M. S. Determining Mineralogy on Mars with the CheMin X-Ray Diffractometer. *Elements* **2015**, *11*, 45. <https://doi.org/10.2113/gselements.11.1.45>.
- [173] NASA. *Curiosity's First 14 Rock or Soil Sampling Sites on Mars*. <https://mars.nasa.gov/resources/7858/curiositys-first-14-rock-or-soil-sampling-sites-on-mars/> (accessed 2021-10-21).
- [174] Beegle, L. W.; Bhartia, R.; DeFlores, L.; Abbey, W.; Miller, E.; Bailey, Z.; Razzell Hollis, J.; Pollack, R.; Asher, S.; Burton, A.; Fries, M.; Conrad, P.; Clegg, S.; Edgett, K. S.; Ehlmann, B.; Hug, W.; Reid, R.; Kah, L.; Nealson, K.; Nelson, T.; Minitti, M.; Popp, J.; Langenhorst, F.; Smith, C.; Sobron, P.; Steele, A.; Tarcea, N.; Wiens, R.; Williford, K.; Yingst, R. A. The SHERLOC Investigations on the Mars 2020 Rover. In *51st Lunar and Planetary Science Conference*; The Woodlands, TX, USA, 2020; Abs 2081.
- [175] Bhartia, R.; Beegle, L. W.; DeFlores, L.; Abbey, W.; Razzell Hollis, J.; Uckert, K.; Monacelli, B.; Edgett, K. S.; Kennedy, M. R.; Sylvia, M.; Aldrich, D.; Anderson, M.; Asher, S. A.; Bailey, Z.; Boyd, K.; Burton, A. S.; Caffrey, M.; Calaway, M. J.; Calvet, R.; Cameron, B.; Caplinger, M. A.; Carrier, B. L.; Chen, N.; Chen, A.; Clark, M. J.; Clegg, S.; Conrad, P. G.; Cooper, M.; Davis, K. N.; Ehlmann, B.; Facto, L.; Fries, M. D.; Garrison, D. H.; Gasway, D.; Ghaemi, F. T.; Graff, T. G.; Hand, K. P.; Harris, C.; Hein, J. D.; Heinz, N.; Herzog, H.; Hochberg, E.; Houck, A.; Hug, W. F.; Jensen, E. H.; Kah, L. C.; Kennedy, J.; Krylo, R.; Lam, J.; Lindeman, M.; McGlowen, J.; Michel, J.; Miller, E.; Mills, Z.; Minitti, M. E.; Mok, F.; Moore, J.; Nealson, K. H.; Nelson, A.; Newell, R.; Nixon, B. E.; Nordman, D. A.; Nuding, D.; Orellana, S.; Pauken, M.; Peterson, G.; Pollock, R.; Quinn, H.; Quinto, C.; Ravine, M. A.; Reid, R. D.; Riendeau, J.; Ross, A. J.; Sackos, J.; Schaffner, J. A.; Schwochert, M.; O Shelton, M.; Simon, R.; Smith, C. L.; Sobron, P.; Steadman, K.; Steele, A.; Thiessen, D.; Tran, V. D.; Tsai, T.; Tuite, M.; Tung, E.; Wehbe, R.; Weinberg, R.; Weiner, R. H.; Wiens, R. C.; Williford, K.; Wollonciej, C.; Wu, Y.-H.; Yingst, R. A.; Zan, J. Perseverance's Scanning Habitable Environments with Raman and Luminescence for Organics and Chemicals (SHERLOC) Investigation. *Space Sci. Rev.* **2021**, *217*, 58. <https://doi.org/10.1007/s11214-021-00812-z>.
- [176] Scheller, E. L.; RazzellHollis, J.; Cardarelli, E. L.; Steele, A.; Beegle, L. W.; Bhartia, R.; Conrad, P.; Uckert, K.; Sharma, S.; Ehlmann, B. L.; Asher, S.; Berger, E. L.; Burton, A. S.; Bykov, S.; Fornaro, T.; Fox, A. C.; Fries, M.; Kah, L. C.; Kizovski, T.; McCubbin, F. M.; Moore, K.; Roppel, R.; Shkolyar, S. O.; Siljeström, S.; Williams, A. J.; Wogsland, B.; Wiens, R. C.; SHERLOCTeam. First-Results from the Perseverance SHERLOC Investigations: Aqueous Alteration Processes and Implications for Organic Geochemistry in Jezero Crater, Mars. In *53rd Lunar and Planetary Science Conference*; The

- Woodlands, TX, USA, 2022; Abs 1652.
- [177] Bernardi, P.; Parès, L.; Newell, R.; Nelson, T.; Gasnault, O.; Réess, J.-M.; Schridar, V.; Contijo, I.; Reyes-Newell, A.; Peterson, G. E.; Legett, C.; Dubois, B.; Robinson, S. H. Optical Design and Performance of the SuperCam Instrument for the Perseverance Rover. In *International Conference on Space Optics — ICSO 2020*; Sodnik, Z., Cugny, B., Karafolas, N., Eds.; SPIE, 2021; p 53. <https://doi.org/10.1117/12.2599243>.
- [178] Wiens, R. C.; Newell, R.; Clegg, S.; Sharma, S. K.; Misra, A.; Bernardi, P.; Maurice, S.; McCable, K.; Cais, P.; Teams, S. S. The SuperCam Remote Raman Spectrometer for Mars 2020. In *Lunar and Planetary Science XLVIII*; The Woodlands, TX, USA, 2017; Abs 2600.
- [179] Clavé, E.; Benzerara, K.; Meslin, P. -Y.; Forni, O.; Royer, C.; Mandon, L.; Beck, P.; Quantin-Nataf, C.; Beyssac, O.; Cousin, A.; Bousquet, B.; Wiens, R. C.; Maurice, S.; Dehouck, E.; Schröder, S.; Gasnault, O.; Mangold, N.; Dromart, G.; Bosak, T.; Bernard, S.; Udry, A.; Anderson, R. B.; Arana, G.; Brown, A. J.; Castro, K.; Clegg, S. M.; Cloutis, E.; Fairén, A. G.; Flannery, D. T.; Gasda, P. J.; Johnson, J. R.; Lasue, J.; Lopez-Reyes, G.; Madariaga, J. M.; Manrique, J. A.; Le Mouélic, S.; Núñez, J. I.; Ollila, A. M.; Pilleri, P.; Pilorget, C.; Pinet, P.; Poulet, F.; Veneranda, M.; Wolf, Z. U. Carbonate Detection with SuperCam in Igneous Rocks on the Floor of Jezero Crater, Mars. *J. Geophys. Res. Planets* **2023**, online ver, in-press. <https://doi.org/10.1029/2022JE007463>.
- [180] Vago, J. L.; Westall, F.; Pasteur Instrument Teams, L. S.; Coates, A. J.; Jaumann, R.; Korablev, O.; Ciarletti, V.; Mitrofanov, I.; Josset, J.-L.; De Sanctis, M. C.; Bibring, J.-P.; Rull, F.; Goesmann, F.; Steininger, H.; Goetz, W.; Brinckerhoff, W.; Szopa, C.; Raulin, F.; Westall, F.; Edwards, H. G. M.; Whyte, L. G.; Fairén, A. G.; Bibring, J.-P.; Bridges, J.; Hauber, E.; Ori, G. G.; Werner, S.; Loizeau, D.; Kuzmin, R. O.; Williams, R. M. E.; Flahaut, J.; Forget, F.; Vago, J. L.; Rodionov, D.; Korablev, O.; Svedhem, H.; Sefton-Nash, E.; Kminek, G.; Lorenzoni, L.; Joudrier, L.; Mikhailov, V.; Zashchirinskiy, A.; Alexashkin, S.; Calantropio, F.; Merlo, A.; Poulakis, P.; Witasse, O.; Bayle, O.; Bayón, S.; Meierhenrich, U.; Carter, J.; García-Ruiz, J. M.; Baglioni, P.; Haldemann, A.; Ball, A. J.; Debus, A.; Lindner, R.; Haessig, F.; Monteiro, D.; Trautner, R.; Volland, C.; Rebeyre, P.; Gouly, D.; Didot, F.; Durrant, S.; Zekri, E.; Koschny, D.; Toni, A.; Visentin, G.; Zwick, M.; van Winnendael, M.; Azkarate, M.; Carreau, C.; the ExoMars Project Team. Habitability on Early Mars and the Search for Biosignatures with the ExoMars Rover. *Astrobiology* **2017**, *17*, 471. <https://doi.org/10.1089/ast.2016.1533>.
- [181] Rull, F.; Maurice, S.; Hutchinson, I.; Moral, A.; Perez, C.; Diaz, C.; Colombo, M.; Belenguer, T.; Lopez-Reyes, G.; Sansano, A.; Forni, O.; Parot, Y.; Striebig, N.; Woodward, S.; Howe, C.; Tarcea, N.; Rodriguez, P.; Seoane, L.; Santiago, A.; Rodriguez-Prieto, J. A.;

- Medina, J.; Gallego, P.; Canchal, R.; Santamaría, P.; Ramos, G.; Vago, J. L.; on behalf of the RLS Team. The Raman Laser Spectrometer for the ExoMars Rover Mission to Mars. *Astrobiology* **2017**, *17*, 627. <https://doi.org/10.1089/ast.2016.1567>.
- [182] Rull, F.; Maurice, S.; Hutchinson, I.; Moral, A. G.; Canora, C. P.; Belenguer, T.; Ramos, G.; Colombo, M.; Lopez-Reyes, G.; García, V.; Forni, O.; Popp, J.; Medina, J.; Team, R. The Raman Laser Spectrometer (RLS) for 2020 Exomars (ESA) Mission: Instrument Development and Operation on Mars. In *European Planetary Science Congress*; Berlin, Germany, 2018; Abs 922.
- [183] *Life As We Don't Know It. SHERLOC*. The Analytical Scientist. <https://theanalyticalscientist.com/techniques-tools/life-as-we-dont-know-it> (accessed 2023-03-14).
- [184] Cabrero, J. F.; Fernández, M.; Colombo, M.; Escribano, D.; Gallego, P.; Canchal, R.; Belenguer, T.; García-Martínez, J.; Encinas, J. M.; Bastide, L.; Hutchinson, I.; Moral, A.; Canora, C.; Prieto, J. A. R.; Gordillo, C.; Santiago, A.; Berrocal, A.; Rull, F. RAMAN Spectrometer: Development of SPU FM Based on Enhanced Qualification Model for Exomars 2020. In *International Conference on Space Optics — ICSO 2018*; Karafolas, N., Sodnik, Z., Cugny, B., Eds.; SPIE, 2019; p 115. <https://doi.org/10.1117/12.2536035>.
- [185] Schröder, S.; Belenguer, T.; Böttger, U.; Buder, M.; Cho, Y.; Dietz, E.; Gensch, M.; Hagelschuer, T.; Hanke, F.; Hübers, H. W.; Kameda, S.; Kopp, E.; Kubitzka, S.; Moral, A.; Caproth, C.; Pertenais, M.; Peter, G.; Rammelkamp, K.; Rodriguez, P.; Rull, F.; Ryan, C.; Säuberlich, T.; Schrandt, F.; Ulamec, S.; Usui, T.; Vance, R. In-Situ Raman Spectroscopy on Phobos: RAX on the MMX Rover. In *51st Lunar and Planetary Science Conference*; The Woodlands, TX, USA, 2020; Abs 2019.
- [186] Silverman, S.; Peralta, R.; Christensen, P.; Mehall, G. Miniature Thermal Emission Spectrometer for the Mars Exploration Rover. *Acta Astronaut.* **2006**, *59*, 990. <https://doi.org/10.1016/j.actaastro.2005.07.055>.
- [187] Christensen, P. R.; Mehall, G. L.; Silverman, S. H.; Anwar, S.; Cannon, G.; Gorelick, N.; Kheen, R.; Tourville, T.; Bates, D.; Ferry, S.; Fortuna, T.; Jeffryes, J.; O'Donnell, W.; Peralta, R.; Wolverton, T.; Blaney, D.; Denise, R.; Rademacher, J.; Morris, R. V.; Squyres, S. Miniature Thermal Emission Spectrometer for the Mars Exploration Rovers. *J. Geophys. Res. Planets* **2003**, *108*, 8064. <https://doi.org/10.1029/2003JE002117>.
- [188] Christensen, P. R.; Wyatt, M. B.; Glotch, T. D.; Rogers, A. D.; Anwar, S.; Arvidson, R. E.; Bandfield, J. L.; Blaney, D. L.; Budney, C.; Calvin, W. M.; Fallacaro, A.; Fergason, R. L.; Gorelick, N.; Graff, T. G.; Hamilton, V. E.; Hayes, A. G.; Johnson, J. R.; Knudson, A. T.; McSween, H. Y.; Mehall, G. L.; Mehall, L. K.; Moersch, J. E.; Morris, R. V.; Smith, M. D.; Squyres, S. W.; Ruff, S. W.; Wolff, M. J. Mineralogy at Meridiani Planum from the Mini-TES Experiment on

- the Opportunity Rover. *Science*. **2004**, 306, 1733. <https://doi.org/10.1126/science.1104909>.
- [189] Christensen, P. R.; Ruff, S. W.; Fergason, R. L.; Knudson, A. T.; Anwar, S.; Arvidson, R. E.; Bandfield, J. L.; Blaney, D. L.; Budney, C.; Calvin, W. M.; Glotch, T. D.; Golombek, M. P.; Gorelick, N.; Graff, T. G.; Hamilton, V. E.; Hayes, A. G.; Johnson, J. R.; McSween, H. Y.; Mehall, G. L.; Mehall, L. K.; Moersch, J. E.; Morris, R. V.; Rogers, A. D.; Smith, M. D.; Squyres, S. W.; Wolff, M. J.; Wyatt, M. B. Initial Results from the Mini-TES Experiment in Gusev Crater from the Spirit Rover. *Science*. **2004**, 305, 837. <https://doi.org/10.1126/science.1100564>.
- [190] Wang, A.; Haskin, L. A.; Squyres, S. W.; Jolliff, B. L.; Crumpler, L.; Gellert, R.; Schröder, C.; Herkenhoff, K.; Hurowitz, J. A.; Tosca, N. J.; Farrand, W. H.; Anderson, R.; Knudson, A. T. Sulfate Deposition in Subsurface Regolith in Gusev Crater, Mars. *J. Geophys. Res. Planets* **2006**, 111, E02S1. <https://doi.org/10.1029/2005JE002513>.
- [191] NASA. *Microdevices Laboratory. Tunable Laser Spectrometer*. <https://microdevices.jpl.nasa.gov/capabilities/in-situ-instruments-tls/> (accessed 2023-03-14).
- [192] Webster, C. R.; Mahaffy, P. R.; Atreya, S. K.; Flesch, G. J.; Mischna, M. A.; Meslin, P.-Y.; Farley, K. A.; Conrad, P. G.; Christensen, L. E.; Pavlov, A. A.; Martín-Torres, J.; Zorzano, M.-P.; McConnochie, T. H.; Owen, T.; Eigenbrode, J. L.; Glavin, D. P.; Steele, A.; Malespin, C. A.; Archer, P. D.; Sutter, B.; Coll, P.; Freissinet, C.; McKay, C. P.; Moores, J. E.; Schwenger, S. P.; Bridges, J. C.; Navarro-Gonzalez, R.; Gellert, R.; Lemmon, M. T. Mars Methane Detection and Variability at Gale Crater. *Science*. **2015**, 347, 415. <https://doi.org/10.1126/science.1261713>.
- [193] Reess, J. M.; Bonafous, M.; Lapauw, L.; Humeau, O.; Fouchet, T.; Bernardi, P.; Cais, P.; Deleuze, M.; Forni, O.; Maurice, S.; Robinson, S.; Wiens, R. C.; Team, S. The SuperCam Infrared Instrument on the NASA Mars2020 Mission, Vol 11180. In *International Conference on Space Optics*; Chania, Greece, 2018; Abs 1118037-2.
- [194] Fouchet, T.; Johnson, J. R.; Forni, O.; Reess, J. M.; Bernardi, P.; Newell, R. T.; Ollila, A.; Leggett, C.; Beck, P.; Cousin, A.; Royer, C.; Pilorget, C.; Poulet, F.; Pilleri, P.; Cloutis, E. A.; McConnochie, T.; Montmessin, F.; Brown, A. J.; Wiens, R.; Maurice, S.; Group, S. V. W. SuperCam Visible/Near-Infrared Spectroscopy Onboard the Perseverance Rover, No. 2548. In *52nd Lunar and Planetary Science Conference*; Virtual Conference, 2021; Abs 1939.
- [195] De Sanctis, M. C.; Altieri, F.; Ammannito, E.; Biondi, D.; De Angelis, S.; Meini, M.; Mondello, G.; Novi, S.; Paolinetti, R.; Soldani, M.; Mugnuolo, R.; Pirrotta, S.; Vago, J. L.; the Ma\_MISS team. Ma\_MISS on ExoMars: Mineralogical Characterization of the Martian Subsurface. *Astrobiology* **2017**, 17, 612. <https://doi.org/10.1089/ast.2016.1541>.

- [196] ESA. *Ma-MISS- Mars Multispectral imager for subsurface studies*. [https://exploration.esa.int/web/mars/-/45103-rover-instruments?section=ma\\_miss---mars-multispectral-imager-for-subsurface-studies](https://exploration.esa.int/web/mars/-/45103-rover-instruments?section=ma_miss---mars-multispectral-imager-for-subsurface-studies) (accessed 2023-03-15).
- [197] Bibring, J.-P.; Hamm, V.; Pilorget, C.; Vago, J. L.; the MicrOmega Team. The MicrOmega Investigation Onboard ExoMars. *Astrobiology* **2017**, *17*, 621. <https://doi.org/10.1089/ast.2016.1642>.



---

# CHAPTER 2

## OBJECTIVES

**“EXPLORATION IS WHAT YOU DO WHEN YOU DO NOT KNOW WHAT YOU ARE DOING. THAT IS WHAT A SCIENTIST DO EVERY DAY. IF SCIENTISTS ALREADY KNEW WHAT THEY WERE DOING, THEY WOULD NOT BE DISCOVERING ANYTHING, BECAUSE THEY ALREADY KNEW WHAT THEY WERE DOING” –**

**Neil de Grasse**

---



## 2. OBJECTIVES

There are common goals of current and future space missions to rocky celestial bodies. On the one hand, to assess the potential habitability of the celestial bodies closest to Earth by searching for evidences of previous life. On the other hand, to characterize its geology, especially the scenarios related to the presence of past water activity. In this sense, the surface and subsurface geochemistry are the best tracers to understand the evolution of the celestial body over the course of history. Through the research of the geochemistry, many questions can be answered, such as the weathering processes that the celestial body underwent, whether there are evidences of biosignatures, the past role of water and evaluation of potential natural resources for future use, among others.

With this in mind, the main objective of this PhD thesis was to expand the geochemical understanding of the planet Mars and the Earth's satellite, the Moon, to support the scientific design of future space missions and to contribute scientifically to the most cutting-edge interests.

The geochemistry of celestial bodies can be studied in many different ways. These include the characterization of meteorites, the study of terrestrial analogs, the use of synthetic simulants, the delivery of missions equipped with a very sophisticated scientific payload and the analysis of return samples. In this PhD, all the mentioned methods were considered, except for the return samples, since there are no samples from Mars yet and those from the Moon are limited and restricted.

In order to achieve the main objective, some operational objectives were established:

- To identify and classify the surface/subsurface Martian and Lunar mineral phases through non-destructive analytical techniques, similar to the ones on board the current and future missions to Mars and Moon.
- To ascertain the weathering processes that led to the formation of secondary mineral phases from the primary ones, in order to know the mineralogical evolution throughout history.
- To simulate, through laboratory work, some of the ancient processes and conditions necessary for the formation of secondary minerals in different aqueous environments.
- To examine some past and present mission data where the developed database can be used to identify key mineral phases and even organic signatures.

- 
- To examine certain formations where biosignatures may be found on Mars, as well as to create a database of minerals related to bioprotector agents through some of the analytical techniques on board the most up-to-date landing missions.
  - To test the protective ability of some phyllosilicates to host relevant organic molecules.
  - To assess the capacity of the Moon's natural resources with the aim of using them in the future for the plant cultivation, considering that human exploration is becoming a near future reality.

Specific tasks were implemented to fulfill these operational objectives that have been applied all along the PhD thesis. There are not specific chapters for each operational objective, although some sections of chapters are more closely related to some of them.



# CHAPTER 3

## SAMPLES AND EXPERIMENTAL PROCEDURE

**“AT FIRST, RESEARCH NEEDS MORE BRAINS  
THAN MEANS” – Severo Ochoa**

---



### **3. SAMPLES AND EXPERIMENTAL PROCEDURE**

#### **3.1. Sample description**

As mentioned in the introductory chapter (Chapter 1), there are different methods for studying the geochemistry of celestial bodies on a microscopic scale: through the characterization of meteorites, the study of terrestrial analogs and the testing of simulants in the laboratory. In this PhD, the different possibilities were considered.

##### **3.1.1. Meteorites**

In order to meet the objectives related to the study of the geochemistry of Mars, Martian meteorites were studied. Likewise, in order to meet the objectives related to the evaluation of disturbed Lunar soils as a preliminary step to plant cultivation, a Lunar meteorite was analyzed.

##### **3.1.1.1. Martian meteorites**

As stated in the introduction, Martian meteorites were originally classified as shergottites, nakhlites, and chassignites (SNC). However, at the present time, the Martian meteorite classification includes more categories based on the rock type. Considering the most recent classification, Martian meteorites are grouped in pyroxene-phyric basalts, lherzolites, olivine-phyric basalts (historically all three are subtypes of shergottites), clinopyroxenites (traditionally nakhlites), dunites and orthopyroxenites (customarily Chassignites) <sup>[1]</sup>.

The Martian meteorites studied for this PhD thesis are the Roberts Massif (RBT) 04262 and the Larkman Nunatak (LAR) 12095 from the ANSMET collection of the Johnson Space Center, JSC/NASA. Both are guarded by the IBeA Research Group of the University of the Basque Country (UPV/EHU) through a loan agreement between the university and the NASA's JSC. Thanks to this agreement, IBeA receives meteorites that are collected by Antarctic Search for meteorites (ANSMET) during its expeditions in the Antarctica for their chemical analysis.

After the expedition, samples are kept frozen until they are ready for initial characterization and classification at the JSC. Then, they are defrosted in a cleanroom nitrogen cabinet and the initial characterization at JSC includes weighing, photographing and macroscopic description. Samples are then prepared and curated to be characterized by electron microprobe, obtaining the enough information to be correctly classified and providing basic data for future deep analyses by scientists of all around the world. The curation process of the Martian meteorites analyzed in this thesis consists in the preparation of thick sections of variable thickness (100-150  $\mu\text{m}$ ). For this purpose, the samples were embedded in a resin and

---

subsequently cut and polished with diamond grinding wheels, as well as SiC slurry for lapping [2].

### 3.1.1.1.1. RBT 04262 Martian Shergottite

The RBT 04262 Martian meteorite (Figure 3.1) was classified as a shergottite Martian meteorite by the Meteoritical Bulletin in 2007 [3]. This meteorite was collected by the US 2004-2005 Antarctic Search for Meteorites (ANSMET) expedition, together with its paired RBT 04261, whose mass was 205 g and the dimensions were 6.5 x 5.5 x 3.5 cm. The RBT 04262 meteorite is characterized by a coarse-grained assemblage of pyroxene, olivine and maskelynite with grain sizes reaching up to 4 mm. Sulfides, chromite, phosphate and oxides are also present [4].

It was initially reported as an olivine-phyric shergottite [4]. However, some petrological studies suggested that it is closer to the lherzolitic shergottite group [5]. The main minerals in olivine-phyric shergottites are pyroxene, olivine and plagioclase, whereas lherzolites are similar to gabbros, composed mainly of olivine and pyroxene. The cosmic ray exposure (CRE) ages of both shergottites are different. On the one hand, olivine-phyric shergottites have CRE ages around 1.2 million years (Ma). On the other hand, all lherzolitic shergottites have CRE ages between 3.8 - 4.7 Ma [6].

In any case, literature refers to the RBT 04262 as a shergottite composed primarily of pyroxene, olivine, and maskelynite with minor chromite, spinel, Ca phosphate, ilmenite, Fe sulfide crystals, and glass with a K feldspar composition [7].

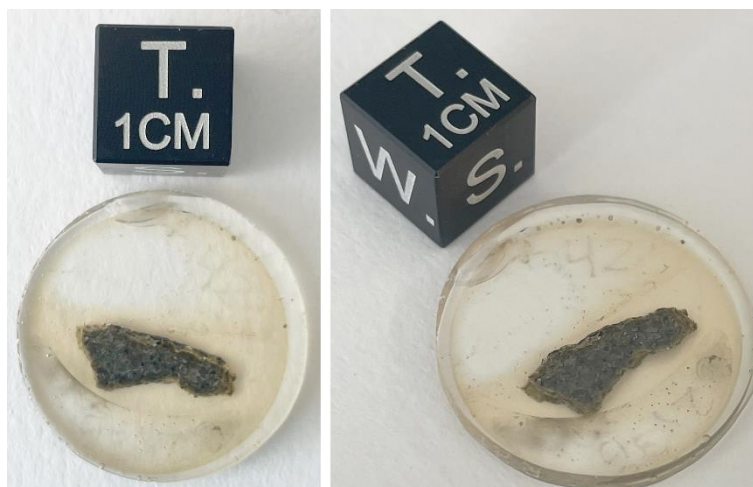


Figure 3.1. Side A of the RBT 04262 Martian meteorite.

In this work, the RBT 04262 elemental and molecular characterization was performed on a thick fragment that weights 1.12 g and has dimensions of 1.4 x 0.6 x 0.2 cm (length x width x height), including the resin in which it is

embedded. Both polished surfaces look similar, having a light grey and ochre matrix with some cracks and fractures. However, at the naked eye it can be seen that there are ochre grains with a black coating and fractures in one of the sides.

### **3.1.1.1.2. LAR 12095 Martian Shergottite**

The LAR 12095 Martian meteorite (Figure 3.2) was found in 2012 in the Larkman Nunataks region of the Transantarctic Mountains, East Antarctica, by the US Antarctic Search for Meteorites program (ANSMET). The weight of the initial meteorite was 133.13 g and its dimensions were 5.5 x 3.8 x 3.4 cm. However, it was cut into thick sections for more detailed analysis. For this work, the measurements were performed on a thick sample that weights 1.26 g and has dimensions of 1.3 x 1.0 x 0.2 cm, including the resin in which is embedded. Both polished surfaces look similar to the naked eye, having a greenish gray matrix with some dark inclusions, separated by cracks and veins.

The initial characterization classified it as a Martian shergottite, according to the Meteoritical Bulletin <sup>[3]</sup>. Literature and the Meteoritical Bulletin reports that the LAR 12095 shergottite is composed by pyroxene (61-62 vol%), olivine (16-17 vol%) and maskelynite (21-23 vol%) groundmass. Minor phosphates (mainly merrillite, with rare apatite), oxides (1 vol%, chromite and Ti-magnetite) and sulfides (1 vol%, mainly Fe-rich pyrrhotite) are also present. In addition, microstructural features of shock metamorphism, including veins and darkened olivine are also observed <sup>[3,8-10]</sup>.



*Figure 3.2. Side A of the LAR 12095 Martian meteorite.*

### **3.1.1.2. Lunar meteorite**

In order to fulfill the objective related to the study of Lunar mineralogy through a meteorite sample and the evaluation of its weathering stage as

---

preliminary step to the cultivation of plants, the Northwest Africa (NWA) 11273 Lunar meteorite was analyzed.

### 3.1.1.2.1. NWA 11273 Feldspathic Breccia Meteorite

The NWA 11273 Lunar meteorite (Figure 3.3) was found in April 2017 near Tindouf, Algeria, with a total mass of 2.81 Kg. A specimen of 37 g was sent to the University of Washington (UWS) to be analyzed and, on October 2017 the NWA 11273 was classified as a lunar feldspathic breccia meteorite with low shock state and low weathering grade by the Meteoritical Society <sup>[11]</sup>.



Figure 3.3. Side A of the NWA 11273 Lunar meteorite.

The sample analyzed in this work was acquired by the IBeA Research Group. It consists on a thin section, whose dimensions are 2.1 x 1.9 cm, with a weight of 0.61 g (0.02 % of the original recovered meteorite mass). It shows heterogeneous fragments of light gray color embedded in a dark color section, which corresponds to a feldspathic breccia meteorite <sup>[12]</sup>.

### 3.2.1. Terrestrial analogs

The results obtained by space missions give rise to a number of scientific hypotheses that must be evaluated on Earth. For this purpose, terrestrial materials that meet the specifications required in non-terrestrial bodies are often used. These materials are known as analogs.

#### 3.2.1.1. Reykjanes, Iceland, terrestrial analogs

On the one hand, three different olivine-bearing Martian analogs were used to develop the olivine calibration models (Chapter 4.1). These samples belong to Reykjanes, Iceland, a region considered to be an optimal analog of Martian olivine-bearing rocks. The samples were collected from areas where the rocks were not weathered or visually altered. Specifically, they

were sampled from two different emplacements: two of them were collected at the geographic coordinates N63 49 01.7 W22 39 03.1 (IS16-0001 and IS16-0002) and the third one was collected at N63 48 58.3 W22 39 38.8 (IS16-0013) <sup>[13]</sup>. These samples were provided by the Department of Condensed Matter Physics, Crystallography and Mineralogy of the University of Valladolid (UVa), Spain, and are part of the Planetary Terrestrial Analogs Library (PTAL) database collection <sup>[14]</sup>.

Due to their origin, they represent basaltic lavas from tissue-fed shield volcanoes that were sourced from the Mid-Atlantic Ridge <sup>[15]</sup>. An in-depth analysis of the geochemistry of these samples and their relevance for the ExoMars 2022 mission has been described, confirming the low degree of alteration and weathering of the selected samples <sup>[13]</sup>.

### **3.2.1.2. Carachi Pampa Oncoid**

On the other hand, there are several terrestrial analogs, but sedimentary deposits developed at high-altitude lakes share some extreme and environmental characteristics that made them excellent analog for planetary geochemistry research. These conditions favor the development of a diverse and abundant microbial biota that influences mineral precipitation and the development of sedimentary deposits of microbial influence typically known as microbialite <sup>[16]</sup>.

In this PhD Thesis, a microbialite from Carachi Pampa volcanic lake was analyzed. Oncoids are microbialites that develop into spherical shapes, unlike stromatolites, which are usually laminated <sup>[17]</sup>. The Carachi Pampa oncooid sample (Figure 3.4) was collected during a biogeochemical sampling campaign in January 2020 on the Salar Carachi Pampa, Catamarca, Argentina.



*Figure 3.4. Carachi Pampa oncooid.*

---

A sample of about 28 g was collected with solvent-cleaned (dichloromethane and methanol) stainless-steel scraper, and transferred to polyethylene containers, where it was kept cold (~ 4°C) until the biogeochemical analysis at the laboratory. Figure 3.4 shows the three sides of the studied microbialite or oncoid, whose dimensions are 51x31x16 mm.

For its analysis, this sample was split into two pieces. It was first analyzed by non-destructive techniques and then ground for destructive analyses.

### 3.2.2. Simulants

When terrestrial analogs do not meet the specifications required by non-terrestrial bodies for a specific study, simulants are often used. These samples are prepared *à la carte* just to test a formulated hypothesis. In this thesis, the following *à la carte analogs* or simulants have been prepared.

#### 3.2.2.1. Sulfates: gypsum, syngenite and görgeyite

The simulants employed for the Martian temperature processes study were three types of sulfates: gypsum, syngenite and görgeyite (Figure 3.5), which were previously synthesized by mimicking hydrothermal conditions (see 4.2.1. chapter).

#### 3.2.2.2. Clay minerals: montmorillonite and hectorite

The simulants employed to study the Martian habitability were two kind of clay minerals: montmorillonite (MMT) and hectorite (HEC). Both were purchased on the Source Clays Repository of the Clay Minerals Society, Purdue University, West Lafayette, IN, USA [18,19].

On the one hand, the MMT used is also known by the acronym SWy-3 and is a Na-rich MMT. It was extracted in Crook County, WY, USA. On the other hand, the HEC used is also known by the acronym SHCa-1 and it was taken from San Bernardino County, CA, USA (Figure 3.5).



Figure 3.5. Simulants used in this work. From left to right: mixed calcium and potassium sulfates; montmorillonite SWy-3 clay; and hectorite SHCa-1 clay.

According to the Clays Minerals Society, the SWy-3 montmorillonite consists of 62.9% SiO<sub>2</sub>, 19.6% Al<sub>2</sub>O<sub>3</sub>, 3.35% Fe<sub>2</sub>O<sub>3</sub>, 3.05% MgO, 1.68 CaO, 1.53% Na<sub>2</sub>O, 0.53% K<sub>2</sub>O, 0.32% FeO, 0.111% F, 0.09% TiO<sub>2</sub>, 0.05% S, 0.049% P<sub>2</sub>O<sub>5</sub> and 0.006% MnO. Regarding to the SHCa-1 hectorite, it is composed of 34.7% SiO<sub>2</sub>, 23.4% CaO, 15.3% MgO, 2.60% F, 2.18% Li<sub>2</sub>O, 1.26% Na<sub>2</sub>O, 0.69% Al<sub>2</sub>O<sub>3</sub>, 0.25% FeO, 0.13% K<sub>2</sub>O, 0.038% TiO<sub>2</sub>, 0.02% Fe<sub>2</sub>O<sub>3</sub>, 0.014% P<sub>2</sub>O<sub>5</sub>, 0.01% S and 0.008% MnO [20].

### **3.3. Experimental procedure**

Throughout the experimental procedure, the following reagents, analytical techniques and laboratory instruments were used.

#### **3.3.1. Reagents**

The reagents are grouped according to the experiment in which they were used. In addition, it should be noted that all reagents were stored in desiccators to ensure their correct maintenance.

##### **3.3.1.1. GC-MS and GC-IRMS analyses**

For the GC-MS and GC-IRMS analyses, which were based on the Carachi Pampa biomolecular identification and quantification, dichloromethane (99.8%, DCM), methanol (99%, MeOH), potassium hydroxide (99%, KOH), n-hexane (C<sub>6</sub>H<sub>14</sub>), bron trifluoride-methanol complex (10%, BF<sub>3</sub>.MeOH) and N,O-bis(trimethylsilyl)trifluoroacetamide (99%, BSTFA) were used. All chemicals and standards were supplied by Sigma Aldrich (St. Luis, MO, USA).

##### **3.3.1.2. Calcium and Magnesium sulfates synthesis**

The synthesis of sulfate simulants was performed by using the following pure solid reagents: pure potassium sulfate (99%, K<sub>2</sub>SO<sub>4</sub>), pure potassium chloride (99%, KCl), magnesium sulfate monohydrate (99%, MgSO<sub>4</sub>.H<sub>2</sub>O), which were purchased from Panreac (Barcelona, Spain), and calcium chloride dehydrate (99%, CaCl<sub>2</sub>.2H<sub>2</sub>O) that was purchased from Merck (Darmstadt, Germany).

##### **3.3.1.3. Sulfates dehydration**

The calcium sulfate hemihydrate (bassanite, 97%, CaSO<sub>4</sub>.0.5H<sub>2</sub>O) and the Chemical Reference Material (CRM) No. 202a plaster (gypsum, CaSO<sub>4</sub>.2H<sub>2</sub>O) reagents were used for the sulfates dehydration experiment. These were purchased from Thermo Fisher Scientific (Waltham, MA, USA) and from Bureau of Analyzed Samples (BAS, Middlesbrough, United Kingdom), respectively.

---

#### **3.3.1.4. Clay mineral doping**

The clay mineral doping was carried out by using the following liquid reagents: sodium hydroxide (NaOH) and sulfuric acid (94-98%, H<sub>2</sub>SO<sub>4</sub>) that were purchased from VWR Chemicals (Radnor, PA, USA). Ethanol (90%, C<sub>2</sub>H<sub>6</sub>O), which was purchased from Thermo Fisher Scientific (Waltham, MA, USA), was also used as liquid reagent. Finally, the unique solid reagent used was dodecanoic acid (99.5%, C<sub>12</sub>H<sub>24</sub>O<sub>2</sub>) that was purchased from Thermo Fisher Scientific (Waltham, MA, USA).

#### **3.3.2. Analytical techniques**

The analytical techniques used in this thesis can be classified as elemental and molecular.

##### **3.3.2.1. Elemental analyses**

###### **3.3.2.1.1. $\mu$ -energy Dispersive X-ray fluorescence ( $\mu$ -EDXRF)**

In order to obtain the elemental composition and distribution of the samples the M4 TORNADO  $\mu$ -EDXRF spectrometer (Bruker Nano GmbH, Berlin, Germany) was used (Figure 3.6). This instrument is equipped with a micro-focus side window Rh X-Ray tube powered by a low-power HV generator and is cooled by air that extends to a maximum current of 700  $\mu$ A and a voltage of 50 kV. It implements an XFlash silicon drift detector with 30 mm<sup>2</sup> sensitive area and energy resolution of 145 eV for the Mn K $\alpha$  line. The micrometric lateral resolution of the instrument, 25  $\mu$ m for the K $\alpha$  line, is achieved thanks to polycapillary lenses.

The spot size varies as a function of the energy, being 17  $\mu$ m at 2.3 KeV and 32  $\mu$ m at 18.3 KeV. Two video-microscopes were used to focus the area under study, one at low magnification (1 cm<sup>2</sup> area) for the exploration of the samples, and the other at high magnification (1 mm<sup>2</sup> area) for the final focusing. As the instrument can detect elements with an atomic number (Z) higher than 10 (starting from the sodium), the measurements must be performed under vacuum (20 mbar) to enhance the detection of the lightest elements. The vacuum was achieved with a diaphragm pump MV 10 N VARIO-B. In order to obtain the hyperspectral maps (elemental chemical images), the K $\alpha$  line of each element was used (at most of the cases) after a previous elemental assignation and deconvolution of the signals in the sum spectrum. After that, the distribution map of each element was represented as a function of the intensity of each detected element K $\alpha$  line, except for Pb, using in this case the L $\beta$  line.



Figure 3.6. M4 TORNADO  $\mu$ -EDXRF spectrometer.

All the  $\mu$ -EDXRF spectra acquisition and the image construction were performed using the M4 TORNADO software (Bruker Nano GmbH, Berlin, Germany).

### 3.3.2.1.2. Laser-induced breakdown spectroscopy (LIBS)

Elemental characterization was also carried out by the LIBS (Figure 3.7) of the LaserLab Research Group of the University of Málaga (UMA), Spain. The equipment used is equipped with a pulsed laser beam (Big Sky, Q-switch Nd:YAG laser; @1064 nm; 8 ns pulse width, 40 mJ/pulse) that was focused onto the sample at normal incidence with a planoconvex quartz lens (FL 100 mm). With this optical configuration, a 250  $\mu$ m crater was generated on the sample surface. Plasma emission was collected at an angle of 90° with a 50 mm focal length fused-silica lens and focused onto the input aperture of a 1.5 m quadrifurcated optical fiber (1.5 m, 200  $\mu$ m of diameter, NA = 0.22) coupled to the entrance slit of a four-channel Czerny-Turner spectrometer (Avantes 2048), providing a FWHM of 0.1 nm FWHM and a spectral range from 202 to 812 nm. Delay and integration time parameters were fixed at 1.28  $\mu$ s and 1.1 ms, respectively. Time resolved studies were carried out using Andor iSTAR (DH740-25F-03) iCCD coupled to an Andor Shamrock SR-303i imaging spectrometer with a monochannel fiber. Temporal parameters were fixed to 17.5  $\mu$ s and 50  $\mu$ s (25 Gain) of delay and integration time respectively.

For microLIBS analysis, the optical configuration was slightly modified so that the focusing lens were replaced by a 15x microscope objective. With

---

this LIBS system, a crater size of approximately 80  $\mu\text{m}$  was left on the surface of the analyzed sample. The sample was placed in XY manual linear stages and monitored using a Dino-Lite digital microscope in axial configuration.

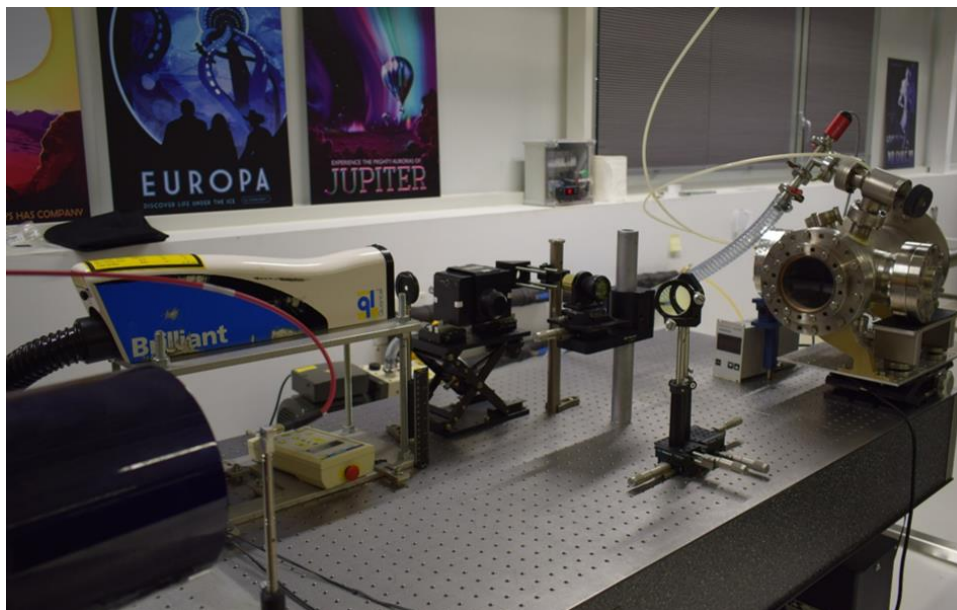


Figure 3.7. LIBS instrument.

### 3.3.2.1.3. Field emission scanning electron microscope (FE-SEM) coupled with an energy dispersive spectrometer (EDS)

FE-SEM-EDS analyses (Figure 3.8) were carried out in the Electron Microanalysis and Imaging Laboratory, Geoscience Department at the University Nevada, Las Vegas (UNLV).

On the one hand, the FE-SEM used was the JSM-6700F FE-SEM (Jeol USA Inc., Peabody, MA, USA), which has high image resolution and optimized for nanoscale topography with magnification ranging 250x to 430000x (5  $\mu\text{m}$  – 10 nm). It is equipped with the lower detector SE (20 mm), SE (9 mm), BSE, Oxford SDD EDS and Oxford HKL EBSD. It can collect images of SEI, BEI and X-ray maps, perform qualitative chemical analysis, collect quantitative crystal structure and orientation information <sup>[21]</sup>. On the other hand, the chemistry of the sample was measured with the INCAx-act (Oxford instruments, Abingdon, United Kingdom), using an accelerating voltage of 5 kV.



Figure 3.8. FE-SEM-EDS spectrometer.

In order to prevent the sample from spilling out during the vacuum process and to increase the conductivity of the sample, the samples were perfectly fixed on graphite tapes. In this sense, as the aim of the EDS analysis was to compare the carbon content between samples in order to avoid interference from the graphite carbon, a low acceleration energy (5 kV) was applied for EDS analysis.

FE-SEM-EDS data was acquired and treated with the INCA software (Oxford Instruments, Abingdon, United Kingdom).

### 3.3.2.2. Molecular analyses

#### 3.3.2.2.1. Raman Spectroscopy

The molecular characterization was performed using four different Raman spectrometers; the Renishaw inVia confocal micro-Raman spectrometer (Renishaw, United Kingdom), the LabRam HR Evolution Raman Spectrometer (Horiba, Japan), the microRaman built by the ERICA research group [22], and the Raman Laser Spectrometer simulator (RLS-Sim) [23]. Each one was used pursuing different aims.

Raman data interpretation was performed by comparing the collected Raman spectra with Raman spectra of pure standard compounds of the

---

public databases RRUFF [24], with bibliography and by comparison with spectra of pure mineral phases proceeding from the Analytical Database of Martian Minerals (ADaMM) library [25].

- **Renishaw inVia confocal micro-Raman spectrometer**

On the one hand, with the Renishaw inVia spectrometer (Figure 3.9) the analyses were carried out both in single point mode and in the spectroscopic imaging mode. Although the instrument is equipped with three diode laser, the 785 nm (Renishaw, UK, RL785 with a nominal 45 mW out-put power) and the 532 nm (Renishaw, UK, RL532C50 with a nominal 300 mW out-put power) excitation diode lasers were used. It is also equipped with a CCD detector cooled by Peltier effect. In addition, the instrument is coupled to a Leica DMLM microscope (Bradford, UK), implementing a XYZ Stage Control toolbar and equipped with a micro-camera for searching the points of interest. 5x N PLAN (0.12 NA), 20x N PLAN EPI (0.40 NA) lenses and 50x N PLAN (0.75 NA) long-range objective were used for visualization and focusing. The nominal power of the source can be modulated between 0,0001% and 100% of the total power to avoid thermo-decomposition of the sample.

The Renishaw inVia confocal micro-Raman spectrometer also allowed to obtain Raman images by using the high-resolution Stream Line™ setup (Renishaw, UK). The control software moves the sample beneath the lens of the inVia's motorized microscope stage, so that the line is rastered across the region of interest with a spatial resolution up to  $\pm 1 \mu\text{m}$  and moving in the snake mapping mode. The data are swept synchronously across the detector as the line moves across the sample and the spectra are read out continuously, recording a Raman spectrum at each pixel of the line raster. At the end, 2D Raman images are obtained containing individual Raman information at pixel level. The InVia spectrometer was daily calibrated setting the  $520.5 \text{ cm}^{-1}$  silicon line.



Figure 3.9. Renishaw InVia Raman spectrometer.

For the variable-temperature analyses, the InVia Renishaw Raman spectrometer was coupled to the THMS600/HFS600 temperature-controlled stage (Linkam Scientific Instrument, UK, Figure 3.10). This is a complete system that provides a stable temperature control that can be programmed from 77 to 873 K. For temperatures above 573 K, a water circulation pump was used to cool the stage. This system allows temperature ramps and holds to be programmed during the required time. The temperature stability is  $<0,1$  K and the sample must be inside the stage between two cover slips 0,2 mm thick to keep the sample in the correct place throughout the experiment. These glass cover slips do not provide Raman signal.



*Figure 3.10. Linkam THMS600/HFS600 temperature-controlled stage.*

For Raman data obtained with the InVia micro-Raman spectrometer, the spectra acquisition and data treatment was carried out with the Wire™ 4.2 software package (Renishaw, UK).

#### **- LabRam HR Evolution Raman Spectrometer**

The biomolecular characterization was performed using the LabRam HR Evolution Raman Spectrometer (Horiba, Japan, Figure 3.11). The analyses were carried out both in single point mode and in the spectroscopic imaging mode. The instrument is equipped with the 266 nm (mtb, CryLas, FQCW266 with a nominal 100 mW out-put power) excitation diode laser. In addition, the instrument is equipped with a Syncerity CCD detector and is coupled to a BXM microscope (Olympus, Japan), implementing a Z motor and XY SCANplus 75x50 2mm motorized microscope stage control toolbar (Märzhäuser Wetzlar, Germany) and equipped with a micro-camera for searching the points of interest. 5x MPlan N (0.10 NA, Olympus), 10x MPlan N (0.25 NA, Olympus) and 100x MPlan N (0.90 NA, Olympus) objectives were used for visualization and focusing, whereas the 74x UVI (0.66 NA, Horiba) objective was used for ultraviolet measurements. The nominal power of the source can be modulated between 0.01-100%. The ultraviolet laser was daily calibrated setting the  $1332.5\text{ cm}^{-1}$  diamond line.

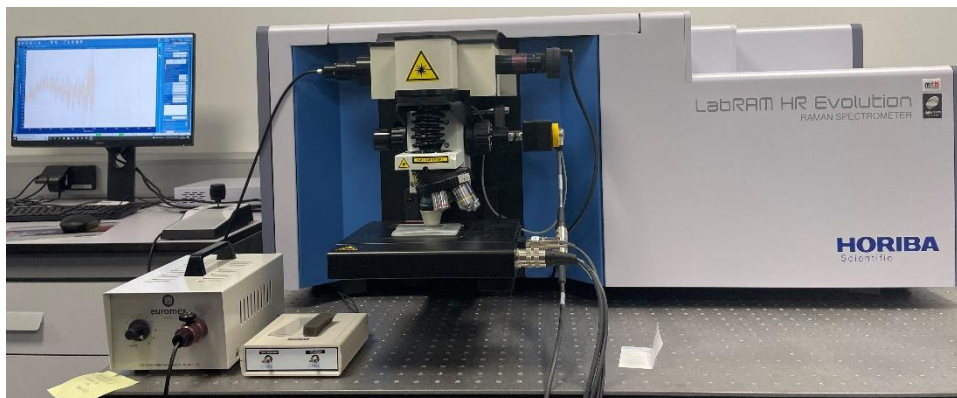


Figure 3.11. Horiba LabRam HR evolution Raman spectrometer.

The Raman data obtained with the LabRam HR Evolution Raman spectrometer was acquired with the LabSpec 6.0 software (Horiba, Japan).

- **ERICA micro-Raman spectrometer**

The ERICA micro-Raman (Figure 3.12) was developed by assembling the following commercial components [22] by the ERICA Research Group of the UVA; a Research Electro-Optics LSRP-3501 excitation laser (Helium–Neon) emitting at 633 nm, a KOSI Holospec 1.8i spectrometer, and an Andor DV420A-OE-130 CCD detector.



Figure 3.12. ERICA micro-Raman spectrometer.

The Nikon Eclipse E600 microscope coupled to the system is equipped with interchangeable long WD objectives of 5x, 10x, 20x, 50x, and 100x. In this study, Raman data were collected from 25 different points of interest that were visually selected by the operator. Spectra were recorded in the

range between 130 and 3780  $\text{cm}^{-1}$  by setting an acquisition time between 30 and 120 seconds, and a number of accumulations from 5 to 50.

- **RLS-Sim Raman spectrometer**

The RLS-Sim (Figure 3.13) of the UVa was used to emulate the scientific outcome of the Raman Laser Spectrometer (RLS) instrument that is implemented on board the Rosalind Franklin rover <sup>[23]</sup>.

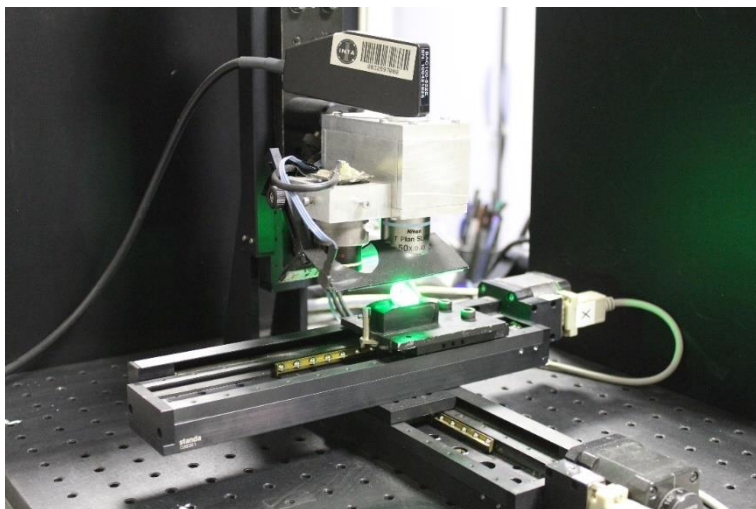


*Figure 3.13. RLS-Sim Raman spectrometer.*

The instrument is composed of the following commercial components: a BWN-532 excitation laser (B&W Tek) emitting at 532 nm, a BTC162 high resolution TE Cooled CCD Array spectrometer (B&W Tek) and an optical head with a long WD objective of 50x. As presented in a dedicated manuscript <sup>[26]</sup>, optical geometry, working distance ( $\sim 15$  mm), laser power output (20 mW), FWHM ( $6\text{--}10$   $\text{cm}^{-1}$ ) and spot size ( $\sim 50$   $\mu\text{m}$ ) are closely resembling those of the RLS instrument. In addition to that, the RLS Simulator integrates the same algorithms the RLS will use on Mars to autonomously perform sequential analyses, autofocus and optimization of the signal-to-noise ratio <sup>[27]</sup>. Using this instrument, a linear raster of 39 spots was carried out, thus simulating the nominal operation mode of the RLS.

For Raman data obtained by the Erica micro-Raman and RLS-Sim, spectra visualization and treatment was carried out by the IDAT/SpectPro, a software developed by the RLS team to receive, decode, calibrate and verify the telemetries generated by the RLS on Mars <sup>[26]</sup>.

**3.3.2.2.2. Infrared Spectroscopy**

Molecular characterization was completed by using some infrared spectrometers in different spectral regions.

---

- **Visible and Near Infrared Reflectance (VNIR) spectroscopy**

The ASD high-resolution FieldSpec4 VNIR spectroradiometer (Analytical Spectral Devices Inc., Boulder, CO, USA), which is equipped with the ASD probe for remote mode operations (Figure 3.14), was used. The light source consisted of a halogen lamp (ASD Illuminator) placed at 30 cm of distance from the samples. The angle between the incident light and the sample, and that between the sample and the detector fiber, is 45° in both cases. The fiber has an acceptance cone with an angle of 25° and was placed to a minimum distance of the sample to minimize the measurement surface. This device works in the 350 to 2500 nm wavelength range and uses three detectors for the different spectroscopic ranges: 350–1000 nm (silicon photodiode array for VNIR), 1001–1800 nm (InGaAs photodiode for SWIR1), and 1801–2500 nm (InGaAs photodiode for SWIR2). The FWHM is of 3 nm in the visible region and 6 nm in the near infrared region. Sensor optimization and calibration was set with a Spectralon white reference scanned once before each sample, and each spectrum was the result of the average of 10 scans.



Figure 3.14. VNIR ASD high-resolution FieldSpec4 VNIR spectroradiometer.

VNIR spectra were collected with RS3 software (ASD Inc.), analyzed with the ViewSpecPro software (ASD Inc.), and compared with those found in bibliography [28–30].

- **Fourier transform infrared (FT-IR) spectrometer – Attenuated total reflection (ATR)**

The ATR/FT-IR spectra were recorded on the Jasco (Tokio, Japan) FT-IR 6300 spectrometer using the Pike MIRacle ATR (diamond crystal with ZnSe focusing lens) accessory from Pike Technologies (Fitchburg, Wisconsin, USA) (Figure 3.15). The instrument is equipped with a 28° Michelson interferometer with corner-cube mirror, with a Ge/KBr beamsplitter and a MCT detector with Peltier temperature control.

The transmittance analyses were performed in the middle infrared region (from 4000 to 700  $\text{cm}^{-1}$ ) recording 128 scans at 4  $\text{cm}^{-1}$  spectral resolution. To collect spectra, a small portion of homogenized sample was placed in the microsample holder, firmly clamped against the ART crystal and analyzed in its pure form. FT-IR-ATR spectra were acquired with the Spectra Manager v.2 software (Jasco).



Figure 3.15. Jasco FT-IR 6300 spectrometer and the Pike ATR accessory.

### 3.3.2.2.3. X-ray diffraction (XRD) spectroscopy

#### - Proto XRD spectrometer

Part of the XRD analyses were performed in the Geoscience Department at the UNLV. The instrument used is a Proto AXRD Benchtop Powder X-ray diffractometer (Proto Manufacturing, Canada, Figure 3.16).

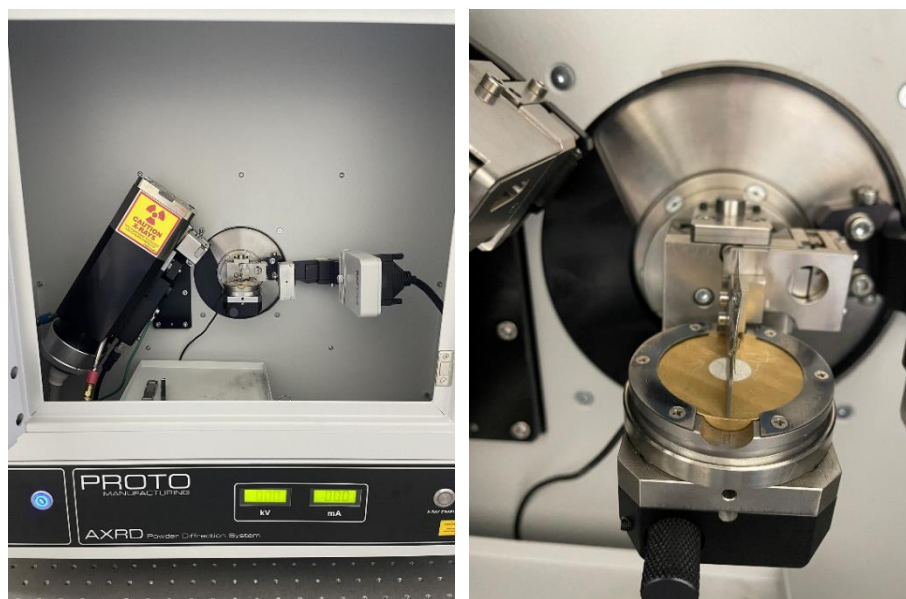


Figure 3.16. XRD Proto AXRD Benchtop Powder X-ray diffractometer.

---

It is equipped with a Cu K $\alpha$ 1 (1.54060 Å) radiation cathode operating at 30 kV and 20mA, provided with a Mynthen 1k (Dectris, Switzerland) detector, in the 2 $\theta$  range of 4-60°, divergence slit of 1°, a 0.01984° of step size ( $\Delta 2\theta$ ) and a measuring time of 1 s per step. The Bragg's equation ( $n\lambda=2\cdot d\cdot \sin\theta$ ) was applied to calculate the d-spacing for each peak and the samples were placed powdered in the middle of the sample holder.

Proto XRD data collection was performed using the XRDWIN PD software and the data treatment was carried out with the Profex software.

- **PANalytical XRD spectrometer**

Other XRD measurements were performed with the powder diffractometer PANalytical Xpert PRO (Almelo, Netherland) of the general research services (SGIker) of the UPV/EHU (Figure 3.17). This XRD is equipped with a Cu tube ( $\lambda_{Cu_{K\alpha media}}=1.5418\text{Å}$ ,  $\lambda_{Cu_{K\alpha 1}}=1.54060\text{ Å}$  and  $\lambda_{Cu_{K\alpha 2}}=1.54439\text{ Å}$ ), a vertical goniometer (Bragg-Brentano geometry), a programmable divergence slit, a secondary graphite monochromator, a PixCel detector, and an automatic sample exchanger. The measurement conditions were 40 KV and 40 mA with 2 $\theta$  range of 5-70°.

Based on XRD analysis, mineral phases can be quantified. To do so, the Reference Intensity Ratio (RIR) values contained in the PDF sheets of the International Center for Diffraction Data (ICDD) database were used. The RIR value corresponds to the intensity (height) ratio of the most intense peak of the mineral phase contained in the PDF from the database to the most intense peak of a standard, corundum (trigonal Al<sub>2</sub>O<sub>3</sub>) in a mixture of 50% by weight of each of the mineral phases. In this way, the different diffraction power of the different mineral phases is corrected, and if all the mineral phases are identified in the samples, a semi-quantitative analysis can be done using the RIR values and the intensity (scale factor) of the most intense peak of each detected mineral phase in the samples. This semi-quantitative method is relative, thus, if amorphous material was present in the samples or other crystalline phases remained unidentified, the obtained values would only represent the relative proportions among the identified phases. Another limitation arises from the fact that quantification is only based on one peak, the most intense one, and its intensity can be greatly affected by the preferred orientation of the crystals in the sample carrier. In this work, this effect could be significant due to the morphology of the obtained crystals, needle-shaped crystals, which can lead to a preferred orientation, enhancing in this way the intensity of some peaks with respect to others. It must also be considered that RIR values may change from some PDF sheets to others, and that some old PDF sheets do not contain the RIR values for some mineral phases.



Figure 3.17. PANalytical Xpert PRO powder diffractometer.

The acquisition and treatment of PANalytical XRD diffractograms was performed with the Xpert GhighScore (PANalytical) software in combination with the specific powder diffraction file ICDD database (Pennsylvania, USA).

#### 3.3.2.2.4. GC-MS and GC-IRMS

In order to study the biomolecular composition of samples, gas chromatography coupled with mass spectrometry (GC-MS) and gas chromatography coupled to isotope-ratio mass spectrometry (GC-IRMS) techniques were used in the Astrobiology Center (CAB, INTA-CSIC, Torrejón de Aroz, Spain, Figure 3.18). To do so, lyophilized subsamples of ~ 5 g were sampled from the oncoid. The extraction method was based on ultrasound sonication (3 cycles of 15 min) with a mixture of dichloromethane and methanol (DCM:MeOH, 3:1, v/v). The concentrated total lipid extract was de-sulfured<sup>[31]</sup> and digested overnight at room temperature with potassium hydroxide (6% MeOH, w/w). Then, lipids were separated into neutral and acidic fractions with n-hexane following the protocol of Grimalt et al.<sup>[32]</sup>. Further separation of the neutral fraction into non-polar (hydrocarbons) and polar (alcohols) sub-fractions was carried out according to procedures described elsewhere<sup>[33]</sup>.

At this point, GC-MS analysis were made using a 6850 GC system coupled to a 5975 VL MSD with a triple axis detector (Agilent Technologies) operating with electron ionization at 70 eV and scanning from m/z 50 to 650<sup>[34]</sup>. All fractions were analyzed by direct injection on hexane (non-polar fraction), or by injection after derivatization, with BF<sub>3</sub> in MeOH to form fatty

---

acid methyl esters or FAMEs (acidic fraction) or with N,O-bis (trimethylsilyl) trifluoroacetamide (BSTFA) to form trimethylsilyl alcohols (polar fraction).



Figure 3.18. CAB GC-MS and GC-IRMS systems.

Subsequently, carbon isotopic composition of individual lipids compounds were determined by coupling GC-MS (Trace GC 1310 ultra/ICQ MS) to the IRMS system (MAT 253 IRMS, Thermo Fisher Scientific). Details on the analytical conditions, sample injection, analysis, and isotopic ratio calculations are provided elsewhere [35]. The isotopic values of the individual lipids separated by GC were calculated using CO<sub>2</sub> – spikes of known isotopic composition, introduced directly into the MS source, three times at the beginning and at the end of every run. Reference mixtures (Indiana University, IN, USA) of known isotopic composition of n-alkanes (A6) and FAMEs (F8) were run every sample in order to check the accuracy of the isotopic ratio determined by the GC-IRMS. For the alkanolic acids, the  $\delta^{13}\text{C}$  data were calculated from the FAME values, correcting them for the one carbon atom added in the methanolysis [36]. The stable-carbon isotopic composition was expressed as the  $\delta^{13}\text{C}$  ratio, in per mille notation (‰) and relative to the Pee Dee Belemnite (PDB) standard.

GC-MS data measurement and identification were performed with the MSD Productivity ChemStation software (Agilent Technologies, Santa Clara, CA, USA). The identification was based on the comparison of mass spectra with reference materials and the NIST library of the MSD Productivity ChemStation software (Agilent Technologies, Santa Clara, CA, USA). In addition, their quantification was based on the use of external calibration curves of n-alkanes (C10 to C40), FAMEs (C8 to C24) and n-alkanols (C14, C16, C18 and C20). Besides that, in order to determine isotopic values of carbon ( $\delta^{13}\text{C}$ ) on the previously biomarkers identified, Isodat software (Thermo Electron Corporation, Waltham, MA, USA) was used.

### **3.4. Laboratory Apparatus**

#### **3.4.1. PARR 4848B reactor controller**

Activation of the clays was carried out using a Parr acid-digestion vessel (acid-washed Teflon) coupled with the Parr 4848B reactor controller (Parr Instrument Company, IL, USA), of the UNLV (Figure 3.19). The reactor system can monitor the motor speed, reactor temperature, heater temperature and pressure.



*Figure 3.19. Parr 4848B reactor controller*

The PARR vessel is communicated with a PC through the SpecView program (Parr Instrument Company, Moline, IL, USA), which can control all setting on the 4848B controller remotely, as well as record and plot the data received from the modules.

#### **3.4.2. Freeze-dryer**

The freeze-drying process at low pressures and temperatures was carried out using the Telstar Cryodos apparatus (Terrassa, Spain, Figure 3.20). The lyophilizer worked at  $-52 \pm 3$  °C and  $1 \pm 0.5$  mBar; and the samples were extracted for analysis at different times (50, 144 and 214 h).



Figure 3.20. Telstar Cryodos lyophilizer.

### 3.4.3. pH and redox determination

Potentiometric and redox measurements were carried out to determine the pH and redox potentials of Saharian sand and clay minerals. Pursuing these aims, the micro-pH-meter 2000 (Crison, Spain, Figure 3.21) was used. It is coupled to a Crison 52-02 electrode (an AgCl electrode was used as reference) for pH measurements and a Crison 52-61 electrode (with the same AgCl reference electrode) for the redox potential. Before performing the pH measurement, the Crison 52-02 electrode was calibrated using two buffer solutions at pH 7.02 and 4.00 (20 °C).

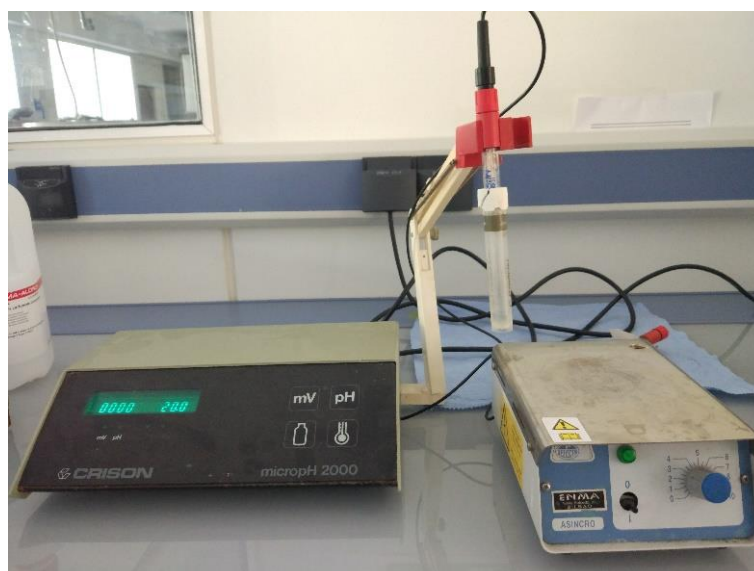


Figure 3.21. Crison micro-pH-meter 2000.

### 3.4.4. Centrifuge

The Eppendorf (Hamburg, Germany) 5804 R Centrifuge (15 amp version, Figure 3.22) was used to separate the solid phase from the liquid one in the clay minerals (see Chapter 5), during the activation procedure. The centrifugation parameters were always 5000 rpm for 5 min.



Figure 3.22. Eppendorf 5804 R Centrifuge.

### 3.4.5. Shaker water bath

All the doped samples of the clay minerals experiment (Chapter 5) were stirred at a constant temperature. For this purpose, the Lab Line 3545 shaker water bath (Figure 3. 23) was used at 60 °C for 2 hour and with 1 unit of speed.



Figure 3. 23. Lab Line 3545 shaker water bath.

---

Apart from these laboratory apparatuses, other basic apparatuses and laboratory materials that can be found in any chemistry laboratory were also used, such as stirring plates, magnets, heat baths, cooling columns, etc.

### **3.5. Mission data acquisition**

All the quantitative data from past space missions used in Chapter 4 were obtained from the NASA repository, PDS Geoscience Node, Washington University, St. Louis, MS, USA <sup>[37]</sup>.

The data and spectra of the Mars2020 mission are directly available to us because we belong to Science Team of that mission.

### **3.6. Chemical and thermodynamic modeling**

In order to select the chemical conditions under which the formation of sulfates is most favored, and to analyze how Lunar iron evolves as function of pH, different thermodynamic simulations and models at room temperature were performed. To do so the Make Equilibrium Diagrams Using Sophisticated Algorithms (MEDUSA) software <sup>[38]</sup> and the free academic software Hydrochemical Equilibrium-Constant (HYDRA) <sup>[39]</sup> database, both from the Royal Institute of Technology of Stockholm, Sweden, were used. Complementary to this, the Visual MINTEQ software <sup>[40]</sup> was used for specific formation constant values. Hydra is linked to the MEDUSA software, setting the chemical system to then create the specific diagrams using MEDUSA. The latter is able to create different kind of diagrams such as fractions diagrams, logarithmic diagrams, predominance area diagrams, etc., and it is based on SOLGASWATER <sup>[41]</sup> and HALTAFALL <sup>[42]</sup> algorithms.

### **3.7. Chemometrics and statistics**

Correlations between elements that compose the Martian soils were calculated by using the Pearson's r Correlation test of the OriginPro (OriginLab Corporation, Northampton, MA, USA) software. The value of the correlation coefficient varies from -1 to 1. A positive value means that the two variables under consideration have a positive linear relationship and are said to be positively correlated. A negative value indicates that the variables considered have a negative linear relationship and are said to be negatively correlated. The closer the value is to 1 or -1, the stronger the degree of linear dependence.

Likewise, the principal component analysis (PCA) of OriginPro software was used for reducing and interpreting large multivariate data (the elements in the Martian soils and their relative abundance) sets with linear structures. This software was also used to plot data.

### 3.8. References

- [1] Papike, J. J.; Karner, J. M.; Shearer, C. K.; Burger, P. V. Silicate Mineralogy of Martian Meteorites. *Geochim. Cosmochim. Acta* **2009**, *73*, 7443. <https://doi.org/10.1016/j.gca.2009.09.008>.
- [2] NASA. *Antarctic meteorite sample preparation*. Curation of Antarctic meteorites. [https://curator.jsc.nasa.gov/antmet/sample\\_preparation.cfm?section=thinandthick](https://curator.jsc.nasa.gov/antmet/sample_preparation.cfm?section=thinandthick) (accessed 2023-03-09).
- [3] Connolly, H. C.; Smith, C.; Benedix, G.; Folco, L.; Richter, K.; Zipfel, J.; Yamaguchi, A.; Chennaoui-Aoudjehane, H. The Meteoritical Bulletin, No. 92, 2007 September. *Meteorit. Planet. Sci.* **2007**, *42*, 1647.
- [4] Richter, K. Shergottites. *Antarct. Meteor. Newsl.* **2007**, *30*, 1.
- [5] Anand, M.; James, S.; Greenwood, R. C.; Johnson, D.; Franchi, I. A.; Grady, M. M. Mineralogy and Geochemistry of Shergottite RBT 04262. In *39th Lunar and Planetary Science Conference, No. 1391*; Texas, USA, 2008; p 2173.
- [6] Lipschutz, M. E.; Schultz, L. Meteorites. In *Encyclopedia of the Solar System*; Spohn, T., Breuer, D., Johnson, T. V., Eds.; Elsevier: Berlin, 2014; pp 625–655.
- [7] Dalton, H. A.; Peslier, A. H.; Brandon, A. D.; Lee, C. T. A.; Lapen, T. J. Petrology and Mineral Chemistry of the New Olivine-Phyric Shergottite RBT04262. In *39th Annual Lunar Planetary Science Conference, No. 1391*; 2008; Abs 2308.
- [8] Clay, P. L.; Joy, K. H.; O'Driscoll, B.; Busemann, H.; Ruzié-Hamilton, L.; Burgess, R.; Fellowes, J.; Joachim-Mrosko, B.; Pernet-Fisher, J.; Strekopytov, S.; Ballentine, C. J. Heavy Halogen Geochemistry of Martian Shergottite Meteorites and Implications for the Halogen Composition of the Depleted Shergottite Mantle Source. *Am. Mineral.* **2020**, *105*, 289. <https://doi.org/10.2138/am-2020-7237>.
- [9] Howarth, G. H.; Liu, Y.; Kohl, I.; Pernet-Fisher, J. F.; Wetteland, C.; Chen, Y.; Bodnar, R. J.; Young, E. D.; Taylor, L. A. Heterogeneous Olivine-Phyric to Pyroxene-Phyric Textures in the Paired Shergottites LAR12095 and LAR12240, N. 1360. In *46th Lunar and Planetary Science Conference*; 2015; Abs 1360.
- [10] Dunham, E. T.; Balta, J. B.; Wadhwa, M.; Sharp, T. G.; McSween, H. Y. Petrology and Geochemistry of Olivine-phyric Shergottites LAR12095 and LAR12240: Implications for Their Petrogenetic History on Mars. *Meteorit. Planet. Sci.* **2019**, *54*, 811. <https://doi.org/10.1111/maps.13262>.
- [11] Gattacceca, J.; Bouvier, A.; Grossman, J.; Metzler, K.; Uehara, M.

- 
- The Meteoritical Bulletin, No. 106. *Meteorit. Planet. Sci.* **2019**, *54*, 2, 469. <https://doi.org/10.1111/maps.13215>.
- [12] Shukla, M.; Sharma, A. A Brief Review on Breccia: It's Contrasting Origin and Diagnostic Signatures. *Solid Earth Sci.* **2018**, *3*, 50. <https://doi.org/10.1016/j.sesci.2018.03.001>.
- [13] Veneranda, M.; Manrique-Martinez, J. A.; Lopez-Reyes, G.; Medina, J.; Torre-Fdez, I.; Castro, K.; Madariaga, J. M.; Lantz, C.; Poulet, F.; Krzesińska, A. M.; Hellevang, H.; Werner, S. C.; Rull, F. Spectroscopic Study of Olivine-Bearing Rocks and Its Relevance to the ExoMars Rover Mission. *Spectrochim. Acta Part A Mol. Biomol. Spectrosc.* **2019**, *223*, 117360. <https://doi.org/10.1016/j.saa.2019.117360>.
- [14] PTAL. *Planetary Terrestrial Analogues Library*. <https://www.ptal.eu/planetary-terrestrial-analogues-library> (accessed 2023-03-28).
- [15] Jakobsson, S. P.; Jonsson, J.; Shido, F. Petrology of the Western Reykjanes Peninsula, Iceland. *J. Petrol.* **1978**, *19*, 669. <https://doi.org/10.1093/petrology/19.4.669>.
- [16] Gomez, F.; Matic, M.; Perez-Valdenegro, P.; Boidi, F.; Mlewski, C. High-Altitude Andean Lakes as Natural Laboratories for Planetary Geology and Astrobiology Research: The Laguna Negra Case (Argentina). In *Europlanet Science Congress 2022*; 2022; Abs 822. <https://doi.org/10.5194/epsc2022-822>.
- [17] Mindat. *Definition of Oncoid*. <https://www.mindat.org/glossary/oncoid> (accessed 2023-03-09).
- [18] Moll, W. F. Baseline Studies of the Clay Minerals Society Source Clays: Geological Origin. *Clays Clay Miner.* **2001**, *49*, 374. <https://doi.org/10.1346/CCMN.2001.0490503>.
- [19] TheClayMineralsSociety. *The Source Clays Repository*. <https://www.agry.purdue.edu/cjohnston/sourceclays/> (accessed 2023-03-09).
- [20] TheClayMineralsSociety. *Physical and chemical data of Source clays*. [https://www.clays.org/sourceclays\\_data/](https://www.clays.org/sourceclays_data/) (accessed 2023-03-09).
- [21] Group, Em. science. *EMil instrumentation*. UNLV. <https://emil.sites.unlv.edu/facilities/#:~:text=JEOL JSM-6700F Field Emission Scanning Electron Microscope&text=The resolution can reach 10,are attached to the JSM6700F>.
- [22] Manrique, J. A.; Santamaria-Sancho, J.; Lopez-Reyes, G.; Veneranda, M.; Arana, G.; Castro, K.; Madariaga, J. M.; Maurice, S.; Prieto-Garcia, C.; Rull, F.; Sanz-Arranz, A.; Wiens, R. C.; Team, S.
-

- Evaluation of Similitudes Between SuperCam and SimulCAM, a Laboratory Standoff Setup for Support Science. In *53rd Lunar and Planetary Science Conference (LPSC)*; The Woodlands, Houston, USA, 2022; p Abs 2589.
- [23] Rull, F.; Maurice, S.; Hutchinson, I.; Moral, A.; Perez, C.; Diaz, C.; Colombo, M.; Belenguer, T.; Lopez-Reyes, G.; Sansano, A.; Forni, O.; Parot, Y.; Striebig, N.; Woodward, S.; Howe, C.; Tarcea, N.; Rodriguez, P.; Seoane, L.; Santiago, A.; Rodriguez-Prieto, J. A.; Medina, J.; Gallego, P.; Canchal, R.; Santamaría, P.; Ramos, G.; Vago, J. L.; on behalf of the RLS Team. The Raman Laser Spectrometer for the ExoMars Rover Mission to Mars. *Astrobiology* **2017**, *17*, 627. <https://doi.org/10.1089/ast.2016.1567>.
- [24] Lafuente, B.; Downs, R. T.; Yang, H.; Stone, N. The Power of Databases: The RRUFF Project. In *Highlights in Mineralogical Crystallography*; Armsbruster, T., Danisi, R. M., Eds.; De Gruyter: Berlin, Germany, 2015; pp 1–30.
- [25] Veneranda, M.; Sanz-Arranz, A.; Manrique, J. A.; Saiz, J.; Garcia-Prieto, C.; Pascual-Sánchez, E.; Medina, J.; Konstantinidis, M.; Lalla, E.; Moral, A.; Nieto, L. M.; Rull, F.; Lopez-Reyes, G. Analytical Database of Martian Minerals (ADaMM): Project Synopsis and Raman Data Overview. *J. Raman Spectrosc.* **2022**, *53*, 364. <https://doi.org/10.1002/jrs.6215>.
- [26] Lopez-Reyes, G.; Veneranda, M.; Manrique, J. A.; González Martín, Á.; Moral, A.; Perez-Canora, C.; Rodríguez Prieto, J. A.; Sanz Arranz, A.; Saiz Cano, J.; Lalla, E.; Konstantinidis, M.; Prieto-Ballesteros, O.; Medina, J.; González, M. Á.; Charro, E.; Lopez, J. M.; Rull, F. The Raman Laser Spectrometer ExoMars Simulator (RLS Sim): A Heavy-duty Raman Tool for Ground Testing on ExoMars. *J. Raman Spectrosc.* **2022**, *53*, 382. <https://doi.org/10.1002/jrs.6281>.
- [27] Lopez-Reyes, G.; Rull Pérez, F. A Method for the Automated Raman Spectra Acquisition. *J. Raman Spectrosc.* **2017**, *48*, 1654. <https://doi.org/10.1002/jrs.5185>.
- [28] Ruiz-Galende, P.; Torre-Fdez, I.; Aramendia, J.; Gomez-Nubla, L.; Castro, K.; Arana, G.; Vallejuelo, S. F.; Maguregui, M.; Medina, J.; Baonza, V. G.; Rull, F.; Madariaga, J. M. New Raman–Visible Near-infrared Database of Inorganic and Mineralogical Planetary and Terrestrial Compounds and Its Implications for Mars: Phyllosilicates. *J. Raman Spectrosc.* **2020**, *51*, 1750. <https://doi.org/10.1002/jrs.5677>.
- [29] Clark, R. N.; Swayze, G. A.; Wise, R. A.; Livo, K. E.; Hoefen, T. M.; Kokaly, R. F.; Sutley, S. J. *USGS Digital Spectral Library Splib06a. Digital Series 231*; 2007; Vol. 231. <https://doi.org/10.3133/ds231>.

- 
- [30] Cloutis, E. A.; Craig, M. A.; Kruzelecky, R. V.; Jamroz, W. R.; Scott, A.; Hawthorne, F. C.; Mertzman, S. A. Spectral Reflectance Properties of Minerals Exposed to Simulated Mars Surface Conditions. *Icarus* **2008**, *195*, 140. <https://doi.org/10.1016/j.icarus.2007.10.028>.
- [31] Sánchez-García, L.; Aeppli, C.; Parro, V.; Fernández-Remolar, D.; García-Villadangos, M.; Chong-Díaz, G.; Blanco, Y.; Carrizo, D. Molecular Biomarkers in the Subsurface of the Salar Grande (Atacama, Chile) Evaporitic Deposits. *Biogeochemistry* **2018**, *140*, 31. <https://doi.org/10.1007/s10533-018-0477-3>.
- [32] Grimalt, R.; Gelmetti, C. Eruptive Vellus Hair Cysts: Case Report and Review of the Literature. *Pediatr. Dermatol.* **1992**, *9*, 98. <https://doi.org/10.1111/j.1525-1470.1992.tb01222.x>.
- [33] Carrizo, D.; Sánchez-García, L.; Menes, R. J.; García-Rodríguez, F. Discriminating Sources and Preservation of Organic Matter in Surface Sediments from Five Antarctic Lakes in the Fildes Peninsula (King George Island) by Lipid Biomarkers and Compound-Specific Isotopic Analysis. *Sci. Total Environ.* **2019**, *672*, 657. <https://doi.org/10.1016/j.scitotenv.2019.03.459>.
- [34] Sánchez-García, L.; Carrizo, D.; Molina, A.; Muñoz-Iglesias, V.; Lezcano, M. Á.; Fernández-Sampedro, M.; Parro, V.; Prieto-Ballesteros, O. Fingerprinting Molecular and Isotopic Biosignatures on Different Hydrothermal Scenarios of Iceland, an Acidic and Sulfur-Rich Mars Analog. *Sci. Rep.* **2020**, *10*, 21196. <https://doi.org/10.1038/s41598-020-78240-2>.
- [35] Megevand, V.; Carrizo, D.; Lezcano, M. Á.; Moreno-Paz, M.; Cabrol, N. A.; Parro, V.; Sánchez-García, L. Lipid Profiles From Fresh Biofilms Along a Temperature Gradient on a Hydrothermal Stream at El Tatio (Chilean Andes), as a Proxy for the Interpretation of Past and Present Biomarkers Beyond Earth. *Front. Microbiol.* **2022**, *13*, 811904. <https://doi.org/10.3389/fmicb.2022.811904>.
- [36] Abrajano, T. A.; Murphy, D. E.; Fang, J.; Comet, P.; Brooks, J. M. Ratios in Individual Fatty Acids of Marine Mytilids with and without Bacterial Symbionts. *Org. Geochem.* **1994**, *21*, 611. [https://doi.org/10.1016/0146-6380\(94\)90007-8](https://doi.org/10.1016/0146-6380(94)90007-8).
- [37] Ward, J.; Byrne, P. *PDS Geoscience Node. Washington University in St. Louis.* PDS Planetary Data System. NASA Repository. <https://pds-geosciences.wustl.edu/> (accessed 2023-02-02).
- [38] Puigdomenech, I. *MEDUSA: Make Equilibrium Diagrams Using Sophisticated Algorithms*; Royal Institute of Technology, KTH: Stockholm, Sweden, 2009.
- [39] Puigdomenech, I. *HYDRA: Hydrochemical Equilibrium-Constant*

*Database*; Royal Institute of Technology, KTH: Stockholm, Sweden, 2009.

- [40] Gustafsson, J. P. *Visual MINTEQ*; Royal Institute of Technology, KTH: Stockholm, Sweden, 2013.
- [41] Eriksson, G. An Algorithm for the Computation of Aqueous Multi-Component, Multiphase Equilibria. *Anal. Chim. Acta* **1979**, *112*, 375. [https://doi.org/10.1016/S0003-2670\(01\)85035-2](https://doi.org/10.1016/S0003-2670(01)85035-2).
- [42] Ingri, N.; Kakolowicz, W.; Sillén, L. G.; Warnqvist, B. High-Speed Computers as a Supplement to Graphical Methods—V1Haltafall, a General Program for Calculating the Composition of Equilibrium Mixtures. *Talanta* **1967**, *14*, 1261. [https://doi.org/10.1016/0039-9140\(67\)80203-0](https://doi.org/10.1016/0039-9140(67)80203-0).

---

---

# CHAPTER 4

BEYOND MARTIAN MINERALOGY: ANALYSES  
OF MARTIAN CHEMICAL PROCESSES THROUGH  
METEORITES, SIMULATION WORK AND  
MISSION DATA TO UNDERSTAND MARTIAN  
GEOCHEMISTRY

**“MARS IS THERE, WAITING TO BE REACHED” –  
Buzz Aldrin**

---



---

#### **4. BEYOND MARTIAN MINERALOGY: ANALYSES OF MARTIAN CHEMICAL PROCESSES THROUGH METEORITES, SIMULATION WORK AND MISISON DATA TO UNDERSTAND MARTIAN GEOCHEMISTRY**

As explained in the introductory chapter (Chapter 1), the Martian mineralogy can be studied in different manners. In this chapter, different alteration processes that the minerals of Mars may undergo are discussed through the study of meteorites, simulants and data from past and/or present missions.

Through the study of meteorites, several research can be performed. On the one hand, the study of Martian geological processes can be studied by the characterization of primary and secondary minerals. On the other hand, it is crucial to discern between Martian minerals and those coming from the Earth after their arrival. In this PhD, two different Martian meteorites were studied to obtain information about the red planet mineralogy and geochemistry.

Likewise, laboratory simulation works allow clarifying the physico-chemical conditions necessary for the formation of certain secondary minerals that were detected on Martian surface. In this work, the formation of some sulfates under Martian conditions was simulated. Moreover, and considering upcoming mission results, the consequences of pressure and temperature episodes on the spectra of these compounds was studied to obtain a reliable database.

#### **4.1. Raman spectroscopy to ascertain the Fa/Fo ratio in olivines: application to Terrestrial analogs and Jezero crater, Mars**

Olivine is a silicate mineral found in igneous rocks together with other mineral phases such as plagioclase and pyroxene. These compounds are considered as primary minerals because they are commonly found in rocky planets formed by solidification of magma <sup>[1,2]</sup>. Likewise, olivine does not present as unique mineral phase, but as a solid solution composed by the two endmembers Forsterite (Fo), as the magnesium-endmember, and Fayalite (Fa), as the iron-endmember <sup>[1]</sup>.

The relative proportion of olivine against other igneous minerals and its Fo/Fa endmembers ratio are used to determine the origin and evolution of its parent magma, since olivine is the first primary mineral to crystallize from it <sup>[3]</sup>. The presence of Fe(II) in the olivine composition is the main disadvantage for its stability, since mild oxidative conditions lead to the formation of Fe(III) species, destroying part of the forsterite ratio. Thus, olivine can undergo different weathering paths, leading to the formation of several secondary minerals <sup>[4]</sup>. The fact that olivine is easily weathered depending on environmental conditions is relevant for space exploration, as the detected mineral phases could provide information about the weathering processes that took place in the past and thus could provide clues about past environmental conditions.

As can be shown in literature <sup>[5,6]</sup>, calibration models can be created from Raman spectroscopy to calculate the Fo/Fa ratio, expressed as  $Fo_xFa_{100-x}$ . Such calibrations are constructed based on the Raman shift of the main olivine Raman bands as function of their Fo and Fa relative proportion content. The first main Raman band (OB1) characteristic of olivine is the one that goes from  $824\text{ cm}^{-1}$  (100% Fo) to  $814\text{ cm}^{-1}$  (100% Fa). The second main Raman band (OB2) characteristic of olivine is the one that transits from  $857\text{ cm}^{-1}$  (100% Fo) to  $840\text{ cm}^{-1}$  (100% Fa). Although works carried out in literature <sup>[5,6]</sup> was able to estimate the Fo and Fa content in olivines, these works are not precise enough to accurately determine the Mg/Fe ratio of olivine, probably because the calibration functions are in the form  $\%Fo=f(B2)$  or similar. This implies uncertainties of  $\pm 10\%$  or even larger, which misleads the interpretation of Martian results. In addition, in this type of studies, it is common to obtain the data for model development with only one or two different Raman instruments. This fact could lead to an important error in the equations of the proposed models, since parameters such as signal-to-noise ratio, bandwidth, spectral resolution, baseline or intensity of the bands are linked to each particular instrument.

After comparing the results provided by these published calibrations <sup>[7]</sup>, the IBeA Research Group became aware of the need to develop a more robust

---

model that would avoid these problems, providing results as accurate and precise as possible regardless of the Raman instrument with which measurements were made. To avoid the possible error generated by the use of a single instrument, a model using data acquired with several Raman spectrometers should be developed.

Preliminary experiments were published in 2019 <sup>[8]</sup> and the applicability of the model, based on a calibration with three equations was demonstrated in the following PhD Thesis <sup>[9]</sup>. Efforts to improve that initial models continued to this date. In this PhD Thesis, an improved model is presented. This work was generated using all olivine Raman data found in the literature that met both of the following requirements: (a) they fit within the uncertainty surfaces for the two main Raman bands of olivine described in our previous model <sup>[8]</sup>; and (b) the amount of Mn should be less than 0.5 % as indicated elsewhere <sup>[10]</sup>.

#### **4.1.1. Methodology**

A large collection of olivine Raman spectra of known composition was compiled from literature to develop the calibration model of the Fo/Fa ratio determination. This data set is summarized in Table 8.1 (Chapter 8) of this PhD Thesis. In Table 8.1, the corresponding Fo content, the position of its two main olivine Raman bands (OB1 from 812 to 824  $\text{cm}^{-1}$  and OB2 from 837 to 856  $\text{cm}^{-1}$ ), their  $\Delta\text{OB}$  (OB2-OB1) difference and the corresponding literature source from which they were extracted are presented.

To increase the accuracy and precision of the models, OB values were collected including the tenth of the wavenumber.

In addition, a standard commercial olivine of known Fo/Fa ratio ( $\text{Fo}_{89}\text{Fa}_{11}$ , Gelest, USA) was used to validate the calibrations models. Likewise, the calibration models were applied on the Raman spectra obtained for three olivine-bearing Martian analogs, and for the results from the SuperCam instrument on board the Perseverance rover of the Séítah formation, Jazero crater, Mars.

In this sense, for the molecular characterization of the commercial olivine and the Martian analog, the Renishaw InVia micro Raman spectrometer, the PANalytical Xpert Pro XRD diffractometer and the PANalytical AXIOS WDXRF spectrometer were used.

#### **4.1.2. Calibration models, validation and implementation**

Three different calibration models were obtained plotting the wavenumber position of OB1, OB2 and  $\Delta\text{OB}$  versus the forsterite ( $\text{Fo}_x$ ) content.

The first fitting process was performed using quadratic regression curves. However, the regression for  $\Delta\text{OB}$  fitted to a straight line. The plots of the

models together with their residuals are shown in Figure 4.1, 4.2 and 4.3. The regression equations for the three models are Equations 4.1, 4.2 and 4.3, respectively.

The two red lines in Figures 4.1, 4.2 and 4.3 represent the calculated confidence interval at a 95 % level of confidence. These lines were computed using the overall standard deviation of each regression model and represent the uncertainty boundary for each equation.

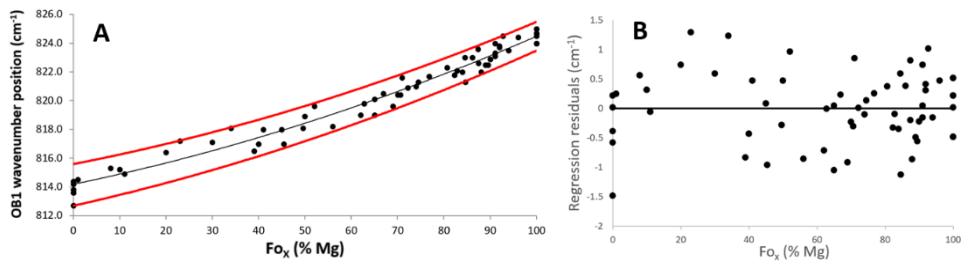


Figure 4.1. (A) Calibration curve of the OB1 as function of %Fo, and (B) their residual plot of the regression model.

The proposed calibration function for the OB1, with less than 0.5% Mn, is:

$$OB1 \text{ (cm}^{-1}\text{)} = 4.13 \cdot 10^{-4} \cdot Fo_x^2 + 0.0599 \cdot Fo_x + 814.39 \quad (\text{Equation 4.1})$$

As observed in Figure 4.1, when using the OB1 Raman signature, all the data fit inside the uncertainty boundaries, which implies that there are not outliers among the set of data used for the calibration model. Regarding its quality parameters, the determination coefficient ( $R^2$ ) obtained for the quadratic regression model expressed in Equation 4.1 was 0.970, and its overall standard deviation of the curve fit was  $\pm 0.61 \text{ cm}^{-1}$ . The residuals are scattered in a random way, as they do not follow a visible trend. In addition, all the points were equally distributed around the zero horizontal line and all of them are within the  $\pm 1.5 \text{ cm}^{-1}$  range, which must be considered the average value for the 95% confidence interval ( $\pm 0.75 \text{ cm}^{-1}$  as the standard deviation for Equation 4.1).

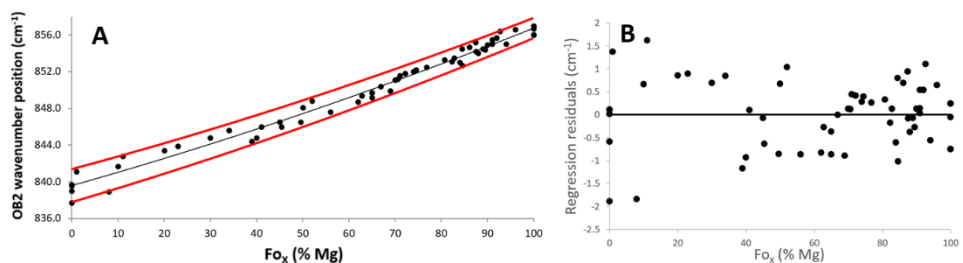


Figure 4.2. (A) Calibration curve of the OB2 as function of %Fo, and (B) their residual plot of the regression model.

The proposed calibration function for the OB2 Raman band for olivine, with less than 0.5% Mn, is:

$$\text{OB2 (cm}^{-1}\text{)} = 3.63 \cdot 10^{-4} \cdot \text{Fo}_x^2 + 0.133 \cdot \text{Fo}_x + 839.85 \quad (\text{Equation 4.2})$$

All the OB2 data points also fit inside the red 95% confidence interval lines of Equation 4.2, supporting the same fact explained in the OB1 model, that is, there are not outliers in the set of data. For this model (Equation 4.2) an  $R^2$  of 0.984 and an overall standard deviation of the curve fit of  $\pm 0.73 \text{ cm}^{-1}$  were obtained. Regarding the residuals model, in this case the points were also distributed in a random way around the horizontal zero line and within the  $\pm 2.0 \text{ cm}^{-1}$  range, that must be considered the average value for the 95% confidence interval ( $\pm 1.0 \text{ cm}^{-1}$  as the standard deviation for Equation 4.2). However, it must be pointed out that for this calibration model the residuals corresponding to the samples with a low magnesium concentration ( $\text{Fo}_x < 20 \%$ ) are slightly further apart from the zero than the rest of them. This implies that the prediction for olivine with low magnesium concentrations will have a higher uncertainty than those for high Fo olivines.

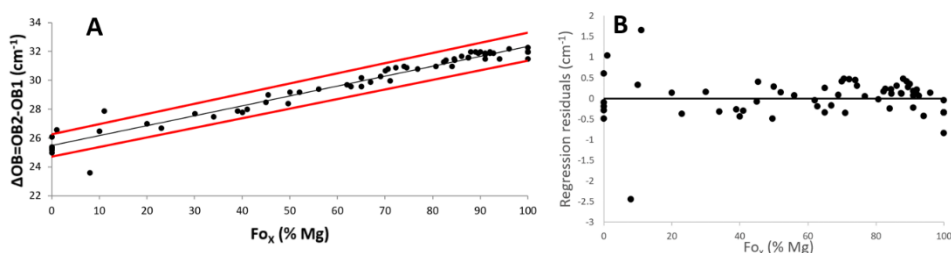


Figure 4.3. (A) Calibration curve of the  $\Delta\text{OB}$  as function of %Fo, and (B) their residual plot of the regression model.

The calibration plot, and uncertainty boundary, using the difference between OB2 and OB1 olivine Raman signals can be seen in Figure 4.3. The proposed calibration function for the  $\Delta\text{OB}$ , with less than 0.5% Mn, is:

$$\Delta\text{OB (cm}^{-1}\text{)} = 0.068 \cdot \text{Fo}_x + 25.5 \quad (\text{Equation 4.3})$$

The regression line (Equation 4.3) possessed an  $R^2$  of 0.951 and an overall standard deviation of the curve fit of  $\pm 0.50 \text{ cm}^{-1}$ . Contrary to the previous two models, in this case not all the data points fit inside the uncertainty boundaries plotted in red. Specifically, about half of the points corresponding to olivines with low Mg content ( $\text{Fo}_x < 20 \%$ ) were outside the interval and they were further away from the horizontal zero line in the residual plot.

#### 4.1.2.1. Calibration models validation by using a commercial standard olivine

In order to check the accuracy of the three models, the standard commercial olivine described above was used. Before that with the aim of verifying the purity of the standard commercial olivine, three different grains were separately analyzed by XRD. Figure 4.4 shows the XRD diffractogram of one of these measurements. The signals of the diffractograms obtained from the three grains were very similar, confirming the homogeneity of the Fo/Fa content. Some minor and trace minerals were also observed, which could be the consequence of microalterations of olivine or the result of contamination of the commercial product. In any case, none of these minor minerals presents Raman signals in the same region as the main Raman bands of olivine, so they did not interfere with the OB signals.

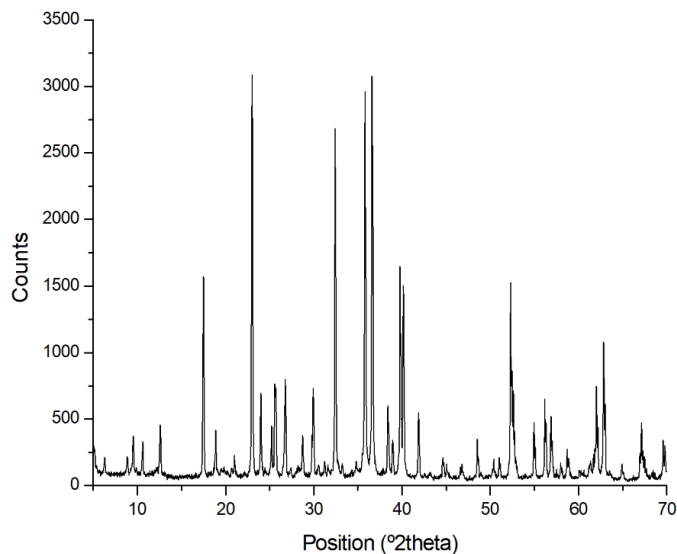


Figure 4.4. XRD diffractogram of one of the analyzed standard commercial olivine grains, corresponding to a pure Mg-rich ( $FO_{89}Fa_{11}$ ) olivine.

In addition, a wavelength dispersive X-ray fluorescence (WDXRF) measurement was carried out to double check the concentration of the commercial olivine and compare the results with those obtained by the proposed Raman model. In this regard, three different borate glass beads were prepared by melting in an induction microfurnace, mixing the ground olivine grains with the Spectromelt A12 flux (Merck, Germany). The beads were then analyzed at vacuum with an AXIOS WDXRF spectrometer (PANalytical, UK), using an Rh tube and three detectors (gas flux, sparkle and Xe sealing).

---

The mean result obtained by WDXRF for the commercial olivine was  $\text{Fo}_{89.5 \pm 1.8} \text{Fa}_{10.5 \pm 0.5}$ , where the confidence interval was calculated at a 95 % using the standard deviation of the three olivine beads analyzed. As noted, the composition stated by the supplier,  $\text{Fo}_{89} \text{Fa}_{11}$ , was within the composition interval obtained by WDXRF.

Finally, in order to calculate de Fo/Fa content, this olivine standard was analyzed by Raman spectroscopy. Different grains (10 samples) were analyzed obtaining the same Raman spectrum in all of them. As can be seen in Figure 4.28, the Raman spectrum did not present any additional signal not related to olivine. In the development of the optimized model, the wavenumber of the two main peaks was obtained with  $\pm 0.1 \text{ cm}^{-1}$ , the same as the data collected in the literature. This is an important factor in increasing the accuracy and precision of the developed calibration equations.

The OB1 ( $823.1 \text{ cm}^{-1}$ ), OB2 ( $855.0 \text{ cm}^{-1}$ ) Raman signals (Figure 4.5) and the  $\Delta\text{OB}$  ( $31.9 \text{ cm}^{-1}$ ) were used to calculate the metallic concentration of the mineral using the respective calibration models. The concentrations obtained were  $\text{Fo}_{89.7 \pm 1.2} \text{Fa}_{10.3 \pm 1.2}$ ,  $\text{Fo}_{91.2 \pm 1.5} \text{Fa}_{8.8 \pm 1.5}$  and  $\text{Fo}_{93.4 \pm 1.0} \text{Fa}_{6.6 \pm 1.0}$  for the OB1, OB2 and  $\Delta\text{OB}$  models, respectively. The uncertainties for Fo values were calculated at a 95 % level of confidence using the overall standard deviation of the calibration curves. The uncertainties for Fa values were calculated through error propagation rules.

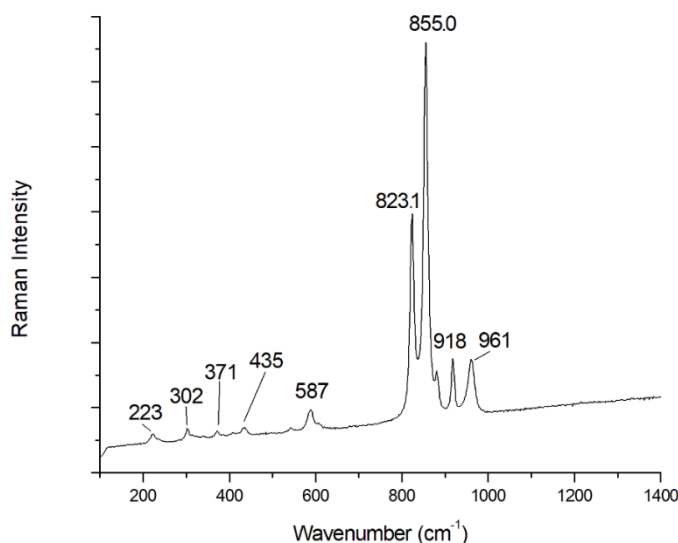


Figure 4.5. Raman spectrum of the standard commercial olivine obtained with the Renishaw InVia microRaman spectrometer, using the 532 nm excitation laser.

As observed, the forsterite confidence interval results obtained with the OB1 and OB2 models overlap perfectly with the WDXRF concentration confidence interval, which means that the predicted concentrations with

these two models were accurate. In contrast, the  $\Delta OB$  model failed in the prediction of the Fo and Fa concentrations. Considering this, that third model was discarded to further ensure the quality parameters, since the resulting methodology for the characterization of the metallic content of olivine had to be as accurate as possible.

In addition to all this, another quality test with the remaining two calibration models was performed. For this purpose, the 64 data values that were used for the models development were used. Position OB1 and OB2 extracted from Table 8.1 were inserted into the respective two models.

OB1 and OB2 values extracted from Tables 4.1 and 4.2 were introduced in the respective two models and the forsterite value corresponding to each data point was calculated. These values were then compared with the ones summarized in the Chapter 8. Table 4.1 and 4.2 summarize this comparison, where the  $Fo_x$  experimental values are compared with those calculated with each calibration model.

In order to check if the calculated results were statistically comparable to the ones provided by literature, a Student's t test of paired samples was carried out for both models (Table 4.3). In this sense, the t values were calculated for a 95 % level of confidence. Since there were differences between high and low forsterite content data points in the residual plot, the Student's t test was also carried out for the  $Fo_{0-50}$  and  $Fo_{52-100}$  ranges separately. As can be seen in Table 4.3, in all cases the obtained t value was smaller than the t critical value for a 95 % level of confidence and, in addition, the p value was higher than 0.05. These facts mean that there are not statistical differences between the forsterite content provided by literature and the ones calculated with both calibration models.

In addition, the t value calculated for the OB2 model in the  $Fo_{52-100}$  range was smaller than the one for the OB1 model in the same range. In addition, the p value for the former model was higher than that one of the latter. These facts suggested that the OB2 model would work better for the fayalite rich olivines. However, the residuals plot of the OB2 model (Figure 4.2) suggested that this model would have more uncertainty in that forsterite concentration range.

To solve this, the use of both models is proposed as the standard procedure to obtain the Fo content for unknown olivine samples, averaging the two results obtained from Equations 4.1 and 4.2, which would provide good results for all the Fo-Fa concentrations range. For example, in the case of the commercial olivine, averaging the results of the OB1 and OB2 models a concentration of  $Fo_{90.1 \pm 1.9} Fa_{9.9 \pm 1.9}$  was obtained, where the confidence interval was calculated at a 95 % level of confidence using the overall standard deviation of both calibration curves and doing variance

propagation. As observed, the concentration is still accurate. The only drawback of using this average method is that the uncertainty associated to the final result increased slightly due to the propagation of the variances of the two calibration curves. However, this uncertainty was still lower ( $\pm 2.1$  % for  $F_{Ox}$ ) than the ones expressed in the literature (around  $\pm 10$  % as stated above), thus, the proposed method of averaging the results of the OB1 and OB2 models is the recommended one.

Table 4.1.  $F_{Ox}$  of the data set used to develop the calibration models and the ones calculated using these models with the OB1 and OB2.

Composition		Calculated composition with the models	
$F_{Ox}$ (Mg %)	Literature reference	OB1 – $F_{Ox}$ (Mg %)	OB2 – $F_{Ox}$ (Mg %)
100	26	100.1	96.2
100	9	96.5	96.2
100	27	96.5	96.2
100	10	96.5	96.2
100	15	101.5	99.7
100	11	103.7	101.2
100	28	101.5	101.2
100	29	103.7	101.2
96	30	99.4	99.2
94	27	92.8	91.2
92.7	16	100.1	98.2
92	30	95.0	94.7
92	30	94.3	94.7
91	15	89.8	91.2
91	29	96.5	93.7
91	30	91.3	91.7
90	30	88.3	90.7
89.5	28	85.2	88.1
89	15	85.2	88.6
88	9	81.2	86.1
87.5	28	86.0	87.1
87.4	16	93.5	92.2
86.1	16	89.0	89.7
84.6	28	75.6	79.3
84.5	11	89.0	88.6
84	29	81.2	80.8
82.8	16	82.0	83.5
82.3	28	79.6	81.4
80.7	16	83.6	82.4
76.8	16	78.8	78.2
74.5	16	75.6	76.6
74	31	73.1	75.5

Table 4.2.  $F_{O_x}$  of the data set used to develop the calibration models and the ones calculated using these models with the OB1 and OB2 (continuation).

Real composition		Calculated composition with the models	
$F_{O_x}$ (Mg %)	Literature reference	OB1 – $F_{O_x}$ (Mg %)	OB2 – $F_{O_x}$ (Mg %)
72.2	16	72.3	74.5
71	30	78.0	73.4
70.6	16	68.0	71.2
70	30	68.0	70.7
69	15	61.0	64.1
66.9	16	68.9	66.9
65	16	65.4	63.0
65	15	55.4	60.2
62.8	16	62.7	61.3
62	15	55.4	57.4
56	15	47.8	51.0
52	30	61.0	57.9
50	30	54.5	53.9
49.6	27	46.8	44.6
45.4	27	35.4	41.6
45	29	45.8	44.6
41	32	45.8	41.6
40	30	35.4	34.3
39	15	29.8	31.8
34	30	46.8	39.2
30	30	36.5	34.3
23	30	37.5	28.7
20	30	28.7	25.5
11	30	10.1	21.7
10	30	14.1	14.5
8	15	15.4	-4.9
1	30	4.6	10.4
0	9	3.1	0.8
0	33	-6.0	-4.2
0	27	0.2	0.1
0	10	-9.3	0.8
0	-	-25.9	-13.7

Table 4.3. Student's *t* test of paired samples results for the *F<sub>ox</sub>* from literature and the calculated ones using OB1 and OB2 calibration models.

<b>F<sub>ox</sub> range (%)</b>	<b>OB1 model</b>			<b>OB2 model</b>		
	0-100	0-50	52-100	0-100	0-50	52-100
<b>Degrees of freedom</b>	63	19	43	63	19	43
<b>t value</b>	0.227	0.0551	0.464	0.0658	0.0529	0.0378
<b>t critical value (2 tails)</b>	2.00	2.09	2.02	2.00	2.09	2.02
<b>p value (2 tails)</b>	0.821	0.957	0.645	0.948	0.958	0.970

As explained above, the calibration models were applied on two different samples: olivine-bearing Martian analog and real samples from the Jezero crater, Mars.

#### 4.1.2.2. Implementation of calibration models on olivine-bearing Martian analog

The olivine-bearing Martian analog samples used in this PhD Thesis were IS16-0001, IS16-0002 and IS16-0013 (for more information see Chapter 3), which belong to Reykjanes, Iceland, a region considered to be an optimal analog of Martian olivine-bearing rocks <sup>[11–13]</sup>.

In order to be analyzed by Raman spectroscopy, the samples were prepared as coarse powder. The three rocky samples did contain a high amount of olivine phenocrysts or, in other words, olivine crystals that were formed early during the rock formation process and are usually larger than the other mineral grains. In the case of the IS16-0001 samples, several dozens of olivine spectra were collected and their main olivine Raman signals varied from 816 and 848 cm<sup>-1</sup> to 823 and 855 cm<sup>-1</sup>. Two of these olivine spectra can be observed in Figure 4.6, where it is clearly seen that there is a shift in the position of the two main Raman bands of the mineral. Using the calibration models proposed above, the forsterite compositions were calculated using the OB1 and OB2, and the results were averaged, calculating all the confidence intervals at a 95 % level using the overall standard deviation of both calibration curves and doing variance propagation. According to the proposed calibration model, the IS16-0001 sample had olivine with a metallic concentration that ranged between  $Fo_{38.7 \pm 0.8}Fa_{61.3 \pm 1.3}$  and  $Fo_{90.1 \pm 1.9}Fa_{9.9 \pm 1.9}$ .

As observed, the difference between the olivines found in this sample regarding their metallic content is very high. This fact is explained due the known differences between the core and the rim metallic composition of olivine grains, where the core is usually richer in magnesium than the rim of the mineral grain. This difference is created during the formation process of the rocks, within the cooling process of the magma, and it is caused by

the difference of the melting point of forsterite (1890 °C) and fayalite (1205 °C) [14]. When the cooling process is slow, the first endmember that crystallizes is forsterite forming the initial bulk (the core) of the olivine crystals. Then, when the cooling process continues, fayalite crystallizes mainly in the rim of the initial forsterite-rich crystals. As a result, when the rock is formed, the olivine grains end up with the highest amount of iron (fayalite) in their rims, while the highest amount of magnesium (forsterite) usually concentrates in their cores. If the cooling process is fast and there is not enough time for this differentiation to happen, the final result is a more homogeneous olivine, where its core and rim have a similar metallic composition.

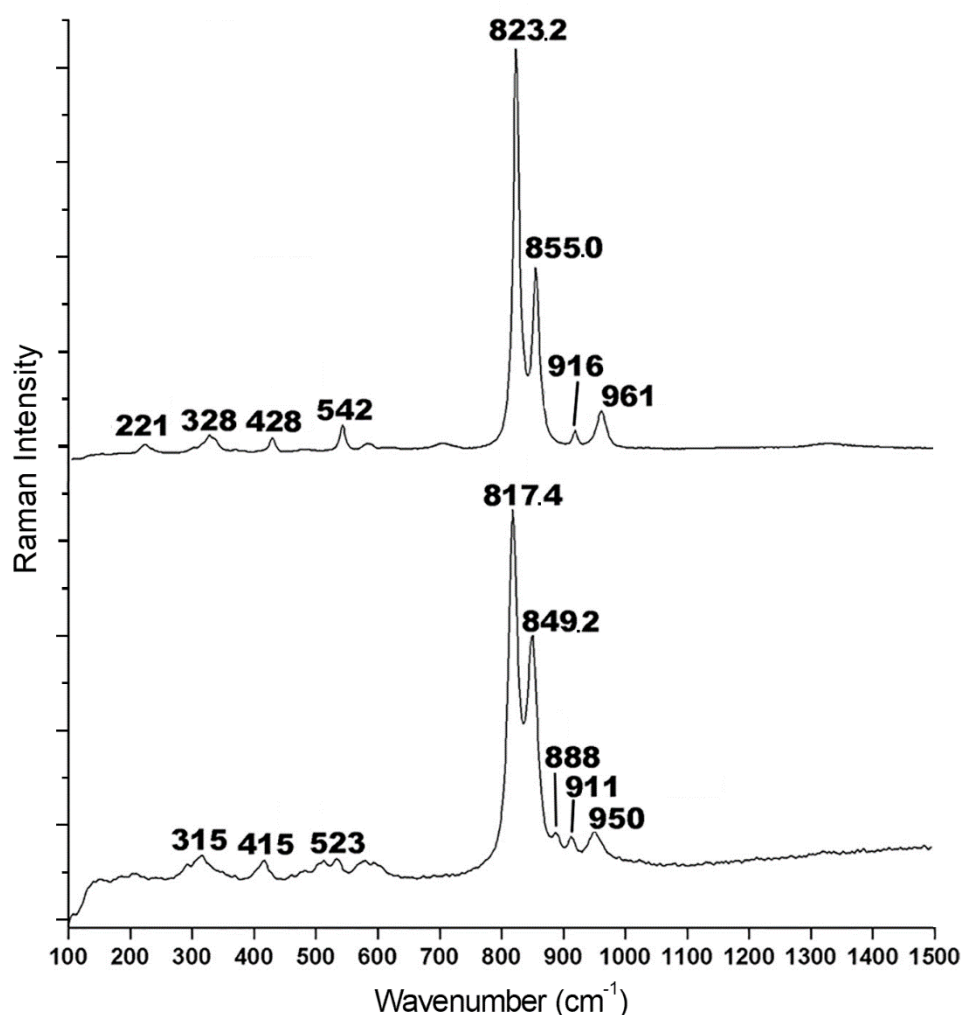


Figure 4.6. Two different olivine spectra observed in the IS 16-0001 sample from Iceland. The spectra were obtained with the 532 nm excitation laser.

---

Regarding the IS16-0002 and IS16-0013 samples, all the olivine spectra collected presented their two main Raman bands in the same positions. Being 822 and 854  $\text{cm}^{-1}$  for IS16-0002 and 818 and 847  $\text{cm}^{-1}$  for IS16-0013. Using the calibration models proposed in this work, the olivine metallic concentration calculated for IS16-0002 was  $\text{Fo}_{83.6\pm 1.8}\text{Fa}_{16.4\pm 1.8}$  and for IS16-0013 it was  $\text{Fo}_{46.7\pm 1.0}\text{Fa}_{53.3\pm 1.1}$ .

As can be appreciated, the difference in metallic content between the rims and the cores of these two samples was not observed. This fact may be due to the fast cooling of the magma that formed these olivines, without having enough time for core-to-rim zoned.

#### **4.1.2.3. Séítah Formation, Jezero crater, Mars, validation**

After optimizing the different instruments of the Perseverance rover, the first science campaign started analyzing rocks, soils and abraded patches of the Crater Floor. Two different geological formations were studied, Mááz and Séítah. Mááz did not show the presence of olivines, while Séítah bedrocks presented olivines <sup>[15]</sup>. In this sense, several Séítah rocks provided positive Raman response with the SuperCam Raman instrument. The OB1 and OB2 of these spectra were extracted from the PDS data repository of NASA <sup>[16]</sup>.

From there, the olivine detection in different targets belonging to the Séítah formation, from Sol 207 to Sol 303, is described. Although not all the data collected showed the two characteristic bands of olivine, in this work, the Raman spectra containing a clear information of those two Raman bands were considered.

Raman observations of the Séítah rocks came from a total of 71 spectra, from Sol 207 (Garde) to Sol 303 (Quartier). The signal-to-noise ratio was poor in more than half of the measurements and the position of the two main olivine bands was difficult to establish. An example of such high noisy Raman spectra with a non-clear definition of the two main Raman bands of olivine is shown in Figure 4.7.

As seen, a clear evidence of olivine was identified but the two Raman bands were not well resolved. The bump in the 300-550  $\text{cm}^{-1}$  range was caused due to the signal promoted by the optic fiber connecting the Mast Unit and the Body Unit, and it is observed when the Raman intensity is not high enough. Some cosmic rays were also observed, a common feature in practically all the Raman spectra collected during the mission by the SuperCam Raman detector <sup>[16]</sup>.

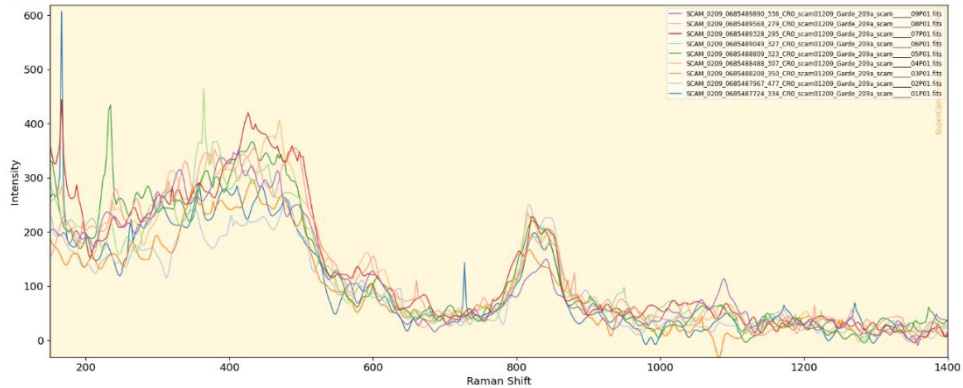


Figure 4.7. Nine olivine Raman spectra collected from a 3x3 raster with the SuperCam instrument on the Garde target on Sol 209<sup>[16]</sup>.

Among all the olivine Raman spectra, 32 were selected for this work. In this sense, the Fo/Fa content was extracted from OB1 and OB2. Then, the average %Fo value was calculated, as well as their standard deviation and relative standard deviation (RSD%).

Half of the values (16) were in the  $50 < \%RSD < 20$  range. As these high %RSD values come from the disagreements between the OB1 and OB2 wavenumbers, they were not considered representative to obtain the Fo/Fa ratio of the detected olivines in Séítah rocks. The values obtained with the other 16 spectra are shown in Table 4.4

Table 4.4. SuperCam Raman data products from Séítah rocks having consistent OB1 and OB2 wavenumbers to calculate the %Fo values using the two calibration models proposed in this work. This table also includes the %Fo average, the standard derivation and the %RSD for each rocky sample.

SuperCam Data Product	OB1	OB2	%Fo from OB1	%Fo from OB2	Average %Fo	Stand. Deviat.	%RSD
SCAM_0207_0685311641_699_CR0_scam01207_Garde_207_scam__05P01	820	847	64,75	47,58	56,2	8,6	15,3
SCAM_0207_0685312080_648_CR0_scam01207_Garde_207_scam__07P01	820	849	64,75	59,22	62,0	2,8	4,5
SCAM_0207_0685312277_656_CR0_scam01207_Garde_207_scam__08P01	820	848	64,75	53,47	59,1	5,6	9,5
SCAM_0210_0685578180_664_CR0_scam01210_Garde_210_scam__03P01	818	848	45,80	53,47	49,6	3,8	7,7
SCAM_0210_0685579716_710_CR0_scam01210_Garde_210_scam__09P01	820	848	64,75	53,47	59,1	5,6	9,5
SCAM_0211_0685669541_593_CR0_scam04211_Penne_____10P01	820	849	64,75	59,22	62,0	2,8	4,5
SCAM_0247_0688865254_040_CR1_scam01247_Brac_247_____02P01	818	849	45,80	59,22	52,5	6,7	12,8
SCAM_0248_0688951962_226_CR1_scam04248_Castellet_____05P01	822	849	81,38	59,22	70,3	11,1	15,8
SCAM_0248_0688951962_226_CR1_scam04248_Castellet_____05P01	822	849	81,38	59,22	70,3	11,1	15,8
SCAM_0248_0688952922_289_CR1_scam04248_Castellet_____09P01	820	849	64,75	59,22	62,0	2,8	4,5
SCAM_0248_0688953248_224_CR1_scam04248_Castellet_____10P01	818	846	45,80	41,53	43,7	2,1	4,9
SCAM_0259_0689932297_708_CR0_scam01259_Dourbes_259_____02P02	820	849	64,75	59,22	62,0	2,8	4,5
SCAM_0259_0689933837_708_CR0_scam01259_Dourbes_259_____08P02	818	847	45,80	47,58	46,7	0,9	1,9
SCAM_0268_0690734362_436_CR1_scam04268_Dourbes_268_____07P01	820	847	64,75	47,58	56,2	8,6	15,3
SCAM_0268_0690734413_573_CR1_scam04268_Dourbes_268_____07P01	820	847	64,75	47,58	56,2	8,6	15,3
SCAM_0268_0690735013_459_CR1_scam04268_Dourbes_268_____10P01	822	849	81,38	59,22	70,3	11,1	15,8
SCAM_0268_0690735065_496_CR1_scam04268_Dourbes_268_____10P01	822	849	81,38	59,22	70,3	11,1	15,8
SCAM_0295_0693130423_577_CR0_scam01295_Quartier_295_scam_10P01	820	849	64,75	59,22	62,0	2,8	4,5

The Garde abrasive patch is shown in Figure 4.8. Before drilling a rock to make a sample to be sealed for the MSR mission, a first abrasion has to be performed on the candidate rock selected by the Mars2020 science team.

In this sense, during sols 207 and 209, several olivine well-resolved Raman spectra were collected at point 5, 7 and 8 on sol 207, and at points 3 and 9

on sol 209. Figure 4.9 shows the stretched mosaics constructed from raw RMI images of both sols.



Figure 4.8. RMI (SuperCam high resolution camera) images superposed over the ZCAM image of the abraded surface (sol 207).

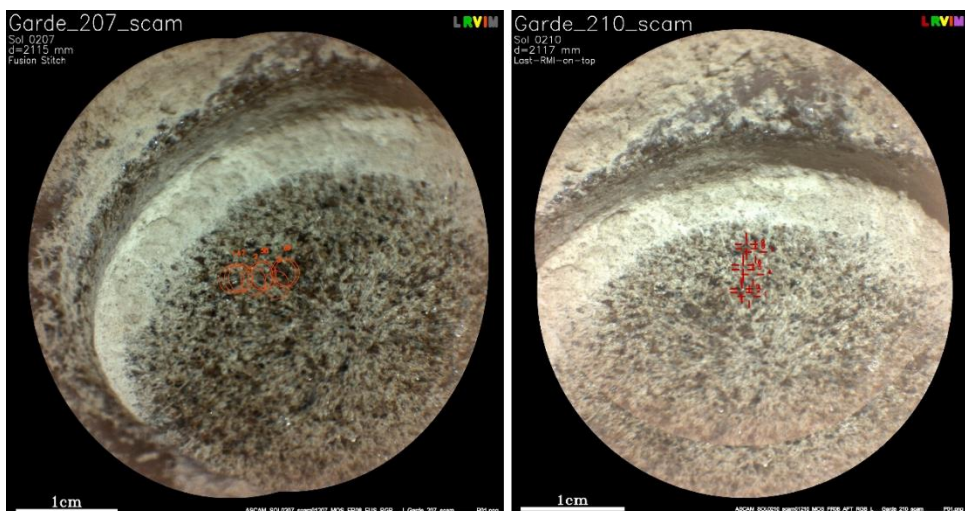


Figure 4.9. The analyzed area inside the Garde abraded patch. The RMI were different for sol 207 and 209. Points 5, 7 and 8 (sol 207) were over high size blackish crystals. Points 3 and 9 (sol 210) were also on similar crystals in other area of the abraded patch.

As can be seen in Table 4.4, the five olivine values obtained for Garde abraded ranged from 50 to 62 %Fo, with average uncertainties around 10% among them. This range fitted well with the proposed range for olivines

---

found by SuperCam LIBS in the surface of Séítah rocks (54 to 72 %Fo) proposed in the first global paper of SuperCam about the geochemistry of rocks in the Carter Floor unit of Jezero crater <sup>[15]</sup>. The Mg-enrichment at the surface of the rocks, with regard to the inner parts analyzed after abrasion, is probably induced by the weathering of the overlying olivines by partial oxidation of Fe(II) in the  $\text{Fe}_2\text{SiO}_4$  fraction with the subsequent loss of fayalite, leading to an enrichment in forsterite.

The second abraded patch at Séítah was the so-called Dourbes (sols 259-268). Figure 4.10 shows a NavCam image (left camera) of the area with the abraded patch and the hole created after removing the core that was sealed to be returned to Earth.



*Figure 4.10. NavCam image (left camera) of the workspace showing the Dourbes abraded patch and the Sallette hole remaining after extracting the core to be returned to Earth. Ref. NLF\_0262\_0690212241\_488CWS\_N0080000NCAM00705\_0A00LLJ01-stretched-v2.*

Two sets of Raman measurements were performed on Dourbes. First, a 3x3 raster in sol 259 (see Figure 4.11 left) and then, a linear 10x1 raster in Sol 268 (see Figure 4.11, right) were performed. The quality of the Raman spectra can be appreciated in Figure 4.12, where the two main Raman bands of olivine are clearly visible. Note the large amount of cosmic rays, which fortunately did not affect the wavenumber range of olivine.

The %Fo values at Dourbes ranged from 47 to 70%. Sol 259 provided higher quality Raman spectra, as is evident from the %RSD of the %Fo values. However, the repeatability observed in the duplicate measurements performed on sol 268 was excellent, although the uncertainties in the %Fo values calculated from the calibration model were higher.

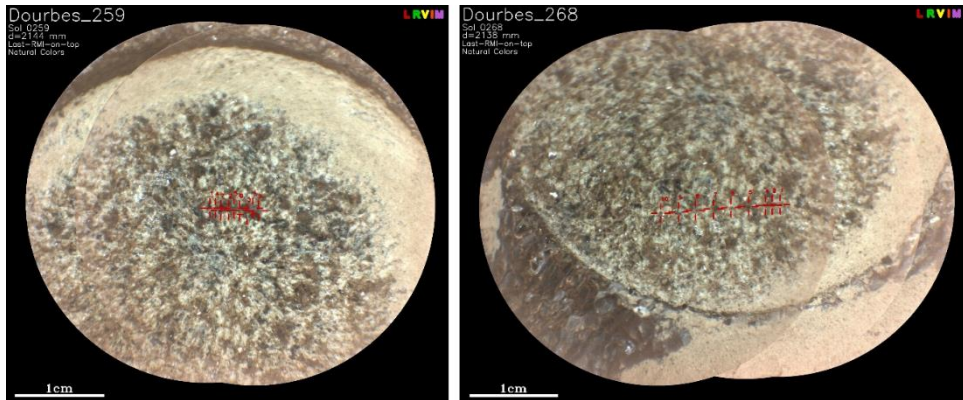


Figure 4.11. The analyzed area inside the abraded patch Dourbes. RMI were different for sol 259 and 268. Points 2 and 8 (sol 259) were over high size blackish crystals. Points 7 and 10 (sol 268) were analyzed twice to check for repetitiveness.

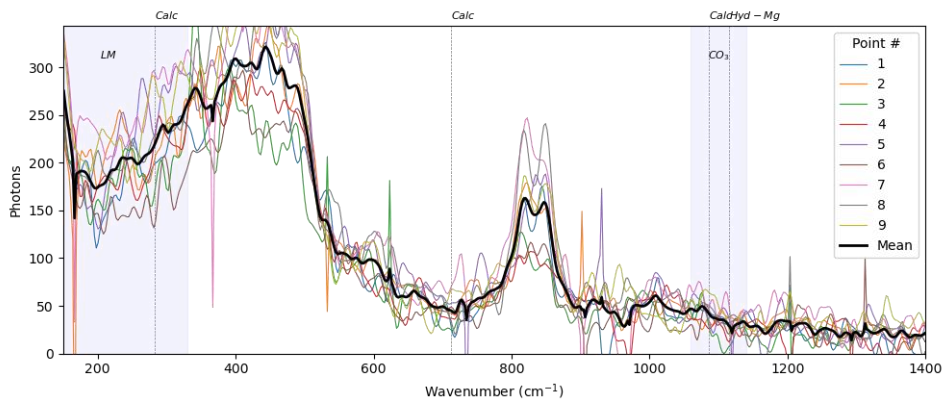


Figure 4.12. Nine spectra collected from 3x3 raster with SuperCam Raman on target Dourbes (abrasion patch on a candidate rock to obtain a sample core) on sol 259.

The other four samples with a positive olivine Raman response were direct measurements on the surface of Séítah rocks (Penne on sol 211, Brac on sol 247, and Castellet on sol 248, Table 4.4) and a surface lightly abraded only to remove surface dust and patina (Quartier on sol 295, Table 4.4). Figure 4.13 shows the SuperCam RMI mosaics of those four targets. The %Fo values calculated from our proposed calibration model provided values ranging from 53% to 70%, completely in agreement with the average range (54 to 72 %Fo), calculated from SuperCam LIBS data, proposed for Séítah rock surfaces <sup>[15]</sup>.

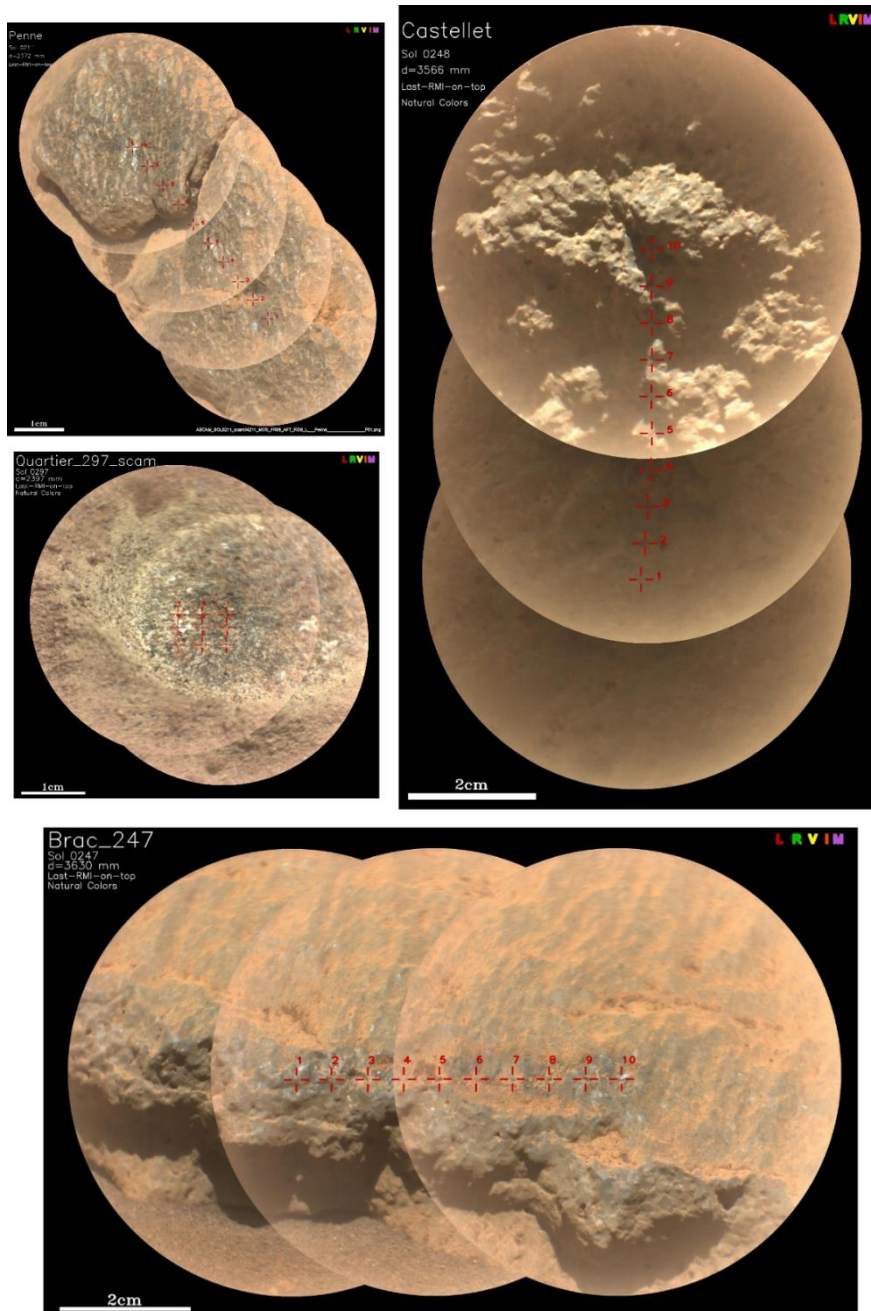


Figure 4.13. The analyzed surfaces with positive olivine Raman response: point 10 for Penne on sol 211, point 2 for Brac on sol 247, points 5, 9 and 10 for Castellet on sol 248, and point 10 for Quartier on sol 295.

### 4.1.3. Discussion

In this work, a new method was optimized to calculate the olivine Fo/Fa ratio by Raman spectroscopy. This method includes three calibration models obtained by quadratic fitting on the main Raman bands, OB1, OB2 and  $\Delta$ OB of olivine.

The three models were developed using a set of 64 data from 14 different research papers, where different Raman instruments and acquisition parameters were used. This fact eliminates any possible bias that the instrumentation could introduce. In order to increase the accuracy of the models, the OB1 and OB2 values were used within a tenth of  $\text{cm}^{-1}$  in wavenumbers.

The developed models were validated with a standard commercial olivine, from which the mineralogical and metallic characterization was performed by XRD and WDXRF to ensure reference values for comparison with the calculated ones from the proposed calibration models. After studying the different quality parameters of the calibration models, and comparing the results obtained for the standard olivine with them, it was determined that the most accurate models were the ones using OB1 and OB2 independently. Unfortunately, the  $\Delta\text{OB}$  calibration model did not provide accurate and precise values. In addition, it was observed that the model that used OB1 became more inaccurate than the one that used OB2 when analyzing iron rich olivines. In order to overcome this issue, it was established that the best way to study the metallic content of any unknown olivine was the use of both calibrations and then average the results. The proposed models in this work improve greatly the precision of the calculated %Fo results obtained for unknown olivine when compared to other calibration functions proposed in the literature. In fact, using the averaging method, the uncertainty associated to the result is around  $\pm 2\text{-}3\%$ , while the models found in the literature <sup>[5,6,17]</sup> have an uncertainty of  $\pm 10\%$  or higher.

The ability to differentiate among different types of olivines in real Martian analog samples from Iceland was also tested. It was observed that for the IS16-0001 sample, Raman spectroscopy was able to differentiate a wide range of olivine compositions. In contrast, IS16-0002 and IS16-0013 did not show different Fo/Fa ratios. Taking into account that IS16-0001 and IS16-0002 were sampled in the same point and IS16-0013 only 500 m away, they could be rocks formed from the same parent magma. However, what differentiated them was the cooling time of the magma. In this sense, when magma cooled slowly, the material was able to zonate from the core to the rim, leaving a heterogeneous olivine rim; but when magma cooled rapidly, materials did not have enough time to core-to-rim zoned, leaving a homogeneous olivine crystal. On Mars a similar observation could happen, where two rocks might seem similar visually but have different formation processes.

This heterogeneity has been observed in the two analyzed abraded surfaces with positive Raman response to olivine, Garde and Dourbes in the Séítah formation, analyzed by SuperCam Raman instrument. Using the two calibration functions proposed in this work, and averaging the %Fo

---

values obtained from both Equations 4.1 and 4.2, the range of %Fo concentrations varied from 50 to 62% in Garde, while the range for Dourbes was 47 to 70%. In addition, some surfaces of Séítah rocks provided positive Raman response to olivine with %Fo variations from 53 to 70%.

These results are really promising for quantification of the olivine Fo/Fa content using Raman spectroscopy. Specially, these models can be used for the olivines analyzed by the SuperCam Raman spectrometer on board of Perseverance rover. Moreover, the same methodology can be applied to Raman data collected in the forthcoming Rosalind Franklin and MMX mission, since both include a Raman spectrometer in their scientific payload.

## **4.2. Martian meteorites study - Pressure, oxidation and hydrothermal alteration processes observed in Martian Shergottites**

The positive aspect about analyzing meteorites is that they can be analyzed in laboratories, with more robust, precise and sensitive instrumentation if compared with those on board rovers, landers or orbiters. Nevertheless, mineral phases found in meteorites may not be the original mineral phases from the parent planet, giving rise to misunderstandings. This is because minerals from meteorites are subjected to different processes that can alter their original composition, such as: (1) the high pressure event during their formation due to the impact of another celestial body against the parent planet; (2) their travel through the space; (3) their entry into a highly oxidizing atmosphere; and (4) their stay on Earth under terrestrial conditions. Therefore, identifying the origin of minerals found on meteorites has become a challenge because it is necessary to differentiate between primary, Martian secondary, terrestrial secondary and terrestrial weathering minerals. This classification can be made based on the minerals already found on Mars by *in situ* analytical techniques and based on their chemical alterations.

In this sense, the RBT 04262 and LAR12095 Martian shergottites were analyzed by using non-destructive analytical techniques. These are micro-Raman spectroscopy and high resolution Raman imaging, assisted with energy dispersive X-ray fluorescence imaging.

The methodology carried out for the analysis of these meteorites consisted on an initial elemental characterization by means of the acquisition of  $\mu$ -EDXRF maps on both sides of the studied specimen. Thanks to the  $\mu$ -EDXRF maps, it was possible to establish coexistence of elements and to detect hot spots of interest for the subsequent molecular characterization by means of point-by-point Raman analyses. When molecular trends were identified, Raman imaging analysis were performed to check, together with  $\mu$ -EDXRF maps, the mineralogical distribution.

The analytical study performed on two different Martian meteorites is shown below.

### **4.2.1. LAR 12095 meteorite**

The analysis of the LAR 12095 Martian meteorite was performed following the same methodology mentioned before. In this sense, Figure 4.14 shows the 12 elements that were detected in the sample. The elements found with a relative abundance higher than 10% wt. were considered as major elements, which are Fe, Si and Mg. Ca and Al were found as minor elements with a relative abundance between 1 and 10 % wt. Finally, Mn, Cr, Ti, S, P, V and Ni were considered as trace elements (<1% wt.). In the

mentioned figure, the intensity of the color is directly correlated to the amount of the element, thus, the higher the color intensity the higher the relative presence of each element.

As can be seen in Figure 4.14, LAR 12095 possessed areas where Fe, Mg and Si coexisted, which suggested the presence of Fe- and Mg-rich silicates. Therefore, in order to find out which minerals were involved in those grains, Raman analyses were performed on those targeted areas.

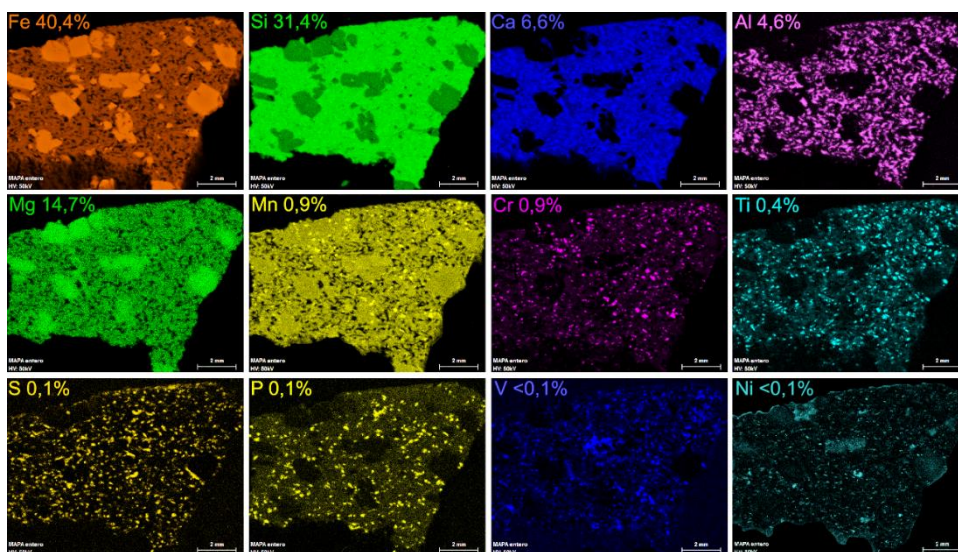


Figure 4.14. Elemental distribution of Fe, Si, Mg, Ca, Al, Mn, Cr, Ti, S, P, V and Ni in the LAR 12095 Martian meteorite obtained by  $\mu$ -EDXRF. The brighter areas of the iron map suggest the presence of olivine phenocrysts, which also match with the areas where magnesium was most abundant.

The spectra obtained were composed by the Raman bands (Figure 4.15 A) that appear at 140 (very weak, vw), 225 (weak, w), 304 (w), 400 (w), 436 (w), 584 (w), 625 (medium, m), 820 (very strong), 849 (vs), 917 (vw) and 959 (vw)  $\text{cm}^{-1}$  [18], which correspond to the bands of olivine. According to the equations (Equations 4.1 and 4.2) of the olivine calibration models developed above and after selecting the main band position of all olivine spectra obtained in this study, the forsterite and fayalite composition in the olivine phenocrysts of the LAR 12095 ranged between  $\text{Fo}_{55.0\pm 1.7}\text{Fa}_{45.0\pm 2.0}$  to  $\text{Fo}_{60.4\pm 1.8}\text{Fa}_{39.6\pm 1.9}$ , in agreement with literature [19]. In this case, no differences between big and small olivine grains were detected, compositionally speaking. Once the point-by-point analyses were done, a Raman map of the central area was acquired. In this way, the spectral range 814-823  $\text{cm}^{-1}$  was selected to obtain the olivine distribution Raman image (Figure 4.15 A, in blue), which corresponds perfectly with the crystals that show the highest content of iron in the elemental distribution (Figure 4.14).

In addition, Figure 4.14 shows that silicon, calcium and aluminum were the main elements that composed the matrix. In this sense, Raman analyses were performed on the matrix and the standard Raman spectrum of pyroxene (Figure 4.15 B) was obtained. This family of aluminosilicates is divided into the orthopyroxene and the clinopyroxene subfamilies. Orthopyroxenes crystallize in the orthorhombic system, whereas clinopyroxene in the monoclinic one. Even though the pyroxene family spectrum is characterized by bands in the 300-400, 650-700 and 980-1020 wavenumber regions, both subfamilies can be differentiated by their own Raman bands. Clinopyroxenes have a single intense peak in the region between 650 and 700  $\text{cm}^{-1}$ , in contrast to the orthopyroxenes which have an intense band with a shoulder in that region <sup>[18]</sup>.

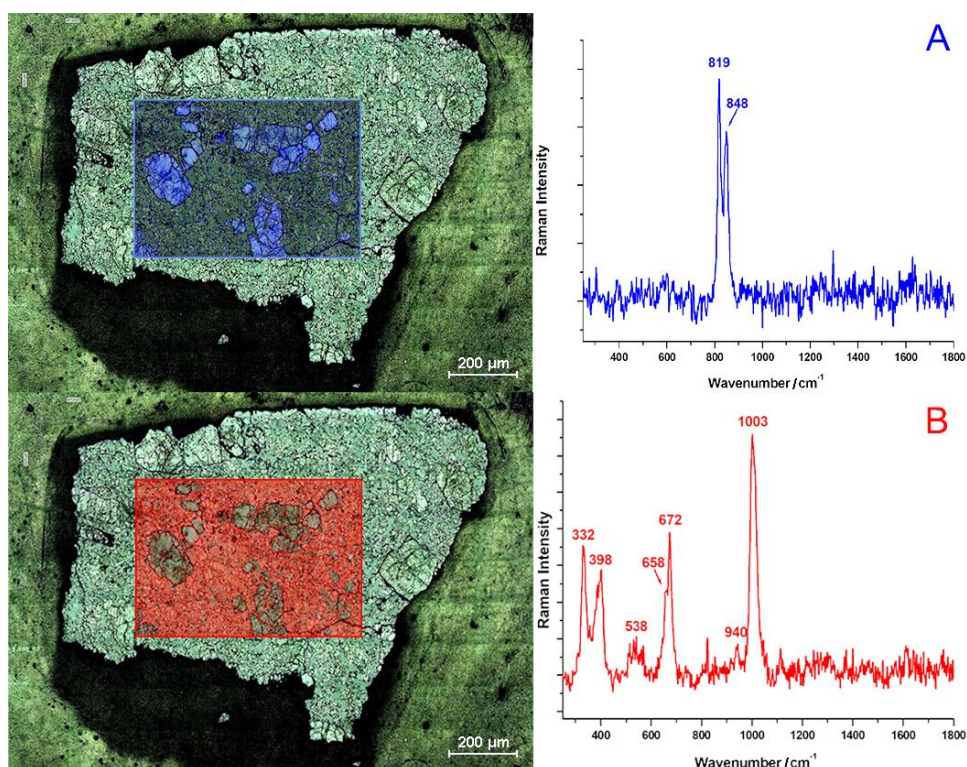


Figure 4.15. (A) Raman image of olivine and its Raman spectrum. The image was obtained using the interval 814-823  $\text{cm}^{-1}$ . (B) Raman image of pyroxene and its Raman spectrum. The image was obtained using the interval 668-680  $\text{cm}^{-1}$ . Both spectra were acquired with the following conditions: 532 nm laser, 1800 l/mm grating, 3 s of exposure time, 2 accumulations, 10% of laser power, 5x objective.

In this case, the pyroxene found possessed a doublet in the 650 and 700  $\text{cm}^{-1}$  region, suggesting the presence of orthopyroxene. In order to verify this hypothesis, the works of Wang et al. <sup>[20]</sup> and Huang et al. <sup>[21]</sup> were used. In this sense, according to the work of Wang et al. <sup>[20]</sup>, the pyroxene spectrum showed in Figure 4.15 B corresponded to a Mg-rich pyroxene with a *Pbca* or *P21/c* crystal structure. This is because the Raman spectrum

---

possessed two doublets, one in the 650-700  $\text{cm}^{-1}$  region and the other in the 300-400  $\text{cm}^{-1}$  region. Likewise, according to the work of Huang et al. [21], this spectrum corresponded to an enstatite-ferrosilite orthopyroxene. Therefore, unequivocally, the pyroxene found consisted of an orthopyroxene.

With the aim of understanding the general distribution of pyroxenes on the sample, a big Raman map in the middle of the sample was carried out. The spectral interval of a characteristic pyroxene band (668-680  $\text{cm}^{-1}$ ) was selected to obtain the pyroxene Raman image (Figure 4.15 B, in red). As can be seen, pyroxene can be considered the main mineral phase of the matrix of the meteorite, in agreement with the initial results published on the Meteoritical Bulletin [22].

Several Al-rich spots identified in the elemental scanning (Figure 4.14) were analyzed by microRaman spectroscopy and the spectra showed broad bands in 450-700  $\text{cm}^{-1}$  region, which correspond to some type of plagioclase [23,24]. These broad bands suggested the low crystallinity of the compound, which may be caused due to an amorphization of the original mineral phase. This amorphization could be produced due to the high impact that ejected the rock from the surface of Mars. As reported in literature [25], that impact caused a shock wave that converted the plagioclase feldspar into maskelynite or into a shocked plagioclase. Therefore, the plagioclase found in this meteorite is maskelynite (Figure 4.16 A) [23].

Besides, by means of both modes, single point analysis and Raman mappings, the oxides hematite [26], anatase [27], ilmenite [28] and chromite [28] were also detected.

The Raman bands position of hematite appear at 223 (w), 292 (m), 403 (m), 605 (w) and 1303 (w, broad, b)  $\text{cm}^{-1}$  (Figure 4.16 D) [26]. This iron oxide was unequivocally identified on Mars, for the first time, in 1996 by the TES on board the Mars Global Surveyor spacecraft [29]. In fact, fine-grained hematite gives Mars its characteristic red color, the reason why this planet is called the "Red Planet". Several studies have confirmed that the presence of hematite on Mars is due to weathering processes [29,30]. On Mars there are many iron-rich minerals that weather, in part, to hematite. Likewise, hematite can also form as product of the oxidation of primary minerals on Earth. Therefore, in order to find out if the hematite found is a Martian secondary or terrestrial secondary mineral phase, its formation process must be estimated [29,30]. However, in this case, hematite is considered a Martian secondary mineral phase.

Regarding, the titanium oxide anatase [27] is a metastable mineral phase (the low temperature polymorph) of titanium dioxide, which is very well

characterized and distinctive from other polymorphs by Raman spectroscopy since its peaks appear at 142 (vs), 194 (w), 396 (w), 517 (w) and 639 (m)  $\text{cm}^{-1}$  (Figure 4.16 B) [27]. It is well known that anatase is usually a secondary mineral derived from other titanium-bearing minerals. In addition, it can be derived from the weathering of rocks by hydrothermal processes or from crystal fractionation of igneous samples [31]. Considering that it is a low-temperature polymorph, its most probable origin is terrestrial (terrestrial secondary mineral).

In addition to hematite and anatase, other oxides were identified. The Fe-Ti-Cr-oxides have similar Raman spectra patterns, which include a main band in the 600-800  $\text{cm}^{-1}$  range, and few minor peaks at lower wavenumbers [28]. Knowing all major and minor Raman peaks it would be possible to distinguish between the different Fe-Ti-Cr-oxides, but when the S/N signal is low and the secondary bands are lacking, it is quite difficult to do so. In this sample, many spectra with a strong band in the range of the Fe-Ti-Cr oxides were found and the secondary Raman bands appeared in different positions allowing us to distinguish among different Fe-Ti-Cr oxides. In this sense, the first Fe-Ti-Cr oxide found features the most intense band at 686  $\text{cm}^{-1}$ , whereas the secondary bands appear at 228 (m), 335 (m) and 376 (w)  $\text{cm}^{-1}$ , which correspond to the characteristic spectrum of ilmenite (Figure 4.16 C) [28]. The rover Spirit of the Mars Exploration Rover Mission detected ilmenite in the Gusev Crater of Mars by the alpha particle-X-ray spectrometer and the Mössbauer spectrometer [32]. In fact, ilmenite was detected in the same sample as pyroxene, olivine, hematite, nanophases of iron oxides and magnetite by Squyres et al. [32]. All this proves that ilmenite is a primary mineral from Mars.

The other Fe-Ti-Cr found oxide presented a broad Raman band at 684  $\text{cm}^{-1}$  and a secondary broad peak at 560  $\text{cm}^{-1}$ . According to Wang et al. [28], the spectrum matches perfectly with the chromite spectrum (Figure 4.16 D). For this compound, the Raman position of the main band reveals the molar ratio  $(\text{Cr}+\text{Fe})/(\text{Cr}+\text{Fe}+\text{Al})$  [28]. In the Raman spectra obtained from the analysis of LAR12095, Raman peak suggested molar ratios between 0.8-1.0. This range indicates that the chromite found may contain traces of aluminum. This fact is consistent with results obtained by  $\mu$ -EDXRF images that showed aluminum regions which coexisted with chromium. In addition, magnesiochromite was also detected thanks to its Raman bands: 560 (m), 598 (m), 645 (strong, s), 689 (vs) and 1363 (w, b)  $\text{cm}^{-1}$  [18]. Martian orbiters, rovers and landers have not yet found chromite on the red planet, maybe because it is a minor compound at surface level. However, there are many Martian meteorites [28,33] with chromite present. This element could come from the mantle-derived magmas of Mars, which may have reached the crust due to the ancient high volcanic activity.

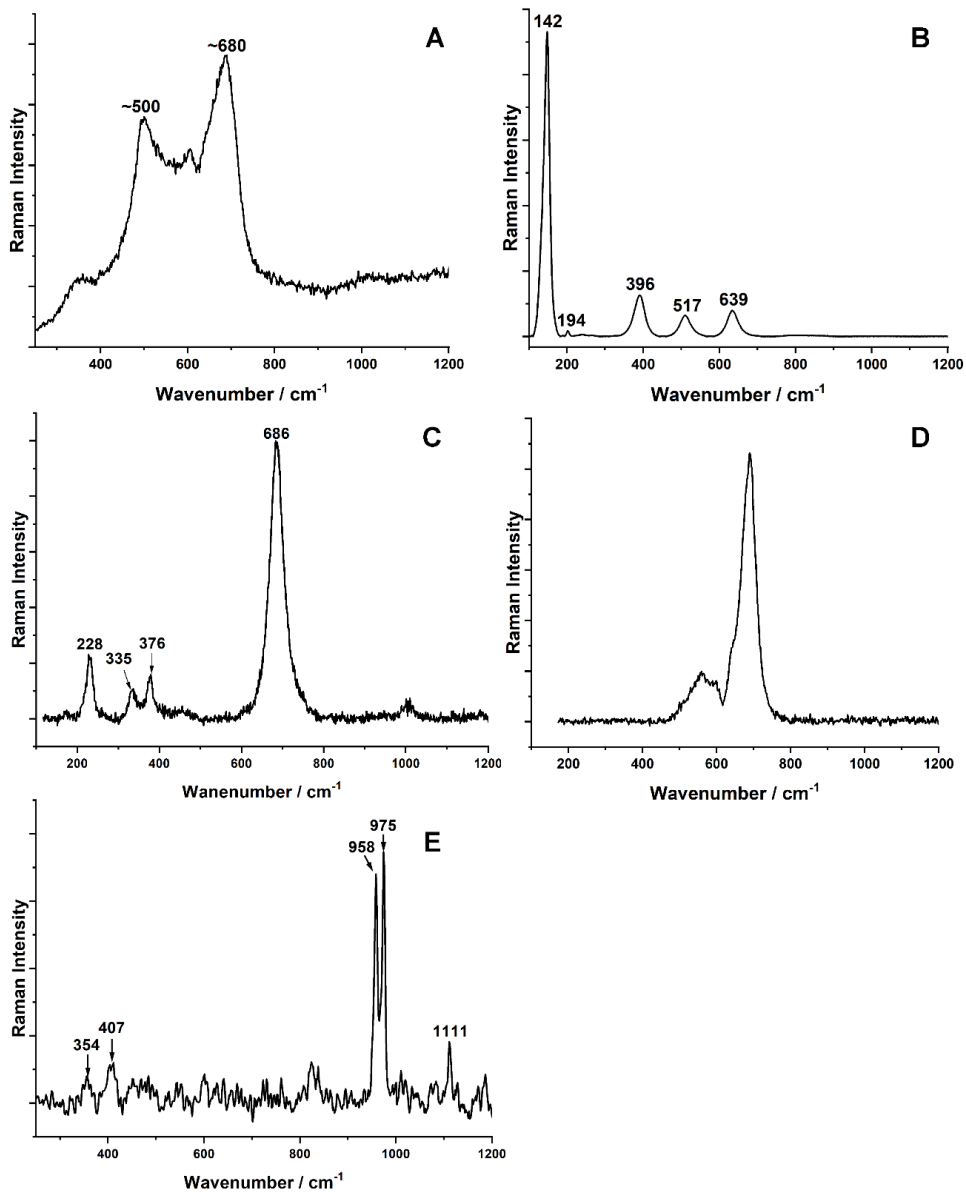


Figure 4.16. Raman spectra of (A) maskelynite, (B) anatase, (C) ilmenite (D) chromite ( $684\text{ cm}^{-1}$ ) and (E) merrillite. Measurement conditions:  $532\text{ nm}$  excitation laser,  $1800\text{ l/mm}$  grating,  $10\text{ s}$  of exposure time, 6 accumulations, 10% of laser power,  $50\times$  objective.

In addition to the major mineral phases and the oxides found, phosphates, sulfides, elemental sulfur and sulfates were also detected as minor mineral phases.

As can be seen in Figure 4.18 A, where some elemental chemical images were overlapping, calcium, magnesium and phosphorus were positively correlated in some areas of the sample. In these points, the calcium phosphate merrillite was detected by single Raman point mode. Its Raman spectrum is characterized by the Raman bands that appear at  $354\text{ (w)}$ ,  $407$

(m), 958 (vs), 975 (vs) and 1111 (m)  $\text{cm}^{-1}$  (Figure 4.16 E) <sup>[34]</sup>. Merrillite is of particular interest to Martian studies because it is the dominant primary phosphate mineral in Martian meteorites, and thus presumably on Mars. It is well known that the single-phase natural merrillite does not occur on Earth as a discrete mineral phase outside of biological systems. In fact, it is only found in extraterrestrial materials and, therefore, studies requiring merrillite must obtain it directly from meteorites or by synthesis. Although merrillite is chemically and structurally similar to the terrestrially occurring mineral whitlockite, the term “merrillite” is used to describe the anhydrous extraterrestrial (and synthetic) Ca-phosphate minerals, while the terms “whitlockite” refers to the hydrated terrestrial mineral form. It is possible that some or all of the merrillite seen in Martian meteorites could come from whitlockite alteration by shock-compression processes. However, whitlockite has never been confirmed in Martian materials, so considering merrillite as a secondary mineral from whitlockite pressure alteration is not yet proven <sup>[35,36]</sup>. Taking into account that merrillite is not an igneous phase, it is considered as a Martian secondary mineral phase.

In addition to the minerals seen so far and considering the positive correlation between sulfur and iron in some regions detected by elemental imaging (see Figure 4.18 B), sulfur-rich compounds were expected to be found. Almost fifty years ago, Viking missions revealed the presence of S- and Cl-rich surface regolith on Mars and since then, sulfur has been confirmed by *in situ* measurements made by landers and rovers, by remote sensing observations made by orbiters, and by analyses of Martian meteorites in terrestrial laboratories <sup>[37]</sup>. It is estimated that most primary igneous sulfur is concentrated in sulfides, including pyrrhotite, rare chalcopyrite, cubanite, troilite, pentlandite and pyrite <sup>[38]</sup>. In addition to primary minerals, sulfur is also found in a variety of secondary mineral phases in Martian meteorites, such as secondary sulfides, sulfates, elemental sulfur, and in impact glasses, among others <sup>[38]</sup>.

After understanding this, it is necessary to emphasize that the sulfur cycle dominates many geochemical processes on Mars. During the formation of Mars, sulfur was distributed in the core to form a liquid Fe-(Ni)S core. Subsequently, the transfer of S to the crust occurred through volcano degassing, magmatism, and hydrothermal processes, which resulted in a considerable amount of S at the surface. Photochemical activity and the presence of oxidizing agents led to rapid formation of S-bearing minerals, such as sulfides <sup>[39]</sup>. If oxidation continued on Mars without the presence of atmospheric oxygen (anaerobic conditions), the primary sulfides may have oxidized to Martian secondary sulfides <sup>[40]</sup>, elemental sulfur and sulfates. In contrast, if the oxidation of sulfur compounds occurs on Earth, under oxygen presence (aerobic conditions), the results are completely

---

different, leading to the formation of iron oxides, such as hematite, goethite, lepidocrocite, among others (terrestrial secondary minerals) [40,41].

Surprisingly, both types of oxidation, aerobic and anaerobic, were observed in the LAR 12095 meteorite. It is well known that mackinawite (metastable) [41] Raman bands appear at 208 (s), 274 (vs) and 385 (s)  $\text{cm}^{-1}$  [41]. However, the ones detected experimentally appear at 214 (vs), 273 (vs) and 382 (b, m)  $\text{cm}^{-1}$  (Figure 4.17 A). In this way, Mendili et al. [40] were able to observe that mackinawite is a metastable iron sulfur and is highly susceptible to transform. In fact, it has been proven that the main mackinawite Raman bands shift towards higher wavenumbers, until the alteration causes a change in the crystal structure from tetragonal to monoclinic (stable) [40]. Therefore, as the detected experimental bands have the same structure as mackinawite but with a small displacement towards higher wavenumbers, it can be concluded that the compound found is an oxidized mackinawite (see Figure 4.17 A).

Figure 4.17 B shows as well the oxidized mackinawite together with the 385 and 582  $\text{cm}^{-1}$  Raman bands [40,41], which means that the metastable iron sulfide formed in anoxic conditions on Mars has started to oxidize in the presence of oxygen, forming the appearance of the first iron oxide bands.

Figure 4.17 C shows the oxidized mackinawite weathering under anaerobic conditions, where part of the mackinawite has been transformed to pyrrhotite [40]. Although the exact Raman peaks for pyrrhotite can vary as function of stoichiometry, as well as with the degree of ordering, and reflect variations in the FeS bond lengths, their standard spectrum is characterized by strong peaks located bellow 400  $\text{cm}^{-1}$  [42]. The ones obtained in the laboratory appear at 329, 363 and 396  $\text{cm}^{-1}$  [43]. Therefore, Figure 4.17 C represents the Raman spectrum of the oxidized mackinawite, pyrrhotite and broad iron oxide bands detected.

Finally, Figure 4.17 D shows the hematite spectrum, which is the product of the complete alteration of iron sulfides in the presence of oxygen.

As mentioned above, anaerobic oxidation of primary sulfides with high sulfur input can produce secondary oxides or  $\text{FeS}_2$  (pyrite or marcasite,  $\text{FeS}_2$ , stable and metastable, respectively [39]), elemental sulfur and  $\text{Fe}^{2+}$  sulfates [44]. Figure 4.17 E shows the Raman bands of marcasite and elemental sulfur, which are 319 (vs) and 381 (s); and 149 (m), 219 (m), 244 (w) and 471 (m)  $\text{cm}^{-1}$ , respectively [18,39].

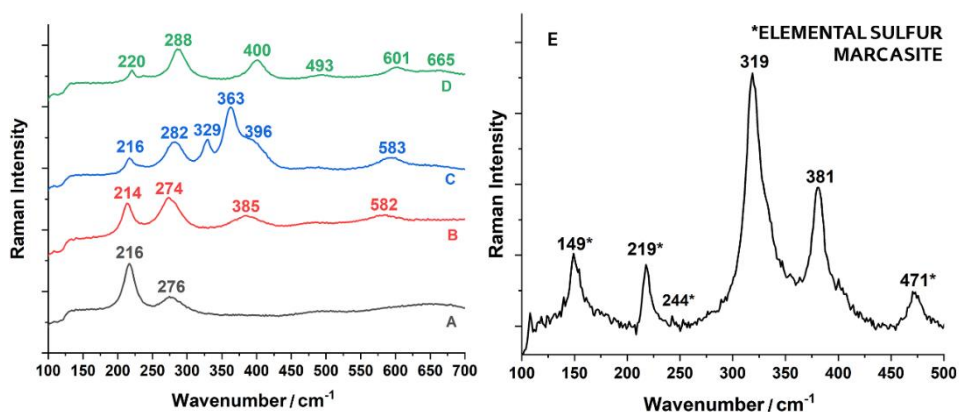


Figure 4.17. Raman spectra of (A) oxidized mackinawite, (B) oxidized mackinawite and broad iron oxide bands, (C) oxidized mackinawite, pyrrhotite and broad iron oxide bands, (D) hematite and (E) elemental sulfur and marcasite. Measurement conditions: 532 nm excitation laser, 1800 l/mm grating, 10 s of exposure time, 10 accumulations, 10% of laser power, 50x objective.

Moreover, in this meteorite it was observed that the oxidation in an anaerobic environment persisted. Sulfides and elemental sulfur continued to oxidize to anhydrous sulfates, which can hydrate through hydrothermal activity, leading to the formation of hydrated sulfates. In this sense, the iron sulfate jarosite<sup>[45]</sup> was detected thanks to its Raman bands that appear at 139 (m), 224 (s), 300 (m), 355 (w), 434 (vs), 454 (m), 573 (m), 625 (m), 1007 (vs), 1051 (w), 1103 (vs) and 1153 (w)  $\text{cm}^{-1}$ <sup>[46]</sup> (Figure 4.19 A). On Earth, jarosite is formed as the result of low-temperature acidic-oxidative weathering of iron-bearing minerals in water presence<sup>[44,45]</sup>. In addition, this compound was reported in 2004 by the Opportunity rover at fine-grained sediments of Meridiani Planum<sup>[45]</sup>. Therefore, the jarosite of this meteorite can be considered as a Martian secondary mineral, as well as a terrestrial weathering mineral phase. Isotopic analysis should be done for determining exactly its origin.

As can be seen in Figure 4.18 C and 4.18 D, the distribution of sulfur along the meteorite often matched with the distribution of calcium and magnesium. In this way, two additional sulfates were detected by Raman spectroscopy: gypsum and epsomite. Both hydrated sulfates have been detected on Mars by the Opportunity rover, the OMEGA on the Mars Express orbiter, the Phoenix lander, the CRISM on the Mars Reconnaissance orbiter, among others<sup>[47]</sup>.

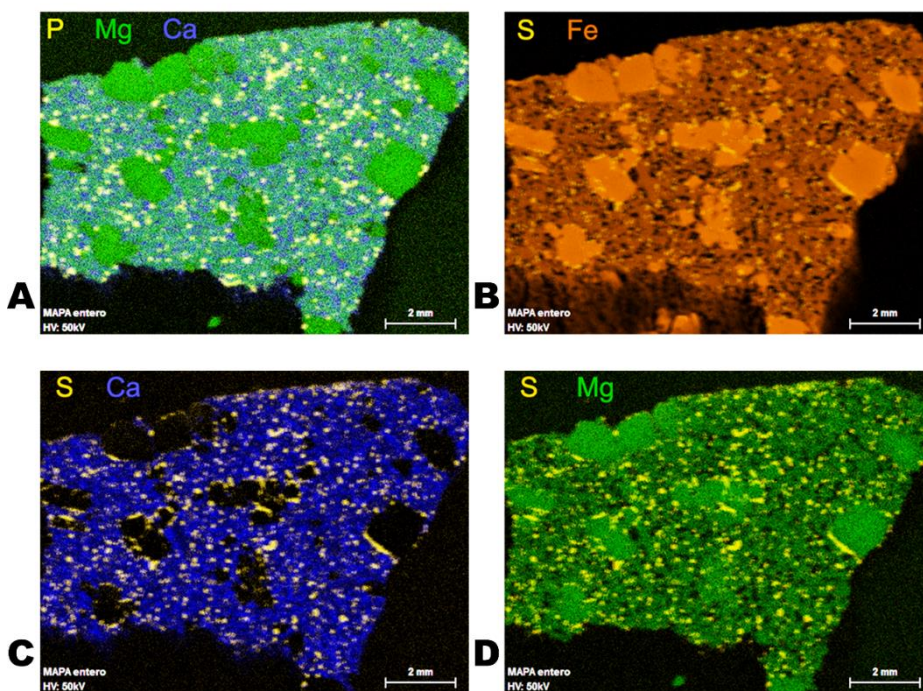


Figure 4.18. Overlapping elemental images of (A) calcium, magnesium and phosphorus; (B) iron and sulfur; (C) calcium and sulfur; and (D) magnesium and sulfur. In Figure 4.18 A, the white areas correspond to the presence of the three elements, which may be merrillite. In Figure 4.18 B, the ochre areas correspond to the presence of iron and sulfur, where the sulfides and jarosite may be present. In Figure 4.18 C, the yellowish-white areas correspond to the match of calcium and sulfur, where gypsum may appear. In Figure 4.18 D, the greenish-yellowish areas correspond to the mixture of magnesium and sulfur, which may be epsomite.

Gypsum was identified thanks to its Raman bands: 133 (w), 183 (w), 224 (w), 328 (w), 416 (w), 435 (w), 495 (m), 620 (w), 674 (w), 1009 (vs), 1103 (w), 1138 (w) and 1454 (w)  $\text{cm}^{-1}$  (Figure 4.19 B). Epsomite was detected through its main Raman band that appears at 984 (vs)  $\text{cm}^{-1}$  (Figure 4.19 C). These minerals are coming from a sulfate-alteration/evaporation process and can be formed in a wide variety of depositional environments. According to literature <sup>[48,49]</sup>, the presence of hydrated sulfates on Mars appears due to the interaction of sulfur-bearing water with Ca/Mg-bearing minerals, precipitating gypsum and epsomite when water is evaporated.

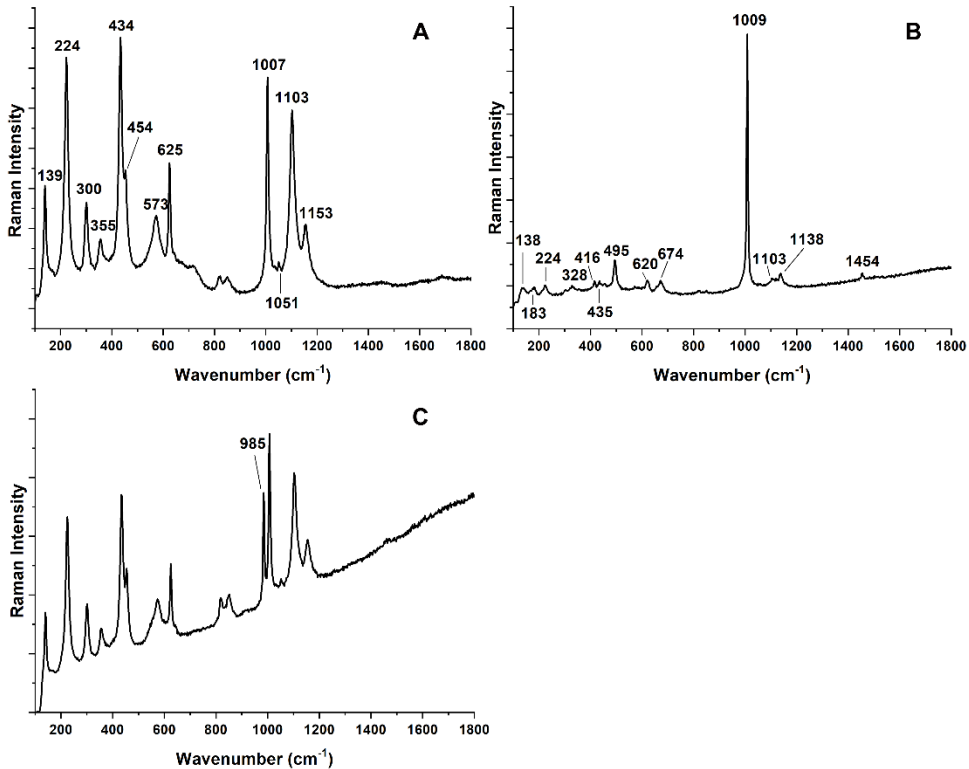


Figure 4.19. Raman spectra of (A) jarosite, (B) gypsum and (C) epsomite. Measurement conditions: 532 nm excitation laser, 1800 l/mm grating, 10 s of exposure time, 3 accumulations, 10% of laser power, 50x objective.

In this case, the gypsum and epsomite of this meteorite may be due to the alteration Ca-bearing minerals on Mars or on the Earth by the action of S bearing water. As both mineral phases appear occasionally in some areas embedded in the matrix of the meteorite and do not have a distribution along the cracks, it seems that both sulfates are likely to have a Martian origin and that are not generated due to an afterwards terrestrial weathering. It should be noted that the analyzed sample belongs to the inner part of the meteorite cut after its collection and there is no other way to reach the inner part of the meteorite once on Earth except through the cracks. After ejection, both hydrated sulfates probably dehydrated, but after the meteorite landing on the Antarctica ices, both could be rehydrated again.

Thus, in the LAR 12095 Martian meteorite it has been possible to verify once again the different stages in which sulfur can be found, from the most reduced form to the most oxidized, which proves the presence of the Martian sulfur cycle.

The cycle would begin with the sulfur contribution to the Martian surface. In this sense, the gaseous  $S^{2-}$  compounds ( $SO_2$  and  $H_2S$ ) and immiscible

sulfide fluids, which came from volcanic and hydrothermal events, were oxidized to  $S^0$ , then to  $S^{4+}$  and, finally to  $S^{6+}$ . However, Mars lost its ancient atmosphere due to the escape of oxygen atoms to space and the absorption and recombination by the surface [50]. Even though nowadays there is not enough oxygen, the presence of perchlorates and ultraviolet rays means that an oxidizing environment still exists, allowing the continuity of the sulfur cycle. In this way, sulfur can participate in the Martian sulfur cycle as  $[SO_4^{2-}]$ ,  $[HSO_4^-]$  and  $SO_3$  in aqueous solutions,  $SO_2$  and  $H_2S$  as gases, as well as elemental sulfur, sulfides and sulfates in solid compounds [51].

Figure 4.20 represents the sulfur cycle proposed in this work. This cycle starts with the emission of sulfur gases due to volcanic emissions and coming from inside the planet. These gases are oxidized to elemental sulfur and sulfide compounds due to ultraviolet radiation that acts as oxidizing agent. These processes are called photo-oxidation and photo-dissociation. If the radiation is sufficient, the compounds continue oxidizing to give rise to sulfates. Once they are on the surface, the compounds can be hydrated due to hydrothermal activity and form the corresponding hydrated sulfates. Apart from the oxidative capacity of radiation, other compounds such as perchlorates can act as oxidizing agents. Until now, there is no knowledge about reducing agents on Mars, so in this work only the oxidation processes are presented.

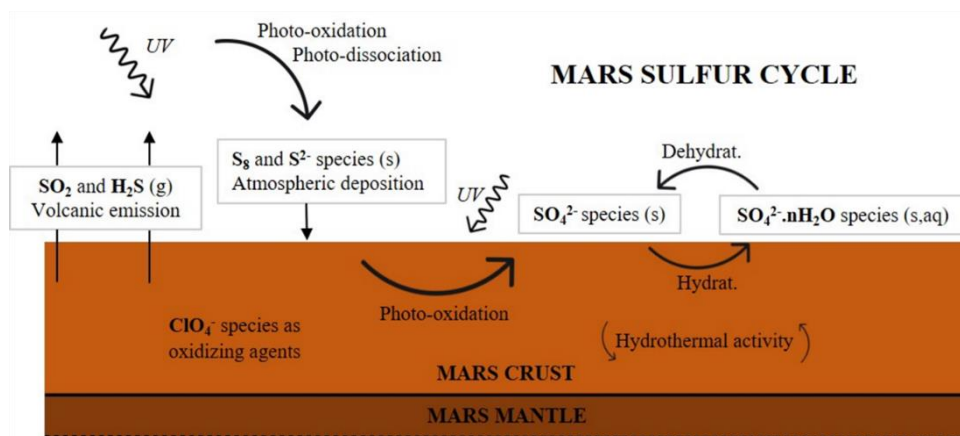


Figure 4.20. Current Mars sulfur cycle, from  $SO_2$  and  $H_2S$  volcanic emissions to hydrated sulfates.

The presence of sulfides in this meteorite ensures that the sulfur cycle is still active. However, oxidation to sulfates can occur on both Earth and Mars. In this regard, primary Martian sulfides can follow three different pathways (Figure 4.21). The first one consist on forming secondary sulfides due to pressure changes. The second one is the anaerobic route, which occurs on Mars, due to oxidizing agents secondary sulfides, elemental sulfur and elemental iron are produced. The third possibility is that primary

or secondary sulfides may be oxidized under aerobic conditions, which occurs on Earth, generating iron oxides, such as hematite, and sulfur oxides (SO<sub>x</sub>).

Finally, the elemental sulfur and the secondary sulfides can be altered until anhydrous or hydrated sulfates. This process may occur due to hydrothermal conditions on Mars or due to terrestrial weathering.

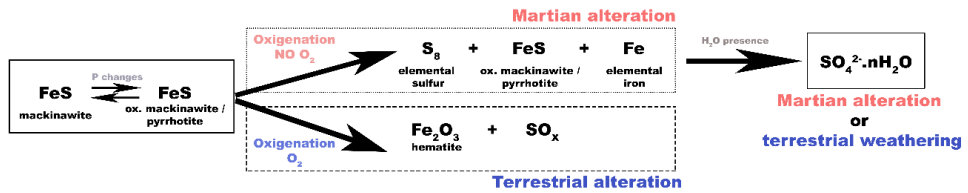


Figure 4.21. Possible alterations of primary Martian sulfides on Mars as a function of the minerals found in the LAR 12095 Martian meteorite by micro-Raman spectroscopy and micro-EDXRF.

### 4.2.2. RBT 04262 meteorite

Thanks to the elemental characterization of this specimen, major (>10% wt.) and minor (<10% wt.) mineral phases could be detected. In this sense, Si, Mg, Fe, Ca and Al were identified as major elements, whereas Mn, Cr, K, Na, Ni, P, S and Ti were detected as minor elements. Figure 4.22 shows the elemental distribution of the major elements through one of the surfaces (Side A).

In this way, Si was distributed in almost all the surface and its higher intensity areas coexisted with Ca and Al. The areas, in which the relative abundance of Si, Ca and Al was high, lead to consider that they could correspond with the distribution of some type of aluminosilicate. Likewise, the areas where the relative presence of Si was low and there was a lack of Ca and Al, the presence of Mg and Fe was higher. This could indicate the presence of Fe- and Mg-rich silicate grains embedded in an aluminosilicate matrix.

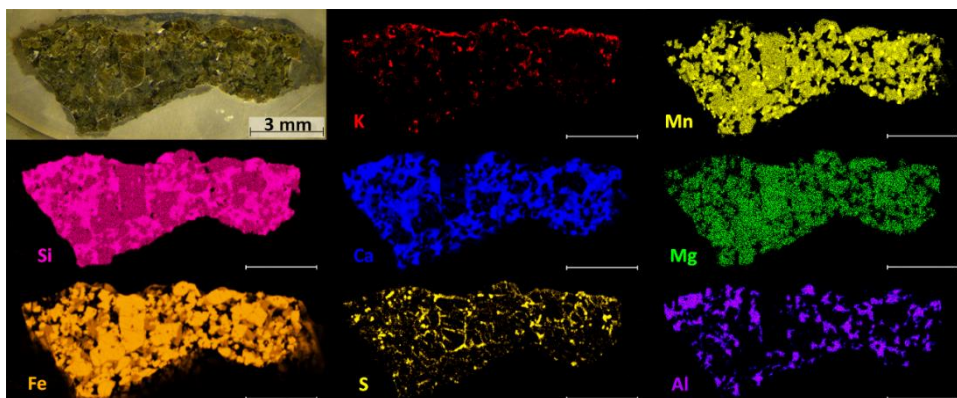


Figure 4.22. The optical image of the mapped area and the elemental distribution for K, Mn, Si, Ca, Mg, Fe, S and Al for one of the surfaces (Side A). The brighter areas of the iron map suggest the presence of olivine phenocrysts.

In order to confirm these hypotheses, Raman analyses were performed as stated before. In this way, it is important to highlight that the accurate composition of the silicate matrix identified by Raman spectroscopy consisted on the feldspar plagioclase. However, as in the previous meteorite analysis, the detected Raman bands were very broad, corresponding to maskelynite or shocked plagioclase. The Raman bands of the compounds concerned appear at a) 479 and 511, and b) 516 and 569  $\text{cm}^{-1}$ , which according to the work of Fritz et al. [52] correspond to weakly shocked plagioclase and shocked plagioclase, respectively. This fact, the coexistence of weakly and heavily shocked plagioclase, could be explained by the heterogeneous exposure of the sample to the pressure. The shock wave, thus, affected the feldspar grains differently, leaving in this case diaplectic crystals and diaplectic glasses. According to the work of Fritz et al. [52], the weakly shocked plagioclase was formed due to a wave of

between 5 and 27 GPa, whereas the range of the shocked plagioclase went from 27 to 30 GPa.

In addition to plagioclase, pyroxenes were also detected as main matrix mineral phases. In this case, as Figure 4.23 shows, in the RBT 04262 Martian meteorite two different types of pyroxene were identified. The first Raman spectrum (Figure 4.23 A) was composed by the following Raman bands: 224 (m), 330 (m), 400 (vw), 433 (w), 570 (vw), 625 (w), 654 (m), 674 (s), 940 (vw), 1003 (vs) and 1010 (w)  $\text{cm}^{-1}$ . The second one (Figure 4.23 B) was composed by the following Raman bands: 329 (w), 394 (w), 434 (vw), 669 (m) and 1005 (s)  $\text{cm}^{-1}$ .

According to the work of Wang et al. [20] and Huang et al. [21], the first Raman spectrum possessed at least a doublet in the 600-800  $\text{cm}^{-1}$  region (625, 654 and 674  $\text{cm}^{-1}$ ), a triplet in the 300-450  $\text{cm}^{-1}$  region (330, 400 and 433  $\text{cm}^{-1}$ ) and a band in the 230-300  $\text{cm}^{-1}$  region (860  $\text{cm}^{-1}$ ). This ensure the presence of a high magnesium orthorhombic *Pbca* pyroxene, which is an orthopyroxene.

Likewise, as the second spectrum only had one peak between 600 and 800  $\text{cm}^{-1}$  (669  $\text{cm}^{-1}$ , at a wavenumber within the range), the compound may be a clinopyroxene or an iron-pyroxenoid. However, as the spectrum had three peaks in the 300-450  $\text{cm}^{-1}$  region (329, 394 and 434  $\text{cm}^{-1}$ ), and no peaks below 300  $\text{cm}^{-1}$ , the compound corresponds to a *C21/c* monoclinic clinopyroxene.

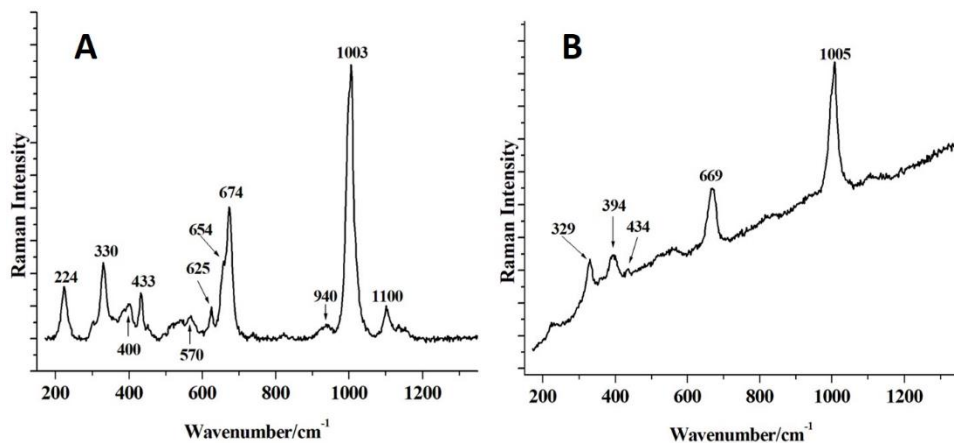


Figure 4.23. (A) Raman spectrum of an orthopyroxene. Measurement conditions: 532 nm laser, objective x50, 20 s exposure time, 5 accumulations, and 10% laser power. (B) Raman spectrum of a clinopyroxene. Measurement conditions: 532 nm laser, objective x50, 10 s exposure time, 5 accumulations, and 10% laser power.

In order to identify possible zoning of pyroxene, further Raman analyses were performed. However, the studied low and high-Ca pyroxenes did not exhibit any core-to-rim distribution.

---

As could be seen from the elemental characterization, there were Si-, Fe, and Mg-rich phenocrysts embedded in the matrix. As in the previous case, thanks to Raman analyses, it was possible to identify that these phenocrysts consisted of olivine. From the calibration models developed in Chapter 4.1, it was possible to calculate the Fo/Fa content of the olivine grains present in this meteorite. After analyzing all the olivine Raman spectra obtained, these calculations revealed that small olivine grains (less than 200  $\mu\text{m}$ ) possessed more variable Fo content than big ones, since their chemical composition went from  $\text{Fo}_{57.5\pm 2.1}\text{Fa}_{42.5\pm 2.1}$  to  $\text{Fo}_{61.3\pm 2.2}\text{Fa}_{38.7\pm 1.9}$ . The most probable explanation for this difference is that the small ones presented core-to-rim zoning.

In contrast, higher grains did not present any core-to-rim zoning and their chemical composition was highly homogeneous:  $\text{Fo}_{57.2\pm 2.2}\text{Fa}_{42.8\pm 2.1}$ . These results are in agreement with other mineralogical studies performed on the meteorite [53].

Figure 4.24 A shows an olivine grain figure, which possessed a discontinuous appearance because its surface was crossed by dark cracks and fractures, and a dark coating surrounded the main grain. Figure 4.24 B shows the Raman image for olivine represented in yellow. This area was represented by selecting the spectral range between 813-826  $\text{cm}^{-1}$  that contained one of the main olivine Raman bands. Figure 4.24 C shows the Raman pyroxene image (in purple represented by the Raman signal at the interval 657-687  $\text{cm}^{-1}$ ), which covered the right surface in which the olivine was not present, being the main compound of the meteorite matrix. It must be highlighted that the pyroxene inclusion inside the olivine grain could be a consequence of the impact that the meteorite suffered at the time of its formation. Most likely, due to the impact process, part of the olivine grain weakened, losing part of its material and revealing the pyroxenitic matrix that was underneath the large olivine grain.

Figure 4.24 D and E correspond to the mineral phases that comprise the coating, cracks and fractures. Concretely, Figure 4.24 D is consistent with epsomite (depicted in red, representing the Raman signal at the spectral range between 982-988  $\text{cm}^{-1}$ ), which was distributed mainly along the coating and, in less proportion, in the outermost cracks. Finally, Figure 4.24 E corresponds to the distribution of gypsum (in green, representing the interval between 1006-1012  $\text{cm}^{-1}$ ). This Ca-sulfate was extended mainly through the innermost cracks and, to a lesser extent, into the coating.

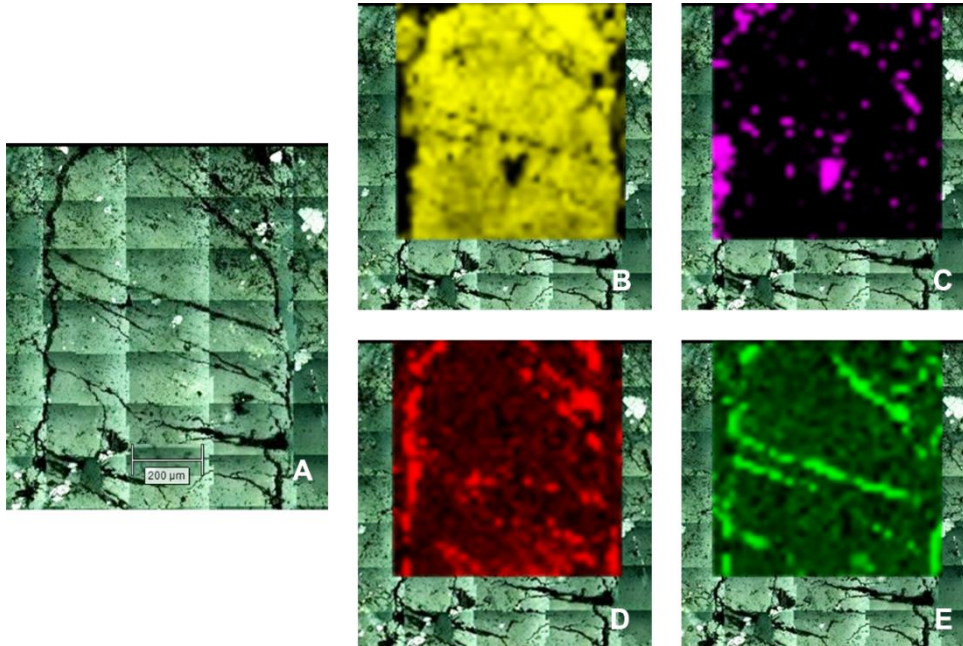


Figure 4.24. (A) Olivine coarse-grain (B) Raman image of olivine, (C) Raman image of pyroxene, (D) Raman image of epsomite, and (E) Raman image of gypsum. Map measurement conditions: 532 nm laser, objective x20, 10 s exposure time, 10 % laser power, slit opening 65  $\mu\text{m}$ , center 1769  $\mu\text{m}$ , step 30x30, and snake direction.

Figure 4.25 A and B show the Raman spectra of epsomite and gypsum, respectively, found in the sample. The Raman bands of the epsomite appear at 252 (vw), 366 (vw), 446 (w), 495 (w), 612 (w), 984 (vs), 1060 (w)  $\text{cm}^{-1}$ , whereas the Raman bands of the gypsum are 183 (vw), 415 (w), 492 (w), 620 (w), 671 (m), 1009 (vs) and 1136 (m)  $\text{cm}^{-1}$  [54].

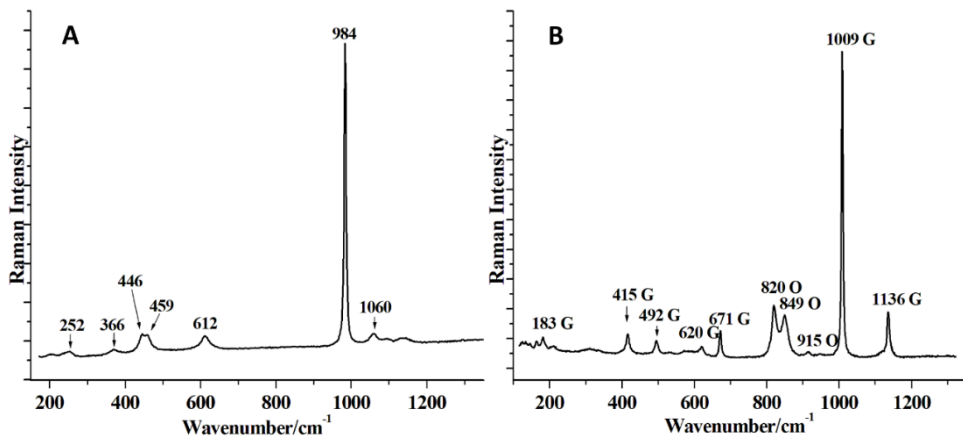


Figure 4.25. (A) Raman spectrum of epsomite. Measurement conditions: 532 nm laser, objective x50, 10 s exposure time, 10 accumulations, and 10% laser power. (B) Raman spectrum of gypsum (G), together with olivine (O). Measurement conditions: 532 nm laser, objective x50, 10 s exposure time, 10 accumulations, and 10% laser power.

Hydrated sulfates are distributed along the cracks and fractures, so it is possible that their presence could be the consequence of the infiltration of salty water that entered through the cracks and fractures, then was evaporated, precipitating the detected sulfates both on Mars (as hydrated sulfates have been found on the surface of Mars [55]) or on Earth. Once again, isotopic analyses could ascertain the origin of these compounds.

Apart from these S-bearing compounds, an iron sulfide and elemental sulfur were also identified. Figure 4.26 A shows the Raman spectrum of elemental sulfur found, together with olivine and orthopyroxene Raman bands. The main Raman bands of elemental sulfur, which appear at 154 (s), 221 (vs), 437 (w) and 474 (s)  $\text{cm}^{-1}$ , are in agreement with literature [56]. In the case of the sulfide, it could be detected thanks to its Raman bands that appear at 216 (vs), 287 (vs) and 390 (m b)  $\text{cm}^{-1}$  [57] (Figure 4.26 B). These bands did not correspond exactly to the most common iron sulfides already found on Mars, [58,59]. As in the study of the previous meteorite, this Raman spectrum represents an oxidized mackinawite together with the 385 and 582  $\text{cm}^{-1}$  Raman bands [40,41], which means that the metastable iron sulfide formed in anoxic conditions on Mars started to oxidize in the presence of oxygen, forming the appearance of the first iron oxide bands. According to the diagram shown in Figure 4.21, the fact that the corresponding iron oxide began to form ensures that the alteration occurred in the presence of oxygen, so it is terrestrial alteration.

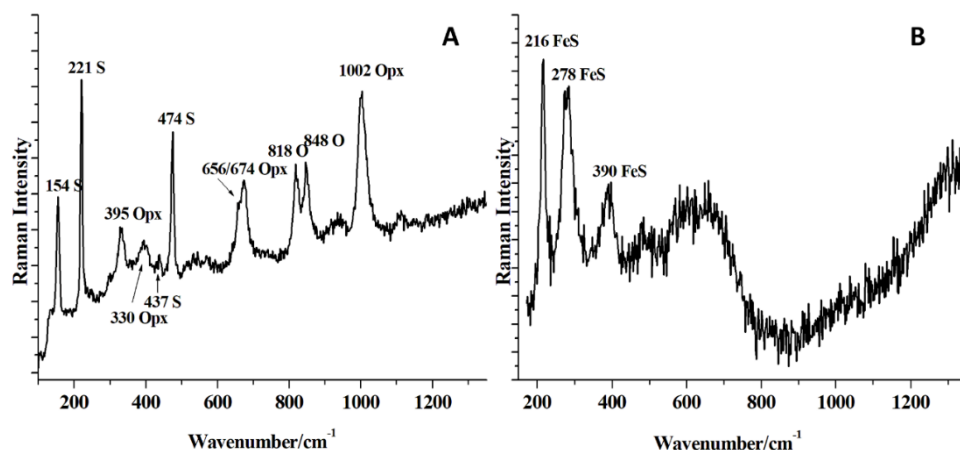


Figure 4.26. (A) Raman spectrum of elemental sulfur (S), together with olivine (O) and orthopyroxene (Opx). Measurement conditions: 532 nm laser, objective x20, 10 s exposure time, 5 accumulations, and 10% laser power. (B) Raman spectrum of FeS. Measurement conditions: 532 nm laser, objective x50, 10 s exposure time, 2 accumulations, and 10% laser power.

In addition to the major crystalline silicates and the S-bearing compounds, accessory minerals such as Ca-phosphate and a possible Fe/Ti oxide were also identified. Both types of compounds were found in Raman single point mode on small crystals of the meteorite. Figure 4.27 A shows the detected

Ca phosphate, identified as merrillite <sup>[34]</sup> through its main Raman bands at 356 (w), 410 (m), 448 (vw), 547 (vw), 595 (vw), 622 (w), 958 (vs), 974 (vs), 1046 (w) and 1082 (w)  $\text{cm}^{-1}$  <sup>[34]</sup>. As in the previous meteorite study, the merrillite presence may be due to the alteration of original whitlockite, but it is not yet proven.

Finally, Figure 4.27 B shows the Raman spectrum of the olivine as well as a broad band at 672  $\text{cm}^{-1}$  and some other minor bands at 302 (w), 410 (w) and 526 (w)  $\text{cm}^{-1}$ . Although the position of these bands did not match perfectly with any particular compound, they may look similar to those of magnetite, which appear at 193 (vw), 306 (w), 538 (m) and 668 (vs)  $\text{cm}^{-1}$  <sup>[60]</sup>. It is well known that shifts in the Raman 665  $\text{cm}^{-1}$  broad band of magnetite can be caused due to the substitution of iron by titanium. This process lead to the formation of mixture of cations called titanomagnetites. Based on the position of the detected bands and according to Zinin et al. <sup>[61]</sup>, the observed spectrum could be the consequence of a high content of impurities of other oxides such as  $\text{TiO}_2$  or  $\text{Al}_2\text{O}_3$ , among others.

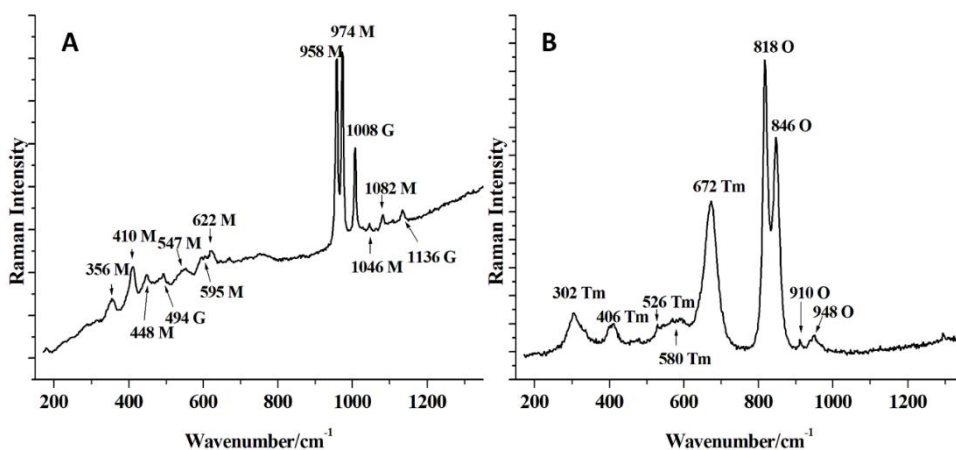


Figure 4.27. (A) Raman spectrum of merrillite (M) together with gypsum (G). Measurement conditions: 532 nm laser, objective x50, 10 s exposure time, 10 accumulations, and 10% laser power. (B) Raman spectrum of a titanomagnetite (Tm), together with olivine (O). Measurement conditions: 532 nm laser, objective x50, 10 s exposure time, 10 accumulations, and 10% laser power.

---

### 4.2.3. Discussion

The initial methodology proposed for meteorite characterization allowed to identify all the mineral phases that compose the sample and to analyze their distribution.

Both meteorites have a similar composition, possessing olivine phenocrysts embedded in a matrix rich in pyroxene and plagioclase. Although some of the secondary minerals were found in the two samples, minor elements and compounds lead to think that both meteorites present different geochemistry. Table 4.5 summarizes all the mineral phases found in each meteorite detailing the kind of compound it is (primary, Martian secondary, terrestrial secondary or terrestrial weathering mineral phases). In addition, their formation process is also indicated. Among all of them, it can be concluded that olivine, pyroxene and ilmenite are primary mineral phases. However, other phases such as maskelynite, hematite, anatase, chromite, merrillite, iron sulfide, oxidized mackinawite, pyrrhotite, elemental sulfur, jarosite, gypsum and epsomite are considered as secondary minerals.

In this sense, the alteration processes that meteorites can undergo since their formation to their finding on Earth are summarized as follows:

- High-pressure processes

Original material from Mars (primary minerals) can lose crystallinity due to high-pressure events, such as meteorite formation. That is, a celestial body impacts with the parent planet generating high pressures and temperatures resulting from the impact. After collision, material is ejected into space, being considered a meteoroid.

The plagioclase found in both meteorites is the clear example of this high pressure transformation of minerals. The primary feldspars from Mars lost crystallinity in the formation of the meteorite, being partially or completely amorphous and leaving maskelynite as result.

It should be noted that it is also possible to find minerals derived from high pressures on Mars, since it is likely that not all altered minerals were ejected and some may remain on Mars.

Another type of high pressure alteration process could be the case of merrillite. It is possible that merrillite comes from the alteration of whitlockite due to pressure shock during the meteorite formation.

- Anaerobic oxidation processes

Oxidation processes were only appreciate in S-bearing compounds. In the case of the anaerobic ones, sulfur is present in Martian atmosphere because it was transferred from the core to the crust through volcano

degassing, magmatism, and hydrothermal processes. In this sense, due to photochemical activity and the presence of oxidizing agents S-bearing gases led to rapid formation of S-bearing minerals, such as primary, sulfides, secondary sulfides, elemental sulfur and sulfates.



- Aerobic oxidation processes

Primary sulfides formed on Mars could have been part of a meteorite, so they continued the oxidation process under terrestrial conditions (aerobic conditions). Following this path, the result is completely different, leading to the formation of iron oxides, such as hematite, goethite, lepidocrocite, among others.



- Hydrothermal alteration processes

Hydrated sulfates were detected in both meteorites. However, their origin is completely different.

On the one hand, the sulfates present on the RBT 04262 Martian meteorites were distributed along the cracks, so it is possible that those mineral phases entered dissolved into the meteorite and, subsequently, precipitated these salts. Therefore, RBT 04262 hydrated sulfates are products of terrestrial weathering.

On the other hand, the hydrated sulfates identified on the LAR 12095 were not distributed along the cracks. In this case, sulfates were distributed as grains along the matrix. This is because secondary sulfates have been hydrated due to hydrothermal processes, leaving hydrated sulfates such as gypsum, epsomite and jarosite. It should be notice that this process can occur both on Earth and on Mars.



In addition to observing hydrothermal alteration processes on S-bearing compounds, terrestrial oxidation in S-bearing compounds, it is well known that anatase is a weathering product of Ti-bearing minerals under hydrothermal conditions, such as ilmenite. As result of this reaction, hematite is also commonly formed.

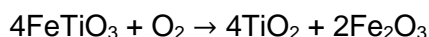


*Table 4.5. Mineral phases found on RBT 04262 and LAR 12095 Martian meteorites. Orange represents primary mineral phases; yellow represents high-pressure alteration processes; green represents anaerobic oxidation processes; pink hydrothermal processes; and blue aerobic hydrothermal processes; purple terrestrial weathering. The origin of chromite is not*

yet established, since Martian *in situ* measurements have not detected chromite on Mars yet, but many Martian meteorites do.

LAR 12095	RTB 04262
Olivine	Olivine
Pyroxene	Pyroxene
Plagioclase-maskelynite	Plagioclase-maskelynite
Hematite	-
Anatase	-
Ilmenite	-
Chromite	Titanomagnetite
Merrillite	Merrillite
Mackinawite	Mackinawite
Pyrrhotite	-
Elemental sulfur	Elemental sulfur
Marcasite	-
Jarosite	-
Gypsum	Gypsum
Epsomite	Epsomite

Taking into account the characterization of both meteorites, it was verified that both belong to the Shergottite group. This is because they are composed by olivine phenocrysts embedded in a silicate matrix, made up mainly of pyroxene and, in a lesser extent, plagioclase. Although more mineral phases were found in the LAR 12095 than in the RBT 04262 Martian meteorites, this study contributes to the further understanding of the minerals phases present in both samples. In addition, the most novel contribution of this work has been to interconnect the different S-bearing mineral phases. In this sense, this work contributes to the scientific community's understanding of why all these phases can coexist and where they come from. Though the diagrams presented in this work about the sulfur cycle and the different paths that iron sulfide can follow, it will be possible to give a better understanding of the presence of these minerals in Martian meteorites.

Considering the significance of S-bearing compounds, a deep study about sulfates was performed in this PhD by laboratory simulation experiments.

### 4.3. Martian simulants study – Hydrothermal, temperature and pressure processes

Evaporite deposits consist of a suite of salt minerals formed from the evaporation of concentrated solution of salt- or fresh-water and from the precipitation of solid minerals crystals. Although the mineralogy of evaporite deposits is complex, with almost 100 minerals potentially present, carbonates, sulfates and chloride minerals [62] are the main families of evaporite minerals. The characterization of evaporite environments is important because assemblages of saline minerals hold the most potential features of present and ancient aqueous fluids on surface and subsurface. Moreover, geological environment containing saline minerals often harbor traces of any primitive life, such as fossil biosignatures, because evaporites require short-term aqueous processes for their formation and they can trap and preserve over geologic times a biological record [63–65]. In fact, organic molecules have already been found in evaporite deposits, such as amino acids and their amine degradation products on sulfate minerals [66], lipids and fatty acids on iron sulfate deposits [67,68] and organic matter in carbonates [69,70], among others.

Huge discoveries have been found on Mars with the detection of evaporite minerals, which has sparked the great purpose of seeking evidences of ancient life on the red planet.

As mentioned above, gypsum has been identified several times throughout the history of Martian landing exploration. This compound was identified for the first time by the APXS and PanCam instruments on board the Opportunity rover [71,72]. Then, the APXS, ChemCam and CheMin instruments on board the Curiosity rover detected gypsum, together with Ca- and cation-mixed sulfates [73]. After analyzing the APXS and LIBS elemental results, the molar ratio of sulfate/calcium was greater than one, which suggested the presence of calcium with other metal-sulfates, or mixed-cation sulfates [71–77]. If mixed-cation sulfates could form under evaporitic (hydrothermal and non-hydrothermal) conditions, they can be expected to be found in Jezero crater and in Oxia Planum, sites where liquid water was present. In this sense, it is necessary to understand how mixed-sulfates can be form under ancient Martian conditions and how they can be altered due to the wide Martian temperature range. In addition, a powerful database must be created that contains not only the single-cation sulfates, but also the mixed-cation sulfates. Such database has to be made by using molecular spectroscopic techniques that are on board the most modern *in situ* missions and that allow the direct identification of these compounds, such as Raman spectroscopy, VNIR and XRD.

Apart from gypsum, ChemCam and CheMin, on board the Curiosity rover, were able to demonstrate that the whitish filler in the cracks consisted of

---

other Ca-sulfates <sup>[76]</sup>. Specifically, though the LIBS hydrogen line that appears at 656 nm, the presence of bassanite was proposed <sup>[77]</sup>. After several interpretations of the results obtained by Curiosity's instruments, the presence of gypsum, bassanite and anhydrite was concluded.

In this regard, this subchapter deals with the conditions at which gypsum and the mixed Ca-sulfates syngenite and görgeyite may be formed. Its sensitivity to Martian temperature was also studied. Finally, the reason for the coexistence of the three Ca-sulfates (anhydrite, bassanite and gypsum) on Mars is discussed.

### 4.3.1. Mixed-sulfate synthesis under the ancient Martian hydrothermal state

Recently, several evidences of the high potassium content of the red planet have been found, such as the presence of K-rich fluids and high alkali feldspars in Martian meteorites [78–81]; and the K-bearing volcanic and sedimentary rock detection made by the APXS, CheMin and ChemCam instruments on board the MSL rover [82–84]. These facts suggest that the possible mixed-cation sulfates on Mars may be of calcium, which has been already found, and potassium. In this sense, the hydrothermal synthesis of the mixed-cation sulfates syngenite and görgeyite is proposed in this thesis chapter. Both are often found in mineral rock salt formation on Earth. On the one hand, syngenite has been found mixed with other sulfates in Death Valley [85]; together with gypsum in efflorescent salts on K-bearing sandstones of outer Carpathians, Poland [86,87]; or in metamorphic evaporite deposits [88] and in volcanic caves of Argentina due to interactions with guano [89]. On the other hand, görgeyite has also been found in a variety of terrestrial natural settings, including the Ischler salt deposit in Salzburg, Austria [90]; Lake Inder, Kazakstan; in Western Greece in a Triassic evaporite sequence; in salt deposits in Germany; in lower-middle Triassic polyhalite rocks in Nongle in sichuan Province, China; and in playa sediments in Iran [90,91]. Moreover, according to Kloprogge et al. [91] syngenite and görgeyite have been found together in a geothermal field in Italy and in guano deposits in South Australia.

#### 4.3.1.1. Preparation of the reactant solutions

The synthesis was performed with the reagents indicated in Chapter 3.1.1. To prepare solutions with different amounts of  $K^+$ ,  $Ca^{2+}$  and  $SO_4^{2-}$ , the following rationale were followed:

- To increase the relative abundance of  $SO_4^{2-}$ ,  $MgSO_4$  solution was added instead of  $K_2SO_4$ , since it was not desired to increase the concentration of  $K^+$ .
- As a  $Ca^{2+}$  input, gypsum was not used due to its insoluble character. Instead,  $CaCl_2 \cdot 2H_2O$  was used because of its high solubility.
- When high  $K^+$  concentrations were required together with low  $SO_4^{2-}$  concentrations, KCl was added. In both cases, the counter ion,  $Cl^-$ , was selected since it is one of the major anions expected in Martian brines [63].
- $MgSO_4 \cdot H_2O$  was also added to reproduce a more realistic geochemical system and to check for the possible presence of other common mixed-cation sulfates, i.e. polyhalite, in the precipitates obtained in the syntheses.

---

#### 4.3.1.2. Synthesis procedure

The different stock solutions of the reactants were mixed at room temperature (RT) or were heated to the boiling point on a heating plate (~100°C). To complete the precipitation process, two methodologies were used.

In the first case, the solutions were left at RT (20-25°C), and in the second case, the reactant mixtures were introduced in flasks into a temperature-controlled water bath to maintain constant temperature at 90°C for 8 hours in order to see if these salts could also precipitate under hydrothermal conditions. The flasks introduced into the water bath were linked to a refrigeration column to avoid complete evaporation (see Figure 4.28). The water bath was heated with a thermostat and a stirrer was used to keep the same temperature in the entire water bath.



Figure 4.28. One of the experiments batches containing three flasks with three different concentrations, submerged in the water bath at 90 °C.

To select the chemical conditions under which the formation of syngenite is theoretically most favored, different thermodynamic simulations were performed using the MEDUSA software at 25°C. The logK data at 25°C contained in the Hydra database were complemented with specific formation constant values extracted from the Visual MINTEQ software.

Once the concentrations at which syngenite should be thermodynamically stable were defined, different combinations of the ion concentrations at which the precipitation of syngenite theoretically occurs were tested. To assess all the possibilities, for each experiment batch three different combinations of the ions involved in the synthesis were selected. Each experiment batch was subjected to different precipitation conditions (Flask 1, 2 and 3), reproducing one of the best conditions designed to obtain pure syngenite derived from the MEDUSA simulations. All the concentration combinations and synthesis conditions employed are described in Tables 4.6 and 4.7 in the results section, and the distribution diagrams used to visualize the best chemical conditions to produce syngenite are shown in Figures 4.29 and 4.30.

The obtained solids were filtered under vacuum through filter paper (25-30  $\mu\text{m}$  pore size and 70 mm diameter) for quantitative analysis and the collected solids were kept in glass vials until their analysis after drying them at 40°C for 2 hours.

### 4.3.1.3. Characterization of the salts

The characterization of the salts synthesized in the laboratory was first carried out by XRD and microRaman spectroscopies; and then, by VNIR spectroscopy. The XRD analyses were carried out by using the SGIker instrument, and thanks to these data, it was possible to estimate the semi-quantitative composition of minerals for each flask (characterizing the proportion of each compound produced in each experiment). Raman measurements were performed with the Renishaw InVia spectrometer and the VNIR with the ASD High Resolution FieldSpec 4 spectroradiometer.

### 4.3.1.4. Results

#### 4.3.1.4.1. Thermodynamic study of salt formation

In order to precipitate syngenite, the best  $\text{SO}_4^{2-}$ ,  $\text{Ca}^{2+}$ ,  $\text{K}^+$ , and  $\text{Mg}^{2+}$  combinations in solution at 25°C are shown in the diagrams obtained with the MEDUSA software (Figures 4.29 and 4.30).

Figure 4.29 shows the effect of increasing the  $\text{Ca}^{2+}$  concentration with constant sulfate and varying  $\text{K}^+$ , with no  $\text{Mg}^{2+}$ . The precipitation of syngenite competes with the formation of gypsum, but syngenite is favored at low calcium and high potassium concentrations.

For the syngenite formation, the concentration of  $\text{Ca}^{2+}$  must be lower than the concentration of  $\text{SO}_4^{2-}$  ( $[\text{Ca}^{2+}] < [\text{SO}_4^{2-}]$ , Figures 4.29 A to 4.29 C), since when  $\text{Ca}^{2+}$  concentration is equal or higher than  $\text{SO}_4^{2-}$  concentration ( $[\text{Ca}^{2+}] \geq [\text{SO}_4^{2-}]$ ), gypsum becomes the most favored compound (Figure 4.29 D).

In addition, the syngenite formation is partially inhibited by the formation of the aqueous  $\text{KSO}_4^-$  complex, which is the main compound formed at any potassium concentration in the presence of low calcium concentration (Figures 4.29 A and 4.29 B). This means that the aqueous  $\text{KSO}_4^-$  complex competes with the solid calcium-potassium-sulfate for the added  $\text{K}^+$ .

Concentrations shown in Figures from 4.29 A to 4.29 C were the ones used for the three flasks comprising each experimental batch for the syngenite synthesis. The red line in the diagrams indicates the final concentration of  $\text{K}^+$  that was selected according to the concentration at which syngenite was the predominant solid compound. The different experimental batches, which always contained the three flasks with the concentrations marked in

---

Figure 4.29, were subjected to different synthesis conditions shown in Table 4.6.

In order to reproduce a more realistic geochemical system,  $\text{Mg}^{2+}$  was added to the system and, under these conditions, the best ion combinations to obtain syngenite precipitation were studied. Figure 4.30 shows the fraction diagrams for some of the simulated ion combinations at 25°C. In this case, not only the aqueous  $\text{KSO}_4^-$  complex but also the soluble  $\text{MgSO}_4$  complex compete with the formation of syngenite (and gypsum).

As can be seen, at a fixed concentration of 200 mM  $\text{SO}_4^{2-}$  (see Figures 4.30 A to 4.30 C), syngenite predominates at higher  $\text{Ca}^{2+}$  concentration ( $[\text{Ca}^{2+}] < [\text{SO}_4^{2-}]$ ). The increase in  $\text{Mg}^{2+}$  concentration reduces the formation of syngenite because of the formation of the soluble  $\text{MgSO}_4$  complex. Under these conditions, the  $\text{K}^+$  concentrations has to be above 600 mM to favor syngenite formation. However, if the concentration of dissolved sulfate is increased, even if  $\text{Mg}^{2+}$  concentrations are up to 100 mM, the amount of precipitated syngenite is increased, especially if  $\text{Ca}^{2+}$  concentration is kept at 200 mM (see Figures 4.30 D and 4.30 E). As syngenite precipitation is favored with the increase of sulfate concentration, the effect of increasing it up to 500 mM, maintaining the  $\text{Mg}^{2+}$  and  $\text{Ca}^{2+}$  concentrations at 100 mM, was also examined.

As seen in Figure 4.30 F, the precipitation of syngenite starts to become less important due to the formation of a new solid sulfate compound, the hydrated mixed potassium-magnesium-calcium sulfate called polyhalite.

In the experiments performed, a concentration of 600 mM of  $\text{K}^+$  was used in most cases (red line in Figures 4.29 and 4.30) to have a concentration high enough to obtain the precipitation of syngenite, but not so high as to be unrealistic relative to the abundance of other ions under earlier Martian conditions.

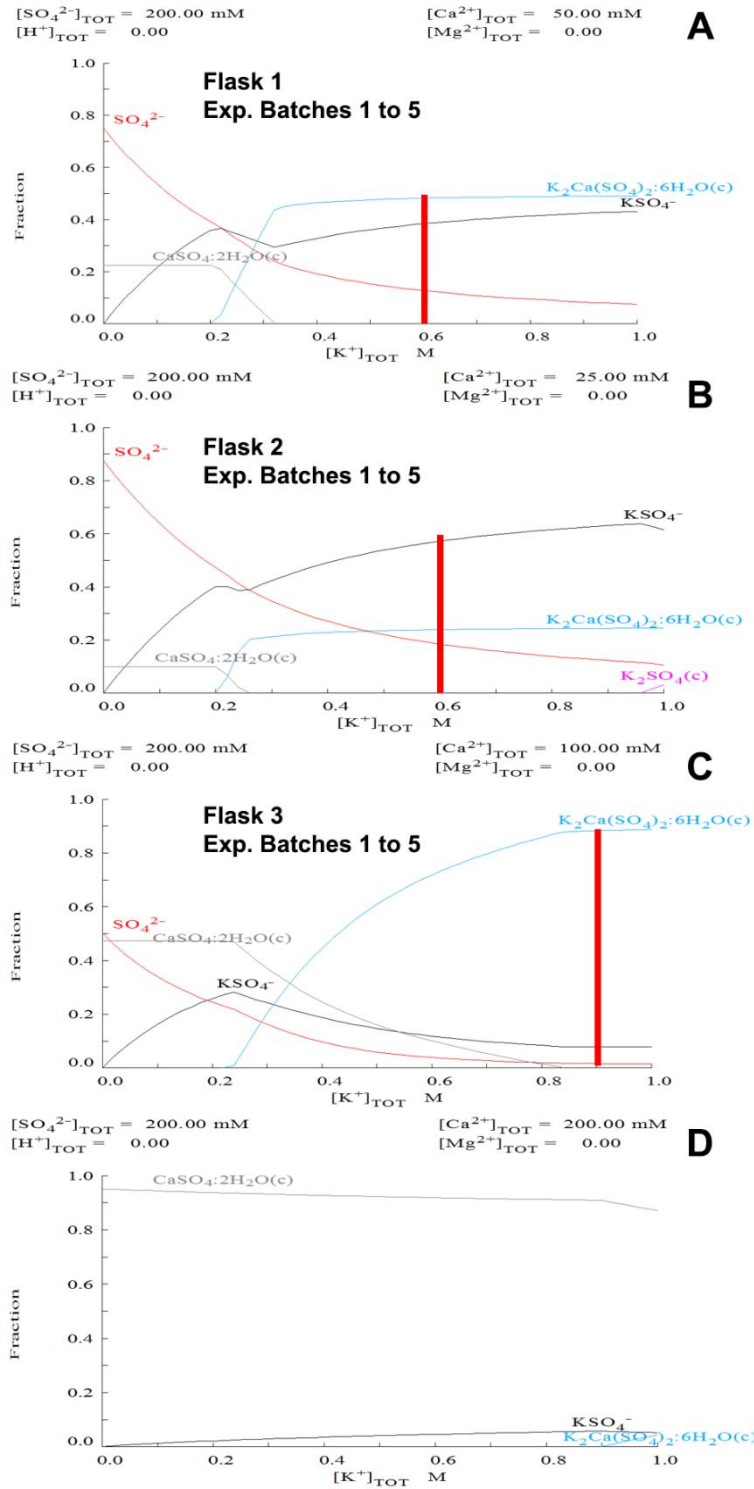
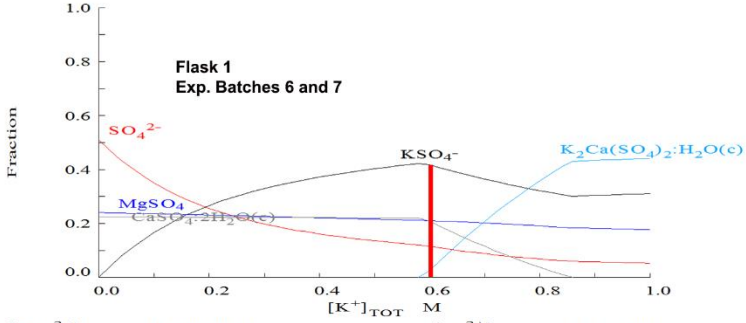


Figure 4.29. Molar fraction diagrams at 25 °C showing different concentrations of ions, but without the presence of magnesium, at which syngenite and görgeyite are thermodynamically favored to precipitate.

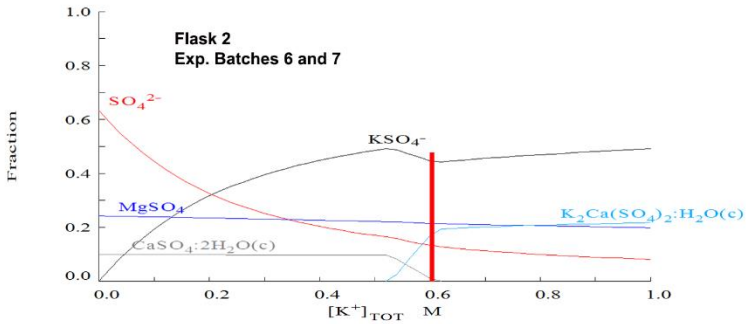
$[\text{SO}_4^{2-}]_{\text{TOT}} = 200.00 \text{ mM}$                        $[\text{Ca}^{2+}]_{\text{TOT}} = 50.00 \text{ mM}$   
 $[\text{H}^+]_{\text{TOT}} = 0.00$                                        $[\text{Mg}^{2+}]_{\text{TOT}} = 50.00 \text{ mM}$

**A**



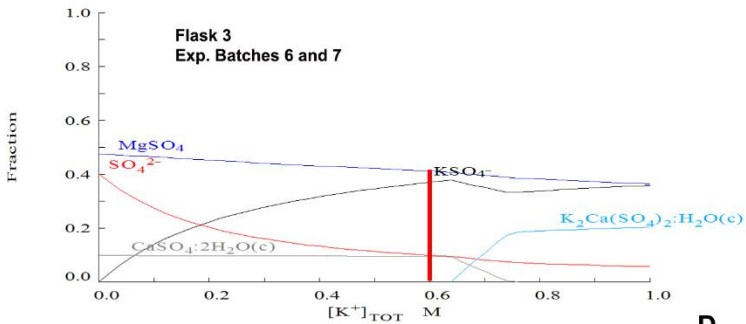
$[\text{SO}_4^{2-}]_{\text{TOT}} = 200.00 \text{ mM}$                        $[\text{Ca}^{2+}]_{\text{TOT}} = 25.00 \text{ mM}$   
 $[\text{H}^+]_{\text{TOT}} = 0.00$                                        $[\text{Mg}^{2+}]_{\text{TOT}} = 50.00 \text{ mM}$

**B**



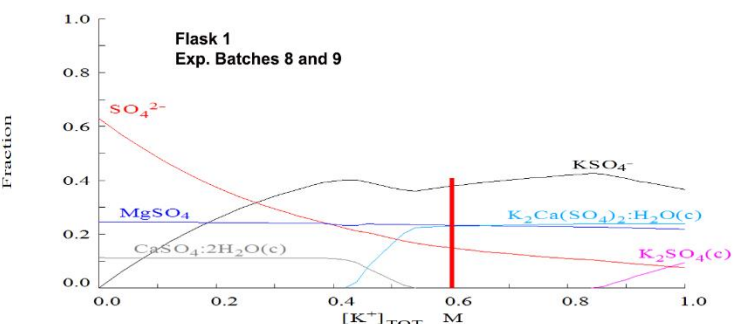
$[\text{SO}_4^{2-}]_{\text{TOT}} = 200.00 \text{ mM}$                        $[\text{Ca}^{2+}]_{\text{TOT}} = 25.00 \text{ mM}$   
 $[\text{H}^+]_{\text{TOT}} = 0.00$                                        $[\text{Mg}^{2+}]_{\text{TOT}} = 100.00 \text{ mM}$

**C**



$[\text{SO}_4^{2-}]_{\text{TOT}} = 400.00 \text{ mM}$                        $[\text{Ca}^{2+}]_{\text{TOT}} = 50.00 \text{ mM}$   
 $[\text{H}^+]_{\text{TOT}} = 0.00$                                        $[\text{Mg}^{2+}]_{\text{TOT}} = 100.00 \text{ mM}$

**D**



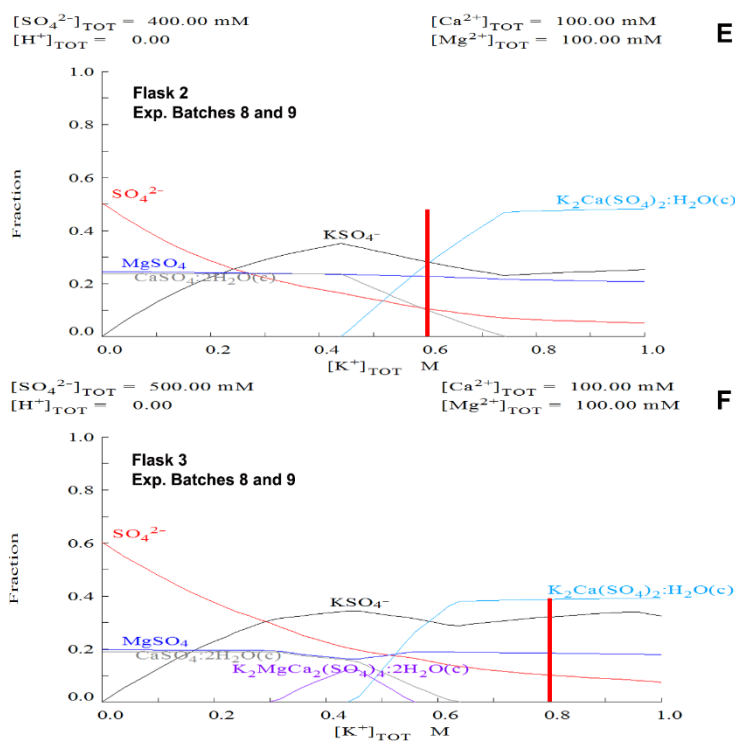


Figure 4.30. Molar fraction diagrams at 25 °C showing different concentrations of ions, with the presence of magnesium, at which syngenite and görgeyite are thermodynamically favored to precipitate.

#### 4.3.1.4.2. Laboratory experiments following thermodynamic studies

After analyzing all the theoretical cases in Figures 4.29 and 4.30, the experiments shown in Table 4.6 and 4.7 were proposed. This table shows the three variations of concentrations for each batch of experiments, as well as the semi-quantitative XRD and qualitative Raman results.

Batches 1 to 5 (Table 4.6) were carried out without the presence of magnesium in the system, whereas batches 6 to 9 (Table 4.7) with magnesium presence. Likewise, different measurement conditions were proposed, taking into account temperature as the main variable. In this sense, experiments were carried out by mixing at RT or at high temperatures, and precipitating at RT or under high temperatures.

In the results of mixed batches at RT (1 to 3), it was observed that the highest amount of syngenite was obtained when precipitating at RT, which is in agreement with the results predicted by the molar fraction diagrams for those concentrations at 25 °C. In these batches, it is also observed that the precipitate is independent of the initial reagent concentrations when reagents are heated in the water bath. According to these first three

batches, it seems that heating favors the precipitation of gypsum rather than favoring syngenite precipitations.

Table 4.6. Synthesis conditions of the experiment batches from 1 to 5 and ion concentrations used in each flask. XRD semi-quantitative and Raman results are also included. RT: room temperature; NP: no significant precipitate; Gp: gypsum; Syn: syngenite; Gör: görgeyite.

Sample	Synthesis conditions	SO <sub>4</sub> <sup>2-</sup> (mM)	K <sup>+</sup> (mM)	Ca <sup>2+</sup> (mM)	%Gypsum CaSO <sub>4</sub> ·2H <sub>2</sub> O	%Syngenite K <sub>2</sub> Ca(SO <sub>4</sub> ) <sub>2</sub> ·H <sub>2</sub> O	%Görgeyite K <sub>2</sub> Ca <sub>3</sub> (SO <sub>4</sub> ) <sub>6</sub> ·H <sub>2</sub> O	Raman observations
EB1_F1	Mixed RT + precipitation at RT	200	600	50	58	42	x	Gp with Syn and Syn
EB1_F2		200	600	25	NP	NP	NP	NP
EB1_F3		200	900	100	35	65	x	Syn and Gp
EB2_F1	Mixed RT+ Water bath at 90° C for 8h	200	600	50	96	4	x	Gp and Syn
EB2_F2		200	600	25	96	4	x	Gp and Gp with Syn
EB2_F3		200	900	100	96	4	x	Gp and Syn
EB3_F1	Mixed RT + water bath at 90° C for 3h	200	600	50	94	6	x	Gp and Gp with Syn
EB3_F2		200	600	25	95	5	x	Gp and Gp with Syn
EB3_F3		200	900	100	93	7	x	Gp and Gp with Syn
EB4_F1	Mixed heating plate for 1h at boiling point	200	600	50	90	10	x	Gp with Syn
EB4_F2		200	600	25	x	95	5	Syn
EB4_F3		200	900	100	7	81	12	Syn and Gp
EB5_F1	Mixed heating plate at boiling point for 1h + water bath at 90° C for 8h	200	600	50	89	7	4	Gp and Gp with Syn
EB5_F2		200	600	25	36	41	23	Gp with Syn
EB5_F3		200	900	100	5	15	80	Gör, Gp and Syn

Although the initial concentrations of batches 1 to 5 were the same, the reagents of the batches 4 and 5 were mixed under high temperatures. For the case of batch 4, these experiments did not avoid solvent evaporation by using a refrigeration column and it seems that syngenite formation is more favored than in the batches where evaporation of water was avoided. For the case of batch 5, which after the initial heating process, the reagents were heated in the water bath with refrigeration, the syngenite percentage was lower than in the 4 batch, but the görgeyite synthesis increased. Moreover, in flasks 3, the amount of initial Ca<sup>2+</sup> was higher, favoring the synthesis of görgeyite under hydrothermal conditions.

## Chapter 4

Table 4.7. Synthesis conditions of the experiment batches from 6 to 9 and ion concentrations used in each flask. XRD semi-quantitative and Raman results are also included. RT: room temperature; NP: no significant precipitate; Gp: gypsum; Syn: syngenite; Gör: görgeyite.

Sample	Synthesis conditions	SO <sub>4</sub> <sup>2-</sup> (mM)	K <sup>+</sup> (mM)	Ca <sup>2+</sup> (mM)	Mg <sup>2+</sup> (mM)	%Gypsum CaSO <sub>4</sub> ·2H <sub>2</sub> O	%Syngenite K <sub>2</sub> Ca(SO <sub>4</sub> ) <sub>2</sub> ·H <sub>2</sub> O	%Görgeyite K <sub>2</sub> Ca <sub>8</sub> (SO <sub>4</sub> ) <sub>8</sub> ·H <sub>2</sub> O	Raman observations
EB6_F1	Mixed RT+precipitation at RT	200	600	50	50	96	4	x	Gp and Gp with Syn
EB6_F2		200	600	25	50	92	8	x	Gp, Gp with Syn and Syn
EB6_F3		200	600	25	100	97	3	x	Gp, Gp with Syn and Syn
EB7_F1	Mixed heating plate at boiling point for 30 min + water bath at 90 C for 8h	200	600	50	50	81	6	13	Gp, Syn and Gör
EB7_F2		200	600	25	50	85	9	6	Gp and Syn
EB7_F3		200	600	25	100	59	13	28	Gp, Syn and Gör
EB8_F1	Mixed RT + precipitation at RT	400	600	50	100	13	87	x	Mainly Syn and Gp with Syn
EB8_F2		400	600	100	100	67	33	x	Syn and Gp with Syn
EB8_F3		500	800	100	100	x	100	x	Syn
EB9_F1	Mixed heating plate for 1h at boiling point + water bath at 90 C for 8h	400	600	50	100	81	19	x	Gp and Gp with Syn
EB9_F2		400	600	100	100	86	14	x	Gp and Gp with Syn
EB9_F3		500	800	100	100	x	100	x	Syn

The objective of this work was also to generate quality Raman and VNIR spectra to support the current and future Martian missions, Mars2020 and Rosalind Franklin, respectively. In this regard, Figure 4.31 shows some Raman spectra of pure syngenite, pure görgeyite and mixtures of them with gypsum. Figure 4.31 A shows the main Raman bands of the syngenite obtained in batch 1, flask 3. Figure 4.31 B shows a mixture of syngenite and gypsum obtained in batch 3, flask 3; being S syngenite and G gypsum. Finally, Figure 4.31 C shows the Raman bands of the görgeyite obtained in batch 7, flask 3.

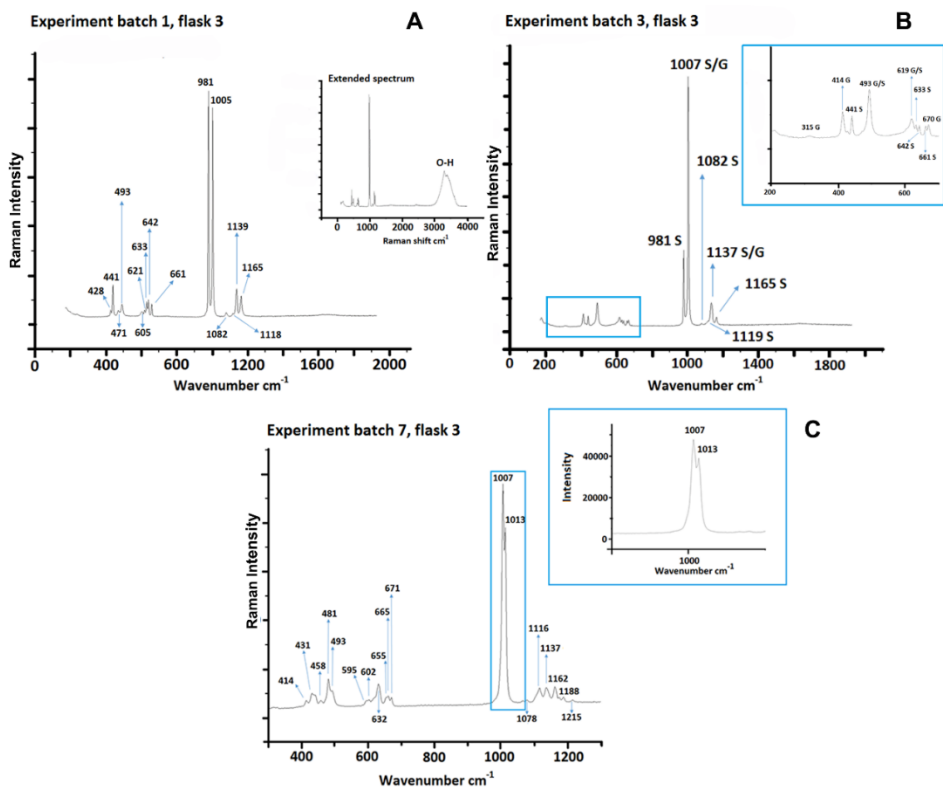


Figure 4.31. Raman spectra of: (A) syngenite acquired in the batch 1, flask 3, together with the extended spectrum of the same point showing the O-H water bands; (B) gypsum and syngenite mixture acquired in the batch 3, flask 3, together with a zoomed figure to appreciate the bands from 200 to 700  $\text{cm}^{-1}$ ; and (C) görgeyite acquired in the batch 7, flask 3, together with a zoomed figure to appreciate the characteristic doublet at 1007 and 1013  $\text{cm}^{-1}$ .

Moreover, Figure 4.32 shows the pure VNIR spectra of the three compounds synthesized. The gypsum VNIR spectrum (Figure 4.32 A) is characterized by a quite weak band at 996 nm due to the combination of the first overtone of the O-H stretching and the first overtone of the H-O-H bending mode. A slightly stronger band around 1200 nm appears due to the combination of the H-O-H bending and the first overtone of the O-H stretching mode. The triplet at 1446, 1494, and 1540 nm is mainly related to the first overtone of the O-H stretching mode. The broad band around 1750 nm is associated to the presence of several signals corresponding to the combination of H-O-H bending, O-H stretching, and low frequency vibration modes of structural water molecules. The strong band, which is actually composed of two bands at 1942 and 1968 nm, is also correlated to the presence of several signals attributed to the combination of the O-H stretching and the H-O-H bending modes [85]. According to Liu et al. [92], the combination bands around 1700 nm and the ones around 2200 to 2300 nm are assigned to the combination modes of  $\text{SO}_4^{2-}$  and  $\text{H}_2\text{O}$  vibrations.

The syngenite VNIR spectrum (Figure 4.32 B) is characterized by bands at 1256 nm (a combination of the H-O-H bending mode and the first overtone of the O-H stretching mode); two overlapped bands at 1498 and 1577 nm (the first overtone of the O-H stretching mode); 1775 nm (a combination of the H-O-H bend and the O-H stretch and vibration modes of the water molecules); and the bands that appear at 1990 and 2082 nm could be associated with the combination of the O-H stretching and the H-O-H bending modes. Finally, the bands at 2190, 2329, and 2422 nm are associated to the combination of the O-H stretch with the first overtone of the water vibration modes [85].

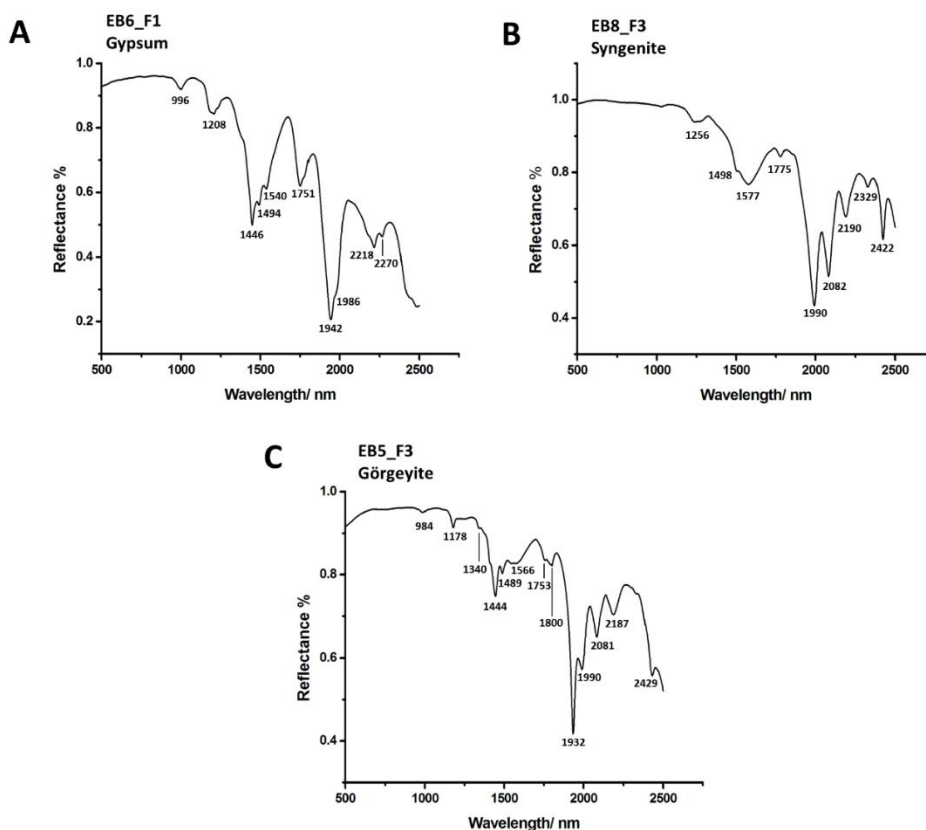


Figure 4.32. VNIR spectra of the synthesized salts. (A) gypsum, (B) syngenite and (C) görgeyite.

Finally, the görgeyite VNIR spectrum (Figure 4.32 C) is reported for the first time in the work already published in *Astrobiology* journal [93]. Even though it cannot be compared with any previous spectra, it is likely that the observed bands are similar to the vibrations observed for gypsum and syngenite. Therefore, the following assignments are proposed for the görgeyite VNIR spectrum: 984 nm band is proposed to be related to the combination of the first overtone of the H-O-H bending and the first overtone of O-H stretching modes. The 1178 and 1340 nm bands are

---

proposed to be associated with the combination of the H-OH bending and the first overtone of the O-H stretch modes. As for gypsum and syngenite, the bands around 1400 nm (specifically 1444, 1489 and 1566 nm) are proposed to be associated with the first overtone of the O-H stretch mode. The bands at 1753 and 1800 nm that form a doublet are proposed to be related to the combination of the bend of H-O-H, the stretch of O-H, and vibration of the water molecules. Bands at 1932, 1990 and 2081 nm are due to the combination of water together with the O-H stretching mode, and bands at 2187 and 2429 nm are attributed to a combination of the O-H stretch and the first overtone of the water and the combination modes of  $\text{SO}_4^{2-}$ .

#### **4.3.1.5. Discussion**

This experiment is of great relevance to expand the knowledge about the geochemistry of the Martian surface and subsurface. In this way, it has been possible to verify how some salts were able to precipitate in aqueous environments without the need for specific conditions, while other salts demanded specific physico-chemical conditions for their precipitation. Thus, the important role of water on ancient Mars is once again evidenced.

On the one hand, under the proper initial concentration in solutions, syngenite easily precipitates with and without the need of hydrothermal conditions. Depending on the ion concentration, it precipitates as the major compound or together with gypsum in different proportions.

On the other hand, it should be noted that, although under hydrothermal conditions syngenite and gypsum precipitate, these specific physico-chemical conditions are the only way in which görgeyite is precipitated. This occurs especially in magnesium-free solutions and high temperatures during the entire formation process.

### 4.3.2. Temperature-sensitive Martian sulfates studied by Raman Spectroscopy

Research done by rovers, orbiters and landers revealed that a substantial portion of the current water on Mars is in the form of ice. In addition, a tiny amount is present as water-vapor in the atmosphere and a low-volume liquid brine can be found in shallow soil areas <sup>[94]</sup>. However, apart from the main areas where water is located (solid, liquid and vapor), another part of the Martian water resides in the structures of plentiful water-rich materials, such as in sulfates and clay minerals (phyllosilicates) <sup>[94]</sup>.

In addition, in many Martian meteorites found in Africa and Antarctica hydrated sulfates have been detected. Taking into account terrestrial weathering, the presence of hydrated sulfates in meteorites may be due to two possibilities. The first consists on the entry of sulfate-rich terrestrial fluids through the cracks into the meteorite, the subsequent evaporation of the water and, finally, the precipitation of the salts. This process would leave sulfate-rich veins easily detectable by means of imaging-spectroscopic techniques <sup>[39]</sup>. The second possibility is that the sulfates present in meteorites are alteration products of primary Martian minerals that, due to different alteration processes from Mars, they may turn into sulfates (secondary minerals), remaining in the sample since its ejection. In this case, meteorites can be considered the key to obtain clues about the primary geologic processes in Mars and to identify its ancient sulfur cycle <sup>[94]</sup>.

As was seen in the previous section, temperature is a very important variable for the synthesis of sulfates. Therefore, in this section, the influence of temperature on the Raman spectra of gypsum, syngenite and görgeyite was studied. Raman spectroscopy is a vibrational spectroscopy, which is a very useful technique for the study of hydrated minerals due to its high sensitivity to structural variations caused by differences in physical magnitudes. In fact, the next robotic mission to the Martian poles could be possibly equipped with a Raman spectrometer to analyze the permafrost and the hydrated minerals that are expected to be found <sup>[95]</sup>. In addition, Raman spectroscopy could be used to determine the temperature of a material Raman bands are sensitive the temperature by shifting in their position. When a Raman band shifts significantly with temperature, the monitoring of the band position is the most straightforward methodology of determining temperature in an indirect way <sup>[96]</sup>. In contrast, if the temperature of the sample is known, using the relationship between Raman signal of the bands and the temperature it is possible to estimate at what wavenumber the Raman peaks may appear.

At least, two distinct effects of a change in scattering could occur with temperature variations. Firstly, the temperature change could cause an

---

alteration in the molecular structure of the compound, such as association of simple molecules into more complex aggregates, or a change in the crystalline form of the substance. Secondly, a change in temperature could produce a new distribution of the molecules in the various rotational and vibrational energy levels <sup>[97]</sup>. What is clear is that a change in temperature would result in band alteration or in the appearance of new bands, an effect that can be monitored by Raman spectroscopy.

Therefore, the aim of this work is to understand how the Raman bands of these three sulfates vary under temperature changes. Considering the wide range of temperatures that Mar surface has experimented along its history, the samples were studied under low (down to 83 K) and high temperatures (up to 673 K). For this purpose, it is necessary to remind the Raman standard spectra at normal conditions for the three studied sulfates: gypsum, syngenite and görgeyite.

In this sense, the Raman spectrum of gypsum is characterized by the bands that appear at 412 (m), 494 (m), 616 (w), 669 (w), 1008 (vs), 1131 (m), 3405 (s) and 3491 (s)  $\text{cm}^{-1}$  <sup>[98]</sup>.

The Raman spectrum of syngenite is characterized by the bands that appear at 132 (vw), 179 (vw), 200 (vw), 239 (vw), 428 (m), 441 (s), 473 (m), 493 (m), 608 (m), 621 (m), 633 (m), 644 (m), 661 (m), 982 (vs), 1006 (vs), 1083 (vw), 1140 (vw), 1166 (vw) and 3309 (m)  $\text{cm}^{-1}$  <sup>[93]</sup>.

The Raman spectrum of görgeyite is characterized by the bands that appear at 429 (w), 439 (w), 475 (w), 480 (m), 604 (w), 631 (m), 661 (w), 980 (s), 1005 (vs), 1012 (vs), 1116 (w), 1138 (w), 1163 (w), 1188 (w), 1216 (vw), 3310 (b), 3412 (b), 3498 (b) and 3527 (b)  $\text{cm}^{-1}$  <sup>[93]</sup>.

For the three samples, and with comparison aims, all the Raman spectra were collected under the same measurement conditions. As the samples did not degrade under high laser powers, the 532 nm excitation diode laser with a 100 % of laser power and the 1800 l/mm (vis) grating was used. Each spectrum was acquired with 10 s of exposure time, with the 5x objective and from 100 to 4000  $\text{cm}^{-1}$ .

The analyses were carried out programming temperature and hold ramps using the Linkam temperature controlled stage. For low-temperature tests, each Raman spectra were collected at every -10 K shift from 273 to 83 K. For high-temperature tests, in contrast, each Raman spectra were collected at every 20 K shift from 313 to 673 K. When the desired temperature was reached, it was hold for 6-minutes. During the hold time, four Raman measurements were performed for checking reproducibility.

After data acquisition, the Raman spectra were treated with the Wire software: the baseline was subtracted from each spectrum and the cosmic rays were removed.

Then, the center, height, full width at half maximum (FWHM), and area of some Raman bands were calculated for several bands of each spectrum. In order to ensure that the experiment was as accurate and precise as possible, the process was systematically repeated for each spectrum.

The curve fitting was also made with the Wire software. This process was carried out by the deconvolution of peaks with a 50% Lorentzian-50% Gaussian curve. The width fit of all bands was limited to  $100\text{ cm}^{-1}$ .

In order to detect outliers, Dixon's Q test was carried out. Then, the parameters versus temperature were plotted, and the linear regression and the Pearson correlation coefficient  $r$  were calculated. Those plots for which the  $R^2$  was higher than 0.80 were considered as significant trend.

#### **4.3.2.1. Low-temperature influence on the Raman spectra of Martian Ca-sulfates results**

The low temperature tests consisted on estimating the relation between the Raman signal and the temperature for the sulfates gypsum, syngenite and görgeyite. The estimation was based on the monitoring of the Raman shift that the temperature-sensitive bands undergo with decreasing temperature between 273 and 83 K. Although a temperature below 133 K has never been recorded on Mars<sup>[99]</sup>, calibrates were performed from 273 to 83 K in order to make the linear estimations more robust.

Even though studies of the influence of temperature or pressure on the Raman spectra of gypsum have been made previously<sup>[100–104]</sup>, this work analyzes for the first time this dependence for syngenite and görgeyite, two hydrated sulfates expected to be found on Mars.

The results obtained from the gypsum study showed conclusively that the main and the two water Raman bands exhibit measurable variations in wavenumber when temperature decreases, while the others remain apparently unaffected. It should be noted that the values of temperature, band position and half-bandwidth of gypsum, syngenite and görgeyite obtained in the experiment are shown in Table 8.2 and 8.3 of appendices (Chapter 8).

In the case of the main gypsum Raman peak ( $\sim 1008\text{ cm}^{-1}$ ), when the temperature decreased, the band shifted to higher wavenumbers (Figure 4.33 and Figure 4.34). From these results, the equation obtained by linear regression for the  $\sim 1008\text{ cm}^{-1}$  band of gypsum is (Equation 4.3):

---

$$\text{Band Position } (\sim 1008 \text{ cm}^{-1}) = -0.01277 \cdot T \text{ (K)} + 1011.88 \quad R^2 = 0.88$$

(Equation 4.3)

In the case of the first -OH band ( $\sim 3407 \text{ cm}^{-1}$ ), its band position shifted linearly towards higher wavenumbers with decreasing temperature (Figure 4.33 and Figure 4.34). Its equation obtained by linear regression is (Equation 4.4):

$$\text{Band Position } (\sim 3407 \text{ cm}^{-1}) = -0.01621 \cdot T \text{ (K)} + 3410.451 \quad R^2 = 0.97$$

(Equation 4.4)

In contrast, the second -OH band shifted ( $\sim 3488 \text{ cm}^{-1}$ ) towards lower wavenumber when temperature decreases (Figure 4.33 and Figure 4.34). Its equation obtained by linear regression is (Equation 4.5):

$$\text{Band Position } (\sim 3488 \text{ cm}^{-1}) = 0.0349 \cdot T \text{ (K)} + 3482.67 \quad R^2 = 0.94$$

(Equation 4.5)

However, as can be seen in Table 8.2 (Chapter 8), the bandwidth of both -OH bands shifted to lower widths when the temperature decreased. In the case of the bandwidth, the distribution of the calibration points are closer to a polynomial function than to a lineal equation. However, the bandwidth is a parameter dependent on several variables apart from the compound itself. In fact, optical elements and collection method could affect this band parameter. Thus, providing linear regressions for bandwidths is not relevant. In any case, it is evident that at low temperature, the -OH bands become fairly sharper.

One of the main Raman bands of syngenite ( $\sim 980 \text{ cm}^{-1}$ ) did not undergo significant changes under the temperature changes, in contrast to its other main band ( $\sim 1006 \text{ cm}^{-1}$ ), which shifted to higher wavenumbers when temperature decreased (Figure 4.33 and Figure 4.34, Table 8.3 of Chapter 8). Its equation obtained by linear regression is (Equation 4.6):

$$\text{Band position } (\sim 1006 \text{ cm}^{-1}) = -0.02606 \cdot T \text{ (K)} + 1013.41 \quad R^2 = 0.96$$

(Equation 4.6)

Likewise, the two -OH bands of syngenite undergo the same band shift, i.e., they shifted towards lower wavenumbers as the temperature decreased (Figure 4.33 and Figure 4.34). However, for the first -OH band ( $\sim 3153 \text{ cm}^{-1}$ ), this trend was only observed from 243 to 163 K, so Equation 4.9 can only be used between these temperatures. Its equation obtained by linear regression is (Equation 4.7):

$$\text{Band position } (\sim 3153 \text{ cm}^{-1}) = 0.418 \cdot T \text{ (K)} + 3039.1 \quad R^2 = 0.84$$

(Equation 4.7)

The equation obtained by linear regression for the second -OH band ( $\sim 3307 \text{ cm}^{-1}$ ) is (Equation 4.8):

$$\text{Band position } (\sim 3307 \text{ cm}^{-1}) = 0.0344 \cdot T \text{ (K)} + 3297.60 \quad R^2 = 0.93$$

(Equation 4.8)

The standard spectrum of görgeyite slightly changes with temperature changes. It could be observed that only one of the main Raman bands ( $\sim 1006 \text{ cm}^{-1}$ ) of görgeyite underwent changes, i.e., the band position of this band shifted to higher wavenumbers when temperature decreased (Figure 4.33 and Figure 4.34). Its equation obtained by linear regression is (Equation 4.9):

$$\text{Band position } (\sim 1006 \text{ cm}^{-1}) = -0.02180 \cdot T \text{ (K)} + 1011.99 \quad R^2 = 0.93$$

(Equation 4.9)

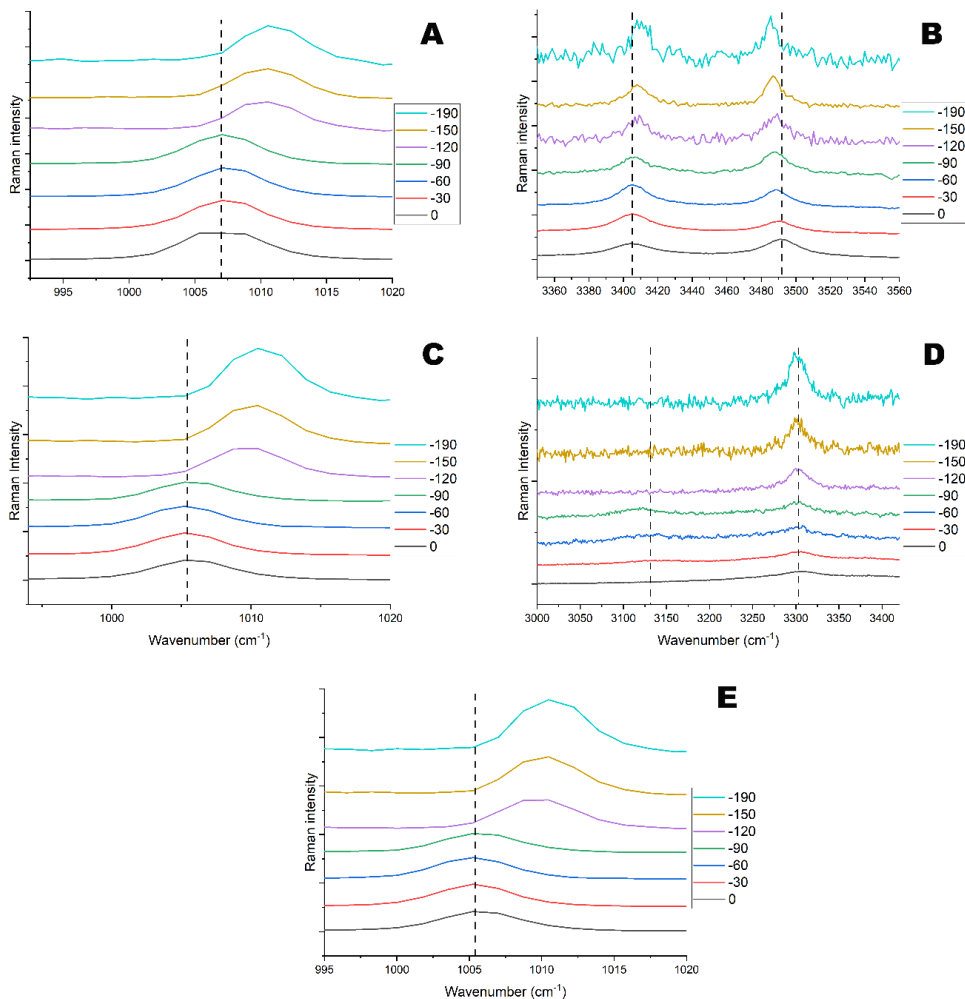


Figure 4.33. Raman spectra of (A) main gypsum band, (B) –OH gypsum bands, (C) main syngenite band, (D) –OH syngenite bands and (E) main görgeyite band from 0 to 190 °C (273 to 83 K).

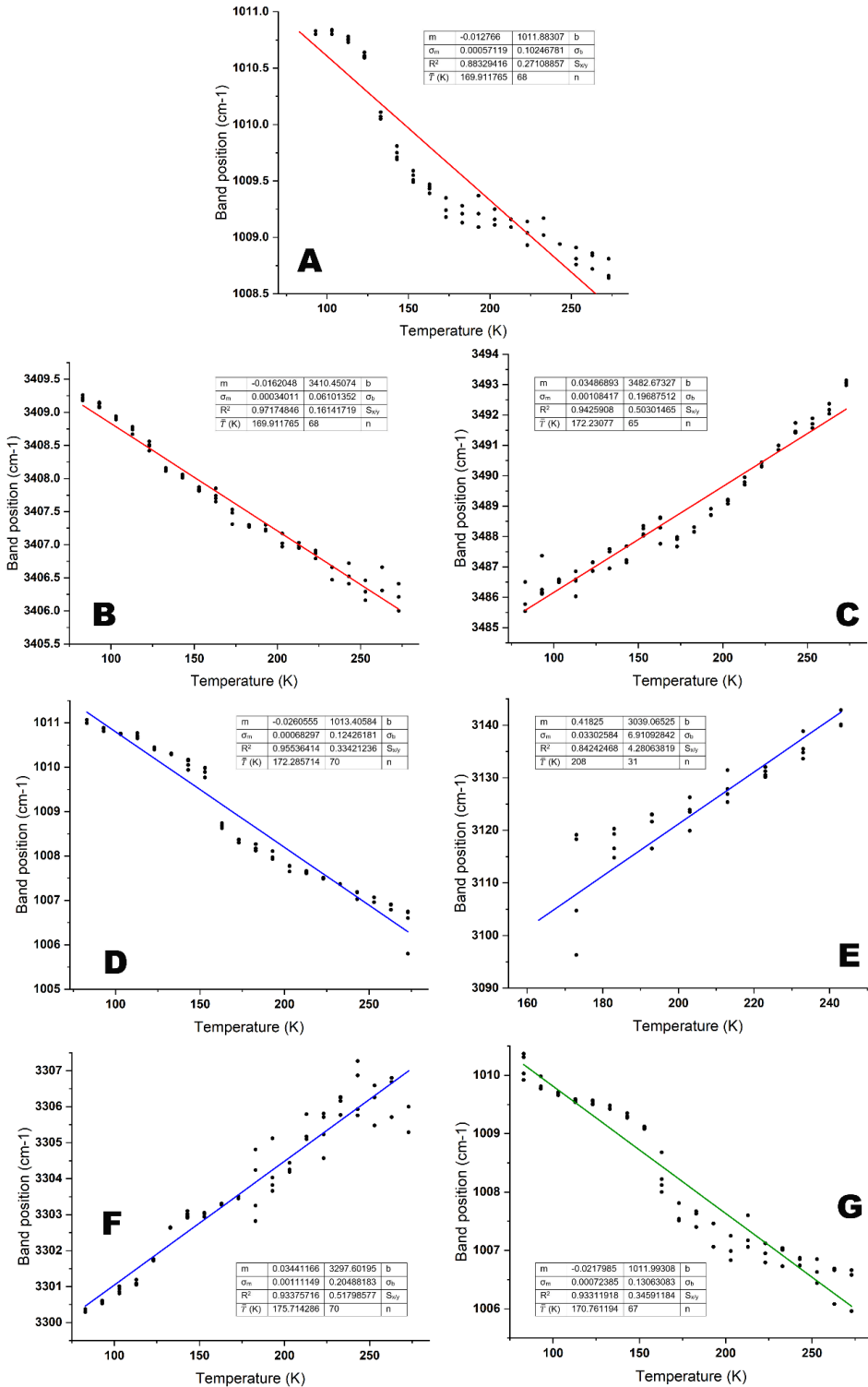


Figure 4.34. Linear Regressions for the band position of (A) main gypsum band (~1008 cm<sup>-1</sup>), (B) first -OH gypsum band (~3407 cm<sup>-1</sup>), (C) second -OH gypsum band (~3488 cm<sup>-1</sup>), (D) main syngenite band (~1006 cm<sup>-1</sup>), (E) first -OH syngenite band (~3153 cm<sup>-1</sup>), (F)

second-OH syngenite band ( $\sim 3307 \text{ cm}^{-1}$ ), and (G) main görgeyite band ( $\sim 1006 \text{ cm}^{-1}$ ) from 273 to 83 K. The calibration data, needed to calculate the global uncertainty, is also provided, being  $m$  the slope,  $\sigma_m$  the uncertainty of the slope,  $b$  the intercept of the line,  $\sigma_b$  the uncertainty of the intercept,  $R^2$  the coefficient of determination (0-1),  $S_{xy}$  is the standard error of the regression and  $n$  the points of the calibrate.

### 4.3.2.2. High-temperature influence on the Raman spectra of Martian Ca-sulfates results

The high temperature tests consisted on studying how the main Raman bands of the salts shifted with temperature until a chemical change took place. In other words, in this work, Raman shift trends were estimated as a function of high temperatures up to the time at which a change in chemical structure took place. The study was based on the monitoring of the Raman shift that the temperature-sensitive bands underwent with increasing temperature between 313 and 673 K. Even if no temperature above 303 K has been recorded on Mars <sup>[99]</sup>, calibrations were performed up to 673 K so that this study can be used for other disciplines related to calcium sulfates.

As mentioned above, studies of the influence of temperature on the gypsum sulfate have already been carried out <sup>[100-104]</sup>. However, the novelty of this work lays on the analysis of the temperature-sensitive Raman bands of görgeyite and syngenite.

Figure 4.35 shows the trend of position change of the gypsum main Raman band ( $\sim 1008 \text{ cm}^{-1}$ ) with temperature. It can be seen how the  $\sim 1008 \text{ cm}^{-1}$  Raman band shifts to lower wavenumbers when temperature increases, following the trend of the Equation 4.10.

$$\text{Band Position } (\sim 1008 \text{ cm}^{-1}) = -0.00586 \cdot T \text{ (K)} + 1009.33 \quad R^2 = 0.98$$

(Equation 4.10)

However, this relationship can be followed only to 433 K. Temperature at which gypsum starts to lose its hydration waters to become anhydrite III, which main Raman band appears at  $1025 \text{ cm}^{-1}$  <sup>[98]</sup>. The total transformation from gypsum to anhydrite ends at the temperature of 473 K. At this temperature, the tendency is preserved for anhydrite III and it shifts towards lower wavenumber with increasing temperature, following the trend of the Equation 4.11 and Figure 4.35.

$$\text{Band Position } (\sim 1025 \text{ cm}^{-1}) = -0.01448 \cdot T \text{ (K)} + 1032.55 \quad R^2 = 0.98$$

(Equation 4.11)

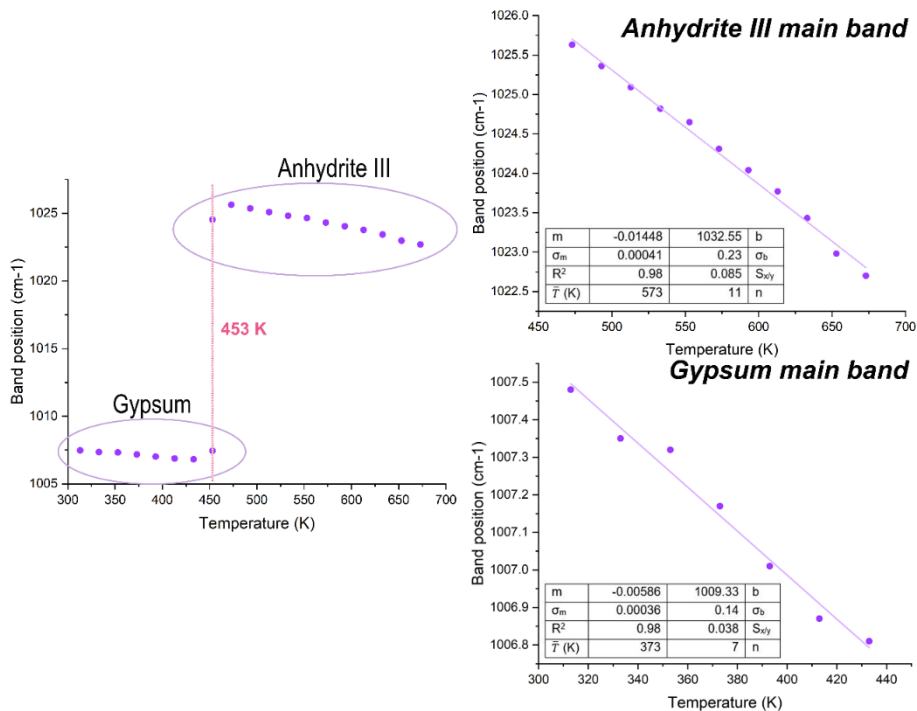


Figure 4.35. Linear Regressions for the band position of main gypsum band from 313 to 673 K. The first plot shows how the gypsum dehydration to anhydrite occurs at 453 K. The second plot shows how the main Raman band of anhydrite III shifts toward lower wavenumber when increasing temperature. The third plot shows how the main Raman band of gypsum shifts towards lower wavenumbers when increasing temperature up to 433 K. At this point the transformation into anhydrite starts. Moreover, the calibration data, needed to calculate the global uncertainty, is also provided, being  $m$  the slope,  $\sigma_m$  the uncertainty of the slope,  $b$  the intercept of the line,  $\sigma_b$  the uncertainty of the intercept,  $R^2$  the coefficient of determination (0-1),  $S_{xy}$  is the standard error of the regression and  $n$  the points of the calibrates.

Similarly, the dehydration process of gypsum can be observed by monitoring the –OH bands. Figure 4.36 shows how the first and second –OH bands disappear at 453 K due to anhydrite formation. On the one hand, the trend observed for the first –OH gypsum band consisted on the shift towards lower wavenumber when temperature increased. Nevertheless, the  $R^2$  remained below 0.80, so it could be said that there is not a good correlation between this band shift and temperature. On the other hand, the trend observed for the second –OH gypsum band consisted on the shift towards higher wavenumbers when temperature increased, following the Equation 4.12.

$$\text{Band Position } (\sim 3494 \text{ cm}^{-1}) = 0.0420 \cdot T \text{ (K)} + 3481.10 \quad R^2 = 0.99$$

(Equation 4.12)

In any case, the trend observed for the three gypsum bands at high-temperatures are the same that the ones observed for the low-temperature tests.

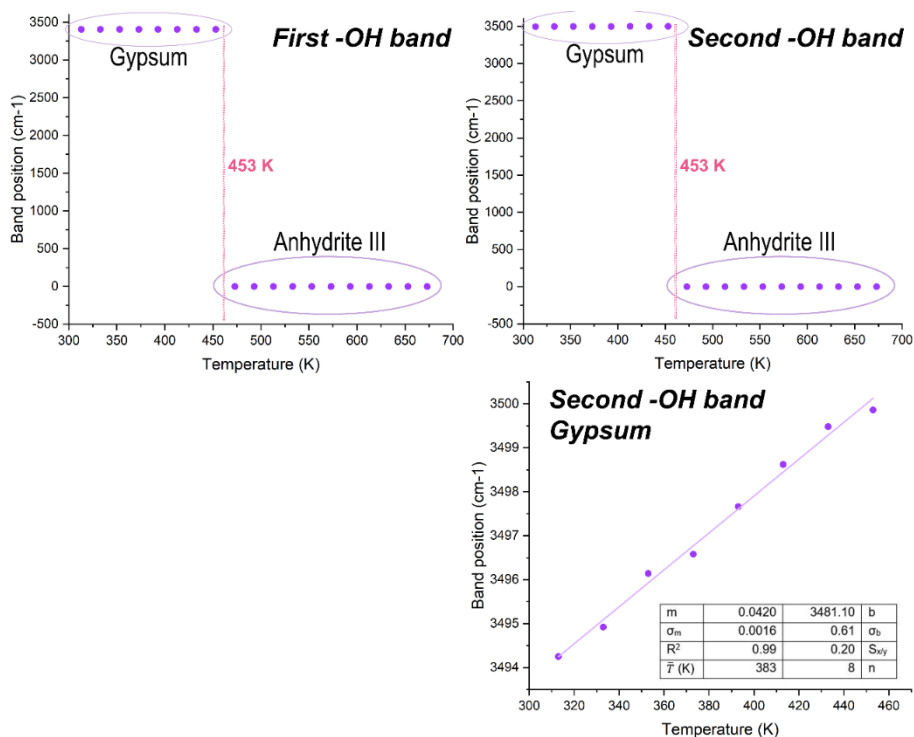


Figure 4.36. Linear Regressions for the band position of the  $-OH$  gypsum bands from 313 to 673 K. The left plot shows how the gypsum dehydration to anhydrite occurs at 453 K, losing the first  $-OH$  band. The right plots show the same process than the other one, but losing the second  $-OH$  gypsum band. In addition, below appears the trend observed for the second  $-OH$  gypsum band until 453 K with the calibration data. Being  $m$  the slope,  $\sigma_m$  the uncertainty of the slope,  $b$  the intercept of the line,  $\sigma_b$  the uncertainty of the intercept,  $R^2$  the coefficient of determination (0-1),  $S_{xy}$  is the standard error of the regression and  $n$  the points of the calibrates.

As occurred in the low-temperature tests, the unique temperature-sensitive syngenite band was the one that appears at  $\sim 1006 \text{ cm}^{-1}$ . This trend was based on the shift towards lower wavenumber when temperature increased, following the Equation 4.13.

$$\text{Band position } (\sim 1006 \text{ cm}^{-1}) = -0.01656 \cdot T \text{ (K)} + 1010.11 \quad R^2 = 0.99$$

(Equation 4.13)

However, as can be seen in Figure 4.37, this equation works only until 633 K, since at this temperature the syngenite is totally transformed into anhydrite I/II, which main Raman band appears at  $1017 \text{ cm}^{-1}$ . This theory is reinforced by the analysis of the syngenite  $-OH$  bands, which, although they do not show any trend with temperature, these bands disappear at 633 K.

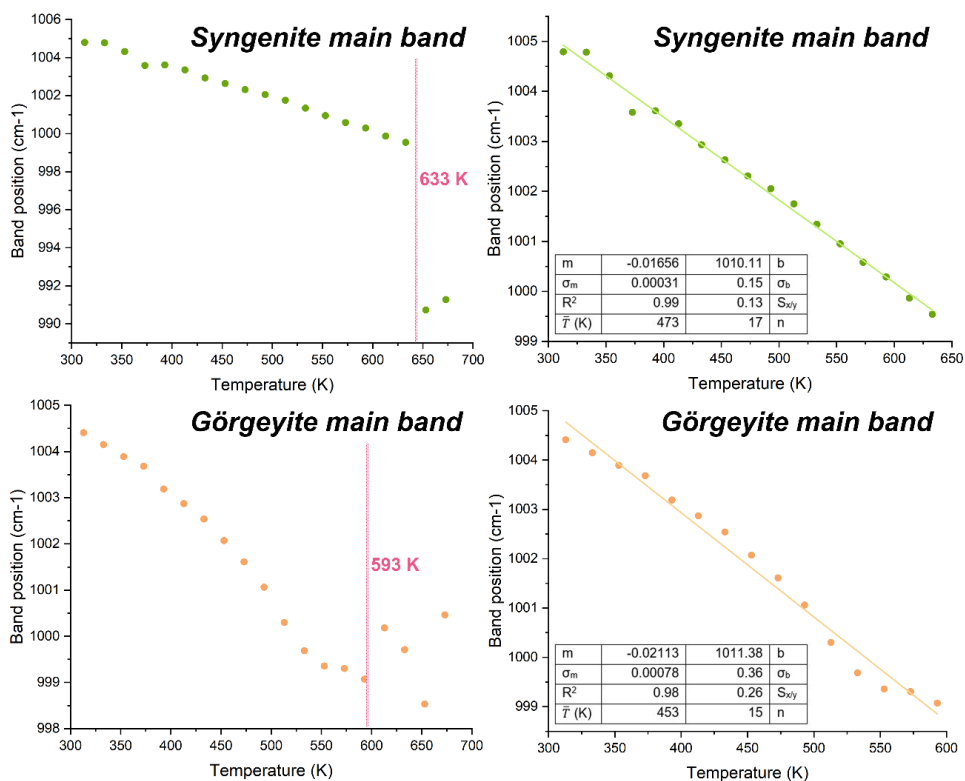


Figure 4.37. Linear Regressions for the  $\sim 1006\text{ cm}^{-1}$  syngenite band and for the  $\sim 1004\text{ cm}^{-1}$  görgeyite band from 313 to 673 K. The first syngenite plot shows how gypsum transforms to anhydrite, langbeinite and arcanite at 633 K. The second syngenite plot shows the calibration data for the main band shift. The first görgeyite plot shows that at 593 K görgeyite degrades; and the second görgeyite plot shows the calibration data for the main görgeyite Raman band. Being  $m$  the slope,  $\sigma_m$  the uncertainty of the slope,  $b$  the intercept of the line,  $\sigma_b$  the uncertainty of the intercept,  $R^2$  the coefficient of determination (0-1),  $S_{xy}$  is the standard error of the regression and  $n$  the points of the calibrates.

In addition to the formation of anhydrite, at 653 K the potassium sulfate arcanite and the mixed calcium and potassium sulfate langbeinite were formed. The presence of these minerals was confirmed by the appearance of Raman bands at  $985$  and  $978\text{ cm}^{-1}$ , respectively. Figure 4.38 shows the Raman spectrum of pure syngenite at 313 K, the spectrum of heated syngenite at 633 K, where anhydrite I/II appears, and the spectrum of heated syngenite at 653 K, where anhydrite I/II, arcanite and langbeinite appear.

Finally, for görgeyite, only the main Raman band underwent changes with temperature (see Figure 4.37). Moreover, this trend, as in the previous cases, was based on the band shift towards lower wavenumbers when temperature increased. However, this trend, which can be seen in Equation 4.14, can be followed only up to 433 K. At this temperature, the main band adopts different positions that cannot be assigned to any compound.

$$\text{Band position } (\sim 1004 \text{ cm}^{-1}) = -0.02113 \cdot T \text{ (K)} + 1011.38 \quad R^2 = 0.98$$

(Equation 4.14)

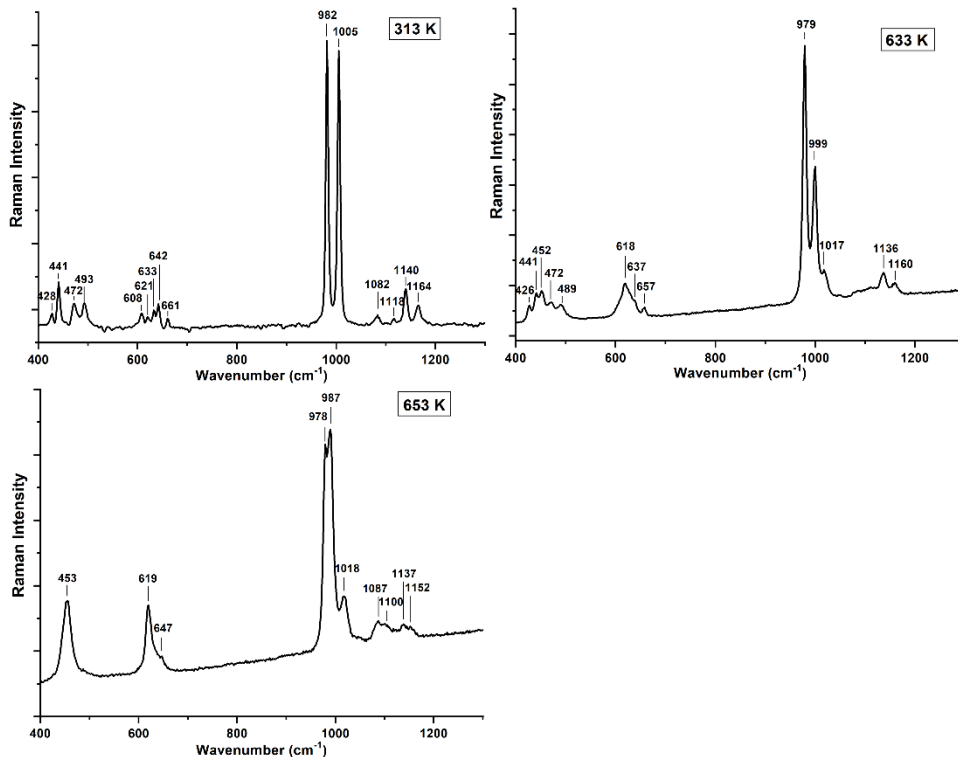


Figure 4.38. Raman spectra of pure syngenite at 313 K; heated syngenite at 633 K, where anhydrite I/II starts to form; and heated syngenite at 653 K, where syngenite is totally degraded into anhydrite I/II, arcanite and langbeinite.

### 4.3.2.3. Discussion

Bandwidth and wavenumber shifts occur due to the thermal contribution and the changes in the population of the vibrational energy levels <sup>[105]</sup>. As can be seen in the trends of the main Raman bands of the three sulfates (both low- and high-temperatures), these bands exhibit a shift to higher wavenumbers with decreasing temperature. This trend is observed because when temperature decreases, the bonds of the molecules are contracted and, consequently, the strain in the bond increases, causing an increase in energy. Thus, according to Planck's equation (Equation 4.15), when energy ( $E$ ) increases, the frequency ( $\nu$ ) increases and the wavelength ( $\lambda$ ) decreases. Since the wavelength is the inverse of the wavenumber ( $\bar{\nu}$ ), it can be concluded that the increase in energy implies an increase in the wavenumber.

$$E \uparrow = h \cdot \nu \uparrow = h \cdot \frac{c}{\lambda \downarrow} = h \cdot c \cdot \bar{\nu} \uparrow \quad (\text{Equation 4.15})$$

---

Comparing both low- and high-temperature slopes for each compound, it can be analyzed if the Raman shift of the temperature-sensitive band follows the same trend both at low- and high- temperatures. Remembering that the slopes of the  $1008\text{ cm}^{-1}$  gypsum main band were  $-0.01277$  and  $-0.00586$  for low- and high-temperatures, respectively, it can be confirmed that both slopes are not significantly similar. In fact, the slope of the low-temperature tests is the double than that of the high-temperature ones, which suggests that this band is more sensitive to low temperatures, since at high temperatures the transformation to anhydrite takes place. However, the slopes of the second  $\text{-OH}$  band trends are significantly comparable up to the moment when anhydrite is formed, being  $0.0349$  and  $0.0420$  for low and high-temperature tests, respectively.

Raman shifts occur up to the time of compound change. That is, as temperature increases, the wavenumber of the main Raman bands become lower. Notwithstanding, this tendency only occurs until a limiting temperature is reached. At this temperature, the analyzed mineral transforms to other minerals, which involves a thermal alteration reaction.

In the case of gypsum, it starts to dehydrate into anhydrite III at  $433\text{ K}$ , which is the metastable form of anhydrite. This can reach its stable form (anhydrite I and anhydrite II) above  $1073\text{ K}$  <sup>[98]</sup>.

However, in the case of syngenite, the similar dehydration process occurs at the temperature of  $633\text{ K}$ . At this point, water molecules are lost and the stable anhydrite I or II are observed. Moreover, with the increase in temperature and apart from the dehydration process, an alteration process also takes place. This one implies that the potassium content of the syngenite transforms to the anhydrous potassium sulfates: langbeinite and arcanite. Finally, no alteration process was observed for görgeyite, which suggests that it is more resistant to high temperatures, even its water molecules.

The dehydration processes described for gypsum and syngenite are also seen in the water bands, which disappear at  $453\text{ K}$  and  $633\text{ K}$ , respectively. In addition, it should be noted that the water bands are more visible in the low-temperatures tests than at high-temperatures, this fact suggests that each frozen hydration water molecule vibrates depending on the type of ice it forms <sup>[106]</sup>.

Thus, based on low-temperature tests, the first gypsum  $\text{-OH}$  band followed the same trend as the main bands of the sulfates. In contrast, the second  $\text{-OH}$  band of gypsum and the two  $\text{-OH}$  bands of syngenite showed drastic changes upon cooling in the region of the  $\text{O-H}$  stretch. These bands moved towards lower wavenumbers as temperature decreased. This fact implies

that the indicated O-H bonds are strengthened as temperature decreases [107].

Finally, the -OH bands of gypsum were the only ones that underwent changes in the FWHM at low temperatures, as the others did not change sufficiently with temperature to be used as Raman-temperature correlation models. The FWHM of these two bands become narrower as temperature decreased and follow a non-linear rate distribution. This is because the -OH bands become more crystalline and, consequently, were at more ordered energy levels. For that reason, they become narrower and sharper with decreasing temperatures [108].

It is worth noting that all results in this work are in agreement with previous works focused on the gypsum Raman spectrum evolution with temperature [102,109,110]. However, the equations and linear regressions vary slightly depending on the employed band deconvolution strategy.

With the equations estimated in this work, both temperatures and wavenumbers can be calculated for gypsum, syngenite and görgeyite, assuming that one of the two magnitudes is known. Moreover, the uncertainties related to the calibration and the reproducibility of the measurement can be calculated as following:

- Estimate the Temperature or Raman wavenumber from the Equation 4.3-4.14.
- Calculate the uncertainty associated with the measurement, following the equations below. Equation 4.16 is to calculate the associated uncertainty for Temperature ( $\sigma_T$ ) [111] and Equation 4.17 for the wavenumber ( $\sigma_{Wn}$ ) [112].

$$\sigma_x = \frac{S_{x/y}}{m} \sqrt{\frac{1}{p} + \frac{1}{n} + \frac{(\bar{X} - X_0)^2}{\sum(\bar{X} - X_i)^2}} \quad (\text{Equation 4.16})$$

$$\sigma_y = S_{x/y} \sqrt{\frac{1}{p} + \frac{1}{n} + \frac{(\bar{X} - X_0)^2}{S_{xx}}} \quad (\text{Equation 4.17})$$

Being  $S_{t/Wn}$  the standard error of regression,  $m$  the slope of the regression,  $p$  the number of replicates of the sample,  $n$  the points of the calibrate,  $\bar{X}$  the average of the calibration points,  $X_0$  the temperature calculated with the linear regression or the temperature at which the wavenumber is calculated.

- The uncertainty associated with the regression (Equation 4.18) and the reproducibility of the measurement (Equation 4.19) can be calculated.

$$\sigma_{regression} = \frac{\sigma_{y \text{ or } x}}{\bar{Y} \text{ or } \bar{X}} \quad (\text{Equation 4.18})$$

---


$$\sigma_{reproducibility} = \frac{desvest}{\bar{Y} \text{ or } \bar{X}} \quad (\text{Equation 4.19})$$

- As well as the combined or global uncertainty (Equation 4.20).

$$combined\ uncertainty = \sqrt{\sigma_{regression}^2 + \sigma_{reproducibility}^2} \quad (\text{Equation 4.20})$$

Two hypothetical examples are given below:

The first hypothetical example would be the estimation of the wavenumber at a certain known temperature: the Martian environmental analyzer of a rover performed four measurements of temperature, being 170.7, 170.5, 171.0 and 169.9 K. Moreover, the instrument equipped with a Raman spectrometer wanted to check if the mineral phase of the analysis point was görgeyite. Thanks to this work, the wavenumber and the uncertainty of the görgeyite main band can be estimated.

- Following the Equation 4.9, the main Raman band would appear at  $1008.276\text{ cm}^{-1}$  with a standard derivation of  $0.010\text{ cm}^{-1}$ .
- The error associated with the wavenumber (Y), following the Equation 4.17:

$$\sigma_y = 0.35 \sqrt{\frac{1}{4} + \frac{1}{67} + \frac{(170.76-170.53)^2}{0.87}} = 34.15$$

- The uncertainty associated with the regression (Equation 4.18) and with the reproducibility of the measurement (Equation 4.19).

$$\sigma_{regression} = \frac{34.15}{1008.28} = 3.4 \cdot 10^{-2}$$

$$\sigma_{reproducibility} = \frac{0.010}{1008.28} = 1.01 \cdot 10^{-5}$$

- The combined uncertainty (Equation 4.20).

$$combined\ uncertainty = \sqrt{(3.4 \cdot 10^{-2})^2 + (1.0 \cdot 10^{-5})^2} = 3.4 \cdot 10^{-2}\text{ cm}^{-1}$$

Therefore, the wavenumber and the global uncertainty of the görgeyite main band would be  $1008.276 \pm 0.034\text{ cm}^{-1}$ .

The second hypothetical example would be the estimation of the temperature knowing the position of the compound main band: during an *in situ* measurement campaign in Antarctica, a Raman spectrum of gypsum obtained with the portable Raman spectrometer was obtained. Three measurements of the wavenumber were performed, which appeared at  $1008.89$ ,  $1008.78$  and  $1008.87\text{ cm}^{-1}$ . However, the scientists were not sure about the measurement since the instrument did not measure well below  $123\text{ K}$ . In this sense, thanks to the equations provided the temperature with its global uncertainty could be calculated.

- The Raman wavenumber from the Equation 4.3. The results would be 237.9 K with a standard derivation of 4.6 K.
- The uncertainty associated with the temperature (X), following the Equation 4.16.

$$\sigma_x = \frac{0.27}{0.013} \sqrt{\frac{1}{3} + \frac{1}{68} + \frac{(169.91-237.85)^2}{13889.03}} = 17.52$$

- The uncertainty associated with the regression (Equation 4.18) and the reproducibility of the measurement (Equation 4.19).

$$\sigma_{regression} = \frac{17.52}{1008.85} = 1.74 \cdot 10^{-2}$$

$$\sigma_{reproducibility} = \frac{4.6}{237.85} = 1.93 \cdot 10^{-2}$$

- The combined uncertainty (Equation 4.20).

$$combined\ uncertainty = \sqrt{(1.74 \cdot 10^{-2})^2 + (1.93 \cdot 10^{-2})^2} = 1.8 \cdot 10^{-2} \text{ K}$$

Therefore, the temperature and the global uncertainty of the gypsum main band is  $237.850 \pm 0.012$  K.

Thanks to this study, it was possible to verify which gypsum, syngenite and görgeyite Raman bands are temperature-sensitive. Likewise, some Raman bands are sensitive to temperature because of two possible effects: (1) they undergo molecular structural changes or (2) temperature causes the distributional change of molecules in various rotational and vibrational energy levels. Moreover, the effect of dehydration was observed for gypsum and syngenite.

In this way, the main bands of the three sulfates shifted towards higher wavenumbers as temperature decreased. The strengthening of the bonds caused an increase in energy and, consequently, higher wavenumbers. However, -OH bands shifted depending on the crystal structure they acquire as the temperature decreased, so not all -OH bands behave in the same way. Finally, the gypsum -OH bands changed to more ordered crystalline structures with decreasing temperature, so their bandwidth decreased.

Based on these trends, it was possible to monitor how temperature-sensitive bands of these sulfates change. In addition, dehydration processes were observed for gypsum and syngenite. On the one hand, the dehydration of gypsum started at 433 K to form anhydrite III. This fact was observed because the intensity of the gypsum main band became smaller, while the anhydrite III main band became bigger. Moreover, the gypsum -OH bands completely disappeared at 453 K. On the other hand, the syngenite dehydration process occur at 633 K, when anhydrite I/II started

---

to form and, then, at 653 K the potassium sulfates arcanite and langbeinite form.

Thus, it is possible to predict the Raman shift of these compounds from 83 to 673 K. This remarkable regularity of Raman shifts and their temperature dependences, regardless the composition or crystal structure, makes it very useful to predict some parameters in cold and hot terrestrial areas such as Antarctica, poles of Mars, hot deserts or industrial sulfate processes. In addition, this study serves as support science for Mars missions, because the daily temperature ranges from 283 to 193 K and it is continuously measured by dedicated instruments in the current Mars2020 and in the forthcoming MMX and Rosalind Franklin missions.

Understanding how the Raman spectra of gypsum, syngenite and görgeyite vary depending on temperature, it is necessary to address other issue related with the presence of the anhydrous and the semi-hydrate calcium sulfates on Mars.

### 4.3.3. Simulation of anhydrite formation at the Delta Front, Jezero crater, Mars

As mentioned above, the Curiosity rover was able to simultaneously identify the presence of three Ca-sulfates: gypsum, bassanite and anhydrite [73,76,77]. This section discusses the different possibilities of this finding.

In order to evaluate the presence of S-bearing compounds and according to the results of the CheMin instrument shown by Vaniman et al. [113], Table 4.8 was assembled. This table shows the targets where some S-bearing compounds coexist on Mars, which are five points from the Stimson and Murray formations, at Gale crater. Likewise, in this table the amount (% units) of the three Ca-sulfates and jarosite measured in the five targets is also reported. As can be seen, anhydrite and gypsum were present in all five samples, being higher the relative abundance of anhydrite than that of gypsum. Bassanite was absent of the Oudam Murray siltstone sample and jarosite was only present in the mudstones of the Murray formation.

*Table 4.8. Abundance (% units over the whole set of minerals) of Ca-sulfates and jarosite detected at five sample sites in Gale crater, Mars.*

Sample / Mineral (%)	Lubango drill, Stimson fracture	Oudam, Murray siltstone	Marimba2, Murray mudstone	Quela, Murray mudstone	Sebina, Murray mudstone
Gypsum	0.9	3.3	2.2	0.4	1.0
Bassanite	2.0	0	0.6	1.5	0.6
Anhydrite	2.8	3.2	3.4	3.3	4.8
Jarosite	0	0	0.5	0.4	0.8

In addition, the relative amounts of the three Ca-sulfates detected by CheMin can be seen in Figure 4.39, which has been extracted from the Vaniman's article [113]. This figure [113] shows the mineral abundances in weight percent as a proportion of the total sample including X-ray amorphous and clay minerals components. As can be seen, anhydrite was present in all the samples except for the Mojave 2 and Confidence Hills samples, where no compound was present. Moreover, there are samples in the Murray formation where the three Ca-sulfates coexisted, being always anhydrite the most abundant component. Likewise, it can be observed how gypsum can coexist with anhydrite, bassanite with anhydrite or all three together.

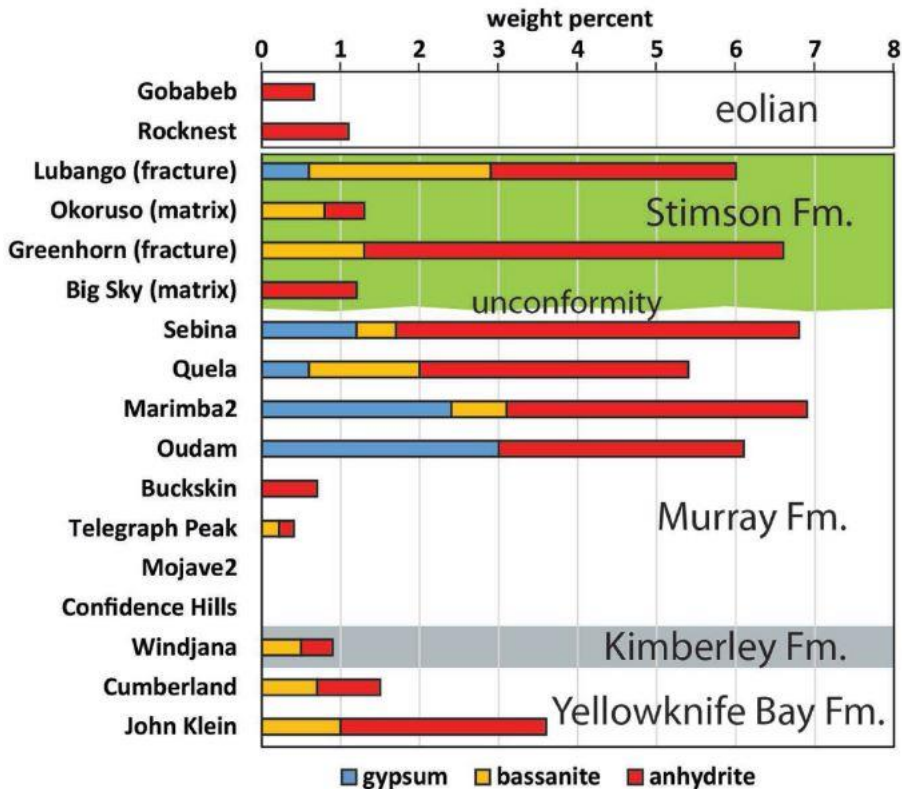


Figure 4.39. Mineral abundances of gypsum, bassanite and anhydrite in CheMin samples. These abundances are in weight percent as a proportion of the total sample including X-ray amorphous and clay minerals components

Besides, the Perseverance rover was also able to detect Ca-sulfates on Mars. The clearest data about the presence of Ca-sulfates were obtained through the SuperCam instrument in the sedimentary deposits at the Delta Front of the Jezero crater paleolake. Figure 4.40 shows the RMI images of the regions called Hogwallow Flats and Yory Pass, which were characterized by being siltstones and sandstones with recurrent presence of light-tones veins. As can be seen, Reids Gap present the thickest vein, but the other five RMI images also show light toned veins.

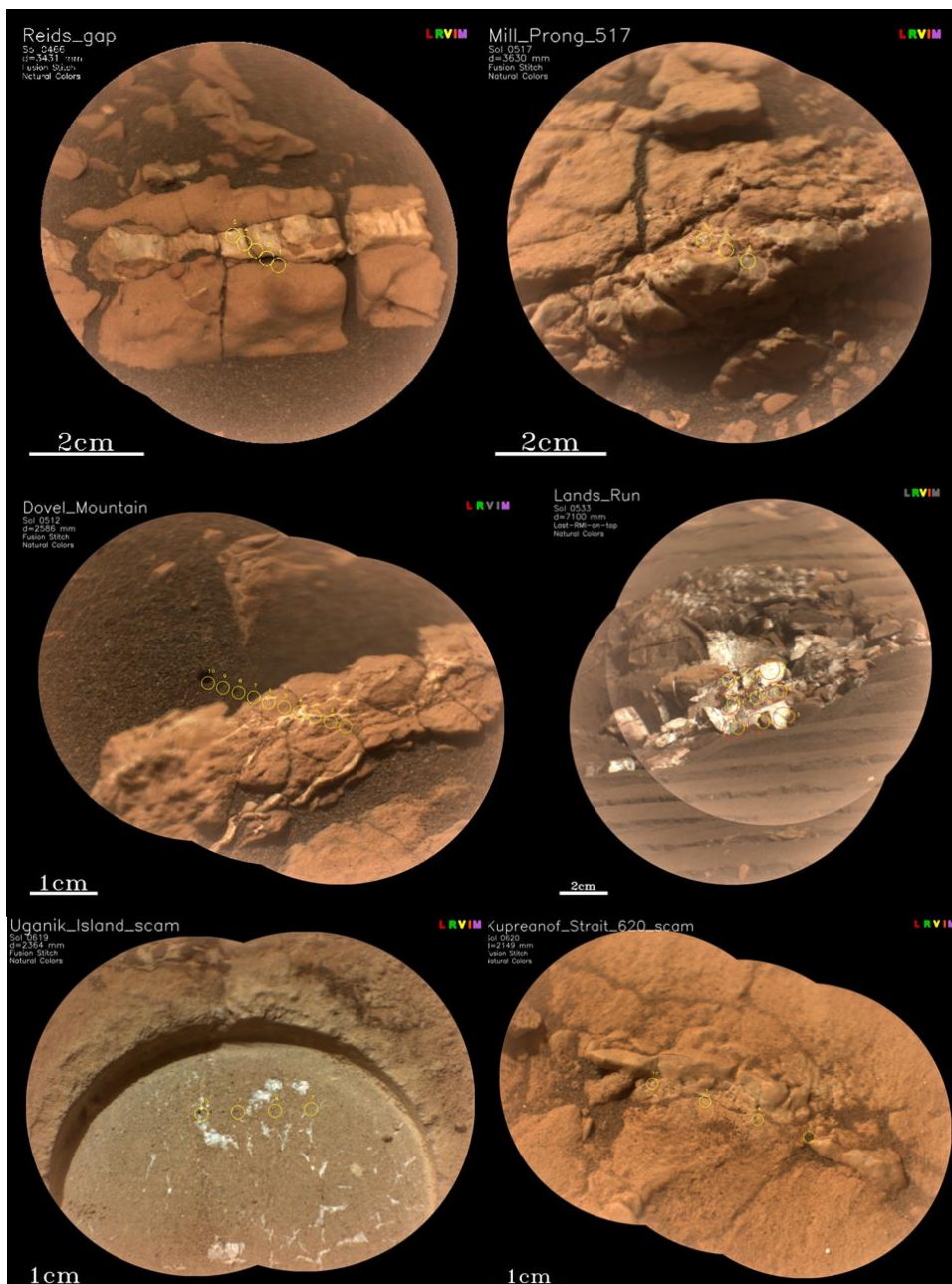


Figure 4.40. Veins and patches analyzed by SuperCam instrument at Hogwallow Flats and Yory Pass.

In order to identify the mineralogical composition of these targets, Raman measurements were performed, which are displayed in Figure 4.41. As seen, all the spectra showed the same Raman band at  $1017\text{ cm}^{-1}$ , and some of them also contained secondary Raman bands, which are consistent with a Ca-sulfate compound. Thanks to Raman spectroscopy,

which is able to differentiate between the three polymorphs of Ca-sulfate, it was possible to verify that it was anhydrite II.

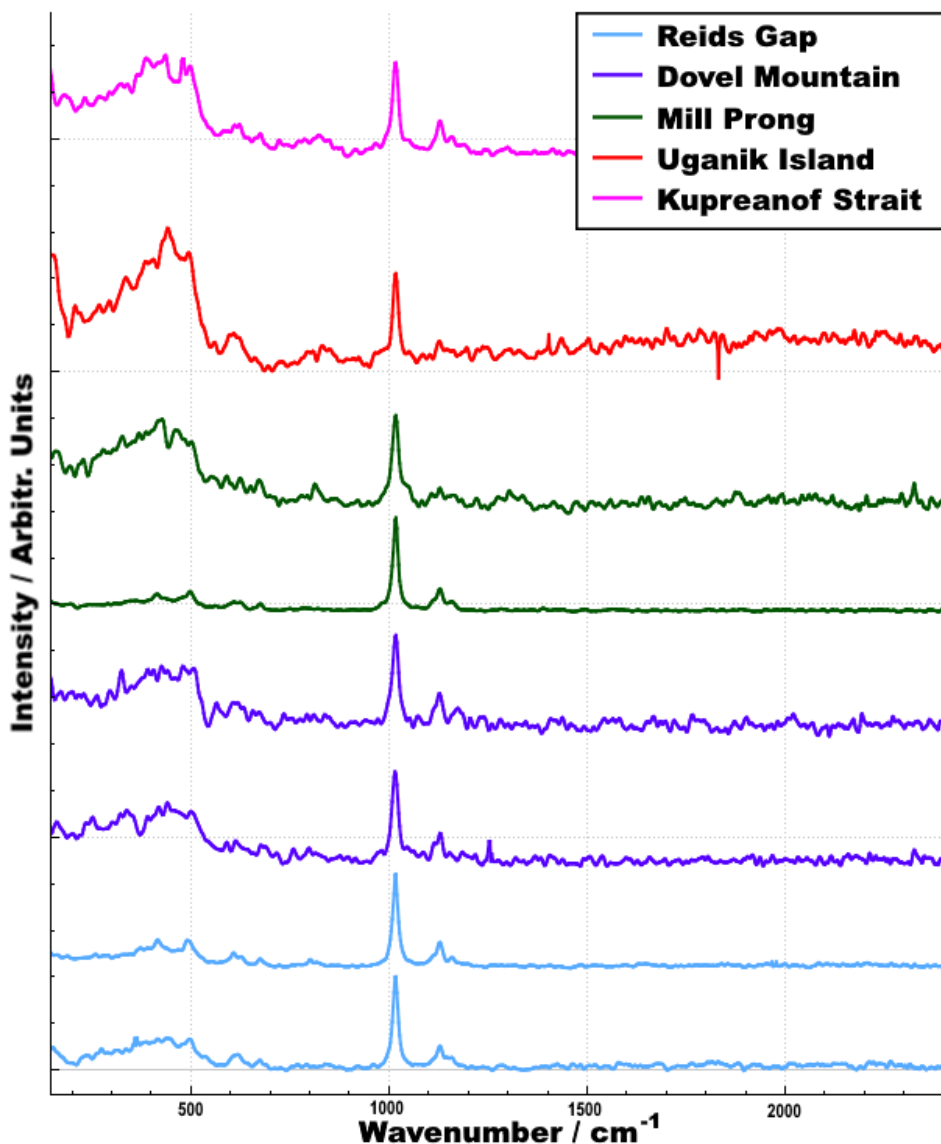


Figure 4.41. Raman spectra obtained in different points of light toned veins at Hogwallow Flats and Yori Pass. The bump between 200-550  $\text{cm}^{-1}$  is due to the signal promoted by the optical fibers of the SuperCam instrument that connects the MU and BU units.

This is because the secondary Raman bands appeared at 609, 1111 and 1060  $\text{cm}^{-1}$ , which correspond with the bands promoted by anhydrite II (orthorhombic polymorph) [98]. This approach was also supported by the lack of bands in the 3350-3650  $\text{cm}^{-1}$  region, where hydration bands appear, and by the position of the main band at 1017  $\text{cm}^{-1}$  corresponding to anhydrite II according to Prieto-Taboada et al. [98].

In order to confirm these statements, Figure 4.42 compares the experimental Raman spectra obtained at Reids Gap with the standard Raman spectra for gypsum, bassanite and anhydrite II. There, it can be seen that both the secondary and the main Raman bands of anhydrite II match with the experimental ones. Likewise, there is no presence of hydration bands. Matching perfectly with the spectrum of anhydrite II.

Finally, the SuperCam LIBS spectra and, subsequent, H analysis on the same targets was also consistent with the presence of anhydrite. However, VNIR showed evidences of hydration.

Considering the unambiguous Raman detection of anhydrous Ca-sulfate and the high sensitivity of IR water bands, the  $\sim 1.4$  and  $\sim 1.9$   $\mu\text{m}$  absorption bands observed in the Reids Gaps IR spectra, are probably related to the minor presence of  $-\text{OH}$  and  $\text{H}_2\text{O}$  molecules, either molecular in trace amounts or absorbed on the sample surface. This fact is probably related to the presence of minor phyllosilicates on the surface of the analyzed vein.

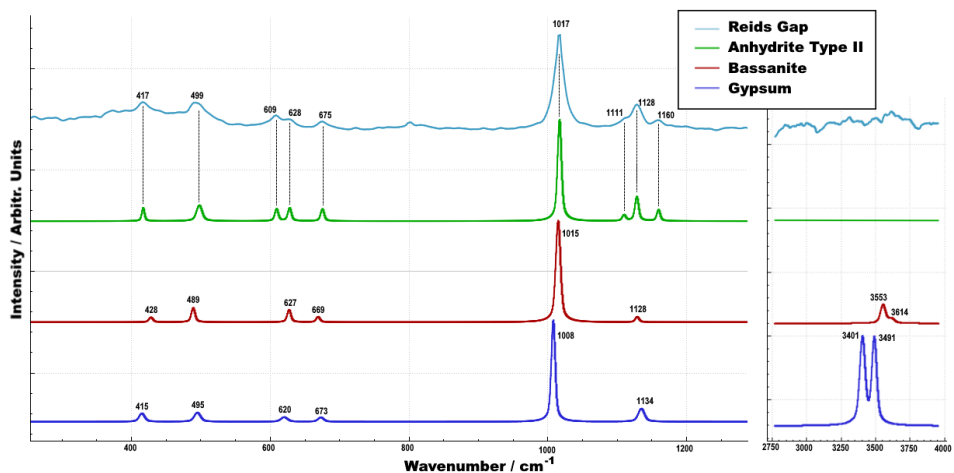


Figure 4.42. Comparison of the Raman spectrum obtained at Reids Gap and standard spectra of anhydrite II, bassanite and gypsum. The absence of  $-\text{OH}$  vibrations around  $3350$  and  $3650$   $\text{cm}^{-1}$  indicate the presence of an anhydrous compound.

According to the work of Li et al. <sup>[114]</sup> that explains the phase transition model for Ca-sulfate compounds as function of temperature, the environmental conditions for the formation of gypsum, bassanite and anhydrite can be understood. In this sense, the figure 1 of this work <sup>[114]</sup> shows how the solubility product ( $k_{\text{sp}}$ ) of the three compounds decrease as temperature increases (considering water activities around 1). At a temperature of  $20$   $^{\circ}\text{C}$ , the less soluble compound is gypsum. At  $43$   $^{\circ}\text{C}$ , the solubility of gypsum and anhydrite are equal, so both precipitate in the same proportion. Finally, above  $43$   $^{\circ}\text{C}$ , anhydrite is the compound with the lowest solubility.

---

Bassanite is never the less soluble compound when the water activity is around 1, so its formation is not thermodynamically favored, unless the water activity increases above 1. That is, under high concentration brine conditions, when the ionic strength is high due to the high concentrations of dissolved ions and less water is present, bassanite precipitates.

Therefore, the presence of Ca-sulfates in Martian veins may be a consequence of the transport of solutions enriched in soluble calcium and sulfate ions along these veins.

At temperatures around 20 °C and with a sufficiently saturated aqueous medium, the formation of gypsum is favored ( $k_{sp \text{ gypsum}} < k_{sp \text{ bassanite}} < k_{sp \text{ anhydrite}}$ )<sup>[114]</sup>.

In contrast, anhydrite precipitation is only achieved under hydrothermal environments. As seen in the figure 1 of the work of Li et al., at 100 °C  $k_{sp \text{ anhydrite}} < k_{sp \text{ gypsum}} = k_{sp \text{ bassanite}}$ . Hence, when the saturated condition is reached, anhydrite will form about 80 % and gypsum and bassanite will form about 10 % each. At temperatures higher than 100 °C, anhydrite is more favored and only bassanite will be the minor compound, while gypsum would be present only at trace levels. This type of formation also occurs on Earth, as in the north coast of Iceland<sup>[115,116]</sup>.

Finally, precipitation of bassanite, over gypsum and/or anhydrite, required high ionic strengths due to the presence of other ions than  $\text{Ca}^{2+}$  or  $\text{SO}_4^{2-}$ , i.e., in brines when the water activity is greater than 1. Only for such conditions at RT,  $k_{sp \text{ bassanite}} < k_{sp \text{ gypsum}} < k_{sp \text{ anhydrite}}$ . For such brines, when water evaporates, the saturation condition is reached and bassanite is the precipitated Ca-sulfate compound.

Considering the precipitation conditions discussed above, when water filled the Jezero crater ambient temperatures were below 40 °C, so gypsum precipitation was favored over bassanite and anhydrite. Then, when water was expelled from Jezero crater, saturated brines could have formed, favoring the formation of bassanite.

Thus, it is most likely that the filling of the veins was done by gypsum and/or bassanite, unless hydrothermal conditions were present to precipitate anhydrite directly. Taking into account that Raman analyses performed on Delta Front rocks shows unequivocally the presence of anhydrite II, dehydration processes to transform the original gypsum and/or bassanite into anhydrite must be occurred for thousands of years.

In this work, two types of dehydration process of hydrated Ca-sulfates are proposed: (1) thermal dehydration of gypsum and bassanite to anhydrite, and (2) dehydration of gypsum and bassanite to anhydrite at Martian pressure and low temperatures.

On the one hand, the first dehydration process proposed is based on the work of Vaniman et al. [117], who observed that gypsum (grain size between 45 and 425  $\mu\text{m}$ ) started to lose water molecules 30 to 40 h at  $\sim 24$  °C and  $\text{RH} < 0.1\%$ . Desiccation to bassanite occurred at 600 h of exposure. In a later work, using gypsum geological forms, it took 150 h for dehydration process to begin, and between  $4 \cdot 10^3$  and  $4 \cdot 10^4$  h to completely dehydrate to bassanite. These results indicate that the time required to transform gypsum into bassanite can vary over two orders of magnitude depending on the crystal form and size. Moreover, this may represent what happens in the summer periods on Mars.

On the other hand, the second dehydration process proposed is based on the formation of bassanite through the dehydration Ca-sulfates at Martian winter conditions, under low pressure and temperature. In order to understand the mechanism for such dehydration, accelerated experiments simulating winter Martian conditions were carried in the laboratory. To do so, the following samples, instrumentation and methodology were employed

#### **4.3.3.1. Samples**

For this experiment, a mixture of the three Ca-sulfates was used. In order to obtain an equilibrium among the three phases, the mixture was left at RT in a desiccator for one month. The equilibrated mixture was characterized by XRD to confirm the relative abundance of each phase, which was 20% of gypsum, 65% of bassanite and 15% of anhydrite II.

#### **4.3.3.2. Instrumentation**

The mineralogical characterization of the initial mixture was performed by using the PANalytical Xpert PRO powder diffractometer. After the freeze-drying experiments, the molecular measurements were performed with the Renishaw InVia Raman spectrometer coupled with the Linkam THMS600/FH600 temperature-controlled stage. The Raman measurement conditions consisted of the use of the 532 nm excitation laser power, 10 s of exposure time, 50 % of laser power, 2 accumulations and a wavenumber range that went from 150 to 4000  $\text{cm}^{-1}$ . Furthermore, the Linkam stage was set to the temperature of the experiment, -52 °C.

In order to guarantee representativeness and to estimate the uncertainties of the results of the accelerated experiment, two equal samples were measured following the same freeze-drying process. In each of these samples 5 Raman measurements were performed.

### 4.3.3.3. Methodology

To simulate the thousand-year influence of environmental Martian conditions, sulfate samples were first frozen at  $-20\text{ }^{\circ}\text{C}$  to remove moisture. Then, they were lyophilized at  $-52 \pm 3\text{ }^{\circ}\text{C}$  and  $1 \pm 0.5\text{ mBar}$  with the Telstar Cryodos lyophilizer during three periods of time. Six samples were coupled to the lyophilizer, two of them were extracted at 50 h, other two at 144h and the last two at 214 h. The samples were molecularly measured as soon as they were extracted from the freeze dryer. After the experiment, they were stored at  $-30\text{ }^{\circ}\text{C}$ .

### 4.3.3.4. Results

After treating all Raman spectra (extracting background noise and removing cosmic rays), they all show a mixture of the three sulfates. Figure 4.43 shows the characteristic Raman spectra of the Ca-sulfates <sup>[98]</sup> acquired after 214 h of freeze-drying, including those  $-\text{OH}$  bands associated to gypsum and bassanite in the  $3500\text{-}3700\text{ cm}^{-1}$  range. However, the main band is broader than the regular one. This is because the analyzed samples were composed of mixtures of the three compounds. In this sense, the relative abundance of the three Ca-sulfates could be calculated by the deconvolution of the main Raman band (see zoomed area of the Figure 4.43).

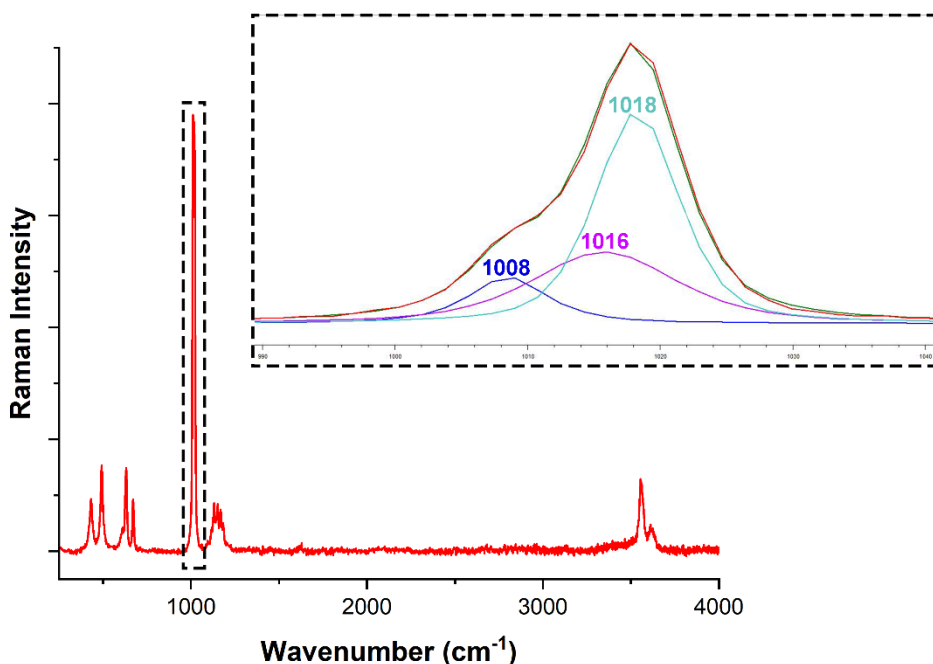


Figure 4.43. Raman spectrum of the mixture after freeze-frying 214h at  $-52 \pm 3\text{ }^{\circ}\text{C}$  and  $1 \pm 0.5\text{ mBar}$ . Likewise, the spectrum range from  $990\text{ to }1040\text{ cm}^{-1}$  was zoomed to obtain the

proposed band deconvolution, which was obtained after treatment with the Wire™ 4.2 software package.

In order to estimate the area under the three characteristic symmetric vibrations of the different Ca-sulfates, the Raman spectra were limited to the range of 990-1040  $\text{cm}^{-1}$  and then the main band of each spectrum was decomposed in three Gaussian-Lorentzian curves (50-50%). The result consisted of three bands with maximums at 1008, 1016 and 1018  $\text{cm}^{-1}$ , corresponding to gypsum, bassanite and anhydrite II, respectively, with uncertainties lower than 1  $\text{cm}^{-1}$ , as expected from the spectral resolution of the Raman spectrometer used. This fitting process was carried out with the Wire™ 4.2. software, which also provided the area for each curve, a value directly related to the relative amount of each compound. Therefore, the average of the areas of the three compounds, together with the uncertainties, were calculated. These values were plotted as a function of time elapsed in the cryogenic and low pressure experiment. As seen in Figure 4.44, the relative abundance of gypsum and bassanite decreased with time, while that of anhydrite increased.

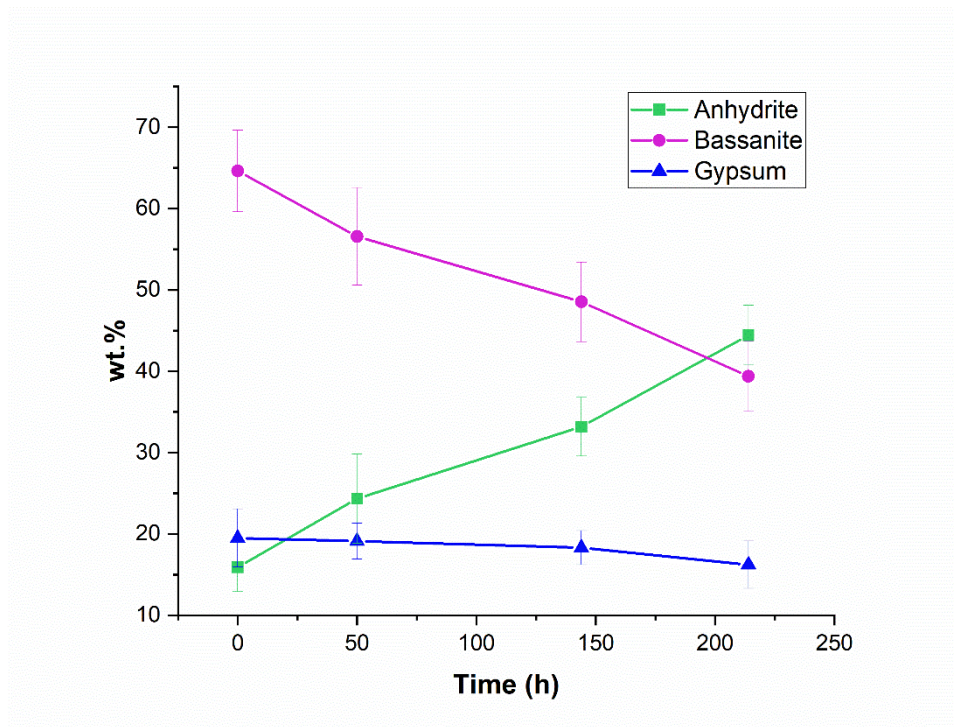


Figure 4.44. Evolution of the relative presence of gypsum, bassanite and anhydrite over time as obtained from the Raman spectra of the Ca-sulfate mixture sample subjected to  $-52 \pm 3$  °C and  $1 \pm 0.5$  mBar.

These experiments demonstrated the favorable conditions of Martian winter to dehydrate both gypsum and bassanite to anhydrite within years.

---

#### 4.3.3.5. Discussion

This experiment showed the gradual transformation of gypsum and/or bassanite to anhydrite at Martian pressure and winter temperature conditions, suggesting that the original hydrated compounds would be transformed to the anhydrous form as time elapses.

Therefore, in this work the dehydration of Ca-sulfate to anhydrite is proposed to take place following two complementary processes, dehydration due to high temperatures in summer and dehydration due to pressure and low temperatures in winter. This is because the temperature cycles on Mars involve about 150 sols per year of summer conditions, in which temperature dehydration occurs, and other 150 sols per year of winter conditions, in which pressure and low temperature dehydrates Ca-sulfates.

Depending on the pore size of hydrated Ca-sulfate deposits, only the most external parts of the initial gypsum (or bassanite) vein may be transformed into anhydrite II, leaving the hydrated forms in the inner part of the veins. This could explain why CheMin found samples with mixtures of anhydrite and other forms of hydrated Ca-sulfates, since CheMin analyses require a prior abrasion of the surface down to a few millimeters. In this sense, anhydrite together with gypsum and/or bassanite were identified.

Moreover, this fact explains the current presence of anhydrite identified on the surface of the veins analyzed in the Delta Front campaign. As it may occur with the CheMin measurements, hydrated Ca-sulfates could be present in the inner parts of the veins. This should be confirmed when the return samples come to Earth and non-destructive spectroscopic analyses are performed with high-resolution instruments.

#### 4.4. Conclusions

Thanks to the study of meteorites, simulation work in the laboratory and the analysis of data obtained by past and present missions, it has been possible to analyze the different processes through which the minerals present on the surface and/or subsurface of Mars have been formed.

It should be noted that all the processes studied form secondary mineral phases. Some of them can only be formed on Earth, which is why the aerobic oxidation processes studied in the meteorite section (Chapter 4.1) are not included in the following list.

- High-pressure processes

Original material from Mars (primary minerals) can lose crystallinity due to high-pressure events, such as meteorite formation. That is, a celestial body impacts with the planet in question generating high pressures and temperatures resulting from the impact.

- Anaerobic oxidation processes

Although oxidation processes were only appreciate in S-bearing compounds, the photochemical activity and the presence of oxidizing agents may oxidize primary and secondary mineral phases.

- Hydrothermal processes

Thanks to the simulation works, it is well known that some sulfates require hydrothermal conditions to be formed. On the one hand, gypsum, bassanite and syngenite can be formed in aqueous media, without the need for high temperatures. On the other hand, görgeyite and anhydrite only can precipitate under aqueous media and high temperature.

In addition, the study of meteorites has shown the presence of hydrated sulfates (jarosite and epsomite) outside the cracks, which also suggests that they were formed under hydrothermal conditions.

- High temperature processes

Due to high temperature, dehydration processes were observed for gypsum and syngenite. On the one hand, the dehydration of gypsum started at 433 K to form anhydrite III and the complete loss of hydration molecules occurred at 453 K. On the other hand, the syngenite dehydration process occur at 633 K, when anhydrite I/II started to form and, then, at 653 K the potassium sulfates arcanite and langbeinite form.

- Low temperature processes

---

Although no mineralogical alteration was observed only at low temperatures, it could be seen that the crystallinity of the hydration molecules of mixed-sulfates changes.

- Low pressure and low temperature

As could be observed in the Chapter 4.3 with the anhydrite II formation, at low pressures and low temperatures, dehydration occurs. This process can take place during Martian winters.

- Low humidity

Thanks to the work of Vaniman et al. <sup>[117]</sup>, it was possible to observe how gypsum may transform into bassanite and anhydrite II at very low relative humidity.

#### 4.5. References

- [1] Papike, J. J. Chemistry of the Rock-Forming Silicates: Ortho, Ring, and Single-Chain Structures. *Rev. Geophys.* **1987**, *25*, 1483. <https://doi.org/10.1029/RG025i007p01483>.
- [2] Taylor, S. R.; McLennan, S. *Planetary Crusts: Their Composition, Origin and Evolution*; Cambridge University Press: Cambridge, UK, 2008.
- [3] Ody, A.; Poulet, F.; Bibring, J.-P.; Loizeau, D.; Carter, J.; Gondet, B.; Langevin, Y. Global Investigation of Olivine on Mars: Insights into Crust and Mantle Compositions. *J. Geophys. Res. Planets* **2013**, *118*, 234. <https://doi.org/10.1029/2012JE004149>.
- [4] Váci, Z.; Agee, C. B.; Herd, C. D. K.; Walton, E.; Tschauner, O.; Ziegler, K.; Prakapenka, V. B.; Greenberg, E.; Monique-Thomas, S. Hydrous Olivine Alteration on Mars and Earth. *Meteorit. Planet. Sci.* **2020**, *55*, 1011. <https://doi.org/10.1111/maps.13479>.
- [5] Kuebler, K. E.; Jolliff, B. L.; Wang, A.; Haskin, L. A. Extracting Olivine (Fo–Fa) Compositions from Raman Spectral Peak Positions. *Geochim. Cosmochim. Acta* **2006**, *70*, 6201. <https://doi.org/10.1016/j.gca.2006.07.035>.
- [6] Ishibashi, H.; Arakawa, M.; Yamamoto, J.; Kagi, H. Precise Determination of Mg/Fe Ratios Applicable to Terrestrial Olivine Samples Using Raman Spectroscopy. *J. Raman Spectrosc.* **2012**, *43*, 331. <https://doi.org/10.1002/jrs.3024>.
- [7] Torre-Fdez, I.; Aramendia, J.; Gomez-Nubla, L.; Castro; Kepa; Madariaga, J. M. Geochemical Study of the Northwest Africa 6148 Martian Meteorite and Its Terrestrial Weathering Processes. *J. Raman Spectrosc.* **2017**, *48*, 1536. <https://doi.org/10.1002/jrs.5148>.
- [8] Torre-Fdez, I.; Ruiz-Galende, P.; Aramendia, J.; Gomez-Nubla, L.; Castro, K.; Arana, G.; Madariaga, J. M. New Quantitative Model to Determine Fayalite-Forsterite Content in Olivine Minerals by Raman Spectroscopy. In *50th Lunar and Planetary Science Conference*; 2019; Abs 2486.
- [9] Torre-Fdez, I. Raman Spectroscopy as a Key Technique for the Interpretation of Geochemistry of Mars and Other Celestial Bodies, University of the Basque Country (UPV/EHU), 2021.
- [10] Mouri, T.; Enami, M. Raman Spectroscopic Study of Olivine-Group Minerals. *J. Mineral. Petrol. Sci.* **2008**, *103*, 100. <https://doi.org/10.2465/jmps.071015>.
- [11] Ehlmann, B. L.; Bish, D. L.; Ruff, S. W.; Mustard, J. F. Mineralogy and Chemistry of Altered Icelandic Basalts: Application to Clay Mineral Detection and Understanding Aqueous Environments on

- 
- Mars. *J. Geophys. Res. Planets* **2012**, *117*, E00J16. <https://doi.org/10.1029/2012JE004156>.
- [12] Black, S. R.; Hynek, B. M.; McHenry, L. J.; McCollom, T.; Cameron, B.; Ludyan, J. Alteration Mineralogy and the Effect of Parent Lithology at Hydrothermal Mars Analog Sites: Initial Results from Hengill and Krafla Volcanoes, Iceland. In *48th Lunar and Planetary Science Conference*; The Woodlands, TX, USA, 2017; Abs 2003.
- [13] Catalano, J. G. Thermodynamic and Mass Balance Constraints on Iron-Bearing Phyllosilicate Formation and Alteration Pathways on Early Mars. *J. Geophys. Res. Planets* **2013**, *118*, 2124. <https://doi.org/10.1002/jgre.20161>.
- [14] King, R. J. Olivine Group. *Geol. Today* **2009**, *25*, 193. <https://doi.org/10.1111/j.1365-2451.2009.00730.x>.
- [15] Wiens, R. C.; Udry, A.; Beyssac, O.; Quantin-Nataf, C.; Mangold, N.; Cousin, A.; Mandon, L.; Bosak, T.; Forni, O.; McLennan, S. M.; Sautter, V.; Brown, A.; Benzerara, K.; Johnson, J. R.; Mayhew, L.; Maurice, S.; Anderson, R. B.; Clegg, S. M.; Crumpler, L.; Gabriel, T. S. J.; Gasda, P.; Hall, J.; Horgan, B. H. N.; Kah, L.; Legett, C.; Madariaga, J. M.; Meslin, P.-Y.; Ollila, A. M.; Poulet, F.; Royer, C.; Sharma, S. K.; Siljeström, S.; Simon, J. I.; Acosta-Maeda, T. E.; Alvarez-Llamas, C.; Angel, S. M.; Arana, G.; Beck, P.; Bernard, S.; Bertrand, T.; Bousquet, B.; Castro, K.; Chide, B.; Clavé, E.; Cloutis, E.; Connell, S.; Dehouck, E.; Dromart, G.; Fischer, W.; Fouchet, T.; Francis, R.; Frydenvang, J.; Gasnault, O.; Gibbons, E.; Gupta, S.; Hausrath, E. M.; Jacob, X.; Kalucha, H.; Kelly, E.; Knutsen, E.; Lanza, N.; Laserna, J.; Lasue, J.; Le Mouélic, S.; Leveille, R.; Lopez Reyes, G.; Lorenz, R.; Manrique, J. A.; Martinez-Frias, J.; McConnochie, T.; Melikechi, N.; Mimoun, D.; Montmessin, F.; Moros, J.; Murdoch, N.; Pilleri, P.; Pilorget, C.; Pinet, P.; Rapin, W.; Rull, F.; Schröder, S.; Shuster, D. L.; Smith, R. J.; Stott, A. E.; Tarnas, J.; Turenne, N.; Veneranda, M.; Vogt, D. S.; Weiss, B. P.; Willis, P.; Stack, K. M.; Williford, K. H.; Farley, K. A. Compositionally and Density Stratified Igneous Terrain in Jezero Crater, Mars. *Sci. Adv.* **2022**, *8*, eabo3399. <https://doi.org/10.1126/sciadv.abo3399>.
- [16] NASA. *PDS Planetary Data System*. Mars 2020: SuperCam (LIBS, Raman, Time-Resolved Fluorescence, VIS/IR, RMI). <https://pds-geosciences.wustl.edu/missions/mars2020/supercam.htm> (accessed 2023-02-27).
- [17] Kolesov, B. A.; Geiger, C. A. A Raman Spectroscopic Study of Fe-Mg Olivines. *Phys. Chem. Miner.* **2004**, *31*, 142. <https://doi.org/10.1007/s00269-003-0370-y>.
- [18] Lafuente, B.; Downs, R. T.; Yang, H.; Stone, N. The Power of Databases: The RRUFF Project. In *Highlights in Mineralogical*
-

- Crystallography*, Armsbruster, T., Danisi, R. M., Eds.; De Gruyter: Berlin, Germany, 2015; pp 1–30.
- [19] Dunham, E. T.; Balta, J. B.; Wadhwa, M.; Sharp, T. G.; McSween, H. Y. Petrology and Geochemistry of Olivine-phyric Shergottites LAR12095 and LAR12240: Implications for Their Petrogenetic History on Mars. *Meteorit. Planet. Sci.* **2019**, *54*, 811. <https://doi.org/10.1111/maps.13262>.
- [20] Wang, A.; Jolliff, B. L.; Haskin, L. A.; Kuebler, K. E.; Viskupic, K. M. Characterization and Comparison of Structural and Compositional Features of Planetary Quadrilateral Pyroxenes by Raman Spectroscopy. *Am. Mineral.* **2001**, *86*, 790. <https://doi.org/10.2138/am-2001-0703>.
- [21] Huang, E.; Chen, C. H.; Huang, T.; Lin, E. H.; Xu, J. Raman Spectroscopic Characteristics of Mg-Fe-Ca Pyroxenes. *Am. Mineral.* **2000**, *85*, 473. <https://doi.org/10.2138/am-2000-0408>.
- [22] Connolly, H. C.; Smith, C.; Benedix, G.; Folco, L.; Richter, K.; Zipfel, J.; Yamaguchi, A.; Chennaoui-Aoudjehane, H. The Meteoritical Bulletin, No. 92, 2007 September. *Meteorit. Planet. Sci.* **2007**, *42*, 1647.
- [23] Shkolyar, S.; Jaret, S. J.; Cohen, B. A.; Johnson, J. R.; Beyssac, O.; Madariaga, J. M.; Wiens, R. C.; Ollila, A.; Holm-Alwmark, S.; Liu, Y. Identifying Shocked Feldspar on Mars Using Perseverance Spectroscopic Instruments: Implications for Geochronology Studies on Returned Samples. *Earth. Moon. Planets* **2022**, *126*, 4. <https://doi.org/10.1007/s11038-022-09546-6>.
- [24] Fritz, J.; Assis Fernandes, V.; Greshake, A.; Holzwarth, A.; Böttger, U. On the Formation of Diaplectic Glass: Shock and Thermal Experiments with Plagioclase of Different Chemical Compositions. *Meteorit. Planet. Sci.* **2019**, *54*, 1533. <https://doi.org/10.1111/maps.13289>.
- [25] Hofmann, B. A. Meteorites: Messengers from the Early Solar System. *Chimia (Aarau)*. **2010**, *64*, 736. <https://doi.org/10.2533/chimia.2010.736>.
- [26] Zoppi, A.; Lofrumento, C.; Castellucci, E. M.; Migliorini, M. G. The Raman Spectrum of Hematite: Possible Indicator for a Compositional or Firing Distinction Among Terra Sigillata Wares. *Ann. Chim.* **2005**, *95*, 239. <https://doi.org/10.1002/adic.200590026>.
- [27] Araújo, E. S.; Libardi, J.; Faia, P. M.; de Oliveira, H. P. Hybrid ZnO/TiO<sub>2</sub> Loaded in Electrospun Polymeric Fibers as Photocatalyst. *J. Chem.* **2015**, *2015*, 1. <https://doi.org/10.1155/2015/476472>.
- [28] Wang, A.; Kuebler, K. E.; Jolliff, B. L.; Haskin, L. A. Raman

- 
- Spectroscopy of Fe-Ti-Cr-Oxides, Case Study: Martian Meteorite EETA79001. *Am. Mineral.* **2004**, *89*, 665. <https://doi.org/10.2138/am-2004-5-601>.
- [29] Christensen, P. R.; Morris, R. V.; Lane, M. D.; Bandfield, J. L.; Malin, M. C. Global Mapping of Martian Hematite Mineral Deposits: Remnants of Water-Driven Processes on Early Mars. *J. Geophys. Res. Planets* **2001**, *106*, 23873. <https://doi.org/10.1029/2000JE001415>.
- [30] Catling, D. C.; Moore, J. M. The Nature of Coarse-Grained Crystalline Hematite and Its Implications for the Early Environment of Mars. *Icarus* **2003**, *165*, 277. [https://doi.org/10.1016/S0019-1035\(03\)00173-8](https://doi.org/10.1016/S0019-1035(03)00173-8).
- [31] Muñoz-Iglesias, V.; Sánchez-García, L.; Carrizo, D.; Molina, A.; Fernández-Sampedro, M.; Prieto-Ballesteros, O. Raman Spectroscopic Peculiarities of Icelandic Poorly Crystalline Minerals and Their Implications for Mars Exploration. *Sci. Rep.* **2022**, *12*, 5640. <https://doi.org/10.1038/s41598-022-09684-x>.
- [32] Squyres, S. W.; Arvidson, R. E.; Bell, J. F.; Brückner, J.; Cabrol, N. A.; Calvin, W.; Carr, M. H.; Christensen, P. R.; Clark, B. C.; Crumpler, L.; Des Marais, D. J.; D'Uston, C.; Economou, T.; Farmer, J.; Farrand, W.; Folkner, W.; Golombek, M.; Gorevan, S.; Grant, J. A.; Greeley, R.; Grotzinger, J.; Haskin, L.; Herkenhoff, K. E.; Hviid, S.; Johnson, J.; Klingelhöfer, G.; Knoll, A.; Landis, G.; Lemmon, M.; Li, R.; Madsen, M. B.; Malin, M. C.; McLennan, S. M.; McSween, H. Y.; Ming, D. W.; Moersch, J.; Morris, R. V.; Parker, T.; Rice, J. W.; Richter, L.; Rieder, R.; Sims, M.; Smith, M.; Smith, P.; Soderblom, L. A.; Sullivan, R.; Wänke, H.; Wdowiak, T.; Wolff, M.; Yen, A. The Spirit Rover's Athena Science Investigation at Gusev Crater, Mars. *Science*. **2004**, *305*, 794. <https://doi.org/10.1126/science.3050794>.
- [33] Lagain, A.; Bouley, S.; Zanda, B.; Miljković, K.; Rajšić, A.; Baratoux, D.; Payré, V.; Doucet, L. S.; Timms, N. E.; Hewins, R.; Benedix, G. K.; Malarewic, V.; Servis, K.; Bland, P. A. Early Crustal Processes Revealed by the Ejection Site of the Oldest Martian Meteorite. *Nat. Commun.* **2022**, *13*, 3782. <https://doi.org/10.1038/s41467-022-31444-8>.
- [34] Jia, M.; Zhai, K.; Gao, M.; Wen, W.; Liu, Y.; Wu, X.; Zhai, S. Raman Spectra and X-Ray Diffraction of Merrillite at Various Temperatures. *Vib. Spectrosc.* **2020**, *106*, 103005. <https://doi.org/10.1016/j.vibspec.2019.103005>.
- [35] Adcock, C. T.; Hausrath, E. M.; Forster, P. M.; Tschauner, O.; Sefein, K. J. Synthesis and Characterization of the Mars-Relevant Phosphate Minerals Fe- and Mg-Whitlockite and Merrillite and a Possible Mechanism That Maintains Charge Balance during
-

- Whitlockite to Merrillite Transformation. *Am. Mineral.* **2014**, *99*, 1221. <https://doi.org/10.2138/am.2014.4688>.
- [36] Adcock, C. T.; Tschauer, O.; Hausrath, E. M.; Udry, A.; Luo, S. N.; Cai, Y.; Ren, M.; Lanzirotti, A.; Newville, M.; Kunz, M.; Lin, C. Shock-Transformation of Whitlockite to Merrillite and the Implications for Meteoritic Phosphate. *Nat. Commun.* **2017**, *8*, 14667. <https://doi.org/10.1038/ncomms14667>.
- [37] Franz, H. B.; King, P. L.; Gaillard, F. Sulfur on Mars from the Atmosphere to the Core. In *Volatiles in the Martian Crust*; Elsevier, 2019; pp 119–183. <https://doi.org/10.1016/B978-0-12-804191-8.00006-4>.
- [38] King, P. L.; McLennan, S. M. Sulfur on Mars. *Elements* **2010**, *6*, 107. <https://doi.org/10.2113/gselements.6.2.107>.
- [39] Huidobro, J.; Aramendia, J.; García-Florentino, C.; Ruiz-Galende, P.; Torre-Fdez, I.; Castro, K.; Arana, G.; Madariaga, J. M. Mineralogy of the RBT 04262 Martian Meteorite as Determined by Micro-Raman and Micro-X-ray Fluorescence Spectroscopies. *J. Raman Spectrosc.* **2022**, *53*, 450. <https://doi.org/10.1002/jrs.6291>.
- [40] El Mendili, Y.; Abdelouas, A.; Bardeau, J.-F. Insight into the Mechanism of Carbon Steel Corrosion under Aerobic and Anaerobic Conditions. *Phys. Chem. Chem. Phys.* **2013**, *15*, 9197. <https://doi.org/10.1039/c3cp50853f>.
- [41] Genchev, G.; Erbe, A. Raman Spectroscopy of Mackinawite FeS in Anodic Iron Sulfide Corrosion Products. *J. Electrochem. Soc.* **2016**, *163*, 333. <https://doi.org/10.1149/2.1151606jes>.
- [42] Wopenka, B. Raman Spectroscopic Investigation of Two Grains from Comet 81P/Wild 2: Information That Can Be Obtained beyond the Presence of Sp<sup>2</sup>-Bonded Carbon. *Meteorit. Planet. Sci.* **2012**, *47*, 565. <https://doi.org/10.1111/j.1945-5100.2011.01317.x>.
- [43] Lara, R. H.; Monroy, M. G.; Mallet, M.; Dossot, M.; González, M. A.; Cruz, R. An Experimental Study of Iron Sulfides Weathering under Simulated Calcareous Soil Conditions. *Environ. Earth Sci.* **2015**, *73*, 1849. <https://doi.org/10.1007/s12665-014-3540-y>.
- [44] King, P. L.; McSween, H. Y. Effects of H<sub>2</sub>O, PH, and Oxidation State on the Stability of Fe Minerals on Mars. *J. Geophys. Res.* **2005**, *110*, E12S10. <https://doi.org/10.1029/2005JE002482>.
- [45] Baccolo, G.; Delmonte, B.; Niles, P. B.; Cibin, G.; Di Stefano, E.; Hampai, D.; Keller, L.; Maggi, V.; Marcelli, A.; Michalski, J.; Snead, C.; Frezzotti, M. Jarosite Formation in Deep Antarctic Ice Provides a Window into Acidic, Water-Limited Weathering on Mars. *Nat. Commun.* **2021**, *12*, 436. <https://doi.org/10.1038/s41467-020-20705-z>.

- 
- [46] Sergeeva, A. V. Infrared Spectra of Alunite-Group Minerals Formed on Thermal Fields. *J. Appl. Spectrosc.* **2019**, *86*, 371. <https://doi.org/10.1007/s10812-019-00828-y>.
- [47] Wang, A.; Feldman, W. C.; Mellon, M. T.; Zheng, M. The Preservation of Subsurface Sulfates with Mid-to-High Degree of Hydration in Equatorial Regions on Mars. *Icarus* **2013**, *226*, 980. <https://doi.org/10.1016/j.icarus.2013.07.020>.
- [48] Fishbaugh, K. E.; Poulet, F.; Chevrier, V.; Langevin, Y.; Bibring, J.-P. On the Origin of Gypsum in the Mars North Polar Region. *J. Geophys. Res.* **2007**, *112*, E07002. <https://doi.org/10.1029/2006JE002862>.
- [49] Marion, G. M., Kargel, J. S. Stability of Magnesium Sulfate Minerals in Martian Environments. In *Lunar and Planetary Science Conference 2005*; 2005; p 2290.
- [50] Zhang, M. H. G.; Luhmann, J. G.; Bougher, S. W.; Nagy, A. F. The Ancient Oxygen Exosphere of Mars: Implications for Atmosphere Evolution. *J. Geophys. Res.* **1993**, *98*, 10915. <https://doi.org/10.1029/93JE00231>.
- [51] Wang, A.; Freeman, J. J.; Jolliff, B. L.; Chou, I.-M. Sulfates on Mars: A Systematic Raman Spectroscopic Study of Hydration States of Magnesium Sulfates. *Geochim. Cosmochim. Acta* **2006**, *70*, 6118. <https://doi.org/10.1016/j.gca.2006.05.022>.
- [52] Fritz, J.; Greshake, A.; Stöffler, D. Micro-Raman Spectroscopy of Plagioclase and Maskelynite in Martian Meteorites: Evidence of Progressive Shock Metamorphism. *Antarct. Meteor. Res.* **2005**, *18*, 96.
- [53] Usui, T.; Sanborn, M.; Wadhwa, M.; McSween Jr., H. Y. Petrology and Trace Element Geochemistry of Robert Massif 04261 and 04262 Meteorites, the First Examples of Geochemically Enriched Lherzolithic Shergottites. *Geochim. Cosmochim. Acta* **2010**, *74*, 7283. <https://doi.org/10.1016/j.gca.2010.09.010>.
- [54] Brotton, S. J.; Kaiser, R. I. In Situ Raman Spectroscopic Study of Gypsum (CaSO<sub>4</sub>·2H<sub>2</sub>O) and Epsomite (MgSO<sub>4</sub>·7H<sub>2</sub>O) Dehydration Utilizing an Ultrasonic Levitator. *J. Phys. Chem. Lett.* **2013**, *4*, 669. <https://doi.org/10.1021/jz301861a>.
- [55] Christensen, P. R.; Wyatt, M. B.; Glotch, T. D.; Rogers, A. D.; Anwar, S.; Arvidson, R. E.; Bandfield, J. L.; Blaney, D. L.; Budney, C.; Calvin, W. M.; Fallacaro, A.; Ferguson, R. L.; Gorelick, N.; Graff, T. G.; Hamilton, V. E.; Hayes, A. G.; Johnson, J. R.; Knudson, A. T.; McSween, H. Y.; Mehall, G. L.; Mehall, L. K.; Moersch, J. E.; Morris, R. V.; Smith, M. D.; Squyres, S. W.; Ruff, S. W.; Wolff, M. J. Mineralogy at Meridiani Planum from the Mini-TES Experiment on

- the Opportunity Rover. *Science*. **2004**, 306, 1733. <https://doi.org/10.1126/science.1104909>.
- [56] Toniazzo, V.; Mustin, C.; Portal, J. S.; Humbert, B.; Benoit, R.; Erre, R. Elemental Sulfur at the Pyrite Surfaces: Speciation and Quantification. *Appl. Surf. Sci.* **1999**, 143, 229. [https://doi.org/10.1016/S0169-4332\(98\)00918-0](https://doi.org/10.1016/S0169-4332(98)00918-0).
- [57] Xi, S.; Zhang, X.; Luan, Z.; Du, Z.; Li, L.; Liang, Z.; Lian, C.; Yan, J. Micro-Raman Study of Thermal Transformation of Sulfide and Oxysalt Minerals Based on the Heat Induced by Laser. *Minerals* **2019**, 9, 751. <https://doi.org/10.3390/min9120751>.
- [58] Vaniman, D. T.; Bish, D. L.; Ming, D. W.; Bristow, T. F.; Morris, R. V.; Blake, D. F.; Chipera, S. J.; Morrison, S. M.; Treiman, A. H.; Rampe, E. B.; Rice, M.; Achilles, C. N.; Grotzinger, J.; McLennan, S. M.; Williams, J.; Bell III, J.; Newsom, H.; Downs, R. T.; Maurice, S.; Sarrazin, P.; Yen, A. S.; Morookian, J. M.; Farmer, J. D.; Stack, K.; Milliken, R. E.; Ehlmann, B.; Summer, D. Y.; Berger, G.; Crisp, J. A.; Hurowitz, J. A.; Anderson, R.; DesMarais, D.; Stolper, E. M.; Edgett, K. S.; Gupta, S.; Spanovich, N.; Team, M. S. Mineralogy of a Mudstone at Yellowknife Bay, Gale Crater, Mars. *Science*. **2013**, 6169, 124380. <https://doi.org/10.1126/science.1243480>.
- [59] Morris, R. V.; Klingelhöfer, G.; Schöder, C.; Fleischer, I.; Ming, D. W.; Yen, A. S.; Gellert, R.; Arvidson, R. E.; Rodionov, D. S.; Crumpler, L. S.; Clark, B. C.; Cohen, B. A.; McCoy, T. J.; Mittlefehldt, D. W.; Schmidt, M. E.; de Souza, P. A.; Squyres, S. W. Iron Mineralogy and Aqueous Alteration from Husband Hill through Home Plate at Gusev Crater, Mars: Results from the Mössbauer Instrument on the Spirit Mars Exploration Rover. *J. Geophys. Res.* **2008**, 113, E12S42. <https://doi.org/10.1029/2008JE003201>.
- [60] Shebanova, O. N.; Lazor, P. Raman Spectroscopic Study of Magnetite (FeFe<sub>2</sub>O<sub>4</sub>): A New Assignment for the Vibrational Spectrum. *J. Solid State Chem.* **2003**, 174, 424. [https://doi.org/10.1016/S0022-4596\(03\)00294-9](https://doi.org/10.1016/S0022-4596(03)00294-9).
- [61] Zinin, P.; Tatsumi-Petrochilos, L.; Bonal, L.; Acosta, T.; Hammer, J.; Gilder, S.; Fuller, M. Raman Spectroscopy of Titanomagnetites: Calibration of the Intensity of Raman Peaks as a Sensitive Indicator for Their Ti Content. *Am. Mineral.* **2011**, 96, 1537. <https://doi.org/10.2138/am.2011.3745>.
- [62] Schwab, F. L. Sedimentary Petrology. In *Encyclopedia of Physical Science and Technology*; Elsevier, 2003; pp 495–529. <https://doi.org/10.1016/B0-12-227410-5/00678-5>.
- [63] Tosca, N. J.; McLennan, S. M. Chemical Divides and Evaporite Assemblages on Mars. *Earth Planet. Sci. Lett.* **2006**, 241, 21. <https://doi.org/10.1016/j.epsl.2005.10.021>.

- 
- [64] Barbieri, R.; Stivaletta, N. Continental Evaporites and the Search for Evidence of Life on Mars. *Geol. J.* **2011**, *46*, 513. <https://doi.org/10.1002/gj.1326>.
- [65] Bridges, J. Evaporite Mineral Assemblages in the Nakhilite (Martian) Meteorites. *Earth Planet. Sci. Lett.* **2000**, *176*, 267. [https://doi.org/10.1016/S0012-821X\(00\)00019-4](https://doi.org/10.1016/S0012-821X(00)00019-4).
- [66] Aubrey, A.; Cleaves, H. J.; Chalmers, J. H.; Skelley, A. M.; Mathies, R. A.; Grunthaler, F. J.; Ehrenfreund, P.; Bada, J. L. Sulfate Minerals and Organic Compounds on Mars. *Geology* **2006**, *34*, 357. <https://doi.org/10.1130/G22316.1>.
- [67] Tan, J.; Lewis, J. M. T.; Sephton, M. A. The Fate of Lipid Biosignatures in a Mars-Analogue Sulfur Stream. *Sci. Rep.* **2018**, *8*, 7586. <https://doi.org/10.1038/s41598-018-25752-7>.
- [68] Johnson, S. S.; Millan, M.; Graham, H.; Benison, K. C.; Williams, A. J.; McAdam, A.; Knudson, C. A.; Andrejkovičová, S.; Achilles, C. Lipid Biomarkers in Ephemeral Acid Salt Lake Mudflat/Sandflat Sediments: Implications for Mars. *Astrobiology* **2020**, *20*, 167. <https://doi.org/10.1089/ast.2017.1812>.
- [69] Goodwin, A.; Papineau, D. Biosignatures Associated with Organic Matter in Late Paleoproterozoic Stromatolitic Dolomite and Implications for Martian Carbonates. *Astrobiology* **2022**, *22*, 49. <https://doi.org/10.1089/ast.2021.0010>.
- [70] Chen, Y.; Sun, Y.; Liu, L.; Shen, J.; Qu, Y.; Pan, Y.; Lin, W. Biosignatures Preserved in Carbonate Nodules from the Western Qaidam Basin, NW China: Implications for Life Detection on Mars. *Astrobiology* **2022**, *23*, 172. <https://doi.org/10.1089/ast.2021.0196>.
- [71] Arvidson, R. E.; Squyres, S. W.; Bell, J. F.; Catalano, J. G.; Clark, B. C.; Crumpler, L. S.; de Souza, P. A.; Fairén, A. G.; Farrand, W. H.; Fox, V. K.; Gellert, R.; Ghosh, A.; Golombek, M. P.; Grotzinger, J. P.; Guinness, E. A.; Herkenhoff, K. E.; Jolliff, B. L.; Knoll, A. H.; Li, R.; McLennan, S. M.; Ming, D. W.; Mittlefehldt, D. W.; Moore, J. M.; Morris, R. V.; Murchie, S. L.; Parker, T. J.; Paulsen, G.; Rice, J. W.; Ruff, S. W.; Smith, M. D.; Wolff, M. J. Ancient Aqueous Environments at Endeavour Crater, Mars. *Science*. **2014**, *343*, 1248097. <https://doi.org/10.1126/science.1248097>.
- [72] Squyres, S. W.; Arvidson, R. E.; Bell, J. F.; Calef, F.; Clark, B. C.; Cohen, B. A.; Crumpler, L. A.; de Souza, P. A.; Farrand, W. H.; Gellert, R.; Grant, J.; Herkenhoff, K. E.; Hurowitz, J. A.; Johnson, J. R.; Jolliff, B. L.; Knoll, A. H.; Li, R.; McLennan, S. M.; Ming, D. W.; Mittlefehldt, D. W.; Parker, T. J.; Paulsen, G.; Rice, M. S.; Ruff, S. W.; Schröder, C.; Yen, A. S.; Zacny, K. Ancient Impact and Aqueous Processes at Endeavour Crater, Mars. *Science*. **2012**, *336*, 570. <https://doi.org/10.1126/science.1220476>.
-

- [73] Yen, A. S.; Ming, D. W.; Vaniman, D. T.; Gellert, R.; Blake, D. F.; Morris, R. V.; Morrison, S. M.; Bristow, T. F.; Chipera, S. J.; Edgett, K. S.; Treiman, A. H.; Clark, B. C.; Downs, R. T.; Farmer, J. D.; Grotzinger, J. P.; Rampe, E. B.; Schmidt, M. E.; Sutter, B.; Thompson, L. M. Multiple Stages of Aqueous Alteration along Fractures in Mudstone and Sandstone Strata in Gale Crater, Mars. *Earth Planet. Sci. Lett.* **2017**, *471*, 186. <https://doi.org/10.1016/j.epsl.2017.04.033>.
- [74] McLennan, S. M.; Bell, J. F.; Calvin, W. M.; Christensen, P. R.; Clark, B. C.; de Souza, P. A.; Farmer, J.; Farrand, W. H.; Fike, D. A.; Gellert, R.; Ghosh, A.; Glotch, T. D.; Grotzinger, J. P.; Hahn, B.; Herkenhoff, K. E.; Hurowitz, J. A.; Johnson, J. R.; Johnson, S. S.; Jolliff, B.; Klingelhöfer, G.; Knoll, A. H.; Learner, Z.; Malin, M. C.; McSween, H. Y.; Pockock, J.; Ruff, S. W.; Soderblom, L. A.; Squyres, S. W.; Tosca, N. J.; Watters, W. A.; Wyatt, M. B.; Yen, A. Provenance and Diagenesis of the Evaporite-Bearing Burns Formation, Meridiani Planum, Mars. *Earth Planet. Sci. Lett.* **2005**, *240*, 95. <https://doi.org/10.1016/j.epsl.2005.09.041>.
- [75] Grotzinger, J. P.; Summer, D. Y.; Kah, L. C.; Stack, K.; Gupta, S.; Edgar, L.; Rubin, D.; Lewis, K.; Schieber, J.; Mangold, N.; Milliken, R.; Conrad, P. G.; DesMarais, D.; Farmer, J.; Siebach, K.; Calef III, F. J.; Hurowitz, J. A.; McLennan, S. M.; Ming, D.; Blake, D.; Gellert, R.; Mahaffy, P.; Wiens, R. C.; Maurice, S.; Grant, J. A.; Wilson, S.; Anderson, R. C.; Beegle, L.; Arvidson, R.; Hallet, B.; Sletten, R. S.; Rice, M.; Bell III, J. F.; Griffes, J.; Ehlmann, B.; Anderson, R. B.; Bristow, T. F.; Dietrich, W. E.; Dromart, G.; Eigenbrode, J. L.; Fraeman, A. A.; Hardgrove, C.; Herkenhoff, K.; Jandura, L.; Kocurek, G.; Lee, S.; Leshin, L. A.; Leveille, R.; Limonadi, D.; Maki, J.; McCloskey, S.; Meyer, M.; Minitti, M.; Newsom, H.; Oehler, D.; Okon, A.; Palucis, M.; Parker, T.; Rowland, S.; Schmidt, M.; Squyres, S.; Steele, A.; Stolper, E.; Summons, R.; Treiman, A.; Williams, R.; Yingst, A.; Team, M. S. A Habitable Fluvio-Lacustrine Environment at Yellowknife Bay, Gale Crater, Mars. *Science*. **2014**, *343*, 12427.
- [76] Nachon, M.; Clegg, S. M.; Mangold, N.; Schröder, S.; Kah, L. C.; Dromart, G.; Ollila, A.; Johnson, J. R.; Oehler, D. Z.; Bridges, J. C.; Le Mouélic, S.; Forni, O.; Wiens, R. C.; Anderson, R. B.; Blaney, D. L.; Bell, J. F.; Clark, B.; Cousin, A.; Dyar, M. D.; Ehlmann, B.; Fabre, C.; Gasnault, O.; Grotzinger, J.; Lasue, J.; Lewin, E.; Léveillé, R.; McLennan, S.; Maurice, S.; Meslin, P.-Y.; Rapin, W.; Rice, M.; Squyres, S. W.; Stack, K.; Sumner, D. Y.; Vaniman, D.; Wellington, D. Calcium Sulfate Veins Characterized by ChemCam/Curiosity at Gale Crater, Mars. *J. Geophys. Res. Planets* **2014**, *119*, 1991. <https://doi.org/10.1002/2013JE004588>.
- [77] Rapin, W.; Meslin, P.-Y.; Maurice, S.; Vaniman, D.; Nachon, M.;

- 
- Mangold, N.; Schröder, S.; Gasnault, O.; Forni, O.; Wiens, R. C.; Martínez, G. M.; Cousin, A.; Sautter, V.; Lasue, J.; Rampe, E. B.; Archer, D. Hydration State of Calcium Sulfates in Gale Crater, Mars: Identification of Bassanite Veins. *Earth Planet. Sci. Lett.* **2016**, *452*, 197. <https://doi.org/10.1016/j.epsl.2016.07.045>.
- [78] Goodrich, C. A.; Treiman, A. H.; Filiberto, J.; Gross, J.; Jercinovic, M. K.  $2\text{O}$ -Rich Trapped Melt in Olivine in the Nakhla Meteorite: Implications for Petrogenesis of Nakhrites and Evolution of the Martian Mantle. *Meteorit. Planet. Sci.* **2013**, *48*, 2371. <https://doi.org/10.1111/maps.12226>.
- [79] Combs, L. M.; Udry, A.; Howarth, G. H.; Righter, M.; Lapen, T. J.; Gross, J.; Ross, D. K.; Rahib, R. R.; Day, J. M. D. Petrology of the Enriched Poikilitic Shergottite Northwest Africa 10169: Insight into the Martian Interior. *Geochim. Cosmochim. Acta* **2019**, *266*, 435. <https://doi.org/10.1016/j.gca.2019.07.001>.
- [80] Agee, C. B.; Wilson, N. V.; McCubbin, F. M.; Ziegler, K.; Polyak, V. J.; Sharp, Z. D.; Asmerom, Y.; Nunn, M. H.; Shaheen, R.; Thiemens, M. H.; Steele, A.; Fogel, M. L.; Bowden, R.; Glamoclija, M.; Zhang, Z.; Elardo, S. M. Unique Meteorite from Early Amazonian Mars: Water-Rich Basaltic Breccia Northwest Africa 7034. *Science*. **2013**, *339*, 780. <https://doi.org/10.1126/science.1228858>.
- [81] Santos, A. R.; Agee, C. B.; McCubbin, F. M.; Shearer, C. K.; Burger, P. V.; Tartèse, R.; Anand, M. Petrology of Igneous Clasts in Northwest Africa 7034: Implications for the Petrologic Diversity of the Martian Crust. *Geochim. Cosmochim. Acta* **2015**, *157*, 56. <https://doi.org/10.1016/j.gca.2015.02.023>.
- [82] Stolper, E. M.; Baker, M. B.; Newcombe, M. E.; Schmidt, M. E.; Treiman, A. H.; Cousin, A.; Dyar, M. D.; Fisk, M. R.; Gellert, R.; King, P. L.; Leshin, L.; Maurice, S.; McLennan, S. M.; Minitti, M. E.; Perrett, G.; Rowland, S.; Sautter, V.; Wiens, R. C.; MarsScienceLaboratoryTeam. The Petrochemistry of Jake\_M: A Martian Mugearite. *Science*. **2013**, *341*, 6153. <https://doi.org/10.1126/science.1239463>.
- [83] Sautter, V.; Toplis, M. J.; Wiens, R. C.; Cousin, A.; Fabre, C.; Gasnault, O.; Maurice, S.; Forni, O.; Lasue, J.; Ollila, A.; Bridges, J. C.; Mangold, N.; Le Mouélic, S.; Fisk, M.; Meslin, P.-Y.; Beck, P.; Pinet, P.; Le Deit, L.; Rapin, W.; Stolper, E. M.; Newsom, H.; Dyar, D.; Lanza, N.; Vaniman, D.; Clegg, S.; Wray, J. J. In Situ Evidence for Continental Crust on Early Mars. *Nat. Geosci.* **2015**, *8*, 605. <https://doi.org/10.1038/ngeo2474>.
- [84] Cousin, A.; Sautter, V.; Payré, V.; Forni, O.; Mangold, N.; Gasnault, O.; Le Deit, L.; Johnson, J.; Maurice, S.; Salvatore, M.; Wiens, R. C.; Gasda, P.; Rapin, W. Classification of Igneous Rocks Analyzed by

- ChemCam at Gale Crater, Mars. *Icarus* **2017**, 288, 265. <https://doi.org/10.1016/j.icarus.2017.01.014>.
- [85] Crowley, J. K. Visible and Near-Infrared (0.4–2.5 Mm) Reflectance Spectra of Playa Evaporite Minerals. *J. Geophys. Res.* **1991**, 96, 16231. <https://doi.org/10.1029/91JB01714>.
- [86] Alexandrowicz, Z.; Marszałek, M.; Rzepa, G. Distribution of Secondary Minerals in Crusts Developed on Sandstone Exposures. *Earth Surf. Process. Landforms* **2014**, 39, 320. <https://doi.org/10.1002/esp.3449>.
- [87] Alexandrowicz, Z.; Marszałek, M. Efflorescences on Weathered Sandstone Tors in the Stone Town Nature Reserve in Ciężkowice (the Outer Carpathians, Poland)—Their Geochemical and Geomorphological Controls. *Environ. Sci. Pollut. Res.* **2019**, 26, 37254. <https://doi.org/10.1007/s11356-019-06778-4>.
- [88] Borchet, H.; Muir, R. O. *Salt Deposits : The Origin, Metamorphism and Deformation of Evaporites*; London, Pinceton, J. J.: Van Nostrand: London, UK, 1964.
- [89] Benedetto, C.; Forti, P.; Galli, E.; Rossi, A. Chemical Deposits in Volcanic Caves of Argentina. *Int. J. Speleol.* **1998**, 27, 155. <https://doi.org/10.5038/1827-806X.27.1.16>.
- [90] Hayrhofer, H. *Görgeyit, Ein Neues Mineral Aus Der Ischler Salzlagertstätte, Neues Jahrbuch Für Mineralogie; Monatshefte*, 1953.
- [91] Klopogge, J. T.; Hickey, L.; Duong, L. V.; Martens, W. N.; Frost, R. L. Synthesis and Characterization of  $K_2Ca_5(SO_4)_6 \cdot H_2O$ , the Equivalent of Görgeyite, a Rare Evaporite Mineral. *Am. Mineral.* **2004**, 89, 266. <https://doi.org/10.2138/am-2004-2-302>.
- [92] Liu, Y. Raman, Mid-IR, and NIR Spectroscopic Study of Calcium Sulfates and Mapping Gypsum Abundances in Columbus Crater, Mars. *Planet. Space Sci.* **2018**, 163, 35. <https://doi.org/10.1016/j.pss.2018.04.010>.
- [93] García-Florentino, C.; Gomez-Nubla, L.; Huidobro, J.; Torre-Fdez, I.; Ruíz-Galende, P.; Aramendia, J.; Hausrath, E. M.; Castro, K.; Arana, G.; Madariaga, J. M. Interrelationships in the Gypsum–Syngenite–Görgeyite System and Their Possible Formation on Mars. *Astrobiology* **2021**, 21, 332. <https://doi.org/10.1089/ast.2020.2319>.
- [94] Nazari-Sharabian, M.; Aghababaei, M.; Karakouzian, M.; Karami, M. Water on Mars—A Literature Review. *Galaxies* **2020**, 8, 40. <https://doi.org/10.3390/galaxies8020040>.
- [95] Huidobro, J.; Aramendia, J.; Arana, G.; Madariaga, J. M. Reviewing

- 
- in Situ Analytical Techniques Used to Research Martian Geochemistry: From the Viking Project to the MMX Future Mission. *Anal. Chim. Acta* **2022**, *1197*, 339499. <https://doi.org/10.1016/j.aca.2022.339499>.
- [96] Tuschel, D. Raman Thermometry. *Spectroscopy* **2016**, *31*, 8.
- [97] Sutherland, G. B. B. M. Experiments on the Raman Effect at Very Low Temperatures. *Proc. R. Soc. London A Math. Phys. Eng. Sci.* **1933**, *141*, 535. <https://doi.org/10.1098/rspa.1933.0137>.
- [98] Prieto-Taboada, N.; Laserna, O.; Martínez-Arkarazo, I.; Olazabal, M.; Madariaga, J. Raman Spectra of the Different Phases in the CaSO<sub>4</sub>-H<sub>2</sub>O System. *Anal. Chem.* **2014**, *86*, 10131. <https://doi.org/10.1021/ac501932f>.
- [99] Science, N. *Mars Facts / Temperature*. Mars Exploration Program. <https://mars.nasa.gov/all-about-mars/facts/#?c=inSPACE&s=distance> (accessed 2023-01-23).
- [100] Chio, C. H.; Sharma, S. K.; Muenow, D. W. Micro-Raman Studies of Gypsum in the Temperature Range between 9 K and 373 K. *Am. Mineral.* **2004**, *89*, 390. <https://doi.org/10.2138/am-2004-2-320>.
- [101] Couty, R.; Velde, B.; Besson, J. M. Raman Spectra of Gypsum under Pressure. *Phys. Chem. Miner.* **1983**, *10*, 89. <https://doi.org/10.1007/BF00309590>.
- [102] Madariaga, J. M.; Huidobro, J.; García-Florentino, C.; Aramendia, J.; Ruiz-Galende, P.; Torre-Fdez, I.; Hausrath, E. M.; Castro, K.; Arana, G. Temperature Transformation of Calcium and Potassium Martian Sulfates as Seen by Exomars 2022 RLS-like Raman Instrument. In *Europlanet Science Congress 2020*; 2020; Abs 1063. <https://doi.org/10.5194/epsc2020-1063>.
- [103] Schofield, P. F.; Wilson, C. C.; Knight, K. S.; Stretton, I. C. Temperature Related Structural Variation of the Hydrous Components in Gypsum. *Zeitschrift für Krist. - Cryst. Mater.* **2000**, *215*, 707. <https://doi.org/10.1524/zkri.2000.215.12.707>.
- [104] Weber, I.; Böttger, U.; Pavlov, S. G.; Stojic, A.; Hübers, H.-W.; Jessberger, E. K. Raman Spectra of Hydrous Minerals Investigated under Various Environmental Conditions in Preparation for Planetary Space Missions. *J. Raman Spectrosc.* **2018**, *49*, 1830. <https://doi.org/10.1002/jrs.5463>.
- [105] Xie, S.; Iglesia, E.; Bell, A. T. Effects of Temperature on the Raman Spectra and Dispersed Oxides. *J. Phys. Chem. B* **2001**, *105*, 5144. <https://doi.org/10.1021/jp004434s>.
- [106] Minceva-Sukarova, B.; Sherman, W. F.; Wilkinson, G. R. The Raman Spectra of Ice (I<sub>h</sub>, II, III, V, VI and IX) as Functions of
-

- Pressure and Temperature. *J. Phys. C Solid State Phys.* **1984**, *17*, 5833. <https://doi.org/10.1088/0022-3719/17/32/017>.
- [107] Goncharov, A. F. Raman Spectroscopy at High Pressures. *Int. J. Spectrosc.* **2012**, *2012*, 1. <https://doi.org/10.1155/2012/617528>.
- [108] Cuscó, R.; Gil, B.; Cassabois, G.; Artús, L. Temperature Dependence of Raman-Active Phonons and Anharmonic Interactions in Layered Hexagonal BN. *Phys. Rev. B* **2016**, *94*, 155435. <https://doi.org/10.1103/PhysRevB.94.155435>.
- [109] Huidobro, J.; Coloma, L.; Poblacion, I.; Arana, G.; Aramendia, J.; García-Florentino, C.; Hausrath, E. M.; Castro, K.; Madariaga, J. M. Temperature Influence on Raman Spectra on Calcium and Potassium Sulfates on the Martian Surface. In *54th Lunar and Planetary Science Conference (LPSC)*; The Woodlands, TX, USA, 2023; Abs 2364.
- [110] Huidobro, J.; Aramendia, J.; Coloma, L.; Poblacion, I.; García-Florentino, C.; Castro, K.; Arana, G.; Madariaga, J. M. Low Temperature Influence on the Raman Spectra of Calcium-Rich Sulfates on Mars: Raman Thermometer for Low Temperatures. In *International Symposium on Ice in a sustainable society (ISS)*; Bilbao, Spain, 2022; Abs 88A3691.
- [111] Miller, J. N. Basic Statistical Methods for Analytical Chemistry. Part 2. Calibration and Regression Methods. A Review. *Analyst* **1991**, *116*, 3. <https://doi.org/10.1039/an9911600003>.
- [112] Draper, N. R.; Smith, H. Checking the Straight Line Fit. In *Applied Regression Analysis*; Draper, N., Smith, H., Eds.; Wiley-Interscience, 1998; pp 47–77. <https://doi.org/10.1002/9781118625590.ch2>.
- [113] Vaniman, D. T.; Martínez, G. M.; Rampe, E. B.; Bristow, T. F.; Blake, D. F.; Yen, A. S.; Ming, D. W.; Rapin, W.; Meslin, P.-Y.; Morookian, J. M.; Downs, R. T.; Chipera, S. J.; Morris, R. V.; Morrison, S. M.; Treiman, A. H.; Achilles, C. N.; Robertson, K.; Grotzinger, J. P.; Hazen, R. M.; Wiens, R. C.; Sumner, D. Y. Gypsum, Bassanite, and Anhydrite at Gale Crater, Mars. *Am. Mineral.* **2018**, *103*, 1011. <https://doi.org/10.2138/am-2018-6346>.
- [114] Li, Z.; Demopoulos, G. P. Model-Based Construction of Calcium Sulfate Phase-Transition Diagrams in the HCl–CaCl<sub>2</sub>–H<sub>2</sub>O System between 0 and 100 °C. *Ind. Eng. Chem. Res.* **2006**, *45*, 4517. <https://doi.org/10.1021/ie0600339>.
- [115] Hannington, M.; Herzig, P.; Stoffers, P.; Scholten, J.; Botz, R.; Garbe-Schönberg, D.; Jonasson, I. R.; Roest, W. First Observations of High-Temperature Submarine Hydrothermal Vents and Massive Anhydrite Deposits off the North Coast of Iceland. *Mar. Geol.* **2001**,

---

177, 199. [https://doi.org/10.1016/S0025-3227\(01\)00172-4](https://doi.org/10.1016/S0025-3227(01)00172-4).

- [116] Kuhn, T.; Herzig, P. .; Hannington, M. .; Garbe-Schönberg, D.; Stoffers, P. Origin of Fluids and Anhydrite Precipitation in the Sediment-Hosted Grimsey Hydrothermal Field North of Iceland. *Chem. Geol.* **2003**, *202*, 5. [https://doi.org/10.1016/S0009-2541\(03\)00207-9](https://doi.org/10.1016/S0009-2541(03)00207-9).
- [117] Vaniman, D. T.; Chipera, S. J. Transformations of Mg- and Ca-Sulfate Hydrates in Mars Regolith. *Am. Mineral.* **2006**, *91*, 1628. <https://doi.org/10.2138/am.2006.2092>.



# CHAPTER 5

## LABORATORY STUDIES TO UNDERSTAND MARTIAN HABITABILITY

**“THE REAL VOYAGE OF DISCOVERY CONSISTS  
NOT IN SEEKING NEW LANDSCAPES, BUT IN  
HAVING NEW EYES” – Marcel Proust**

---



---

## 5. LABORATORY STUDIES TO UNDERSTAND MARTIAN HABITABILITY

Assessing the habitability of the red planet has been one of the main objectives for scientists during years. In fact, all Martian landing missions have tried to identify past or present presence of biosignatures on the surface or subsurface of the planet. This is the reason why the landing site of most of the surface missions were usually selected in areas where water was present at some point of the history of Mars.

However, under current Martian conditions, unprotected organic molecules would be degraded by one of the following destructive agents: (1) ultraviolet radiation, which would interact with the first millimeters of the regolith; (2) oxidation processes at the surface/subsurface, which could be efficient until 100 cm of depth depending on the characteristic of the materials; and/or (3) energetic particles radiation from galactic cosmic rays, which would interact with organics in the first meters of depth<sup>[1]</sup>. In this sense, at present, clay minerals and hydrated minerals are the most viable targets for tracing the history of Martian habitability, as they are compounds that are capable of preserving organic molecules despite the Martian inhospitable environment.

Moreover, other structures that probed to preserve organic molecules and microorganisms, protecting them from critical conditions on Earth have also been found on Mars by Opportunity<sup>[2]</sup>, Spirit<sup>[3]</sup> and Curiosity<sup>[4]</sup> rovers. Some of those formations are known as microbialites<sup>[5]</sup>, which are organo-sedimentary deposits formed by sediment trapping, binding and *in situ* precipitation of calcium carbonate due to the growth and metabolic activities of microorganisms<sup>[6,7]</sup>. Although microbialites have not been analyzed in depth on Mars, similar structures that may also protect microorganisms from the harsh Martian conditions were observed.

Hence, the presence of certain key mineral on Martian soils can trace the history of the planet's habitability. Likewise, biosignatures preservation is also expected within protective matrices, such as clay minerals or microbialites<sup>[8,9]</sup>.

Therefore, this thesis chapter discusses two possible trajectories for tracing Martian habitability over time: (1) the geochemistry of Martian soils as reservoirs of key minerals for habitability; (2) the evaluation of the potential preservation of different clay minerals; and (3) the characterization and study of a Martian analog in the form of microbialites, which are remains left by microorganisms.

## 5.1. Soils at Jezero Crater Floor and at different landing sites of past missions

Martian surface is composed by two morphologically different materials: outcrops and soils. On the one hand, outcrops are defined as visible exposures of bedrock or other geologic formations at the surface, including paver rocks, boulders, cumulates, all the rigid and immovable materials from centimeters to meters in size, etc. On the other hand, soils include fine grained materials, coarse grained materials, crusts, small pebbles, materials from microns to milliliters in size that are potentially movable by the wind.

Recently, a generic definition of soils for terrestrial like bodied has been proposed as: an unconsolidated and chemically weathered surficial layer of fine-grained mineral and organic materials exceeding centimeter scale thickness, with or without coarse elements and cemented portions <sup>[10]</sup>.

Due to all these features, Martian soils are critically important for understanding the history of Mars, past potentially habitable environments, returned samples and future human exploration.

Crustless soils (cemented portions) are easily moved by winds and dust devils, with consequence formation of dunes and ripples that are not stable over time in the same location. In contrast, crusted soils are not easily moved and have been recorded in immovable dunes and ripples. However, very little is known of the entire Martian surface and some authors suggest using the term soil to indicate the unconsolidated sediment of Mars <sup>[11]</sup>.

Martian soil also represents the surface that would interact most immediately with future human explorers, as they will need *in situ* resources to colonize Mars. The characterization of local unconsolidated sediments is a work in continuous progress. In this chapter the main characteristics of soils at different landing sites will be reviewed aiming to search for common grouping, if possible, of the analyzed soils in past and current Martian missions.

### 5.1.1. Soils at the Viking landing site

The Viking landers analyzed 15 elements by XRF in 21 samples <sup>[12]</sup> and a first mineralogical and petrological implications were published elsewhere <sup>[13]</sup>. It was the first time to differentiate duricrusts (crust soils) from unconsolidated fine-grained soils on Mars. After a thorough recalibration of the XRF instruments the new elemental composition, expressed as percent oxide, was published by Clark et al. <sup>[14]</sup> in 1982, for 9 samples at the Chryse Planitia (the Viking 1 landing site) and for 8 samples at Utopia Planitia (the Viking 2 landing site).

Unfortunately, sodium cannot be measured by XRF and some problems with the spectrometer of the Viking 2 did not allowed to obtain accurate enough values for aluminum and magnesium. By using the values for 2 duricrust samples and for 4 fine soil samples, the mean concentration values (Table 5.1) were calculated in this work for the Viking 1 landing site. As seen, totals do not add up to 100% because (a) Na and K values are not included, (b) chlorine could be present as oxychloride anions, (c) there could be carbonate minerals, and (d) hydrated mineral phases could be present.

*Table 5.1. Mean elemental composition of duricrust and fine soils at the Viking 1 landing site on Chryse Planitia [14].*

Type of Soil	SiO <sub>2</sub>	TiO <sub>2</sub>	Al <sub>2</sub> O <sub>3</sub>	FeO <sub>T</sub>	MgO	CaO	SO <sub>3</sub>	Cl	Total
Duricrust	42,5±3,0	0,60±0,15	7,0±2,9	16,0±3,5	6,5±4,0	5,7±1,3	9,3±2,8	0,9±0,3	88,3±7,4
Fines	43,5±3,0	0,70±0,15	7,3±2,9	16,4±3,5	5,8±4,0	6,0±1,3	6,6±2,8	0,7±0,3	86,8±7,4

Although duricrusts seem to be enriched in chlorine, sulfur and magnesium, the high uncertainty values derived from the XRF measurements do not allow to observe significant differences in the elemental composition of duricrust and fines. The Viking mission science team suggested that trends in the variation of elemental composition at Viking landing sites are evidence of multiple geochemical components in the soils [14].

Later, in 1993, Clark et al. [15] proposed the minimum geochemical components of the Martian soils from the final results of the XRF instruments, by using a linear least squares fitting to analyze variations of elemental concentrations between pairs of element. That work concluded on the need of only a two components model to explain the observed diversity in the XRF concentrations. On the one hand, component A represents 84% of the nominal sample, and includes all Si, Al, Ca and most (>75%) or all Fe, with Ti associated with that Fe. On the other hand, component B, representing 16% of the nominal sample, includes Mg, S, and Cl, with Mg associated with Cl and S (about 60-100 %), leaving some of the Mg (<40%) associated with silicate minerals.

### **5.1.2. Soils at the Pathfinder landing site**

Pathfinder was the first Martian mission including an APXS for the elemental characterization of samples. This instrument analyzed 6 soil samples and 5 rock targets, obtaining linear correlations between Si, Ti, Al and Mg with S in the rock values [16].

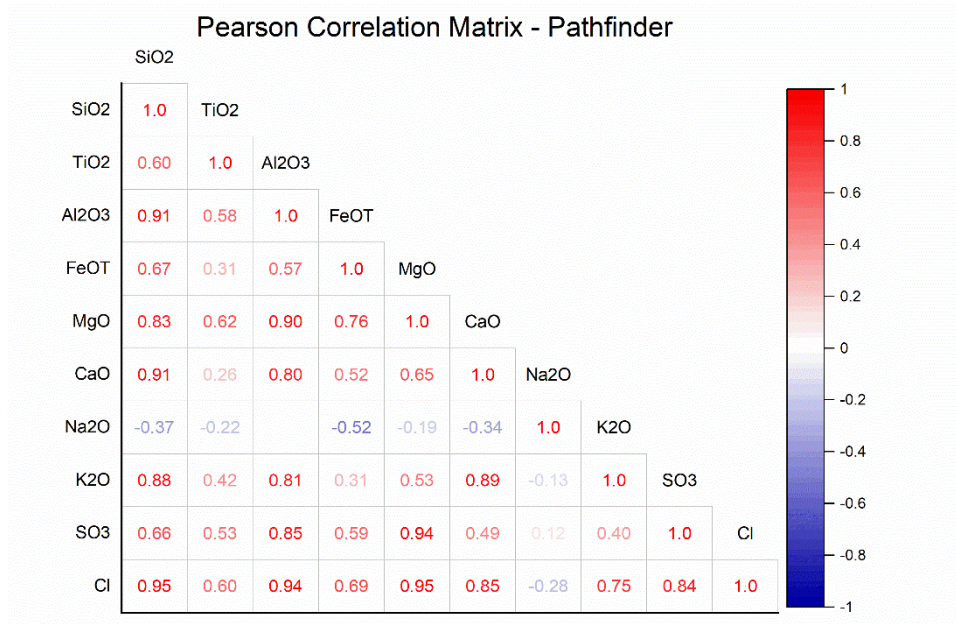
In this work, the original, not normalized values of the percent element concentrations (as oxides) of 6 soil samples have been treated PCA. Sample 1 is the disturbed soil after landing (it was collected about 10 cm from the surface), sample 6 was declared by the mission as cemented soil, while samples 1-4 were assigned to undisturbed soils, i.e. crust soils. The average elemental composition (in percent oxides) of these 3 soils is summarized in Table 5.2.

Table 5.2. Mean elemental composition of soils at the Pathfinder landing site

Type of Soil	SiO <sub>2</sub>	TiO <sub>2</sub>	Al <sub>2</sub> O <sub>3</sub>	FeO <sub>T</sub>	MgO	CaO	Na <sub>2</sub> O	K <sub>2</sub> O	SO <sub>3</sub>	Cl	Total
Disturbed	35,7±1,8	0,84±0,14	5,18±0,49	11,6±1,2	5,5±0,8	4,8±0,7	1,61±0,63	0,14±0,07	2,8±0,6	0,35±0,07	68,6±2,6
Fines	44,6±5,6	1,07±0,26	7,88±0,92	15,3±3,0	7,1±1,1	5,6±1,2	2,08±1,22	0,24±0,12	5,3±1,1	0,59±0,20	89,7±6,8
Cemented	52,2±2,6	1,11±0,20	9,21±0,92	13,6±1,3	7,2±1,1	7,4±1,1	2,03±0,81	0,51±0,10	5,4±1,1	0,71±0,20	99,3±3,7

The Pearson's Coefficient of Correlation obtained in the PCA treatment (see Table 5.3) for all samples show a high positive correlation among Si, Cl, Al, Ca, K and Mg, while Na is the only element with a negative correlation.

Table 5.3. Pearson's Coefficient of Correlation among elements from the 6 soil samples.



Observing the values in Table 5.2, the so called “cemented soil”, in spite of its consolidated rock-like appearance, could be misinterpreted as a crustal soil. This is not because it has a total sum of oxides close to 100%, which

---

means that the minerals explaining the elemental data could not be hydrated, carbonates could not be present, and probably chlorine is totally as chloride probably bound to magnesium, as extracted from the correlation analysis.

On the contrary, the “disturbed soil” from the landing impact shows an opposite composition with very low totals, suggesting the presence of volatiles like carbonate, hydrated phases and probably oxychlorine minerals, at depths higher than 10 cm.

The average composition of the other four soil samples is quite close to the fine soils at the Viking 1 landing site. If we add the Na and K values, i.e.  $2,32 \pm 1,22$  of Ares Vallis fines to the total of Chryse Planitia (shown in Table 5.1), we obtain  $89,1 \pm 7,5\%$  for those soils, suggesting their classification as fine grained soil, probably with the absence of crust.

The concentration uncertainties of Ares Vallis soils are lower than those reported for the Chryse Planitia soils, due to the better performance of the APXS instrument with regard to the XRF one. Moreover, data for Na and K are more accurate.

It is interesting to emphasize the high correlation of Mg with S and Cl, and in less extent with Al and Si. This is in agreement with the distribution of component B in the Viking soils, suggesting the presence of salts containing MgO, SO<sub>3</sub>, and Cl in the analyzed soils of Chryse Planitia and Ares Vallis landing sites.

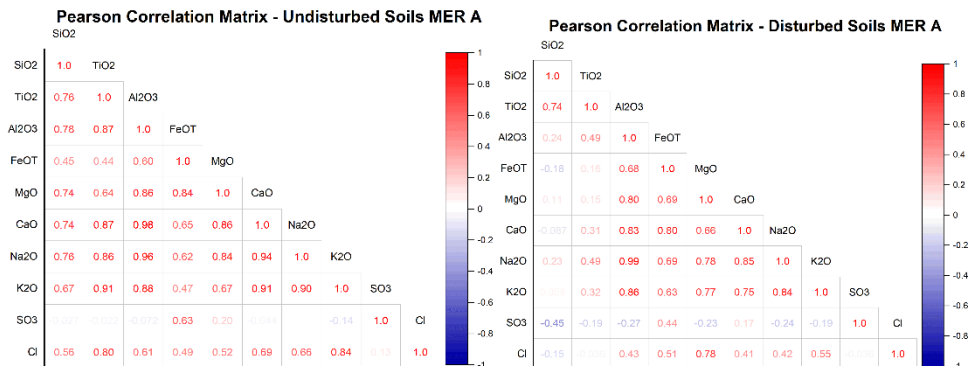
### **5.1.3. Soils at the MER traverse sites**

The MER rovers were also equipped with an APXS for the elemental characterization. The most recent report of oxide abundance measured by APXS was published in September 2021 on the PDS Geoscience Node site <sup>[17]</sup>.

Spirit rover explored Columbia Hills, Gusev crater, from sol 1410 to sol 2169, and just before getting embedded in the 8 m Toy crater, the rover broke a thin sulfate-rich soil crust that covered an underlying mix of sulfate and basaltic sands <sup>[18]</sup>. In this PhD Thesis, the element oxide abundances of disturbed and undisturbed soils were treated by PCA and CA chemometric tools.

Table 5.4 shows the Pearson's Coefficient of Correlation obtained in our CA treatment for undisturbed and disturbed soils analyzed by Spirit (MER A).

Table 5.4. Pearson's Coefficient of Correlation among elements from the undisturbed and disturbed soil samples analyzed by Spirit rover at Columbia Hills, Gusev crater, Mars.



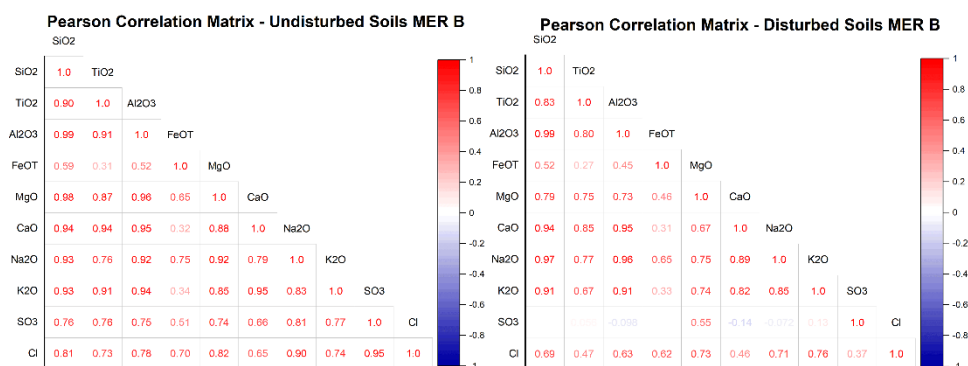
The most interesting finding of the CA for undisturbed soils is the correlation of SO<sub>3</sub> with FeO<sub>T</sub>, and the absence of correlation of sulfate with other cations. This is in agreement with the experimental observation when the rover wheels excavated soils discovering ferric-sulfate materials just beneath the crusty surface layer [18]. For undisturbed soils, there are also important correlation between chlorine and K, Ca, Na and Mg, suggesting that crusts in the soils of Columbia Hills (Gale crater, Mars) are enriched in iron-sulfate salts and chlorine (probably oxychlorine) salts of potassium, calcium, sodium and magnesium salts.

For disturbed soils sulfate is barely correlated with Fe and is not correlated to other cations. However, chlorine is highly correlated to Mg, and to K in a lower extent. Thus, fine grained soils down the surface of Columbia Hills are enriched in chlorine salts of magnesium and potassium.

Spirit detected highly altered Fe-oxyhydroxides (by Mossbauer measurements) during this traverse over Columbia Hills [18]. As their crusty soils are enriched in iron-sulfate salts, it looks like dissolved iron bounded to dissolved sulfates to form iron-sulfate compounds at the surface, being one of the salts acting as cementer for the crusty soils. Both undisturbed and disturbed soils showed the absence of correlation between sulfate and chlorine related compounds.

Opportunity rover explored Meridiani Planum sites and analyzed bedrocks, soils and even metallic meteorites [19]. The undisturbed and disturbed soils analyzed by the Opportunity rover were also subjected to Correlation Analysis. Table 5.5 shows the Pearson's Coefficient of Correlation obtained in our CA treatment for undisturbed and disturbed soils analyzed by Opportunity (MER B).

Table 5.5. Pearson's Coefficient of Correlation among elements from the undisturbed and disturbed soil samples analyzed by Opportunity rover at Meridiani Planum, Mars.



The undisturbed soils of Meridiani Planum showed an important correlation between sulfate and chlorine compounds, in contrast to the observation for Columbia Hill undisturbed soils. These soils of Meridiani Planum showed an important correlation between sulfate and Na, K, Mg and to less extent Ca. A similar correlation is observed for chlorine. Thus, a variety of sulfate and chlorine salts may act as cementers of the crusty soils at Meridiani Planum.

For disturbed soils, the situation is completely different. Sulfate is barely correlated to magnesium, it is not correlated to any other cation and it is slightly correlated to chlorine. However, chlorine is correlated to potassium, magnesium and sodium. These correlations of disturbed (the fine grained fraction) soils at Meridiani Planum is similar to some extent to the correlations for disturbed soils at Columbia Hills.

To visualize the differences among the soils of the traverses analyzed by Spirit and Opportunity, a PCA was performed with the four types of soils. Figure 5.1 shows the scores and loading plots we obtained with the whole set of soil data from MER A and MER B rovers, together with the 95% confidence level boundary for both MER A and MER B soils.

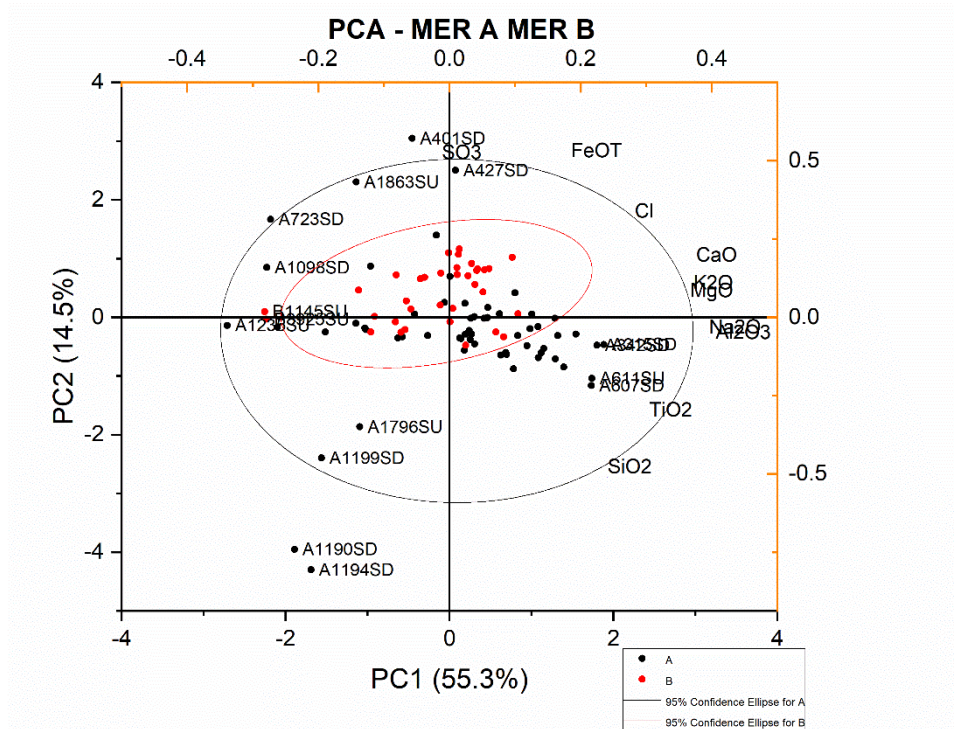


Figure 5.1. Score and loading plots of the whole set of data used in Tables 5.4 and 5.5.

The two first PCs explain 70% of the total variance. As seen, the data of MER B soils (points in red referred to the reddish axis) show a lower diversity than soils of MER A, while there is not a clear grouping between disturbed and undisturbed soils.

The total amount of oxides for both MER A and MER B soils is always below 80%, showing the important contribution of volatile compounds (carbonates, oxychlorides, hydrated minerals). Apart from the sulfate-enriched soils, the sulfate abundance varies between 1 and 6% for undisturbed soils and between 4 and 14% for disturbed ones. There is not a clear distinction between the chlorine concentrations for disturbed and undisturbed soils, being always in the range of 0,2 to 0,8 %Cl. As seen, the amount of sulfates is higher than those of chlorine-based salts, representing an important fraction of the whole set of altered minerals (phyllosilicates mainly) in the soils.

#### 5.1.4. Soils at the Phoenix landing site

The analysis performed by the Phoenix lander WCL equipment of water soluble salts in soils showed an average  $\text{ClO}_4^-$  concentration of  $2.4 \pm 0.2$  mM and  $0.54 \pm 0.07$  mM of  $\text{Cl}^-$ . That dissolved perchlorate concentration

---

correspond to an equivalent amount of 0.4-0.6 %  $\text{ClO}_4^-$  if all the perchlorate salts were soluble enough <sup>[20]</sup>. The chemical modelling of dissolved ions suggested  $\text{ClO}_4^-$  mainly found as  $\text{Mg}(\text{ClO}_4)_2$  with minor amounts of Ca and/or Na perchlorates. Chloride was about of 20-25% of the total perchlorate concentration.

This analysis by the Phoenix wet chemistry laboratory also showed  $5.3 \pm 1.5$  mM of  $\text{SO}_4^{2-}$  equivalent to  $1.1 \pm 0.3\%$  of soluble sulfate compounds in the soil <sup>[21]</sup>. Taken into account the dissolved concentration of other cations, the chemical modelling of the data is consistent with a major magnesium-sulfate mineral (epsomite was suggested) and a minor calcium-sulfate (gypsum was suggested). In the molar scale, the ration of dissolved  $\text{SO}_3/\text{Cl} \sim 2.2 \pm 0.2$ , while in the solid oxide fraction  $\text{SO}_3/\text{Cl} \sim 2.3 \pm 0.7$ .

Sulfate crusts on Mars have been proposed as resulting from the alteration of *in situ* sulfides and pyroxenes by melt water leading to their formation <sup>[22]</sup>, and these observations from multiple landing sites on Mars indicate the importance of salts in Martian soil crusts.

#### **5.1.5. Soils at Gale crater up to sol 100. The Rocknest dune shadow and indurated soils**

The MSL on board Curiosity rover was equipped with three instruments, CheMin, to perform XRD analysis, the APXS, to perform XRF analysis, and ChemCam, to perform LIBS analysis, to check the geochemistry of bedrocks and soils at Gale crater.

As the mission is still at work, here we give information on the soils analyzed up to sol 100 because they are representative of soil diversity at Gale crater. One of such soils was analyzed by those four instruments, the Rocknest dune shadow, an unconsolidated (equivalent to disturbed soils of MER landing sites) material taken from an aeolian dune shadow <sup>[23]</sup>. The aeolian bedform at Rocknest is quite similar to coarse-grained ripples encountered at Gusev by the MER Spirit <sup>[18]</sup> and at Meridiani Planum by the MER Opportunity <sup>[19]</sup> in that a coarse-grained, indurated, dust-coated surface overlies an interior of markedly finer sediment. These finer sediments were mainly sampled to perform the analysis with Chemin and SAM instruments, while APXS and ChemCam performed the analysis on the remaining soil surface.

Rocknest had both crystalline (54.7%) and X-Ray amorphous component (45.3%). The crystalline component is basaltic, like in other Martian soils, composed of plagioclase feldspar, forsteritic olivine, the pyroxenes augite and pigeonite and a minor amount (1.5%) of anhydrite; consequently, the amorphous component must contain water altered basaltic minerals (phyllosilicates) and salts. The SAM instrument analyzed Rocknest for volatile species and organic molecules [24], and detected  $\text{H}_2\text{O} > \text{SO}_2 > \text{CO}_2 > \text{O}_2$ . As the crystalline phases did not include these species as a part of their structure, they must either be present in the amorphous component or be present in the crystalline component at levels below the XRD detection limit of CheMin. This information is consistent with the presence of hydrated compounds, sulfate salts and carbonates, either hydrated or anhydrous.

Rocknest soils pressed by wheels of the rover (called Rocknest Portage, that are indurated soils) were directly analysed by the APXS instrument, without taken any sample. The results are showed in Table 5.6, and compared with averaged indurated (undisturbed) soils at Gusev crater (MER A crust soils) and Meridiani Planum (MER B crust soils).

Table 5.6. Undisturbed soils at Rocknest portage site, compared with the average undisturbed soils at Gusev crater (average of 48 sites) and Meridiani Planum (average of 48 sites). Taken from table 2 of the work of Blake et al. [23].

	Rocknest	Gusev	Meridiani
Number	1*	48†	29†
SiO <sub>2</sub> (wt %)	42.88 ± 0.47	46.1 ± 0.9	45.7 ± 1.3
TiO <sub>2</sub>	1.19 ± 0.03	0.88 ± 0.19	1.03 ± 0.12
Al <sub>2</sub> O <sub>3</sub>	9.43 ± 0.14	10.19 ± 0.69	9.25 ± 0.50
Cr <sub>2</sub> O <sub>3</sub>	0.49 ± 0.02	0.33 ± 0.07	0.41 ± 0.06
Fe <sub>2</sub> O <sub>3</sub> + FeO	19.19 ± 0.12	16.3 ± 1.1	18.8 ± 1.2
MnO	0.41 ± 0.01	0.32 ± 0.03	0.37 ± 0.02
MgO	8.69 ± 0.14	8.67 ± 0.60	7.38 ± 0.29
CaO	7.28 ± 0.07	6.30 ± 0.29	6.93 ± 0.32
Na <sub>2</sub> O	2.72 ± 0.10	3.01 ± 0.30	2.21 ± 0.18
K <sub>2</sub> O	0.49 ± 0.01	0.44 ± 0.07	0.48 ± 0.05
P <sub>2</sub> O <sub>5</sub>	0.94 ± 0.03	0.91 ± 0.31	0.84 ± 0.06
SO <sub>3</sub>	5.45 ± 0.10	5.78 ± 1.25	5.83 ± 1.04
Cl	0.69 ± 0.02	0.70 ± 0.16	0.65 ± 0.09
Br (µg/g)	26 ± 6	53 ± 46	100 ± 111
Ni	446 ± 29	476 ± 142	457 ± 97
Zn	337 ± 17	270 ± 90	309 ± 87
Sum (wt %)	99.85	99.88	99.88
Cl/SO <sub>3</sub>	0.13 ± 0.02	0.12 ± 0.02	0.11 ± 0.01

The uncertainties for most of the APXS measurements at Rocknest are lower than similar APXS measurements with Spirit and Opportunity

---

instruments. As seen, the abundances of  $\text{SiO}_2$ ,  $\text{CaO}$ , and  $\text{Na}_2\text{O}$ , do not match among the three sites. The ratio of solid chlorine/sulfate is the same for the three locations, with an average of  $\text{SO}_3/\text{Cl} \sim 8.3 \pm 1.4$ . Comparing this value with the one obtained for Phoenix soils, using dissolved concentrations ( $\text{SO}_3/\text{Cl} \sim 2.3 \pm 0.7$ ), the presence of a higher amount of insoluble sulfates with regard to soluble ones must be considered for undisturbed (crusted, or indurated) soils.

ChemCam observations on the first 100 sols account for 139 LIBS points. Those analysed in the walls left in the dune after taken the samples shown strong emissions from hydrogen <sup>[25]</sup>. Comparison of this result with those of CheMin and SAM suggests that ChemCam detections of hydrogen in soils most likely correspond to the  $\text{H}_2\text{O}$  (hydrated salts) and/or  $-\text{OH}$  (phyllosilicates) associated with the amorphous component detected by CheMin. As stated before, the perchlorate salts seem to be soluble compounds while part of the sulfate salt are soluble and other important part is formed by insoluble sulfate minerals.

Figure 5.2 shows the traverse of the first 100 sols, from the Bradbury landing site to the entry of Yellow Knife Bay, through the Rocknest area (see Figure 5.2 A). The Image taken with the RMI on the vertical profile of the trench dug performed to collect the sand shadow analysed by CheMin, APXS and SAM, showed a crust of about 1-2 mm thick, with small coarse grain size material and bellow a homogeneous fine-grained soil. The fine-grained soils are mafic and enriched in hydrated compounds as shown by the high hydrogen LIBS signals, while the coarse-grained soils are more felsic and anhydrous <sup>[25]</sup>.

Other RMI images on surface soils found in those first 100 sols show a diversity of soil targets, that range from homogeneous soils made of fine-sand particles (Figure 5.2 C) to mixtures of fines and pebbles with typical grain sizes of  $<4$  mm, classified as "fine gravels" (Figure 5.2 D). Observe the pits left by the laser shots after the ChemCam LIBS analysis. A chemometric analysis on the LIBS spectra (cluster analysis by using ICA, Independent Component Analysis, and PLS2, Partial Least Square), revealed a compositional trend between two endmembers, a mafic component (cluster 1 or mafic type, with the strongest H signals among the soil targets) and a alkali-, silica-rich component (cluster 2 or felsic type with high Si, Na, and K signals, and H signal like those of anhydrous calibration targets). Cluster 3 is formed by the spectra on small pebbles with high Mg and Na, and low H signals.

The eight points of Crestaurum (Figure 5.2 C) and Beaulieu point#1 (Figure 5.2 D) belong to cluster 1, i.e. the points showing a deeper hole after the LIBS shots, that looks unconsolidated soils. Beaulieu points #2, #3 and #4 belong to cluster 2, while Beaulieu point #5 and points of Epworth on top of the Rocknest dune belong to cluster 3. The mean composition of cluster 1 is close to the APXS composition of Rocknest Portage and to the composition of the dust measured by ChemCam on the surfaces of rocks.

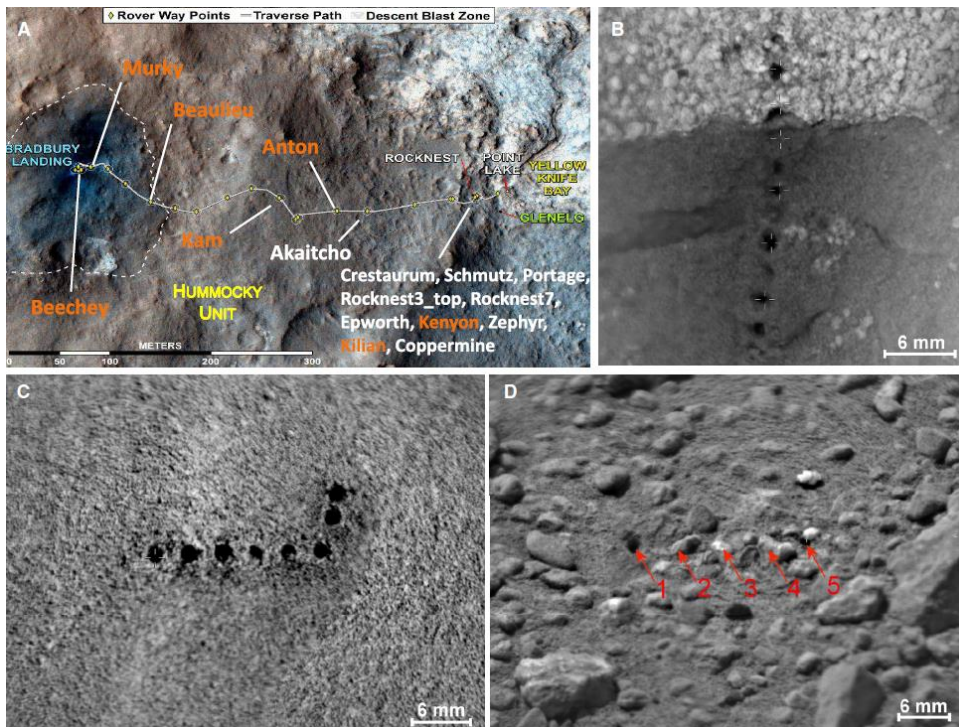


Figure 5.2. ChemCam analysis of soil targets: (A) Rover traverse and locations where soils targets (until sol 100) were analyzed by ChemCam. All the analyzed soils were of mafic nature (cluster 1), except those at names in orange that were of felsic nature (cluster 2). (B) Vertical raster of pits left by the laser shot in the points analyzed by ChemCam on the trench dug at Rocknest sand shadow (Epworth3, sol 84). (C) Homogeneous fine-grained soil (Crestaurum, sol 83). (D) Heterogeneous soil containing pebbles of different (< 4 mm) size (Beaulieu, sol 33). Image taken from figure 1 of reference <sup>[25]</sup>.

### 5.1.6. Crust soils at the Jezero crater, Mars

For the Mars 2020 mission, understanding the Martian soils is an essential task in order to meet some of its objectives, such as to a) determine whether life ever existed on Mars, b) characterize the climate of Mars, c) characterize its geology, and d) prepare for human exploration <sup>[26]</sup>. In this regard, the Perseverance rover explored the soil of the Jezero crater until sol 378, when the Crater Floor Science Campaign ended.

---

A comprehensive understanding of soils is also valuable to the success of the Mars Sample Return Program <sup>[27]</sup> and to the future design of manned missions.

Soils crusts represent increased cohesion of material at the surface, and have been reported at all previous mission landing sites. On Mars, soil crusts can also protect subsurface minerals from direct exposure to Martian surface conditions, allowing otherwise unstable minerals to persist at depth <sup>[28]</sup>. An understanding of these crusts and their origins may therefore shed light on potentially habitable environments at or near the surface in the ancient Mars. In addition to thin surface crusts, Martian soil is weakly cohesive to depths of 10 cm or more. Understanding soil crusts and subsurface cohesion through *in situ* measurements on Mars is also critical to understanding returned soil samples. This is because the spatial distribution in returned samples will not be preserved within the sample tube after sampling <sup>[29]</sup>. Despite the prevalence and importance of Martian surface crusts, however, their characteristics and formative mechanisms remain poorly understood.

The observations reported above this chapter for undisturbed soils at the different landing sites indicate the importance of salts in Martian soil crusts. On Earth, studies of sulfate rich minerals have detected amino acids <sup>[9]</sup> and lipids <sup>[30]</sup> revealing the utility of these salt-rich deposits for capturing and preserving molecular markers of past life. Sulfate minerals and salt crusts have also been shown to be effective at trapping whole organisms within crystals, protecting surficial microorganisms from the surface environment and impeding their detection <sup>[31]</sup>.

The whole set of instruments on board the Perseverance rover were used to characterize soils all along the traverse of the crater floor unit at Jezero crater, aiming to understand soil crusts in Jezero crater, their formation mechanisms, and their importance to sample return and human exploration. In this chapter, the measurements and results related to SuperCam will be described.

#### **5.1.6.1. Experimental section**

All LIBS observations (SuperCam instrument) of soils up to sol 378 were analyzed in this study, including the LIBS observations of rocks that contained soils on them. Table 5.7 summarizes the analyzed soils in the Crater Floor Campaign. The dusty rock Naltsos (sol 126) was included to compare with the PIXL data. SuperCam's RMI provides pictures for local context and site imaging at a high-resolution. The 110-mm SuperCam

telescope, with a focal length of 563 mm, allows to take RGB color images of 2048x2048 pixels with a CMOS camera over a bandwidth from ~375 to ~655 nm. This is useful to preselect and visualize grains, textures, color differences, and other features of the potential soil targets (contextualizing them in their respective geomorphological settings), which can help interpret further chemical analyses. RMI data are available on the Planetary Data System <sup>[17]</sup>.

The LIBS data set at each point analyzed contains information on the 30 successive shots at the same point. The LIBS measurements of the soils were analyzed in the following ways. First, the hydrogen independent component analysis (ICA) score, which is a unitless measure of the hydrogen peak that can correspond to hydrogen content <sup>[32]</sup>, was examined as a function of shot number, to analyze differences with depth. The recovered H component is shown for the 10 points of the raster executed on the Queh\_eh\_Scam soil (sol 115). The average hydrogen ICA score of points 6-10 (the top 5 points are removed to avoid the effect of dust) was compared with the average of the deepest 10 shots (shots 21 to 30) of each sample to determine whether a statistically significant decrease in H from the surface was observed; the averages of scores 6-10 were also compared to determine whether different points were above or below the average of all of the points.

For comparison with the RMI images of the soils, we also measured the standard deviation of the total emissivity of the LIBS measurements for shots >10. The standard deviation of the total emissivity of the LIBS measurement has been previously shown to indicate the presence of a coarse grain versus a fine grain <sup>[32]</sup>. Soils at the Crater Floor unit show a natural break into two groups between 11 and 12 %. Therefore, standard deviations of the total emissivity of <11.5% were interpreted as more likely to be coarse grains, and standard deviations of the total emissivity of >11.5% were interpreted as more likely to be fine-grained soils, and were compared with RMI images. The SuperCam total emissivity data are included in the Planetary Data System <sup>[17]</sup>.

The LIBS major element oxide composition data comprising the eight most common major elements <sup>[33]</sup>, the H and S and Cl scores averaged for each point were analyzed using PCA to check for different elemental correlations. To account for grain size, coarse grains were removed based on a standard deviation of the total emissivity of >11.4% as described above. PCA analysis was also performed for selected shot-to-shot data including Naltsos for comparison with the PIXL data.

---

A special subset of soil surfaces includes soils that were disturbed by the wheel track, including targets Rougon (sol 282), Brandis (sol 302), Chandon (sol 315) and Toudon (sol 333). Those Points that were disturbed were not included in the PCA analysis of the SuperCam points, but were analyzed separately, averaged and compared to the average of the undisturbed soils that are high in H, and the VISIR measurements of Toudon as described below.

Reflectance spectra in the NIR were collected by the SuperCam IR spectrometer on various regolith targets. The field of view of the IR instrument is 1.15 mrad, which corresponds to a footprint of ~2.3 mm for a mast-to-target distance of 2 m. This implies that, for fine soils where the particle size is less than the diameter of the laser beam (250-350  $\mu\text{m}$ ) overall homogeneous materials are observed by the spectrometer. This also implies that the surface measured in VNIR is larger than the LIBS footprint (0.25–0.45 mm) and that comparison of LIBS and VNIR data might not always be straightforward due to the different field of views of both spectrometers.

Table 5.7. LIBS points used in this work up to sol 378<sup>[17]</sup>.

Target	Sol	Points	Comments
Daa	357	1, 4-10	2 and 3 are on a rock
Toudon	333	1-9	4-9 = disturbed
Sigonce	319	1-10	
Chandon	315	1, 5, 10	only 1,5,10 in focus; 10 = disturbed
Tanaron	313	1,5,10	only 1,5,10 in focus
Brandis	302	1-10	all points disturbed - not used due to apparent rock surface
Rougon	282	1-10	4-10 = disturbed
Courbaissa	238	2-3	points 2-3 in soil on a rock
Vaire	236	1-10	
Vaire	214	1-10	
Chambares	185	1-10	
Reglet	151	8-10	soil at the edge of a paver
Clave	150	1-10	
Croix	145	1-10	
Beujeau	140	6	soil on a rock
Roque	137	1	soil next to a rock
Whoosh	123	1-10	
Cheskeh	116	1-10	
Que eh scam	115	1-10	
Lha tsaadah	110	1-10	
Hastaa	106	1-10	
Asdzoh	103	1-4	soil at the edge of a rock
Sei	84	1-5	
Naakih	84	1-5	
A koo	72	1-10	
Naltsos	126	1-5	on dusty rock for comparison with PIXL analyses

### 5.1.6.2. Results

Figure 5.3 summarizes the location of soil crusts identified along the rover traverse. Soil crusts were apparent at 45 of 101 rover stops evaluated with images from the different cameras on board Perseverance rover. Crusts

---

were evident also at 2 of 6 locations where helicopter flights crossed wheel tracks. There was clear evidence of soil crust in 4 of the 8 coring/abrasion locations. These results likely represent an underestimate of the presence of soil crusts in the study area, because soil crusts are detected most readily when relatively extensive disturbances occur by the wheels or coring/abrasion activities and can be examined closely. These results indicate that the process of crust formation is widespread in the study area on the floor of Jezero crater, consistent with observations at previous landing sites on Mars.

An examination of the average H score in shots 6-10 versus the deepest 10 shots show that most points indicate either 1) a statistically significant decrease from shots 6-10 to the deepest 10 shots (92 points total), or 2) the H score of the surface, even though it does not show a statistically significant decrease, is above the average H score (56 total points), with a few points not corresponding to either of these trends (12 total points). Figure 5.4 A shows an RMI of the Que\_ah\_Scam target, with Figure 5.4 B showing the H points for points 1-10 (indicated in Figure 5.4 A), and whether or not they decrease from the surface. Figure 5.4 B illustrates the most common types of variation in the H score with depth throughout the early mission; the greatest number of points are on coarse grains with a decrease in the H score from the surface (65 points), with a nearly equal number of fine-grained points that do not decrease from the surface (50 points), with a substantial number of points that are fine-grained with a decrease in H from the surface (27), followed by small numbers of fine soils that are consistently low in H (7), coarse grains that are consistently high in H (6), and coarse grains that are consistently low in H (5) (Figure 5.4 C). These measurements were all made during the day time, and hydration may differ at night.

The greatest number of points are coarse grains with a decrease in the H score from the surface (65 points from samples A\_koo, Naakih, Hastaa, Lha\_tsaadah, Que\_Eh\_Scam, Cheskeh, Whoosh, Croix, Clave, Chambares, Vaire 214 and 236, Beaujeu, Rougon, Tanaron, Sigonce, Toudon, and Daa), with a nearly equal number of fine-grained points that do not decrease from the surface (50 points from samples Akoo, Sei, Naakih, As\_dzoh, Lha\_tsaadah, Que\_Eh\_Scam, Cheskeh, Whoosh, Roque, Croix, Clave, Reglet, Chambares, Vaire 214 and 236, Courbaissa, Chandon, Sigonce, and Daa), with a substantial number of points that are fine-grained with a decrease in H from the surface (27 points from samples Akoo, Sei, Naakih, As\_dzoh, Hastaa, Lha\_tsaadah, Que\_Eh\_Scam, Cheskeh, Croix, Clave, Chambares, Vaire 214 and 236, Courbaissa, Rougon, Sigonce, and Daa), followed by small numbers of fine soil that are consistently low in H (7 points from samples As\_dzoh, Hastaa,

Lha\_tsaadah, Whoosh, and Sigonce), coarse grains that are consistently high in H (6 from samples Cheskeh, Whoosh, Chambares, and Vaire 214), and coarse grains that are consistently low in H (5 points from samples Hastaa, Lha\_tsaadah, Rougon, and Tanaron).

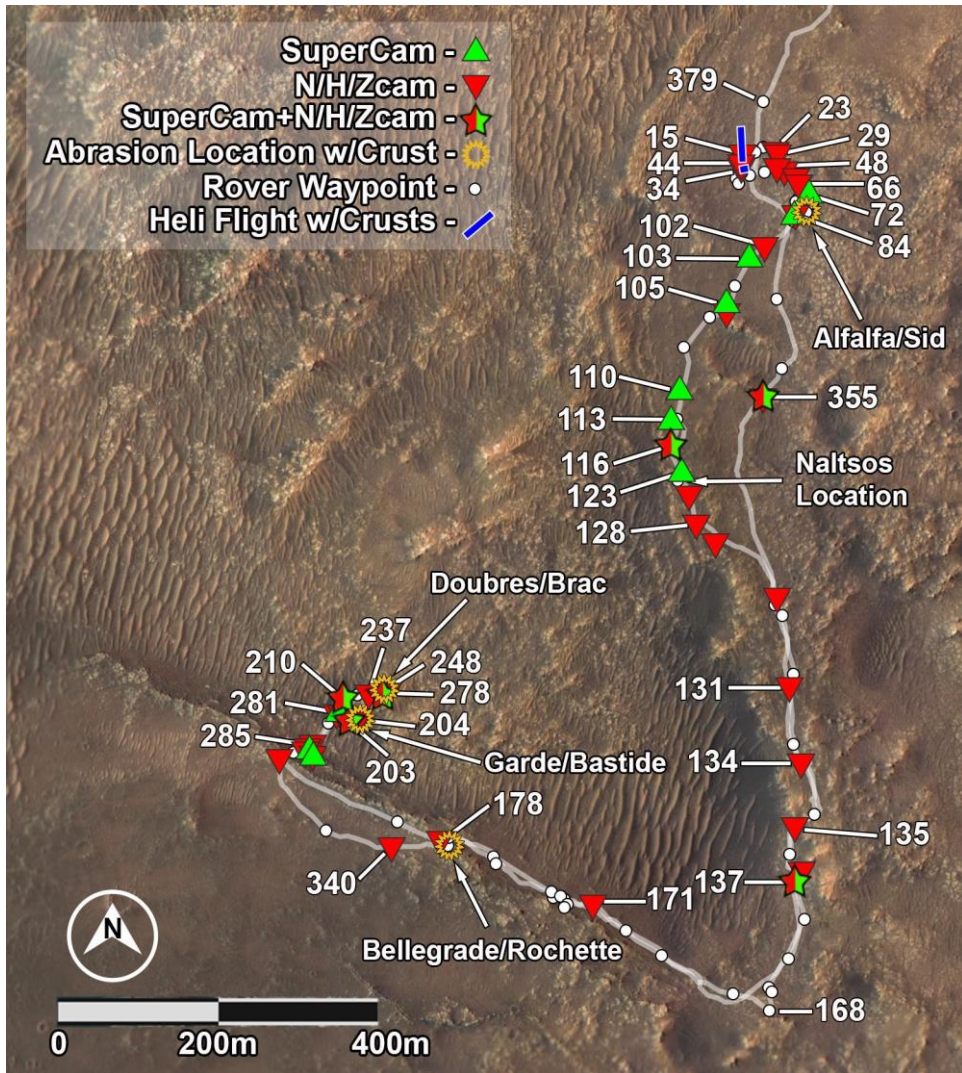


Figure 5.3. A map of the rover traverse indicating rover stops (white points), SuperCam analyses (indicated in green), and evidence of crusts observed near wheel tracks (red points/half stars), by the helicopter (blue lines), at abrasion locations (indicated with orange circles) and the Naltsos target measured by PIXL is labeled on the map<sup>[17]</sup>.

The points in Figure 5.4 B are color-coded to correspond to the most common types of grains observed throughout the mission, coarse grains with a decrease in H score = blue, fine grains with a consistently high H

score = red, and fine grains with a decrease in H score = orange.

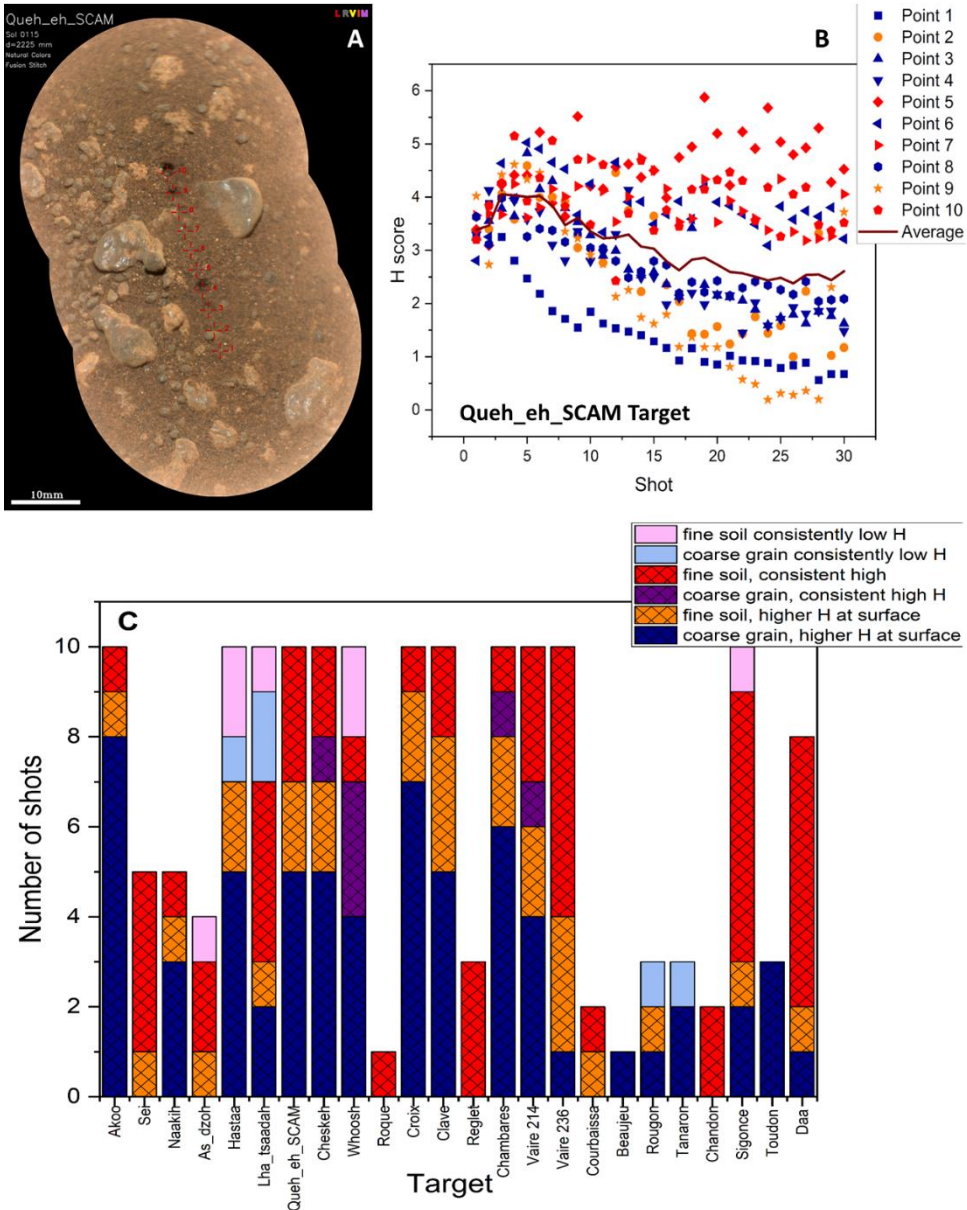


Figure 5.4. (A) RMI mosaic of Que\_eh\_Scam, showing the location of the pits formed by the LIBS shots. (B) Image showing decrease of H with depth from the surface of Que\_eh\_Scam, which contains the most common types of grains. (C) Image showing the breakdown of points by low variation in emissivity (more indicative of a coarse grain), and higher variation in emissivity, and a decrease in H from the surface, versus more constant, higher and lower H scores at the surface.

Figure 5.5 shows the mean NIR reflectance spectra of all fine soils observed during the first year of the mission, along with the mean spectra of two disturbed soils (*Keyah* and *Toudon* targets), and compared with laboratory reflectance spectra.

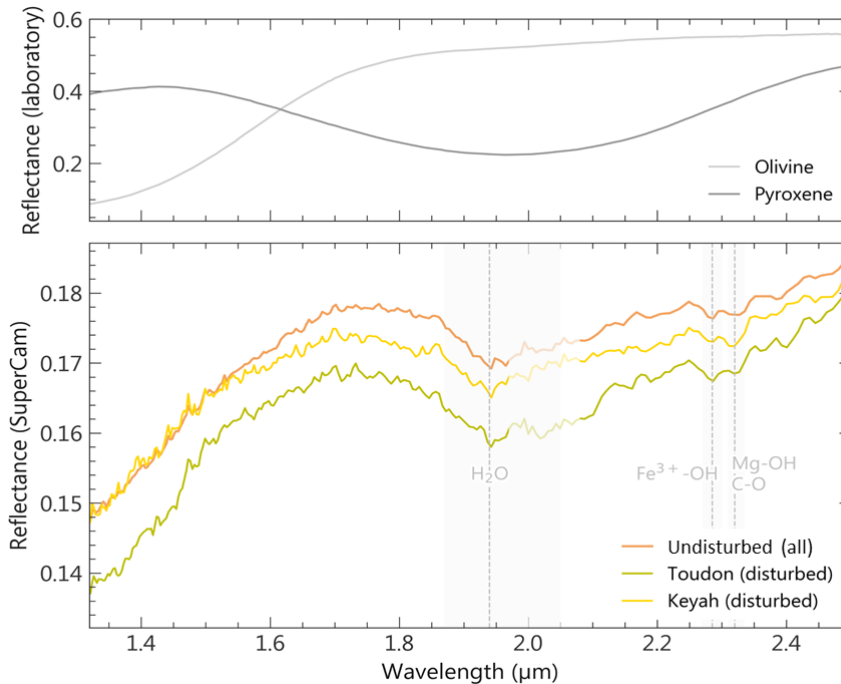


Figure 5.5. Mean reflectance spectra of fine soils observed during the first year of the mission and measured by the SuperCam IR, compared with laboratory reflectance of the RELAB library (olivine C1PO47, pyroxene CASB52 <sup>[34]</sup>). The correlation of the VNIR band depth with the LIBS H Score suggests the presence of H<sub>2</sub>O, which is consistent with atmospheric observations from MEDA about the frost events and hydration of the salts. All SuperCam raw data and processed calibrated data files are included in the Planetary Data System <sup>[17]</sup>.

Disturbed soils are similar to other fine soils and exhibit a spectral positive trend in the 1.3–1.7 μm range consistent with the presence of olivine detected from orbit, which is also strongly associated with coarse-grained material. An absorption near 1.9 μm is also observed, a band related to the combination of elongation and bending modes of the water molecule. Additional shallow absorptions at 2.28 (Fe<sup>3+</sup>-OH) and 2.32 μm (Mg-OH and/or CO<sub>3</sub><sup>2-</sup>) are observed, indicating that water is present in hydrated minerals phases, probably Fe/Mg-phyllsilicates such as nontronite <sup>[35]</sup>, maybe with carbonates. The enlargement of the 1.9 μm band and the blue slope in the 2–2.5 μm range is indicative of the presence of pyroxene inducing a large absorption band centered near 2 μm.

A comparison of the averaged major-element oxide composition and S, Cl, and H scores of the disturbed soils Rougon, Chandon, and Toudon with the average of the undisturbed fine-grained soils that are high in H indicates that the chemistry of the soils is the same within (the high) uncertainty (see Table 5.8).

Table 5.8. A comparison of the average of disturbed soils and fine soils that are high in H show that they are the same within uncertainty

		SiO <sub>2</sub>	TiO <sub>2</sub>	Al <sub>2</sub> O <sub>3</sub>	FeOT	MgO	CaO	Na <sub>2</sub> O	K <sub>2</sub> O	Cl fit	H <sub>score</sub>	S <sub>score</sub>
Disturbed	Average	37.6	1.05	7.91	16.1	7.2	5.3	1.79	1.03	0.0045	3.1	0.43
	SD	8.5	0.63	0.72	4.4	2.2	3.3	0.29	0.59	0.0045	1.4	0.27
Undisturbed	Average	44.6	0.68	7.3	16.9	10.2	4.04	1.69	0.68	0.013	4.0	0.53
	SD	2.3	0.25	1.8	6.3	6.6	0.82	0.51	0.40	0.016	1.0	0.15

PCA analysis of the averaged shots for each point shows that H, Cl, and S are tightly correlated. These results suggest the presence of hydrated salts that may be contributing to the formation of the soil crusts. For specific comparison with the PIXL measurements, PCA analysis of the shot-to-shot SuperCam data on Naltsos indicate tight correlation of Mg with H, suggesting that the Mg sulfates observed by PIXL might be hydrated (Figure 5.6).

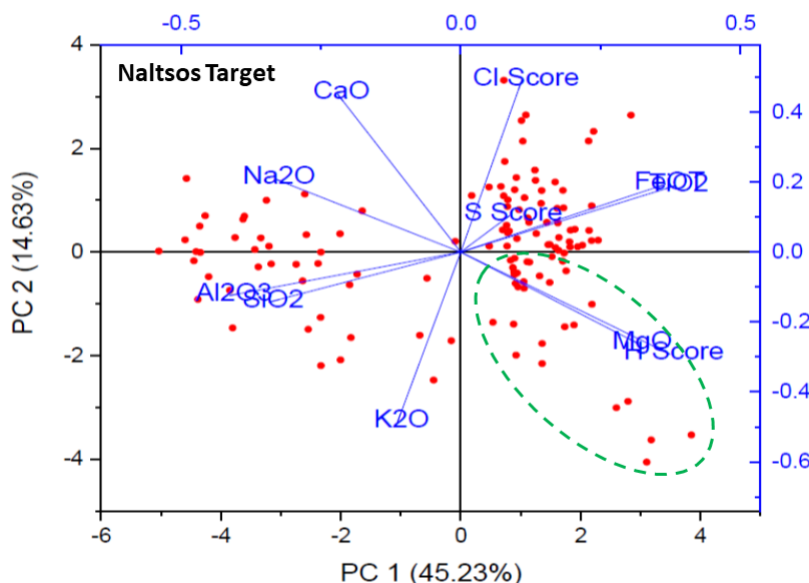


Figure 5.6. PCA analysis of the shot-to-shot LIBS data (the first 5 are excluded) of the Naltsos target. A tight correlation between MgO and H score is observed in the downward right quadrant, suggesting that Mg-rich minerals are probably hydrated.

### 5.1.7. Discussion

This work examined crusts of Martian soils analyzed by several landing missions. These crusts were analyzed with the aim of understanding their characteristics, possible formation mechanisms, and the implications of this material for the history, possible past habitability and future human exploration. Soil crust is more cohesive than the subsurface cohesion. This cohesion may be due to the presence of liquid water, the presence of salts, as well as the characteristics of the grains themselves, such as their smaller size or morphology.

The very fine-grained material present below the surface observed in the wheel tracks may therefore be contributing to this evidence of subsurface cohesion. It is likely that this very fine-grained material may be transported from long distances and is therefore strongly impacted by the geochemical processes that take place on Martian surfaces, which also generate the surface crusts observed in Jezero crater.

During the traverse of the Jezero Crater Floor, several indications of disturbed crusts have been observed in wheel track images at 45 of the 101 rover stops, on 2 helicopter flights of the 6 that crossed the rover wheel tracks, as well as clear evidence at 4 of the 8 drilling/abrasion locations (see Figure 5.3). Evidence of soil crusts and cohesive soil beneath the surface are prevalent in Jezero crater, and their formation mechanisms are important for understanding the surface of Mars.

Shot-by-shot examination of the LIBS data indicates characteristically higher H-scores at the soil surface (Figure 5.4). Comparing the changes in H-scores to grain size estimates based on the standard deviation of total emissivity shows that SuperCam LIBS H-scores from thin soils are consistently high (50 points), but with a substantial number of points showing a decrease from the surface (27 points). This is consistent with a hydrated crustal thickness that is in most cases thicker than the depth of the SuperCam LIBS-generated pits (probably 1-2 mm), but in some cases less than this thickness. This is consistent with crustal thickness measurements from 3D data analysis of MastCam-Z stereo images, which indicate crustal thicknesses of 1 and 2 mm.

The high H values commonly observed with SuperCam LIBS for fine-grained soils (Figure 5.4 B) are also consistent with SuperCam VISIR measurements that measure an H<sub>2</sub>O band depth of 1.9 microns for fine-grained samples, specifically including Toudon and Keyah (Figure 5). The correlation of the 1.9 micron H<sub>2</sub>O VNIR band depth with the LIBS H-score

---

suggests that the presence of H<sub>2</sub>O contributes to the LIBS-measured H-score.

To examine the chemical characteristics of this hydrated soil crust, a PCA analysis was performed on the MOC values, and LIBS scores of H, Cl, and S. The correlation of H, Cl, and S values with LIBS scores is shown in Figure 5.1. The correlation of H, Cl, and S scores, separated from a correlation of Fe and Mg, and K, Ca, Al, and Na, suggest evidence of crusting over two different types of grains, more mafic grains (cluster 1) and more felsic grains (cluster 2).

PIXL analyses of the Naltsos target surface indicate a correlation between Mg and Ca and S, as well as potentially Na with Cl. These results suggest the presence of Mg and Ca sulfates, and potentially halite or Na-perchlorate consistent with the Raman observation of anhydrous NaClO<sub>4</sub> in the Bellegarde pores observed after abrasion of the rock. By way of comparison, PCA analysis of shot-by-shot SuperCam data at Naltsos indicate a close correlation of Mg with H for SuperCam points measured at Naltsos (Figure 5.6), suggesting that the Mg sulfates observed by PIXL are likely hydrated. Both SuperCam and PIXL clearly indicate the presence of salts that probably contribute to soil particle cohesion and thus crusting, as well as cohesion below the surface.

Can we determine the dominant process that forms the crusts observed in the soils at the bottom of Jezero crater? To answer this question, we examined the geochemistry measured by SuperCam on multiple soil targets. The soil surfaces show correlation of sulfur, chlorine, and hydrogen, suggesting the input of these three ions from the same source to form salts that act as cementing agents for soil grains. Sulfate can be adsorbed to the mineral phase, whereas perchlorate or chloride cannot. Thus, depositions from solutions containing S and Cl ions appear to be disfavored, suggesting that a different, non-aqueous mechanism is depositing the S and Cl species.

Atmospheric deposition of S and Cl is, however, consistent with the correlation of S, Cl, and H, as well as with Cl enrichment in Jezero crater. The deposited Cl and S may form different mineral phases, which could hydrate with changes in relative humidity and possible frost, cementing the surfaces. Further work is needed to examine soil crusts throughout the Jezero crater mission to determine if soil crusts elsewhere could be the result of groundwater or melting ice.

## 5.2. Martian simulant study – Clay minerals as hosts for organic molecules on Mars

Clay minerals crystallize in aqueous environments being formed from the weathering of primary minerals such as olivines, pyroxenes, feldspars, micas, quartz and others that were formed under extreme heat and pressure conditions. Normally, they are less than 2  $\mu\text{m}$  particle size and they are chemically composed of hydrated aluminum silicates, with magnesium, iron, calcium, potassium or sodium, arranged in different ways as alternating layers<sup>[36,37]</sup>. A feature that makes them very special minerals is their ability to host other compounds, such as organics, quartz particles, pyrite, calcite, soluble salts, other non-clay minerals and amorphous components. These compounds are absorbed by the interlayers of the expandable clays<sup>[36,38]</sup>, forming mineral complexes like organo-minerals<sup>[8]</sup>.

The variety of clay minerals can be distinguished by the configuration of tetrahedral and octahedral sheets. 1:1 clay minerals are characterized by one tetrahedral and one octahedral sheet per clay layer, whereas 2:1 clay minerals contain two tetrahedral sheets and one octahedral central sheet. In any case, clay layers are negatively charged, so the interlayers are able to absorb cations to balance the charge of the whole crystal. Interlayers bonds and interlayer cations may be due to Vander Walls forces, hydrogen bonding or electrostatic forces<sup>[39]</sup>. The most common 1:1 clay mineral on Earth is the kaolinite  $[\text{Al}_2\text{Si}_2\text{O}_5(\text{OH})_4]$ <sup>[40]</sup>, while the most common 2:1 clays are: smectite  $[(\text{Ca},\text{Na},\text{H})(\text{Al},\text{Mg},\text{Fe},\text{Zn})_2(\text{Si},\text{Al})_4\text{O}_{10}(\text{OH})_2.n\text{H}_2\text{O}]$ <sup>[37]</sup>, vermiculite  $[(\text{Mg},\text{Fe},\text{Al})_3((\text{Al},\text{Si})_4\text{O}_{10})(\text{OH})_2.n\text{H}_2\text{O}]$ <sup>[37]</sup>, illite  $[(\text{K},\text{Na},\text{H})(\text{Al},\text{Fe},\text{Mg})_2(\text{Si},\text{Al})_4\text{O}_{10}(\text{OH})_2.n\text{H}_2\text{O}]$ <sup>[41]</sup> and chlorite  $[(\text{Mg},\text{Fe})_3(\text{Si},\text{Al})_4\text{O}_{10}(\text{OH})_2(\text{Mg},\text{Fe})_3(\text{OH})_6]$ <sup>[42]</sup>.

Smectites have already been found on Mars. For example, in 2013, the CheMin instrument on board the Curiosity rover was able to detect, at least, 20 wt.% of the smectite clay mineral on Mars<sup>[43,44]</sup>. In addition, the Curiosity's SAM instrument detected some organic compounds (organic-carbon, organo-chlorinated and sulfur-rich molecules) in two mudstones acquired at the Yellowknife Bay within Gale crater on Mars<sup>[45–47]</sup>. In this context, clay minerals, with a long residence time in Martian soils and sediments, are particularly interesting on Mars because, in addition to serving as geochemical markers of past aqueous conditions, they are excellent reservoirs for preserving organic compounds over geological time scales<sup>[48]</sup>.

Taking all this into account, the first goal of this work is to study the different methods by which organic molecules can be absorbed by smectite interlayers. Likewise, the second objective is to test the produced samples by the analytical techniques used in space exploration, both for laboratory and *in situ* sample analyses. In this way, it will be possible to create a

---

database with the results obtained that can serve as support science for current and future Martian missions.

### 5.2.1. Samples

There are already many types of smectite found on Mars, being the most common the nontronite (Fe-smectite), montmorillonite (Al-smectite), saponite (Mg-smectite) and beidellite (Al-smectite), among others [49–51]. Furthermore, evidences of the possible presence of other smectites, such as hectorite has been found [52,53].

Therefore, in this work one of the most and one of the less common smectites on Mars were selected to perform the experiments. These are: montmorillonite  $[(\text{Na,Ca})_x(\text{Al,Mg})_2(\text{Si}_4\text{O}_{10})(\text{OH})_2.n\text{H}_2\text{O}]$  [54] and hectorite  $[(\text{Li,Mg})_3\text{Si}_4\text{O}_{10}(\text{OH})_2.n\text{Na}^+]$  [55]. The montmorillonite used was the Na-rich one (SWy-3, MMT) from Crook Country, Wyoming, USA; and the hectorite (SHCa-1, HEC) was extracted from San Bernardino Country, California, USA.

The organic compound selected to dope the smectite samples was the dodecanoic acid ( $\text{C}_{12}\text{H}_{24}\text{O}_2$ ) [56], or more commonly called lauric acid. Fatty acids have been found indirectly on Mars, through the SAM instrument on board the Curiosity rover, which detected undecane and decane, alkyl molecules probably derived from the thermal decomposition of the  $-\text{COOH}$  from undecanoic and dodecanoic acids [57]. Moreover, they already were found in Martian analogs [58,59]. Dodecanoic acid was also chosen because it has a long carbon chain and is quite bulky. Therefore, if dodecanoic acid can be absorbed by using the proposed method in this work, it can be assumed that other fatty acids with shorter chain would be absorbed as well.

### 5.2.2. Doping methodology

In order to prepare the clays for a correct absorption of organic molecules, first an acid activation was carried out. Acid activation causes dehydroxilation of smectite clays, followed by the removal of cations from the surfaces and edges of the layers. This results in the formation of a silica-rich amorphous phase that exhibit substantial overall negative charge. The negative charge is adjusted with monovalent hydrogen ions that comes from the acid activation. The final result consist of altered smectite layers through increasing the specific surface area and porosity [60,61].

To do so, the smectite activation was carried out dissolving 80 g of pure smectite (MMT, HEC) on sulfuric acid 2 M (1:3 in weight). The reaction was performed with 18.2  $\Omega\text{Ohm}$  water in the Teflon Parr acid digestion vessel, where temperature was controlled ( $90 \pm 8$  °C for 4 hours) at constant stirring (80 rpm). After completing the reaction and reaching room

temperature, the solution was transferred to four 50 mL Falcon tubes for centrifugation at 5000 rpm for 5 min. Liquid supernatant was removed by several centrifugations and washing cycles, mixing with the vortex (5 mL per adding), until the final pH arrived at 7.0 (x8 times). Finally, the solid part was filtrated under vacuum, dried at 60°C for 72 hours and ground with an agate mortar and pestle.

For a correct absorption of organic molecules by clays, the molecules must be in solution. For this purpose, lauric acid (partially apolar) was brought into solution by two methods: the first by synthesizing the corresponding sodium salt (sodium laurate) in aqueous medium, and the second by dissolution in a partially apolar solvent such as ethanol.

The first method consisted of dissolving the clay (20.32 g) in 1 M sodium hydroxide (100 mL) in a 1:1 ratio. For correct dissolution, 42 mL of ultrapure water were added, obtaining a final salt concentration of 0.7 M.

The second method consisted of dissolving the lauric acid with ethanol. Taking into account that the solubility of the lauric acid in ethanol is approximately 30 mg/mL <sup>[62]</sup> and that 100 mL of 60% ethanol was to be used, 1.8 g of clay was weighed and 1.8 mL of ethanol was used. Leaving a final concentration of 0.09 M.

Then the doping process was the same for both methods. However, in this process the pH plays a very important role, since the pKa of lauric acid is 5.5 <sup>[63]</sup>. In fact, at pH values below 5.5 the compound is in its acid form (C<sub>11</sub>H<sub>23</sub>COOH), while at pH values above 5.5 the compound is ionized (C<sub>11</sub>H<sub>23</sub>COO<sup>-</sup>). Thus, in order to understand better the role of pH in the absorption capacity of organic molecules by smectites, in this work different pH were assessed. For this purpose, the two pHs chosen were: 3.5 and 7.5 (two units below and above the pKa to be at least 99% hydrated or ionized).

Considering all this, 4 samples of 10 g of activated smectite were mixed with 20 mL of lauric acid solutions (both methods) and the pH desired was adjusted by using HCl 1 M and NaOH 1M solutions using the vortex to keep the mixture homogeneous. Then, the samples were agitated in a shaker bath (60 ± 1 °C for 2 hours), centrifuged (5000 rpm) and the supernatant was removed. The solid part was filtrated under vacuum and dried at 60°C for 24 hours.

Table 5.9 summarizes all the samples prepared for this experiment specifying each sample code, the smectite mass, the solvent and the pH to which they were adjusted. It should be noted that, due to the solubility of lauric acid in ethanol, the two solutions had different concentrations. The molar ratio of smectite to salt solution was 1:1, whereas that of smectite to ethanol solution was 7:1.

All the samples were analyzed by three techniques: XRD, FE-SEM-EDS and FT-IR. XRD was employed to understand if the size of the interlayer changed (increased or remained the same). For this aim, smectite was analyzed before and after activation. By this means, the correct absorption of lauric acid was evaluated. Whereas, by FE-SEM-EDS an estimation of the amount of carbon was performed, the higher relative abundance of carbon meant the higher amount of lauric acid absorbed. Finally, through FT-IR analysis it was possible to characterize molecularly the compounds that formed the samples.

*Table 5.9. Summary of the samples prepared of montmorillonite and hectorite taking into account the lauric acid dissolution method and the pH of adjustment.*

Sample	Activated smectite (g)	Lauric acid solution (mL)	pH
NM1	9.95 MMT	20 salt	3.5
NM2	9.90 MMT	20 salt	7.5
EM1	9.92 MMT	20 with ethanol	3.5
EM2	9.93 MMT	20 with ethanol	7.5
NH1	9.98 HEC	20 salt	3.5
NH2	9.89 HEC	20 salt	7.5
EH1	9.94 HEC	20 with ethanol	3.5
EH2	9.97 HEC	20 with ethanol	7.5

### 5.2.3. Results

#### 5.2.3.1. XRD analyses

In order to evaluate the features of clay minerals, their XRD patterns are often used. For instance, an important factor to study when dealing with clays is the interlayer space, which usually retains cations and water molecules. In this sense, the clays XRD patterns are characterized by the parameter so called d-spacing ( $d_{001}$ ). This parameter consists of the distance between atomic parallels layers in a crystal <sup>[64]</sup>. In this sense, the most common  $d_{001}$  values for SWy and SHCa-1 are 1.19 and 1.10 nm, respectively <sup>[65]</sup>. In this work the region of the diffractogram from 4 to 18° was specifically analyzed (5.15 B and 5.16 B) to verify the interlayer size of smectites, as this is the region that characterizes the  $d_{001}$  parameter.

##### 5.2.3.1.1. Montmorillonite XRD analyses

Figure 5.7 A shows the XRD patterns of regular montmorillonite (RM), activated montmorillonite (AM), EM1, EM2, NM1, NM1 and lauric acid (LA) in the range of  $2\theta = 4-60^\circ$ .

In this way, the typical XRD reflection pattern of RM was characterized by having a basal spacing between the clay sheets that appeared at  $2\theta = 7.28^\circ$  ( $d_{001} = 1.21$  nm). This reflection shifted to  $2\theta = 7.03^\circ$  when it was acid activated (AM;  $d_{001} = 1.26$  nm). This increase in d-spacing is explained by

the growth of interlayer between the montmorillonite sheets, which implies that the acid activation of the RM was carried out correctly.

Doping experiments with ethanol indicated that the interlayer size grew more at low pH (EM1, pH=3.5) than at neutral pH (EM2, pH=7.5), since the d-values were 1.35 and 1.24, respectively. For the sodium hydroxide experiments, the test at low pH (NM1, pH=3.5) worked better than at neutral pH (NM2, pH=7.5), as at pH of 7.5 the peak at  $2\theta \approx 7^\circ$  disappeared. It is possible that the distribution of the layers lost homogeneity, increasing the disorder and losing crystallinity. Therefore, this band was hardly noticeable due to its high FWHM.

A second group of reflections occurred for  $2\theta$  values close to  $11^\circ$ , but only in the tests at a pH of 3.5 (EM1 and NM1). These reflections indicate a partial ordering of the lauric acid in the interlayers of the smectite.

Considering these tests, it can be assumed that the experiments at low pH lead to higher peak shifts ( $\Delta 2\theta$ ) and higher d-values, which means higher compound retention. Therefore, the integration of organic molecules on montmorillonite structure is more favored at low pHs. Considering that the pH of the ancient Martian regolith was acid due to the acidic contribution of volcanic gases on the ancient Mars <sup>[66]</sup>, Martian montmorillonite rich areas imply to be a perfect target for biosignatures searching missions.

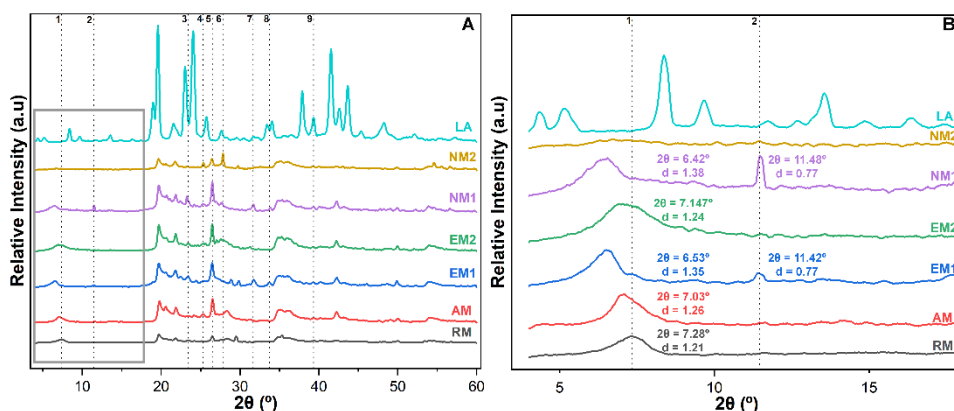


Figure 5.7. (A) XRD patterns of RM, AM, EM1, EM2, NM1, NM2 and LA in the range of  $2\theta = 4-60^\circ$ . (B) Zoom of the region of interest marked with a rectangle in A. The d-spacing is expressed in nm.

### 5.2.3.1.2. Hectorite XRD analyses

Figure 5.8 A shows the XRD patterns of regular hectorite (RH), activated hectorite (AH), EH1, EH2, NH1, NH1 and LA in the range of  $2\theta = 4-60^\circ$ .

As in the previous case, the region of the graph between 4 and  $18^\circ$  was carefully studied, since it is representative of the interlayers size (Figure 5.8 B). In this case, no peak corresponding to the interlayer could be

appreciated in the XRD pattern of the RH and AH. This may be due to the fact that initially the hectorite did not have enough interlayer space. The interlayer band is not noticeable in any doped sample except for NH1 and EH2. Based on these peaks, the one belonging to EH2 appeared at  $2\theta = 7.50^\circ$  ( $d = 1.18$  nm), whereas the one belonging to NH1 appears at  $2\theta = 6.47^\circ$  ( $d = 1.37$  nm). As the  $d$ -spacing value for the RH and AH interlayers could not be calculated due to the non-existence of bands, the literature<sup>[65]</sup> value of 1.10 nm, which corresponds to a regular hectorite, was taken as a reference. Thus, considering this value, a higher value of  $\Delta d$  occurred for NH1. This is in agreement with what was found in the case of montmorillonite, which had a higher interlayer spacing for sample NM1. These experiments indicate that at low pH of 3.5 and with the formation of the sodium salt, there is a greater increase in interlayer.

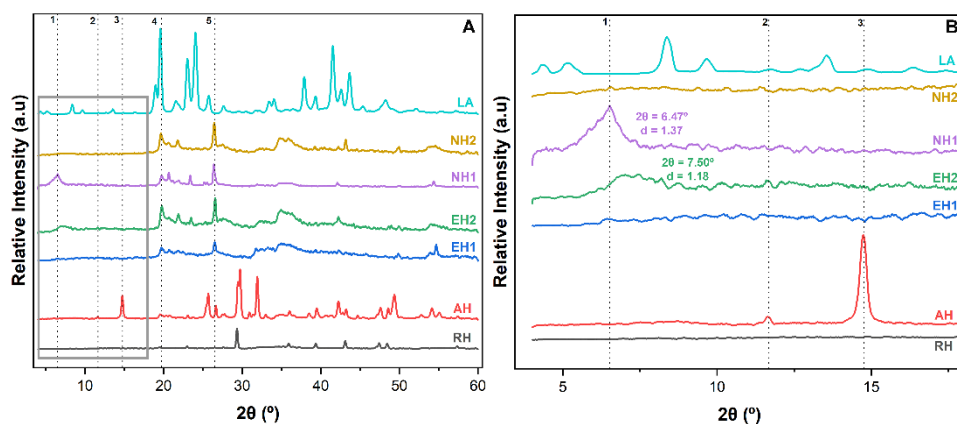


Figure 5.8. (A) XRD patterns of RH, AH, EH1, EH2, NH1, NH2 and LA in the range of  $2\theta = 4$ - $60^\circ$ . (B) Zoom of the region of interest marked with a rectangle in A. The  $d$ -spacing is expressed in nm

In order to verify that the organic molecule was retained by the interlayers of the clays, FE-SEM-EDS and FT-IR analyses were carried out.

### 5.2.3.2. FE-SEM-EDS results

Montmorillonite and hectorite FE-SEM images can be seen in Figure 5.9 and Figure 5.10, respectively. All these figures were obtained with the SEI mode, at 15 kV and vacuum condition. The space between smectite layers is less than  $\sim 2$  nm and the lower limit for the spatial resolution of this equipment is 10 nm. Therefore, with this technique it is not possible to measure the distance between the layers or to see the presence of lauric acid between them. Nevertheless, with EDS analysis it was possible to compare the carbon content in each sample by analyzing the intensity of element C EDS band. In this way, the higher the carbon counts, the higher the relative concentration of lauric acid in each sample. To ensure the representability of the study, at least 6 EDS analyses were performed at

different points for each sample and then, statistical analysis was performed to reject outliers. The results can be found in Table 5.10.

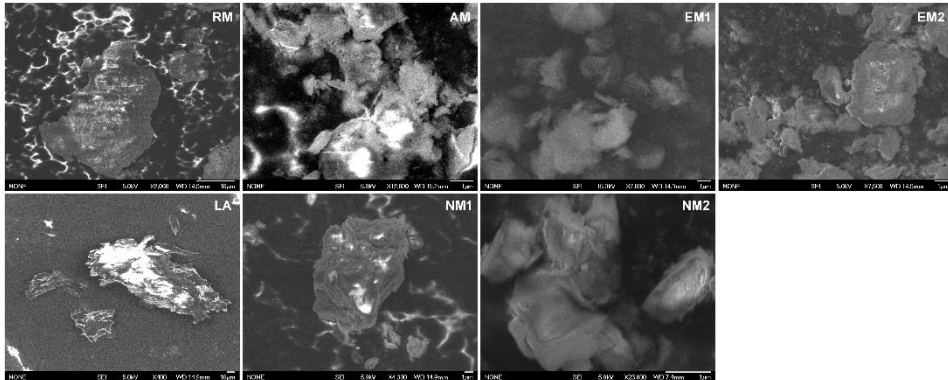


Figure 5.9. FE-SEM figures of RM, AM, EM1, EM2, LA, NM1 and NM2.

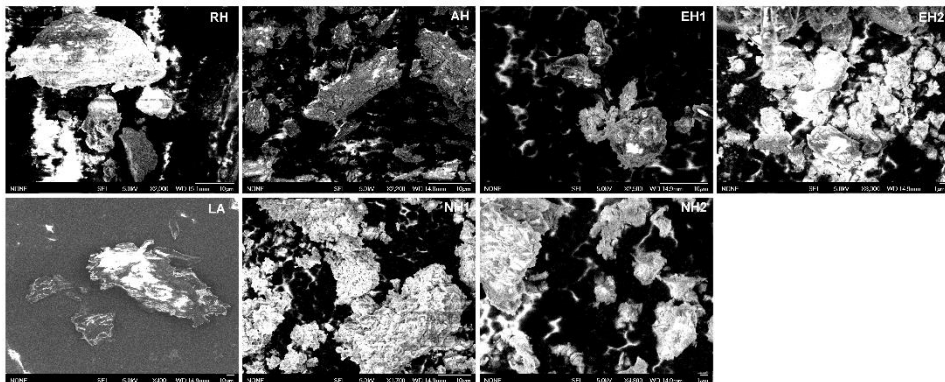


Figure 5.10. FE-SEM figures of RH, AH, EH1, EH2, LA, NH1 and NH2.

### 5.2.3.2.1. Montmorillonite EDS analyses

Although no signal for carbon was expected for the RM EDS spectrum, a small amount was found likely related to the residual carbon signal emitted from the graphite tape. Thus, the RM sample was considered as the “blank” for this experiment. To get rid of this background, the rest of the samples were measured following the same experimental conditions used during the blank analysis for comparison purposes. The counts for C band in the different samples are shown in Table 5.10.

In Table 5.10., it can be appreciated that the highest carbon content was found for EM1 sample. Then, in decreasing order considering C content, we got NM1, EM2 and NM2.

---

### 5.2.3.2.2. Hectorite EDS analyses

Surprising results were obtained from the EDS analysis of hectorite (Table 5.10). No significant differences were observed between RH/AH and EH2, which could mean that EH2 did not retain the lauric acid. In addition, it was observed that the carbon counts of the EH1 sample were considerably higher than those of any other sample.

Table 5.10. Intensity of carbon detected by EDS analyses on RM, RH, AM, AH, EM1, EH1, EM2, EH2, NM1, NH1, NM2, NH2 and LA, expressed in Counts. Energy of 5 kV.  $C_{MMT}$ : Carbon band counts for montmorillonite samples;  $C_{HEC}$ : Carbon band counts for hectorite samples;  $SD_{MMT}$ : standard derivation of carbon band counts for montmorillonite; and  $SD_{HEC}$ : standard derivation of carbon band counts for hectorite.

SAMPLE	$C_{MMT}$	$SD_{MMT}$	$C_{HEC}$	$SD_{HEC}$
RM/RH	6	6	5	4
AM/AH	6	7	6	6
EM1/EH1	139	88	124	74
EM2/EH2	36	29	5	3
NM1/NH1	41	37	44	40
NM2/NH2	13	10	23	19
LA	167	2	167	2

It should be noted the carbon counts for each sample should be considered as relative values and not absolute ones. This is because, taking into account the high values of the standard deviations, each grain in each sample is not homogeneous, thus showing different magnitudes of organic retention. Although absolute values are not shown, Table 5.10 shows the trend of carbon present in each sample and can be considered to draw conclusions.

### 5.2.3.3. FT-IR Results

The lauric acid FTIR spectrum (Figure 5.11 and Figure 5.12) is mainly characterized by alkanes and the carbonyl groups. The  $-CH-$  bands appear from  $3000$  to  $2850\text{ cm}^{-1}$ , the ones of  $-CH_2-$  from  $1470$  to  $1450\text{ cm}^{-1}$ , and the ones of  $-CH_3$  at  $1375$  and  $1450\text{ cm}^{-1}$ . In addition, the peak at  $1697\text{ cm}^{-1}$  is attributed to the carbonyl functional group ( $C=O$ ) while that at  $1292\text{ cm}^{-1}$  could be assigned to the stretching vibration of  $C-O$  [67].

The region below  $1300\text{ cm}^{-1}$  (fingerprint region) is where each organic compound shows its own fingerprint. However, this region is quite complex and difficult to interpret because many different compounds are overlapped. Therefore, for this study it was decided to work just with the main IR bands of the lauric acid ( $3000$ - $2850$ ,  $1697$ ,  $1470$ - $1450$ ,  $1375$  and  $1292\text{ cm}^{-1}$ ).

It should be noted that all the small bands appearing around  $2300\text{ cm}^{-1}$  correspond to the atmospheric  $\text{CO}_2$  [68] that could not be completely corrected by the subtraction of the previously acquired background spectrum.

#### 5.2.3.3.1. Montmorillonite FT-IR results

The experimental RM FT-IR spectrum (Figure 5.11) is characterized by the  $\text{-OH}$  stretching band that appears at  $3625\text{ cm}^{-1}$ . It is also characterized by a broad band between  $3500$  and  $3000\text{ cm}^{-1}$  corresponding to the  $\text{-OH}$  stretching band for interlayer water. The overlaid absorption peaks in the region of  $1640\text{ cm}^{-1}$  are attributed to the  $\text{-OH}$  bending mode of water ( $1634\text{ cm}^{-1}$ , absorbed water). The characteristic peak at  $1119\text{ cm}^{-1}$  corresponds to the Si-O stretching (out-of-plane) and the  $1001\text{ cm}^{-1}$  is attributed to the Si-O stretching (in-plane) vibration for layered silicates. The IR bands at  $916$ ,  $883$  and  $846\text{ cm}^{-1}$  are attributed to  $\text{AlAlOH}$ ,  $\text{AlFeOH}$  and  $\text{AlMgOH}$  bending vibrations, respectively [69].

It can be seen how the characteristic smectite bands (RH) are maintained in the AM FT-IR spectrum (Figure 5.11), which ensures that the treated samples did not lose much crystallinity due to acid activation. No further differences can be seen since the size of the interlayer can only be studied by XRD.

For the doped montmorillonite samples (Figure 5.11), the characteristic lauric acid bands are only seen for low pH tests (EM1 and NM1), supporting XRD and EDS results.

In addition to the clay and lauric acid bands, a new band can be also appreciated in the EM1 and NM1 FT-IR spectra (Figure 5.11). This band appears at  $1582\text{ cm}^{-1}$  and corresponds to the  $\text{-O-Na}$  bond. The presence of this bond leads to think that the sodium ions present in the interlayer reacted with the doping organic molecule to form the corresponding salt, the sodium laurate [70].

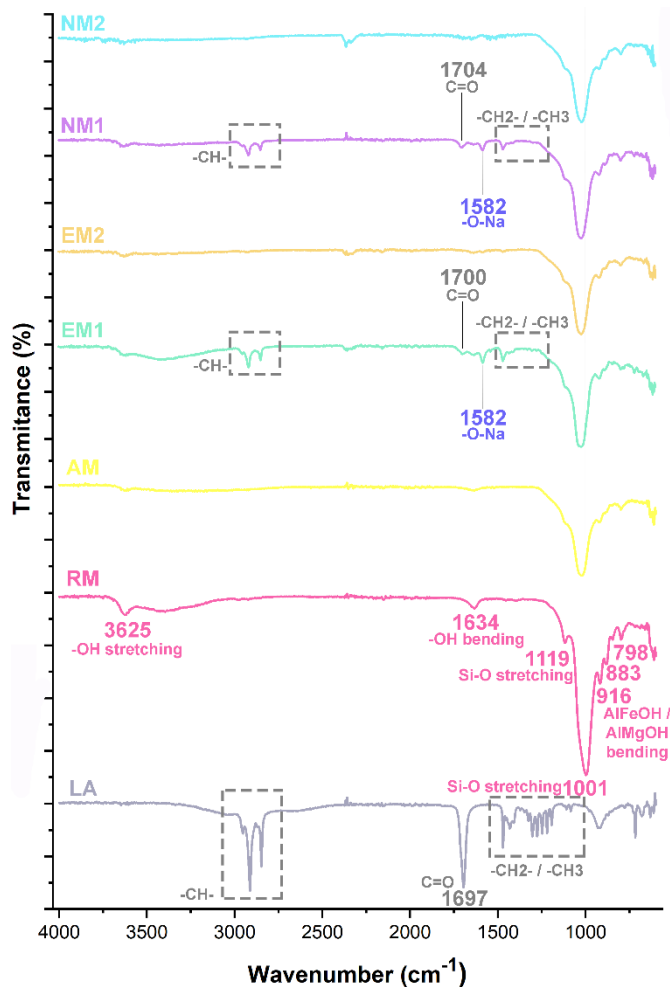


Figure 5.11. FT-IR spectra of AL, RM, AM, EM1, EM2, NM1 and NM2 acquired from 4000 to 700  $\text{cm}^{-1}$  using 128 scans.

### 5.2.3.3.2. Hectorite FT-IR analyses

The infrared spectrum of hectorite <sup>[71]</sup> is similar to that of montmorillonite. However, in this work, certain differences were observed. In this sense, the experimental hectorite spectrum (Figure 5.12) consisted of the 1634  $\text{cm}^{-1}$  band that corresponded to the hydration  $\text{-OH}$  bending mode; the one of Si-O stretching in-the-plane that appeared at 992  $\text{cm}^{-1}$ ; and the 874  $\text{cm}^{-1}$  band that was attributed to the AlFeOH bending vibration <sup>[69]</sup>.

As can be seen, there was no presence of  $\text{-OH}$  bands corresponding to the Si-OH and/or Al-OH stretching. The out-of-plane stretching band corresponding to the Si-O bond was not observed either (it usually appears at  $\sim 1084 \text{ cm}^{-1}$  <sup>[71]</sup>), nor were those corresponding to the AlAlOH and AlMgOH bending vibrations. Finally, the band that appeared at 1407  $\text{cm}^{-1}$

corresponds to the vibration of the  $\text{CO}_3^{2-}$  anion of calcite [72], which is a mineral that is usually found together with smectites [73].

Regarding the AH experiment, the spectrum shown in Figure 5.12 was quite similar to that of the RH, but the calcite band was greatly reduced in intensity since part of calcite was dissolved during the acid activation. Finally, after analyzing all the different doping samples of hectorite (Figure 5.12), results were similar to those obtained for montmorillonite samples. The organic bands were only detected in the spectra of the samples taken at low pH (EH1 and NH1). In addition, the  $-\text{O}-\text{Na}$  band was observed on these spectra, suggesting the formation of sodium laurate. As in the previous case, the method of dissolving lauric acid by forming the salt with NaOH provided better results. This was evidenced by the  $-\text{CO}-$  band, which appeared very subtle for EH1.

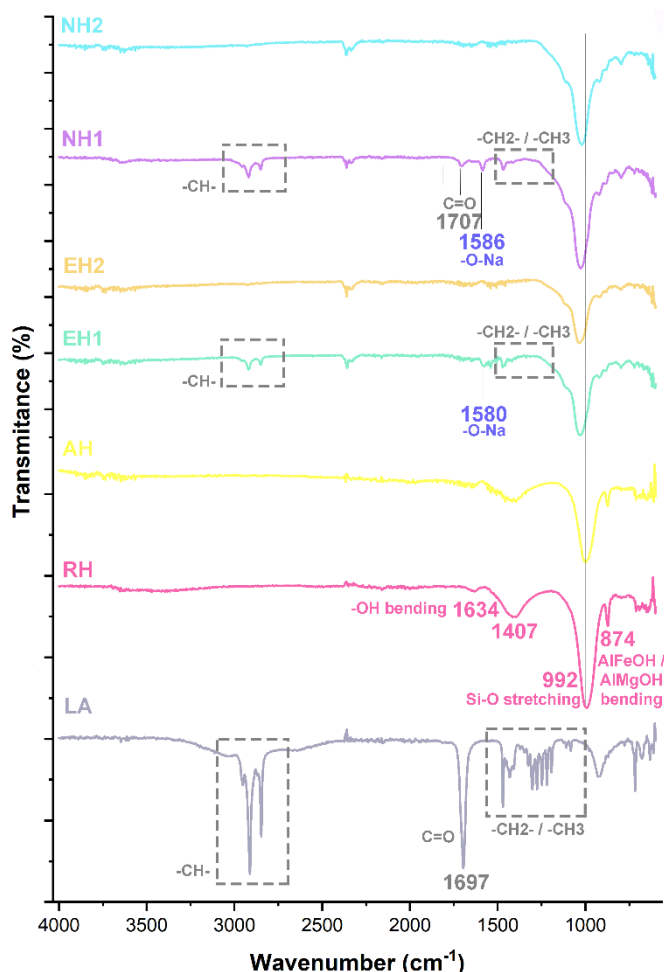


Figure 5.12. FT-IR spectra of AL, RH, AH, EH1, EH2, NH1 and NH2 acquired from 4000 to 700  $\text{cm}^{-1}$  using 128 scans.

---

#### 5.2.4. Discussion

Acid activation caused the dissolution of the octahedral layers (M-OH) of the two phyllosilicates and resulted on an enrichment of amorphous SiO<sub>2</sub>. This process increased the specific surface area and provided more sites of binding, which surely increased the affinity of organics for SiO<sub>2</sub>. During the acid activation, protons entered into the clay structure, partially dissolving the octahedral layers. This amorphization process could be verified thanks to the XRD diffractograms, where there is less crystalline structure in the activated samples than in the regular ones.

After studying the XRD results, it was found that the experiments carried out at a pH of 3.5 had a greater increase in the interlayer with the exception of the sample EH1, which did not present interlayer increase. For the case of the experiments carried out at 7.5, only the ethanol tests showed a broad interlayer band.

Considering the calcium counts detected by EDS, pH 3.5 tests were those with the highest number of counts, while those at pH 7.5 were significantly lower. According to the NM2 XRD diffractogram that did not present any interlayer band, the carbon counts of this sample were practically null, so it makes sense that no organic molecule was retained. Moreover, the EH2 sample did not show any carbon counts, while its XRD diffractogram showed a broad interlayer band. This may mean that there were compounds absorbed on the interlayer, such as cations and water, but not lauric acid. Finally, the EDS detected few carbon atoms in the NH2 sample, unlike the XRD diffractogram which did not show any interlayer band. This may be due to the presence of lauric acid on the surface of the hectorite grains and not retained by the interlayers. However, it should be said that the statistics of the C estimation should be improved by increasing the number of EDS punctual analysis by sample obtaining a more robust dataset. In any case, the EDS results obtained suggest that retention did not occur equally in all grains, so the values given in Table 5.10 should be considered as relative and not absolute values. This reason is why different C count values were obtained for each sample, resulting in a very large standard derivations.

The FT-IR data showed that organic molecules were only present in tests carried out at low pH for both montmorillonite and hectorite. In addition, thanks to this molecular analysis technique, it was possible to verify that the organic molecule generated after the applied methodologies was sodium laurate.

As sodium laurate was formed by both the salt method and the ethanol method to dissolve the lauric acid, the sodium contribution did not come only from the salt formation. This contribution may also be due to the presence of free sodium cations in the interlayer or from the sodium ions

(NaOH) added to the solution to reach the desired pH, which was initially ~2. An important amount of NaOH must be added to neutralize pH=2 until pH=3.5.

Therefore, although the two methods used for the dissolution of lauric acid gave good results, thanks to the FT-IR spectra, it could be observed that the bands of sodium laurate were more intense for the samples that used sodium hydroxide than for those that used ethanol. This makes sense because a small amount of lauric acid could be dissolved in ethanol (solubility of lauric acid in ethanol). This solution (7:1) was less concentrated than that of sodium hydroxide (1:1).

After analyzing all the results obtained through the techniques, it can be considered that the results of the experiments with montmorillonite were more homogeneous and stable. In contrast, the experiments with hectorite were not so homogeneous. This suggests that the retention capacity of montmorillonite, in this case, was better than that of hectorite. In other words, montmorillonite is a safer choice as biosignatures protector.

Finally, it should be noted that evaluating the samples with transmission electron microscopy (TEM) could provide further information about the absorption of the organic molecules by the smectite layers. This is because its resolution is higher than that of SEM. Therefore, the combined methodology applied in this work (XRD for interlayer size study, FE-SEM-EDS for C estimation and FT-IR for molecular identification), plus possible TEM analyses would result the best way to assess proper doping.

---

### 5.3. Martian analog study – The case of finding organic molecules on the Carachi Pampa oncoid

The fact that ancient Mars possessed water creates the possibility of habitability and the presence of microorganisms in spite of the current inhospitable Martian environment. However, at the time of the formation of sedimentary structures, water was liquid with dissolved oxygen and probably with an atmosphere much higher than the current one. The types of microorganisms that could have existed on early Mars would have been tiny and from about a micron to a few microns in size. Although the individual cells would be too small to distinguish, their microbial colonies would be much larger <sup>[5]</sup> and, consequently, visible through rover's analytical instruments.

Microbes can live in many environments, but those living in extreme ones face inhospitable Martian conditions with different strategies, including formation of complex extremophilic microbial communities driven by light and water presence (O<sub>2</sub> availability). In this way, mats, biofilms, domes, endo-evaporitic mats and microbialites can be formed <sup>[6]</sup>. Therefore, these long-lived sedimentary structures are formed by the synergy between microbial metabolism and the environment in shallow waters, such as salars, lagoons, and even volcanic fumaroles <sup>[74]</sup>. Geological records indicate that these communities dated to 3.5 billion years in age, thus, they are the main evidence of ancient life on Earth <sup>[6,75]</sup>. Microbialites are organo-sedimentary deposits formed by sediment trapping, binding and *in situ* precipitation of calcium carbonate due to the growth and metabolic activities of microorganisms <sup>[6,7]</sup>. They can take the form of layered mound, spheres, columns or sheet-like sediments that can be conical, domal, stratiform or branching <sup>[75]</sup>.

Depending on their mesoscopic features, microbialites are classified into five groups: stromatolites, oncoids, thrombolites, dendrolites and leiolites. The main structures found on Earth are stromatolites, oncoids and thrombolites. Stromatolites display a laminated mesostructure, oncoids exhibit a concentrically laminated mesostructure and thrombolites show a clotted mesostructure <sup>[74,76]</sup>.

On Earth, microbialites have been found along the seashores and reefs, fresh water lakes, lagoons and hypersaline lakes salars and even volcanic fumaroles. In addition, they have been also identified in lakes analogs to Martian paleolakes, such as Lake Thetis and other western Australian lakes <sup>[77,78]</sup>. In fact, microbialite-like structures were found by Opportunity <sup>[2]</sup>, Spirit <sup>[3]</sup> and Curiosity <sup>[4]</sup> rovers in Mars. These facts support the use of a microbialite as a Martian analog.

Moreover, landing sites selected for the mentioned missions were directly related to water, since a common objective for them was to search for signs of ancient and present life in water environments on Mars <sup>[79,80]</sup>.

Considering the aqueous past character of both sites, if there was life in Mars it is very likely that microbialite-like structures were formed. If this happens, rovers may find them on the Martian surface and may analyze them by using their analytical payload.

In order to understand if microscale spectroscopic techniques that are being and will be used *in situ* on Mars (Mars2020 and Rosalind Franklin) are appropriate tools for detecting biosignatures in this kind of structures, a microbialite was studied in this work as an analog of Mars biomediated structure. Specifically, an oncoïd from the Salar Carachi Pampa (Catamarca, Argentina) was analyzed. This Salar is an extreme environment characterized by a high altitude (3018 masl), with high UV radiation expositions, high levels of desiccation, highly daily temperature fluctuations and a different chemical composition of the water (e.g., high arsenic concentration) attributable to the volcanic activity <sup>[74]</sup>.

### **5.3.1. Mission-like analytical instruments used for the study of habitability in the Carachi Pampa oncoïd**

In order to serve as a supportive science of the Mars2020 and Rosalind Franklin missions, the Carachi Pampa oncoïd sample was characterized by some of the *in situ* analytical techniques that are currently being used and will be used on Mars in the near future. These techniques are part of the analytical payload of the Perseverance rover and the Rosalind Franklin rover.

In this sense, in order to study the biomolecular composition, PIXL, SuperCam, SHERLOC, RLS and MOMA-like instruments were used. Table 5.11 summarizes the instruments that were used to simulate the real instruments of the Perseverance and Rosalind Franklin rovers. The PIXL like instrument selected was the  $\mu$ -EDXRF Tornado instrument, due to both can acquire high spectral resolution observations of rock and soil chemistry. Moreover, both instruments can correlate elemental results with visual image acquired by instrument's camera, proving maps that can reveal the distribution and abundance of chemical elements making up the rock <sup>[81]</sup>.

Regarding the SuperCam instrument, it is provided with versatile remote-sensing techniques, such as LIBS, time-resolved Raman and luminescence spectroscopies, and VNIR spectroscopy. In this sense, the LaserLab LIBS was used to recreate the SuperCam's measurements. This is because both use a laser with the same wavenumber (1064 nm), although of different

powers [29]. In order to simulate the SuperCam Raman measurement, the ERICA Raman spectrometer was used. This is because both are time-resolved spectrometers and both use a single CCD detector to maximize the product of spectral range and resolution [82,83]. Moreover, the VNIR ASD high-resolution FieldSpec4 spectroradiometer was used to recreate the SuperCam VNIR measurements. This instrument was used because it is a portable equipment and covers the spectral range of the SuperCam VNIR, which will go from 1300 to 2600 nm [84,85]. In order to complement the molecular data, the InVia Raman spectrometer was used to perform Raman imaging, but it should be highlighted that this equipment is not considered an analog of SuperCam's.

In order to recreate the SHERLOC analyses, the Horiba LabRam HR Evolution Raman spectrometer was used. This is because they both use a deep UV excitation laser to identify possible biosignatures [86]. SHERLOC uses a pulsed laser while the LabRam instrument has a continuous wave laser. However, the Raman spectra obtained by both excitation lasers provide the same wavenumber for the Raman bands of compounds, although the form of the bands (intensity, HWMC, area) is different.

Table 5.11. Techniques used to recreate the real instruments of the Perseverance and Rosalind Franklin rovers. RS: Raman spectroscopy; and IRS: Infrared spectroscopy.

Rover	Analytical techniques	Corresponding instrument on Mars	Corresponding analog-instrument used on terrestrial laboratories
Perseverance rover	μ-EDXRF	PIXL	M4 Tornado μ-EDXRF spectrometer
	RS	SuperCam	ERICA micro-Raman spectrometer
	LIBS		LaserLab LIBS
	IRS		ASD high-resolution FieldSpec4 spectroradiometer
	RS	SHERLOC	LabRam HR Evolution UV-laser Raman spectrometer
Rosalind Franklin rover	RS	RLS	RLS-Sim
	GC-MS	MOMA	GC-MS + GC-IRMS

In relation to the Rosalind Franklin rover analytical payload, the RLS-simulator was used in this work. The RLS instrument and the RLS-simulator share the same characteristics.

Finally, in order to analyze organic molecules, the GC-MS and GC-IRMS techniques were used as MOMA's analog. This is because MOMA will use GC-MS for volatile molecule characterization and LDMS for non-volatile molecules. Although the same method was used for volatile molecules analysis, the technique for non-volatile molecules was not the same. In this

work, in order to determine the carbon isotopic composition of individual lipids, the GC coupled to IRMS was used [87].

It should be noted that the specificities of the analog-instruments used in this work are described in Chapter 3.2.2.

### 5.3.2. Results and discussion

#### 5.3.2.1. Results of the PIXL-like instrument

Figure 5.13, 5.14 and 5.15 show the  $\mu$ -EDXRF imaging results for the main elements present in the three sides of the sample. The images were acquired with a motor step of 20  $\mu\text{m}$  between every single measurement, ensuring that the sample was completely scanned.

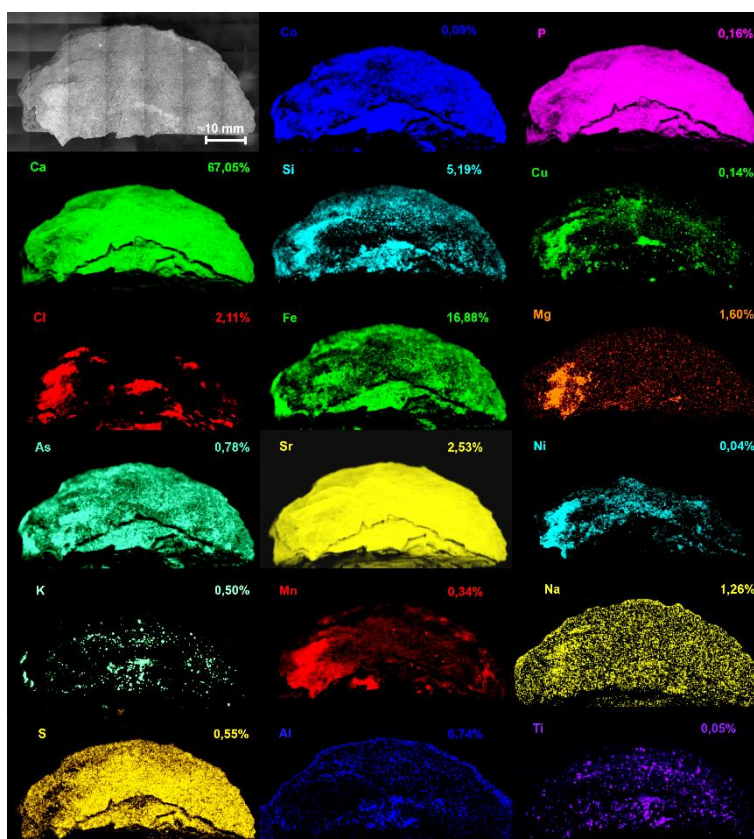


Figure 5.13. Optical and  $\mu$ -EDXRF image of the side A and the elemental distribution for Co, P, Ca, Si, Cu, Cl, Fe, Mg, As, Sr, Ni, K, Mn, Na, S, Al and Ti. These elemental maps were performed at 40 ms of real time and 2 cycles/frame counts.

The color intensity of the mapping for each element is directly correlated to the concentration of the given elements on the analyzed sample. Thus, brighter color means higher relative presence of element and vice versa, being the absence of the element represented by a black hole. In this sense, when the elemental distribution of more than one element matches

in the image, is likely due to the presence of a mineral that contains both (or three, four, etc.) chemical elements (positive correlation). Thus,  $\mu$ -EDXRF allows a) to ascertain the elemental composition of the samples, as well as b) to locate areas of potential minerals by analyzing the spatial distribution of the elements and c) pre-sampling procedure for molecular analysis.

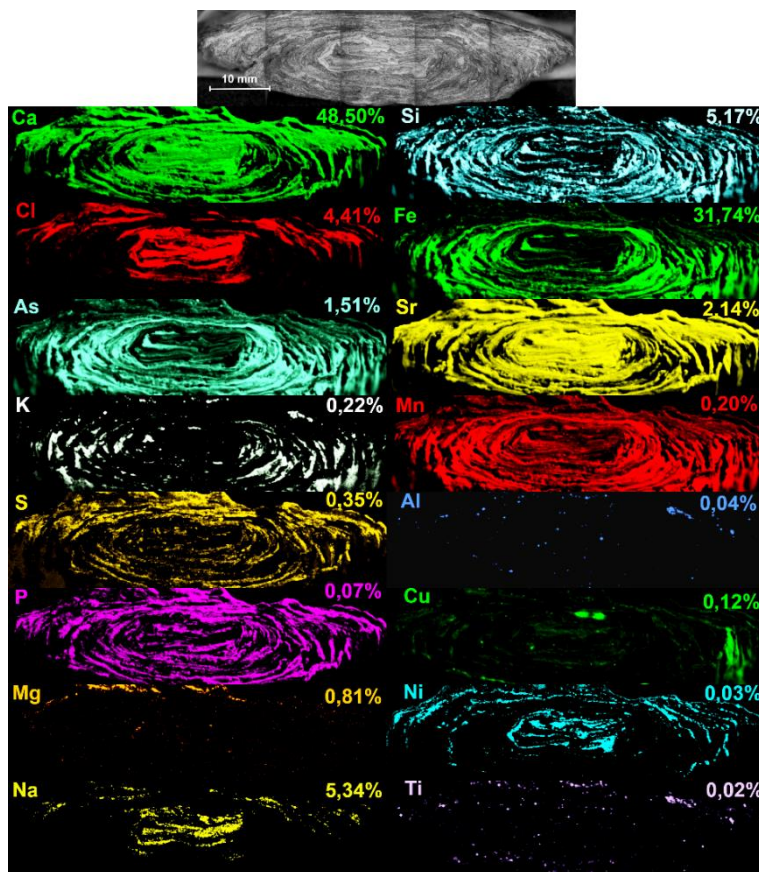


Figure 5.14. Optical and  $\mu$ -EDXRF image of the side B and the elemental distribution for Co, P, Ca, Si, Cu, Cl, Fe, Mg, As, Sr, Ni, K, Mn, Na, S, Al and Ti. These elemental maps were performed at 40 ms of real time and 2 cycles/frame counts.

As Figure 5.13 shows, the main element on side A of the sample is Ca, showing a wt. % higher than 67, among all the elements found. Fe, Si, Sr, Cl, Mg and Na are present in an abundance between 17 and 1 wt.%. Finally, the composition is completed by traces of As, Al, S, K, Mn, P, Cu, Ti, Ni and Co at below 1 wt.%. After analyzing the elemental chemical images of Figure 5.13, it can be seen that calcium, the major element in the sample, is distributed over the entire surface. It is necessary to remember that one of the limitations of  $\mu$ -EDXRF is to not detect elements with an atomic number lower than that of sodium, so it does not detect carbon. Carbon is the other elements expected to be found in abundance,

as microorganisms form these types of structures by forming calcium carbonate layers.

Figure 5.14 shows the elemental composition of side B. The elemental composition of this side is quite different from side A, since it has a lower Ca content (48.50 wt.%) and higher content of other elements such as Fe (31.75 wt.%). Each of the elements: Na, Si, Cl, Sr, As, Mg, S, K, Mn, Cu, P, Al, Ni and Ti, have a relative abundance less than 5.5 wt.%.

The distribution of chlorine, mainly in the core of the sample, is quite striking. This suggests that the early stages of oncoïd formation took place in chlorine-rich waters. What is also noteworthy is the high amount of iron and silicon on side B. This could be due to the presence of silicates and/or some iron-bearing oxides.

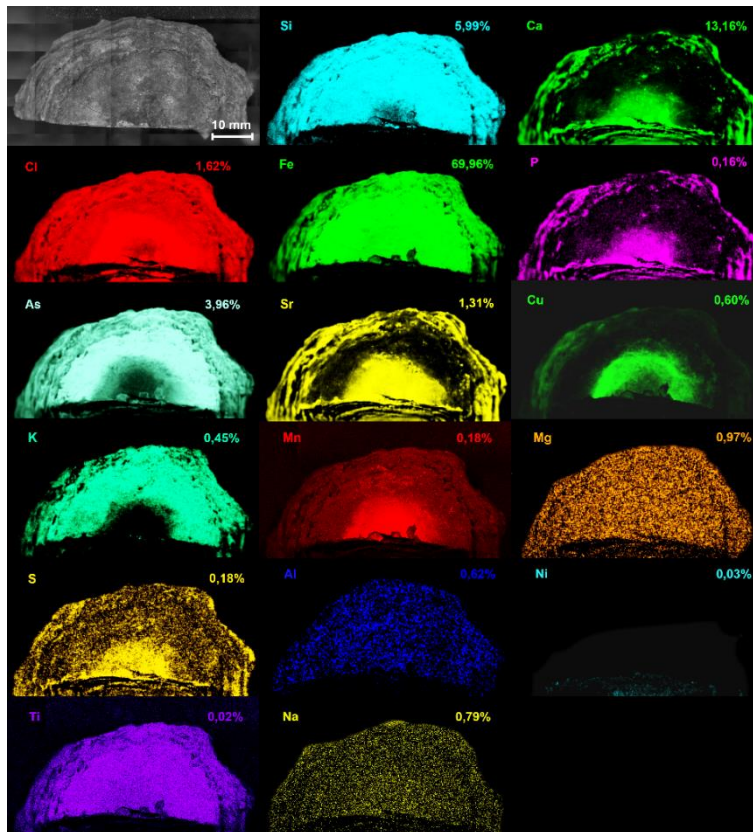


Figure 5.15. Optical and  $\mu$ -EDXRF image of the side C and the elemental distribution for Co, P, Ca, Si, Cu, Cl, Fe, Mg, As, Sr, Ni, K, Mn, Na, S, Al and Ti. These elemental maps were performed at 40 ms of real time and 2 cycles/frame counts.

Figure 5.15 shows the elemental composition of side C. In this case, the major element present in the sample was Fe (69.96 wt.%), instead of Ca (13.16 wt.%), which was the main element in A and B sides. Si, As, Cl, Sr,

---

Mg, Na, Al, Cu, K, Mn, S, P, Ti and Ni are the minor elements, each of them having a relative abundance lower than 6 wt.%.

Therefore, based on the elemental characterization, it can be said that side C is very different from the other two. Calcium, which in the other two sides was the major component, is in lower relative concentration. Possibly, this is due to how the sample rested in the field, as it will be explained below.

### 5.3.2.2. Results of the SuperCam-like instrument (LIBS and Raman instrument)

To complete the compositional characterization of the sample by SuperCam-like instrument, Raman and LIBS instruments were used. LIBS analysis was performed at 6 selected sampling positions on the oncoid surface. These positions were chosen attending to the different colorations of the sample, which could suggest a distinction of composition. A photographic detail of the 6 sampling locations are shown in Figure 5.16. LIBS analysis revealed the presence of emission lines for Ca I (at 422.67 nm), Fe I (at 404.58 nm), K I (at 766.49 nm), Li I (at 670.79 nm), Mg I (at 285.21 nm), Mn I (at 403.37 nm), Na I (at 589.59 nm), Si I (at 288.15 nm) and Sr I (at 460.73 nm) in all the sampling positions.

Significant compositional differences were observed regarding minor elements such as Al I, Ba II, Cu I, H<sub>α</sub>, O and Ti I (see Table 5.12). In addition, the CaO molecular band, ranging from 590 to 625 nm, was also identified in the LIBS spectra.

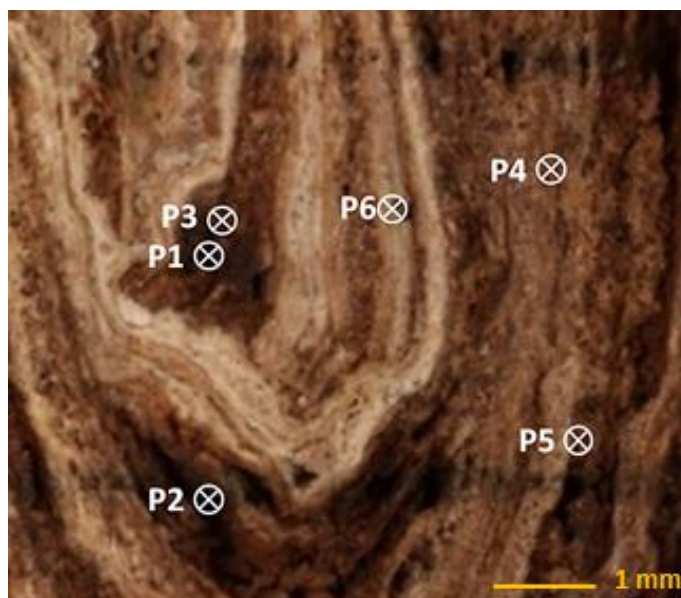


Figure 5.16. Sampling positions analyzed by LIBS.

Table 5.12. Minor elements detected by LIBS of the 6 sampling positions.

Atomic element	Wavelength (nm)	P1	P2	P3	P4	P5	P6
Al	394.40	X	-	-	X	X	-
Ba	455.40	X	-	X	X	-	X
Cu	324.75, 327.39	X	-	X	X	-	X
H	656.28	X	-	X	-	-	X
O	777.19, 777.42, 777.54	X	-	X	-	-	X
Rb	780.03	X	X	X	X	-	X

For positions 1, 3 and 6, LIBS detection of atomic hydrogen and oxygen lines could indicate the presence of certain hydrated salts or hydrogen-carbonate at these points. A more exhaustive analysis was proposed to evaluate the elemental distribution along the growing axis of the microbialite sample.

The sedimentary nature of the sample and its inherent roughness affected LIBS signal collection. To minimize the fluctuations in the acquired signal and to reduce the laser energy oscillation caused by changes in the plasma temperature and amount of ablated material, each spectrum was normalized to the total intensity of the spectra. Normalized LIBS results are shown in Figure 5.17.

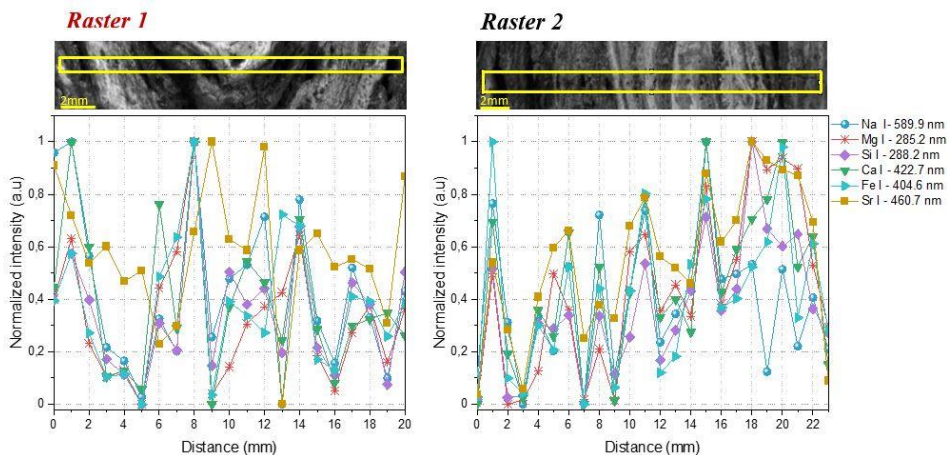
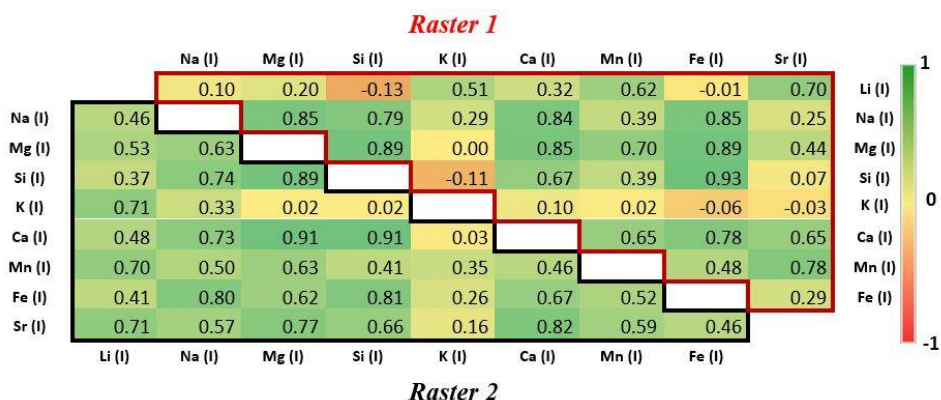


Figure 5.17. Lateral profile of the major elements along raster 1 and 3 (10 and 23 positions, respectively) under atmospheric conditions, 15 laser shots per sampling position. Energy used was 40 mJ per pulse. Spatial resolution 1 mm.

The emission lines Na (I) 589.9 nm, Mg (I) 285.2 nm, Si (I) 288.2 nm, Ca (I) 422.7 nm, Fe (I) 404.6 nm and Sr (I) 460.7 nm were monitored along the growing axis. In addition, as commented above, spectra were normalized to unity. As shown, differences among elements are noticeable.

From data plotted in Figure 5.17, a statistical study was performed using Pearson's correlation coefficients to verify the degree of variation between the input variables (see Table 5.13). Al and Ti were excluded, as they were not detected at all sampling points. As observed, in raster #1, Mg presents a high correlation with several of the rest of elements, with a Pearson's correlation coefficient value close to 0.90 for Na, Si and Fe. However, correlation coefficients for raster #2 are better than for raster #1. For both rasters, Ca (the major element) shows a higher correlation for all detected elements. It should be noted that when comparing to Figure 5.14, Fe and Si have a similar spatial distribution. In Table 5.13 some negative correlations appear between variables, like for K distributed in different zones with respect to Ca, Fe or Si. This fact is consistent with  $\mu$ -EDXRF results.

Table 5.13. Pearson correlations for the detected elements in the two sampled areas. In the upper triangular matrix are the relationships obtained from the net intensity data, collected from the spectra normalized to the total area, over the 24 positions of raster 1. The lower triangular matrix shows the same but for raster 2.



Due to the interest in detecting halogens Cl and F, the LIBS setup was modified. The atomic emissions of both elements have a lower relative intensity when compared to their potential molecular species, which produce an intense response even at low elemental concentrations. The detection strategy was focused on the identification of CaF ( $B\ 2\Sigma^+ \rightarrow X\ 2\Sigma^+$ ,  $\Delta v=0$ ) and CaCl ( $A^2\Pi \rightarrow X^2\Sigma$ ,  $\Delta v=0$ ) molecular bands. The formation of these molecular species takes place from recombination processes occurring during plasma cooling<sup>[88]</sup>, thus requiring both longer delay and integration times<sup>[89]</sup>. In addition, the collection angle was adjusted to 45° with respect to plasma expansion direction, which favors the sensitivity of the molecular emission signal. For comparative purposes, the acquired

LIBS spectra were compared with different patterns of fluorite, aragonite and  $\text{CaCl}_2$  (see Figure 5.18).

The  $\text{CaF}_2$  and  $\text{CaCl}_2$  molecular bands were analyzed in different spectral windows of the analyzed oncoïd. Figure 5.19 shows the chemical distribution of  $\text{CaF}_2$  and  $\text{CaCl}_2$  in different areas. The concentrations of chlorine and fluorine do not appear constant in the sample. Likewise, the dependence of the signal on the sample structure is evident.

The observed trend of each molecular emission,  $\text{CaCl}_2$  and  $\text{CaF}_2$ , was coincident with respect to the distribution of calcium in both spectral windows. The monitored calcium line was  $\text{Ca(I)}\ 611.76\ \text{nm}$  for the  $\text{CaCl}$  spectral region and  $\text{Ca(I)}\ 526.56\ \text{nm}$  for the  $\text{CaF}_2$  spectral region. The chlorine distribution was mainly located in the core of the sample and at one extreme side (see distance #11.5-14.5 mm). It must be considered that these data agree with the elemental maps for Cl obtained by  $\mu\text{-EDXRF}$ . Moreover, fluorine seems to be located, at higher concentration, in the outermost zones of the sample. The fluorine data cannot be  $\mu\text{-EDXRF}$ -checked because the atomic number of F is lower than that of Na.

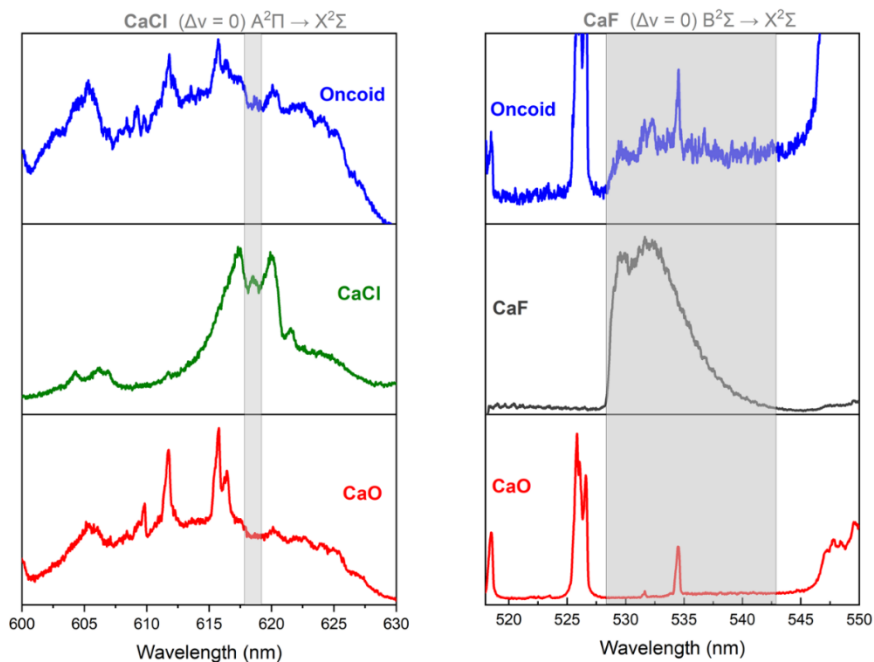


Figure 5.18. Comparative spectra between fluorite, aragonite,  $\text{CaCl}_2$  patterns and the oncoïd samples, in the regions where the  $\text{CaCl}_2$  (red system) and  $\text{CaF}_2$  (green system) molecular bands are located. Single shot, 50 ml per pulse.

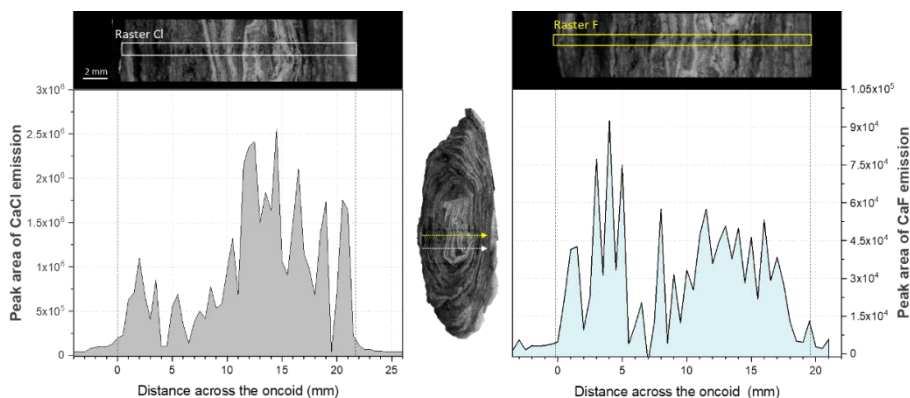


Figure 5.19. Comparison between gray value profile and the intensity of the CaF ( $B^2\Sigma^+ \rightarrow X^2\Sigma^+$ ,  $\Delta v = 0$ ), CaCl ( $A^2\Pi \rightarrow X^2\Sigma$ ,  $\Delta v = 0$ ) along of linear raster of 60 and 53 sampling locations, respectively, single shots per position. The energy used was 50 mJ per pulse. Spatial resolution 0.5 mm.

With regard to Raman spectroscopy, the aim was to identify the spectra of expected compounds after analyzing the elemental data from PIXL-like instrument and the combined technique with SuperCam-like instrument-LIBS. In this sense, the ERICA microRaman spectrometer was used.

As shown in Figure 5.20 B, the spectral signatures of aragonite were detected in association with additional Raman peaks of its polymorph, calcite. Although aragonite forms the skeletal structure of microbialites, its preservation in this sample was relatively low. This could be a consequence of the fact that under ambient conditions and in the presence of water, aragonite transforms into its polymorph calcite, which is the most stable polymorph [90].

However, after band decomposition in pure Lorentzian-Gaussian bands of the non-symmetric experimental Raman band (Figure 5.20 B), the main peak of calcite was found to be centered at  $1093\text{ cm}^{-1}$ , which supposes a shifting of  $6\text{-}7\text{ cm}^{-1}$  compared to nominal calcite standards. Similarly, secondary peaks also resulted shifted towards higher wavenumbers (from  $281$  to  $286\text{ cm}^{-1}$  and from  $711$  to  $720\text{ cm}^{-1}$  for lattice and  $\nu_4$  modes, respectively). As presented in previous works, peak shifting can be related to the cation substitution of Ca for Mg, which lead to the crystallization of the so-called high-magnesium calcite (HMC) [91]. Knowing the linear correlation between peak shifting and magnesium substitution, that has been experimentally confirmed in previous works [92], it can be assumed that the calcite detected in this sample has a Mg content above 20 wt.%. As reported elsewhere [93,94], the crystallization of HMC in water environment is often mediated by biological activity. Similarly, the simultaneous detection of HMC and aragonite is mostly found in biogenic structures, including oncoïds. Considering the application of Raman spectroscopy in planetary missions, this result highlights the relevance of

a high resolution mineral characterization of geological targets for astrobiology research.

Besides carbonate materials, Raman analysis also enabled the detection of two broad bands at 1330 and 1570  $\text{cm}^{-1}$  fitting the D and G vibrational bands of the kerogen, a compound that can either be related to biotic or abiotic processes.

As shown in Figure 5.20 A, pyroxene was also detected by its characteristic peaks at 315, 382, 658 and 1000  $\text{cm}^{-1}$  [95]. According to the flow chart for pyroxene discrimination presented by Wang et al. [95], peak position indicated the detection of a monoclinic mineral phase (e.g. augite). The presence of minor amounts of feldspars was also confirmed by the detection of the main doublet at 473 and 512  $\text{cm}^{-1}$ , followed by the secondary peak at 282  $\text{cm}^{-1}$ . By comparing the spectrum displayed in Figure 5.20 A with the reference pattern provided elsewhere [96], it can be assumed the detection of a K-feldspar (e.g. sanidine). Finally, hematite inclusions were also found, as proved by the identification of Raman peaks at 222, 291, 409, 495, 606, 662 and 1318  $\text{cm}^{-1}$  [96] in some of the studied spots.

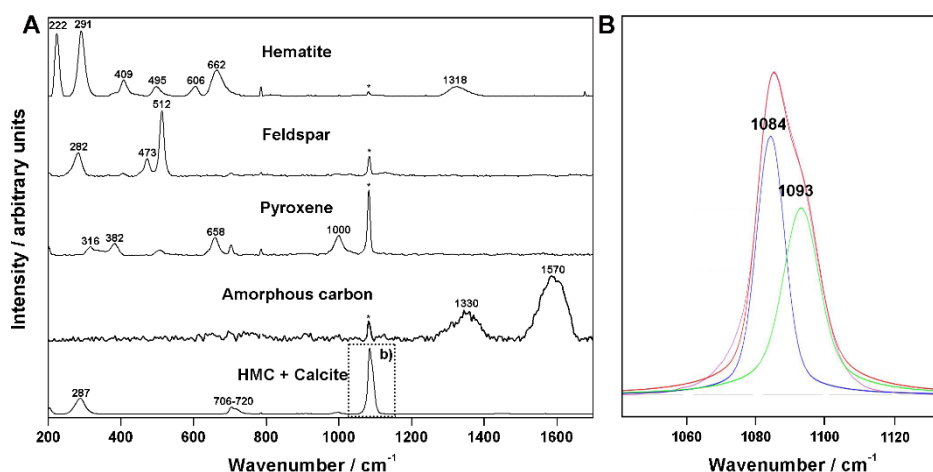
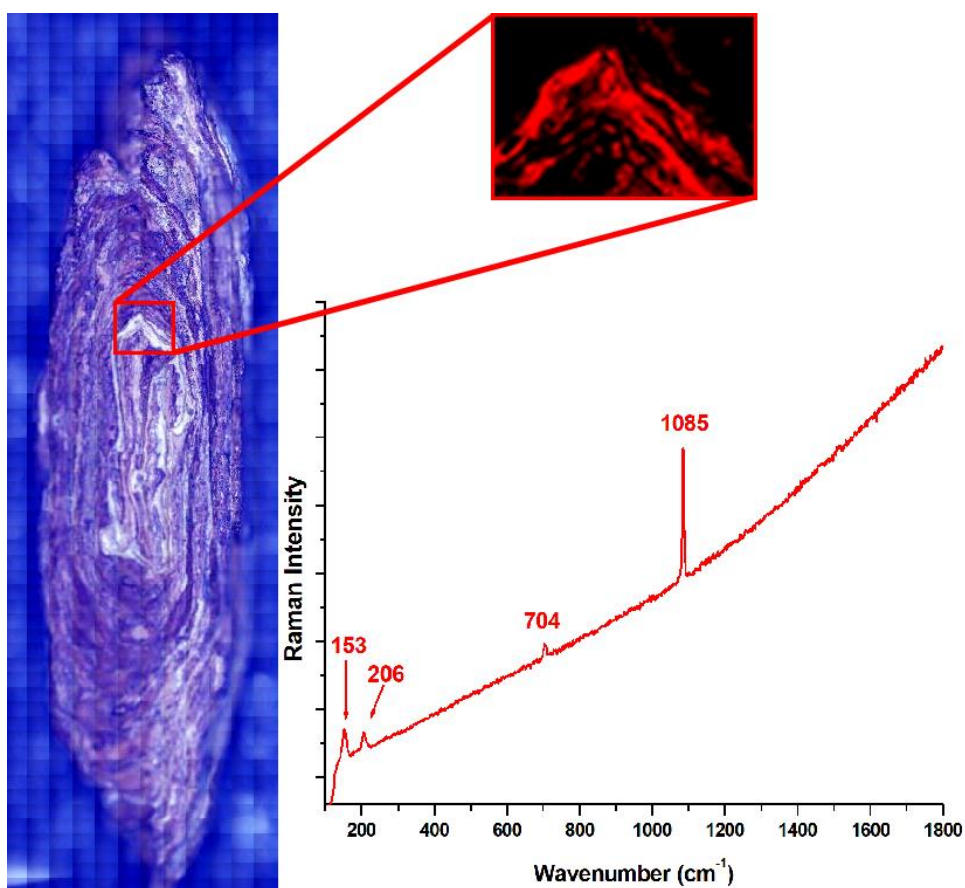


Figure 5.20. (A) Raman spectra of hematite, feldspar, pyroxene, kerogen, HMC\* and calcite, detected by the ERICA microRaman. (B) Band deconvolution of the v1 band of  $\text{CaCO}_3$  (purple: original spectra; blue: aragonite peak; green: calcite peak; and red: deconvoluted spectra).

The presence of pyroxene, feldspar and hematite could be related to the presence of soil remains on which the oncoïd was formed [97]. In fact, after analyzing the high presence of iron in the C side of the oncoïd (Figure 5.15), it can be established that this side was the one in contact with the ground.

In order to complete the Raman analyses, another Raman instrument was used, the Renishaw InVia system. It should be noted that this instrument is

not an analog to that of SuperCam and it was used just to complete the oncoïd molecular characterization. In this way, most of the Raman spectra collected with this instrument possessed the characteristic bands that appear at 153 (m, medium), 206 (w, weak), 704 (w) and 1085 (vs, very strong)  $\text{cm}^{-1}$  [98], which match with the aragonite Raman bands. Figure 5.21 shows the Raman spectrum of the aragonite found and its distribution along side B of the oncoïd sample. The Raman image on that part of side B indicates that aragonite is only distributed in the lighter colored layers. However, single Raman analyses were performed on the dark layers and aragonite was also identified. The reason that the Raman image did not represent correctly the presence of calcium carbonate is due to the sample's relief. The dark areas are deeper than the light areas, which were well focused by the Raman spectrometer, while the dark ones were not.



*Figure 5.21.* Optical image, Raman image and Raman spectrum of the aragonite distribution in a small part of the side B of the sample, using the SuperCam-like instrument. The Raman image of aragonite was obtained using the interval 201-210  $\text{cm}^{-1}$  that contains the one of the secondary Raman bands of aragonite. The Raman band at 1085  $\text{cm}^{-1}$  was not selected, since calcite and aragonite overlap their main Raman band at this wavenumber. In this way, possible confusions of mineralogical distribution are avoided. Measurement parameters: 532 nm laser, grating 1800 l/mm (vis), 7 s of exposure time, 10% of laser power and objective 5x. The Raman map was obtained from a mosaic acquired with the Renishaw

InVia microscope. This image is composed of 7980 points and was performed following the snake mapping mode.

In addition, thanks to these complementary Raman analyses, it was possible to detect a carotenoid through their main Raman bands detected at 959 (w), 1000 (m), 1151 (vs), 1193 (w), 1281 (w) and 1707 (vs) (Figure 5.22). According to literature <sup>[99,100]</sup>, this carotenoid is associated with halophilic archaeas. This finding links the oncoïd to the place where it was found, that is, a salt-saturated lake, and explains the high presence of halogens, such as chlorine and fluorine, already detected by  $\mu$ -EDXRF and LIBS.

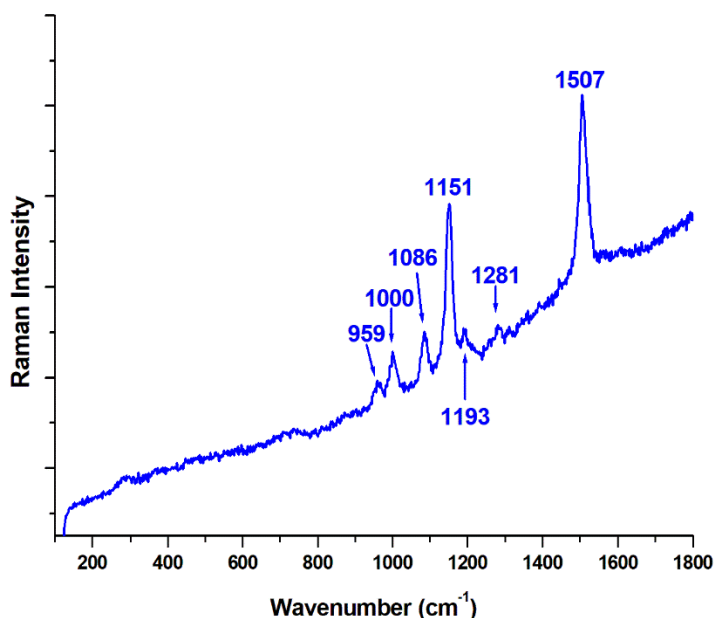


Figure 5.22. Halophilic archaea carotenoid Raman spectrum obtained by the InVia micro-Raman of the SuperCam-like instrument.

### 5.3.2.3. Results of the SHERLOC-like instrument

Although SHERLOC is used to identify potential biosignatures and to understand the aqueous history of the Jezero region in the Mars2020 mission, the SHERLOC-like instrument showed no evidence of the existence of organics in the oncoïd sample. Nevertheless, the SHERLOC-like instrument was able to identify the Raman bands of the aragonite. The measurement parameters used to obtain the aragonite spectrum were: 266 nm laser, extended mode (100-4000 cm<sup>-1</sup>), grating 2400 l/mm, 10 s of exposure time, 10% of laser power and objective 75x.

### 5.3.2.4. Results of the RLS-Sim instrument

The linear raster of 39 spots autonomously analyzed by the RLS-Sim, using the operational conditions constrained by the Rosalind Franklin mission,

confirmed the results provided by the SuperCam-like instrument. Results indicated the presence of aragonite in most of the investigated spots through its main Raman peaks (Figure 5.23). In addition to this, calcite was also detected in some occasions (main peaks at 282 and 1085  $\text{cm}^{-1}$ , see Figure 5.23). Moreover, the presence of K-feldspars was also confirmed by the identification of the characteristic peaks at 283, 473 and 512  $\text{cm}^{-1}$  (Figure 5.23).

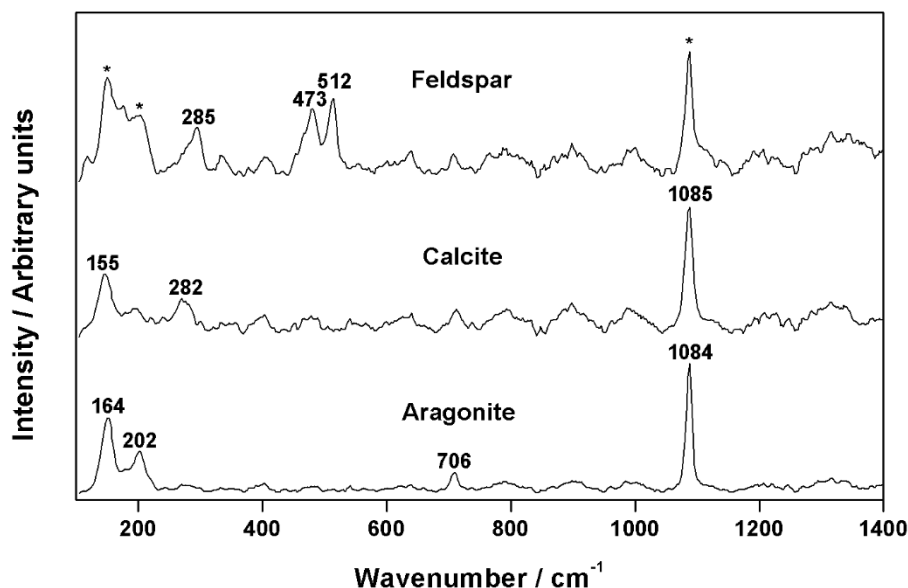


Figure 5.23. Raman spectra of aragonite, calcite and feldspar, detected by the RLS-like instrument.

### 5.3.2.5. Results of the MOMA-like instrument

The molecular profile of lipid biomarkers (hydrocarbons, fatty acids, alkanols and sterols) was similar in the inner and outer oncoïd layers (Figures 5.24, 5.25 and 5.26), but with concentrations an order of magnitude higher detected in the later. The relative abundance of lipids in the outer layer may be explained by the more recent synthesis relative to the older compounds preserved in the inner layer. Upon accretion, the oncoïd mineral matrix would have favored the preservation of the entombed biomarkers from damaging UV radiation.

On both layers a wide variety of hydrocarbons were found in the non-polar fraction (Figure 5.24), including a dominant series of n-alkanes from C<sub>15</sub> to C<sub>31</sub>, a few 1-alkenes (C<sub>16:1</sub>, C<sub>17:1</sub>, C<sub>18:1</sub> and C<sub>19:1</sub>), an organo-sulfur compound (2, 5 di-n-alkylthiophene), an organo-chlorine heptadecane (Chloro-17), and isoprenoids (squalene and dihydrosqualene).

The acidic fraction was dominated by a series of *n*-alkanoic acids from C<sub>12:0</sub> to C<sub>26:0</sub> (mostly C<sub>16:0</sub>), and some mono- (C<sub>14:1</sub>[ $\omega$ 5], C<sub>16:1</sub>[ $\omega$ 7], C<sub>17:1</sub>[ $\omega$ 7], C<sub>18:1</sub>[ $\omega$ 7] and C<sub>18:1</sub>[ $\omega$ 9]) and polyunsaturated alkanolic acids (C<sub>16:2</sub>[ $\omega$ 6], C<sub>18:2</sub>[ $\omega$ 6], C<sub>20:4</sub>[ $\omega$ 3], and C<sub>20:5</sub>[ $\omega$ 3]), cyclopropyl- acids (Cy<sub>17:0</sub> and Cy<sub>19:0</sub>), terminal branched (*iso/anteiso* C<sub>15:0</sub> and C<sub>17:0</sub>) and other monomethyl (MMe) alkanolic acids (Figure 5.25).

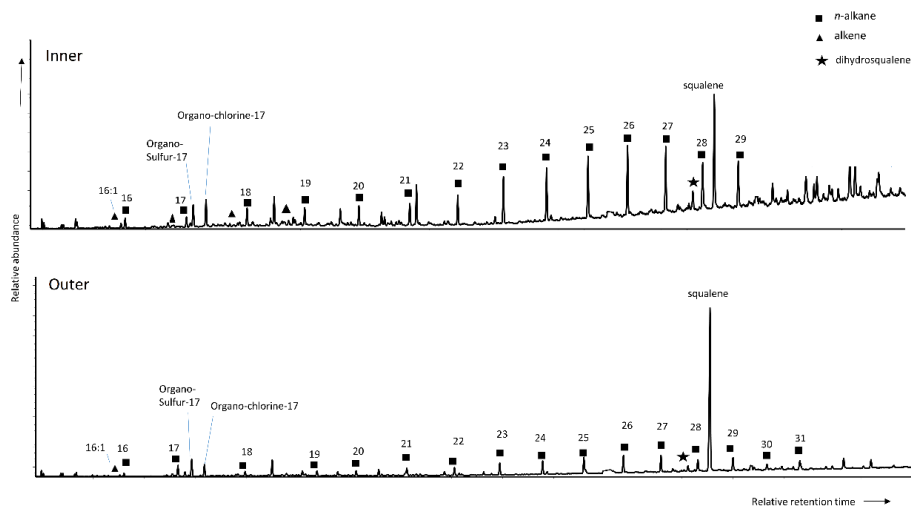


Figure 5.24. Total ion chromatogram of the non-polar fraction in the inner and outer layer samples of the oncoid measured by the MOMA-like instrument. The different families of hydrocarbons are represented by different symbols.

The polar fraction was dominated by phytol and relatives (neophytadiene and dihydrophytol), saturated alkanols from 14 to 22 carbons (C<sub>14</sub> to C<sub>22</sub>) and some of their monounsaturated homologs (C<sub>16:1</sub> and C<sub>18:1</sub>), and sterols such as cholesterol, ergosterol and a few phytosterols (stigmasterol, campesterol and  $\beta$ -sitosterol, Figure 5.26).

The lipid molecular profile of the oncoid suggested contribution from different prokaryotic and eukaryotic sources. On the one hand, the detection of short chain *n*-alkanes (C<sub>17</sub>) and alkenes (C<sub>16:1</sub>, C<sub>17:1</sub>, C<sub>18:1</sub> and C<sub>19:1</sub>) (Figure 5.24) was related to oxygenic phototrophic cyanobacteria [101,102], whereas that of cyclopropyl nonadecanoic acid (Cy<sub>19:0</sub>) to anoxygenic phototrophs such as purple sulfur bacteria (PSB) and/or green sulfur bacteria (GSB) [103]. On the other hand, the co-detection of the terminally branched *i/a*-C<sub>15:0</sub> and *i/a*-C<sub>17:0</sub>, the cyclopropyl Cy<sub>17:0</sub>, and the mid-chain branched 10Me-C<sub>16:0</sub> (Figure 5.25) was associated with sulfate reducing bacteria [103–105].

In addition, biomass from phototrophic eukaryotes such as diatoms was deduced from the identification of the polyunsaturated alkanolic acids C<sub>20:4</sub> and C<sub>20:5</sub> [106]. The detection of the phytosterols campesterol, stigmasterol,

and  $\beta$ -sitosterol support the microalgae inputs, although contribution from allochthonous sources (i.e. local higher plants) could also be possible. The relative abundance of photosynthetic microorganisms was supported by the relative abundance of phytol (i.e. a side chain of chlorophyll-*a*; Figure 5.26) and the  $\delta^{13}\text{C}$  values (26.2 to -35.6 ‰) measured for the lipids, overall compatible with a carbon fixation by the Calvin–Benson–Bassham cycle [107] typically used by cyanobacteria, PSB, algae, and higher plants [108]. Still, the most depleted  $\delta^{13}\text{C}$  values (lower than ca. -32 ‰) might represent the use of the alternative Wood-Ljungdahl (reductive acetyl CoA) pathway [109] by fermentative and acetogen SRB [108]. The biomarkers profile in the oncoïd is comparable to that found in similar hypersaline settings in the Argentinean Andes and have been related to induced mineral precipitation of stromatolites in Andean lakes.

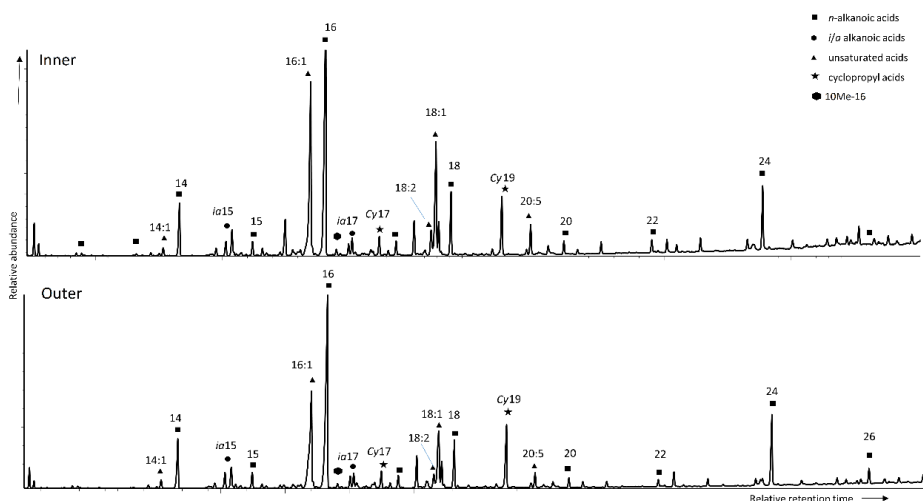


Figure 5.25. Total ion chromatogram of the acid fraction from the inner and outer layers of the oncoïd measured by the MOMA-like instrument. The different families of alkanolic acids are represented by different symbols.

The detection of lipidic biomarkers by GC-MS is relevant for the search of organics on Mars. Lipids are ubiquitous and relatively more geostable biomolecules than others with potential to persist in the geological record for up to billions of years [110] under ideal conditions (i.e. mild diagenesis). They provide a testimony of life that can be unequivocal when their molecular detection is combined with their compound-specific isotopic analysis.

Mineral protection such as that exerted by aragonite in the oncoïd sample can favor the preservation of biomarkers by acting as a shield of strong UV radiation or other aggressive environmental factors. Ideally, the SAM or MOMA instruments could detect organic signals in Martian settings harboring water bodies in the past similar to those described in this work.

Thus, interpreting the molecular and isotopic lipid fingerprints in the oncoid provides insights for the interpretation of potentially similar signals in samples with comparable structure (stromatolitic) from Noachian Mars. In fact, the SAM instrument has already detected a number of short-chain hydrocarbons (C<sub>10</sub>-C<sub>12</sub>) at the Gale crater [57] that have been hypothesized to be potential degradation products of carboxylic acids.

The plausible discovery of more short-chain lipids in other Martian samples highlights the need for further decoding of biomarker records in aquatic environments analogous to ancient Mars.

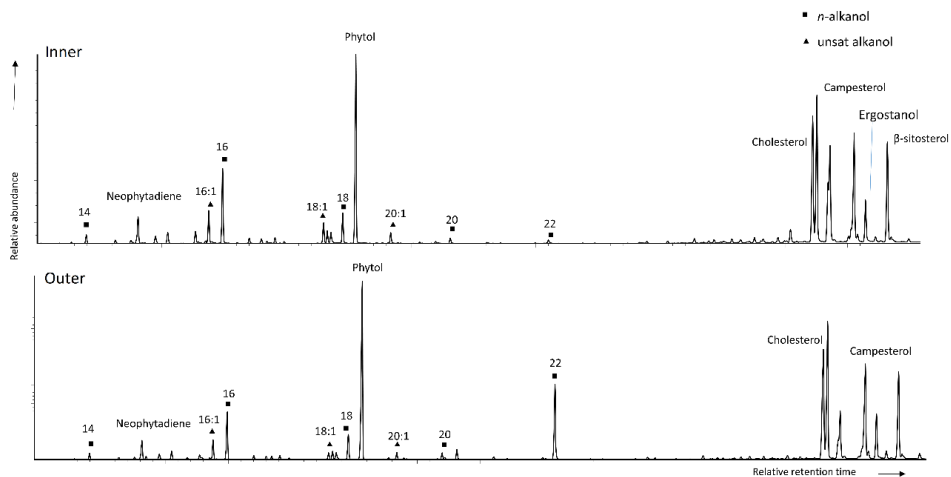


Figure 5.26. Total ion chromatogram of the polar fraction from the inner and outer layers of the oncoid measured by the MOMA-like instrument. Different symbols over the peaks indicate the type of alcohol compound.

### 5.3.3. Discussion

By using all techniques described above, it was possible to verify that a good methodology in sample characterization consists of a first recognition by elemental techniques (PIXL and LIBS of SuperCam-like instruments). For example, the presence of halogens suggests that in the first stages of the oncoid formation the surrounding environment was rich in salts. Although that presence could also indicate that, the microorganisms that formed the oncoid had the capacity to deposit halogens. In addition, by identifying the distribution of elements along the sample, it was possible to detect hotspots where more than one element coexisted. In this way, elemental techniques also gave clues about which minerals could possibly be found before the subsequent use of molecular analytical techniques.

Raman analyses performed with SuperCam-, SHERLOC- and RLS-like instruments revealed that the dominant mineral, distributed along the whole sample, was aragonite. This data agrees with the elemental distribution of

---

calcium obtained with the PIXL-like instrument. Besides, after performing more detailed analysis, the SuperCam-like instrument was able to detect minor compounds, such as calcite, HMC, feldspars, pyroxenes, kerogen and hematite. Calcite was likely present because under specific ambient conditions and in the presence of water, aragonite transforms into calcite, which is the most stable polymorph. It is worthy to point out that the presence of HMC is relevant from a biogeochemical point of view since the cation substitution of Ca for Mg may occur in aqueous environments dominated by biological activity. In this way, the finding of kerogen by Raman spectroscopy is also very relevant as probes the presence of ancient carbonaceous material.

The abundances of Al, Si, Fe and other elements reflect the soil influence on which the oncoïd was formed. This fact was also reflected in the detection of pyroxene, feldspar and hematite. In fact, after analyzing the high presence of iron in the C side of the oncoïd, it was inferred that, this side was likely the one in contact with the ground.

As mentioned above, it should also be noted that the sample was cut, allowing access to the side B for analysis. Taking into account that it is a soft carbonate sample, when it was split, material was removed, leaving holes that could not be detected by spectroscopic imaging techniques, such as  $\mu$ -EDXRF, LIBS and Raman images. In response to this, the images show dark areas that could not be focused with the microscope because the surface was not smooth and homogeneous.

Finally, it is known that the Salar Carachi Pampa is characterized by being a salt-saturated lake, where only extremophile microorganisms can live. A wide variety of lipids biomarkers were found thanks to the MOMA-like instrument, which are similar to those reported on similar hypersaline lakes from the same location, and correspond to a wide microbial community. Besides, some eukaryotes biomarkers could also be found, as well as a halophilic bacteria carotenoid by Raman spectroscopy.

Thanks to this work, it has been possible to see how all the techniques used in a complementary way allowed a complete comprehension of the formation of Martian relevant complex biostructure. It is important to notice that the results of the instruments should be analyzed as a whole, which can provide more relevant information than using only the data from one instrument. In this way, the lack of information generated by the drawbacks related to some instruments, such as low detection limits and/or critical spectral resolutions, are complemented by the information coming from other instruments.

## 5.4. Conclusions

Thanks to the experiments carried out in this chapter, it was possible to study three manners in which biosignatures can be found on Mars.

Firstly, biosignatures could be retained and protected under the crust of Mars. It has been proven that these crusts could be formed due to the evaporation of water and the precipitation of dissolved salts. Thus allowing the biosignatures to be protected. However, more studies about this issue should be carried out.

Secondly, it was proved that the preservation of long-chain organic molecules is favorable on clay minerals, in particular montmorillonite and hectorite. This preservation is favored at low pH values because organic molecules seem to be trapped. These ideal conditions could be found in Martian regolith because it was rich in sulfur acids due to the high volcanism.

Moreover, it was proved that it is possible to find traces of biomolecules retained in the interlayers of Martian clays by the payload of the current and future landed missions. As future work, a complementary experiment to this study would assess the residence time of the protected molecules against ultraviolet radiation.

The third pathway for the detection of possible biosignatures is the identification of microbialites on Mars. Thanks to this study, it has been possible to evaluate what results would be obtained after studying a microbialite, specifically an oncoïd, using the analytical techniques on board the Perseverance and Rosalind Franklin rovers.

Regarding biosignatures, a wide variety of lipids biomarkers, eukaryotes biomarkers and halophilic bacteria could be identified. Thus, as in the terrestrial oncoïd analyzed in this work, it is possible that biosignatures can be found in the Martian microbialites. However, as in the previous case, future works should be done to ensure the protection of these biomolecules in their respective protective structures against ultraviolet radiation.

It is well known that the high bombardment of ionizing particles from the Sun and stars, including ultraviolet radiation, causes the decomposition of any organic molecule. Thus, it would be interesting to evaluate the protective capacity of smectites and microbialites to preserve biosignatures against different intensities of ultraviolet radiation. This could be carried out by simulating Martian radiation at different exposure times and analyzing the samples with the same analytical techniques used above. Following this methodology, it would be possible to trace the history of organics on Mars as a function of UV-exposure-time.

---

Finally, as a general conclusion, it has been possible to verify the existence of organic molecules protective structures on Mars, as well as to predict the possible responses of the instruments on board the Perseverance and Rosalind Franklin rovers to the analysis of these structures.

## 5.5. Referencies

- [1] Poch, O.; Noblet, A.; Stalport, F.; Correia, J. J.; Grand, N.; Szopa, C.; Coll, P. Chemical Evolution of Organic Molecules under Mars-like UV Radiation Conditions Simulated in the Laboratory with the “Mars Organic Molecule Irradiation and Evolution” (MOMIE) Setup. *Planet. Space Sci.* **2013**, *85*, 188. <https://doi.org/10.1016/j.pss.2013.06.013>.
- [2] Bianciardi, G.; Rizzo, V.; Cantasano, N. Opportunity Rover’s Image Analysis: Microbialites on Mars? *Int. J. Aeronaut. Sp. Sci.* **2014**, *15*, 419. <https://doi.org/10.5139/IJASS.2014.15.4.419>.
- [3] Bianciardi, G.; Rizzo, V. Microbialites at Gusev Crater, Mars. *J. Astrobiol. Outreach* **2015**, *03*, 1000143. <https://doi.org/10.4172/2332-2519.1000143>.
- [4] Elewa, A. M. T. Fossils on Mars: A Brief Review of the Evidence. *J. Astrobiol.* **2021**, *7*, 29.
- [5] Vago, J. L.; Westall, F.; Pasteur Instrument Teams, L. S.; Coates, A. J.; Jaumann, R.; Korablev, O.; Ciarletti, V.; Mitrofanov, I.; Josset, J.-L.; De Sanctis, M. C.; Bibring, J.-P.; Rull, F.; Goesmann, F.; Steininger, H.; Goetz, W.; Brinckerhoff, W.; Szopa, C.; Raulin, F.; Westall, F.; Edwards, H. G. M.; Whyte, L. G.; Fairén, A. G.; Bibring, J.-P.; Bridges, J.; Hauber, E.; Ori, G. G.; Werner, S.; Loizeau, D.; Kuzmin, R. O.; Williams, R. M. E.; Flahaut, J.; Forget, F.; Vago, J. L.; Rodionov, D.; Korablev, O.; Svedhem, H.; Sefton-Nash, E.; Kminek, G.; Lorenzoni, L.; Joudrier, L.; Mikhailov, V.; Zashchirinskiy, A.; Alexashkin, S.; Calantropio, F.; Merlo, A.; Poulakis, P.; Witasse, O.; Bayle, O.; Bayón, S.; Meierhenrich, U.; Carter, J.; García-Ruiz, J. M.; Baglioni, P.; Haldemann, A.; Ball, A. J.; Debus, A.; Lindner, R.; Haessig, F.; Monteiro, D.; Trautner, R.; Volland, C.; Rebeyre, P.; Goult, D.; Didot, F.; Durrant, S.; Zekri, E.; Koschny, D.; Toni, A.; Visentin, G.; Zwick, M.; van Winnendael, M.; Azkarate, M.; Carreau, C.; the ExoMars Project Team. Habitability on Early Mars and the Search for Biosignatures with the ExoMars Rover. *Astrobiology* **2017**, *17*, 471. <https://doi.org/10.1089/ast.2016.1533>.
- [6] Farías, M. E.; Saona-Acuña, L. A. Modern Microbial Mats and Endoevaporite Systems in Andean Lakes: A General Approach. In *Microbial Ecosystems in Central Andes Extreme Environments*; Farías, M. E., Ed.; Springer International Publishing: Cham, 2020; pp 21–28. <https://doi.org/10.1007/978-3-030-36192-1>.
- [7] Burne, R. V.; Moore, L. S. Microbialites: Organosedimentary Deposits of Benthic Microbial Communities. *Palaeos* **1987**, *2*, 241. <https://doi.org/10.2307/3514674>.
- [8] Keil, R. G.; Mayer, L. M. Mineral Matrices and Organic Matter. In *Treatise on Geochemistry*; Holland, H. D., Turekian, K. K., Eds.; Elsevier, 2014; pp 337–359. <https://doi.org/10.1016/B978-0-08-095975-7.01024-X>.
- [9] Aubrey, A.; Cleaves, H. J.; Chalmers, J. H.; Skelley, A. M.; Mathies,

- 
- R. A.; Grunthner, F. J.; Ehrenfreund, P.; Bada, J. L. Sulfate Minerals and Organic Compounds on Mars. *Geology* **2006**, *34*, 357. <https://doi.org/10.1130/G22316.1>.
- [10] Certini, G.; Ugolini, F. C. An Updated, Expanded, Universal Definition of Soil. *Geoderma* **2013**, *192*, 378. <https://doi.org/10.1016/j.geoderma.2012.07.008>.
- [11] Certini, G.; Karunatillake, S.; Zhao, Y.-Y. S.; Meslin, P.-Y.; Cousin, A.; Hood, D. R.; Scalenghe, R. Disambiguating the Soils of Mars. *Planet. Space Sci.* **2020**, *186*, 104922. <https://doi.org/10.1016/j.pss.2020.104922>.
- [12] Clark, B. C.; Baird, A. K.; Rose, H. J.; Toulmin III, P.; Castro, A. J.; Kelliher, W. C.; Rowe, C. D.; Evans, P. H. Inorganic Analysis of Martian Surface Samples at the Viking Landing Sites. *Science*. **1976**, *194*, 1283.
- [13] Bairs, A. K.; Toulmin III, P.; Clark, B. C.; Rose, H. J.; Keil, K.; Christian, R. P.; Gooding, J. L. Mineralogic and Petrologic Implications of Viking Geochemical Results From Mars: Interim Report. *Science*. **1976**, *194*, 1288. <https://doi.org/10.1126/science.194.4271.1288>.
- [14] Clark, B. C.; Baird, A. K.; Weldon, R. J.; Tsusaki, D. M.; Schnabel, L.; Candelaria, M. P. Chemical Composition of Martian Fines. *J. Geophys. Res.* **1982**, *87*, 10059. <https://doi.org/10.1029/JB087iB12p10059>.
- [15] Clark, B. C. Geochemical Components in Martian Soil. *Geochim. Cosmochim. Acta* **1993**, *57*, 4575. [https://doi.org/10.1016/0016-7037\(93\)90183-W](https://doi.org/10.1016/0016-7037(93)90183-W).
- [16] Rieder, R.; Economou, T.; Wänke, H.; Turkevich, A.; Crisp, J.; Brückner, J.; Dreibus, G.; McSween, H. Y. The Chemical Composition of Martian Soil and Rocks Returned by the Mobile Alpha Proton X-Ray Spectrometer: Preliminary Results from the X-Ray Mode. *Science*. **1997**, *278*, 1771. <https://doi.org/10.1126/science.278.5344.1771>.
- [17] Ward, J.; Byrne, P. *PDS Geoscience Node. Washington University in St. Louis*. PDS Planetary Data System. NASA Repository. <https://pds-geosciences.wustl.edu/> (accessed 2023-02-02).
- [18] Arvidson, R. E.; Bell, J. F.; Bellutta, P.; Cabrol, N. A.; Catalano, J. G.; Cohen, J.; Crumpler, L. S.; Des Marais, D. J.; Estlin, T. A.; Farrand, W. H.; Gellert, R.; Grant, J. A.; Greenberger, R. N.; Guinness, E. A.; Herkenhoff, K. E.; Herman, J. A.; Iagnemma, K. D.; Johnson, J. R.; Klingelhöfer, G.; Li, R.; Lichtenberg, K. A.; Maxwell, S. A.; Ming, D. W.; Morris, R. V.; Rice, M. S.; Ruff, S. W.; Shaw, A.; Siebach, K. L.; de Souza, P. A.; Stroupe, A. W.; Squyres, S. W.; Sullivan, R. J.; Talley, K. P.; Townsend, J. A.; Wang, A.; Wright, J. R.; Yen, A. S. Spirit Mars Rover Mission: Overview and Selected Results from the Northern Home Plate Winter Haven to the Side of Scamander Crater. *J. Geophys. Res.* **2010**, *115*, E00F03.
-

- <https://doi.org/10.1029/2010JE003633>.
- [19] Arvidson, R. E.; Ashley, J. W.; Bell, J. F.; Chojnacki, M.; Cohen, J.; Economou, T. E.; Farrand, W. H.; Fergason, R.; Fleischer, I.; Geissler, P.; Gellert, R.; Golombek, M. P.; Grotzinger, J. P.; Guinness, E. A.; Haberle, R. M.; Herkenhoff, K. E.; Herman, J. A.; Iagnemma, K. D.; Jolliff, B. L.; Johnson, J. R.; Klingelhöfer, G.; Knoll, A. H.; Knudson, A. T.; Li, R.; McLennan, S. M.; Mittlefehldt, D. W.; Morris, R. V.; Parker, T. J.; Rice, M. S.; Schröder, C.; Soderblom, L. A.; Squyres, S. W.; Sullivan, R. J.; Wolff, M. J. Opportunity Mars Rover Mission: Overview and Selected Results from Purgatory Ripple to Traverses to Endeavour Crater. *J. Geophys. Res.* **2011**, *116*, E00F15. <https://doi.org/10.1029/2010JE003746>.
- [20] Hecht, M. H.; Kounaves, S. P.; Quinn, R. C.; West, S. J.; Young, S. M. M.; Ming, D. W.; Catling, D. C.; Clark, B. C.; Boynton, W. V.; Hoffman, J.; DeFlores, L. P.; Gospodinova, K.; Kapit, J.; Smith, P. H. Detection of Perchlorate and the Soluble Chemistry of Martian Soil at the Phoenix Lander Site. *Science*. **2009**, *325*, 64. <https://doi.org/10.1126/science.1172466>.
- [21] Kounaves, S. P.; Hecht, M. H.; Kapit, J.; Quinn, R. C.; Catling, D. C.; Clark, B. C.; Ming, D. W.; Gospodinova, K.; Hredzak, P.; McElhoney, K.; Shusterman, J. Soluble Sulfate in the Martian Soil at the Phoenix Landing Site. *Geophys. Res. Lett.* **2010**, *37*, L09201. <https://doi.org/10.1029/2010GL042613>.
- [22] Fishbaugh, K. E.; Poulet, F.; Chevrier, V.; Langevin, Y.; Bibring, J.-P. On the Origin of Gypsum in the Mars North Polar Region. *J. Geophys. Res.* **2007**, *112*, E07002. <https://doi.org/10.1029/2006JE002862>.
- [23] Blake, D. F.; Morris, R. V.; Kocurek, G.; Morrison, S. M.; Downs, R. T.; Bish, D.; Ming, D. W.; Edgett, K. S.; Rubin, D.; Goetz, W.; Madsen, M. B.; Sullivan, R.; Gellert, R.; Campbell, I.; Treiman, A. H.; McLennan, S. M.; Yen, A. S.; Grotzinger, J.; Vaniman, D. T.; Chipera, S. J.; Achilles, C. N.; Rampe, E. B.; Sumner, D.; Meslin, P.-Y.; Maurice, S.; Forni, O.; Gasnault, O.; Fisk, M.; Schmidt, M.; Mahaffy, P.; Leshin, L. A.; Glavin, D.; Steele, A.; Freissinet, C.; Navarro-González, R.; Yingst, R. A.; Kah, L. C.; Bridges, N.; Lewis, K. W.; Bristow, T. F.; Farmer, J. D.; Crisp, J. A.; Stolper, E. M.; Des Marais, D. J.; Sarrazin, P.; MarsScienceLaboratoryTeam. Curiosity at Gale Crater, Mars: Characterization and Analysis of the Rocknest Sand Shadow. *Science*. **2013**, *341*, 12395. <https://doi.org/10.1126/science.1239505>.
- [24] Leshin, L. A.; Mahaffy, P. R.; Webster, C. R.; Cabane, M.; Coll, P.; Conrad, P. G.; Archer, P. D.; Atreya, S. K.; Brunner, A. E.; Buch, A.; Eigenbrode, J. L.; Flesch, G. J.; Franz, H. B.; Freissinet, C.; Glavin, D. P.; McAdam, A. C.; Miller, K. E.; Ming, D. W.; Morris, R. V.; Navarro-González, R.; Niles, P. B.; Owen, T.; Pepin, R. O.; Squyres, S.; Steele, A.; Stern, J. C.; Summons, R. E.; Sumner, D. Y.; Sutter, B.; Szopa, C.; Teinturier, S.; Trainer, M. G.; Wray, J. J.; Grotzinger,

---

J. P.; MarsScienceLaboratoryTeam. Volatile, Isotope, and Organic Analysis of Martian Fines with the Mars Curiosity Rover. *Science*. **2013**, *341*, 12389. <https://doi.org/10.1126/science.1238937>.

- [25] Meslin, P.-Y.; Gasnault, O.; Forni, O.; Schröder, S.; Cousin, A.; Berger, G.; Clegg, S. M.; Lasue, J.; Maurice, S.; Sautter, V.; Le Mouélic, S.; Wiens, R. C.; Fabre, C.; Goetz, W.; Bish, D.; Mangold, N.; Ehlmann, B.; Lanza, N.; Harri, A.-M.; Anderson, R.; Rampe, E.; McConnochie, T. H.; Pinet, P.; Blaney, D.; Lèveillé, R.; Archer, D.; Barraclough, B.; Bender, S.; Blake, D.; Blank, J. G.; Bridges, N.; Clark, B. C.; DeFlores, L.; Delapp, D.; Dromart, G.; Dyar, M. D.; Fisk, M.; Gondet, B.; Grotzinger, J.; Herkenhoff, K.; Johnson, J.; Lacour, J.-L.; Langevin, Y.; Leshin, L.; Lewin, E.; Madsen, M. B.; Melikechi, N.; Mezzacappa, A.; Mischna, M. A.; Moores, J. E.; Newsom, H.; Ollila, A.; Perez, R.; Renno, N.; Sirven, J.-B.; Tokar, R.; de la Torre, M.; D'Uston, L.; Vaniman, D.; Yingst, A.; Kemppinen, O.; Minitti, M.; Cremers, D.; Bell, J. F.; Edgar, L.; Farmer, J.; Godber, A.; Wadhwa, M.; Wellington, D.; McEwan, I.; Newman, C.; Richardson, M.; Charpentier, A.; Peret, L.; King, P.; Weigle, G.; Schmidt, M.; Li, S.; Milliken, R.; Robertson, K.; Sun, V.; Baker, M.; Edwards, C.; Farley, K.; Griffes, J.; Miller, H.; Newcombe, M.; Pilorget, C.; Rice, M.; Siebach, K.; Stack, K.; Stolper, E.; Brunet, C.; Hipkin, V.; Marchand, G.; Sánchez, P. S.; Favot, L.; Cody, G.; Steele, A.; Flückiger, L.; Lees, D.; Nefian, A.; Martin, M.; Gailhanou, M.; Westall, F.; Israël, G.; Agard, C.; Baroukh, J.; Donny, C.; Gaboriaud, A.; Guillemot, P.; Lafaille, V.; Lorigny, E.; Paillet, A.; Pérez, R.; Saccoccio, M.; Yana, C.; Armiens-Aparicio, C.; Rodríguez, J. C.; Blázquez, I. C.; Gómez, F. G.; Gómez-Elvira, J.; Hettrich, S.; Malvitte, A. L.; Jiménez, M. M.; Martínez-Frías, J.; Martín-Soler, J.; Martín-Torres, F. J.; Jurado, A. M.; Mora-Sotomayor, L.; Caro, G. M.; López, S. N.; Peinado-González, V.; Pla-García, J.; Manfredi, J. A. R.; Romeral-Planelló, J. J.; Fuentes, S. A. S.; Martinez, E. S.; Redondo, J. T.; Urqui-O'Callaghan, R.; Mier, M.-P. Z.; Chipera, S.; Mauchien, P.; Manning, H.; Fairén, A.; Hayes, A.; Joseph, J.; Squyres, S.; Sullivan, R.; Thomas, P.; Dupont, A.; Lundberg, A.; DeMarines, J.; Grinspoon, D.; Reitz, G.; Prats, B.; Atlaskin, E.; Genzer, M.; Haukka, H.; Kahanaää, H.; Kauhanen, J.; Kemppinen, O.; Paton, M.; Polkko, J.; Schmidt, W.; Siili, T.; Wray, J.; Wilhelm, M. B.; Poitrasson, F.; Patel, K.; Gorevan, S.; Indyk, S.; Paulsen, G.; Gupta, S.; Schieber, J.; Geffroy, C.; Baratoux, D.; Cros, A.; Lee, Q.-M.; Pallier, E.; Parot, Y.; Toplis, M.; Brunner, W.; Heydari, E.; Achilles, C.; Oehler, D.; Sutter, B.; Cabane, M.; Coscia, D.; Israël, G.; Szopa, C.; Robert, F.; Nachon, M.; Buch, A.; Stalport, F.; Coll, P.; François, P.; Raulin, F.; Teinturier, S.; Cameron, J.; Dingler, R.; Jackson, R. S.; Johnstone, S.; Little, C.; Nelson, T.; Williams, R. B.; Jones, A.; Kirkland, L.; Treiman, A.; Baker, B.; Cantor, B.; Caplinger, M.; Davis, S.; Duston, B.; Edgett, K.; Fay, D.; Hardgrove, C.; Harker, D.; Herrera, P.; Jensen, E.; Kennedy, M. R.; Krezoski, G.; Krysak, D.; Lipkaman, L.; Malin, M.; McCartney, E.; McNair, S.; Nixon, B.; Posiolova, L.; Ravine, M.;

Salamon, A.; Saper, L.; Stoiber, K.; Supulver, K.; Van Beek, J.; Van Beek, T.; Zimdar, R.; French, K. L.; Iagnemma, K.; Miller, K.; Summons, R.; Goesmann, F.; Hviid, S.; Johnson, M.; Lefavor, M.; Lyness, E.; Breves, E.; Fassett, C.; Bristow, T.; DesMarais, D.; Edwards, L.; Haberle, R.; Hoehler, T.; Hollingsworth, J.; Kahre, M.; Keely, L.; McKay, C.; Wilhelm, M. B.; Bleacher, L.; Brinckerhoff, W.; Choi, D.; Conrad, P.; Dworkin, J. P.; Eigenbrode, J.; Floyd, M.; Freissinet, C.; Garvin, J.; Glavin, D.; Harpold, D.; Jones, A.; Mahaffy, P.; Martin, D. K.; McAdam, A.; Pavlov, A.; Raaen, E.; Smith, M. D.; Stern, J.; Tan, F.; Trainer, M.; Meyer, M.; Posner, A.; Voytek, M.; Anderson, R. C.; Aubrey, A.; Beegle, L. W.; Behar, A.; Brinza, D.; Calef, F.; Christensen, L.; Crisp, J. A.; Feldman, J.; Feldman, S.; Flesch, G.; Hurowitz, J.; Jun, I.; Keymeulen, D.; Maki, J.; Morookian, J. M.; Parker, T.; Pavri, B.; Schoppers, M.; Sengstacken, A.; Simmonds, J. J.; Spanovich, N.; Vasavada, A. R.; Webster, C. R.; Yen, A.; Cucinotta, F.; Jones, J. H.; Ming, D.; Morris, R. V.; Niles, P.; Nolan, T.; Radziemski, L.; Berman, D.; Dobreá, E. N.; Williams, R. M. E.; Lewis, K.; Cleghorn, T.; Huntress, W.; Manhès, G.; Hudgins, J.; Olson, T.; Stewart, N.; Sarrazin, P.; Grant, J.; Vicenzi, E.; Wilson, S. A.; Bullock, M.; Ehresmann, B.; Hamilton, V.; Hassler, D.; Peterson, J.; Rafkin, S.; Zeitlin, C.; Fedosov, F.; Golovin, D.; Karpushkina, N.; Kozyrev, A.; Litvak, M.; Malakhov, A.; Mitrofanov, I.; Mokrousov, M.; Nikiforov, S.; Prokhorov, V.; Sanin, A.; Tretyakov, V.; Varenikov, A.; Vostrukhin, A.; Kuzmin, R.; Wolff, M.; McLennan, S.; Botta, O.; Drake, D.; Bean, K.; Lemmon, M.; Schwenzer, S. P.; Lee, E. M.; Sucharski, R.; Hernández, M. Á. de P.; Ávalos, J. J. B.; Ramos, M.; Kim, M.-H.; Malespin, C.; Plante, I.; Muller, J.-P.; Navarro-González, R.; Ewing, R.; Boynton, W.; Downs, R.; Fitzgibbon, M.; Harshman, K.; Morrison, S.; Dietrich, W.; Kortmann, O.; Palucis, M.; Sumner, D. Y.; Williams, A.; Lugmair, G.; Wilson, M. A.; Rubin, D.; Jakosky, B.; Balic-Zunic, T.; Frydenvang, J.; Jensen, J. K.; Kinch, K.; Koefoed, A.; Stipp, S. L. S.; Boyd, N.; Campbell, J. L.; Gellert, R.; Perrett, G.; Pradler, I.; VanBommel, S.; Jacob, S.; Owen, T.; Rowland, S.; Atlaskin, E.; Savijärvi, H.; Boehm, E.; Böttcher, S.; Burmeister, S.; Guo, J.; Köhler, J.; García, C. M.; Mueller-Mellin, R.; Wimmer-Schweingruber, R.; Bridges, J. C.; Benna, M.; Franz, H.; Bower, H.; Brunner, A.; Blau, H.; Boucher, T.; Carmosino, M.; Atreya, S.; Elliott, H.; Halleaux, D.; Rennó, N.; Wong, M.; Pepin, R.; Elliott, B.; Spray, J.; Thompson, L.; Gordon, S.; Williams, J.; Vasconcelos, P.; Bentz, J.; Nealson, K.; Popa, R.; Kah, L. C.; Moersch, J.; Tate, C.; Day, M.; Kocurek, G.; Hallet, B.; Sletten, R.; Francis, R.; McCullough, E.; Cloutis, E.; ten Kate, I. L.; Kuzmin, R.; Arvidson, R.; Fraeman, A.; Scholes, D.; Slavney, S.; Stein, T.; Ward, J.; Berger, J. Soil Diversity and Hydration as Observed by ChemCam at Gale Crater, Mars. *Science*. **2013**, *341*, 1238670. <https://doi.org/10.1126/science.1238670>.

- [26] Mustard, J. F.; Adler, M.; Allwood, A.; Bass, D. S.; Beaty, D. W.; Bell III, J. F.; Brinckerhoff, W. B.; Carr, M.; Des Marais, D. J.; Drake, B.;

- 
- Edgett, K. S.; Eigenbrone, J.; Elkins-Tanton, L. T.; Grant, J. A.; Milkovich, S. M.; Ming, D.; Moore, C.; Murchie, S.; Onstott, T. C.; Ruff, S. W.; Sephton, M. A.; Steele, A.; Treiman, A. *Report of the Mars 2020 Science Definition Team*; 2013. [https://mepag.jpl.nasa.gov/reports/MEP/Mars\\_2020\\_SDT\\_Report\\_Final.pdf](https://mepag.jpl.nasa.gov/reports/MEP/Mars_2020_SDT_Report_Final.pdf).
- [27] Beaty, D. W.; Grady, M. M.; McSween, H. Y.; Sefton-Nash, E.; Carrier, B. L.; Altieri, F.; Amelin, Y.; Ammannito, E.; Anand, M.; Benning, L. G.; Bishop, J. L.; Borg, L. E.; Boucher, D.; Brucato, J. R.; Busemann, H.; Campbell, K. A.; Czaja, A. D.; Debaille, V.; Des Marais, D. J.; Dixon, M.; Ehlmann, B. L.; Farmer, J. D.; Fernandez-Remolar, D. C.; Filiberto, J.; Fogarty, J.; Glavin, D. P.; Goreva, Y. S.; Hallis, L. J.; Harrington, A. D.; Hausrath, E. M.; Herd, C. D. K.; Horgan, B.; Humayun, M.; Kleine, T.; Kleinhenz, J.; Mackelprang, R.; Mangold, N.; Mayhew, L. E.; McCoy, J. T.; McCubbin, F. M.; McLennan, S. M.; Moser, D. E.; Moynier, F.; Mustard, J. F.; Niles, P. B.; Ori, G. G.; Raulin, F.; Rettberg, P.; Rucker, M. A.; Schmitz, N.; Schwenger, S. P.; Sephton, M. A.; Shaheen, R.; Sharp, Z. D.; Shuster, D. L.; Siljeström, S.; Smith, C. L.; Spry, J. A.; Steele, A.; Swindle, T. D.; ten Kate, I. L.; Tosca, N. J.; Usui, T.; Van Kranendonk, M. J.; Wadhwa, M.; Weiss, B. P.; Werner, S. C.; Westall, F.; Wheeler, R. M.; Zipfel, J.; Zorzano, M. P. The Potential Science and Engineering Value of Samples Delivered to Earth by Mars Sample Return. *Meteorit. Planet. Sci.* **2019**, *54*, 667. <https://doi.org/10.1111/maps.13242>.
- [28] Wang, A.; Bell, J. F.; Li, R.; Johnson, J. R.; Farrand, W. H.; Cloutis, E. A.; Arvidson, R. E.; Crumpler, L.; Squyres, S. W.; McLennan, S. M.; Herkenhoff, K. E.; Ruff, S. W.; Knudson, A. T.; Chen, W.; Greenberger, R. Light-Toned Salty Soils and Coexisting Si-Rich Species Discovered by the Mars Exploration Rover Spirit in Columbia Hills. *J. Geophys. Res.* **2008**, *113*, E12S40. <https://doi.org/10.1029/2008JE003126>.
- [29] Wiens, R. C.; Maurice, S.; Robinson, S. H.; Nelson, A. E.; Cais, P.; Bernardi, P.; Newell, R. T.; Clegg, S.; Sharma, S. K.; Storms, S.; Deming, J.; Beckman, D.; Ollila, A. M.; Gasnault, O.; Anderson, R. B.; André, Y.; Angel, S. M.; Arana, G.; Auden, E.; Beck, P.; Becker, J.; Benzerara, K.; Bernard, S.; Beyssac, O.; Borges, L.; Bousquet, B.; Boyd, K.; Caffrey, M.; Carlson, J.; Castro, K.; Celis, J.; Chide, B.; Clark, K.; Cloutis, E.; Cordoba, E. C.; Cousin, A.; Dale, M.; Deflores, L.; Delapp, D.; Deleuze, M.; Dirmyer, M.; Donny, C.; Dromart, G.; Duran, M. G.; Egan, M.; Ervin, J.; Fabre, C.; Fau, A.; Fischer, W.; Forni, O.; Fouchet, T.; Fresquez, R.; Frydenvang, J.; Gasway, D.; Gontijo, I.; Grotzinger, J.; Jacob, X.; Jacquino, S.; Johnson, J. R.; Klisiewicz, R. A.; Lake, J.; Lanza, N.; Laserna, J.; Lasue, J.; Le Mouélic, S.; Lucero, B.; Madariaga, J. M.; Madsen, M.; Madsen, S.; Mangold, N.; Manrique, J. A.; Martinez, J. P.; Martinez-Frias, J.; McCabe, K. P.; McConnochie, T. H.; McGlown, J. M.; McLennan, S.
-

- M.; Melikechi, N.; Meslin, P.; Michel, J. M.; Mimoun, D.; Misra, A.; Montagnac, G.; Montmessin, F.; Mousset, V.; Murdoch, N.; Newsom, H.; Ott, L. A.; Ousnamer, Z. R.; Pares, L.; Parot, Y.; Pawlucyk, R.; Peterson, C. G.; Pilleri, P.; Pinet, P.; Pont, G.; Poulet, F.; Provost, C.; Quertier, B.; Quinn, H.; Rapin, W.; Reess, J.; Regan, A. H.; Reyes-Newell, A. L.; Romano, P. J.; Royer, C.; Rull, F.; Sandoval, B.; Sarrao, J. H.; Sautter, V.; Schoppers, M. J.; Schöder, S.; Seitz, D.; Shepherd, T.; Sobron, P.; Dubois, B.; Sridhar, V.; Toplis, M. J.; Torre-Fdez, I.; Trettel, I. A.; Underwood, M.; Valdez, A.; Valdez, J.; Venhaus, D.; Willis, P. The SuperCam Instrument Suite on the NASA Mars 2020 Rover: Body Unit and Combined System Tests. *Space Sci. Rev.* **2021**, *217*, 4. <https://doi.org/10.1007/s11214-020-00777-5>.
- [30] Tan, J.; Lewis, J. M. T.; Sephton, M. A. The Fate of Lipid Biosignatures in a Mars-Analogue Sulfur Stream. *Sci. Rep.* **2018**, *8*, 7586. <https://doi.org/10.1038/s41598-018-25752-7>.
- [31] Cloutis, E.; Applin, D.; Connell, S.; Kubanek, K.; Kuik, J.; Parkinson, A.; Ramirez, M.; Turenne, N.; Mertzman, S. A Simulated Rover Exploration of a Long-Lived Hypersaline Spring Environment: The East German Creek (MB, Canada) Mars Analogue Site. *Planet. Space Sci.* **2021**, *195*, 105130. <https://doi.org/10.1016/j.pss.2020.105130>.
- [32] Cousin, A.; Meslin, P. Y.; Wiens, R. C.; Rapin, W.; Mangold, N.; Fabre, C.; Gasnault, O.; Forni, O.; Tokar, R.; Ollila, A.; Schröder, S.; Lasue, J.; Maurice, S.; Sautter, V.; Newsom, H.; Vaniman, D.; Le Mouélic, S.; Dyar, D.; Berger, G.; Blaney, D.; Nachon, M.; Dromart, G.; Lanza, N.; Clark, B.; Clegg, S.; Goetz, W.; Berger, J.; Barraclough, B.; Delapp, D. Compositions of Coarse and Fine Particles in Martian Soils at Gale: A Window into the Production of Soils. *Icarus* **2015**, *249*, 22. <https://doi.org/10.1016/j.icarus.2014.04.052>.
- [33] Anderson, R. B.; Forni, O.; Cousin, A.; Wiens, R. C.; Clegg, S. M.; Frydenvang, J.; Gabriel, T. S. J.; Ollila, A.; Schröder, S.; Beyssac, O.; Gibbons, E.; Vogt, D. S.; Clavé, E.; Manrique, J.-A.; Legett, C.; Pilleri, P.; Newell, R. T.; Sarrao, J.; Maurice, S.; Arana, G.; Benzerara, K.; Bernardi, P.; Bernard, S.; Bousquet, B.; Brown, A. J.; Alvarez-Llamas, C.; Chide, B.; Cloutis, E.; Comellas, J.; Connell, S.; Dehouck, E.; Delapp, D. M.; Essunfeld, A.; Fabre, C.; Fouchet, T.; Garcia-Florentino, C.; García-Gómez, L.; Gasda, P.; Gasnault, O.; Hausrath, E. M.; Lanza, N. L.; Laserna, J.; Lasue, J.; Lopez, G.; Madariaga, J. M.; Mandon, L.; Mangold, N.; Meslin, P.-Y.; Nelson, A. E.; Newsom, H.; Reyes-Newell, A. L.; Robinson, S.; Rull, F.; Sharma, S.; Simon, J. I.; Sobron, P.; Fernandez, I. T.; Udry, A.; Venhaus, D.; McLennan, S. M.; Morris, R. V.; Ehlmann, B. Post-Landing Major Element Quantification Using SuperCam Laser Induced Breakdown Spectroscopy. *Spectrochim. Acta Part B At. Spectrosc.* **2022**, *188*, 106347.

- 
- <https://doi.org/10.1016/j.sab.2021.106347>.
- [34] Pieters, C. M.; Hiroi, T. *RELAB (Reflectance Experiment Laboratory): A NASA Multiuser Spectroscopy Facility*. <https://ntrs.nasa.gov/citations/20040129713> (accessed 2023-04-03).
- [35] Turenne, N.; Sishu, S.; Applin, D.; Cloutis, E. Nontronite Spectral Reflectance Characteristics with Implications for Mars. In *53rd Lunar and Planetary Science Conference*; The Woodlands, TX, USA, 2022; Abs 1571.
- [36] Matsui, M. S.; Carle, T.; Costa, M. The Interaction of Metals and the Skin: The Good, Bad, and the Ugly. In *Handbook on the Toxicology of Metals*; Elsevier, 2022; pp 407–420. <https://doi.org/10.1016/B978-0-12-823292-7.00011-5>.
- [37] Schulze, D. G. Clay Minerals. In *Encyclopedia of Soils in the Environment*, Elsevier, 2005; pp 246–254. <https://doi.org/10.1016/B0-12-348530-4/00189-2>.
- [38] Ovesen, R. G.; Nielsen, J.; Bruun Hansen, H. C. Biomedicine in the Environment: Sorption of the Cyclotide Kalata B2 to Montmorillonite, Goethite, and Humic Acid. *Environ. Toxicol. Chem.* **2011**, *30*, 1785. <https://doi.org/10.1002/etc.579>.
- [39] Uddin, F. Clays, Nanoclays, and Montmorillonite Minerals. *Metall. Mater. Trans. A* **2008**, *39*, 2804. <https://doi.org/10.1007/s11661-008-9603-5>.
- [40] Gruner, J. W. The Crystal Structure of Kaolinite. *Zeitschrift für Krist. - Cryst. Mater.* **1932**, *83*, 75. <https://doi.org/10.1524/zkri.1932.83.1.75>.
- [41] Nieto, F.; Mellini, M.; Abad, I. The Role of H<sub>3</sub>O<sup>+</sup> in the Crystal Structure of Illite. *Clays Clay Miner.* **2010**, *58*, 238. <https://doi.org/10.1346/CCMN.2010.0580208>.
- [42] Akisanmi, P. Classification of Clay Minerals. In *Mineralogy*; IntechOpen, 2022; p 2. <https://doi.org/10.5772/intechopen.103841>.
- [43] Bristow, T. F.; Bish, D. L.; Vaniman, D. T.; Morris, R. V.; Blake, D. F.; Grotzinger, J. P.; Rampe, E. B.; Crisp, J. A.; Achilles, C. N.; Ming, D. W.; Ehlmann, B. L.; King, P. L.; Bridges, J. C.; Eigenbrode, J. L.; Sumner, D. Y.; Chipera, S. J.; Moorokian, J. M.; Treiman, A. H.; Morrison, S. M.; Downs, R. T.; Farmer, J. D.; Marais, D. D.; Sarrazin, P.; Floyd, M. M.; Mischna, M. A.; McAdam, A. C. The Origin and Implications of Clay Minerals from Yellowknife Bay, Gale Crater, Mars. *Am. Mineral.* **2015**, *100*, 824. <https://doi.org/10.2138/am-2015-5077CCBYNCND>.
- [44] Bristow, T. F.; Rampe, E. B.; Achilles, C. N.; Blake, D. F.; Chipera, S. J.; Craig, P.; Crisp, J. A.; Des Marais, D. J.; Downs, R. T.; Gellert, R.; Grotzinger, J. P.; Gupta, S.; Hazen, R. M.; Horgan, B.; Hogancamp, J. V.; Mangold, N.; Mahaffy, P. R.; McAdam, A. C.; Ming, D. W.; Moorokian, J. M.; Morris, R. V.; Morrison, S. M.; Treiman, A. H.; Vaniman, D. T.; Vasavada, A. R.; Yen, A. S. Clay

- Mineral Diversity and Abundance in Sedimentary Rocks of Gale Crater, Mars. *Sci. Adv.* **2018**, *4*, eaar3330. <https://doi.org/10.1126/sciadv.aar3330>.
- [45] Ming, D. W.; Archer, P. D.; Glavin, D. P.; Eigenbrode, J. L.; Franz, H. B.; Sutter, B.; Brunner, A. E.; Stern, J. C.; Freissinet, C.; McAdam, A. C.; Mahaffy, P. R.; Cabane, M.; Coll, P.; Campbell, J. L.; Atreya, S. K.; Niles, P. B.; Bell, J. F.; Bish, D. L.; Brinckerhoff, W. B.; Buch, A.; Conrad, P. G.; Des Marais, D. J.; Ehlmann, B. L.; Fairén, A. G.; Farley, K.; Flesch, G. J.; Francois, P.; Gellert, R.; Grant, J. A.; Grotzinger, J. P.; Gupta, S.; Herkenhoff, K. E.; Hurowitz, J. A.; Leshin, L. A.; Lewis, K. W.; McLennan, S. M.; Miller, K. E.; Moersch, J.; Morris, R. V.; Navarro-González, R.; Pavlov, A. A.; Perrett, G. M.; Pradler, I.; Squyres, S. W.; Summons, R. E.; Steele, A.; Stolper, E. M.; Sumner, D. Y.; Szopa, C.; Teinturier, S.; Trainer, M. G.; Treiman, A. H.; Vaniman, D. T.; Vasavada, A. R.; Webster, C. R.; Wray, J. J.; Yingst, R. A.; MSLScienceTeam. Volatile and Organic Compositions of Sedimentary Rocks in Yellowknife Bay, Gale Crater, Mars. *Science*. **2014**, *343*, 1245267. <https://doi.org/10.1126/science.1245267>.
- [46] Stern, J. C.; Malespin, C. A.; Eigenbrode, J. L.; Webster, C. R.; Flesch, G.; Franz, H. B.; Graham, H. V.; House, C. H.; Sutter, B.; Archer, P. D.; Hofmann, A. E.; McAdam, A. C.; Ming, D. W.; Navarro-Gonzalez, R.; Steele, A.; Freissinet, C.; Mahaffy, P. R. Organic Carbon Concentrations in 3.5-Billion-Year-Old Lacustrine Mudstones of Mars. *Proc. Natl. Acad. Sci.* **2022**, *119*, e2201139119. <https://doi.org/10.1073/pnas.2201139119>.
- [47] Szopa, C.; Freissinet, C.; Glavin, D. P.; Millan, M.; Buch, A.; Franz, H. B.; Summons, R. E.; Sumner, D. Y.; Sutter, B.; Eigenbrode, J. L.; Williams, R. H.; Navarro-González, R.; Guzman, M.; Malespin, C.; Teinturier, S.; Mahaffy, P. R.; Cabane, M. First Detections of Dichlorobenzene Isomers and Trichloromethylpropane from Organic Matter Indigenous to Mars Mudstone in Gale Crater, Mars: Results from the Sample Analysis at Mars Instrument Onboard the Curiosity Rover. *Astrobiology* **2020**, *20*, 292. <https://doi.org/10.1089/ast.2018.1908>.
- [48] Gil-Lozano, C.; Fairén, A. G.; Muñoz-Iglesias, V.; Fernández-Sampedro, M.; Prieto-Ballesteros, O.; Gago-Duport, L.; Losa-Adams, E.; Carrizo, D.; Bishop, J. L.; Fornaro, T.; Mateo-Martí, E. Constraining the Preservation of Organic Compounds in Mars Analog Nontronites after Exposure to Acid and Alkaline Fluids. *Sci. Rep.* **2020**, *10*, 15097. <https://doi.org/10.1038/s41598-020-71657-9>.
- [49] Craig, P. I.; Mickol, R. L.; Archer, P. D.; Kral, T. A. Nontronite and Montmorillonite as Nutrient Sources for Life on Mars. In *48th Lunar and Planetary Science Conference*; The Woodlands, TX, USA, 2017; Abs 1997.
- [50] Cuadros, J.; Michalski, J. R. Investigation of Al-Rich Clays on Mars: Evidence for Kaolinite–Smectite Mixed-Layer versus Mixture of End-

- 
- Member Phases. *Icarus* **2013**, 222, 296. <https://doi.org/10.1016/j.icarus.2012.11.006>.
- [51] Zhang, L.; Fu, X.; Wang, A.; Ling, Z. Crystallinity Effects on the Vibrational Spectral Features of Saponite: Implications for Characterizing Variable Crystalline Phyllosilicates on Mars. *Icarus* **2022**, 379, 114951. <https://doi.org/10.1016/j.icarus.2022.114951>.
- [52] Liu, C.; Ling, Z.; Wu, Z.; Zhang, J.; Chen, J.; Fu, X.; Qiao, L.; Liu, P.; Li, B.; Zhang, L.; Xin, Y.; Shi, E.; Cao, H.; Tian, S.; Wan, S.; Bai, H.; Liu, J. Aqueous Alteration of the Vastitas Borealis Formation at the Tianwen-1 Landing Site. *Commun. Earth Environ.* **2022**, 3, 280. <https://doi.org/10.1038/s43247-022-00614-3>.
- [53] Che, C.; Glotch, T. D. Characterizing Possible Dehydrated and/or Dehydroxylated Phyllosilicate Deposits on Mars Using Thermal and near-IR Spectroscopy. In *American Geophysical Union, Fall Meeting*; San Francisco, CA, USA, 2011; p Abs P31D-1727.
- [54] Jadhav, A. C.; Jadhav, N. C. Treatment of Textile Wastewater Using Adsorption and Adsorbents. In *Sustainable Technologies for Textile Wastewater Treatments*; Elsevier, 2021; pp 235–273. <https://doi.org/10.1016/B978-0-323-85829-8.00008-0>.
- [55] GRANQUIST, W. T.; POLLACK, S. S. A Study of the Synthesis of Hectorite. In *Clays and Clay Minerals*; Elsevier, 1960; pp 150–169. <https://doi.org/10.1016/B978-0-08-009351-2.50019-2>.
- [56] Sarier, N.; Onder, E.; Ersoy, S. The Modification of Na-Montmorillonite by Salts of Fatty Acids: An Easy Intercalation Process. *Colloids Surfaces A Physicochem. Eng. Asp.* **2010**, 371, 40. <https://doi.org/10.1016/j.colsurfa.2010.08.061>.
- [57] Freissinet, C.; Glavin, D. P.; Buch, A.; Szopa, C.; Teinturier, S.; Archer, D. P.; Williams, A. J.; Williams, R.; Millan, M.; Steele, A.; Navarro-Gonzalez, R.; House, C. H.; Malespin, C. A.; Mahaffy, P. Detection of Long-Chain Hydrocarbons on Mars with the Sample Analysis at Mars (SAM) Instrument. In *9th International Conference on Mars*; Pasadena, CA, USA, 2019; Abs 6123.
- [58] Williams, A. J.; Eigenbrode, J.; Floyd, M.; Wilhelm, M. B.; O'Reilly, S.; Johnson, S. S.; Craft, K. L.; Knudson, C. A.; Andrejkovičová, S.; Lewis, J. M. T.; Buch, A.; Glavin, D. P.; Freissinet, C.; Williams, R. H.; Szopa, C.; Millan, M.; Summons, R. E.; McAdam, A.; Benison, K.; Navarro-González, R.; Malespin, C.; Mahaffy, P. R. Recovery of Fatty Acids from Mineralogic Mars Analogs by TMAH Thermochemolysis for the Sample Analysis at Mars Wet Chemistry Experiment on the Curiosity Rover. *Astrobiology* **2019**, 19, 522. <https://doi.org/10.1089/ast.2018.1819>.
- [59] Fernández-Remolar, D. C.; Gomez-Ortiz, D.; Huang, T.; Anglés, A.; Shen, Y.; Hu, Q.; Amils, R.; Rodríguez, N.; Escudero, C.; Banerjee, N. R. The Molecular Record of Metabolic Activity in the Subsurface of the Río Tinto Mars Analog. *Astrobiology* **2021**, 21, 1387. <https://doi.org/10.1089/ast.2020.2431>.
-

- [60] Komadel, P. Acid Activated Clays: Materials in Continuous Demand. *Appl. Clay Sci.* **2016**, *131*, 84. <https://doi.org/10.1016/j.clay.2016.05.001>.
- [61] Ayati, B.; Newport, D.; Wong, H.; Cheeseman, C. Acid Activated Smectite Clay as Pozzolan Supplementary Cementitious Material. *Cem. Concr. Res.* **2022**, *162*, 106969. <https://doi.org/10.1016/j.cemconres.2022.106969>.
- [62] ChemicalCayman. *Lauric Acid - Product Information*. Item No. 10006626. <https://cdn.caymanchem.com/cdn/insert/10006626.pdf> (accessed 2023-03-03).
- [63] PubChem. *Lauric Acid - Compound Summary*. National Library of Medicine. <https://pubchem.ncbi.nlm.nih.gov/compound/Lauric-acid> (accessed 2023-03-03).
- [64] Matusik, J.; Koteja-Kunecka, A.; Maziarz, P.; Kunecka, A. Styrene Removal by Surfactant-Modified Smectite Group Minerals: Efficiency and Factors Affecting Adsorption/Desorption. *Chem. Eng. J.* **2022**, *428*, 130848. <https://doi.org/10.1016/j.cej.2021.130848>.
- [65] Chipera, S. J. Baseline Studies of the Clay Minerals Society Source Clays: Powder X-Ray Diffraction Analyses. *Clays Clay Miner.* **2001**, *49*, 398. <https://doi.org/10.1346/CCMN.2001.0490507>.
- [66] Burns, R. G.; Fisher, D. S. Rates of Oxidative Weathering on the Surface of Mars. *J. Geophys. Res. Planets* **1993**, *98*, 3365. <https://doi.org/10.1029/92JE02055>.
- [67] Jiang, J.; Zheng, Q.; Yan, Y.; Guo, D.; Wang, F.; Wu, S.; Sun, W. Design of a Novel Nanocomposite with C-S-H@LA for Thermal Energy Storage: A Theoretical and Experimental Study. *Appl. Energy* **2018**, *220*, 395. <https://doi.org/10.1016/j.apenergy.2018.03.134>.
- [68] Falk, M.; Miller, A. G. Infrared Spectrum of Carbon Dioxide in Aqueous Solution. *Vib. Spectrosc.* **1992**, *4*, 105. [https://doi.org/10.1016/0924-2031\(92\)87018-B](https://doi.org/10.1016/0924-2031(92)87018-B).
- [69] Patel, H. A.; Somani, R. S.; Bajaj, H. C.; Jasra, R. V. Nanoclays for Polymer Nanocomposites, Paints, Inks, Greases and Cosmetics Formulations, Drug Delivery Vehicle and Waste Water Treatment. *Bull. Mater. Sci.* **2006**, *29*, 133. <https://doi.org/10.1007/BF02704606>.
- [70] Hadjiivanov, K. I.; Panayotov, D. A.; Mihaylov, M. Y.; Ivanova, E. Z.; Chakarova, K. K.; Andonova, S. M.; Drenchev, N. L. Power of Infrared and Raman Spectroscopies to Characterize Metal-Organic Frameworks and Investigate Their Interaction with Guest Molecules. *Chem. Rev.* **2021**, *121*, 1286. <https://doi.org/10.1021/acs.chemrev.0c00487>.
- [71] Jaynes, W. F. Preparation and Characterization of Reduced-Charge Hectorites. *Clays Clay Miner.* **1992**, *40*, 397. <https://doi.org/10.1346/CCMN.1992.0400404>.
- [72] Hopkinson, L.; Rutt, K.; Kristova, P.; Blows, J.; Firth, C. Sourcing Limestone Masonry for Restoration of Historic Buildings, a

- 
- Spectroscopic Pilot Study. *J. Cult. Herit.* **2015**, *16*, 822. <https://doi.org/10.1016/j.culher.2015.03.007>.
- [73] Van Rompaey, K.; Van Ranst, E.; De Coninck, F.; Vindevogel, N. Dissolution Characteristics of Hectorite in Inorganic Acids. *Appl. Clay Sci.* **2002**, *21*, 241. [https://doi.org/10.1016/S0169-1317\(02\)00086-8](https://doi.org/10.1016/S0169-1317(02)00086-8).
- [74] Vignale, F. A.; Lencina, A. I.; Stepanenko, T. M.; Soria, M. N.; Saona, L. A.; Kurth, D.; Guzmán, D.; Foster, J. S.; Poiré, D. G.; Villafañe, P. G.; Albarracín, V. H.; Contreras, M.; Farías, M. E. Lithifying and Non-Lithifying Microbial Ecosystems in the Wetlands and Salt Flats of the Central Andes. *Microb. Ecol.* **2022**, *83*, 1. <https://doi.org/10.1007/s00248-021-01725-8>.
- [75] Joseph, R. G.; Planchon, O.; Duxbury, N. S.; Latif, K.; Kidron, G. J.; Consorti, L.; Armstrong, R. A.; Gibson, C.; Schild, R. Oceans, Lakes, and Stromatolites on Mars. *Adv. Astron.* **2020**, *2020*, 1. <https://doi.org/10.1155/2020/6959532>.
- [76] Riding, R. Microbialites, Stromatolites, and Thrombolites. In *Encyclopedia of Geobiology. Encyclopedia of Earth Sciences Series*; Reitner, J., Thiel, V., Eds.; Springer, 2011; pp 635–654. [https://doi.org/10.1007/978-1-4020-9212-1\\_196](https://doi.org/10.1007/978-1-4020-9212-1_196).
- [77] Planavsky, N.; Grey, K. Stromatolite Branching in the Neoproterozoic of the Centralian Superbasin, Australia: An Investigation into Sedimentary and Microbial Control of Stromatolite Morphology. *Geobiology* **2007**, *33*. <https://doi.org/10.1111/j.1472-4669.2007.00116.x>.
- [78] Xiao, L.; Wang, J.; Dang, Y.; Cheng, Z.; Huang, T.; Zhao, J.; Xu, Y.; Huang, J.; Xiao, Z.; Komatsu, G. A New Terrestrial Analogue Site for Mars Research: The Qaidam Basin, Tibetan Plateau (NW China). *Earth-Science Rev.* **2017**, *164*, 84. <https://doi.org/10.1016/j.earscirev.2016.11.003>.
- [79] Quantin-Nataf, C.; Carter, J.; Mandon, L.; Thollot, P.; Balme, M.; Volat, M.; Pan, L.; Loizeau, D.; Millot, C.; Breton, S.; Dehouck, E.; Fawdon, P.; Gupta, S.; Davis, J.; Grindrod, P. M.; Pacifici, A.; Bultel, B.; Allemand, P.; Ody, A.; Lozach, L.; Broyer, J. Oxia Planum: The Landing Site for the ExoMars “Rosalind Franklin” Rover Mission: Geological Context and Prelanding Interpretation. *Astrobiology* **2021**, *21*, 345. <https://doi.org/10.1089/ast.2019.2191>.
- [80] Farley, K. A.; Williford, K. H.; Stack, K. M.; Bhartia, R.; Chen, A.; de la Torre, M.; Hand, K.; Goreva, Y.; Herd, C. D. K.; Hueso, R.; Liu, Y.; Maki, J. N.; Martinez, G.; Moeller, R. C.; Nelessen, A.; Newman, C. E.; Nunes, D.; Ponce, A.; Spanovich, N.; Willis, P. A.; Beegle, L. W.; Bell, J. F.; Brown, A. J.; Hamran, S.-E.; Hurowitz, J. A.; Maurice, S.; Paige, D. A.; Rodriguez-Manfredi, J. A.; Schulte, M.; Wiens, R. C. Mars 2020 Mission Overview. *Space Sci. Rev.* **2020**, *216*, 142. <https://doi.org/10.1007/s11214-020-00762-y>.
- [81] Allwood, A. C.; Wade, L. A.; Foote, M. C.; Elam, W. T.; Hurowitz, J.
-

- A.; Battel, S.; Dawson, D. E.; Denise, R. W.; Ek, E. M.; Gilbert, M. S.; King, M. E.; Liebe, C. C.; Parker, T.; Pedersen, D. A. K.; Randall, D. P.; Sharrow, R. F.; Sondheim, M. E.; Allen, G.; Arnett, K.; Au, M. H.; Basset, C.; Benn, M.; Bousman, J. C.; Braun, D.; Calvet, R. J.; Clark, B.; Cinquini, L.; Conaby, S.; Conley, H. A.; Davidoff, S.; Delaney, J.; Denver, T.; Diaz, E.; Doran, G. B.; Ervin, J.; Evans, M.; Flannery, D. O.; Gao, N.; Gross, J.; Grotzinger, J.; Hannah, B.; Harris, J. T.; Harris, C. M.; He, Y.; Heirwegh, C. M.; Hernandez, C.; Hertzberg, E.; Hodyss, R. P.; Holden, J. R.; Hummel, C.; Jadusingh, M. A.; Jørgensen, J. L.; Kawamura, J. H.; Kitiyakara, A.; Kozaczek, K.; Lambert, J. L.; Lawson, P. R.; Liu, Y.; Luchik, T. S.; Macneal, K. M.; Madsen, S. N.; McLennan, S. M.; McNally, P.; Meras, P. L.; Muller, R. E.; Napoli, J.; Naylor, B. J.; Nemere, P.; Ponomarev, I.; Perez, R. M.; Pootrakul, N.; Romero, R. A.; Rosas, R.; Sachs, J.; Schaefer, R. T.; Schein, M. E.; Setterfield, T. P.; Singh, V.; Song, E.; Soria, M. M.; Stek, P. C.; Tallarida, N. R.; Thompson, D. R.; Tice, M. M.; Timmermann, L.; Torossian, V.; Treiman, A.; Tsai, S.; Uckert, K.; Villalvazo, J.; Wang, M.; Wilson, D. W.; Worel, S. C.; Zamani, P.; Zappe, M.; Zhong, F.; Zimmerman, R. PIXL: Planetary Instrument for X-Ray Lithochemistry. *Space Sci. Rev.* **2020**, *216*, 134. <https://doi.org/10.1007/s11214-020-00767-7>.
- [82] Bernardi, P.; Parès, L.; Newell, R.; Nelson, T.; Gasnault, O.; Réess, J.-M.; Schridar, V.; Contijo, I.; Reyes-Newell, A.; Peterson, G. E.; Legett, C.; Dubois, B.; Robinson, S. H. Optical Design and Performance of the SuperCam Instrument for the Perseverance Rover. In *International Conference on Space Optics — ICSO 2020*; Sodnik, Z., Cugny, B., Karafolas, N., Eds.; SPIE, 2021; Abs 53. <https://doi.org/10.1117/12.2599243>.
- [83] Wiens, R. C.; Newell, R.; Clegg, S.; Sharma, S. K.; Misra, A.; Bernardi, P.; Maurice, S.; McCable, K.; Cais, P.; Teams, S. S. The SuperCam Remote Raman Spectrometer for Mars 2020. In *Lunar and Planetary Science XLVIII*; The Woodlands, TX, USA, 2017; Abs 2600.
- [84] Reess, J. M.; Bonafous, M.; Lapauw, L.; Humeau, O.; Fouchet, T.; Bernardi, P.; Cais, P.; Deleuze, M.; Forni, O.; Maurice, S.; Robinson, S.; Wiens, R. C.; Team, S. The SuperCam Infrared Instrument on the NASA Mars2020 Mission, Vol 11180. In *International Conference on Space Optics*; Chania, Greece, 2018; Abs 1118037-2.
- [85] Fouchet, T.; Johnson, J. R.; Forni, O.; Reess, J. M.; Bernardi, P.; Newell, R. T.; Ollila, A.; Legett, C.; Beck, P.; Cousin, A.; Royer, C.; Pilorget, C.; Poulet, F.; Pilleri, P.; Cloutis, E. A.; McConnochie, T.; Montmessin, F.; Brown, A. J.; Wiens, R.; Maurice, S.; Group, S. V. W. SuperCam Visible/Near-Infrared Spectroscopy Onboard the Perseverance Rover, No. 2548. In *52nd Lunar and Planetary Science Conference*; Virtual Conference, 2021; Abs 1939.
- [86] Bhartia, R.; Beegle, L. W.; DeFlores, L.; Abbey, W.; Razzell Hollis,

- 
- J.; Uckert, K.; Monacelli, B.; Edgett, K. S.; Kennedy, M. R.; Sylvia, M.; Aldrich, D.; Anderson, M.; Asher, S. A.; Bailey, Z.; Boyd, K.; Burton, A. S.; Caffrey, M.; Calaway, M. J.; Calvet, R.; Cameron, B.; Caplinger, M. A.; Carrier, B. L.; Chen, N.; Chen, A.; Clark, M. J.; Clegg, S.; Conrad, P. G.; Cooper, M.; Davis, K. N.; Ehlmann, B.; Facto, L.; Fries, M. D.; Garrison, D. H.; Gasway, D.; Ghaemi, F. T.; Graff, T. G.; Hand, K. P.; Harris, C.; Hein, J. D.; Heinz, N.; Herzog, H.; Hochberg, E.; Houck, A.; Hug, W. F.; Jensen, E. H.; Kah, L. C.; Kennedy, J.; Krylo, R.; Lam, J.; Lindeman, M.; McGlowan, J.; Michel, J.; Miller, E.; Mills, Z.; Minitti, M. E.; Mok, F.; Moore, J.; Nealon, K. H.; Nelson, A.; Newell, R.; Nixon, B. E.; Nordman, D. A.; Nuding, D.; Orellana, S.; Pauken, M.; Peterson, G.; Pollock, R.; Quinn, H.; Quinto, C.; Ravine, M. A.; Reid, R. D.; Riendeau, J.; Ross, A. J.; Sackos, J.; Schaffner, J. A.; Schwochert, M.; O Shelton, M.; Simon, R.; Smith, C. L.; Sobron, P.; Steadman, K.; Steele, A.; Thiessen, D.; Tran, V. D.; Tsai, T.; Tuite, M.; Tung, E.; Wehbe, R.; Weinberg, R.; Weiner, R. H.; Wiens, R. C.; Williford, K.; Wollonciej, C.; Wu, Y.-H.; Yingst, R. A.; Zan, J. Perseverance's Scanning Habitable Environments with Raman and Luminescence for Organics and Chemicals (SHERLOC) Investigation. *Space Sci. Rev.* **2021**, *217*, 58. <https://doi.org/10.1007/s11214-021-00812-z>.
- [87] Goesmann, F.; Brinckerhoff, W. B.; Raulin, F.; Goetz, W.; Danell, R. M.; Getty, S. A.; Silijeström, S.; Mibach, H.; Steininger, H.; Arevalo, R. D.; Buch, J. A.; Freissinet, C.; Grubisic, A.; Meierhenrich, U. J.; Pinnick, V. T.; Stalport, F.; Szopa, C.; Vago, J. L.; Lindner, R.; Schulte, M. D.; Brucato, J. R.; Glavin, D. P.; Grand, N.; Li, X.; van Amerom, F. H. W. The Mars Organic Molecule Analyzer (MOMA) Instrument: Characterization of Organic Material in Martian Sediments. *Astrobiology* **2017**, *17*, 655. <https://doi.org/10.1089/ast.2016.1551>.
- [88] Lazic, V.; Palucci, A.; Jovicevic, S.; Poggi, C.; Buono, E. Analysis of Explosive and Other Organic Residues by Laser Induced Breakdown Spectroscopy. *Spectrochim. Acta Part B At. Spectrosc.* **2009**, *64*, 1028. <https://doi.org/10.1016/j.sab.2009.07.035>.
- [89] Moros, J.; Laserna, J. Laser-Induced Breakdown Spectroscopy (LIBS) of Organic Compounds: A Review. *Appl. Spectrosc.* **2019**, *73*, 963. <https://doi.org/10.1177/0003702819853252>.
- [90] Janiszewska, K.; Mazur, M.; Machalski, M.; Stolarski, J. From Pristine Aragonite to Blocky Calcite: Exceptional Preservation and Diagenesis of Cephalopod Nacre in Porous Cretaceous Limestones. *PLoS One* **2018**, *13*, e0208598. <https://doi.org/10.1371/journal.pone.0208598>.
- [91] Borromeo, L.; Zimmermann, U.; Andò, S.; Coletti, G.; Bersani, D.; Basso, D.; Gentile, P.; Schulz, B.; Garzanti, E. Raman Spectroscopy as a Tool for Magnesium Estimation in Mg-Calcite. *J. Raman Spectrosc.* **2017**, *48*, 983. <https://doi.org/10.1002/jrs.5156>.
- [92] Perrin, J.; Vielzeuf, D.; Laporte, D.; Ricolleau, A.; Rossman, G. R.;
-

- Floquet, N. Raman Characterization of Synthetic Magnesian Calcites. *Am. Mineral.* **2016**, *101*, 2525. <https://doi.org/10.2138/am-2016-5714>.
- [93] Greinert, J.; Bohrmann, G.; Elvert, M. Stromatolitic Fabric of Authigenic Carbonate Crusts: Result of Anaerobic Methane Oxidation at Cold Seeps in 4,850 m Water Depth. *Int. J. Earth Sci.* **2002**, *91*, 698. <https://doi.org/10.1007/s00531-001-0244-9>.
- [94] Pederson, C. L.; McNeill, D. F.; Klaus, J. S.; Swart, P. K. Deposition and Diagenesis of Marine Oncoids: Implications For Development of Carbonate Porosity. *J. Sediment. Res.* **2015**, *85*, 1323. <https://doi.org/10.2110/jsr.2015.77>.
- [95] Wang, A.; Jolliff, B. L.; Haskin, L. A.; Kuebler, K. E.; Viskupic, K. M. Characterization and Comparison of Structural and Compositional Features of Planetary Quadrilateral Pyroxenes by Raman Spectroscopy. *Am. Mineral.* **2001**, *86*, 790. <https://doi.org/10.2138/am-2001-0703>.
- [96] Freeman, J. J.; Wang, A.; Kuebler, K. E.; Jolliff, B. L.; Haskin, La. A. Characterization of Natural Feldspars by Raman Spectroscopy for Future Planetary Exploration. *Can. Mineral.* **2008**, *46*, 1477. <https://doi.org/10.3749/canmin.46.6.1477>.
- [97] Heindel, L.; Birgel, D.; Peckmann, J.; Kuhnert, H.; Westphal, H. Formation of Deglacial Microbialites in Coral Reefs off Tahiti (IODP 310) Involving Sulfate-Reducing Bacteria. *Palaios* **2010**, *25*, 618. <https://doi.org/10.2110/palo.2010.p10-032r>.
- [98] Lafuente, B.; Downs, R. T.; Yang, H.; Stone, N. *Highlights in Mineralogical Crystallography*, Armbruster.; De Gruyter: Berlin, 2015.
- [99] Winters, Y. D.; Lowenstein, T. K.; Timofeeff, M. N. Identification of Carotenoids in Ancient Salt from Death Valley, Saline Valley, and Searles Lake, California, Using Laser Raman Spectroscopy. *Astrobiology* **2013**, *13*, 1065. <https://doi.org/10.1089/ast.2012.0952>.
- [100] Verkaaik, M. F. C.; Hooijschuur, J.-H.; Davies, G. R.; Ariese, F. Raman Spectroscopic Techniques for Planetary Exploration: Detecting Microorganisms through Minerals. *Astrobiology* **2015**, *15*, 697. <https://doi.org/10.1089/ast.2015.1329>.
- [101] Grimalt, J. .; Yruela, I.; Saiz-Jimenez, C.; Toja, J.; de Leeuw, J. .; Albaigés, J. Sedimentary Lipid Biogeochemistry of an Hypereutrophic Alkaline Lagoon. *Geochim. Cosmochim. Acta* **1991**, *55*, 2555. [https://doi.org/10.1016/0016-7037\(91\)90373-D](https://doi.org/10.1016/0016-7037(91)90373-D).
- [102] Coates, R. C.; Podell, S.; Korobeynikov, A.; Lapidus, A.; Pevzner, P.; Sherman, D. H.; Allen, E. E.; Gerwick, L.; Gerwick, W. H. Characterization of Cyanobacterial Hydrocarbon Composition and Distribution of Biosynthetic Pathways. *PLoS One* **2014**, *9*, e85140. <https://doi.org/10.1371/journal.pone.0085140>.
- [103] Grimalt, J. O.; de Wit, R.; Teixidor, P.; Albaigés, J. Lipid Biogeochemistry of Phormidium and Microcoleus Mats. *Org.*

- 
- Geochem.* **1992**, 19, 509. [https://doi.org/10.1016/0146-6380\(92\)90015-P](https://doi.org/10.1016/0146-6380(92)90015-P).
- [104] Killops, S. D.; Killops, V. J. An Introduction to Organic Geochemistry. In *Geological Magazine*; Farrimond, P., Ed.; 1994; Vol. 131, p 702. <https://doi.org/10.1017/S0016756800012656>.
- [105] Kuever, J. The Family Syntrophaceae. In *The Prokaryotes*; Springer Berlin Heidelberg: Berlin, Heidelberg, 2014; pp 281–288. [https://doi.org/10.1007/978-3-642-39044-9\\_269](https://doi.org/10.1007/978-3-642-39044-9_269).
- [106] Dijkman, N.; Kromkamp, J. Phospholipid-Derived Fatty Acids as Chemotaxonomic Markers for Phytoplankton: Application for Inferring Phytoplankton Composition. *Mar. Ecol. Prog. Ser.* **2006**, 324, 113. <https://doi.org/10.3354/meps324113>.
- [107] Hayes, J. M. Fractionation of Carbon and Hydrogen Isotopes in Biosynthetic Processes. *Rev. Mineral. Geochemistry* **2001**, 43, 225. <https://doi.org/10.2138/gsrmg.43.1.225>.
- [108] Hügler, M.; Sievert, S. M. Beyond the Calvin Cycle: Autotrophic Carbon Fixation in the Ocean. *Ann. Rev. Mar. Sci.* **2011**, 3, 261. <https://doi.org/10.1146/annurev-marine-120709-142712>.
- [109] Sirevg, R.; Buchanan, B. B.; Berry, J. A.; Troughton, J. H. Mechanisms of CO<sub>2</sub> Fixation in Bacterial Photosynthesis Studied by the Carbon Isotope Fractionation Technique. *Arch. Microbiol.* **1977**, 112, 35. <https://doi.org/10.1007/BF00446651>.
- [110] Brocks, J. J.; Love, G. D.; Summons, R. E.; Knoll, A. H.; Logan, G. A.; Bowden, S. A. Biomarker Evidence for Green and Purple Sulphur Bacteria in a Stratified Palaeoproterozoic Sea. *Nature* **2005**, 437, 866. <https://doi.org/10.1038/nature04068>.

---

## CHAPTER 6

### POSSIBLE HABITABILITY ON THE MOON?

**“NOTHING IN LIFE IS TO BE FEARED, IT IS ONLY  
TO BE UNDERSTOOD. NOW IS THE TIME TO  
UNDERSTAND MORE, SO THAT WE MAY FEAR  
LESS” – Marie Curie**

---



---

## 6. Possible habitability on the Moon? Evaluating the mineralogy of the lunar regolith for plant cultivation

Moon is not a homogeneous system, since it has experienced planetary evolution, catastrophic meteoroid bombardment, and intense igneous activity. In fact, the strongest evidence of lunar chemical segregation can be observed on the lunar surface, with two distinct zones: the highlands and the maria. The highlands are characterized by a light color due to the presence of Ca- and Al-rich ancient impact-shocked plutonic rocks. Whereas, what most characterizes maria is the dark color, because they are covered by younger basaltic lavas, rich in Fe and Ti, being mostly pyroxenes<sup>[1-3]</sup>.

Although the Moon is not affected by atmosphere, water or life, which are the three major agents that alter rock surfaces, the lunar surface is strongly weathered with respect to its origins, since it has always been exposed to meteoroid impact. Unlike the Earth, the Moon has no atmosphere to slow down or disintegrate the bodies that impact it. Actually, this is the reason why Moon's surface presents so many impact craters. The impacts cause a melting of some minerals in the crust and part of the lunar mantle, emerging mantle materials to the surface and leaving, consequently, the maria regions rich in lunar mantle materials such as basalts. This are the so-called mare basalts, extrusive rocks that are derived from partial melting of the mantle<sup>[4]</sup>.

In terms of mineralogy, silicate minerals are the most abundant lunar components, representing more than 90% by volume of lunar rocks. The most common silicate minerals are pyroxenes, plagioclase feldspars and olivines. Minerals containing oxidized iron Fe(III) are missing on the Moon and the most notable aspect of lunar geologic composition is the lack of minerals that contain water, such as hydrated minerals, clays, micas and amphiboles<sup>[5]</sup>.

After silicates, oxides are the most abundant minerals. They are especially concentrated in the mare basalts and can represent up to 20% by volume of these rocks. The most abundant lunar oxides are ilmenite, spinel and armalcolite. As in the case of silicates, none oxides in the Moon contain water<sup>[5]</sup>.

Two minor minerals, which reflect the highly reducing and low-oxygen environment under which the lunar rocks were formed, are also found on the Moon. These are the native iron, which is sometimes accompanied with Ni and Co, and troilite, which contains the most of the sulfur in lunar rocks. The sulfur not bounded to troilite, can be mobilized during impacts, producing more sulfurization of the native iron<sup>[5]</sup>.

In addition, other minor minerals found on the Moon are apatite and its associated mineral merrillite, among others at trace levels <sup>[5]</sup>.

All these minerals are organized together forming different types of lunar rocks: basaltic volcanic rocks, pristine rocks and polymict breccias, as well as lunar soils. The basaltic volcanic rocks include lava flows and pyroclastic rocks or ash. Pristine rocks come from the lunar highlands, which composition is not affected (contaminated) by impact mixing. Polymict breccias are formed by impacts that destroy, mix and re-compact the lunar surface and by impact melts that are formed by the melting of ancient Lunar rocks during meteoroid impacts. Finally, the lunar soils are fragmentary remnants of the lunar regolith that covers the surface <sup>[6]</sup>.

As mentioned in previous chapters, regolith is a general term for the layer of fragmentary unconsolidated rock material (<1 cm) that overlies bedrock <sup>[7]</sup> and it commonly includes rocky remains of all types <sup>[8]</sup>. On Earth, regolith is produced by the presence of oxygen, the influence of wind and water, life activities, etc. In contrast, lunar regolith is formed under characteristic environmental conditions i.e. continuous impact of large and small meteoroids and by the constant bombardment of charged atomic particles coming from the Sun and the stars <sup>[8]</sup>.

All this information has been collected from observations, satellites, lunar meteorites and returned samples analysis. There are two types of Lunar returned samples, surface samples and core samples at different depths, depending on the mission from which they were brought back. Between 1969 and 1972 six Apollo missions brought back 381.7 Kg of rocks, core samples, pebbles, sand and dust from the lunar surface. The six landed manned missions returned 2200 separate samples from six different exploration sites on the Moon. In addition, three automated Soviet spacecraft (Luna 16, 20 and 24 missions) collected soil and small rock fragments by drilling 35, 27 and 160 cm into the surface, with a total mass of 321 g <sup>[1,9]</sup>.

In laboratories, apart from lunar samples, our understanding of the Moon is limited to the study of meteorites. Lunar meteorites can be divided into 3 different types based on lithology, texture, petrography, chemistry and mineral composition: anorthositic breccias, basaltic breccias, and impact-melt breccias. Anorthositic breccias come from the lunar highlands and are rich in aluminum (26-31%), iron (3-6%) and incompatible elements, such as thorium. Incompatible elements are those which, due to their characteristics, could not form crystalline minerals <sup>[10,11]</sup>.

Basalt breccias come from the maria and are characterized by a relative presence of iron around 18-22%, moderately low aluminum (8-10%) and moderate levels of incompatible elements (thorium). Finally, impact-melt

---

breccias are mix of anorthositic and basaltic ones, with aluminum and iron levels located between the previously mentioned ones and have very high thorium presence <sup>[10-12]</sup>.

The mineralogy of the Moon continues to be studied through the analysis of lunar meteorites, together with returned samples and lunar simulants seeking innovative information about our natural satellite. In this way, one of the greatest challenges regarding the space exploration consists of returning humans to the Moon <sup>[13]</sup>. The upcoming long-term manned missions are critically focused on finding resources to survive on the Moon, including food production <sup>[13,14]</sup>. Therefore, the current challenge is to design methods for growing food in lunar regolith.

In advance to future manned missions, scientists are trying to evaluate how plants could be grown under lunar conditions and resources. In this regard, this chapter focuses on the study of the mineralogy of the NWA 11273 Lunar meteorite, to understand (a) how it has been altered after its ejection from the Moon and how it has been weathered on Earth, and (b) how the highly reduced lunar regolith could be oxidized as a preliminary step to plant cultivation.

## 6.1. Mineralogy of lunar meteorites – the case of the NWA 11273 Lunar meteorite

To understand lunar mineralogy as a preliminary step to define actions aiming at plant cultivation, it is necessary to check literature information as well as to analyze available samples from the Moon. In this work, the mineralogy of the feldspathic breccia NWA 11273 Lunar meteorite was studied in depth through two non-destructive analytical techniques:  $\mu$ -EDXRF and microRaman spectroscopies. In particular, the M4 TORNADO  $\mu$ -EDXRF and the Renishaw InVia microRaman spectrometers (described in Chapter 3) were selected to perform the geochemical characterization of the NWA 11273 Lunar meteorite.

### 6.1.1. Results

Firstly, a general analysis of the surface was performed by means of  $\mu$ -EDXRF imaging for assessing the elemental composition of the whole surface of the sample. Figures 6.1 and 6.2 show the  $\mu$ -EDXRF images of all the elements detected in both sides of the specimen. It can be seen that the matrix of the meteorite is mainly composed of Si, Al, Ca, Cr, Fe, Mg, Mn and Ti. Likewise, there are specific areas where Ca, K, Ni and S are abundant.

Taking into account these element mappings, some hotspots where different elements coexisted were detected. Afterwards, microRaman analyses were carried out in those areas to identify the mixture of minerals the meteorite was composed of.

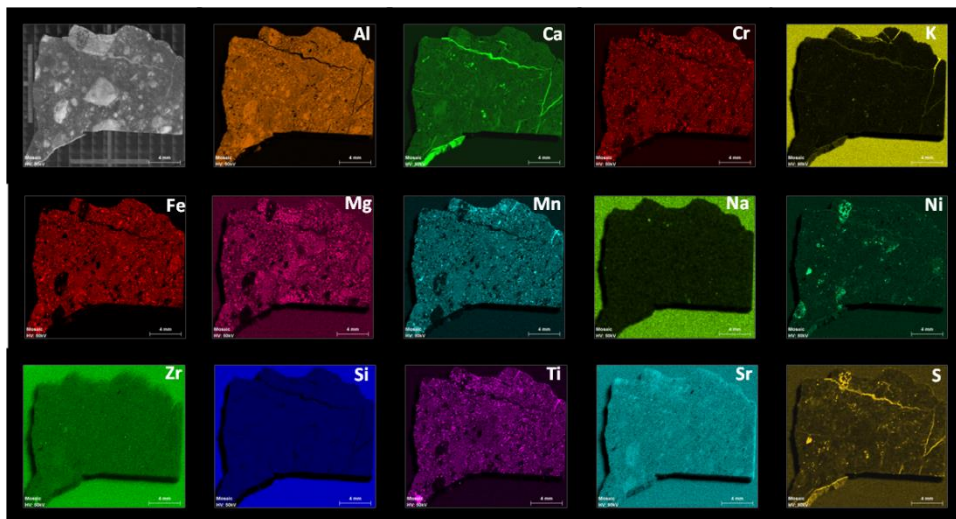


Figure 6.1.  $\mu$ -EDXRF images of the elements found on side A of the meteorite.

According to  $\mu$ -EDXRF and microRaman analyses, the most abundant discrete mineral imbedded in the feldspathic breccia family of meteorites belongs to the plagioclase group <sup>[15]</sup>, which is a solid solution ranging from

pure albite <sup>[16]</sup> to pure anorthite <sup>[16]</sup>. The Raman peaks of the identified anorthite appeared at 281, 487 and 505  $\text{cm}^{-1}$  <sup>[17,18]</sup>, which correspond to the single band around 280  $\text{cm}^{-1}$  and a doublet peak between 480 and 508  $\text{cm}^{-1}$  <sup>[19]</sup> that compose the common plagioclase Raman spectrum, as seen in Figure 6.3 B. This compound was detected as the main mineral phase of the matrix of the NWA 11273 Lunar meteorite as depicted in Al map shown in Figures 6.1 and 6.2.

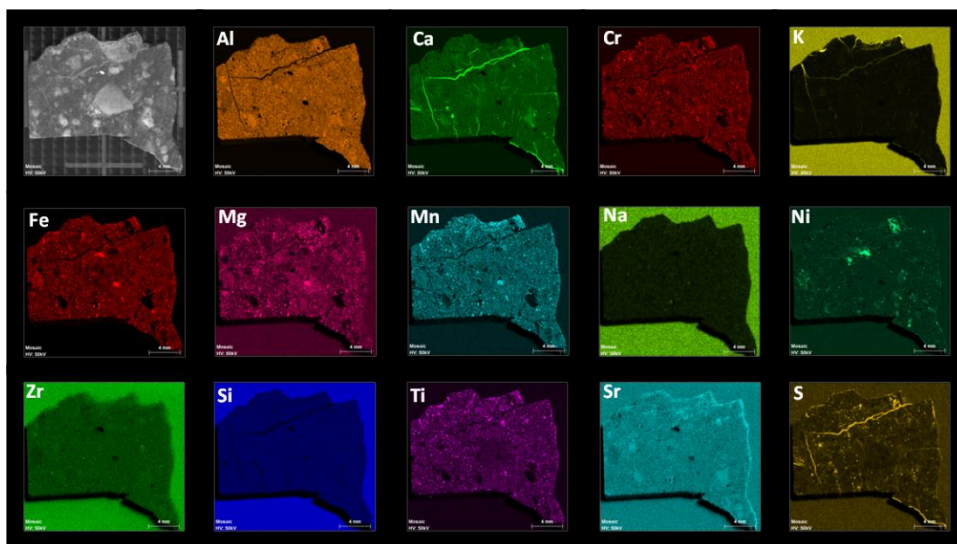


Figure 6.2.  $\mu$ -EDXRF images of the elements found on side B of the meteorite.

The second major mineral family found was pyroxene, which is divided into two subfamilies: orthopyroxene and clinopyroxene. On the one hand, orthopyroxenes crystallize in the orthorhombic system <sup>[20]</sup> and its chemical composition ranges from pure magnesium silicate, enstatite <sup>[21]</sup>, to pure ferrous iron silicate, ferrosilite <sup>[22]</sup>. On the other hand, clinopyroxenes crystallize in the monoclinic system <sup>[20]</sup> and its chemical formula is composed by single chains of  $\text{SiO}_4$  shared with a large variety of cations. Even though the pyroxene family has a Raman spectrum pattern, which consist on bands in the 300-400, 650-700 and 980-1020 wavenumber region, both subfamilies can be differentiated by their own Raman bands.

Orthopyroxenes have a doublet in the 650-700  $\text{cm}^{-1}$  region, whereas clinopyroxenes show only one intense band in that region <sup>[23]</sup>. In this way, two types of spectra were found. On the one hand, the Raman bands that appear at 296, 330, 363, 391, 660, 678 and 1001  $\text{cm}^{-1}$  compose the first spectrum (see Figure 6.3 A). On the other hand, the peaks of the second one appear at 323, 355, 389, 666 and 1010  $\text{cm}^{-1}$ . According to the bases proposed above, the first spectrum is an orthopyroxene because it has a doublet in the 650-700  $\text{cm}^{-1}$  region, and the second one is a clinopyroxene because it only has one band in that region. In addition, thanks to the flow

chart published by Wang et al.<sup>[24]</sup>, the space group of both compounds can be known. On the one side, as the first spectrum showed a doublet in the 600-800  $\text{cm}^{-1}$  region (660 and 678  $\text{cm}^{-1}$ ), a triplet in the 300-450  $\text{cm}^{-1}$  region (330, 363 and 391  $\text{cm}^{-1}$ ) and a band in the 230-450  $\text{cm}^{-1}$  region (296  $\text{cm}^{-1}$ ), the compound found corresponds to a high magnesium orthorhombic *Pbca* pyroxene. On the other side, as the second spectrum only shows one peak between 600 and 800  $\text{cm}^{-1}$  (666  $\text{cm}^{-1}$ , at a wavenumber higher than the limit of 660  $\text{cm}^{-1}$ ), the compound may correspond to a clinopyroxene or an iron-pyroxenoid. However, as this spectrum has 3 peaks in the 300-450  $\text{cm}^{-1}$  range (323, 355 and 389  $\text{cm}^{-1}$ ), and no peaks below 300  $\text{cm}^{-1}$ , the compound found corresponds to a  $C2_1/c$  monoclinic pyroxene.

Although there are 120 Raman active modes for *Pbca* pyroxenes<sup>[24]</sup>, the magnesium end member of the orthopyroxene mineral group, enstatite, was identified with its characteristic Raman bands that appear at 128(m), 234(m), 338(vs), 402(w), 435(w), 539(w), 659(s), 680(vs), 749 and 1007(s)  $\text{cm}^{-1}$ <sup>[25]</sup> (Figure 6.3 A). In this case, all Raman bands of enstatite were identified together with the main olivine Raman bands. Taking into account that the Raman measurements were performed with 785 nm excitation laser, the 50x objective and that the Raman spot size was of 1.3  $\mu\text{m}$ , it can be said that enstatite and olivine appeared in the same micrometric grain. This fact led to think that enstatite is very close related to olivine. Other spots showed only the two vs bands and other the two vs and s bands.

The third major mineral present in the sample was olivine (Figure 6.3 A) that is thought to be the dominant component in the Earth's upper mantle<sup>[26]</sup> and it normally appears in the general composition of stone and stony-iron meteorites<sup>[27]</sup>. As stated above (see Chapter 4.1), the position of the main Raman bands of olivine are sensitive to the Fo/Fa content, being displaced according to this ration. In this sense, according to the equations (Equations 4.1 and 4.2) of the olivine calibration models developed above and after selecting the main Raman band position of all olivine spectra obtained in this study, the forsterite and fayalite composition in the olivine grains of the NWA 11273 Lunar meteorite ranged between  $\text{Fo}_{62.2\pm 0.9}\text{Fa}_{37.8\pm 1.4}$  to  $\text{Fo}_{91.3\pm 1.8}\text{Fa}_{8.7\pm 1.2}$ .

The Fo/Fa values indicate that the concentration of magnesium silicate was higher than the iron silicate in the olivines of NWA 11273, i.e. there is more forsterite than fayalite. This ratio was consistent with literature values because the most mare basalt olivine grains contain only 20% of Fa and very few olivines have more content of Fe than Mg<sup>[30]</sup>.

Apart from the three major mineral phases found, other lunar minerals were identified in minor relative abundances. One of these minerals is troilite, which was occasionally identified, although literature refers as the most abundant sulfide mineral<sup>[5]</sup>. Its main Raman peaks appeared at 218, 281

and  $396\text{ cm}^{-1}$  (Figure 6.3 B). Troilite is often found in various extraterrestrial objects from meteorites to cosmic dust [31]. Besides, it is the most common sulfur component found on the Moon because the low oxygen partial pressure in the lunar environment does not permit the formation of sulfate minerals [30].

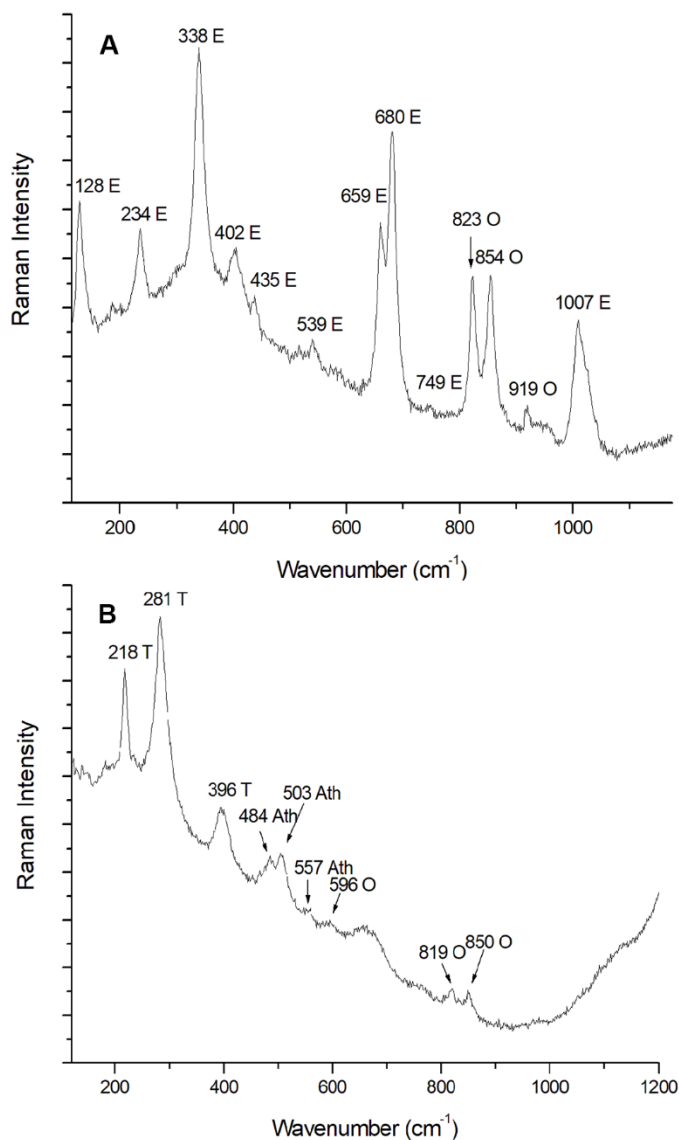


Figure 6.3. Primary mineral phases detected by microRaman spectroscopy on NWA11273. (A) Raman spectrum of enstatite, E, together with olivine, O. Measurement parameters: Renishaw inVia microRaman spectrometer, 785 nm laser, 10% laser power, objective 50x, 4s of exposure time and 5 accumulations. (B) Raman spectrum of troilite, T, together with anorthite, Ath, and olivine, O. Measurement parameter: Renishaw inVia microRaman spectrometer, 785 nm laser, 10% laser power, objective 50x, 10s of exposure time and 20 accumulations.

Furthermore, some areas of the meteorite showed a metallic appearance, which was distinguished by the naked eye (Figure 6.4 A). Those areas were studied by  $\mu$ -EDXRF and semi-quantitative analyses were carried out obtaining a ratio of 93:7% in weight of Fe:Ni. This relation of iron and nickel indicated the presence of kamacite, the alpha iron-nickel phase solution, that contains approximately 6 % of nickel <sup>[32]</sup>. When the nickel content increases, the alloy changes to the gamma iron-nickel phase, taenite, that contains between 25% and 50% of nickel <sup>[32]</sup>. Figure 6.4 B and Figure 6.4 C show the distribution of iron and nickel in the meteorite surface. The intensity of color is directly correlated to the concentration of the element; thus, higher intensity means higher relative presence of each element and vice versa. The circled area in the Figure 6.4 corresponds to the main kamacite grain. The studied sample is an achondrite and the metallized area is located in the middle of the sample. Hence, the kamacite presence may be due to the fusion between materials from the celestial body that impacted the Moon and the lunar regolith at the time of the meteorite's formation, as a metallic mineral is not expected in the magmas for this kind of meteorites <sup>[33]</sup>.

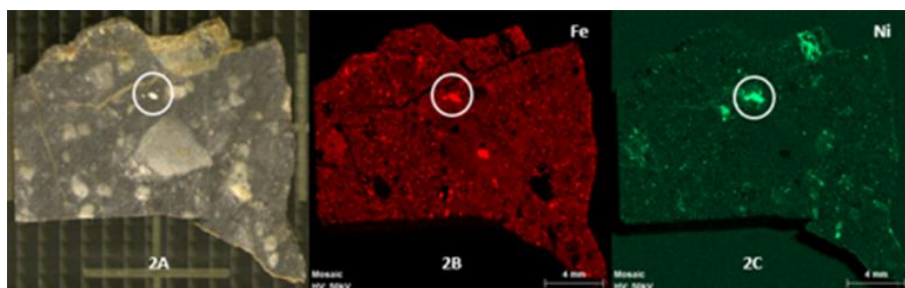


Figure 6.4. (A)  $\mu$ -EDXRF image of the B meteorite side, with the metallic area marked. (B)  $\mu$ -EDXRF image for the iron and (C) the nickel.

Figure 6.5 shows the regions where nickel and sulfur coexisted, suggesting the presence of stable nickel sulfur compounds, as sulfide or sulfate <sup>[34]</sup>.

In order to find out the actual molecular composition of the region marked, microRaman analyses were carried out. In this way, a unique and sharp band at  $989\text{ cm}^{-1}$  (Figure 6.6 A) was obtained.

This band is related to the sulfate anion <sup>[35]</sup>. Even if, it was impossible to detect any secondary band to identify the actual sulfate, this band matched perfectly with the Raman band of the tetragonal retgersite. There is another stable nickel sulfate, morenosite, which presence was rejected as its main Raman band appears at  $986\text{ cm}^{-1}$  <sup>[36]</sup>.

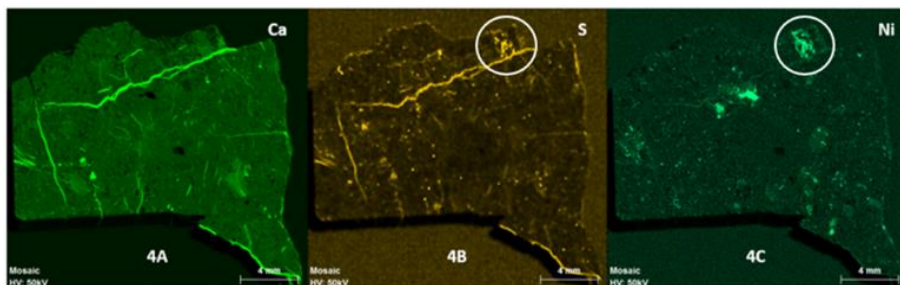


Figure 6.5.  $\mu$ -EDXRF images of (A) calcium, (B) sulfur, and (C) nickel.

It has to be highlighted that morenosite is the main mineral phase when nickel and sulfate reacts to form the solid at room temperature, which crystallizes in the orthorhombic system. However, when temperature raises 35 °C, the heptahydrate transforms to the hexahydrate tetragonal retgersite, requiring more than 65 °C to evolve to the monoclinic one [36]. Taking into account that the NWA 11273 Lunar meteorite could be exposed for decades to the hot environment of the Sahara desert (annual average is 30 °C [37]), the presence of tetragonal phase was more expected. Moreover, the presence of nickel-sulfate is probably due to a terrestrial secondary mineral phase, which is the results of the weathered original lunar nickel-sulfide compound.

Ilmenite [38] and zircon [39] were also found in the NWA 11273 meteorite. Ilmenite is the most abundant oxide mineral in lunar rocks and forms as much as 15-20% by volume of many Apollo 11 and 17 mare basalts [30]. It was identified by its Raman bands that appear at 229, 370 and 680  $\text{cm}^{-1}$  [40] (Figure 6.6 B).

Regarding the zircon, which appears in less lunar rocks than ilmenite, it is worthy highlighting that it has the great capability to release the pressure it had been previously subjected to. This is because when the zircon is subjected to a pressure higher than 20 GPa [41], its tetragonal structure (with space group  $D4h\ 19$  or  $I41/amd$ ;  $a = 6.607\ \text{\AA}$ ;  $c = 5.981\ \text{\AA}$ ) [41] changes into the structural phase transition of the mineral reidite, the scheelite-structure phase (space group  $I41/a$ ;  $a = 4.734\ \text{\AA}$ ;  $c = 10.51\ \text{\AA}$ ) [41].

In this way, Gucsik et al. [41] proposed that the main band of zircon shifts its wavenumber by two units, in  $\text{cm}^{-1}$ , for every extra 10 GPa that it undergoes after a shock event. Taking as reference the position of the unshocked zircon, which appear at 202, 214, 225, 269, 355, 393, 439, 975 and 1008  $\text{cm}^{-1}$  [39], the pressure that the sample underwent can be calculated with the experimental position of the shocked zircon. Figure 6.7 A shows the Raman bands of the detected zircon. This presented a band at 1004  $\text{cm}^{-1}$ , so as the main band of zircon suffered a displacement of 4  $\text{cm}^{-1}$  (from 1008 to 1004  $\text{cm}^{-1}$ ), it was calculated that the impact pressure suffered by the NWA 11273 Lunar meteorite was estimated to be at least around 20 GPa.

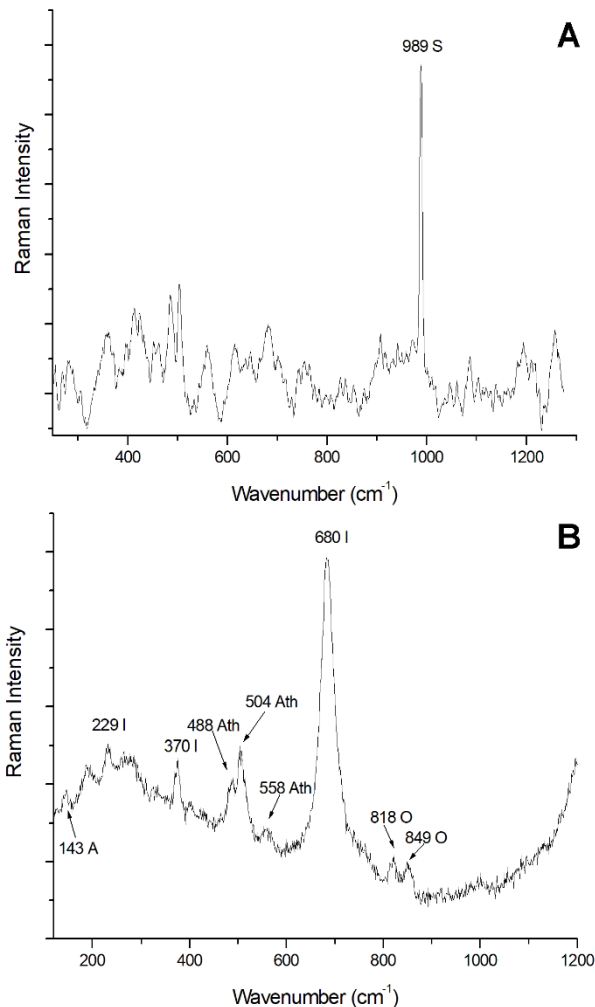


Figure 6.6. (A) Raman spectrum of retgersite, S. Measurement parameters: Renishaw inVia microRaman spectrometer, 785 nm laser, 1% laser power, objective 20 $\times$ , 25 s of exposure time, and 5 accumulations. Spectrum treatment: baseline. (B) Raman spectrum of ilmenite, I, together with anatase, A, anorthite, Ath, and olivine, O. Measurement parameters: Renishaw inVia microRaman spectrometer, 532 nm laser, 5% laser power, objective 50 $\times$ , 20s of exposure time and 2 accumulations.

Finally, three oxides were found in the sample: hematite [42], quartz [43] and anatase [44]. Hematite was found occasionally through point-by-point microRaman analysis with bands at 225, 290, 405, 495 and 605  $\text{cm}^{-1}$  [45] (Figure 6.7 B). With regard to iron oxides, magnetite [46] and hematite have been detected so far in lunar rocks and soils by a variety of techniques [46]. The appearance of iron oxides may be due to alteration of other primary mineral phases. For example, some studies [47,48] have checked that the observation of hematite by microRaman spectroscopy can be caused by the oxidation of lunar ilmenite or the elemental iron during the analysis

process in the presence of terrestrial atmosphere. However, in this study the thermodecomposition of the sample was certainly avoided by using different lasers at very low intensity.

Besides, quartz was found by its Raman bands that appear at 205, 266, 352 and 464  $\text{cm}^{-1}$  [49] (Figure 6.7 B). Although it is one of the major compounds on terrestrial igneous, metamorphic, and sedimentary rocks, this mineral phase is rarely found on the Moon. In fact, this distinction is one of the major mineralogical differences between the Moon and the Earth.

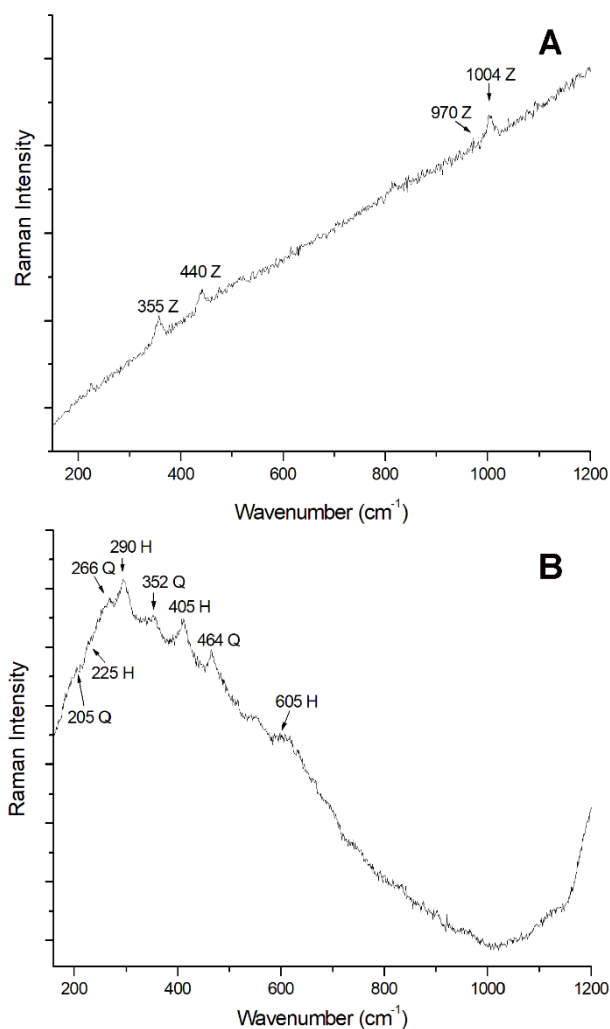


Figure 6.7. (A) Raman spectrum of the shocked zircon, Z. Measurement parameters: Renishaw inVia microRaman spectrometer, 532 nm laser, 5% laser power, objective 20x, 4s of exposure time and 1 accumulation. (B) Raman spectrum of quartz, Q, and hematite, H. Measurement parameters: Renishaw inVia microRaman spectrometer, 785 nm laser, 1% laser power, objective 50x, 25s of exposure time and 5 accumulations.

On the Moon, the silica minerals tend to concentrate with (a) chemical elements that are also rare on the Moon, such as the KREEP elements (potassium, Rare-Earth Elements, EE, and phosphorous) <sup>[30]</sup>, or with (b) variable amounts of plagioclase, potassium feldspar and pigeonite, mixture so-called quartz monzodiorite <sup>[50]</sup>. The quartz detected in the studied sample did not appear accompanied with the mentioned elements and mineral phases. In contrast, all quartz Raman spectra were always accompanied by hematite and olivine. Therefore, the presence of quartz and hematite seems to be a consequence of an alteration product of other primary lunar minerals, such as olivines, induced by terrestrial weathering.

The last oxide found was anatase, whose main Raman band appears at  $143\text{ cm}^{-1}$  <sup>[51]</sup> (Figure 6.8 A). It is one of the most abundant mineral phases in the terrestrial nature, but anatase has not been found yet in the Moon, so its presence in the NWA 11273 Lunar meteorite could be associated with an alteration of other primary minerals, such as ilmenite, which is the most abundant oxide mineral on the Moon <sup>[30]</sup>.

Apart from the previously discussed lunar minerals, other compound that is not related with the Moon was found. The most abundant unexpected mineral found in the sample was calcite <sup>[52]</sup>, which was identified by combining  $\mu$ -EDXRF and microRaman measurements. The  $\mu$ -EDXRF technique indicated that the calcium was distributed all along the meteorite (Figure 6.5 A), but cracks showed higher concentration of this element than the rest of the surface.

As Figure 6.5 B shows, these fractures were also rich in sulfur, so, in order to know which mineral was present in the cracks, microRaman analysis were carried out, obtaining bands at  $280$ ,  $711$  and  $1087\text{ cm}^{-1}$  (Figure 6.8 B), which correspond to those of calcite <sup>[34]</sup>. It is possible that the high amount of calcite in the cracks masks the Raman signal of other compounds. Taking into account that Figures 6.5 A and 6.5 B show the coexistence of calcium and sulfur on the cracks, it is possible that calcite masks the possible Raman signal of gypsum <sup>[53]</sup>. The most reliable hypothesis about the presence of calcite in the cracks of the meteorite is the precipitation of a solution saturated with the ions  $\text{Ca}^{2+}$  and  $\text{HCO}_3^-$  at a pH higher than 8. These ions were transported in the water that entered in the meteorite through the cracks once on Earth. Then water was evaporated, and the ions precipitated forming the mentioned calcium carbonate.

Complementary to point-by-point analysis, big areas of the meteorite were analyzed by Raman imaging. Raman imaging was carried out in both sides of the meteorite sample. In this way, Figure 6.9 A shows an optical image of the selected area for a Raman image which was performed on the side A of the sample.

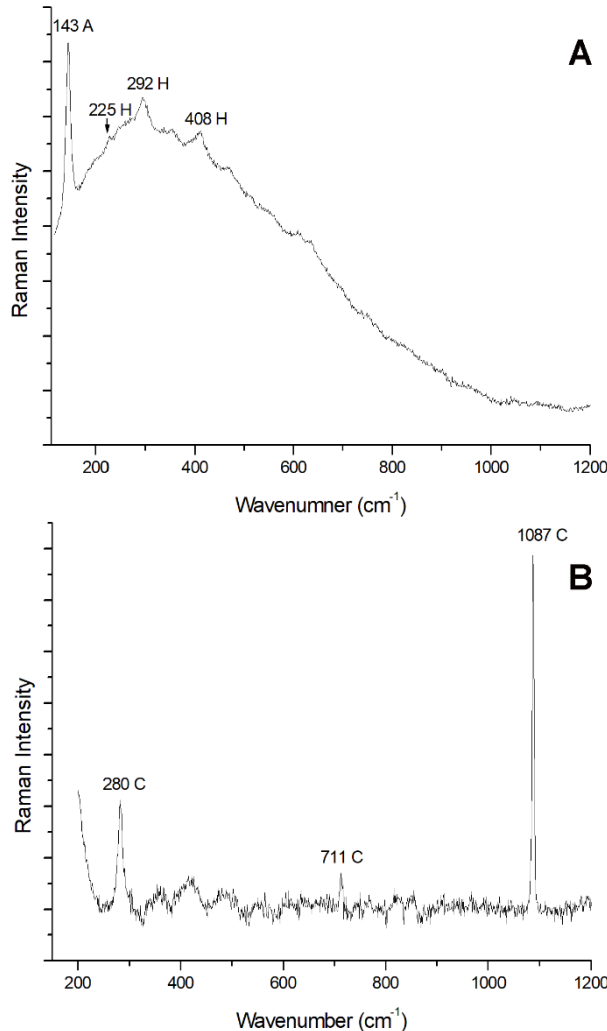


Figure 6.8. (A) Raman spectrum of anatase, A, together with hematite, H. Measurement parameters: Renishaw inVia microRaman spectrometer, 785 nm laser, 1% laser power, objective 20x, 25s of exposure time and 5 accumulations. (B) Raman spectrum of calcite, C. Measurement parameters: Renishaw inVia microRaman spectrometer, 785 nm laser, 1% laser power, objective 50x, 25 s of exposure time, and 5 accumulations. Spectrum treatment: baseline done.

Figure 6.9 B shows the anorthite rich area (in green), which was constructed after selecting the interval 498-512 cm<sup>-1</sup> that contains the main Raman bands for anorthite. Figures 6.9 C and 6.9 D show the spatial distribution of pyroxene (in purple the area with signal at the 665-685 cm<sup>-1</sup> interval containing the common band of both types of pyroxenes) and olivine (in green, which was created using the range 815-834 cm<sup>-1</sup> that contains one of the main bands for olivine). By this means, it can be said that pyroxene and olivine were distributed along the matrix, like anorthite. However, as can be seen in Figure 6.9, there is a grain that is not composed by olivine, as it is made of anorthite, pyroxene and some calcite (Figure 6.9

E). The Raman image of calcite (in red) was performed using the interval  $1082\text{-}1093\text{ cm}^{-1}$  that contains the main Raman band for calcite at  $1084\text{ cm}^{-1}$ . It has to be considered that due to the lack of flatness in the area analyzed (the crack is deeper than the rest of the region) the Raman signals of the compounds present in the crack do not appear in this Raman image. Other Raman measurements performed, focused on the cracks, showed the presence of calcite along them. The same happened with the retgersite present in the crack. However, Figure 6.9 F shows the scarce distribution of retgersite (in blue) also out of the crack. This figure was constructed after selecting the  $980\text{-}991\text{ cm}^{-1}$  where the main and unique band of the sulfate appears.

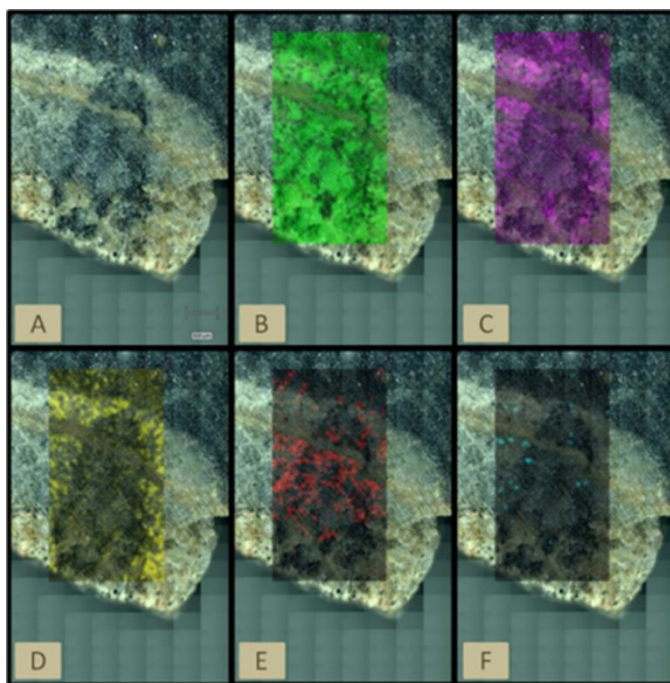


Figure 6.9. Raman images of the (A) sample area mapping, (B) anorthite, (C) pyroxene, (D) olivine, (E) calcite, and (F) retgersite obtained with the Renishaw inVia microRaman spectrometer.

### 6.1.2. Discussion

By using this analytical strategy, it was possible to identify primary (lunar origin), secondary (formed by alteration of the primary ones on both the Moon and the Earth, being Martian secondary and terrestrial secondary mineral phases), and terrestrial weathering mineral phases. According to the Meteoritical Bulletin, this work confirms the presence of anorthite, olivine, pyroxene, troilite and kamacite as primary mineral phases. In addition, thanks to the high resolution techniques used, two more primary minerals were identified: ilmenite and zircon.

---

Besides the primary minerals, retgersite, hematite, quartz, enstatite and anatase were detected as secondary minerals. In this work, it is proposed that retgersite comes from the millerite oxidation (terrestrial secondary mineral); hematite, quartz and enstatite are minerals formed through the pressure alteration of olivine (lunar secondary minerals); and another proportion of hematite and all of the anatase comes from the terrestrial oxidation of ilmenite (terrestrial secondary mineral).

As mentioned, thanks to the use of high spectral resolution techniques used a pressure study of zircon was performed. This allowed to estimate that the NWA 11273 Lunar meteorite was subjected to a pressure of about 20 GPa at the time of its formation (Figure 6.10). Hence, it can be confirmed that the proposed alteration processes may be due to the high pressures.

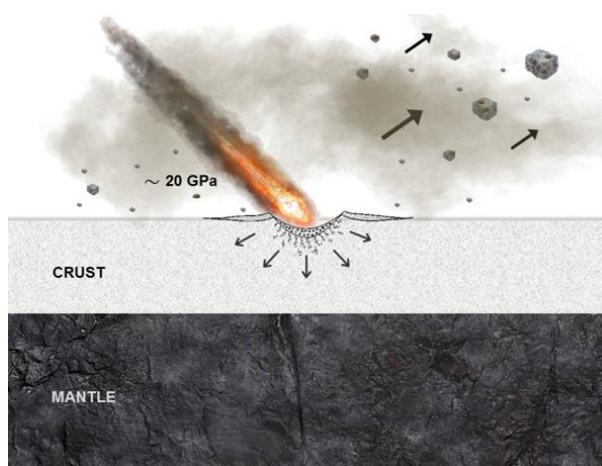


Figure 6.10. Process in which a celestial body hit the Moon with a pressure of 20 GPa. This event formed the meteorite analyzed in this work, the NWA 11273 Lunar meteorite.

Although the point-by-point analyses gave us relevant information about the sample, it is important to highlight the great advantage provided by the imaging analyses. Both microRaman and  $\mu$ -EDXRF chemical imaging provide a visual distribution of the sample composition (mineral phases and chemical elements), which helped to interpret the results. Thanks to imaging analyses, it was possible to identify the distribution of calcium and sulfur along the cracks, as well as nickel and sulfur in a detached area in the upper part of the meteorite. These zones correspond to calcite and a retgersite, respectively.

As can be seen, by combining high resolution non-destructive techniques such as  $\mu$ -EDXRF and microRaman spectroscopies, a deeper mineralogical analysis can be carried out, being able to differentiate between primary, secondary, which can be formed on the Moon or on the Earth, and terrestrial weathering mineral phases.

## **6.2. Weathering of lunar soils, as seen from the NWA 11273 Lunar meteorite, as the first step for plant cultivation**

As demonstrated by Paul et al. <sup>[54]</sup>, future plant cultivation on the Moon will require using amended soils (nutrients, organic matter and water). However, first, the raw soils must be treated to transform the anoxic compounds into the oxic ones to avoid the presence of harmful reduced ions that could be released after amending soils. Thus, this subchapter evaluates how the lunar regolith can be altered and, consequently, oxidized, giving rise to oxidized soils ready for plant cultivation. In this sense, the NWA 11273 Lunar meteorite was used as the model sample.

The weathering of the NWA 11273 Lunar meteorite was studied as a model to understand the expected reactions that raw lunar soils can undergo after treating them to transform the reduced minerals into the oxidized ones. As oxidized minerals can be included hydrated minerals containing water molecules and/or hydroxyl functions groups in their structures.

By using the previous strategy based on the combination of  $\mu$ -EDXRF and microRaman spectroscopies (Chapter section 6.2), it was possible to identify primary (lunar origin), secondary (formed through the alteration of the primary ones on the Earth or on the Moon), and terrestrial weathering mineral phases. According to the Meteoritical Bulletin, this work confirms the presence of anorthite, olivine, pyroxene, troilite and kamacite as primary mineral phases. In addition, thanks to the high resolution of the techniques used, two more primary minerals were identified: ilmenite and zircon. All these minerals have in common that they are in their most reduced form, which indicates a complete anoxic environment during the cooling of the lunar magma.

Soils coming directly from highlands are poorly weathered and cannot be used directly for cultivation processes. For this reason, the secondary and the terrestrial weathering minerals found on the NWA 11273 Lunar meteorite were carefully studied. In this sense, retgersite, hematite, quartz, enstatite and anatase were detected as secondary minerals. In this work, it is proposed that retgersite comes from the millerite oxidation (terrestrial secondary mineral); hematite, quartz and enstatite are minerals formed through the pressure alteration of olivine (lunar secondary minerals); and another proportion of hematite and all of the anatase comes from the terrestrial oxidation of ilmenite (terrestrial secondary mineral).

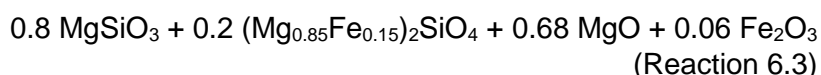
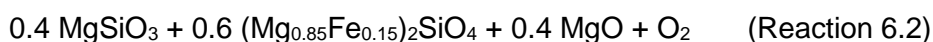
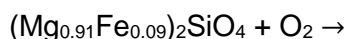
On the one hand, we propose that millerite can be a primary mineral from the Moon, since the magma was cooled in anoxic environmental conditions. Under an oxidizing environment and in the presence of water,

---

this mineral can be oxidized to retgersite, following the reaction on Reaction 6.1.

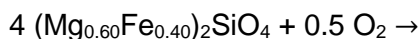


On the other hand, we propose that hematite, quartz and enstatite are minerals formed through the pressure alteration of olivine (lunar secondary minerals). It is well known that this type of oxidation is a commonly recognized natural phenomenon caused first by a high-pressure event and then by an oxidation <sup>[52]</sup>. In this way, the reaction occurs by an initial breakdown of the fayalite and forsterite components due to the high-pressure effect, then the oxidation of the fayalite component, and subsequent reaction with the forsterite one, to give rise to two different options depending on the oxygen consumption. The detection of olivine remnants indicates that the alteration process was not complete. Reaction 6.2 shows the possible reaction that would occur without total oxygen consumption, whereas Reaction 6.3 shows the reaction with a total oxygen consumption. In any case, the final products proposed are a less magnesium-concentrated olivine, enstatite and MgO. Hematite is joined to these compound if the Reaction 6.4 is followed <sup>[55]</sup>.



Unfortunately, the MgO Raman scattering is low enough to be in the range of noise and the amount of hematite is quite low to be observed.

However, in the border of the same olivine grains, quartz and hematite were also observed, together with olivine. According to the calibration model proposed in Chapter 4.1, the olivine Raman bands are consistent with an olivine with 40% of fayalite. Therefore, the oxidative degradation of a more Fe-enriched olivine is proposed on Reaction 6.6.



Here, an initial  $(\text{Mg}_{0.60}\text{Fe}_{0.40})_2\text{SiO}_4$  olivine is completely transformed to the three minerals showed in the spectrum. With these two oxidative reactions of olivine, where water does not take part, although an aqueous medium is always required, three important mineral for plant cultivation have been

formed ( $\text{MgO}$ ,  $\text{SiO}_2$  and  $\text{Fe}_2\text{O}_3$ ). Remaining, also, an important amount of olivine to generate Mg- and Fe-rich phyllosilicates after a more acidic attack.

Another important oxidative weathering reaction detected was the transformation of ilmenite into anatase and hematite. In order to understand the formation of the anatase and other weathered compounds explained below, soils near Tinduf were sampled and analyzed. To determine the pH and redox potential of the Sahara soil, the UNE-ISO 10390 norm and the 2000  $\mu\text{-pH}$ meter were used. Therefore, 5 g of the soils were mixed with 25 mL of deionized water, stirred in a plate heated at 20 °C for 10 hours and then, filtered to obtain a clean water extract. After obtaining three replicates, the average values were  $9.45 \pm 0.25$  of pH and  $490 \pm 8$  mV of redox potential. These values were later used as references in the thermodynamic modelling.

In this sense, the oxidative weathering of ilmenite is thermodynamically possible at the water extractable conditions of Sahara soils (pH=9.45 and 490 mV of potential redox). This fact is also observed in the fraction diagram shown in Figure 6.11, where only ilmenite and an aqueous media have been considered for the modelling process.

In this model, solid ilmenite (at an equivalent total concentration of 50 mM) without any dissolved titanium species was fixed at 0.49 V of redox potential. As seen at 9.45 of pH, the most stable specie is the solid  $\text{Fe}(\text{OH})_3$ , which transforms into hematite with temperature.

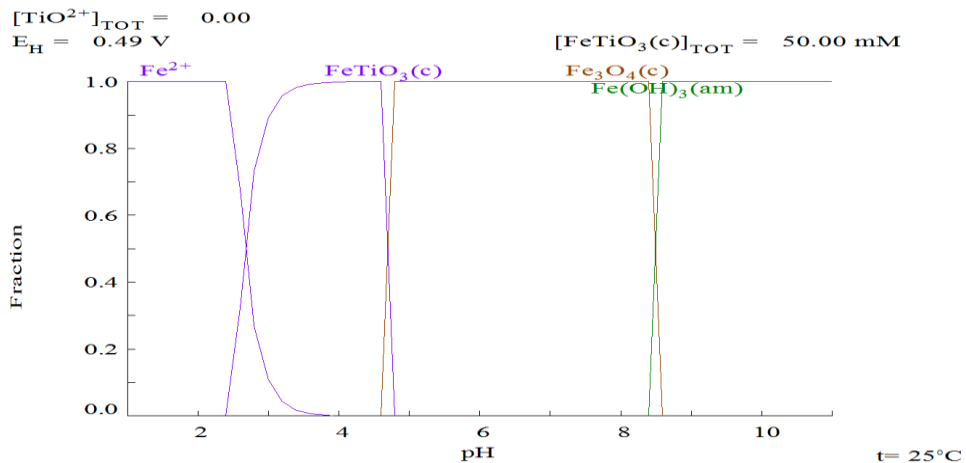


Figure 6.11. Iron fraction diagram created with Hydra and Medusa software to explain how iron evolves as a function of pH.

Besides, anatase transforms irreversibly to the other titanium dioxide polymorph, rutile, at temperatures higher than 800 °C [56,57]. Therefore, the transformation of the titanium-bearing compound into anatase happened

after the high-temperature events of the travel to the ground. Taking this into account, it is highly probable that the presence of anatase in the NWA 11273 meteorite may due to an alteration related to the oxidation of the Fe (II) in ilmenite to form irreversibly hematite and anatase [58].

Thus, the Reaction 6.5 is proposed for ilmenite oxidation.



It was also possible to verify that the meteorite was subjected to high pressures since one of the primary minerals, the zircon, was capable to reveal the pressure to which the sample was subjected to measuring the displacement of its Raman bands. Thus, in this work we have estimated that the NWA 11273 Lunar meteorite was subjected to a pressure of about 20 GPa at the time of its formation. Hence, it can be confirmed that the proposed alteration processes may be due to the high pressures.

Table 6.1 summarizes all the mineral phases found in this meteorite, including primary, secondary and terrestrial weathering mineral phases.

*Table 6.1. Mineral phases found in the NWA 11273 Lunar meteorite, including the name, the molecular formula, the type of mineral phase (1°: primary; L2°: lunar secondary; T2°: terrestrial secondary; TW: terrestrial weathering; and S: space), and the Raman bands of each compound (v: very; s: strong; m:medium; w: weak; br: broad; and sh: shoulder).*

Mineral Phase	Molecular Formula	Type	Raman Bands (cm <sup>-1</sup> )
Anorthite	CaAl <sub>2</sub> Si <sub>3</sub> O <sub>8</sub>	1°	281 (m), 402 (m), 487 (sh s), 505 (vs), 560 (m), 681 (m), 766 (w)
Clinopyroxene	(Ca,Mg,Fe,Mn,Na,Li)	1°	321 (m), 388 (s), 663 (s), 1010 (vs)
Orthopyroxene	(Al,Mg,Fe,Mn,Cr,Sc,Ti) (Si,Al) <sub>2</sub> O <sub>6</sub>	1°	335 (m), 660 (sh s), 678 (vs), 1004 (vs)
Enstatite	MgSiO <sub>3</sub>	L2°	128 (s), 234 (m),338 (vs), 402 (m), 435 (w), 539 (w), 659 (sh s), 680 (vs), 1007 (s)
Olivine	(Fe,Mg) <sub>2</sub> SiO <sub>4</sub>	1°	421 (w), 600 (w), 673 (w), 820 (vs), 850 (vs), 958 (w)
Kamacite	Fe:Ni alloy	1°/S	-
Troilite	FeS	1°	218 (s), 281 (vs), 396 (m)
Ilmenite	FeTiO <sub>3</sub>	1°	229 (w), 370 (m), 682 (vs)
Zircon	ZrSiO <sub>4</sub>	1°/L2°	355 (s), 440 (s), 970 (w), 1004 (vs)
Hematite	Fe <sub>2</sub> O <sub>3</sub>	L2°/T2°	225 (s), 290 (vs), 405 (s), 495 (w), 605 (m)
Quartz	SiO <sub>2</sub>	L2°	205 (w), 266 (w), 352 (m), 464 (s)
Calcite	CaCO <sub>3</sub>	TW	153 (w), 280 (m), 711 (w), 1087 (vs)
Retgersite	NiSO <sub>4</sub> .6H <sub>2</sub> O	T2°	989 (m)
Anatase	TiO <sub>2</sub>	T2°	143 (s)

### 6.3. Conclusions

Most of the secondary minerals phases identified in this meteorite ( $\text{MgSiO}_3$ ,  $\text{Fe}_2\text{O}_3$ ,  $\text{SiO}_2$ ,  $\text{NiSO}_4 \cdot 6\text{H}_2\text{O}$  and  $\text{TiO}_2$ ) have been formed by oxidative weathering of original lunar minerals (primary minerals). Although they have been found in the NWW 11273 Lunar meteorite, these phases are also expected to be found in the lunar regolith when it is oxidized as a preliminary step to plant cultivation. The remaining olivine, pyroxenes and plagioclases (primary mineral phases) are sources for phyllosilicate formation when acidic attack is applied in oxidizing conditions. However, this must be conducted carefully due to the risk of destroying the ilmenite of the regolith, which is a very important mineral for habitability.

Ilmenite has been recognized for years as an important mineral for human habitability in the Moon <sup>[59]</sup> due to its capability to absorb volatile elements such as H, N, C, He and other noble gases in the anoxic lunar environment. In particular, ilmenite-rich regolith with grain sizes lower than  $75 \mu\text{m}$  (this grain size indicate a mature soil) host the highest content of such volatiles <sup>[59]</sup>.

According to the modelling diagram of Figure 6.11, if a more acidic ( $\text{pH} < 3$ ) oxidation is applied to lunar regolith, phyllosilicates can be formed from primary minerals and the ilmenite can be dissolved, releasing  $\text{Fe}^{2+}$  ions in dissolution. Due to an oxidation process,  $\text{Fe}^{2+}$  transforms into the dissolved  $\text{Fe}^{3+}$ , which precipitates at  $\text{pH} > 3$ . The dissolved  $\text{Fe}^{3+}$  can react with carboxylic acids (added as ammenders for plant cultivation), forming quelated Fe-compounds that are better captured by the roots of plants, enhancing their absorption capability for iron. This positive effect (formation of phyllosilicates and absorbable iron) has an associated problem: the destruction of ilmenite and that trapped volatiles would be released to atmosphere.

Using lunar meteorite analyses to evaluate possible reactions that may occur in the lunar regolith as a preliminary step to plant cultivation is very successful. This is because the primary minerals identified in the Chapter section 6.2 by  $\mu\text{-EDRF}$  and microRaman spectroscopies are very similar to those described for the LZS-1 lunar basaltic soil simulant <sup>[60]</sup>. This simulant is dominated by Ca-rich plagioclases, high-Ca pyroxenes, Mg-rich olivines (mean  $\text{Fo}_{70}$ ) and Fe-Ti-Cr oxides. This clear parallelism between the NWA 11273 Lunar meteorite and the LZS-1 simulant will help to perform in the future, on the one hand, high scale experiments for habitability with the simulant and, on the other hand, confirm their results at low scale with the NWA 11273 materials.

Next experiments will consist of detecting if the weathered oxides described previously in NWA 11273 meteorite are found in the LZS-1 lunar soil simulant <sup>[60]</sup> using microRaman spectroscopy. Then, searching for

---

soluble ions and their concentrations in NWA 11273 Lunar meteorite and LZS-1 materials will be conducted to confirm the parallelism between NWA 11273 and LZS-1. Finally, acidic oxidative tests will be performed to detect new mineral phases and released compounds in both materials, checking carefully the conditions for the complete destruction of ilmenite just to define the extreme environmental conditions that never should be trespassed to avoid the destruction of this key mineral in the lunar regolith.

## 6.4. References

- [1] Vaniman, D.; Dietrich, J.; Taylor, G. J.; Heiken, G. Exploration, Samples, and Recent Concepts of the Moon. In *Lunar Sourcebook*; Heiken, G. H., Vaniman, D. T., French, B. M., Eds.; Cambridge University Press: Cambridge, UK, 1991; pp 5–25.
- [2] Vaniman, D.; French, B. M.; Heiken, G. Afterword. In *Lunar Sourcebook*; Heiken, G., Vaniman, D. T., French, B. M., Eds.; Cambridge University Press: Cambridge, UK, 1991; pp 633–650.
- [3] Spudis, P. D. Volcanism on the Moon. In *The Encyclopedia of Volcanoes*; Elsevier, 2015; pp 689–700. <https://doi.org/10.1016/B978-0-12-385938-9.00039-0>.
- [4] Hörz, F.; Grieve, R.; Heiken, G.; Spudis, P.; Binder, A. Lunar Surface Processes. In *Lunar Sourcebook*; Heiken, G., Vaniman, D. T., French, B. M., Eds.; Cambridge University Press: Cambridge, UK, 1991; pp 61–111.
- [5] Papike, J.; Taylor, L.; Simon, S. Lunar Minerals. In *Lunar Sourcebook*; Heiken, G., Vaniman, D. T., French, B. M., Eds.; Cambridge University Press: Cambridge, UK, 1991; pp 121–155.
- [6] Taylor, G. J.; Warren, P.; Ryder, G.; Delano, J.; Pieters, C.; Lofgren, G. Lunar Rocks. In *Lunar Sourcebook*; Heiken, G., Vaniman, D. T., French, B. M., Eds.; Cambridge University Press: Cambridge, UK, 1991; pp 183–261.
- [7] Bates, R. L.; Jackson, J. A. *The Glossary of Geology*, 2nd ed.; American Geological Institute: Washington D. C., 1980.
- [8] McKay, D. S.; Heiken, G.; Basu, A.; Blanford, G.; Simon, S.; Reedy, R.; French, B. M.; Papike, J. The Lunar Regolith. In *Lunar Sourcebook*; Heiken, G., Vaniman, D. T., French, B. M., Eds.; Cambridge University Press: Cambridge, UK, 1991; pp 285–356.
- [9] NASA. *Lunar rocks and soils from Apollo missions*. <https://curator.jsc.nasa.gov/lunar/> 1969 and 1972 six,exploration sites on the Moon. (accessed 2023-03-30).
- [10] Yanai, K.; Kohima, H. Varieties of Lunar Meteorites Recovered from Antarctica. *Proc. NIPR Symp. Antarct. Meteorites* **1991**, *4*, 70.
- [11] Korotev, R. L. Lunar Geochemistry as Told by Lunar Meteorites. *Geochemistry* **2005**, *65*, 297. <https://doi.org/10.1016/j.chemer.2005.07.001>.
- [12] Grier, J. A.; Rivkin, A. S. Comparing Sample and Remote-Sensing Data—Understanding Surface Composition. In *Airless Bodies of the Inner Solar System*; Elsevier, 2019; pp 95–119. <https://doi.org/10.1016/B978-0-12-809279-8.00005-6>.

- 
- [13] Cyclic, L. M.; Hausrath, E. M.; Ming, D. W.; Adcock, C. T.; Raymond, J.; Remias, D.; Rueschle, W. P. Investigating the Growth of Algae Under Low Atmospheric Pressures for Potential Food and Oxygen Production on Mars. *Front. Microbiol.* **2021**, *12*, 733244. <https://doi.org/10.3389/fmicb.2021.733244>.
- [14] Revellame, E. D.; Aguda, R.; Chistoserdov, A.; Fortela, D. L.; Hernandez, R. A.; Zappi, M. E. Microalgae Cultivation for Space Exploration: Assessing the Potential for a New Generation of Waste to Human Life-Support System for Long Duration Space Travel and Planetary Human Habitation. *Algal Res.* **2021**, *55*, 102258. <https://doi.org/10.1016/j.algal.2021.102258>.
- [15] Nagaoka, H.; Karouji, Y.; Arai, T.; Ebihara, M.; Hasebe, N. Geochemistry and Mineralogy of a Feldspathic Lunar Meteorite (Regolith Breccia), Northwest Africa 2200. *Polar Sci.* **2013**, *7*, 241. <https://doi.org/https://doi.org/10.1016/j.polar.2013.09.001>.
- [16] Sims, M.; Jaret, S. J.; Carl, E.-R.; Rhymer, B.; Schrod, N.; Mohrholz, V.; Smith, J.; Konopkova, Z.; Liermann, H.-P.; Glotch, T. D.; Ehm, L. Pressure-Induced Amorphization in Plagioclase Feldspars: A Time-Resolved Powder Diffraction Study during Rapid Compression. *Earth Planet. Sci. Lett.* **2019**, *507*, 166. <https://doi.org/10.1016/j.epsl.2018.11.038>.
- [17] Matson, D. W.; Sharma, S. K.; Philpotts, J. A. Raman Spectra of Some Tectosilicates and Glasses along the Orthoclase-Anorthite and Nepheline-Anorthite Joins. *Am. Mineral.* **1986**, *71*, 694.
- [18] Freeman, J. J.; Wang, A.; Kuebler, K. E.; Jolliff, B. L.; Haskin, L. A. Characterization of Natural Feldspars by Raman Spectroscopy for Future Planetary Exploration. *Can. Mineral.* **2008**, *46*, 1477. <https://doi.org/10.3749/canmin.46.6.1477>.
- [19] S., K. B.; Lin, J.-F.; Cisneros, M.; Fu, S. Feldspar Raman Shift and Application as a Magmatic Thermobarometer. *Am. Mineral.* **2018**, *103*, 600. <https://doi.org/10.2138/am-2018-6157>.
- [20] Morimoto, C. N. Nomenclature of Pyroxenes. *Mineral. Petrol.* **1988**, *39*, 55. <https://doi.org/10.1007/BF01226262>.
- [21] Sanchez-Valle, C.; Bass, J. Elasticity and Pressure-Induced Structural Changes in Vitreous MgSiO<sub>3</sub>-Enstatite to Lower Mantle Pressures. *Earth Planet. Sci. Lett.* **2010**, *295*, 523. <https://doi.org/10.1016/j.epsl.2010.04.034>.
- [22] Stalder, R.; Kronz, A.; Schmidt, B. C. Raman Spectroscopy of Synthetic (Mg,Fe)SiO<sub>3</sub> Single Crystals. An Analytical Tool for Natural Orthopyroxenes. *Eur. J. Mineral.* **2009**, *21*, 27. <https://doi.org/10.1127/0935-1221/2009/0021-1846>.

- [23] Mernagh, T. P.; Hoatson, D. M. Raman Spectroscopic Study of Pyroxene Structures from the Munni Munni Layered Intrusion, Western Australia. *J. Raman Spectrosc.* **1997**, *28*, 647. [https://doi.org/10.1002/\(SICI\)1097-4555\(199709\)28:9<647::AID-JRS155>3.0.CO;2-H](https://doi.org/10.1002/(SICI)1097-4555(199709)28:9<647::AID-JRS155>3.0.CO;2-H).
- [24] Wang, A.; Jolliff, B. L.; Haskin, L. A.; Kuebler, K. E.; Viskupic, K. M. Characterization and Comparison of Structural and Compositional Features of Planetary Quadrilateral Pyroxenes by Raman Spectroscopy. *Am. Mineral.* **2001**, *86*, 790. <https://doi.org/10.2138/am-2001-0703>.
- [25] Jung, H.; Lee, J.; Ko, B.; Jung, S.; Park, M.; Cao, Y.; Song, S. Natural Type-C Olivine Fabrics in Garnet Peridotites in North Qaidam UHP Collision Belt, NW China. *Tectonophysics* **2013**, *594*, 91. <https://doi.org/10.1016/j.tecto.2013.03.025>.
- [26] Mitchell, T. E.; Heuer, A. H. *Chapter 68 - Dislocations and Mechanical Properties of Ceramics*; Nabarro, F., Hirth, J., Eds.; Elsevier: New York, 2004; Vol. 12. [https://doi.org/10.1016/S1572-4859\(05\)80007-5](https://doi.org/10.1016/S1572-4859(05)80007-5).
- [27] Guo, S.-L.; Chen, B.-L.; Durrani, S. A. *Chapter 4 - Solid-State Nuclear Track Detectors*; Academic Press: Amsterdam, 2012. <https://doi.org/10.1016/B978-0-12-384873-4.00004-9>.
- [28] Torre-Fdez, I.; Ruiz-Galende, P.; Aramendia, J.; Gomez-Nubla, L.; Castro, K.; Arana, G.; Madariaga, J. M. New Quantitative Model to Determine Fayalite-Forsterite Content in Olivine Minerals by Raman Spectroscopy. In *50th Lunar and Planetary Science Conference*; 2019; Abs 2486.
- [29] Torre-Fdez, I.; Aramendia, J.; Gomez-Nubla, L.; Castro; Kepa; Madariaga, J. M. Geochemical Study of the Northwest Africa 6148 Martian Meteorite and Its Terrestrial Weathering Processes. *J. Raman Spectrosc.* **2017**, *48*, 1536. <https://doi.org/10.1002/jrs.5148>.
- [30] Papike, J.; Taylor, L.; Simon, S. Lunar Minerals, Lunar Sourcebook: A User's Guide to the Moon. In *Lunar Sourcebook. A User's Guide to the Moon*; Heiken, G., Vaniman, D., M., B. F., Eds.; Cambridge University Press: Cambridge, 1991; pp 121–181.
- [31] Oshtrakh, M. I.; Klencsár, Z.; Petrova, E. V.; Grokhovsky, V. I.; Chukin, A. V.; Shtoltz, A. K.; Maksimova, A. A.; Felner, I.; Kuzmann, E.; Homonnay, Z.; Semionkin, V. A. Iron Sulfide (Troilite) Inclusion Extracted from Sikhote-Alin Iron Meteorite: Composition, Structure and Magnetic Properties. *Mater. Chem. Phys.* **2016**, *174*, 100. <https://doi.org/https://doi.org/10.1016/j.matchemphys.2016.02.056>.
- [32] Blau, P. J.; Goldstein, J. I. Investigation and Simulation of Metallic Spherules from Lunar Soils. *Geochim. Cosmochim. Acta* **1975**, *39*,

---

305. [https://doi.org/10.1016/0016-7037\(75\)90199-4](https://doi.org/10.1016/0016-7037(75)90199-4).

- [33] Scott, D.; Schwab, R. *Metallography in Archaeology and Art*, 1st ed.; Springer: Switzerland, 2019.
- [34] Lafuente, B.; Downs, R. T.; Yang, H.; Stone, N. *Highlights in Mineralogical Crystallography*, Armbruster.; De Gruyter: Berlin, 2015.
- [35] Börjesson, L.; Torell, L. M. Raman Scattering Evidence of Rotating SO<sub>4</sub><sup>2-</sup> in Solid Sulphate Electrolytes. *Solid State Ionics* **1986**, *18–19*, 582. [https://doi.org/10.1016/0167-2738\(86\)90182-7](https://doi.org/10.1016/0167-2738(86)90182-7).
- [36] Krishnamurti, D. Raman Spectra of Nickel Sulphate Crystals. *Proc. Indian Acad. Sci. - Sect. A* **1955**, *42*, 77. <https://doi.org/10.1007/BF03053494>.
- [37] *Interesting facts about the Sahara desert*. <https://rb.gy/uza4gl> (accessed 2023-02-13).
- [38] Raghavender, A. T.; Hong, N. H.; Lee, K. J.; Jung, M.-H.; Skoko, Z.; Vasilevskiy, M.; Cerqueira, M. F.; Samantilleke, A. P. Nano-Ilmenite FeTiO<sub>3</sub>: Synthesis and Characterization. *J. Magn. Magn. Mater.* **2013**, *331*, 129. <https://doi.org/10.1016/j.jmmm.2012.11.028>.
- [39] Rendtorff, N. M.; Grasso, S.; Hu, C.; Suarez, G.; Aglietti, E. F.; Sakka, Y. Zircon–Zirconia (ZrSiO<sub>4</sub>–ZrO<sub>2</sub>) Dense Ceramic Composites by Spark Plasma Sintering. *J. Eur. Ceram. Soc.* **2012**, *32*, 787. <https://doi.org/10.1016/j.jeurceramsoc.2011.10.021>.
- [40] Tan, W.; Liu, P.; He, H.; Wang, C. Y.; Liand, X. Mineralogy and Origin of Exsolution In Ti-Rich Magnetite From Different Magmatic Fe-Ti Oxide-Bearing Intrusions. *Can. Mineral.* **2016**, *54*, 539. <https://doi.org/10.3749/canmin.1400069>.
- [41] Gucsik, A.; Zhang, M.; Koeberl, C.; Salje, E. K. H.; Redfern, S. A. T.; Pruneda, J. M. Infrared and Raman Spectra of ZrSiO<sub>4</sub> Experimentally Shocked at High Pressures. *Mineral. Mag.* **2004**, *68*, 801. <https://doi.org/10.1180/0026461046850220>.
- [42] Zhang, M.; Salje, E.; Farnan, I.; Graeme-Barber, A.; Daniel, P.; C, R.; Ewing, R.; Clark, A.; Leroux, H. Metamictization of Zircon: Raman Spectroscopic Study. *J. Phys. Condens. Matter* **2000**, *12*, 1915. <https://doi.org/10.1088/0953-8984/12/8/333>.
- [43] Yu, H.; Jiang, Y.; Lu, Y.; Li, X.; Zhao, H.; Ji, Y.; Wang, M. Quartz Fiber Reinforced Al<sub>2</sub>O<sub>3</sub>-SiO<sub>2</sub> Aerogel Composite with Highly Thermal Stability by Ambient Pressure Drying. *J. Non. Cryst. Solids* **2019**, *505*, 79. <https://doi.org/10.1016/j.jnoncrysol.2018.10.039>.
- [44] Castro, A. L.; Nunes, M. R.; Carvalho, A. P.; Costa, F. M.; Florêncio, M. H. Synthesis of Anatase TiO<sub>2</sub> Nanoparticles with High

- Temperature Stability and Photocatalytic Activity. *Solid State Sci.* **2008**, *10*, 602. <https://doi.org/10.1016/j.solidstatesciences.2007.10>.
- [45] Froment, F.; Tournié, A.; Colomban, P. Raman Identification of Natural Red to Yellow Pigments: Ochre and Iron-containing Ores. *J. Raman Spectrosc.* **2008**, *39*, 560. <https://doi.org/10.1002/jrs.1858>.
- [46] Joy, K. H.; Visscher, C.; Zolensky, M. E.; Mikouchi, T.; Hagiya, K.; Ohsumi, K.; Kring, D. A. Identification of Magnetite in Lunar Regolith Breccia 60016: Evidence for Oxidized Conditions at the Lunar Surface. *Meteorit. Planet. Sci.* **2015**, *50*, 1157. <https://doi.org/10.1111/maps.12462>.
- [47] Shearer, C. K.; Sharp, Z. D.; Burger, P. V.; McCubbin, F. M.; Provencio, P. P.; Brearley, A. J.; Steele, A. Chlorine Distribution and Its Isotopic Composition in “Rusty Rock” 66095. Implications for Volatile Element Enrichments of “Rusty Rock” and Lunar Soils, Origin of “Rusty” Alteration, and Volatile Element Behavior on the Moon. *Geochim. Cosmochim. Acta* **2014**, *139*, 411. <https://doi.org/10.1016/j.gca.2014.04.029>.
- [48] Ling, Z. C.; Wang, A.; Jolliff, B. L. Mineralogy and Geochemistry of Four Lunar Soils by Laser-Raman Study. *Icarus* **2011**, *211*, 101. <https://doi.org/10.1016/j.icarus.2010.08.020>.
- [49] Popp, J.; Tarcea, N.; Kiefer, W.; Hilchenbach, M.; Thomas, N.; Stuffer, T.; Hofer, S.; Stöffler, D.; Greshake, A. The Effect of Surface Texture on the Mineralogical Analysis of Chondritic Meteorites Using Raman Spectroscopy. *Planet. Space Sci.* **2002**, *50*, 865. [https://doi.org/10.1016/S0032-0633\(02\)00061-2](https://doi.org/10.1016/S0032-0633(02)00061-2).
- [50] Sharkov, E.; Bogatikov, O. A. Early Stages of the Tectonic and Magmatic Development of the Earth and Moon: Similarities and Differences. *Petrology* **2001**, *9*, 97.
- [51] Lakshminarayana, A.; Hussain, O.; Mauger, A.; Julien, C. Transport Properties of Nanostructured Li<sub>2</sub>TiO<sub>3</sub> Anode Material Synthesized by Hydrothermal Method. *Science*. **2019**, *1*, 39. <https://doi.org/10.3390/sci1020039>.
- [52] Al Omari, M. M. H.; Rashid, I. S.; Qinna, N. A.; Jaber, A. M.; Badwan, A. A. *Chapter Two - Calcium Carbonate*; Academic Press, 2016; Vol. 41. <https://doi.org/10.1016/bs.podrm.2015.11.003>.
- [53] Prieto-Taboada, N.; Laserna, O.; Martínez-Arkarazo, I.; Olazabal, M.; Madariaga, J. Raman Spectra of the Different Phases in the CaSO<sub>4</sub>-H<sub>2</sub>O System. *Anal. Chem.* **2014**, *86*, 10131. <https://doi.org/10.1021/ac501932f>.
- [54] Paul, A.-L.; Elardo, S. M.; Ferl, R. Plants Grown in Apollo Lunar Regolith Present Stress-Associated Transcriptomes That Inform Prospects for Lunar Exploration. *Commun. Biol.* **2022**, *5*, 382.

---

<https://doi.org/10.1038/s42003-022-03334-8>.

- [55] Goode, A. D. T. Oxidation of Natural Olivines. *Nature* **1974**, *248*, 500. <https://doi.org/10.1038/248500a0>.
- [56] Hanaor, D. A. H.; Sorrell, C. C. Review of the Anatase to Rutile Phase Transformation. *J. Mater. Sci.* **2011**, *46*, 855. <https://doi.org/10.1007/s10853-010-5113-0>.
- [57] Palliyaguru, L.; Kulathunga, U. S.; Jayarathna, L. I.; Jayaweera, C. D.; Jayaweera, P. M. A Simple and Novel Synthetic Route to Prepare Anatase TiO<sub>2</sub> Nanopowders from Natural Ilmenite via the H<sub>3</sub>PO<sub>4</sub>/NH<sub>3</sub> Process. *Int. J. Miner. Metall. Mater.* **2020**, *27*, 846. <https://doi.org/10.1007/s12613-020-2030-3>.
- [58] García-Florentino, C.; Torre-Fdez, I.; Ruiz-Galende, P.; Aramendia, J.; Castro, K.; Arana, G.; Maguregui, M.; Fdez-Ortiz de Vallejuelo, S.; Madariaga, J. M. Development of Innovative Non-Destructive Analytical Strategies for Mars Sample Return Tested on Dar Al Gani 735 Martian Meteorite. *Talanta* **2020**, *224*, 121863. <https://doi.org/10.1016/j.talanta.2020.121863>.
- [59] Neal, C. R. The Moon 35 Years after Apollo: What's Left to Learn? *Geochemistry* **2009**, *69*, 3. <https://doi.org/10.1016/j.chemer.2008.07.002>.
- [60] Alberquilla, F.; Martínez-Frías, J.; García-Baonza, V.; Lunar, R. LZS-1, Lanzarote (Canary Island, Spain) Lunar (Apollo 14) Basaltic Soil Simulant. *Sci. Rep.* **2022**, *12*, 16470. <https://doi.org/10.1038/s41598-022-20960-8>.

---

# CHAPTER 7

## GENERAL CONCLUSIONS AND FUTURE WORKS

**“ADVANCES ARE MADE BY ANSWERING  
QUESTIONS. DISCOVERIES ARE MADE BY  
QUESTIONING ANSWERS” – Bernard Haisch**

---



## **7. GENERAL CONCLUSIONS AND FUTURE WORKS**

The tasks included in the different operational objectives were carried out to fulfill the main objective of this PhD thesis: to expand the geochemical understanding of the planet Mars and the Earth's satellite, the Moon, to support the scientific design of future space missions and to contribute scientifically to the most cutting-edge interests.

A reliable and complete methodology for meteorite analysis has been proposed in this PhD thesis. The methodology is based on an initial elemental reconnaissance observation followed by an in-depth molecular identification. The elemental characterization was carried out by  $\mu$ -EDXRF spectroscopy. Through this technique, it was possible to create elemental maps to show the distribution of the different elements in the samples, through which it was possible to identify hotspots based on the coexistence of two or more elements. These hotspots with matching elements are always related to particular mineral phases, providing some ideas about the nature of such minerals. Besides, it provided valuable information for further future analyses such as the molecular ones. Therefore, this procedure could be considered a previous step for targeting molecular analyses. It should be highlighted that this technique was selected for being one of the pioneering techniques in space exploration, traveling for the first time to Mars on board the Viking lander and it is still used in current missions due to its good performance. On the other side, the molecular characterization was carried out by using Raman spectroscopy. Firstly, point-by-point analyses were performed using microRaman spectroscopy. When some mineralogical distributions were considered interesting to be studied, Raman maps were created using a High Resolution Raman Imaging spectrometer. Raman spectroscopy was selected for being one of the cutting-edge techniques in space exploration, having traveled into space for the first time on board the Perseverance rover to Mars, and expected to be incorporated in the Rosalind Franklin mission to Mars and in the MMX mission to Martian Moons. Moreover, it has to be highlighted that both selected analytical techniques,  $\mu$ -EDXRF and microRaman spectroscopies, are non-destructive and non-invasive. In addition, the sample does not require any pre-treatment for performing the analyses. Considering all this, it can be said that the combination of both techniques proved to be the perfect procedure for performing a deep characterization of a meteorite.

Taking into account previously mentioned goodness, it can be said that this methodology is an optimal procedure for the first study of Martian return samples.  $\mu$ -EDXRF and microRaman spectroscopies are very robust techniques, allowing a complete initial characterization. In addition, semiquantitative data can be also obtained from a post-treatment of the data in both cases. All this make them the most suitable analytical

combination for routine preliminary analysis in a non-destructive way. Moreover, their microscopic character allows as well to perform in deep analysis by the detection of minor elements and compounds.

Regarding the study of meteorites, as a manner to obtain geochemical information from their parent bodies, this PhD has demonstrated the importance to perform an analytical strategy that permits ascertaining the origin of the detected compounds. In this sense, it is necessary to consider how they have been exposed to atypical conditions and processes, such as the ejection, the space travel and their entry and stay on Earth. This involves mainly structural changes of key minerals due to the shock pressures and high temperatures when ejected from the parent body; the fusion of the meteoritic crust during the entry in the Earth atmosphere; the aerobic alterations; and the common terrestrial weathering processes. Thus, it is mandatory to identify and differentiate among the major and minor mineral phases found as well as where such minerals are located in any type of meteorite. The proposed methodology combining point-by-point and spectroscopic image analysis proved to be successful for that aim.

In addition, thanks to a solid classification basis between original and altered minerals, it is possible to estimate the processes that led to the formation of secondary minerals from primary ones. In this manuscript, several Martian and lunar processes have been described. Likewise, as future work, it is proposed to perform isotopic analysis to corroborate whether the minerals found are of terrestrial or extraterrestrial origin.

Considering all this, it can be said that the study of meteorites provides valuable data about parent body geochemistry. Moreover, the selected methodology proved to be successful for the proposed aim.

Unfortunately, by this means, the formation of some secondary minerals could not be explained considering the current Martian and lunar conditions. Some minerals already found on Mars contain hydration molecules in their crystalline structure, so they must be formed on ancient environments due to brine precipitation. Therefore, in order to contribute to the knowledge of ancient Martian conditions, which possessed liquid water, this PhD thesis proposes to carry out some research. Such as laboratory experiments to simulate the formation of certain secondary minerals, as a complementary methodology to better understand the geochemistry of celestial bodies. These laboratory experiments showed the adequate conditions required for the formation of gypsum, syngenite and görgeyite, hydrated and mixed compounds that are probably present in Martian environments. Thanks to these simulations, it was possible to verify that some secondary minerals, apart from aqueous conditions, also required hydrothermal ones.

To confirm the presence of such compounds through the *in situ* techniques on board exploration rovers, the development of a complete spectroscopic databases is crucial for their unequivocal confirmation. Therefore, the correct interpretation of *in situ* results by comparing the collected spectra with the proper database is critical to ensure a good traceability of the whole scenario. In this way, this thesis has contributed to the expansion of a reliable and rich Raman database.

Actually, new Raman spectra were discovered in almost all the chapters of this PhD e.g. meteorite analysis, simulants experiments or temperature assays. It must be highlighted that a quality Raman database of sulfates at extreme temperature conditions has been created, which could serve both for already planned missions and/or for future missions to the landing sites where extreme conditions are present (e.g. Martian poles). Considering the promising future of Raman spectroscopy in space exploration this database will be extremely useful.

As stated in the objectives of this PhD, the study of both, past and future, habitability potential of planets and satellites is a recurrent issue in space exploration. In this thesis, it has been proved that by using analytical techniques analog to those on board the Perseverance and Rosalind Franklin rovers, it is possible to identify organic molecules retained by bioprotector agents related with water.

The first bioprotector agent studied were clay minerals, specifically montmorillonite and hectorite. In this way, it was possible to prove the importance of clay minerals as future target for landing missions to find biosignatures. Although several of the simulants à la carte were favorable, the montmorillonite in acidic media stood out against all, suggesting that the retention capacity of montmorillonite was greater than that of hectorite. This information is extremely useful for target selection processes in surface missions. Besides, this finding is very promising for the missions that have among their main objectives the discovery of past live evidences, since montmorillonite is one of the most abundant phyllosilicates on Mars.

The second bioprotector agent studied was a microbialite. This characterization was extremely robust because several analytical techniques were employed. In fact, this PhD thesis highlights the importance of performing collaborative science, using complementary techniques and evaluating the results globally and not individually. Following this methodology, this type of collaborative science allowed to establish broader and more solid conclusions. Nevertheless, it is mandatory to emphasize the excellent results provided by GC-MS. In this PhD thesis it has been confirmed that the most useful technique for organic molecules identification was GC-MS, in the considered case of study, as it provided the most significant information in terms of biosignatures.

Taking into account that the Perseverance rover is not equipped with a GC-MS, the greatest hope of finding organics rests with the Rosalind Franklin rover. Unfortunately, this rover proceed for GC-MS analysis at the analytical laboratory of in-depth drilled samples. However, microbialites are found on the surface. Therefore, this PhD thesis demonstrates the importance of future rovers being equipped with GC-MS to analyze also the inner (protected) parts of surface samples, where microbialites may harbor biosignatures, even if acquiring samples for this kind of structures for GC-MS analyses supposes a great challenge.

As a conclusion of this PhD some future works arose. On the one hand, it is well known that the high bombardment of ionizing particles from the Sun and stars causes the decomposition of any organic molecule. Thus, as future work, it would be interesting to evaluate the protective capacity of these bioprotector agents to preserve biosignatures against different intensities of UV radiation. Such experiments can be carried out by using environmental simulation chambers to expose the already prepared samples (spiked phyllosilicates) to different UV radiation times monitoring the possible alteration of the biomarkers by using the same analytic strategy employed in this PhD.

Other future works are related to the search and use of the Moon's natural resources. What is clear after this work is that oxidative reactions can be expected to be induced in the lunar regolith as a previous step for plant cultivation. The clear parallelism established between the NWA 11273 Lunar meteorite and the LZS-1 simulant will help to perform, on the one hand, high scale experiments for habitability with the mentioned simulant and, on the other hand, confirm then the results at low scale using NWA 11273-like materials. In this sense, future experiments will consist of detecting if the weathered oxides described previously in NWA 11273 meteorite are found in the LZS-1 lunar soil simulant using Raman spectroscopy. Then, searching for soluble ions and their concentrations both in NWA 11273 Lunar meteorite (or similar) and LZS-1 materials. Finally, acidic oxidative tests should be performed to detect new mineral phases and compounds released in both materials, just to define the extreme environmental conditions that never should be trespassed to avoid the destruction of key minerals in the lunar regolith.

To sum up, it can be said that the results attained through the tasks and methods used in all the operational objectives of this PhD thesis, indicate that the main objective was completely fulfilled. In addition, innovative research emerged that will be the basis of future works to expand the geochemical understanding of Mars and the Moon, as well as to support the scientific design of future space missions and to contribute scientifically to most cutting-edge interests.



---

# CHAPTER 8

## APPENDICES

**“AN EXPERT IS A PERSON WHO HAS MADE ALL  
THE MISTAKES THAT CAN BE MADE IN A VERY  
NARROW FIELD” – Neils Bohr**

---



## 8. APPENDICES

This chapter summarizes all the glossary of acronyms, the mineral phases indicated along the thesis and all the scientific publications made by the author, including articles and congresses.

### 8.1. Glossary of acronyms

<b><i>μ-EDXRF</i></b>	μ-Energy Dispersive X-Ray Fluorescence
<b><i>ACI</i></b>	Autofocusing Contextual Imager
<b><i>ADaMM</i></b>	Analytical Database of Martian Minerals
<b><i>ADRON-RM</i></b>	Autonomous Detector of Radiation of Neutron On board -Rover at Mars
<b><i>AH</i></b>	Activated Hectorite
<b><i>ALD</i></b>	Analytical Laboratory Drawer
<b><i>AM</i></b>	Activated Montmorillonite
<b><i>ANSMET</i></b>	Antarctic Search for Meteorites
<b><i>AOTF</i></b>	Acousto-Optic Tunable Filter
<b><i>APSS</i></b>	Auxiliary Payload Subsystem
<b><i>APXS</i></b>	Alpha Pronto X-Ray Spectrometer
<b><i>ASPERA-3</i></b>	Analyzer of Space Plasmas Energetic Neutral Atoms
<b><i>ATR</i></b>	Attenuated Total Reflection
<b><i>BU</i></b>	Body Unit
<b><i>CAB</i></b>	Astrobiology Center
<b><i>ChemCam</i></b>	Chemical Camera
<b><i>CheMin</i></b>	Chemistry and Mineralogy
<b><i>CHIMRA</i></b>	Collection and Handling for In Situ Martian Rock Analysis
<b><i>CLUPI</i></b>	Close-Up Imager
<b><i>CMDM</i></b>	Circum-Martian Dust Monitor
<b><i>CNES</i></b>	Centre National d'Estudes Spatiales
<b><i>CNSA</i></b>	China National Space Administration
<b><i>CRE</i></b>	Cosmic Ray Exposure
<b><i>CRISM</i></b>	Compact Reconnaissance Imaging Spectrometer for Mars
<b><i>CRM</i></b>	Chemical Reference Material
<b><i>CTX</i></b>	Context Imager
<b><i>d001</i></b>	d-spacing
<b><i>DAN</i></b>	Dynamic Albedo of Neutron
<b><i>DLR</i></b>	German Aerospace Center
<b><i>DSC</i></b>	Differential Scanning Calorimetry
<b><i>DTGS</i></b>	Deuterated Triglycine Sulphate
<b><i>EDS</i></b>	Energy Dispersive Spectrometer
<b><i>EETA</i></b>	Elephant Moraine
<b><i>EH1</i></b>	Hectorite doping experiments with ethanol at pH=3.5

---

<b><i>EH2</i></b>	Hectorite doping experiments with ethanol at pH=7.5
<b><i>EM1</i></b>	Montmorillonite doping experiments with ethanol at pH=3.5
<b><i>EM2</i></b>	montmorillonite doping experiments with ethanol at pH=7.5
<b><i>ESA</i></b>	European Space Agency
<b><i>FE-SEM</i></b>	Field Emission Scanning Electron Microscope
<b><i>FREZCHEM</i></b>	Freezing Chemistry
<b><i>FT-IR</i></b>	Fourier Transform
<b><i>FTS</i></b>	Fourier Transform Spectrometer
<b><i>FWHM</i></b>	Full Width at Half Maximum
<b><i>GAP</i></b>	Gas Analysis Package
<b><i>GC-IRMS</i></b>	Gas Chromatography coupled to Isotope-Ratio Mass Spectrometry
<b><i>GC-MS</i></b>	Gas Chromatography coupled to Mass Spectrometry
<b><i>GEX</i></b>	Gas Exchange
<b><i>HEC</i></b>	Hectorite
<b><i>HiRISE</i></b>	High-Resolution Imaging Science Experiment
<b><i>HMC</i></b>	High-Magnesium Calcite
<b><i>HP3</i></b>	Heat Flow and Physical Properties Package
<b><i>HRSC</i></b>	High-Resolution Stereo Camera
<b><i>HYDRA</i></b>	Hydrochemical Equilibrium-Constant database
<b><i>IC</i></b>	Interband Cascade laser
<b><i>ICDD</i></b>	International Center for Diffraction Data
<b><i>IDD</i></b>	Instrument Deployment Devices
<b><i>IMP</i></b>	Imager for Mars Pathfinder
<b><i>InSight</i></b>	Interior Exploration using Seismic Investigations, Geodesy and Heat Transport
<b><i>IR</i></b>	Infrared
<b><i>IRTM</i></b>	Infrared Radiometer for Thermal Mapping
<b><i>ISE</i></b>	Ion Selective Electrode
<b><i>ISRO</i></b>	Indian Space Research Organisation
<b><i>ISS</i></b>	International Space Station
<b><i>JAXA</i></b>	Japan Exploration Agency
<b><i>JPL</i></b>	Jet Propulsion Laboratory
<b><i>KREEP</i></b>	potassium, REE and phosphorous elements
<b><i>K<sub>sp</sub></i></b>	solubility product
<b><i>LA</i></b>	Lauric Acid
<b><i>LAR</i></b>	Larkman Nunatak
<b><i>LDMS</i></b>	Laser Desorption coupled to the MS
<b><i>LIBS</i></b>	Laser-Induced Breakdown Spectroscopy
<b><i>LIDAR</i></b>	Light Detection and Ranging
<b><i>LOD</i></b>	Limit Of Detection

---

---

<b>LR</b>	Labeled Release
<b>MAHLI</b>	Mars Hand Lens Imager
<b>Ma-MISS</b>	Mars Multispectral Imager for Subsurface Studied
<b>MARCI</b>	Mars Color Imager
<b>MARDI</b>	Mars Descent Imager
<b>MaRS</b>	Mars Express Radio Science Experiment
<b>MarsCoDe</b>	Mars Surface Composition Detector
<b>MARSIS</b>	Mars Advanced Radar for Subsurface and Ionospheric Sounding
<b>MastCam</b>	Mast Cameras
<b>MAWD</b>	Infrared Spectrometer for Water Vapor Mapping
<b>MBS</b>	Mössbauer Spectroscopy
<b>MCS</b>	Mars Climate Station
<b>MECA</b>	Microscopy Electrochemistry, and Conductivity Analyzer
<b>MECA</b>	Microscopy, Electrochemistry and Conductivity Analyzer
<b>MEDA</b>	Mars Environmental Dynamics Analyzer
<b>MEDLI</b>	Mars Science Laboratory Entry Descent and Landing Instrument
<b>MEDUSA</b>	Make Equilibrium Diagrams Using Sophisticated Algorithms
<b>MEGANE</b>	Mars-moon Exploration with Gamma Rays and Neutrons
<b>MER</b>	Mars Exploration rovers
<b>MES</b>	Mars Express
<b>MET</b>	Meteorological Station
<b>MGS</b>	Mars Global Surveyor
<b>MI</b>	Microscopic Imager
<b>MIMOS</b>	Mössbauer Spectrometer
<b>miniRAD</b>	Thermal mapper
<b>Mini-TES</b>	Miniature Thermal Emission Spectrometer
<b>MIRS</b>	MMX Infrared Spectrometer
<b>MMT</b>	Montmorillonite
<b>MMX</b>	Martian Moons eXploration
<b>MOC</b>	Mars Orbital Camera
<b>MOLA</b>	Mars Orbiter Laser Altimeter
<b>MOMA</b>	Mars Organic Molecule Analyzer
<b>MOXIE</b>	Mars Oxygen In Situ Resource Utilization Experiment
<b>MRO</b>	Mars Reconnaissance Orbiter
<b>MS</b>	Mass Spectroscopy
<b>MSA</b>	Mass Spectrum Analyzer
<b>MSCam</b>	Multispectral Camera
<b>MSL</b>	Mars Science Laboratory
<b>MSP</b>	Mars Surveyor Program

---

---

<b>MU</b>	Mast Unit
<b>NASA</b>	National Aeronautics and Space Administration
<b>NaTeCam</b>	Navigation and Terrain Camera
<b>NH1</b>	Hectorite doped experiments with NaOH at pH=3.5
<b>NH2</b>	Hectorite doped experiments with NaOH at pH=7.5
<b>NIR</b>	Near-Infrared
<b>NM1</b>	Montmorillonite doped experiment with NaOH at pH=3.5
<b>NM2</b>	Montmorillonite doped experiment with NaOH at pH=7.5
<b>NWA</b>	Northwest Africa
<b>OB1</b>	Olivine first main Raman band position
<b>OB2</b>	Olivine second main Raman band position
<b>OMEGA</b>	Observatoire por la Minéralogie, l'Eau, les Glaces et l'activité
<b>OROCHI</b>	Optical Radiometer composed of Chromatic Imagers
<b>PanCam</b>	Panoramic Camera
<b>PCA</b>	Principal Component Analysis
<b>PES</b>	Planetary Fourier Spectrometer
<b>PIXL</b>	Planetary Instrument for X-Ray Lithochemistry
<b>PMIRR</b>	Pressure Modulated Infrared Radiometer
<b>PR</b>	Pyrolytic Release
<b>R2</b>	coefficient of determination
<b>RAD</b>	Radiation Assessment Detector
<b>RAT</b>	Rock Abrasion Tool
<b>RAX</b>	Raman Spectrometer
<b>RBT</b>	Roberts Massif
<b>REE</b>	Rare-Earth Elements
<b>REMS</b>	Rover Environmental Monitoring Station
<b>RH</b>	Regular Hectorite
<b>RIFMA</b>	Roentgen Isotopic Fluorescent Method of Analysis
<b>RIMFAX</b>	Radar Imager for Mars' Subsurface Experiment
<b>RIR</b>	Reference Intensity Ratio
<b>RISE</b>	Rotation and Interior Structure Experiment
<b>RLS</b>	Raman Laser Spectrometer
<b>RLS-Sim</b>	Raman Laser Spectrometer Simulator
<b>RM</b>	Regular montmorillonite
<b>RoMAG</b>	Mars Rover Magnetometer
<b>RoPeR</b>	Mars Rover Penetrating Radar
<b>Roscosmos</b>	Russian State Space Corporation
<b>RT</b>	room temperature
<b>SA/SPaH</b>	Sample Analysis/Sample Processing and Handling
<b>SAM</b>	Sample Analysis at Mars

---

---

<b>SEIS</b>	Seismic Experiment for Interior Structure
<b>SHERLOC</b>	Scanning Habitable Environments with Radar and Luminescence for Organics and Chemicals
<b>SNC</b>	Shergotty, Nakhla and Chassigny
<b>SOx</b>	Sulfur oxides
<b>SPICAM</b>	Spectroscopy for the Investigation of the Characteristics of the Atmospheric of Mars
<b>SWIR</b>	Short-Wave Infrared
<b>TEGA</b>	Thermal and Evolved Gas Analyzer
<b>TEM</b>	Transmission Electron Microscopy
<b>TENGOO</b>	Telescopic Nadir imager for FeOmOrphology
<b>TES</b>	Thermal Emission Spectrometer
<b>THEMIS</b>	Thermal Emission Imaging System
<b>TLS</b>	Tunable Laser Spectroscopy
<b>TV-GC-MS</b>	Thermal Volatilization Gas Chromatograph - mass spectrometer
<b>UMA</b>	University of Málaga
<b>UNLV</b>	University of Nevada, Las Vegas
<b>UPV/EHU</b>	University of the Basque Country
<b>UV</b>	Ultraviolet
<b>Uva</b>	University of Valladolid
<b>UWS</b>	University of Washington
<b>VNIR</b>	Visible and Near Infrared
<b>WCL</b>	Wet Chemistry Laboratory
<b>WISDOM</b>	Water Ice Subsurface Deposit Observation on Mars
<b>XRD</b>	X-Ray Diffraction
<b>XRF</b>	X-Ray Fluorescence Spectrometer

## 8.2. Glossary of mineral phases

<b>Albite</b>	$\text{NaAlSi}_3\text{O}_8$
<b>Anatase</b>	$\text{TiO}_2$
<b>Anhydrite</b>	$\text{CaSO}_4$
<b>Anorthite</b>	$\text{CaAl}_2\text{Si}_2\text{O}_8$
<b>Apatite</b>	$\text{Ca}_5(\text{PO}_4)_3(\text{F}, \text{Cl}, \text{OH})$
<b>Aragonite</b>	$\text{CaCO}_3$
<b>Arcanite</b>	$\text{K}_2\text{SO}_4$
<b>Armcolite</b>	$(\text{Fe}, \text{Mg})\text{Ti}_2\text{O}_5$
<b>Augite</b>	$(\text{Ca}, \text{Mg}, \text{Fe})_2(\text{Si}, \text{Al})_2\text{O}_6$
<b>Bassanite</b>	$\text{CaSO}_4 \cdot 0.5\text{H}_2\text{O}$
<b>Beidelite</b>	$(\text{Na}, \text{Ca}_{0.5})_{0.3}\text{Al}_2((\text{Si}, \text{Al})_4\text{O}_{10})(\text{OH})_2 \cdot n\text{H}_2\text{O}$
<b>Calcite</b>	$\text{CaCO}_3$

---

<b>Chlorite</b>	$(\text{Mg,Fe})_3(\text{Si,Al})_4\text{O}_{10}(\text{OH})_2(\text{Mg,Fe})_3(\text{OH})_6$
<b>Chromite</b>	$(\text{Fe,Mg})\text{Cr}_2\text{O}_4$
<b>Elemental sulfur</b>	$\text{S}_8$
<b>Enstatite</b>	$\text{MgSiO}_3$
<b>Epsomite</b>	$\text{MgSO}_4 \cdot 7\text{H}_2\text{O}$
<b>Fayalite</b>	$\text{Fe}_2\text{SiO}_4$
<b>Feldspar</b>	$(\text{K,Na,Ca,Ba,NH}_4)(\text{Si,Al})_4\text{O}_8$
<b>Ferrosilite</b>	$\text{FeSiO}_3$
<b>Forsterite</b>	$\text{MgSiO}_4$
<b>Glauberite</b>	$\text{Na}_2\text{Ca}(\text{SO}_4)_2$
<b>Goethite</b>	$\alpha\text{-FeO}(\text{OH})$
<b>Görgeyite</b>	$\text{K}_2\text{Ca}_5(\text{SO}_4)_6 \cdot \text{H}_2\text{O}$
<b>Gypsum</b>	$\text{CaSO}_4 \cdot 2\text{H}_2\text{O}$
<b>Halite</b>	$\text{NaCl}$
<b>Hectorite</b>	$(\text{Li,Mg})_3\text{Si}_4\text{O}_{10}(\text{OH})_2 \cdot n\text{Na}^+$
<b>Hematite</b>	$\text{Fe}_2\text{O}_3$
<b>HMC</b>	$(\text{Ca,Mg})\text{CO}_3$
<b>Hydromagnesite</b>	$3\text{MgCO}_3 \cdot \text{Mg}(\text{OH})_2 \cdot 3\text{H}_2\text{O}$
<b>Illite</b>	$(\text{K,Na,H})(\text{Al,Fe,Mg})_2(\text{Si,Al})_4\text{O}_{10}(\text{OH})_2 \cdot n\text{H}_2\text{O}$
<b>Ilmenite</b>	$\text{FeTiO}_3$
<b>Jarosite</b>	$\text{KFe}_3(\text{SO}_4)_2 \cdot 2(\text{OH})_6$
<b>Kamacite</b>	$\text{A}-(\text{Fe,Ni})$
<b>Kaolinite</b>	$\text{Al}_2\text{Si}_2\text{O}_5(\text{OH})_4$
<b>Kieserite</b>	$\text{MgSO}_4 \cdot \text{H}_2\text{O}$
<b>Langbeidite</b>	$\text{K}_2\text{Ca}_2(\text{SO}_4)_3$
<b>Lepidochrocite</b>	$\gamma\text{-FeO}(\text{OH})$
<b>Mackinawite</b>	$\text{FeS}$
<b>Magnetite</b>	$\text{Fe}_3\text{O}_4$
<b>Marcasite</b>	$\text{FeS}_2$
<b>Meridianiite</b>	$\text{MgSO}_4 \cdot 11\text{H}_2\text{O}$
<b>Merrillite</b>	$\text{Ca}_9\text{NaMg}(\text{PO}_4)_7$
<b>Millerite</b>	$\text{NiS}$
<b>Montmorillonite</b>	$(\text{Na,Ca})_x(\text{Al,Mg})_2(\text{Si}_4\text{O}_{10})(\text{OH})_2 \cdot n\text{H}_2\text{O}$
<b>Morenosite</b>	$\text{NiSO}_4 \cdot 7\text{H}_2\text{O}$
<b>Nontronite</b>	$(\text{CaO}_{0.5},\text{Na})_{0.3}\text{Fe}_2(\text{Si,Al})_4\text{O}_{10}(\text{OH})_2 \cdot n\text{H}_2\text{O}$
<b>Olivine</b>	$(\text{Mg,Fe})_2\text{SiO}_4$
<b>Plagioclase</b>	$\text{CaAl}_2\text{Si}_2\text{O}_8 - \text{NaAlSi}_3\text{O}_8$
<b>Polyhalite</b>	$(\text{K}_2\text{Ca}_2\text{Mg}(\text{SO}_4)_4 \cdot 2\text{H}_2\text{O})$
<b>Pyrite</b>	$\text{FeS}_2$

---

<b>Pyroxene</b>	$R_2[(Si,Al)_2O_6]$ (R: Mg, Fe, Ca, Al, Ti, Mn, Na, K, or Li)
<b>Pyrrhotite</b>	$Fe_{1-x}S$
<b>Quartz</b>	$SiO_2$
<b>Retgersite</b>	$NiSO_4 \cdot 6H_2O$
<b>Sanidine</b>	$K(AlSi_3O_8)$
<b>Saponite</b>	$(Ca,Na)_{0.3}(Mg,Fe)_3(Si,Al)_4O_{10}(OH)_2 \cdot 4H_2O$
<b>Smectite</b>	$(Ca,Na,H)(Al,Mg,Fe,Zn)_2(Si,Al)_4O_{10}(OH)_2 \cdot nH_2O$
<b>Syngenite</b>	$K_2Ca(SO_4)_2 \cdot H_2O$
<b>Taenite</b>	$\gamma-(Fe,Ni)$
<b>Ti-magnetite</b>	$Fe(Fe,Ti)_2O_4$
<b>Troilite</b>	$FeS$
<b>Vermiculite</b>	$(Mg,Fe,Al)_3((Al,Si)_4O_{10})(OH)_2 \cdot nH_2O$
<b>Whitlockite</b>	$Ca_9Mg(PO_4)_6PO_3OH$
<b>Wollastonite</b>	$CaSiO_3$
<b>Zircon</b>	$ZrSiO_4$

### 8.3. Annexes with Data

On the one hand, Table 8.1 shows the metallic composition and main Raman band positions of the olivines used for the calibration models, including the bibliographic source, used in Chapter 4.1. In the other hand, Tables 8.2 and 8.3 represent the values of temperature, band position and half-bandwidth of gypsum, syngenite and görgeyite obtained in the experiment described in Chapter 4.2.2.

Table 8.1. Metallic composition and main Raman signals position of the olivines used for the calibration model

Composition		Spectral information (cm <sup>-1</sup> )			Literature reference
Fo <sub>x</sub>	Fa <sub>x</sub>	OB1	OB2	ΔOB	
(Mg %)	(Fe %)				
100	0	824.5	856	31.5	26
100	0	824	856	32	9
100	0	824	856	32	27
100	0	824	856	32	10
100	0	824.7	856.7	32	15
100	0	825	857	32	11
100	0	824.7	857	32.3	28
100	0	825	857	32	29
96	4	824.4	856.6	32.2	30
94	6	823.5	855	31.5	27

---

92.7	7.3	824.5	856.4	31.9	16
92	8	823.8	855.7	31.9	30
92	8	823.7	855.7	32	30
91	9	823.1	855	31.9	15
91	9	824	855.5	31.5	29
91	9	823.3	855.1	31.8	30
90	10	822.9	854.9	32	30
89.5	10.5	822.5	854.4	31.9	28
89	11	822.5	854.5	32	15
88	12	822	854	32	9
87.5	12.5	822.6	854.2	31.6	28
87.4	12.6	823.6	855.2	31.6	16
86.1	13.9	823	854.7	31.7	16
84.6	15.4	821.3	852.7	31.4	28
84.5	15.5	823	854.5	31.5	11
84	16	822	853	31	29
82.8	17.2	822.1	853.5	31.4	16
82.3	17.7	821.8	853.1	31.3	28
80.7	19.3	822.3	853.3	31	16
76.8	23.2	821.7	852.5	30.8	16
74.5	25.5	821.3	852.2	30.9	16
74	26	821	852	31	31
72.2	27.8	820.9	851.8	30.9	16
71	29	821.6	851.6	30	30
70.6	29.4	820.4	851.2	30.8	16
70	30	820.4	851.1	30.7	30
69	31	819.6	849.9	30.3	15
66.9	33.1	820.5	850.4	29.9	16
65	34.7	820.1	849.7	29.6	16
65	35	819	849.2	30.2	15
62.8	37.2	819.8	849.4	29.6	16
62	38	819	848.7	29.7	15
56	34	818.2	847.6	29.4	15
52	48	819.6	848.8	29.2	30
50	50	818.9	848.1	29.2	30
49.6	50.4	818.1	846.5	28.4	27
45.4	54.6	817	846	29	27
45	55	818	846.5	28.5	29
41	59	818	846	28	32
40	60	817	844.8	27.8	30
39	61	816.5	844.4	27.9	15
34	66	818.1	845.6	27.5	30

---

30	70	817.1	844.8	27.7	30
23	77	817.2	843.9	26.7	30
20	80	816.4	843.4	27	30
11	89	814.9	842.8	27.9	30
10	90	815.2	841.7	26.5	30
8	92	815.3	838.9	23.6	15
1	99	814.5	841.1	26.6	30
0	100	814.4	839.7	25.3	9
0	100	813.8	839	25.2	33
0	100	814.2	839.6	25.4	27
0	100	813.6	839.7	26.1	10
0	100	812.7	837.7	25	This work

Table 8.2. Center and width parameters calculated for the three gypsum Raman bands from 273 to 83 K.

Temperature (K)	Center ~1008 cm <sup>-1</sup>	Center ~3407 cm <sup>-1</sup>	Width ~3407 cm <sup>-1</sup>	Center ~3488 cm <sup>-1</sup>	Width ~3488 cm <sup>-1</sup>
273	1008.7	3406.0	33.7	3493.1	29.7
273	1008.8	3406.4	38.7	3493.1	30.7
273	1008.6	3406.2	34.6	3493.0	27.5
263	1008.7	3406.3	33.9	3492.4	30.7
263	1008.9	3406.7	35.9	3492.0	30.0
263	1008.8	3406.7	35.8	3492.2	25.2
253	1008.9	3406.5	32.7	3491.9	26.3
253	1008.8	3406.2	32.2	3491.7	23.9
253	1008.8	3406.3	27.8	3491.6	24.7
243	1008.9	3406.4	25.3	3491.4	25.5
243	1008.9	3406.7	30.4	3491.5	25.3
243	1008.9	3406.5	26.6	3491.7	20.9
233	1009.2	3406.7	24.5	3491.0	21.4
233	1009.0	3406.5	24.2	3490.9	19.8
223	1009.0	3406.9	22.9	3490.3	20.7
223	1009.1	3406.9	24.4	3490.3	20.2
223	1008.9	3406.8	23.6	3490.4	19.2
213	1009.1	3407.0	20.9	3489.7	19.1
213	1009.2	3407.0	22.0	3489.8	19.9
213	1009.2	3407.0	21.6	3490.0	18.1
203	1009.1	3407.0	20.9	3489.2	18.1
203	1009.2	3407.0	19.5	3489.1	18.0
203	1009.3	3407.2	20.3	3489.2	17.1

193	1009.2	3407.2	19.1	3488.7	17.4
193	1009.4	3407.3	18.8	3488.9	17.6
193	1009.1	3407.2	18.4	3488.7	16.6
183	1009.1	3407.3	18.6	3488.2	15.7
183	1009.2	3407.3	17.5	3488.2	16.2
183	1009.3	3407.3	17.6	3488.3	15.4
173	1009.2	3407.3	17.8	3487.7	15.7
173	1009.2	3407.5	17.2	3488.0	15.5
173	1009.4	3407.5	16.6	3488.0	16.1
163	1009.4	3407.7	16.1	3488.3	17.4
163	1009.4	3407.9	16.3	3488.6	-
163	1009.5	3407.7	-	3487.8	-
163	1009.5	3407.7	-	3488.6	14.9
153	1009.5	3407.8	16.2	3488.1	-
153	1009.5	3407.8	15.3	3488.3	16.4
153	1009.6	3407.8	16.5	3488.4	14.7
153	1009.2	3407.9	-	3488.0	13.5
143	1009.7	3408.0	-	3487.1	13.5
143	1009.7	3408.0	17.4	3487.2	-
143	1009.8	3408.1	15.0	3487.7	12.8
143	1009.8	3408.0	16.9	-	15.6
133	1010.1	3408.1	16.23	3487.6	16.1
133	1010.1	3408.1	16.1	3487.5	12.7
133	1010.1	3408.1	16.2	347.0	11.9
133	1010.1	3408.2	-	-	11.6
123	1010.6	3408.4	17.1	3487.2	11.7
123	1010.6	3408.5	14.1	3487.1	9.6
123	1010.6	3408.5	-	3486.9	8.8
123	1010.6	3408.6	-	3487.2	-
113	1010.8	3408.7	16.2	3486.6	9.0
113	1010.8	3408.8	14.9	3486.0	-
113	1010.8	3408.8	18.4	3486.5	8.9
113	1010.7	3408.7	19.2	3486.9	-
103	1010.8	3408.9	14.4	3486.5	9.0
103	1010.8	3408.9	13.4	3486.6	9.0
103	1010.8	3408.9	17.9	3486.6	10.8
103	1010.8	3408.9	-	3486.6	11.8
93	1010.8	3409.1	17.4	3486.2	10.4
93	1010.8	3409.1	15.2	3486.3	-
93	1010.8	3409.2	13.0	3487.4	-
93	1010.8	3409.1	14.3	3486.1	11.7
83	1011.1	3409.2	15.2	-	-

83	1011.02	3409.2	13.4	3485.8	-
83	1011.08	3409.3	16.1	3486.5	-
83	1011.08	3409.2	-	3485.5	-

Table 8.3. Center position calculated for the three syngenite Raman bands and for the Görgeyite main band from 273 to 83 K.

SYNGENITE				GÖRGEYITE	
Temperature (K)	Center ~1006 cm <sup>-1</sup>	Center ~3153 cm <sup>-1</sup>	Center ~3307 cm <sup>-1</sup>	Temperature (K)	Center ~1006 cm <sup>-1</sup>
273	1005.8	0.00	3305.3	273	-
273	1006.7	0.00	3306.0	273	1006.7
273	1006.8	0.00	-	273	1006.6
273	1006.6	0.00	-	273	1006.0
263	1006.9	0.00	3305.7	273	-
263	1006.9	0.00	3306.7	263	1006.7
263	1006.8	0.00	3306.8	263	1006.7
263	-	0.00	-	263	1006.1
253	1007.1	0.00	3306.6	253	-
253	1007.1	0.00	3306.3	253	1006.6
253	1007.0	0.00	3305.5	253	1006.9
253	-	0.00	-	253	1006.4
243	1007.0	3139.9	3305.8	243	-
243	1007.2	3140.1	3305.9	243	1006.7
243	1007.2	3145.4	3307.3	243	1006.9
243	-	3142.9	3306.9	243	1006.9
233	1007.4	3138.9	3305.8	233	-
233	1007.4	3134.8	3306.3	233	1006.7
233	1007.4	3133.6	3306.3	233	1007.0
233	-	3135.5	3306.2	233	1007.0
223	1007.5	3132.0	3304.6	223	-
223	1007.5	3130.2	3305.8	223	1006.8
223	1007.5	3131.2	3305.2	223	1007.0
223	-	3130.5	3305.7	223	1007.1
213	1007.7	3131.5	3305.8	213	-
213	1007.6	3125.4	3305.1	213	1007.1
213	1007.6	3127.9	3305.2	213	1007.2
213	-	3126.9	-	213	1007.6
203	1007.7	3126.3	3304.3	203	-
203	1007.8	3119.9	3304.4	203	1007.0

203	1007.8	3123.5	3304.2	203	1007.2
203	-	3123.9	3304.2	203	1006.8
193	1007.9	3123.0	3303.8	193	-
193	1008.0	3121.6	3303.7	193	1007.5
193	1008.1	3116.5	3304.0	193	1007.1
193	-	3122.9	3305.1	193	-
183	1008.3	3119.3	3302.8	183	1007.7
183	1008.1	3120.3	3303.3	183	1007.6
183	1008.2	3114.8	3304.8	183	1007.4
183	-	3116.6	3304.2	183	-
173	-	-	-	173	-
173	1008.4	3118.3	3303.5	173	1007.8
173	1008.4	3104.7	3303.5	173	1007.5
173	1008.3	3119.2	-	173	1007.5
173	-	3096.3	-	163	1008.0
163	1008.7	3095.8	3303.3	163	1008.2
163	1008.6	3081.6	3303.3	163	1008.1
163	1008.7	-	3303.3	163	1008.7
163	1008.7	-	3303.2	153	1009.1
153	1010.0	3072.7	3302.9	153	1009.1
153	1009.8	-	3303.1	153	1009.1
153	1010.0	-	3302.9	153	-
153	1009.9	-	3303.0	143	1009.3
143	1010.1	3074.8	3302.9	143	1009.3
143	1010.2	-	3303.0	143	1009.4
143	1009.9	-	3303.1	143	1009.4
143	1010.2	-	3303.0	133	1009.4
133	1010.3	3034.7	3302.6	133	1009.5
133	1010.3	-	3302.7	133	1009.4
133	1010.3	-	3302.6	133	1009.5
133	1010.3	-	3302.6	123	1009.5
123	1010.4	3024.1	3301.7	123	1009.6
123	1010.5	-	3301.7	123	1009.6
123	1010.4	-	3301.8	123	1009.5
123	1010.4	-	-	113	1009.6
113	1010.7	3065.4	3301.2	113	1009.6
113	1010.7	3038.5	3301.1	113	1009.5
113	1010.8	2996.2	3301.1	113	1009.5
113	1010.7	-	-	103	1009.7
103	1010.7	3024.8	3300.9	103	1009.7
103	1010.8	3026.9	3300.9	103	1009.7
103	1010.8	-	3300.8	103	1009.7

103	1010.8	-	3301.0	93	1009.8
93	1010.8	2926.5	3300.6	93	1009.8
93	1010.9	3291.1	3300.5	93	1010.0
93	1010.9	-	3300.6	93	1009.8
93	1010.9	-	3300.6	83	1009.9
83	1011.0	2981.4	3300.3	83	1010.3
83	1011.0	2924.8	3300.3	83	1010.0
83	1011.0	-	3300.4	83	1010.4
83	1011.1	-	-	83	-

## 8.4. Scientific Publications

The published articles, articles under review and conferences shown below have been extracted from the work carried out in this PhD thesis.

### 8.4.1. Published articles

- **Huidobro, J.**; Aramendia, J.; Arana, G.; Madariaga, J. M. Geochemical Characterization of the NWA 11273 Lunar Meteorite Using Nondestructive Analytical Techniques: Original, Shocked, and Alteration Mineral Phases. *Earth Sp. Chem.* **2021**, *5*, 1333. <https://doi.org/10.1021/acsearthspacechem.0c00329>
- García-Florentino, C.; Gomez-Nubla, L.; **Huidobro, J.**; Torre-Fdez, I.; Ruíz-Galende, P.; Aramendia, J.; Hausrath, E. M.; Castro, K.; Arana, G.; Madariaga, J. M. Interrelationships in the Gypsum–Syngenite–Görgeyite System and Their Possible Formation on Mars. *Astrobiology* **2021**, *21*, 332. <https://doi.org/10.1089/ast.2020.2319>
- **Huidobro, J.**; Aramendia, J.; Arana, G.; Madariaga, J. M. Reviewing in Situ Analytical Techniques Used to Research Martian Geochemistry: From the Viking Project to the MMX Future Mission. *Anal. Chim. Acta* **2022**, *1197*, 339499. <https://doi.org/10.1016/j.aca.2022.339499>
- **Huidobro, J.**; Aramendia, J.; García-Florentino, C.; Ruiz-Galende, P.; Torre-Fdez, I.; Castro, K.; Arana, G.; Madariaga, J. M. Mineralogy of the RBT 04262 Martian Meteorite as Determined by Micro-Raman and Micro-X-ray Fluorescence Spectroscopies. *J. Raman Spectrosc.* **2022**, *53*, 450. <https://doi.org/10.1002/jrs.6291>.
- Torre-Fdez, I.; García-Florentino, C.; **Huidobro, J.**; Coloma, L.; Ruiz-Galende, P.; Aramendia, J.; Castro, K.; Arana, G.; Madariaga, J. M. Characterization of Olivines and Their Metallic Composition: Raman Spectroscopy Could Provide an Accurate Solution for the Active and Future Mars Missions. *J. Raman Spectrosc.* **2023**, *54*, 340. <https://doi.org/10.1002/jrs.6485>

- Hausrath, E. M.; Adcock, C. T.; Bechtold, A.; Beck, P.; Benison, K.; Brown, A.; Cardarelli, E. L.; Carman, N. A.; Chide, B.; Christian, J.; Clark, B. C.; Cloutis, E.; Cousin, A.; Forni, O.; Gabriel, T. S. J.; Gasnault, O.; Golombek, M.; Gómez, F.; Hecht, M. H.; Henley, T. L. J.; **Huidobro, J.**; Johnson, J.; Jones, M. W. M.; Kelemen, P.; Knight, A.; Lasue, J. A.; Le Mouélic, S.; Madariaga, J. M.; Maki, J.; Mandon, L.; Martinez, G.; Martínez-Frías, J.; McConnochie, T. H.; Meslin, P.; Zorzano, M.; Newsom, H.; Paar, G.; Randazzo, N.; Royer, C.; Siljeström, S.; Schmidt, M. E.; Schröder, S.; Sephton, M. A.; Sullivan, R.; Turenne, N.; Udry, A.; VanBommel, S.; Vaughan, A.; Wiens, R. C.; Williams, N.; the SuperCam team; the Regolith working group. An Examination of Soil Crusts on the Floor of Jezero Crater, Mars. *J. Geophys. Res. Planets* **2023**, e3033JE007433. <https://doi.org/10.1029/2022JE007433>

- **Huidobro, J.**; Aramendia, J.; Arana, G.; Hausrath, E. M.; Madariaga, J. M. The effect of low temperature on the Raman spectra of Calcium-rich sulfates on Mars. *Ann. Glaciol.* **2023**, In press.

#### 8.4.2. Articles under review

- **Huidobro, J.**; Madariaga, J. M.; Carrizo, D.; Laserna, J. L.; Rull, F.; Martínez-Frías, J.; Aramendia, J.; Sánchez-García, L.; García-Gómez, L.; Veneranda, M.; Población, I.; Cabalín L. M.; López-Reyes, G.; Coloma, L.; García-Florentino, C.; Arana, G.; Castro, K.; Delgado, T.; Alvarez-Llamas, C.; Fortes, F. J.; Manrique, J. A.; and the SIGUE-MARS team. Multi-analytical characterization of an oncoïd from a high altitude hypersaline lake using techniques employed in the Mars2020 and Rosalind Franklin missions on Mars. *Anal. Chim. Acta.* **2023**, Under review.

- **Huidobro, J.**; Aramendia, J.; García-Florentino, C.; Población, I.; Castro, K.; Arana, G.; Madariaga, J. M. Mineralogy of the LARS 12095 Martian shergottite as determined by micro-Raman and micro-X-ray Fluorescence spectroscopies. *J. Raman Spectrosc.* **2023**, Under review.

#### 8.4.3. Contributions to national and international conferences

At the end of each conference contribution it is specified whether it is international or national conference, and whether it is a poster or an oral contribution.

*ICO: International Conference, Oral communication*

*ICP: International Conference, Poster*

*NCP: National Conference, Poster*

*VM: Virtual Meeting*

- 
- **Huidobro, J.**; Aramendia, J.; Madariaga, J. M. Raman and XRF Analysis of the New NWA 11273 Lunar Meteorite. In *European Planetary Science Congress (EPCS)*; Berlin, Germany, 2018; Abs 883. **ICP**
- **Huidobro, J.**; Torre-Fdez, I.; García-Florentino, C.; Ruiz-Galende, P.; Aramendia, J.; Madariaga, J. M. Terrestrial Weathering of Ilmenite and Olivine in the Northwest Africa 11273 Lunar Meteorite. In *Goldschmidt*; Barcelona, Spain, 2019; Abs 1439. **ICP**
- **Huidobro, J.**; Aramendia, J.; Ruiz-Galende, P.; Torre-Fdez, I.; Madariaga, J. M. Raman Spectroscopy on the New Northwest Africa 11273 Lunar Meteorite to Understand the Initial Impact and Final Terrestrial Weathering. In *50th Lunar and Planetary Science Conference (LPSC)*; The Woodlands, TX, USA, 2019; Abs 2132. **ICP**
- Madariaga, J. M.; **Huidobro, J.**; García-Florentino, C.; Aramendia, J.; Ruiz-Galende, P.; Torre-Fernández, I.; Hausrath, E. M.; Castro, K.; Arana, G. Temperature Transformation of Calcium and Potassium Martian Sulfates as Seen by an Exomars 2022 RLS-like Raman Instrument. In *Europlanet Science Congress 2020*; 2020; Abs 1063. **VM**
- **Huidobro, J.**; García-Florentino, C.; Aramendia, J.; Ruiz-Galende, P.; Torre-Fdez, I.; Castro, K.; Arana, G.; Madariaga, J. M. Sulfate Covering on the Olivine RBT 04262 Grains as Probe of the Acid-Weathering on Mars. In *14th GeoRaman 2020*; 2020. **VM**
- **Huidobro, J.**; Madariaga, J. M.; Carrizo, D.; Laserna, J. J.; Rull, F.; Martínez-Frías, J.; Belenguer, T.; Taravillo, M.; Aramendia, J.; Arana, G.; Castro, K.; Cabalín, L. M.; García-Gómez, L.; Alvarez-Llamas, C.; Delgado, T.; Fortes, F. J.; Sigue-MarsTeam. Multi-Analytical Approach for the Detection and Interpreting Biosignatures in a Microbialite from a Hypersaline High Altitude Lake. In *Astrobiology Science Conference (AbSciCon)*; Atlanta, GA, USA, 2022; Abs 421. **ICO**
- **Huidobro, J.**; Aramendia, J.; Coloma, L.; Población, I.; García-Florentino, C.; Castro, K.; Arana, G.; Madariaga, J. M. Low Temperature Influence on the Raman Spectra of Calcium-Rich Sulfates on Mars: Raman Thermometer for Low Temperatures. In *International Symposium on Ice in a sustainable society (ISS)*; Bilbao, Spain, 2022; Abs 88A3691. **ICO**
- **Huidobro, J.**; Aramendia, J.; García-Florentino, C.; Población, I.; Castro, K.; Arana, G.; Madariaga, J. M. Unaltered Martian Hydrated Sulfates in the LAR 12095 Martian Shergottite Detected by Raman Spectroscopy. In *15th GeoRaman 2022*; Prague, Czech Republic, 2022. **ICP**
- **Huidobro, J.**; Aramendia, J.; Adcock, C.; Hausrath, E. M.; Madariaga, J. M. New Methodology for Doping Smectites with Fatty Acids and for Their

Spectroscopic Analysis Using Mars Exploration Techniques. In *1 PhD Multidisciplinary Chemical Congress*; Gijón, Spain, 2023; Abs 92. **NCP**

- **Huidobro, J.**; Coloma, L.; Población, I.; Arana, G.; Aramendia, J.; García-Florentino, C.; Hausrath, E. M.; Castro, K.; Madariaga, J. M. Temperature Influence on Raman Spectra on Calcium and Potassium Sulfates on the Martian Surface. In *54th Lunar and Planetary Science Conference (LPSC)*; The Woodlands, TX, USA, 2023; Abs 2364. **ICP**

- **Huidobro, J.**; Población, I.; Alberquilla, F.; Madariaga, J. M.; Coloma, L.; Aramendia, J.; García-Florentino, C.; Martínez-Frías, J.; Castro, K.; Arana, G. Weathering of Moon Soils, as Seen from the Feldspathic Breccia Northwest Africa 11273 Meteorite, as the First Step for Plant Cultivation. In *54th Lunar and Planetary Science Conference (LPSC)*; The Woodlands, TX, USA, 2023; Abs 2386. **ICP**

- Lopez-Reyes, G.; Nachon, M.; Veneranda, M.; Beyssac, O.; Madariaga, J. M.; Manrique, J. A.; Clavé, E.; Ollila, A.; Castro, K.; Sharma, S. K.; Johnson, J. R.; Schröder, S.; Cloutis, E.; Dehouck, E.; **Huidobro, J.**; Martínez-Frías, J.; Rull, F.; Maurice, S.; Wiens, R. C.; SuperCamTeam. Anhydrite Detections by Raman Spectroscopy with SuperCam at the Jezero Delta, Mars. In *54th Lunar and Planetary Science Conference (LPSC)*; The Woodlands, TX, USA, 2023; Abs 1721. **ICP**

### **8.5. Scientific Disclosure**

In addition to making scientific contributions to a specialized audience, Jennifer has contributed to the science dissemination to all audience.

- Science Week at the chemistry stand. Held in Bilbao, Spain, in November 2019.
- One of the main speakers of the Webinar: “From ancient relics to life on Mars: temperature-controlled experiments for material characterization”. Held virtually in February 2021.
- Keynote speaker in the interview conducted by high school students of the IES Valle de Camargo school in Revilla de Camargo Cantabria, Spain. Held virtually in April 2022.
- One of the main speakers of the roundtable discussion: “Discoveries and surprises in the (bio)geochemical processes in the Jezero crater of Mars”. Held in Leioa, Spain, in April 2022.
- Keynote speaker in the interview conducted by primary school students of the La Salle school in Burgos, Spain. Held virtually in March 2023.



---

